# Deformation mechanisms in micas and mica-bearing mylonites in regional scale shear zones


UNIVERSITY OF LIVERPOOL

Thesis submitted in accordance with the requirements of the University of Liverpool for the degree of Doctor in Philosophy by

**Joseph Merlin Aslin**

**September 2019**

# Abstract

Mica minerals are ubiquitous constituents of the Earth's crust, occurring commonly within faults and shear zones. They are widely understood to be weaker than most other silicate minerals across a range of pressure, temperature and strain rate conditions and, as a result, accommodate a disproportionately large amount of strain within lithospheric faults and shear zones. Despite this, the mechanisms and processes which govern mica deformation are not fully understood. This is due primarily to the strong crystallographic anisotropy of micas, which sets them apart from the majority of other minerals. This thesis reports microstructural work carried out on naturally deformed mica-bearing and mica-dominated mylonites from the upper-greenschist to amphibolite facies Cossato-Mergozzo-Brissago (CMB) line and Pogallo line shear zones in North West Italy. The principal objectives are to identify the mechanisms of intracrystalline deformation within micas, investigate the interaction of stress, chemistry and fluids within mica-bearing mylonites and examine how the degree of mica content affects the distribution of strain within polyphase rocks.

Transmission electron microscope (TEM) images reveal evidence of ripplocations, a novel defect proposed for layered materials, in naturally deformed biotite. Nanoscale lenticular delaminations and bending of biotite lattice planes are observed in en-echelon arrays. These features cannot be explained within the framework of existing understanding of intracrystalline defects within micas as basal dislocations contain no component of c-axis parallel strain. The features closely resemble those resulting from ripplocations, modelled and observed within layered engineering materials, that are theoretically applicable to phyllosilicates. The existence of ripplocations within phyllosilicates opens up ripplocation motion as a potential deformation mechanism in geological phenomena which is able to explain many of the existing ambiguities relating to non-brittle intracrystalline deformation of phyllosilicates.

Biotite within the studied mylonites derived from granitic orthogneiss protoliths underwent a dramatic grain size reduction with increasing strain, forming 1-5 μm aggregates. The breakdown was focussed initially at sites of high strain, such as kink band boundaries, grain tips and grain surfaces, but eventually entirely replaced coarse grains. Electron probe microanalysis (EPMA) data suggests the fine grains represent a subtly different compositional population to the parent grains, centred on a reduction in Ti. TEM images reveal irregular boundaries between fine-grained biotite and quartz in the matrix, with the transition from coarse to fine grains having occurred in a single stage, with no evidence of subgrain

formation. Muscovite in the same thin sections did not undergo the same process. It is suggested that the grain-size reduction occurred by means of a stress-induced, fluid facilitated dissolution-precipitation reaction rather than a purely mechanical recrystallisation mechanism. This process facilitated the formation of an interconnected weak network of fine-grained polyphase material which likely deformed by grain-size sensitive creep, ultimately leading to rheological weakening of the mylonite.

While the grain size reduction of biotite is critical to forming interconnected weak networks in orthogneiss mylonites, its occurrence is distinctly less pronounced in mylonites with higher mica content. In these rocks (with mica content up to and over 50%) the mica phase forms an interconnected weak network from the outset of deformation. This enables strain to be distributed more evenly, as the microstructure is dominated by a weak framework, and contrasts with the high strain C' shear bands formed in orthogneiss rocks where biotite grain size has been dramatically reduced. Such a pattern is also evident at the scale of hundreds of metres, with mica-rich rocks forming a 200 m to 300 m wide region of distributed deformation and orthogneiss rocks producing ~50 m wide zones characterised by heterogeneous deformation, high strain shear zones and ultramylonites. It is proposed that strain localisation is most important in rocks with mica content between around 5% - 25%, whereas deformation of rocks with mica content above around 25% promotes more distributed accommodation of strain.

In granitic orthogneiss ultramylonites, K-feldspar porphyroclasts are decorated along high stress interfaces by fine grained plagioclase feldspar and a small amount of quartz. The reverse occurs at low stress sites of plagioclase porphyroclasts such as fractures and surfaces in contact with pressure shadows. Microstructural observations and electron backscatter diffraction (EBSD) data suggest the fine grains have grown topotactically at the expense of the porphyroclasts, indicating that this is a form of mineral replacement reaction controlled by local stress heterogeneities. Molar volume calculations show that the driving force for the reaction may be a re-distribution of volume from sites of high stress to those of low stress, making this process a form of incongruent pressure solution as it involves a phase change. These reactions are facilitated by ionic exchange and local chemical gradients within an aqueous phase and serve to accelerate the transformation of feldspars from coarse, rigid porphyroclasts to fine-grained components of a polyphase matrix.

# Acknowledgements

Firstly, I would like to thank my principal supervisor, Betty Mariani, for the guidance, support and encouragement she has given me throughout the course of this project. It has been a privilege to work with someone as passionate and knowledgeable as her. She has taught me a great deal. Many thanks also to my other supervisors John Wheeler and Dan Faulkner for many informative and enlightening discussions in the department, in the field and in the pub. Their insights have been invaluable.

A huge thanks to Karl Dawson for introducing me to the dark arts of TEM. Though not one of my official supervisors he has been an enormous source of assistance and expertise. I am also very grateful to Giulia Degli-Alessandrini, Jon Fellowes and James Utley for their technical wizardry with the microprobes and the QEMSCAN.

I would like to extend my sincere thanks to everyone who has passed through the Rock Deformation lab and the postgrad offices during my time, for their advice, enthusiasm, encouragement and not least for their friendship. In particular, cheers to Mike, John, Julia, Anthony and Gary who have been there throughout, and to Joe Gardner, who from the day I arrived has been nothing but welcoming and supportive. He has been my perpetual officemate, my mentor for the last 4 years and, I'm sure, a good friend for many more.

My long-suffering housemates Arthur and Stephan have made my time at Liverpool incredibly happy and enjoyable and have given me countless memories. They have seen the best and endured the worst of me and I look forward many future misadventures with them both.

I owe an awful lot to my parents and to the rest of my family for their unconditional love and support through the good times and the bad. I am incredibly lucky to know I can always count on them.

And finally, to my partner Katie. Thank you for your companionship, your patience and your trust, especially over this past year.

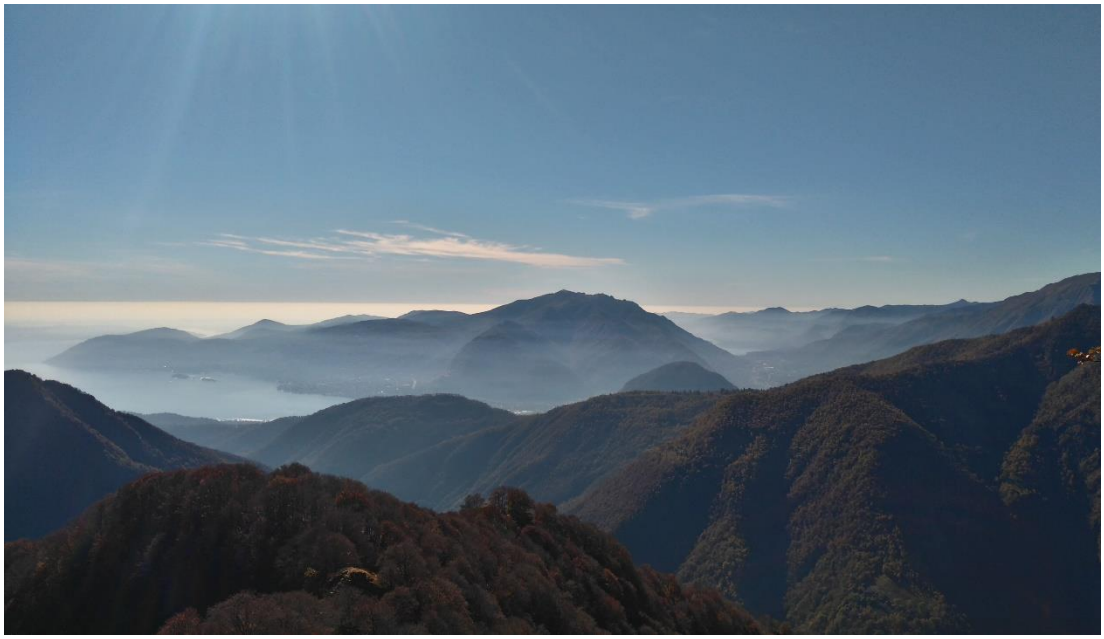

Mottarone and Lago Maggiore

From the Val Grande National Park

Piedmont, Italy

# Table of Contents

# List of Figures and Tables

# 1. Introduction to this thesis

## 1.1. The dynamic lithosphere

The Earth's lithosphere (comprising the crust and lithospheric mantle), much like the biosphere, cryosphere, hydrosphere and atmosphere above it, is a dynamic and complex system, which involves the interactions of stress and chemistry with a range of rocks and fluids via a multitude of interrelated processes. Arguably the most important among these, with regard to the evolution of the lithosphere, is plate tectonics (Wilson, 1965), which describes the movement and cycling of matter and energy between the planetary surface and the deeper Earth. The deformation of the lithosphere, which enables this motion, occurs largely on timescales that preclude direct observation, hence the historical misconception that the Earth, and the landscapes with which we interact, are constant and unchanging, as immovable as a mountain. The occasional events that occur rapidly enough to break this temporal veil — earthquakes, volcanic eruptions, landslides — have, throughout history, hinted at the unseen powers and energies beneath our feet. In truth, the Earth's lithosphere, at any given time, is a transient manifestation of the outer part of our planet: mountain ranges rise and fall, ocean basins open and close, and the internal structures of the crust evolve and develop over time. The difference in how we perceive these fluctuations relative to those on and above the Earth's surface, is merely a consequence of our perspective as short-lived observers.

## 1.2. The importance of phyllosilicates in crustal deformation

The deformation of the Earth's lithosphere, through plate tectonics, is facilitated by displacement along discrete fault and shear zones (Ramsay and Graham, 1970) with the largest of these forming the boundaries of tectonic plates (Wilson, 1965). As these boundaries accommodate the majority of strain in the Earth's crust, the physical properties and processes at play within them govern the strength and structural evolution of the lithosphere. These properties and processes are strongly affected by the conditions of temperature, pressure, strain rate and the composition of the rocks being deformed. Faults and shear zones can also themselves account for variations in these conditions, for example by distorting the geotherm or influencing the flow and distribution of fluids. For these reasons, the study of the behaviour of different minerals and rocks under varying conditions applicable to the Earth's crust has been a cornerstone of structural geology for many decades.

Within the field of structural geology, phyllosilicate minerals (such as the micas) have been both a critical interest and a persistent enigma. They are a ubiquitous constituent of crustal lithologies and commonly occur in association with faults and shear zones (Boulton *et al.*, 2012; Hunter *et al.*, 2016). In these settings, phyllosilicates are generally observed to be weaker than other silicate minerals at a range of conditions and, as the weakest phase, regularly serve to accommodate a disproportionate amount of deformation (Shea and Kronenberg, 1992; Wintsch *et al.*, 1995; Holyoke and Tullis, 2006b; Mariani *et al.*, 2006; Hirth and Guillot, 2013; Hunter *et al.*, 2016). In addition, phyllosilicates have an extensive influence on the deformation of other minerals through their role as sources and sinks of volatiles, as reaction products, and as second phases within polyphase aggregates. As a result, understanding phyllosilicate behaviour and properties is critical to understanding those of faults and shear zones at the larger scale. However, due primarily to their complex rheology and difficulties associated with studying them experimentally, studies of mica deformation have been far outweighed by those of phases such as quartz, feldspar and olivine. Much of this stems from the strong physical anisotropy of phyllosilicate crystal structures which are platy, sheet silicates whose behaviour is greatly influenced by their orientation relative to the principal stress axes (Kronenberg, Kirby, *et al.*, 1990; Shea and Kronenberg, 1993). This anisotropy pertains also to deformation mechanisms, rendering processes that are common in other minerals, such as dislocation creep and dynamic recrystallisation (see Chapter 2 section 2.2.2), unable to explain the deformation of phyllosilicates. Instead, there are a range of deformation microstructures, such as kinking (see Chapter 3 section 3.2.4) which are almost unique to phyllosilicates and are poorly explained within the exiting theoretical framework.

Interest in phyllosilicate deformation has ebbed and flowed over the past few decades. Several studies in the 1970s and early 1980s focussed on microstructural observations of deformed micas, attempting to explain observed microstructures in the context of existing understanding of deformation mechanisms (Etheridge *et al.*, 1973; Etheridge and Hobbs, 1974; Bell and Wilson, 1977; Bell, 1978; Wilson and Bell, 1979; Bell *et al.*, 1986). In the early 1990s, Andreas Kronenberg and others focussed on determining the physical properties of micas through experimental deformation (Kronenberg, *et al.*, 1990; Shea and Kronenberg, 1992, 1993; Christoffersen and Kronenberg, 1993; Mares and Kronenberg, 1993). Experiments and observations on deformed micas and mica bearing rocks were revisited by researchers in the early part of this century (Bos and Spiers, 2001, 2002; Rawling, 2002; ten Grotenhuis *et al.*, 2003; Mariani *et al.*, 2006; Niemeijer and Spiers, 2007; Basu *et al.*, 2009)

and has more recently seen a revival with a focus on anisotropy and strain localisation (Wenk *et al.*, 2010; Dempsey *et al.*, 2011; Tesei *et al.*, 2012; Bolognesi and Bistacchi, 2016; Hunter *et al.*, 2016). Throughout this period, detailed transmission electron microscopy (TEM) studies have examined the deformation of micas at the nanoscale (Bell and Wilson, 1981; Meike, 1989; Goodwin and Wenk, 1990; Noe and Veblen, 1999b, 1999a). Despite this work, numerous questions and challenges remain with regard to the deformation of phyllosilicates and phyllosilicate bearing rocks. The fundamental viscous mechanism by which micas accommodate intracrystalline strain parallel to the c-axis is not known, nor is the precise physical process that facilitates kinking. Grain size reduction is a key process in the microstructural evolution of deforming rocks and plays a critical role in the interconnection of weak mica-rich layers within mylonites (see Section 2.5), however, the mechanism by which this is achieved in micas is ambiguous. Additionally, the extent to which micas undergo dissolution and reprecipitation has been contentious for some time, as has the influence they have on the solubility of other minerals in close proximity. With dissolution-precipitation increasingly recognised to play a key role in the viscous deformation of rocks, the extent to which this process affects micas and mica-bearing lithologies remains to be seen.

The purpose of this thesis is to address these questions by analysing natural microstructures using powerful observational and analytical techniques. By applying novel ideas and perspectives to these existing problems, this thesis aims to propose new interpretations and update our understanding of mica deformation in the light of recent advances. In order to examine the influence of mica on the rheology of shear zones at the larger scale, this thesis focusses on natural rocks collected from shear zones in north western Italy which serve as an ideal natural laboratory for this study.

## 1.3. Geological context of the field area

The samples used in this thesis were collected from the Cossato-Mergozzo-Brissago (CMB) line and the Pogallo line shear zones in north western Italy. The principal areas of study were within the Val Grande National Park and the lower parts of Valle d'Ossola to the west of Lago Maggiore.

The CMB line is an amphibolite facies mid-crustal shear zone of late Variscan age, first identified by Boriani *et al.* (1990). It forms a tectonic discontinuity which crops out along an approximately 70 km long stretch and defines the boundary between the Ivrea Verbano Zone (IVZ) and the Serie dei Laghi (SdL) (Boriani, Burlini, *et al.*, 1990; Boriani, Giobbi Origoni, *et al.*, 1990) (Fig. 1.1a). The CMB line itself is a steeply dipping band of mylonites which varies in

thickness along its length but is on the order of hundreds of metres wide. The exact boundaries of the viscous shear zone are difficult to define, partly as a result of the generally poor exposure of the CMB line along its outcrop, but also due to the gradational nature of the boundaries, as strongly foliated schist and gneiss protoliths transition to protomylonites and higher strain mylonites. The Pogallo line is a slightly younger (160 – 240 Ma) shear zone (Zingg, 1983), active under upper greenschist to lower amphibolite facies conditions (Hodges and Fountain, 1984; Handy, 1987; Handy and Streit, 1999), which meets the CMB line at a very low angle and forms the boundary between the IVZ and the SdL between Val d'Ossola and the peak of La Piota near the town of Gurro. In some literature (Handy, 1987) the Pogallo ductile fault zone (PDFZ) is defined as an approximately 1 km wide zone of distributed deformation along the edge of the IVZ, with the Pogallo line itself forming the south eastern boundary of the zone. Ductile overprinting is concordant with that of the Pogallo line and increases gradually as the Pogallo line is approached. The deformation in the PDFZ and along the Pogallo line are believed to be related to the same event, with the PDFZ representing more diffuse deformation away from the tectonic contact and the Pogallo line forming the more localised deformation along the contact itself (Handy, 1987).

Two distinct models exist for the formation of the CMB line and Pogallo line. One interpretation is that they represent a deep-crustal low-angle extensional detachment system later tilted to vertical by the Alpine orogeny (Hodges and Fountain, 1984; Handy, 1987; Handy and Streit, 1999; Mulch *et al.*, 2002; Siegesmund *et al.*, 2008). In this model the current geological map approximates the paleo crustal cross-section, with the SdL representing the upper crust and the IVZ the lower crust (Fig. 1.1b). Evidence for this is centred on the continuous metamorphic pressure gradient observed across the CMB line (Handy *et al.*, 1999) as well as structural and age data suggesting a sub-horizontal orientation with little if any vertical displacement (Mulch *et al.*, 2002; Siegesmund *et al.*, 2008). The Pogallo line displays an increasing grade of syntectonic assemblages and conditions of deformation along strike, from upper greenschist facies in the SW to mid-amphibolite facies in the NE (Handy, 1987). This suggests the NE section was deeper in the crust during activity on the Pogallo line, leading to its interpretation as a low angle normal fault and explaining how the lower crustal IVZ became juxtaposed against the mid-crustal SdL (Hodges and Fountain, 1984).

A separate interpretation for the CMB/Pogallo line system characterizes these lineaments as oblique strike-slip faults which resulted in the lateral emplacement of the IVZ alongside

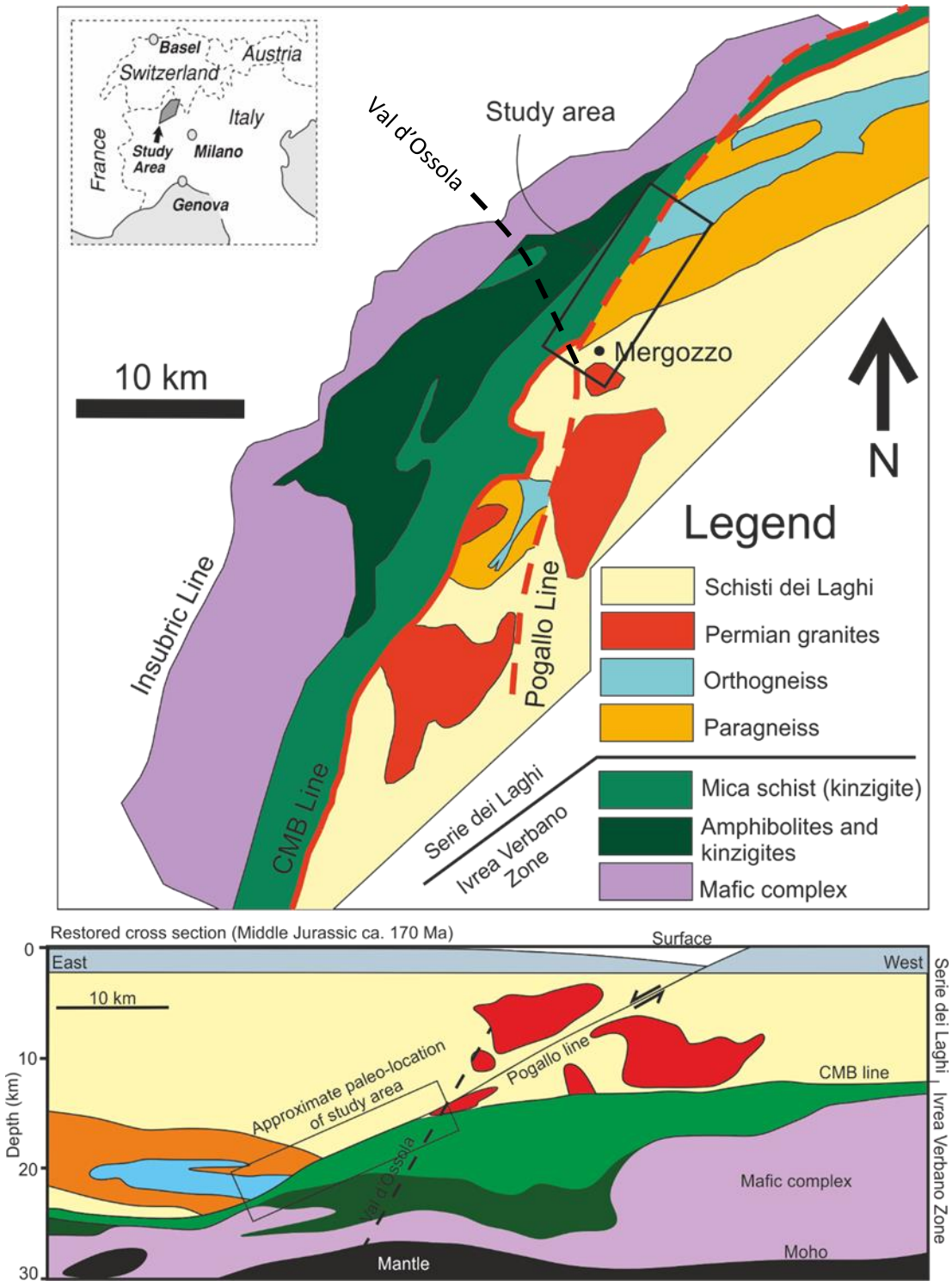


**Figure 1.1:** (a) Simplified geological map of the Ivrea Verbano Zone and Serie dei Laghi in the vicinity of the study area (black box). The CMB line forms the boundary between the two sections, with the IVZ to the northwest and the SdL to the southeast (adapted from Rutter et al. 2007 and Siegesmund et al. 2008). (b) Tentative restored cross section of the area during the middle Jurassic displaying the Pogallo line as a low angle normal fault juxtaposing upper crustal rocks against those of the lower crust. Colour scheme is the same as in (a) (adapted from Schaltegger and Brack, 2007).

the SdL (Boriani, Burlini, *et al.*, 1990; Boriani, Giobbi Origoni, *et al.*, 1990; Boriani, Origoni, *et al.*, 1995; Boriani and Giobbi, 2004). This model states that the shear zones were always subvertical and argues against significant tilting of the crustal section based on evidence of sub-horizontal layering and miarolitic cavities (crystal lined irregular vugs) in the Graniti dei Laghi plutons. These suggest shallow emplacement and no more than 15-20° of tilting, despite the Permian age of the granites and their association with the tectonic contact (Boriani, Burlini, *et al.*, 1990; Boriani and Giobbi, 2004). More recently (Boriani *et al.*, 2016), this interpretation has been extended to suggest that the CMB line represents part of a major intra-Pangea strike-slip fault which accommodated several thousand km of displacement during the Permian (Muttoni *et al.*, 1996). In this scenario the SdL and IVZ would have originated extremely far away from each other and are in no way part of the same crustal section (Boriani *et al.*, 2016).

Interest in the IVZ has centred primarily around the idea that it represents a largely intact, exposed section of the lower continental crust (Berckhemer, 1969; Fountain and Salisbury, 1981; Brodie and Rutter, 1987; Burke and Fountain, 1990), with its deepest section, composed of mafic and ultramafic rocks, to the NW, and its upper section, composed of the high to medium grade schists of the Kinzigite Formation, to the SE (Handy *et al.*, 1999; Rutter *et al.*, 2007). The Kinzigite Formation crops out along the entire IVZ side of the CMB line and is one of the major lithologies incorporated into the shear zone. It is comprised primarily of medium grade metapelites, interspersed with infrequent layers of marble and amphibolite. The protolith has been inferred to be fine grained sediments and interlayered limestones of an oceanic origin with depositional ages between 700 and 480 Ma (Hunziker and Zingg, 1980), with some basaltic lava flows or dykes (Boriani, Burlini, *et al.*, 1990).

The rocks on the south east side of the CMB line are a varied group of paragneisses, orthogneisses and granitic rocks belonging to the SdL. They represent a metamorphosed mid to upper crustal section with a protolith of sediments and granitic to granodioritic intrusions (Boriani, Giobbi Origoni, *et al.*, 1990; Boriani, Origoni, *et al.*, 1995). The paragneisses include the Scisti dei Laghi, the coarser, arenaceous Ceneri gneiss and the fine-grained Gneiss Minuti (Boriani, Giobbi Origoni, *et al.*, 1990). There is also a limited occurrence of layered amphibolites, including retrogressed eclogites, metagabbros and ultramafites, in a narrow band named the Strona Ceneri border zone (SCBZ). These are inferred to be derived from early paleozoic back-arc bimodal volcanics (Giobbi Mancini *et al.*, 2003).

## 1.4. Thesis aims

The aim of this thesis is to gain further insights into the processes and mechanisms which govern the deformation of mica and mica-bearing rocks in the Earth's crust. It will examine intracrystalline deformation mechanisms within micas, the interaction between fluids and mica minerals, and the ways in which micas influence the deformation of other phases in a mylonite, through the examination of naturally deformed microstructures from the amphibolite to upper greenschist facies CMB line and Pogallo line mylonites of North West Italy. The specific objectives of this study are:

1) To investigate the intracrystalline mechanism(s) by which mica deforms in viscous mylonites given that dislocation glide is impossible outside of the basal plane, dislocation creep is not applicable, and kinking cannot be fully explained by existing known mechanisms.
2) To characterise the influence of micas on the rheology and deformation mechanisms active within the CMB and Pogallo line mylonites by determining the mechanism responsible for substantial grain size reduction of biotite.
3) To examine the role of mica content on strain partitioning and deformation microstructures in mylonites of different protolith compositions across the CMB and Pogallo line shear zones.
4) To study natural examples of the interaction between stress and fluids and the influence of this on phase distribution and rheology in mica-bearing granitic rocks deformed by simple shear.

The key processes examined, their variable scales and the methodologies used are summed up schematically in Fig. 1.2.

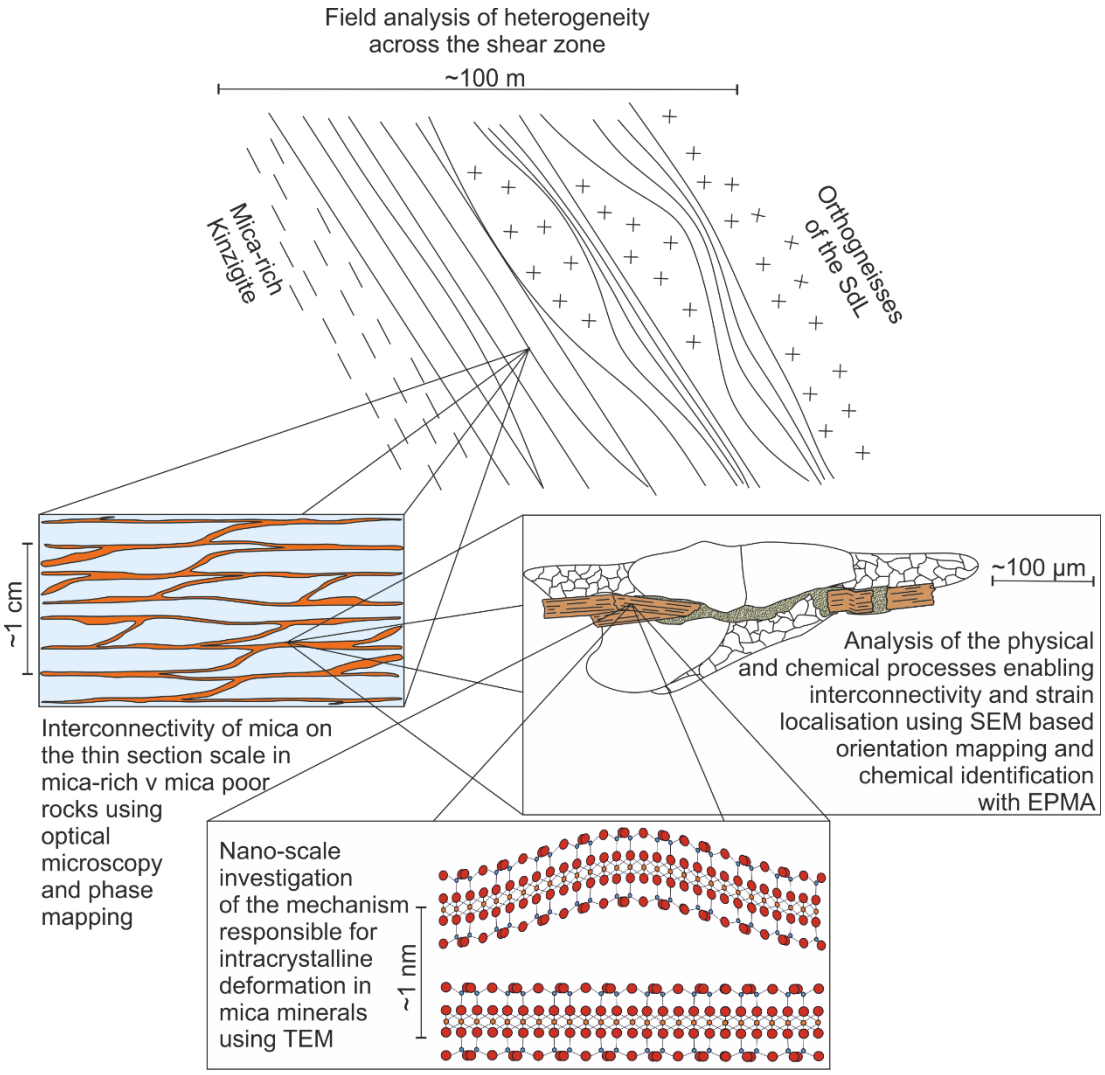


***Figure 1.2:*** *Schematic diagram illustrating the sections of the shear zone targeted in this thesis, the processes examined and the main techniques used. The scale of investigations in this thesis range from the outcrop-scale to the nano-scale: Field analysis of the shear zone is used to determine outcrop-scale heterogeneity; Optical microscopy of thin sections is utilised to identify clear differences in the microstructures of mica-rich vs mica bearing rocks; Scanning electron microscope-based techniques such as electron backscatter diffraction and electron probe microanalysis are used to investigate the physical and chemical processes which facilitate deformation and strain localisation; Transmission electron microscopy is applied to solve the problem of how highly anisotropic layered mica minerals are able to accommodate intracrystalline strain.*

## 1.5. Outline of thesis structure

This chapter, along with Chapters 2, 3 and 4 outline the motivations and methodology of this thesis and place the work in the context of previous studies.

***Chapter 2 –*** gives a broad introduction to deformation within the Earth's lithosphere focussing on types of deformation mechanisms, the conditions in which they are prevalent and the types of deformed rocks that they produce. Mention is also given to the phenomenon of strain localisation and the role of fluids in the crust as these are particularly pertinent when discussing micas.

***Chapter 3 –*** introduces the crystal structure and chemical composition of micas in order to provide the necessary context for further in-depth discussion of these minerals. This is followed by a review of existing understanding with regard to the processes and mechanisms involved in the deformation of mica and mica-bearing rocks.

***Chapter 4 –*** outlines the methods and techniques used during the collection and analysis of data reported in this thesis.

Chapters 5, 6, 7 and 8 report the original research carried out as part of this study. These chapters were written as stand-alone manuscripts intended (with the exception of Chapter 7) for publication in peer reviewed journals. For this reason, there is repetition of some concepts, motivations, background discussions and parts of figures across these chapters.

***Chapter 5 –*** details the first reported evidence for a novel defect type and deformation mechanism, termed ripplocations, within naturally deformed phyllosilicates. This chapter uses TEM observations to identify nanoscale bending in biotite lattice planes and explores the potential of ripplocations to solve several key ambiguities of phyllosilicate deformation.

***Chapter 6 –*** utilises electron backscatter diffraction (EBSD), electron probe microanalysis (EPMA) and TEM to investigate the mechanism responsible for the dramatic grain size reduction of biotite within orthogneiss and paragneiss mylonites in which biotite is a secondary phase relative to quartz and feldspar.

***Chapter 7 –*** presents microstructural observations of mylonites of different protolith compositions from across transects of the CMB and Pogallo lines in order to assess to what extent differences in mica content influence the distribution of strain both spatially and between different phases.

***Chapter 8 –*** focusses on the effect of stress induced, fluid facilitated reactions on the distribution and strength of feldspars within mica-bearing granitic orthogneiss mylonites of the Pogallo line. This chapter develops a model for these reactions, which are a form of incongruent pressure solution, and discusses the implications for the rheological and microstructural evolution of the mylonite.

***Chapter 9 –*** summarises the findings of the previous chapters, synthesises the implications of the work and suggests possible directions for future investigations.

Included in the digital appendices attached to this thesis are a selected number of poster and oral conference presentations which have been delivered by the author in relation to this thesis. Oral presentations included were delivered at the TSG, VMSG, BGA Joint Assembly 2017, the AGU Fall Meeting 2017, the EGU General Assembly 2018 and the TSG Annual Meeting 2019. Poster presentations included were produced for the EBSD 2016 Conference, the MSG annual meeting 2017, DRT 2017 and the EGU General Assembly 2018. Also included is a PDF copy of this thesis.

## 1.6. Status of Manuscripts and co-author contributions

**Chapter 5:** Aslin, J.[1], Mariani, E.[1], Dawson, K.[2] and Barsoum, M.W.[3], 2019. Ripplocations provide a new mechanism for the deformation of phyllosilicates in the lithosphere. *Nature Communications*, *10*(1), p.686.

Status: Published in Nature Communications

Co-author contributions:

Joseph Aslin: Principal investigator, primary author, sample collection and preparation, data collection, analysis and interpretation.

Elisabetta Mariani: Sample collection, analysis and interpretation, manuscript review and discussion.

Karl Dawson: Sample preparation, data collection and technical support, manuscript review and discussion.

Michel W. Barsoum: Manuscript review and discussion

**Chapter 6:** Aslin, J.[1], Mariani, E.[1] and Wheeler, J.[1], Grain size reduction of biotite in mid-crustal mylonites: implications for shear zone rheology

Status: Near completion, to be submitted to the Journal of Geophysical Research: Solid Earth.

Co-author contributions:

Joseph Aslin: Principal investigator, primary author, sample collection and preparation, data collection, analysis and interpretation.

Elisabetta Mariani: Analysis and interpretation, technical support, manuscript review and discussion.

John Wheeler: Discussion

**Chapter 8:** Aslin, J.[1], Mariani, E.[1] and Wheeler, J.[1], Incongruent pressure solution of feldspars in granitic orthogneiss mylonites

Status: Near completion, to be submitted to the journal Geochemistry, Geophysics, Geosystems.

Co-author contributions:

Joseph Aslin: Principal investigator, primary author, sample collection and preparation, data collection, analysis and interpretation.

Elisabetta Mariani: Analysis and interpretation, technical support, manuscript review and discussion.

John Wheeler: Analysis and interpretation, manuscript review and discussion

**Author affiliations**

1: Department of Earth, Ocean and Ecological Sciences, University of Liverpool, Liverpool, UK.

2: Imaging Centre at Liverpool, University of Liverpool, Liverpool, UK.

3: Department of Materials Science and Engineering, Drexel University, Philadelphia, USA.

## 1.7. Funding information

This work was funded by a NERC studentship (NE/L002469/1) within the Earth, Atmosphere and Oceans (EAO) doctoral training programme at the Universities of Liverpool and Manchester.

# 2. Deformation in the Earth's lithosphere

## 2.1. Fault zones and shear zones

In order to study the deformation of the lithosphere, one must first identify where such deformation takes place. Throughout the Earth, deformation is localised to a greater or lesser extent within discreet zones, or regions, across which displacement of one body of rock relative to another occurs (Ramsay and Graham, 1970). These shear zones exist at all scales from the continental, for example plate boundaries and subduction zones, down to the microscopic, in the case of intracrystalline deformation and micro-fractures within mineral grains. At all scales, shear zones are finite regions of increased levels of predominantly simple shear which enable deformation at a strain rate greater than that which could be accommodated by bulk deformation (White *et al.*, 1980). On the larger scale, a general trend can be seen in terms of the distribution of deformation with depth in the lithosphere, from distinct narrow fractures and fault zones near the surface, to diffuse regions of distributed strain at greater depths (Fig. 2.1). This transition is instigated primarily by a mechanistic change from brittle deformation to viscous flow, brought about, to a first approximation, by changes in the conditions of temperature and pressure at different depths in the Earth. This brittle-viscous transition, as it is known, will be considered further after a discussion of the mechanisms which constitute brittle and viscous deformation.

## 2.2. Deformation mechanisms

### 2.2.1. Brittle deformation mechanisms

Brittle behaviour is the non-recoverable deformation of a material under applied stress through the permanent breakage of bonds, after which it loses cohesion. The fundamental brittle mechanisms of micro-cracking and frictional sliding (Blenkinsop, 2002) are inhibited by high lithostatic pressures but are nominally independent of temperature, making them favourable in the relatively low pressure, low temperature environment of the upper crust. Microcracks are grain scale, planar discontinuities with a component of dilation but little if any displacement (Passchier and Trouw, 2005). They nucleate at minor lattice flaws, mineral inclusions or grain boundaries and can propagate and coalesce to form larger fractures (Tapponnier and Brace, 1976, Moore and Lockner, 1995). Fractures which involve lateral displacement may be termed faults, and continued deformation by movement along these features is controlled by the process of frictional sliding (Scholz, 1998; Blenkinsop, 2002). The strength of rocks deforming by frictional sliding is strongly dependent on normal stress and

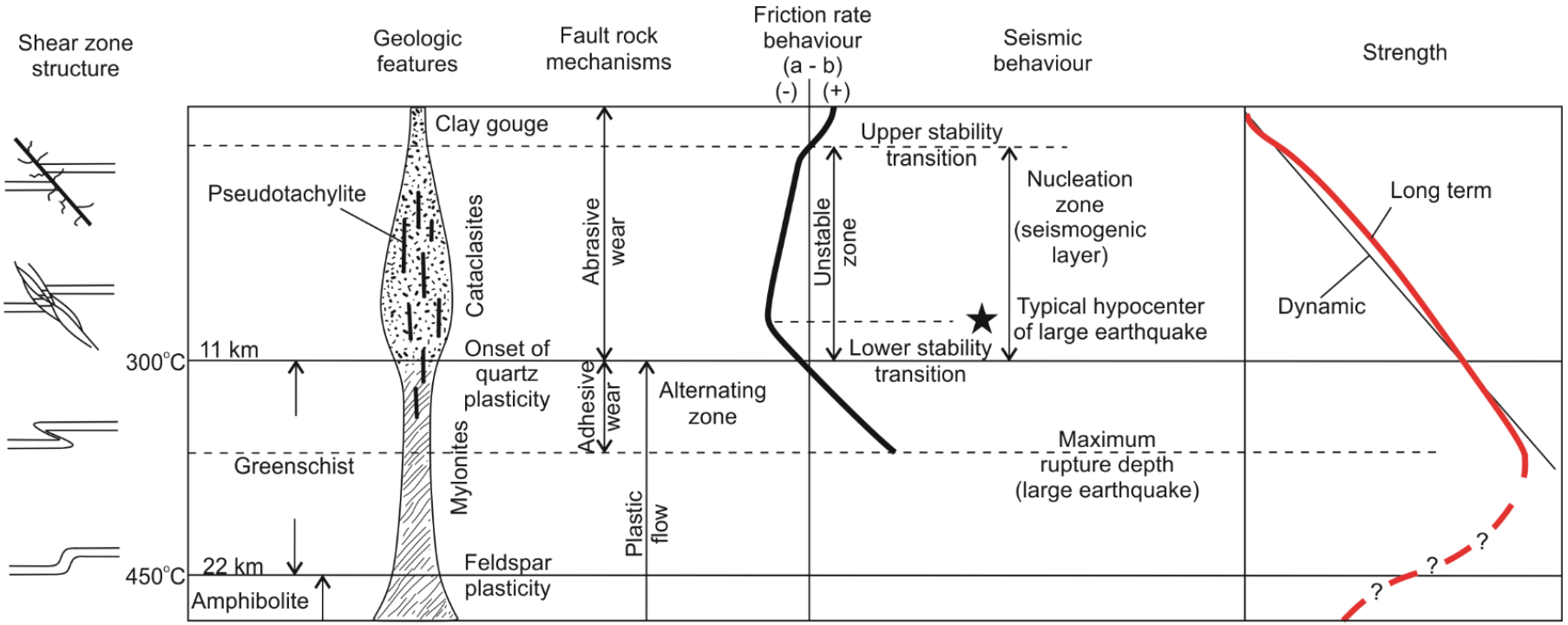


**Figure 2.1:** Conceptual representation of shear zone structure, deformation processes and strength with depth in the crust. From the model of Scholz (1988).

is influenced by surface roughness, pore fluid pressure, temperature and the velocity of sliding (Byerlee, 1978). Phyllosilicates, and especially clays, have a very low coefficient of friction relative to other silicate minerals (Morrow *et al.*, 1992), meaning that their presence can significantly reduce the frictional strength of fault zones in which they occur (Mariani *et al.*, 2006).

Unstable or dynamic frictional sliding is termed stick-slip behaviour and results in earthquakes in nature, in contrast to stable sliding during which displacement occurs steadily. Earthquakes generate seismic waves when frictional sliding occurs at strain rates equal to seismogenic velocities (0.1-2 $ms^{-1}$) (Scholz, 1998). Progressive deformation by micro-cracking and frictional sliding is termed cataclasis and leads to the development of complex fault zones with brittle damage zones (Scholz, 1998; Faulkner *et al.*, 2010). Cataclasis (and cataclastic flow) involves brittle comminution of rocks by the formation of fractures coupled with frictional sliding and abrasion of fragments. It is an entirely brittle process which can produce apparently ductile microstructures at larger scales (Curran *et al.*, 1993).

### 2.2.2. Viscous deformation mechanisms

Viscous deformation involves non-recoverable deformation of a material during which the strain rate is directly proportional to the differential stress. Prior to a yield point, strain is stored elastically, meaning it is instantaneously recoverable on releasing the stress. Unlike in brittle deformation, materials undergoing viscous processes maintain their cohesion and resistance to strain throughout the deformation. With depth in the lithosphere, pressure increases due to gravity and the weight of the rock mass above, and temperature generally increases, although the gradient and morphology of the geotherm varies greatly with location. Viscous deformation mechanisms are more common in rocks and minerals of the deeper lithosphere as they are not inhibited by high pressures and generally become more favourable at higher temperatures. Viscous deformation mechanisms can be divided into two principal types: intracrystalline plasticity and diffusive mass transfer.

#### *Intracrystalline plasticity*

Intracrystalline plasticity involves the accommodation of permanent strain within a crystal lattice through the formation and motion of defects such as dislocations and vacancies. Dislocations are formed by an extra half-plane within the crystal lattice, while vacancies refer to individual missing atoms or molecules (Passchier and Trouw, 2005). The process in which dislocations move by breaking and reforming bonds along specific crystallographic planes and directions (slip systems) is known as dislocation glide (Fig. 2.2a). The movement of

dislocations outside of these planes in order to circumvent obstacles such as impurities is called dislocation climb and relies on the movement of vacancies within the crystal lattice (Fig. 2.2a). In this way, glide is a strain producing mechanism while climb is a recovery mechanism. The two processes acting together constitute dislocation creep. Dislocation creep is usually accompanied by a variety of dynamic recrystallisation mechanisms which result in the generation of new, strain-free grains at the expense of older strained grains. Dynamic recrystallisation can lead to substantial grain size reduction and the production of the fine grained mylonites which characterise most viscous shear zones (Urai *et al.*, 1986; Drury and Urai, 1990). While dynamically recrystallised material is regularly finer than its undeformed protolith, it has been argued that dynamic recrystallisation represents a balance between grain size reduction and grain growth from recovery, representing an equilibrium state at the boundary between dislocation creep and diffusion creep (De Bresser *et al.*, 1998, 2001). However, this has been strongly challenged by Platt and Behr (2011), who argue that the process is dominated by the nucleation of new grains and that the resulting transition to a finer grain size leads to permanent weakening of lithospheric-scale shear zones. A significant amount of energy is required in order to facilitate the motion of dislocations, hence dislocation creep in rocks only becomes feasible at higher temperatures. Dislocation climb in particular has a very strong temperature dependence as the rate at which vacancies can move through the lattice increases with higher temperature. The occurrence of glide without climb, or at rates that are too fast for successful recovery by climb, produces dislocation tangles at obstacles and leads to strain hardening and eventually brittle fracture.

Dislocation creep in silicate minerals is characterised by a range of microstructures produced by dynamic recrystallisation processes. The initial development at low strains is a distortion of the crystal lattice as dislocations are generated and move individually throughout the grain. This is observable in thin sections of geologic materials as undulose extinction and can be further characterised and quantified by techniques such as electron backscatter diffraction (see Chapter 4 section 4.4). As the strain increases, dislocations line up to form dislocation walls across which the lattice is misoriented. Eventually further addition of dislocations to the wall produces enough misorientation between the lattice on either side that it becomes a subgrain boundary and eventually a grain boundary. This process, known as subgrain rotation (SGR) recrystallisation, reduces the free energy of the system by transforming large, strained grains with high dislocation densities into numerous, smaller,

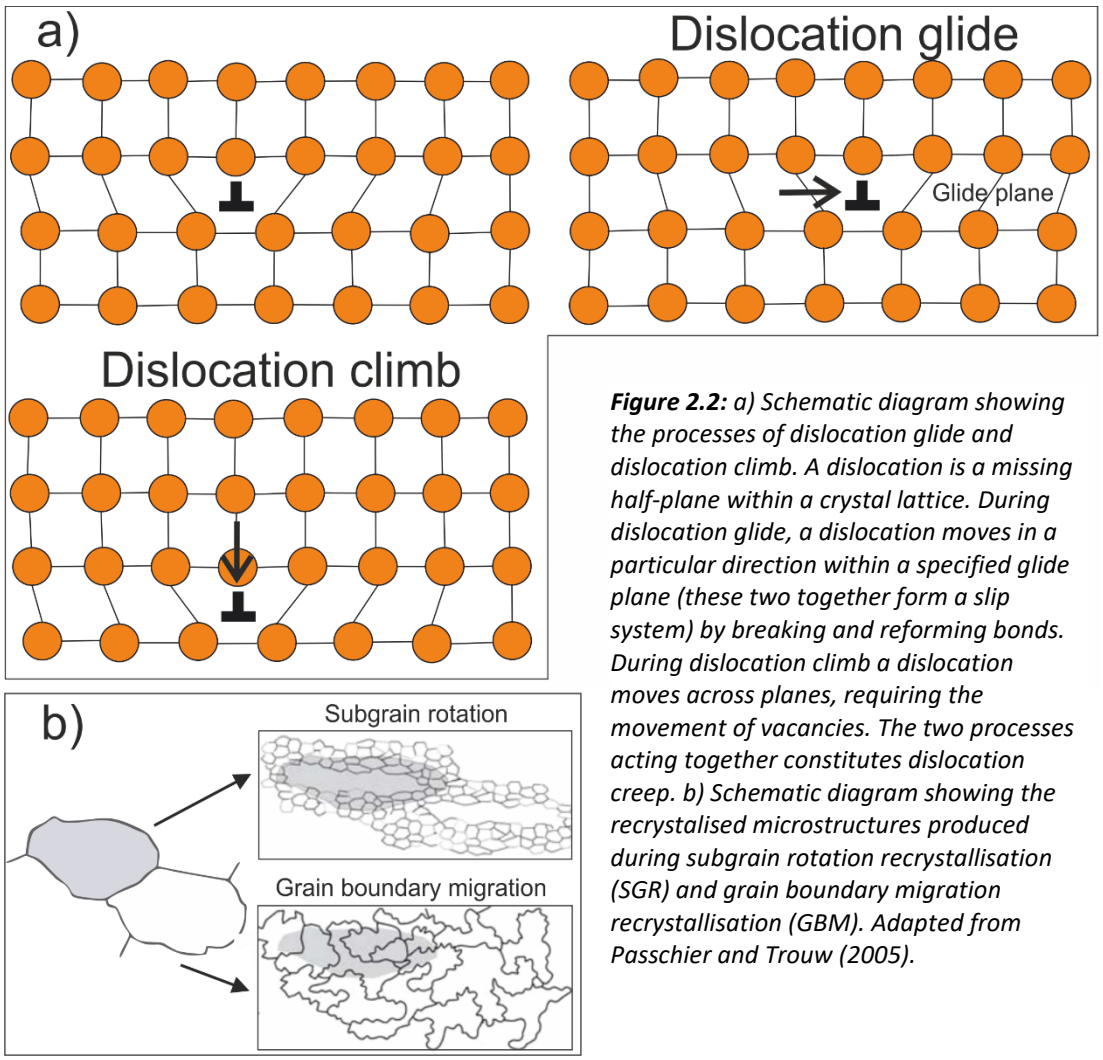


***Figure 2.2:*** *a) Schematic diagram showing the processes of dislocation glide and dislocation climb. A dislocation is a missing half-plane within a crystal lattice. During dislocation glide, a dislocation moves in a particular direction within a specified glide plane (these two together form a slip system) by breaking and reforming bonds. During dislocation climb a dislocation moves across planes, requiring the movement of vacancies. The two processes acting together constitutes dislocation creep. b) Schematic diagram showing the recrystalised microstructures produced during subgrain rotation recrystallisation (SGR) and grain boundary migration recrystallisation (GBM). Adapted from Passchier and Trouw (2005).*

strain free grains and subgrains (Fig. 2.2b). At lower temperatures, where dislocation mobility is lower, recrystallisation may occur by bulging (BLG), whereby a boundary migrates locally into the side with higher dislocation density, removing dislocations it passes. These localised bulges of low strain lattice can then rotate away from their original host grain, via a subgrain boundary, and form distinct fine grains decorating the edges of larger grains. In this case the grain boundary mobility is limited and localised to the small bulging area, however, at much higher temperatures the grain boundaries are mobile enough to sweep across entire grains, removing dislocations and alleviating strain energy. The new dislocations that continue to be generated in the grain behind this boundary are then removed by another boundary sweeping across from elsewhere. This third process is termed grain boundary migration (GBM) recrystallisation and, unlike in BLG and SGR, does not necessarily lead to significant grain size reduction, although all vestige of the original grains is lost (Fig. 2.2b). These

processes have been observed and described most clearly in quartz (eg. Hirth and Tullis, 1992; Stipp *et al.*, 2002) but are applicable to other minerals and materials (Urai *et al.*, 1986).

The activation of dislocation glide on specific crystallographic planes at certain temperatures and levels of differential stress can result in the development of a crystallographic preferred orientation (CPO) in aggregates deforming by dislocation creep. This is because preferential activity of favourably oriented slip systems rotates grains towards similar orientations. Rocks which have deformed by dislocation creep will therefore possess a CPO, and the presence of a CPO is often used as strong evidence of dislocation creep. However, CPOs, especially weak or poorly developed ones, can also be generated by other mechanisms such as those outlined in the section below.

### *Diffusive mass transfer*

Diffusive mass transfer (DMT) enables shape change and the accommodation of strain by the diffusion of material around or within grains without the need for mechanical lattice distortion or fracturing (Poirier, 1985). It can refer to the processes of diffusion creep, which can itself be divided into Coble creep and Nabarro-Herring creep, and dissolution-precipitation creep (or pressure solution). Dissolution-precipitation creep involves diffusive transfer of matter within a fluid phase (Rutter, 1983), while diffusion creep does not require a fluid phase and is most prevalent at greater depths where elevated temperatures sufficiently increase the rate of diffusion in dry rocks. In both dissolution-precipitation creep and diffusion creep, deformation is driven by gradients in stress and/or chemistry around mineral grains induced by differential loading within a fault or shear zone or during compaction (Poirier, 1985; Wheeler, 1992).

Diffusion creep involves the diffusive migration of vacancies. In the case of Coble creep the diffusion occurs around the boundaries of grains (grain boundary diffusion) whereas with Nabarro-Herring creep vacancies diffuse through the crystal lattice (bulk diffusion). Vacancies move towards the sites of highest stress and away from those of lower stress which results in a net transfer of mass towards low stress interfaces. DMT mechanisms are greatly enhanced by finer grain sizes as grain boundaries provide fast diffusion pathways, thus they are sometimes referred to as grain size sensitive (GSS) creep mechanisms(White *et al.*, 1980; Wheeler, 1992). Deformation of an aggregate by diffusion creep necessarily includes the process of grain boundary sliding (GBS), during which grains rotate and translate relative to each other. In this situation diffusion accounts for the change in shape of grains required to satisfy intergranular compatibility constraints (Paterson, 2001), preventing the formation of

voids between grains by diffusion of material to such locations. This can also be achieved by crystal plastic deformation and/or dissolution and precipitation in the presence of a fluid phase. In diffusion accommodated GBS, the rate of diffusion of material is the rate limiting factor, so diffusion creep is favoured at low stresses and strain rates. DMT mechanisms become particularly important in the deformation of polyphase aggregates (Wheeler, 1992) as an abundance of phase boundaries leads to second phase (or Zener) pinning and the inhibition of dynamic recrystallisation processes (Herwegh and Berger, 2004; Song and Ree, 2007). The presence of a fine-grained second phase evenly distributed within a single phase matrix has the effect of pinning grain boundaries that would otherwise move through the primary framework phase (Smith, 1948; Evans *et al.*, 2001; Herwegh *et al.*, 2011). This impedes grain growth through recovery, and results in a finer grained overall aggregate. In well mixed polyphase aggregates this can lead to a transition from dislocation creep to diffusion creep once the grain size is reduced sufficiently by crystal plasticity (Kilian *et al.*, 2011; Little *et al.*, 2015) or by metamorphic reactions (de Ronde *et al.*, 2005; Holyoke and Tullis, 2006c).

Dissolution-precipitation creep (or pressure solution) is similar in concept to diffusion creep but occurs at a faster rate in the middle and upper crust due to the presence of an aqueous fluid phase as a fast diffusive medium (Rutter, 1983; Gratier *et al.*, 2013). Material is dissolved at asperities or sections of grain boundaries that experience high normal stress and is transported down a stress or chemical gradient to be precipitated elsewhere (Wheeler, 1992; Shimizu, 1995; Renard *et al.*, 1997). The process is therefore more similar to Coble creep than to Nabarro-Herring creep as the diffusive mass transfer occurs around grains rather than through them. The new grains often nucleate at the interfaces of existing grains and grow in a similar orientation (Menegon, Pennacchioni and Spiess, 2008; Ceccato *et al.*, 2018). This process is known as epitaxy. However, in some instances new grains can be precipitated in random orientations generating little if any CPO (Mcpherren and Kuiper, 2013). It is important to distinguish the deformation mechanism of dissolution-precipitation creep from the mineral-replacement mechanism of dissolution-precipitation (Putnis and John, 2010). The two processes are essentially the same except that dissolution-precipitation creep requires differential stress and results in a shape change, while dissolution-precipitation does not require differential stress and results in the replacement of one mineral with another driven by changes in the chemical equilibrium between a solid and an aqueous phase (Putnis, 2002; Putnis and Putnis, 2007; Putnis and John, 2010; Ruiz-Agudo *et al.*, 2014). Instances where differential stress drives a mineral replacement reaction in the presence of an aqueous

fluid can be termed incongruent pressure solution, in which the phase or phases which dissolves is not the same as that or those which precipitate. In this way, incongruent pressure solution is effectively a form of stress induced chemical reaction (Beach, 1979; Fry, 1982; Simpson and Wintsch, 1989; Menegon *et al.*, 2006; Wheeler, 2014, 2018). This process is discussed in detail in Chapter 8 of this thesis.

## 2.3. The brittle-viscous transition and strength profile of the crust

The strength of rocks deforming by brittle processes increases linearly with depth, as increasing confining pressure hinders the opening of fractures. Conversely, the strength profile of rocks deforming by viscous processes decreases exponentially with depth as the increasing temperature aids crystal plastic processes. The combination of these two relationships results in a transition, with depth, from dominantly brittle processes to dominantly viscous deformation mechanisms. The switch from brittle to viscous deformation takes the form of a gradual transition within the middle-crust, the brittle-viscous transition (Kohlstedt *et al.*, 1995; Marti *et al.*, 2017). This simplified picture is complicated by the fact that different materials can behave differently at the same conditions, so one mineral type behaves viscously at a particular location in the crust where another in close proximity and under the same conditions behaves in a brittle manner (Fagereng *et al.*, 2014). This means that throughout the brittle-viscous transition, both brittle and viscous processes can occur simultaneously within the same rock, interacting with each other on the grain-scale (Fusseis and Handy, 2008). Aside from confining pressure and temperature, other factors which affect whether a material deforms by brittle or viscous mechanisms include the strain rate and the presence of fluids. A material deforming viscously at a slow strain rate may fracture and deform by frictional sliding if the strain rate is increased sufficiently. The presence of water has a significant weakening effect on viscous mechanisms (as discussed in section 2.6), which can significantly alter the depth of the brittle-viscous transition by raising the depth at which viscous processes take precedent over brittle ones. Consequently, the presence of dry, strong granulitic lower crust has the opposite effect, deepening the brittle-viscous transition and producing microstructures reminiscent of lower grade wet rocks in much higher temperature dry rocks (Wex *et al.*, 2019).

Because of this relationship (brittle strength increasing with depth and viscous strength decreasing with depth) the brittle-viscous transition is generally viewed as the strongest part of the crust and, indeed, it coincides with the depth at which a significant proportion of large

earthquakes nucleate (Sibson, 1984). However, the strength profile of the lithosphere as a whole, taking into account the lower crust and the upper part of the mantle, has been a matter of debate for some time and is still ambiguous (Burov and Watts, 2006). The classic model is that of a 'jelly sandwich', with a strong upper and middle crust overlying a very weak, lower crust which itself lies above a strong dry upper mantle (Chen and Molnar, 1983; Handy and Brun, 2004). This has been challenged by the re-evaluation of earthquake depth distributions and gravity anomalies which suggests that the upper mantle is weaker than the lower crust and significant lithospheric strength resides throughout the crust, with little influence from the upper mantle (Jackson, 2002; Priestley *et al.*, 2008). This is known colloquially as the 'crème brulee' model. In either case the profile of strength in the crust is likely to be dynamic and highly variable with location and tectonic environment due to factors such as rock type, mineralogy, geothermal gradient and fluid availability.

## 2.4. The classification and characteristics of deformed rocks

Regardless of the mechanism and character of deformation, fault and shear zones generally comprise a finite region of damaged or altered rocks. Generally, rocks which have undergone a greater degree of strain possess a larger modal percentage of fine-grained material, and the terminology for categorising fault lithologies is based on this as well as the nature of the processes (brittle or viscous) which dominated during deformation. Brittle fault zones can contain incohesive fault breccia (>30% visible fragments) or fault gouge (<30% visible fragments) as well as cohesive cataclasites ranging from protocataclasites (10-50% matrix) to ultracataclasites (>90% matrix), crush breccias (0-10% matrix) and pseudotachylites (Sibson, 1977). In the case of viscous shear zones, the deformed rocks are all cohesive and foliated and are termed mylonites. The classifications of mylonites range from protomylonites (10-50% matrix), through mesomylonites (50-90% matrix) (usually just termed mylonites), to ultramylonites (>90% matrix) with a separate term (blastomylonites) for rocks which have undergone substantial grain growth (Sibson, 1977). These lithologies, formed by deformation, are important rocks to study as they represent the material into which strain has localised, with strain rates or degrees of strain in excess of those experienced by the less deformed wall rocks around them. Often, multiple types of fault lithologies are present within the same fault zone, producing composite fault zone structures comprised of a fault core and a surrounding damage zone (Faulkner *et al.*, 2010). Composite fault lithologies are also characteristic of the brittle-viscous transition in which rocks are deformed by brittle and viscous processes and hence possess elements of different types of fault rock and mylonites, or where a fault or shear zone has been re-activated under different pressure, temperature

or strain rate conditions from those of its original activity (Menegon *et al.*, 2013, 2017; Salomon *et al.*, 2015; Papeschi *et al.*, 2018).

If a viscous shear zone is a zone of inhomogeneous deformation which has undergone strain softening, then a mylonite is the softened medium within that zone (White *et al.*, 1980). Mylonites, a term first used by Lapworth (1885), are fine grained viscously deformed lithologies and are the viscous equivalent of brittle fault rocks like cataclasites. Both mylonites and cataclasites have undergone strain softening by means of a reduction in grain size. In the case of cataclasites, comminution is achieved through brittle fracturing along with frictional sliding and rotation, whereas in mylonites, this has usually occurred via dynamic recrystallisation and crystal plasticity (e.g. White *et al.*, 1980). That being said, it should be noted that grain boundary sliding, diffusive mass transfer and even some cataclasis are also common during the deformation of mylonites. Stronger minerals commonly resist grain size reduction in mylonites and remain as coarse grained, rigid, rotating porphyroclasts as strain is partitioned into the weaker, fine-grained matrix (White *et al.*, 1980; Handy *et al.*, 1998).

Mylonites are commonly banded and display a mylonitic foliation, which, rather than being simply planar, often forms S, C, C’ and/or C’’ foliations (Fig. 2.3) (Lister and Snoke, 1984). In S-C mylonites the S surfaces are related to the accumulation of finite strain and are parallel to the maximum extension direction of the minerals, while the C surfaces represent bands of localised high shear strain which are parallel to the boundaries of the shear zone and have the same sense of shear (Berthe *et al.*, 1979). C’ surfaces are also micro-shear bands like C surfaces, however they occur at an angle to the shear zone boundary (< 45°) and are often less continuous, wavey structures which facilitate large displacements across the mylonitic foliation (Passchier and Trouw, 2005). C’’ shear bands are the far less common, antithetic, conjugate counterparts to C’ shear bands (Passchier and Trouw, 2005). Shear fabrics at such angles to regular C planes have been referred to as ‘steady-state foliations’ (Means, 1981). Lister and Snoke (1984) defined two different types of S-C mylonites based on the relative importance of S and C surfaces. Type 1 S-C mylonites are dominated by the S surfaces which are well defined and bend into the C surfaces, with mineral domains between the S surfaces often continuous across the C planes. In type 2 S-C mylonites by contrast, S surfaces are less well defined and the microstructure is dominated by C planes which involve transient displacement discontinuities, often highlighted by boudinaged mica fish (Lister and Snoke, 1984).

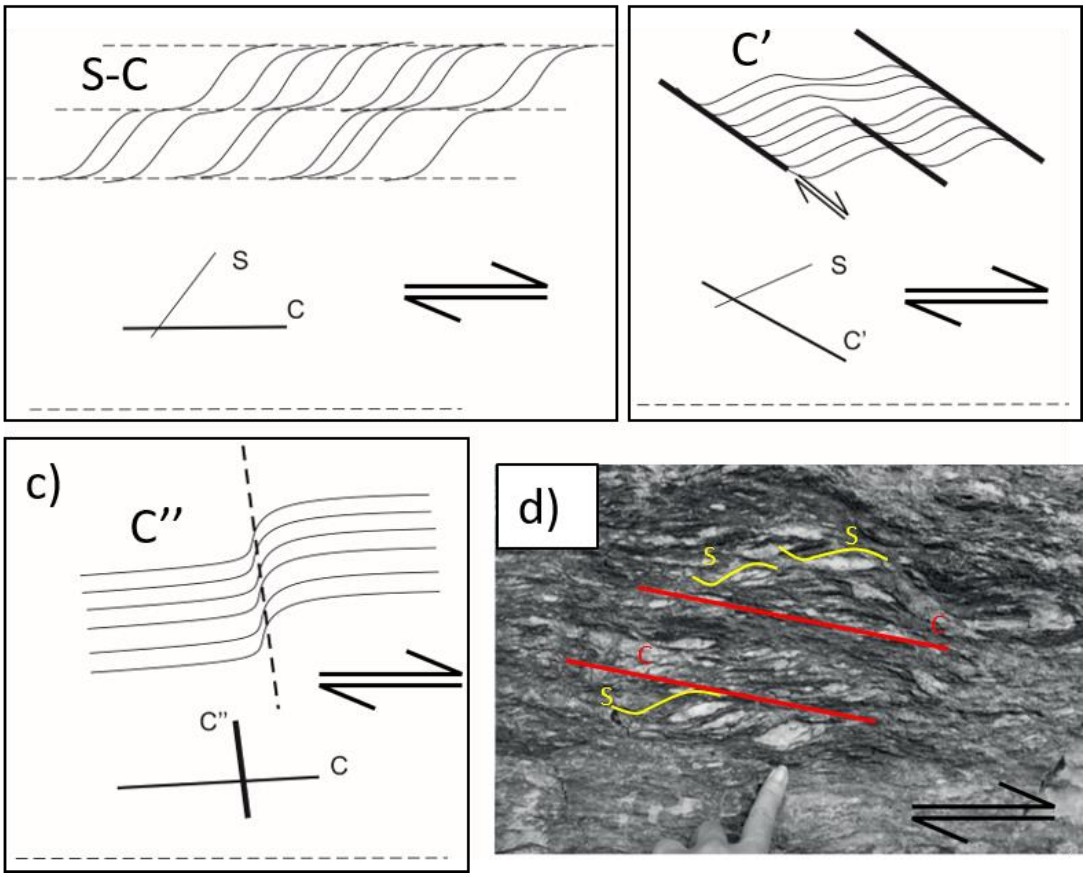


***Figure 2.3:*** *Sketches of the geometries of foliations in S-C mylonites. a) S surfaces usually represent the original foliation in the rock. C surfaces are generally straighter, accommodate a small amount of shear and are parallel to the shear zone boundaries. b) C' surfaces are micro-scale shear bands which are differentiated from C surfaces by having greater displacement, often being less continuous and by forming at a relatively high angle to the shear zone boundary. c) C'' surfaces are much less common than other types of foliation. They are antithetic with respect to the overall shear zone sense of shear and form at very high angles to the shear zone boundary. In all cases the orientation of the shear zone boundary is horizontal, given by the dashed line at the base of each panel. d) Example of S-C mylonitic fabric displayed within an outcrop in the field, from Montegmagni et al. (2016).*

## 2.5. Strain localisation in polymineralic rocks

How and why deformation in the crust localises into high strain zones has been the subject of much interest and discussion over the past decade or so (Cole *et al.*, 2007; Sullivan *et al.*, 2013; Oliot *et al.*, 2014; Czaplińska *et al.*, 2015; Goncalves *et al.*, 2015, 2016; Peters *et al.*, 2016). It is a critically important question because the vast majority of strain in the crust is localised at a multitude of scales. Therefore, in order to model the evolution of the crust, the occurrence and drivers of strain localisation must be addressed. Brittle deformation is inherently localised to some extent by the fact that it occurs along discrete fractures and results in the breaking of bonds across a plane. The localisation of viscous deformation is less intuitive. There are many possibilities as for why shear zones nucleate but the fundamental condition is the presence of a strength heterogeneity. Simply, weaker material will deform at lower stresses than stronger material at the same strain rate and faster than a stronger

material under the same stress. Any factor that makes a certain region weaker than another can lead to the localisation of strain into that region. In polyphase rocks such a weakness can be the result of the increased abundance of a weaker mineral phase, a different texture such as a finer grain size (Fitz Gerald and Stunitz, 1993; Kilian *et al.*, 2011; Oliot *et al.*, 2014), an existing fabric such as a crystallographic preferred orientation (CPO) or shape preferred orientation (SPO) (Menegon, Pennacchioni, Heilbronner, *et al.*, 2008; Montési, 2013), reaction softening (Dixon and Williams, 1983; Gueydan *et al.*, 2003; Oliot *et al.*, 2010), shear heating (Platt, 2015) or the presence of fluids (Griggs, 1974; Kronenberg, Segall, *et al.*, 1990; Menegon, Pennacchioni and Spiess, 2008; Menegon *et al.*, 2015; Finch *et al.*, 2016). Once a shear zone has nucleated, strain softening plays an important role, this is the process by which continued deformation leads to the strained rock mass becoming weaker than the surrounding material, ensuring deformation continues to be localised within the same zone (Means, 1995).

Almost all rocks in the Earth's crust are polymineralic, containing multiple mineral phases. These systems introduce additional complexities to the problem of strain localisation, especially on the meso-scale within fault lithologies. In studies of polymineralic rocks, the overall strength of the bulk aggregate is related to the end-member strengths of the constituent phases, their volume proportions and their distribution (the fabric). The bulk flow law of an aggregate is constrained to lie between the flow laws of its constituent phases on a log stress vs log strain rate plot (Tullis *et al.*, 1991). Handy (1990) defined three key types of deformation in polyphase rocks based on the fabric and distribution of phases of different strength; Type 1: a load bearing framework of strong minerals controls the bulk rock rheology over a small amount of isolated grains of the weaker phase by constraining the weak grains to deform at the same rate. Type 2: two phases with a small phase strength contrast form elongate boudins and matrix. Type 3: a large amount of a weaker matrix phase dominates the rheology, with stronger minerals forming isolated clasts (Fig. 2.4.). Which regime is applicable is a function of the contrast between the strengths of the stronger and weaker minerals and the volume proportion of each phase in the bulk aggregate. Handy *et al.*, (1998) developed this to define the three end-member types of a steady state mylonitic fabric for bimineralic rocks as; 1) a load bearing framework in which both strong and weak phases deform viscously ($LBF_{vv}$), 2) interconnected weak layers in which both strong and weak phases deform viscously ($IWL_{vv}$) and 3) interconnected weak layers in which the strong phase

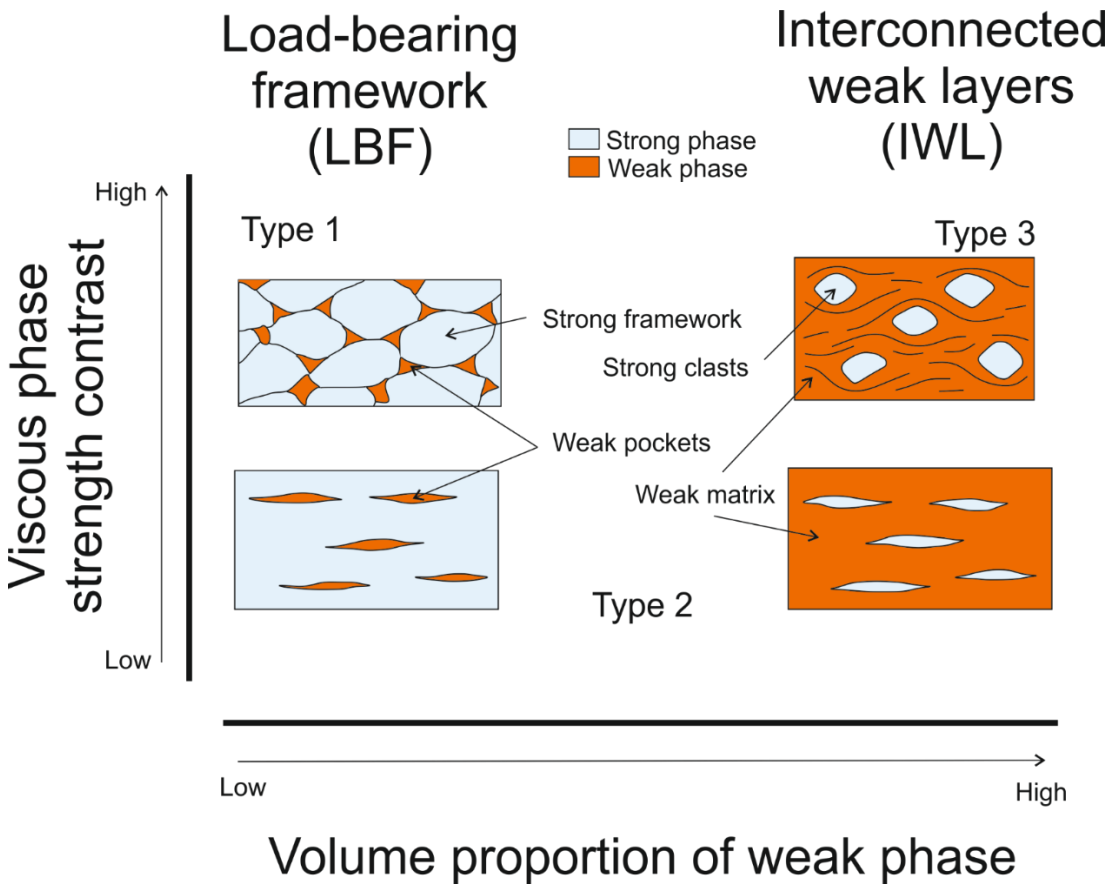


***Figure 2.4:*** *Schematic sketches of microstructural types in two phase rocks, differentiated by the volume proportion of strong and weak phases and the viscous strength contrast between those phases. After Handy (1994).*

deforms by frictional sliding but the weak phase deforms viscously ($IWL_{fv}$). For bimineralic mylonites with a $LBF_{vv}$ fabric an upper bound approximation of composite viscous shear strength of the composite rock ($\tau_r^{LBF}$) at uniform strain rate can be given as:

$$\tau_r^{LBF} = \tau_{wr}\phi_w + \tau_{sr}(1 - \phi_w) \tag{2.1}$$

where $\tau_{wr}$ and $\tau_{sr}$ are the shear strengths of the weak and strong phases respectively and $\phi_w$ is the volume proportion of the weak phase. The shear strengths of the weak and strong phases are defined at a set temperature (T) and at a reference strain rate equal to that of the bulk rock ($\dot{\gamma}_r$) (Handy, 1994). This simple relationship means that in rocks with a large proportion of strong minerals and a small amount of isolated weak minerals, it is the strong phase which dominates the bulk rock strength as it limits the isolated pockets of weak phase to deform at the same strain rate. However, this relationship changes when the weak phase becomes interconnected, as the relative strain rates of the two phases become important, as does the viscous strength contrast ($\tau_c$) between the phases. The strain rates of the weak ($\dot{\gamma}_w$) and strong ($\dot{\gamma}_s$) phases are:

$$\dot{\gamma}_w = \dot{\gamma}_r {\phi_w}^{-1/\tau_c} \tag{2.2}$$

and

$$\dot{\gamma}_s = \dot{\gamma}_r \frac{1-{\phi_w}^{1-(1/\tau_c)}}{1-\phi_w} \tag{2.3}$$

The viscous strength contrast is the ratio between the shear strengths of the strong phase and the weak phase such that: $\tau_c = \tau_{sr}/\tau_{wr}$ (Handy, 1994). The connectivity of the weak phase in IWL microstructures allows the weak phase to accommodate an amount of shear strain that is inversely and non-linearly proportional to the volume proportion and viscous strength contrast of the constituent minerals (Handy *et al.*, 1998). The shear strength of a mylonite with an IWL fabric ($\tau_r^{IWL}$) is given by:

$$\tau_r^{IWL} = \tau_w \phi_w^{-1/\tau_c} + \tau_s \left(1 - \phi_w^{-1/\tau_c}\right) \tag{2.4}$$

where $\tau_w$ and $\tau_s$ are the shear strengths of the weak and strong phases deforming at the strain rates $\dot{\gamma}_w$ and $\dot{\gamma}_s$ respectively (Handy *et al.*, 1998). In the case of a type 3 fabric, a frictional-viscous clastomylonite in which brittle porphyroclasts are surrounded by a weak matrix, usually with a very high phase strength contrast, Handy, Wissing and Streit, (1998) input a frictional sliding version of $\tau_s$, such that:

$$\tau_s = \frac{1}{2}\left[a + P_{eff}(b-1)\right] sin(90 - arctan\, \mu_d) \tag{2.5}$$

where effective pressure ($P_{eff}$) is the lithostatic pressure minus the pore fluid pressure and a and b are constants relating to the coefficient of dynamic friction ($\mu_d$) and the critical shear strength.

These equations derived by Handy, (1994) and Handy *et al.*, (1998) describe how the distribution of strain between weak and strong phases depends on T, $\dot{\gamma}_r$, $\tau_c$, $\phi_w$ and, where the deformation of the strong phase includes a brittle component, $P_{eff}$. Ultimately, as the proportion of weak phase increases so does its influence on the strength of the bulk aggregate, but this is increased markedly when the weak phase becomes interconnected and the fabric switches from LBF type to IWL type and especially when there is a high shear strength contrast between the two phases. As the shear strength contrast increases, strain is increasingly partitioned into the weak phase and away from the stronger phase, meaning the strain rate of the porphyroclasts approaches 0, and they become essentially passive, rigid clasts in a deforming matrix.

In the above equations (Equations 2.1 - 2.5) it is assumed that 'viscous deformation' constitutes dislocation creep, and therefore that the difference in shear strength of the weak and strong volumes of a rock is due to them being composed of different phases with different strengths. However, a variation in strength can also be derived from a difference in viscous deformation mechanism between different phases or within the same phase. An example of this is the switch from grain size-insensitive dislocation creep to grain size-sensitive diffusion creep, which becomes more efficient at finer grain sizes (see section 2.2.2). If the strain rate in the fine-grained aggregate deforming by diffusion creep can become greater than that of the coarser grained material, then it effectively represents a weaker material into which strain is partitioned to a greater extent. The development of shear zones is almost always accompanied by some degree of grain size reduction in the deformed material. A resulting switch to diffusion creep can therefore constitute a strain weakening effect that localises further deformation predominantly within the volume that has already deformed (Behrmann and Mainprice, 1987; Kilian *et al.*, 2011; Menegon *et al.*, 2013; Viegas *et al.*, 2015).

## 2.6. The role of fluids in crustal deformation

Fluids (predominantly $H_2O$, but also $CO_2$, $CH_4$ and others) are ubiquitous throughout the Earth's crust and have a substantial effect on the strength and deformation behaviour of the rocks with which they interact. The principal origins of fluids in the crust include: meteoric water, usually buried within wet sediments and expelled during compaction and digenesis; sea water that reacts with minerals of the oceanic lithosphere (e.g. serpentinisation reactions) and is subducted at destructive plate margins, where it is in part released at depth through dehydration reactions and in part integrated in crystal structures and grain boundaries as intracrystalline water (Rupke *et al.*, 2004; Tielke *et al.*, 2019); metamorphic fluids derived from the devolatilization and reaction of minerals such as phyllosilicates and clays during prograde metamorphism; and magmatic fluids generated through aqueous fractionation during melt crystallisation. In the upper crust, the abundance of fluids plays an important role in fault zone dynamics. Fault zones can act as either conduits or barriers to fluid flow often depending on the structure's position temporally within the seismic cycle. The fractured and damaged rock immediately after an earthquake can provide a region of high permeability and fluid flow. However, precipitation of minerals from this fluid, in combination with compaction of the fine grained, often clay-rich, gouge in the fault core during the interseismic period, can form an impermeable hydraulic seal, producing high fluid pressure gradients in the surrounding rocks (Wibberley and Shimamoto, 2003; Faulkner *et*

*al.*, 2010; Sutherland *et al.*, 2012). The interplay of fluid pressure, fault friction and far-field stresses is likely to play a critical role in the earthquake cycles of many major fault zones (Faulkner *et al.*, 2010, 2011; Sutherland *et al.*, 2012).

Although the middle and lower crust are generally considered to be drier than the upper crust, fluids retain a significant influence on the rheology of viscous shear zones through processes such as hydrolytic weakening and fluid-rock interactions as well as in aiding diffusive mass transfer (see section 2.2.2). Hydrolytic weakening is applicable to nominally anhydrous minerals such as quartz (Griggs, 1967, 1974; Kronenberg, Segall, *et al.*, 1990) and olivine (Girard *et al.*, 2013; Tielke *et al.*, 2017), and involves the inclusion of hydrogen as point defects within the crystal lattices of minerals that deform by dislocation creep (Tielke *et al.*, 2017). The weakening occurs due to hydrolysis of Si-O-Si or Si-O-M bridges in silicates, meaning that dislocation slip can be accommodated simply by hydrogen bond exchange with no need to break Si-O bonds (Griggs, 1967). In crustal mylonites the combination of high fluid flux within shear zones (Menegon *et al.*, 2015) and the effects of hydrolytic weakening on quartz, constitute a significant strain weakening process driving strain localisation (Kronenberg and Tullis, 1984; Tullis and Yund, 1989; Kronenberg, Segall, *et al.*, 1990). Alternatively, the redistribution of fluids during the syntectonic evolution of shear zones and the resulting re-localisation of hydrolytic weakening in different areas, may be a process which facilitates the growth of wide regions of high strain ultramylonites by progressively moving the loci of fluid flow outward from the centre of the shear zone during deformation (Finch *et al.*, 2016). Traditional ideas of strain softening would otherwise preclude the development of ultramylonite zones with thicknesses wider than several metres.

Throughout the crust, fluids enable chemical reactions by providing an effective means for the transport of material through dissolution and reprecipitation and by diffusive mass transfer (Rutter, 1983; Wheeler, 1992). In some instances these processes, and the shape change they enable, can constitute an important or even dominant mechanism of deformation (Cox and Paterson, 1991; Wintsch and Yi, 2002; Menegon, Pennacchioni and Spiess, 2008). High water content in mylonites also aids the mobility of grain boundaries during dynamic recrystallisation relative to dry conditions, promoting GBM recrystallisation. Mancktelow and Pennacchioni (2004), found that dry amphibolite facies quartz-feldspar mylonites preserved a similar recrystallised microstructure to regular wet greenschist facies mylonites of similar composition, suggesting rocks deforming by dislocation creep are stronger under dry conditions or, conversely, weakened by high intergranular water content. This is different to hydrolytic weakening which involves intragranular hydrolysis and weakens

the slip systems of minerals (Griggs, 1967, 1974; Kronenberg, Segall, *et al.*, 1990; Girard *et al.*, 2013; Tielke *et al.*, 2017).

Reaction softening is a process of weakening that does not inherently require the involvement of fluids but is strongly enhanced by the increased diffusion rates — and therefore reaction rates — afforded by the presence of fluids. Reaction weakening involves the reaction of a strong mineral phase either to a weaker phase or to a fine-grained aggregate inducing a change in deformation mechanism (Brodie and Rutter, 1986). The reactions induce a change in strength of the rock aggregate, making it weaker than the surrounding country rock and serving to localise or even nucleate shear zones. The most commonly documented form of reaction softening is the growth of weak phyllosilicates, at the expense of feldspar or other minerals, driven by an abundance of aqueous fluid (Dixon and Williams, 1983; Wintsch *et al.*, 1995; Gueydan *et al.*, 2003; Oliot *et al.*, 2010). This can occur in granitic rocks in the shallow crust and in mafic rocks to greater depths, producing a reaction product that is weaker than the original rock due to the relative weakness of phyllosilicates at a range of conditions (Wintsch *et al.*, 1995). Conversely, it has been argued that the precipitation of quartz, which accompanies the above reaction, could serve to strengthen some parts of fault zones and actually lead to reaction hardening (Wibberley, 1999). The development of an interconnected weak network also benefits from reactions, where the weak material is a reaction product (Holyoke and Tullis, 2006c; Goncalves *et al.*, 2015). The formation of a fine grained aggregate by reaction of a coarse grained initial lithology can, in some instances, occur without abundant fluids and may be an important mechanism for strain localisation and shear zone nucleation in the lithospheric mantle (Handy and Stunitz, 2002; de Ronde *et al.*, 2005).

# 3. Structure and deformation mechanisms of mica minerals

## 3.1. The structure and chemistry of mica minerals

Micas are a major member of the larger group of minerals known as phyllosilicates. These layer silicates are notable for the strong anisotropy of their crystal lattices with generally much weaker bonding in one crystallographic orientation in comparison to others. This results in a perfect cleavage and gives them a distinctive 'flaky' or 'platy' texture when observed in hand specimen. Aside from micas, minerals of the phyllosilicate group include clays, serpentines and chlorite, among others, and share many similarities with engineering materials such as ceramics and the MAX phases (Barsoum and Tucker, 2017; Barsoum *et al.*, 2019). Micas include biotite, muscovite, paragonite, phengite and glauconite, and are ubiquitous throughout the Earth's crust occurring within sedimentary, metamorphic and igneous rocks of a range of compositions (Deer *et al.*, 1980).

The general chemical formula for micas is:

$$X_2Y_{4-6}Z_8O_{20}(OH,F)_4 \tag{3.1}$$

Where X is an alkali or alkaline earth cation, usually K, Na or Ca, Y is an octahedrally coordinated cation usually Al, Fe or Mg and Z is a tetrahedrally coordinated cation usually Si with some substitution of Al and in some cases Ti (Deer *et al.*, 1980). Many mica species exist in solid solution and can contain a range of these cations between defined end members. The presence of $OH^-$ groups defines micas as hydrous minerals which dehydrate at high temperatures but also readily form in volatile rich settings such as the diagenesis of wet sediments and the crystallisation of intermediate arc magmas. In metamorphic settings, micas are a common product of the prograde evolution of clays and clay-rich sediments and give way to other hydrous species such as amphiboles at still higher-grade conditions.

The basic structure of micas consists of an octahedral layer (M) sandwiched between two tetrahedral layers (T) forming a TMT layer which is connected to other TMT layers across an interlayer region (I) (Fig. 3.1a and b). In the general chemical formula above, 'Y', 'Z' and 'X' correspond to cations in the 'M', 'T' and 'I' layers respectively (Brigatti and Guggenheim, 2002). The TMT layers are bonded internally via covalent bonding producing a strong, pseudohexagonal, monoclinic crystal structure with rings of six tetrahedral sites in the T layers surrounding groups of 3 octahedral sites in the M layers (Fig. 3.1c). The extreme

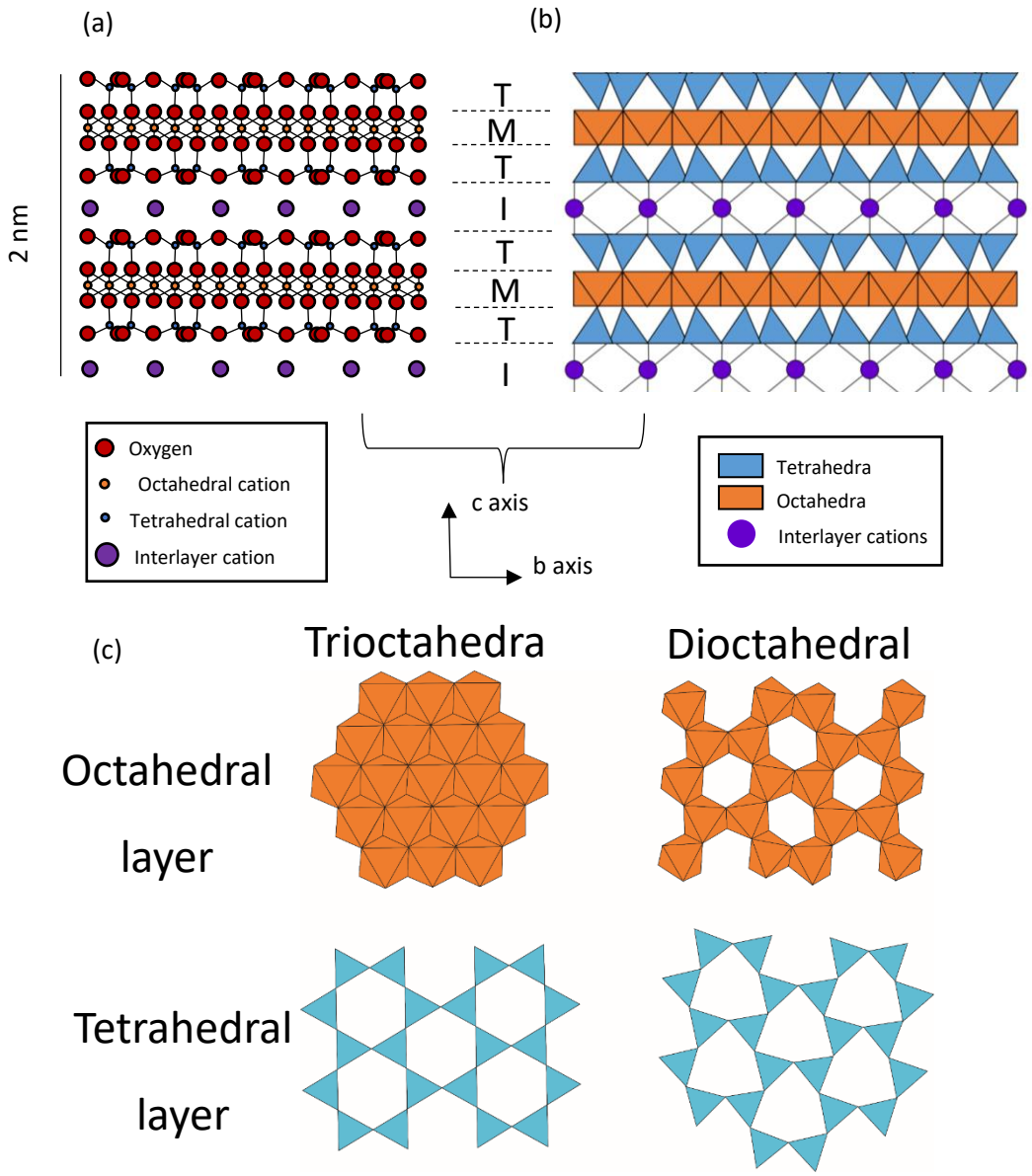


***Figure 3.1:*** *Illustrations of mica crystal structures. a) Ball and stick model of a trioctahedral mica structure viewed from the a direction. Tetrahedral (T), octahedral (M) and interlayer (I) layers are highlighted to the right. b) Block model of the same mica lattice also viewed from the a direction showing the arrangement of octahedral and tetrahedral structures, which form TMT layers separated by interlayers. c) Block diagrams viewed from the c direction of octahedral and tetrahedral layers for both trioctahedral and dioctahedral micas. In a dioctahedral mica, one in every three octahedral spaces is vacant, the unevenly distributed charges distort the shapes of the resulting octahedral and tetrahedral layers.*

anisotropy of micas is a result of the comparatively weak bonding between one TMT layer and another across the interlayer region. This weak bonding is what allows mica to split along the interlayers and form a perfect cleavage. The $OH^-$ groups in micas are located at the apex of three octahedral sites where they fall within a ring of tetrahedra and thus do not connect with the apical oxygen of a tetrahedron.

Micas can be separated into two principal categories; trioctahedral micas and dioctahedral micas (Deer *et al.*, 1980). As the nomenclature suggests, this distinction is based on the number of octahedrally coordinated cations (Y in the general formula above) present in the structure. There are three octahedral spaces in the unit cell of a mica lattice, in a trioctahedral mica all three are occupied by a cation with a valence of 2+, in a dioctahedral mica two of these spaces are occupied by a cation with a valence of 3+ and the other space is vacant (Fig. 3.1c) (Deer *et al.*, 1980). Hence micas with $Al^{3+}$ in these locations, such as muscovite, are generally dioctahedral, whereas those with $Mg^{2+}$ or $Fe^{2+}$, such as biotite, are trioctahedral. There is some flexibility, however, with some micas lying somewhere in between true dioctahedral and trioctahedral structures. It is also possible for divalent cations to be present in dioctahedral micas and trivalent cations in trioctahedral micas by balancing the charge through the relative abundance of $Si^{4+}$ and $Al^{3+}$ in the tetrahedral sites (Z in the general formula above). Examples include the presence of $Fe^{3+}$ in trioctahedral biotite and $Mg^{2+}$ in dioctahedral phengite. The vacant octahedral site in dioctahedral micas produces a pronounced distortion in the lattice within the hexagonal rings of tetrahedra (Fig. 3.1c) (Brigatti and Guggenheim, 2002). This is caused by the rotation of tetrahedra with basal oxygens moving towards occupied octahedral sites. The unoccupied octahedral sites also become slightly larger than the occupied ones due to the O anions which surround them moving away from the vacancies and towards regions of greater positive charge (Brigatti and Guggenheim, 2002).

## 3.2. Current understanding of deformation mechanisms in micas

### 3.2.1. Brittle deformation and friction

Brittle fracturing occurs in mica minerals at conditions of low confining pressure and comminution of mica grains by cataclasis is common in brittle fault rocks. Fracturing is particularly common when mica is shortened perpendicular to the basal plane. However, the picture is more complicated in other orientations as crystal plastic processes, namely dislocation glide, can be active in micas at low temperatures and low levels of differential stress, conditions which are associated with brittle behaviour and fracturing in other minerals (Kronenberg, Kirby, *et al.*, 1990; Mares and Kronenberg, 1993). Interestingly, experiments suggest the deformation of micas is confining pressure sensitive even at very high temperatures (Mariani, 2002). Such a confining pressure dependency is generally associated with brittle deformation mechanisms, however micas display this behaviour

even when no brittle microstructures are observed. Frictional sliding in micas is characterised by a very low coefficient of friction, between 0.25 and 0.5 (Mariani *et al.*, 2006), although this is generally higher than in other phyllosilicates such as clays (Morrow *et al.*, 1992). This, coupled with the generally high abundance of phyllosilicates within brittle fault gouges, makes phyllosilicates very important minerals with regard to the frictional properties of faults (Byerlee, 1978; Mariani *et al.*, 2006).

### 3.2.2. Crystal plasticity in micas

A number of studies have proposed that crystal plastic processes within mica are essentially limited to dislocation glide and slip parallel to (001) which can be activated at relatively low differential stress (< 200 MPa) and at a very wide range of temperatures from 20°C to 700°C (Etheridge *et al.*, 1973; Bell *et al.*, 1986; Meike, 1989; Kronenberg, Kirby, *et al.*, 1990; Christoffersen and Kronenberg, 1993; Mares and Kronenberg, 1993; Mariani *et al.*, 2006). The specific slip directions within (001) have been determined to be [100] and <110> (Etheridge *et al.*, 1973; Meike, 1989) which correspond with the closest packing vectors in a mica crystal lattice (Christoffersen and Kronenberg, 1993). Unequivocal evidence for dislocation climb and cross slip on other planes has not been observed, making micas highly anisotropic with regard to properties such as strength and resistance to shear. As a result, micas are deformed reasonably easily when $\sigma_1$ is oriented at a low angle to (001) and strain can be accommodated predominantly by basal slip (Kronenberg, Kirby, *et al.*, 1990). Interestingly, when $\sigma_1$ is oriented parallel to (001), deformation results in the nucleation of high angle kink bands and strain cannot simply be accommodated by slip on (001) (Kronenberg, Kirby, *et al.*, 1990). This means micas are weakest when $\sigma_1$ is oriented at a low angle to (001) (Kronenberg, Kirby, *et al.*, 1990) or parallel to it under conditions of simple shear (Mariani *et al.*, 2006). Crucially, non-basal slip does not occur even under experimental conditions where $\sigma_1$ is oriented perpendicular to (001), and the directions of slip systems in mica do not appear to change with temperature (Christoffersen and Kronenberg, 1993). Even at temperatures as high as 600°C the dominance of dislocation glide and a lack of climb or cross-slip can result in work hardening (brought about by tangles of dislocations that cannot leave their glide plane to bypass obstacles) in experimentally deformed phyllosilicate-rich fault gouges (Rutter and Maddock, 1992). The lack of climb and non-basal slip precludes dislocation creep, in the classic sense, as a deformation mechanism in micas, and the mechanisms by which intracrystalline strain is accommodated perpendicular to the basal plane, without brittle cataclasis, is currently unknown.

A new type of defect and associated deformation mechanism, termed ripplocations, have recently been proposed within materials science and have the potential to explain intracrystalline c-axis parallel strain in layered materials (Kushima *et al.*, 2015; Gruber *et al.*, 2016; Barsoum and Tucker, 2017; Griggs *et al.*, 2017; Freiberg *et al.*, 2018; Barsoum *et al.*, 2019). Ripplocations take the form of atomic scale ripples with the dual character of a ripple and a basal dislocation and are potentially applicable to phyllosilicates. Chapter 6 of this thesis (also Aslin *et al.*, 2019) details the first evidence for the presence of ripplocations in naturally deformed micas.

As described in section 3.1, the interlayer is the weakest region of bonding in a mica lattice. As a result, this is the part of the crystal within which the characteristic perfect cleavage of micas is accommodated and along which basal plane parallel fracturing and frictional sliding is most likely to occur. It has been a common assumption that basal dislocation glide also occurs within this interlayer region, especially when considering the strong structural anisotropy of micas and the occurrence of dislocation glide only on the basal plane. However, perhaps counterintuitively, the interlayer region is not the structural layer within which it is most energetically favourable for dislocations to glide (Noe and Veblen, 1999a). While the bonding is weak here, the length of the bonds is large and the energy required to form and glide a dislocation is significant. Noe and Veblen (1999) found that the most energetically favourable locations for glide, which produced the least structural disruption, was between the apical oxygens in the hydroxyl plane and either the octahedral or tetrahedral cations (see Fig. 3.1 for reference).

### 3.2.3. Mica fish

Mica minerals are some of the best exhibitors of mineral 'fish' structures within mylonites and other sheared rocks. White mica in particular, very commonly forms these lozenge shaped porphyroclasts which allow a single crystal to maintain a semi-stable structure within a finer grained deforming matrix. Mica fish can occur in several different characteristic shapes including lenticular fish, rhomboidal fish and fish with either low or high aspect ratios (ten Grotenhuis *et al.*, 2003) (Fig. 3.2). Mica fish are believed to form by a combination of rigid body rotation and crystal plastic deformation in the form of slip on (001). They commonly contain kink folds and isoclinal folds and have strong undulose extinction (ten Grotenhuis et al. 2003). Rotation occurs in order to re-orient an elongate grain towards a low angle (-8° to 32°) to shear (ten Grotenhuis *et al.*, 2003). During, after or instead of this process the mica grain can deform by slip on (001) to produce a distorted lozenge shape (ten Grotenhuis *et al.*, 2003). Mica fish are useful shear sense indicators and often define the S

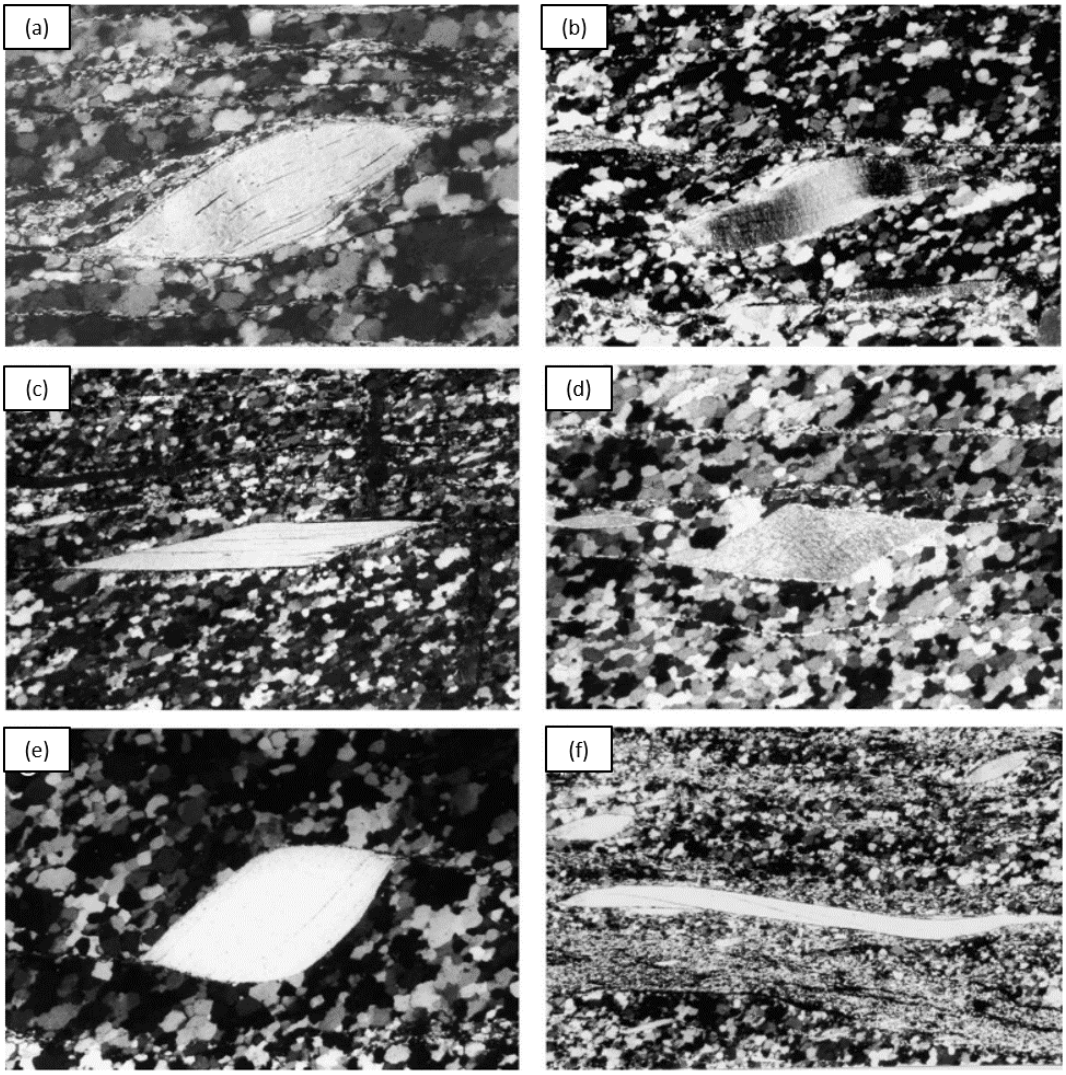


***Figure 3.2:*** *Examples of different types of mica fish. (a) and (b) lenticular fish, (c) and (d) rhomboidal fish, (e) mica fish with a low aspect ratio and (f) mica fish with a high aspect ratio. From ten Grotenhuis et al. 2003. Samples are from Conceicao do Rio Verde, Brazil and all have a dextral shear sense. All images taken with crossed polars and with widths of view (a) 3 mm, (b) 0.75 mm, (c), (d) and (e) 3 mm, (f) 6 mm.*

and C surfaces in S/C mylonitic fabrics, with their basal planes bent to follow this fabric as well. Many mica fish also show long, thin trails of very fine-grained mica which protrude from the corners of the fish and trail out into the fine-grained matrix parallel to shear. This material is understood to be produced either by recrystallisation of the mica along the top and bottom of the fish or by folding and cataclastic grain size reduction at the fish tips (ten Grotenhuis *et al.*, 2003). A clear distinction between white mica fish and biotite fish is the fact that biotite appears to subvert to grain size reduction far more easily than white mica. As a result the tails of biotite fish are larger and their survivability is far lower (ten Grotenhuis *et al.*, 2003).

### 3.2.4. Kinking

A common way in which micas express c-axis parallel (basal plane perpendicular) strain is the formation of tight intracrystalline folds known as kinks, with a parallel pair of these folds being known as kink band boundaries either side of a kink band (Fig. 3.3a). Kinking can be observed in other minerals but is only common in phyllosilicates and appears to require very pronounced crystallographic and physical anisotropy. Kink bands can be described as primary or secondary based on whether slip has occurred on one side or both sides of the boundary respectively. On the grain scale, kink bands interact to form complicated anastomosing networks that accommodate basal plane-parallel shortening within larger mica grains. Three main stages are apparent in the formation of kink bands; nucleation, longitudinal propagation and lateral growth (Weiss, 1980). The original nuclei of kink bands are lensoidal regions of lattice in which the basal planes are misoriented with respect to those of their host grains by the angle of bending (ω) (Etheridge *et al.*, 1973) (Fig. 3.3b). The ends of these elongate lenses propagate longitudinally due to high elastic strain concentrations in the surrounding undeformed lattice at their tips, increasing the size of the deformed and misoriented region. These ends may reach the edges of the mineral grain, at which point the kink band boundaries at the sides will straighten and become parallel. During and after this process the kink band boundaries can migrate laterally into the undeformed lattice, widening the kink band (Weiss, 1980). Where a new kink band nucleates within the deformed region of an existing kink band due to rotation of the lattice with respect to the principle stress axes, it is referred to as a second generation kink band. Before the ends of a propagating kink band have intersected the edges of the host mineral grain, it is possible that the deformation could be entirely reversible, with the lensoidal regions of misoriented lattice shrinking back and disappearing. Such features are termed incipient kink bands and have been invoked to explain observations of fully reversible, reproducible hysteretic stress-strain loops during experimental deformation of kinking materials (Basu *et al.*, 2009).

The precise mechanism by which kink bands form is not clear, principally because it is difficult to account for such sharp bending and deformation parallel to the c-axis using basal dislocation glide alone. The most comprehensive models invoke complex arrays of dislocation walls and stacking faults focussed within a small area (Etheridge *et al.*, 1973; Bell *et al.*, 1986), but even these concede that another mechanism is required to explain c-axis strain and satisfy kink band asymmetry. Kink band asymmetry is defined as:

$$|\phi - \phi_K| \tag{3.2}$$

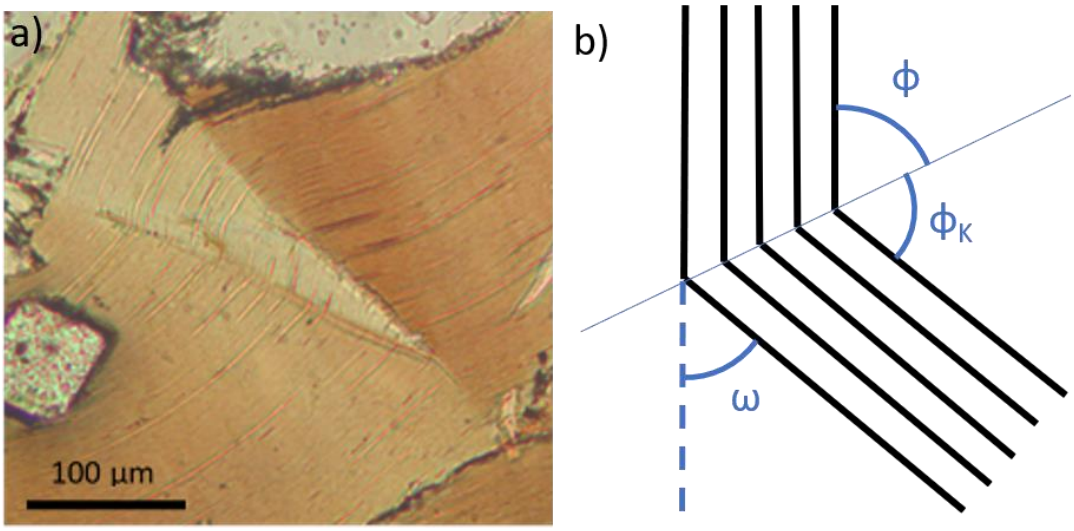


***Figure 3.3:*** *a) Plane polarised light optical micrograph of a kink band within a biotite grain. The sharp fold axes are the kink band boundaries, the orientation of the basal planes is highlighted by dark micro-cleavages. b) Conceptual diagram illustrating the components of a kink band as described by (Etheridge et al. 1973).*

Where ϕ is the angle between (001) in the limb outside the kink band and the axial plane of the KBB and $\phi_K$ is the angle between (001) in the limb inside the kink band and the axial plane of the KBB (Etheridge *et al.*, 1973) (Fig. 3.3b). Asymmetric kink bands occur at all conditions though more commonly in micas deformed at higher temperatures and compressed along [010] (Etheridge *et al.*, 1973). The asymmetry results in an expansion in the basal plane spacing within the kink band which cannot be explained by basal dislocation glide but is not clearly a brittle or cataclastic phenomenon either.

### 3.2.5. Grain size reduction and recrystallisation of micas

Grain size reduction is regularly interpreted to result in significant rheological weakening within localised regions. A change in dominant deformation mechanism from dislocation creep to diffusion creep processes within these regions may be the process that brings about this weakening (Warren and Hirth, 2006; Kilian *et al.*, 2011). Alternatively, it may be true that a balance between grain growth processes and grain size reduction may be struck at a certain point with conditions remaining near the boundary of the dislocation creep and diffusion creep fields. This is known as the field boundary hypothesis (De Bresser *et al.*, 1998, 2001) although it has been contested by Platt and Behr (2011) who argue that grain growth is inhibited by the dominance of strain energy driven-grain boundary migration over surface energy driven-grain boundary migration. This would imply grain size reduction results in permanent weakening through a switch in dominant deformation mechanism from dislocation creep to grain-size sensitive creep (Platt and Behr, 2011). The presence of fine mica (or another mineral) as a secondary phase appears to have a strong effect on the degree

and manner of dynamic recrystallisation within surrounding minerals (Little *et al.*, 2015; Andrew J. Cross *et al.*, 2017). Where mica is present as multiple dispersed grains within a quartz-muscovite mylonite, the average size of recrystallised quartz grains is significantly reduced with respect to a region of the same mylonite where muscovite is less abundant or is clustered into smaller areas (Song and Ree, 2007). This effect is very sensitive to mica fraction, being evident even with mica fractions below 3% (Song and Ree, 2007). The implication of this observation is that the presence of mica grains works to inhibit dynamic recrystallisation processes within neighbouring or nearby quartz grains, by pinning the grain boundaries of recrystalising quartz grains. However, the precise mechanisms of grain size reduction in micas remain ambiguous.

The occurrence of classical dynamic recrystallisation mechanisms in micas is contentious. A strong mechanical anisotropy and a tendency to kink distinguishes micas from materials such as quartz and metals. Low angle subgrain boundaries are rarely observed in micas and as a result the typical microstructures used to identify dynamic recrystallisation in quartz, such as core and mantle structures and chessboard grains are not apparent. Several mechanisms for grain size reduction in micas have been suggested including bulging recrystallisation at high angle boundaries (Etheridge and Hobbs, 1974), segmentation by means of the production of a series of slight misorientations parallel and subnormal to (001) (Wilson and Bell, 1979) and intracrystalline folding and cataclasis (Goodwin and Wenk, 1990; ten Grotenhuis *et al.*, 2003).

In samples which had undergone varying degrees of annealing, Etheridge and Hobbs (1974) observed serrated kink boundaries which were interpreted as equivalent to the undulating boundaries characteristic of bulging recrystallisation. This is perhaps supported by the evolution of the microstructure to eventually replace the high angle kink boundaries with bleb-like regions at places along its length. Indeed, the process of bulging recrystallisation could be applicable to layer silicates as it is common in materials where dislocation climb and subgrain formation are not favourable. Once nucleated, the orientations and rate at which new grains grow may be determined by coincidence lattice relationships between old and new grains or the preference of new grains to grow with the fastest growing direction (001) parallel to the strong diffusion pathways afforded by the kink boundaries (Etheridge and Hobbs, 1974).

### 3.2.6. Segmentation and cataclasis

Segmentation is a process of grain size reduction involving the production of smaller grains at the expense of larger ones through a series of slight misorientations across boundaries

that are parallel or subnormal to (001) (Wilson & Bell 1979, Bell & Wilson, 1981). It appears to be restricted to (or at least favoured in) crystal structures with a low number of slip systems, such as micas and specifically biotite, due to the lack of examples of similar processes within the mineralogical or metallurgical literature, as noted by Bell & Wilson (1981). A similar process is described by Bell (1978) whereby minute internal kinking of small portions of the host lattice creates high angle boundaries that then migrate into the highly strained lattice of the parent grain. These boundaries eventually connect around portions of the lattice to produce new grains with lower internal strain and therefore a driving force for growth. This mechanism does not require the nucleation of new grains but rather the formation and migration of new grain boundaries.

Grain size reduction of micas by means of intracrystalline folding and cataclasis was put forward by Goodwin & Wenk (1990). This mechanism is focused initially within lens shaped (or parallel sided) zones that are visible as darker regions with a higher refractive index. It begins with opening of cavities along cleavage planes and leads to eventual detachment of layers parallel to (001). Alternatively, these layers can be torn apart at the boundaries of micro shear zones. Subsequent folding and fragmentation of these layers produces an intracrystalline cataclasite. This process has geochemical implications, as it locally increases both the surface energy and strain energy. Also, the surface area becomes larger so fluid penetration is enhanced and metamorphic reactions may proceed more rapidly.

The existence of a single active slip plane in micas (001) produces significant anisotropy with regard to the strength and resistance to fracture of micas under conditions favouring brittle deformation. Micas fracture easily along (001) making them very weak when resisting shear in this orientation. Mares & Kronenberg (1993) found muscovite to have very weak basal shear strengths under a variety of conditions and a strong sensitivity to temperature and strain rate at high confining pressures. Micas are weakest when (001) is oriented ~45° to compression and are stronger when (001) is normal or even parallel to σ1.

Brittle deformation and cataclasis of micas is a significant mechanism for the production of fault gauges from the re-activation of phyllosilicate-rich mylonites. This process proceeds by nucleation of brittle deformation along the planes of mylonitic foliation where phyllosilicates have become concentrated and homogenously oriented by earlier ductile shear (Bolognesi and Bistacchi, 2016). Deformation is particularly focussed on the tips of favourably oriented micas which are weak enough along (001) to act almost like cohesion-less Griffith cracks, concentrating stresses at their tips (Rawling, 2002). These cataclastic layers, once nucleated,

then develop, under ongoing deformation, first by growing in thickness and then by changing from a foliated fabric to a random one with increasing strain (Bolognesi and Bistacchi, 2016). It has been suggested that the presence of pre-existing phyllosilicate-rich mylonites with established foliation could be weak enough so as to facilitate the nucleation of faults on misoriented planes (Bolognesi and Bistacchi, 2016).

## 3.3. The role of mica in accommodating crustal strain

The presence of mica minerals within fault and shear zones is likely to have a significant weakening effect on the features themselves (Shea and Kronenberg, 1993; Mariani *et al.*, 2006; Bolognesi and Bistacchi, 2016). Micas and other phyllosilicates display velocity strengthening behaviour under sub-seismic slip rates. This promotes aseismic slip within fault zones containing phyllosilicate rich fault gouge, such as those within sedimentary sequences in the upper crust. Under conditions of increased temperature and pressure, such as those that dominate lower levels in the continental crust, experimental evidence suggests the shear strength of mica reduces significantly. Coefficients of friction of between 0.25-0.5 are expected for mica rich shear zones in the mid-crust with shear strengths of 1-10 MPa for similar features in the lower crust (Mariani *et al.*, 2006). It has been suggested that this may be a result of a mechanism of viscous glide of basal dislocations becoming favourable and dominant at lower strain rates such as those apparent in deeper shear zones and detachments (Mariani *et al.*, 2006).

An important factor in the way that micas influence the rheological properties of polyphase rocks is the formation of an interconnected network of mica. Mica minerals commonly form the weakest component of polyphase rocks and are usually present as a secondary, rather than a dominant, phase. When individual isolated mica grains exist within a dominant framework of stronger minerals, such as in granite, the rheology of the aggregate is very heavily influenced by the strong, load-bearing framework minerals (see microstructure 'Type 1' of Handy, 1990). However, if the grains of the weak phase (mica) are interconnected rather than isolated, then strain can be partitioned into this network, dramatically increasing the role of micas in the deformation of the bulk aggregate (Wintsch *et al.*, 1995; Handy *et al.*, 1998; Hunter *et al.*, 2016). Such interconnection of mica and other types of weak phases actively develops during deformation under both viscous and brittle conditions (Holyoke and Tullis, 2006b, 2006a; Rutter *et al.*, 2013; Goncalves *et al.*, 2015). This leads to a dynamic syn-tectonic change from a LBF (Type 1 of Handy, 1990) microstructure to an IWL (Type 3 of

Handy, 1990) type system in mylonites, constituting significant strain weakening, or to a distinct reduction in friction within brittle fault gouges (Rutter *et al.*, 2013).

The strong structural and mechanical anisotropy of micas (Kronenberg, Kirby, *et al.*, 1990) can be translated up to a larger scale when micas are aligned into a shape preferred orientation within a specific fabric in a mica bearing rock, as often occurs under conditions of differential stress. Micas can form a variety of different fabrics depending on the stress field they are exposed to. A simple alignment can be produced by pure shear in compressive, extensional or even diagenetic environments (Shea and Kronenberg, 1993; Rawling, 2002; Wenk *et al.*, 2008). This may take the form of a primary foliation in which micas are rotated so that the long axis of each grain becomes perpendicular to $\sigma_1$ and parallel to $\sigma_3$, or it could produce a secondary foliation such as a crenulation cleavage by folding an existing foliation under a different orientation of $\sigma_1$. Production of a single penetrative foliation such as this results in high levels of seismic anisotropy (Burke and Fountain, 1990; Lloyd *et al.*, 2009; Dempsey *et al.*, 2011). Conditions of simple shear however, can produce more complicated fabrics where micas become aligned in multiple orientations within mylonites or fault rocks (Dempsey *et al.*, 2011; Bolognesi and Bistacchi, 2016). An S-C fabric is often formed under such conditions, with the S and C surfaces defined by the basal planes of mica grains. The asymmetry produced by these CPOs can be used as a kinematic indicator for the mylonite or shear zone (Dempsey *et al.*, 2011). Lloyd et al. (2009) conducted seismic anisotropy studies on orthogneiss from the Himalayan Nanga Parbit Massif, which possessed a penetrative S-C fabric. They found that the presence of such a composite fabric served to reduce seismic anisotropy of the rock relative to samples with a single penetrative fabric. Mica content also had a significant effect on the results, with samples containing a higher concentration of micas recording higher levels of seismic anisotropy.

# 4. Methods

## 4.1. Introduction

This chapter details the techniques, and equipment used in this thesis. This includes techniques utilised in the field area along the CMB and Pogallo shear zones for mapping and sample collection; the equipment and methods used to prepare samples for analysis; the analytical instruments and techniques used to observe and measure sample microstructures; and the steps taken to process and interpret the data collected.

Samples were collected during three field seasons in the Val Grande and Val d'Ossola area in North Western Italy in 2016 and 2017. All scanning electron microscope (SEM) work, including electron backscatter diffraction (EBSD) analyses and energy dispersive spectroscopy (EDS), were carried out at the Electron Microscopy Laboratory (Liverpool Earth Sciences) using Camscan X500 CrystalProbe and Phillips XL30 SEMs. Transmission electron microscopy (TEM) was carried out at the University of Liverpool's Imaging Centre at Liverpool (ICaL) using JEOL 2000FX and JEOL 2100 FCs TEMs, the former operated by the author and the latter by Dr Karl Dawson who also operated a FEI Helios Nanolab™ 600 I DualBeam™ Ga ion focussed ion beam (FIB) SEM for TEM sample preparation purposes. Electron probe microanalysis (EPMA) was conducted using Cameca SX100 electron probe microanalysers at the Earth Science departments of the Open University (under the instruction of Dr Giulia Degli-Alessandrini) and the University of Manchester (under the instruction of Dr Jonathon Fellowes). Quantitative evaluation of minerals by scanning electron microscopy (QEMSCAN®) was performed by James Utely using a FEI WellSite Qemscan SEM at the University of Liverpool (Department of Earth Science). All mineral abbreviations used are based on the recommendations laid out by Siivola and Schmid, (2007).

## 4.2. Sampling

### 4.2.1. Field mapping and sampling strategy

The samples used in this thesis were collected from the CMB line and Pogallo line mylonites in NW Italy (see Chapter 1 section 1.3). In order to understand the larger tectonic picture and select samples from across the mylonite zones, the shear zones and spatial relationships were examined through geological mapping. Large scale reconnaissance mapping was conducted by crossing from the SdL to the IVZ and back again at multiple locations in order

to assess the width and structure of the shear zone and identify the best exposed sections for more detailed transects and sample collection. The field area for this study consists almost entirely of very steep and highly forested terrain, with outcrops very limited and difficult to locate. This means that most outcrops are relatively small and often not continuous across the shear zone. Two sites where exposure of the mylonites was fairly continuous across the trace of the CMB/Pogallo line were selected for more detailed transects across the shear zone. The locations of these transects were; 1) across the CMB line near Ornavasso from approximately 45°57'27" 8°25'16" (UTM 32 N 455141 5089488) to approximately 45°57'38" 8°24'59" (UTM 32 N 454778 5089831) and 2) across the Pogallo line along the footpath in Val Pogallo from approximately 46°01'26" 8°29'34" (UTM 32 N 460742 5096827) to approximately 46°01'30" 8°29'32" (UTM 32 N 460699 5096950) (Fig. 4.1) (see Chapter 7 section 7.4 for detailed description of these transects). At these sites, 1:1000 scale mapping was conducted, focussing predominantly on lithological composition, degree of strain and the presence of narrow high-strain shear zones. Base maps were produced using ESRI ArcMap software from topographic maps freely accessible via the Geoportale Piemonte. Previous geological mapping by Boriani *et al.*, (1988; 1995) was used to locate the best regions in which to conduct reconnaissance of the outcrop quality and exposure.

The thin section sample CMB5A, was collected by Dr Elisabetta Mariani for previous work but was used in this study due to its proximity to the studied areas and direct applicability as a mica-bearing mylonite from the CMB line. Oriented hand specimen samples were collected for this study from several locations along the shear zone during reconnaissance mapping in order to assess strain distribution and lithological variation. However, those used for detailed microstructural analyses were taken specifically from the two transects detailed above. Sampling along these transects was conducted with the aim of collecting a full picture of the variation across the shear zone with regard to both lithological composition and distribution of strain. In this way, as near as possible direct comparisons could be made between rocks of approximately the same composition but deformed to different extents and between rocks of different composition but within similar parts of the shear zone. This sampling was done also with consideration to the quality of the outcrop and the ability to collect as fresh a specimen as possible. Sampling permissions were not required but sampling strategy was conservative and care was taken not to damage outcrops unnecessarily. The hazardous nature of the terrain meant most outcrops were accessed on or a short distance from footpaths.

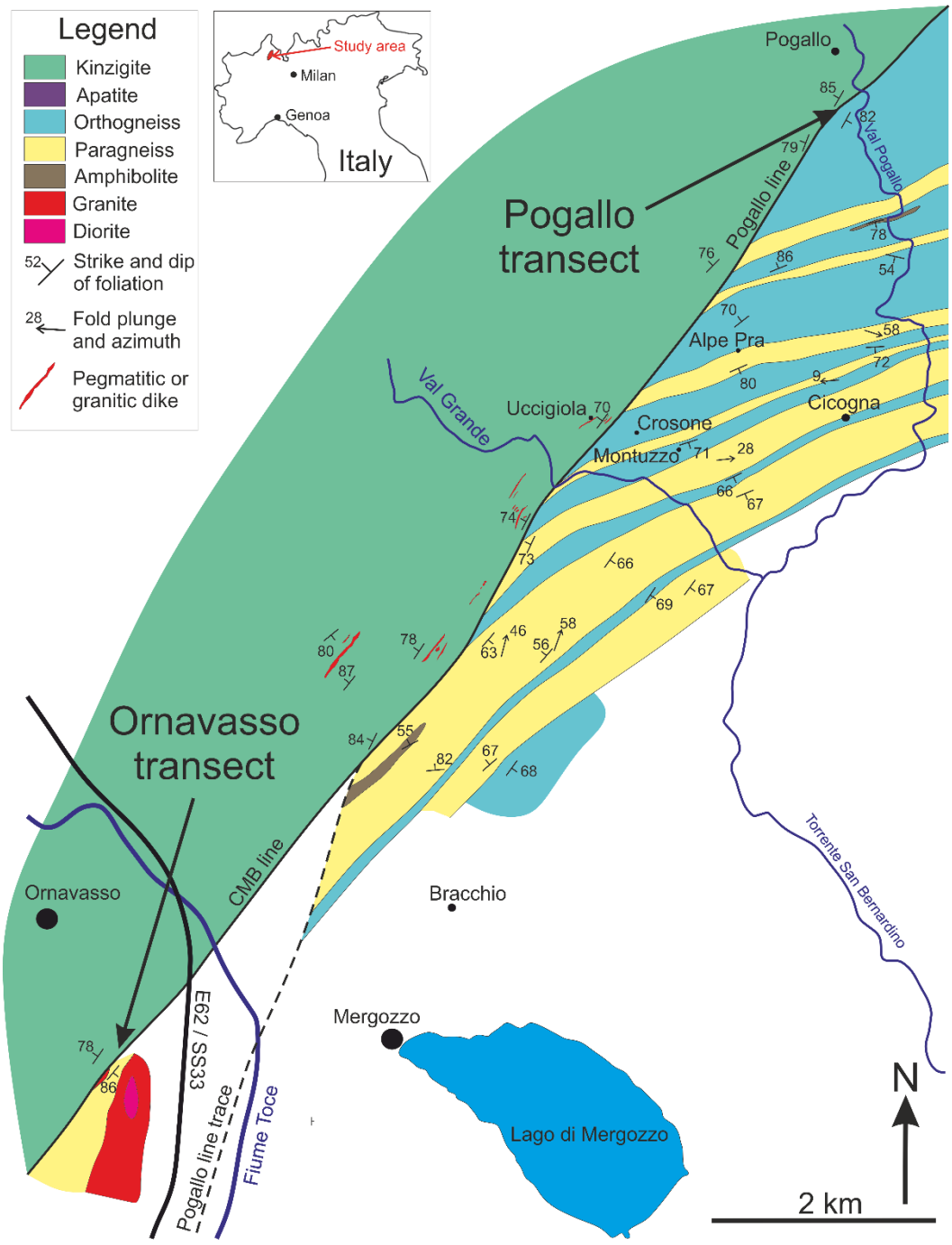


***Figure 4.1:*** *Geological map of the study area with the locations of the two transects where detailed mapping and sample collection took place.*

## 4.2.2. Sample preparation

Hand specimens collected in the field were cut at the University of Liverpool using a circular water-cooled rock saw, with the cut being made such that the plane was perpendicular to foliation and parallel to lineation, where lineation could be determined. Principal markers used to identify lineation direction were quartz rods and lineations on exposed foliation surfaces. Samples were then re-oriented using a plasticine base in order to measure the

orientation of the newly cut surfaces with respect to a geographical reference frame. The samples were cut in this orientation as it represents the principal kinematic surface, in which strain markers and deformation microstructures are best observed. Dempsey *et al.*, (2011) prepared mica-rich samples with surfaces parallel to foliation in order to improve polishing quality and increase the indexing potential during EBSD (see Section 4.4). However, for the work described in this thesis it was critical to examine the role (and abundance) of mica within each rock as well as the influence it has on other minerals, so cutting along individual mica-rich foliation planes would not have been suitable.

Thin section billets of approximately 2 cm x 1.5 cm x 0.5 cm were produced from the cut surface by selecting areas that were representative of the structure and composition of the whole hand specimen. These billets were then used to produce standard, polished, 30 µm thick petrographic thin sections by Paul Hands of Hands On Thin Sections Ltd. using standard thin section preparation techniques including water based polishing at progressively finer grit sizes. Samples were then prepared for EBSD work (which requires a very high-quality polish) by further polishing for 2 hours using SYTON in the Electron Microscopy Laboratory of the University of Liverpool Department of Earth Sciences. SYTON is a chemo-mechanical colloidal silica polishing fluid consisting of 0.005 µm to 0.006 µm particles suspended within an alkali solution. It minimises the thickness of the damaged or amorphous layer that is produced by conventional polishing, ensuring that undamaged crystalline material is present for analysis at the sample surface. Despite these efforts, the polish quality of micas, and particularly fine-grained micas, oriented with their basal planes perpendicular to the thin section surface, was far lower than that of quartz and feldspar in the same samples. This is a common but unfortunate occurrence when dealing with polyphase samples consisting of minerals with very different hardness. Polished thin section samples which were not collected specifically for this study but were lent by Dr Elisabetta Mariani were re-polished using standard mechanical polishing techniques. Water based polishing using silicon carbide grit of increasingly finer size was conducted at the electron microscope laboratories (Liverpool Earth Sciences) before SYTON polishing following the same technique as the other samples.

Before each fully polished sample was analysed inside an SEM, its edges were painted with carbon paint and a very thin layer of carbon (~5-15 nm thick) was deposited on top of the sample using an Emitech K950X carbon coater. This is a necessary step for analysing non-conducting samples within an SEM as the coat of carbon and the carbon paint contacts the sample holder and ensures the charge of electrons from the electron beam is carried away and not allowed to build up at the sample surface, distorting the images and data. EBSD

works best with the thinnest possible carbon coat sufficient to carry away the charge, as it enables the signal from the diffracted electrons to be stronger. This was therefore the aim when carbon coating in the majority of cases, however when samples were specifically prepared for phase mapping in the QEMSCAN (see section 4.3.3) a much thicker coat was applied as this is optimal for EDS measurements. Further specimen preparation was employed for TEM analysis and is detailed in section 4.6.2.

## 4.3. Scanning electron microscopy

### 4.3.1. The scanning electron microscope

Scanning electron microscopes are versatile instruments commonly used for the micro-scale analysis and characterisation of a wide range of materials and objects within geology, engineering, environmental science, biology and many other disciplines. They work fundamentally by detecting the interaction between a focussed beam of electrons and the atoms and structure of the sample surface. The electron beam is scanned in a raster pattern across the sample, collecting information in order to build up an image. They are able to operate with much greater resolution than optical microscopes as the wavelength of an electron is orders of magnitude smaller than the wavelength of a photon of the same energy, enabling the resolution of much finer details of a specimen (Trimby and Prior, 1999). The major components of an SEM are: a sample chamber, which is usually kept at high vacuum during operation to minimise the effect of atmospheric atoms interacting with the electron beam or the signal from the specimen; an electron column, which is typically positioned vertically above the sample chamber and serves to focus an electron beam generated by an electron source at the top; and the detectors which are mounted around the sample chamber in a configuration that can be customised to optimise the microscope for a particular purpose.

Several types of interaction occur when the electron beam reaches the sample surface. These occur within a small, approximately tear drop shaped, volume of the sample termed the interaction volume which defines the depth to which primary electrons originating in the electron beam can penetrate the sample with enough energy to induce an interaction. This volume varies based on the type of interaction and the ability of the signal produced to leave the sample and reach a detector. Secondary electrons (SE) are generated when electrons from the primary electron beam eject electrons from the outer shells of atoms in the sample. These secondary electrons have very low energies so only those from the upper few nm of the sample are able to leave the sample and reach the detectors. As a result, the intensity of

secondary electrons is strongly influenced by sample topography and this technique is regularly used to produce high magnification images of 3 dimensional specimens or to identify surface features. When secondary electrons are emitted from an inner shell, they induce an electron from an outer shell to drop into the vacant space. The resultant change in energy is expressed by the emission of X-rays with an energy equivalent to the difference between the two shells (Goodhew *et al.*, 2014). These characteristic X-rays form the basis of elemental analysis through energy dispersive spectroscopy (EDS) and wavelength dispersive spectroscopy (WDS). Occasionally, the energy from an electron moving shells can be released by the ejection of another electron from the atom, this is known as the Auger effect. Backscattered electrons, by contrast, are those originating from the primary beam whose trajectories are altered by elastic scattering from atoms in the sample such that they are reflected or scattered back, away from the sample surface. Such interactions are intensified if the sample material contains heavy elements with a high atomic number. These regions therefore appear brighter in a backscattered electron (BSE) image, which can be used for phase contrast and qualitative evaluation of compositional variation (Lloyd, 1987; Prior *et al.*, 1999; Trimby *et al.*, 2000; Wheeler *et al.*, 2001). Backscattered electrons are also useful for identifying crystallographic orientations using electron backscatter diffraction (EBSD) (Prior *et al.*, 1999, 2009).

### 4.3.2. The Phillips XL30 SEM

In this thesis, BSE imaging and EDS analysis was conducted using a Phillips XL30 tungsten filament SEM in the electron microscopy laboratories at the University of Liverpool, Department of Earth, Ocean and Ecological Sciences (Fig. 4.2). This instrument is a conventional SEM with a vertical column and a tungsten filament electron source. An adjustable stage enables the sample surface to be tilted up to 70° from horizontal. The instrument is equipped with SE, BSE and cathodoluminescence (CL) detectors for imaging purposes as well as an Oxford Instruments X-act 10 $mm^2$ silicon drift detector (SDD) for fast EDS compositional analysis. The XL30 is also capable of acquiring crystallographic orientation data by means of a Nordlys EBSD detector, although for this project a more optimised instrument (the Camscan X500 described in section 4.4.2) was used for this purpose. Typical operating conditions for the XL30 were an accelerating voltage of 20 kV, a beam current of 43-44 nA and a spot size of 5 nm.

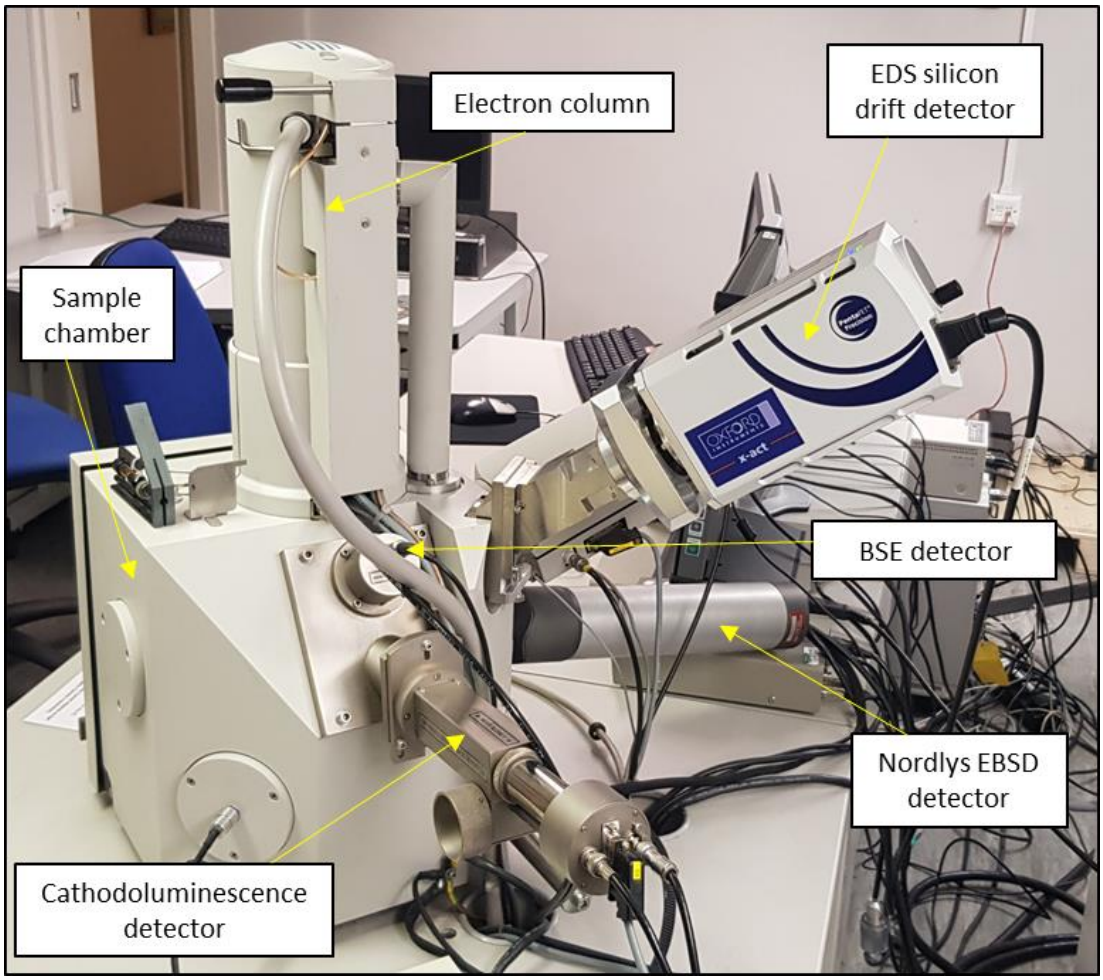


**Figure 4.2:** Photograph of the Phillips XL30 SEM at the electron microscopy laboratory of the Department of Earth, Ocean and Ecological Sciences, University of Liverpool. The instrument uses a tungsten filament electron source located at the top of the electron column. The configuration for EBSD acquisition is that of most conventional SEMs, with the electron column vertical, the EBSD detector mounted 20° below horizontal and the specimen inside the sample chamber tilted at 70° towards the EBSD detector.

### 4.3.3. Energy dispersive X-ray spectroscopy and QEMSCAN® mapping

Energy dispersive X-ray spectroscopy (EDS or sometimes EDX) involves the detection of characteristic X-rays emitted from atoms when an electron moves from an outer shell to an inner shell as a result of interaction with an electron beam. Silicon drift EDS detectors (SDDs) measure electrical charge pulses across a surface of semiconducting silicon induced by an incident X-ray, which is proportional to the energy of that X-ray (Goodhew *et al.*, 2014). The frequency with which X-rays of different energies excite the detector can be plotted in a histogram to produce an EDS spectrum. As the X-ray energy is characteristic of the element it was generated from, the peaks on this spectrum hold information on the elements present and their relative abundance within the electron interaction volume. EDS can be used in combination with phase contrast BSE imaging to characterise the phases present and their

distribution within a sample by collecting EDS spectra from point analyses of each different phase. EDS element maps are generated by repeatedly scanning a sample region and defining each pixel on a scale of intensity of a particular element. This enables the spatial distribution of elements within a sample to be investigated.

The FEI quantitative evaluation of minerals by scanning electron microscopy (QEMSCAN®) system enables rapid phase mapping of Earth or engineering materials through the use of an optimised SEM equipped with multiple EDS detectors. The integrated iDiscover software package compares the measured spectrum of each pixel to a database of known mineral species and assigns each pixel a phase, producing a phase map of the scanned area of the specimen and phase statistics based on the abundance of each mineral at the sample surface. The QEMSCAN® system is useful for detailed or large-scale phase mapping and for visualisation of mineral distributions and spatial relationships. The instrument employed in this study was a FEI WellSite Qemscan SEM with a tungsten filament electron source and equipped with two Bruker light-element energy dispersive X-ray spectrometers facilitating EDS maps to be collected at a rate of c. 10 ms per pixel (Pirrie *et al.*, 2004). One limitation of the system, which was encountered during this study, was its inability to differentiate between mineral polymorphs such as the aluminosilicates: kyanite, sillimanite and andalusite, which have identical chemical composition but different crystal structures. As these phases rarely occur together in the same specimen, simple optical characterisation of the sample was employed to identify which phase was present.

## 4.4. Electron backscatter diffraction

### 4.4.1. Theory of EBSD

Electron backscatter diffraction (EBSD) is a now widely employed technique for the determination of crystallographic orientations within crystalline materials. The datasets produced can be used to quantify fabric strengths through the presence or lack of a crystallographic preferred orientation (CPO) and to analyse in detail the relationship between different grains across grain, subgrain or phase boundaries. As such, it has been applied to a wide range of Earth science applications within petrology, metamorphic geology, ice dynamics and particularly structural geology (Prior *et al.*, 2009, 2015). EBSD in the SEM relies on the diffraction of electrons from the incident beam as they interact with the lattice planes of a crystalline material, such that they satisfy Bragg's equation:

$$n\lambda = 2d\ sin\theta \tag{4.1}$$

where n is an integer, λ is the wavelength of the electron beam, d is the lattice spacing and θ is the angle of incidence. The geometry of this relationship is displayed in Figure 4.3a. The diffracted electrons are backscattered out of the interaction volume and into a detector. This produces a pair of wide-angle cones of diffracted electrons for each lattice plane (Fig. 4.3b). The projections of these cones intersect to form an electron backscatter diffraction pattern (EBSP) which is characteristic of the spacing and orientation of diffracting lattice planes. This pattern will appear different depending on the orientation of the source crystal with respect to the detector. Hence, information about both the phase type and its orientation can be gleaned from identifying, or 'indexing', these patterns. To produce the strongest signal, the optimal incidence angle of the electron beam relative to the sample surface is 20°, with the

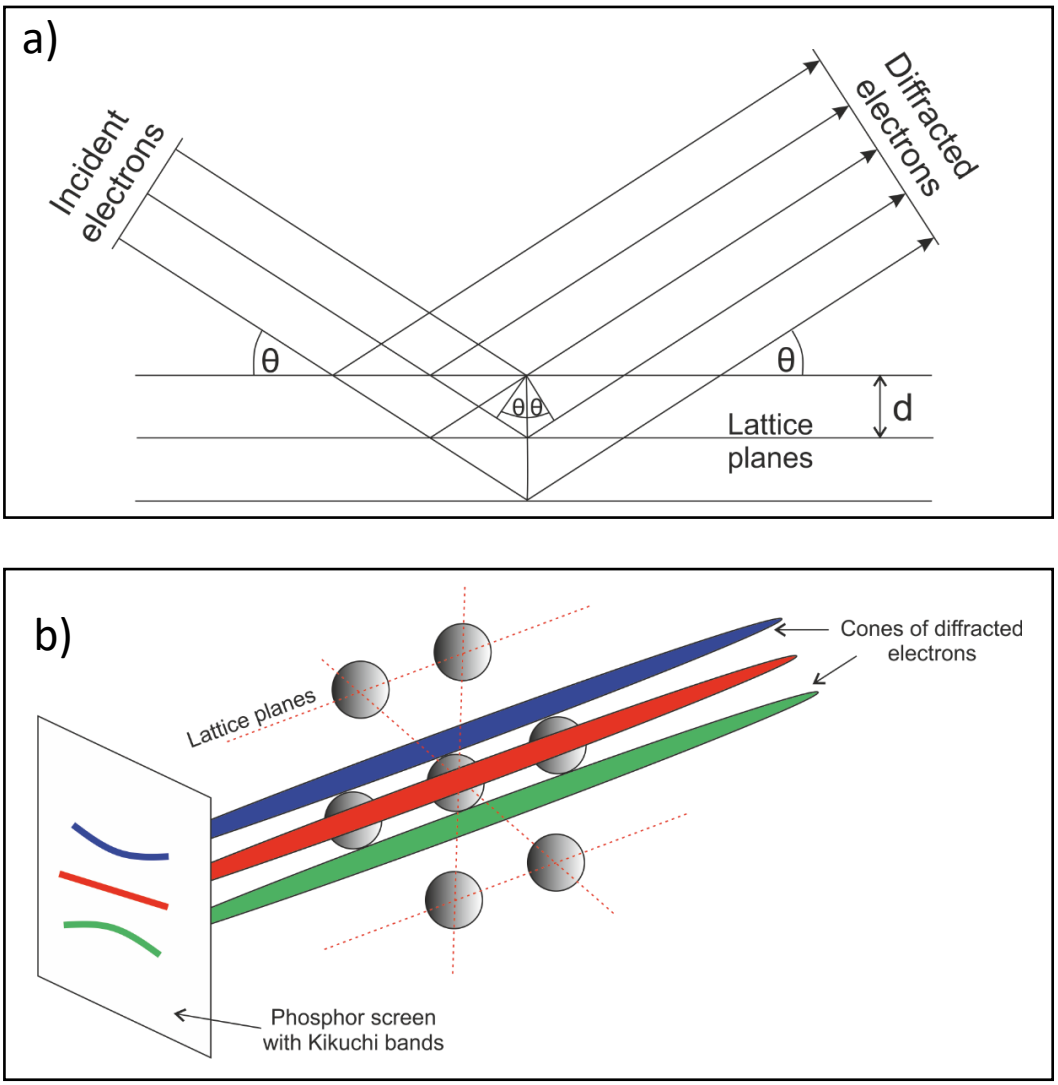


***Figure 4.3:*** *a) Sketch of the geometry of electron diffraction in a crystal lattice. b) Sketch showing the generation of an electron backscatter diffraction pattern (EBSP) on the phosphor screen of an EBSD detector. Wide-angle cones of diffracted electrons are produced by lattice planes in a crystal. These then form bands known as Kikuchi bands on the phosphor screen.*

detector mounted directly opposite the electron beam to catch forescattered electrons (Fig. 4.4a). This geometry is usually achieved by titling the specimen within the sample chamber and is necessary as it allows more diffracted electrons within the interaction volume to leave the sample surface, reach the detector and contribute to the signal. Most EBSD detectors work by receiving the diffracted electrons on a phosphor screen which fluoresces to display the diffraction pattern as an array of 'Kikuchi bands' which are the projections of the diffracted cones of electrons (Fig. 4.3b). Due to the low angle of these cones the bands appear as almost straight lines when they reach the detector. Low light charge couple device (CCD) cameras are generally then used to image the fluorescing phosphor screen, producing a digital version of the EBSP which can be indexed by dedicated EBSD acquisition software.

### 4.4.2. The Camscan X500 Crystal Probe SEM

All EBSD data as well as qualitative EDS analysis in this thesis was conducted using a Camscan X500 Crystal Probe field-emission gun (FEG) SEM located at the electron microscopy laboratories at the University of Liverpool (Department of Earth, Ocean and Ecological Sciences). The instrument was designed and built by Obducat Camscan Ltd and Professor David Prior with the purpose of optimising the acquisition of EBSD data from Earth and engineering materials. It is one of only two microscopes of this type in the world. The principal unique feature of the X500 is an electron gun column which is inclined at 70° from vertical (Fig. 4.4a). This enables the geometric requirements for optimal EBSD (20° electron beam incidence angle) to be met, whilst maintaining a horizontal sample surface. This greatly simplifies the design of advanced sample stages to enable in situ heating and deformation experiments within the SEM (Seward *et al.*, 2002, 2004). The geometry of the X500 also enables greater stage speed and accuracy in specimen positioning, relative to the vertical column and tilted specimen setup of conventional SEMs (Allen, 2017). In addition, the design of the X500 incorporates a large sample chamber which enables the analysis of large samples (up to 10 cm x 10 cm) and the separation of the chamber into a lower section, for the stage and specimen and an upper section in which the detectors are mounted (Fig. 4.4b). These sections are divided by a heatshield which prevents damage to the detectors when the heating stage is in use (Prior *et al.*, 1999; Seward *et al.*, 2002; Mariani and Ghassemieh, 2010) (Fig. 4.4 b, c). The electron source in the X500 is a thermionic field-emission warm cathode consisting of a single crystal tungsten tip coated with $ZrO_2$. This FEG source is superior to a tungsten filament in that it produces a highly focussed and more stable electron beam enabling greater resolution for imaging and data acquisition. The EBSD detector mounted on the instrument is a F+ Nordlys EBSD detector which utilises a 1344 x 1024 resolution CCD

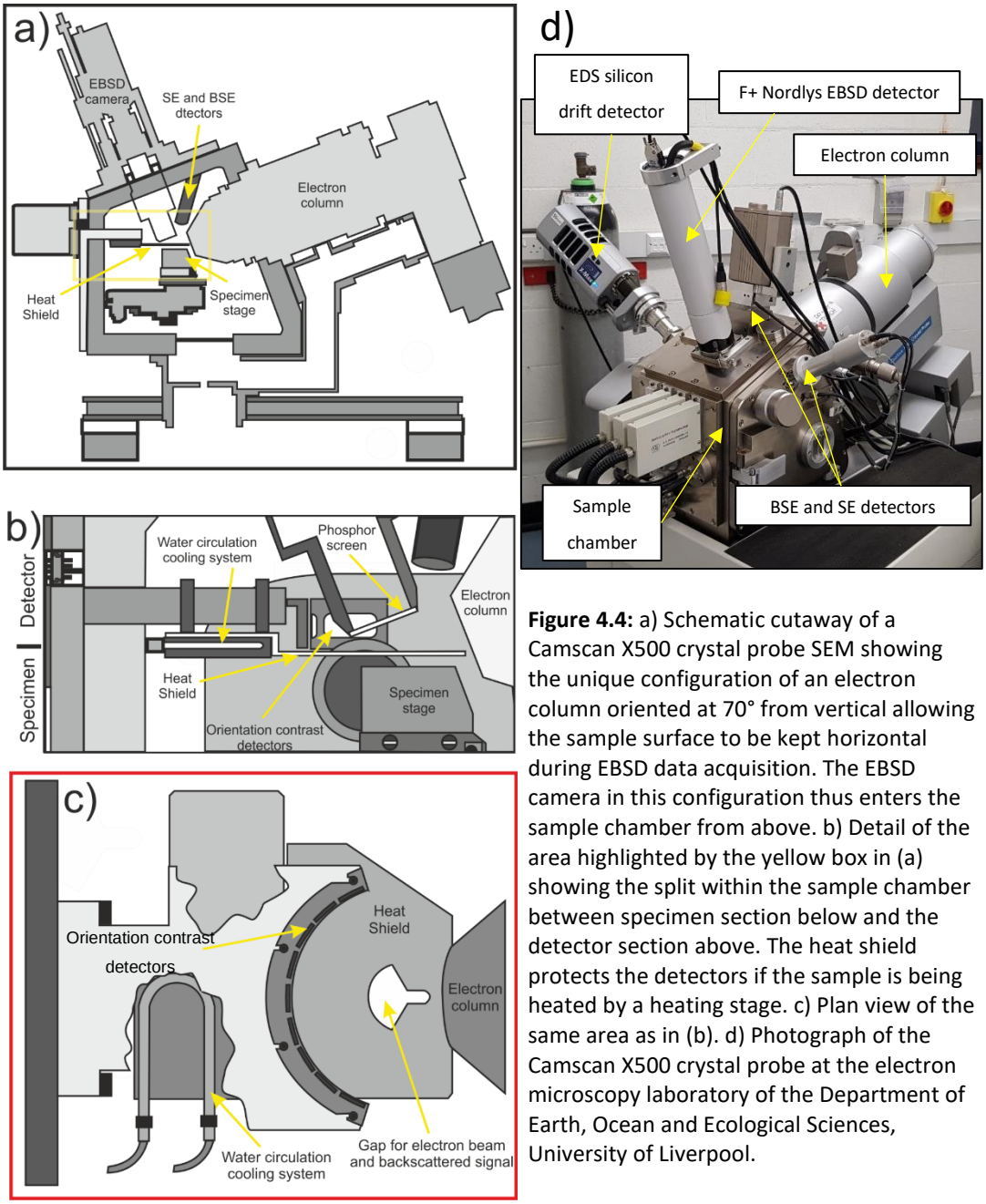


**Figure 4.4:** a) Schematic cutaway of a Camscan X500 crystal probe SEM showing the unique configuration of an electron column oriented at 70° from vertical allowing the sample surface to be kept horizontal during EBSD data acquisition. The EBSD camera in this configuration thus enters the sample chamber from above. b) Detail of the area highlighted by the yellow box in (a) showing the split within the sample chamber between specimen section below and the detector section above. The heat shield protects the detectors if the sample is being heated by a heating stage. c) Plan view of the same area as in (b). d) Photograph of the Camscan X500 crystal probe at the electron microscopy laboratory of the Department of Earth, Ocean and Ecological Sciences, University of Liverpool.

camera to image EBSPs captured on a phosphor screen, mounted in front. This detector is capable of EBSD analyses at rates of 600 points/sec or can work in parallel with a X-Max 50 mm silicon drift detector (SDD) (Fig. 4.4 d) to enable simultaneous EBSD and EDS acquisition at rates of 400 points/sec. Throughout the work detailed in this thesis, simultaneous EBSD and EDS mapping was conducted under typical operating conditions of 20.00 kV accelerating voltage, 20-30 nA beam current and a spot size of 5.5 nm. Step sizes varied according to the grain size of the sample and the desired level of spatial resolution for each analysis. Other detectors mounted on the X500 are; an Everhart-Thornley SE detector, a K.E. Developments Ltd. solid-state BSE detector and nine further forward mounted solid-state BSE detectors

arrayed in an arc around the sample to facilitate detailed orientation contrast imaging to complement EBSD orientation data.

### 4.4.3. Visualisation of EBSD data

EBSD datasets in this thesis are visualised by means of several types of map and by pole figures. Maps of EBSD data are built up by rastering the beam across a user-defined area of the sample surface with steps of a chosen size, indexing and storing the data from each point. The data recorded in these maps can be colour-coded by phase, to give the spatial distribution of phases in that part of the sample (phase maps) or by crystallographic orientation in several different ways to display the crystallographic relationship within or between grains and domains.

The most commonly employed form of orientation map is an all Euler map, in which each data point is colour-coded according to its orientation with respect to the SEM reference frame and a set of angles called Euler angles. The three Euler angles are defined as $\phi 1$, $\Phi$ and $\phi 2$ and describe the three rotations required to 'rotate' the crystal from the SEM reference frame into its measured orientation. The Euler colour scale applies a base colour to each angle (red for $\phi 1$, green for $\Phi$ and blue for $\phi 2$) with the magnitude of each rotation defining the value for each colour, which are then combined to form a single RGB colour. This means that, for the most part, similar colours indicate similarly oriented lattices, allowing both a quantitative determination of the orientation and the capability for a qualitative assessment of orientation relationships in the map. However, if one or more Euler angle values reaches its maximum magnitude, then a so called 'wraparound effect' can produce two very different colours for two orientations that are very similar, producing speckling in grains where there is, in reality, little significant lattice distortion. Other indexing issues occur where the lattice of a crystal diffracts similarly in several different orientations due to the symmetry of that crystal system. An example of this 'systematic mis-indexing' is the presence of three different apparent orientations displayed within a single mica grain, each exactly 120° apart. In truth the grain may have the same orientation, but the pseudo-hexagonal symmetry of the mica crystal induces incorrect indexing in the software. This effect can usually be corrected during post processing by defining the likely angles at which mis-indexing could occur for each crystal system.

Many orientation maps in this thesis are displayed using an inverse pole figure (IPF) colour scheme to avoid these drawbacks. IPF colours work by assigning three colours (red, blue and green) to three corners of an inverse pole figure (which is a segment of a pole figure of

different size based on the crystal symmetry of the phase in question). A reference sample direction is then selected – the z or 001 direction for the maps in this thesis – and the colour of the grain in the map is assigned by the crystallographic direction in that grain which is parallel to the sample direction.

Chapter 8 of this thesis also makes use of texture component maps produced from EBSD orientation data. These maps assign a colour to each data point of a chosen phase based the magnitude of the misorientation of that point with respect to a reference orientation (in the cases in this thesis this is the centre of a porphyroclast). These maps are useful for highlighting small missorientations within grains or between parent grains and subtly misoriented subgrains.

Within this thesis, 3-dimensional orientation data is plotted in lower hemisphere equal area pole figures. These project given crystallographic directions, or the poles to given crystallographic planes, onto a sphere which is visualised as a circle with the outer edge representing the equator of the sphere and the area of the circle representing the lower hemisphere. In equal are projections such as these, a random distribution of crystal orientations results in a uniform distribution across the pole figure. Pole figures can be plotted to show individual data points or contoured to give a representation of variation in the density distribution. For this purpose, a statistical method known as the multiple of uniform distribution (MUD) is used. MUD values of 1 represent a random distribution, while MUD values greater than 1 indicate a non-random fabric or a CPO. MUD contouring must be interpreted carefully as each colour scale is calculated independently for each pole figure or set of pole figures from a data set, so pole figures from different data sets can only be qualitatively compared. Pole figures in this thesis were plotted using either the Mtex MatLab toolbox (Chapters 6 and 7) or HKL Channel 5 software (Chapter 8).

### 4.4.4. Acquisition software and techniques

Acquisition of EBSD data (and associated EDS element maps) was performed using the Oxford Instruments AZtec HKL® software package. In this thesis, samples selected for EBSD analysis were first analysed by optical microscopy (and in some cases SEM based analysis using the Phillips XL30) to characterise the mineralogy and identify sites of specific interest for focussed EBSD analyses. During acquisition, indexing was conducted automatically by comparing EBSPs to a database of phases which were selected based on the previously determined mineralogy of the sample. In some cases, accessory phases which were not identified in optical work or were present in very low abundances were not included in the list of

reference phases for EBSD indexing, and thus are represented as unindexed pixels in the corresponding datasets. Detailed, high resolution maps were collected over small areas at high magnifications and using small step sizes of down to 1 µm. Large area maps (approximately 10 mm x 5 mm but varying substantially between samples), used for the collection of representative orientation data, were acquired using the automation function in the AZtec software, whereby a grid of smaller area maps was scanned in sequence and then digitally stitched together to produce a single large dataset. Such maps typically used a step size of 5-20 µm and a magnification of 100 x although step size especially was varied according to the specimen grain size. Ideally, maps of even larger areas or full thin sections would have been collected to give the best representation of specimen fabric (especially within coarse-grained samples). However, during the course of this project the Camscan X500 Crystal Probe SEM suffered a recurring issue involving a loss of communication with the Aztec acquisition software, which made it impossible to set automated acquisitions for the long periods of time required for such large high-resolution maps. The large area maps which were collected and are reported in this thesis represent the largest automations which were achievable and cover regions selected to give the best representation of the overall thin section fabric, including several thousand grains of each phase of interest. Despite these steps to ensure the data are representative, it should be noted that this may not always be the case, particularly in coarse-grained samples.

In all cases, EDS data was acquired simultaneously with EBSD to produce element maps of the scanned area. Where indexing was poor due to the presence of two phases of similar structure but differing chemistry (such as biotite and muscovite or K-feldspar and plagioclase) the TruPhase function was applied during the acquisition set up in Aztec. This requires the assignment of reference EDS spectra to each phase prior to EBSD analysis. During indexing the spectrum of each phase is compared to that collected at each point and the diffraction pattern is only indexed if the spectrum sufficiently matches the reference spectrum for the phase in question. Allowing EDS spectra to have an influence on phase ID reduces erroneous indexing of phases and improves the validity of the EBSD dataset generated.

Band contrast maps were also generated by comparing the clarity of EBSPs, determined by means of the Hough transform, which relates the average intensity of the Kikuchi bands to the overall intensity of the pattern, and plotting this in greyscale. Such maps are useful for highlighting grain boundaries (which appear dark due to poor indexing where two different phases or lattice orientations meet) and can be used to sub-sample poorly indexed data points during data-cleaning procedures. Band contrast maps collected in this thesis clearly

show how mica grains, and in particular fine mica grains, with their basal planes roughly perpendicular to the sample surface, return very poor quality EBSPs and as a result, contain a large proportion of unindexed pixels in EBSD maps. This issue is due to the difficulties associated with producing a high-quality polish on micas within polyphase samples in which they represent the softest phase. Some improvement in the surface quality is achieved in larger grains, or those with basal planes oriented approximately parallel to the sample surface. This is reflected in a higher proportion of correctly indexed pixels. Grain boundaries are regions were indexing is always poor as the signal received is a mixture of diffracted electrons from two different grains. This means that fine-grained aggregates will usually have lower proportions of indexed pixels than course-grained areas, although this can be improved by increasing the resolution of the acquisition through a reduction in the step size.

### 4.4.5. Post-acquisition processing

EBSD data can contain erroneous pixels associated with incorrect or incomplete indexing of EBSPs. Such erroneous data, if left un-processed, can lead to the misrepresentation of grain boundaries, spurious misorientation analyses and the visualisation of artefacts that have no bearing on the true microstructure of the specimen. In the case of the samples analysed in this study, poor indexing and mis-indexing were very significant problems and limited the applicability of some of the data sets (Fig. 4.5). Fine micas in particular, displayed very poor indexing potential due to the difficulties associated with producing a good polish on these softest phases within polyphase specimens.

The impacts of mis-indexing or poor indexing can be mitigated by 'cleaning' data during post-processing. Unindexed (or zero solution) pixels are filled by extrapolation of the surrounding orientations of 1 to 8 neighbouring pixels. Care must be taken to do this proportionately and to ensure that the new dataset is more representative of the true microstructure, not less so. If grains are allowed to expand into regions where they do not in reality exist in the sample, then the new dataset becomes less valid. The cleaning procedure utilised for all EBSD data in this study was applied using the Tango application of the Channel 5 software package. Firstly, band contrast maps were thresholded to remove pixels with the lowest band contrast. This corresponds to grain boundaries and regions of poor surface finish. The remaining pixels were then run through an initial zero solution algorithm using 7 neighbouring pixels which was iterated until no more solutions could be extrapolated in this way. This was then repeated using 5 neighbours. Finally, wild spikes (isolated measurements with mis-indexing) were replaced. Systematic mis-indexing is another issue that can arise in EBSD data (Fig. 4.5c-f). This is when the diffraction patterns of two or more orientations of the same crystal

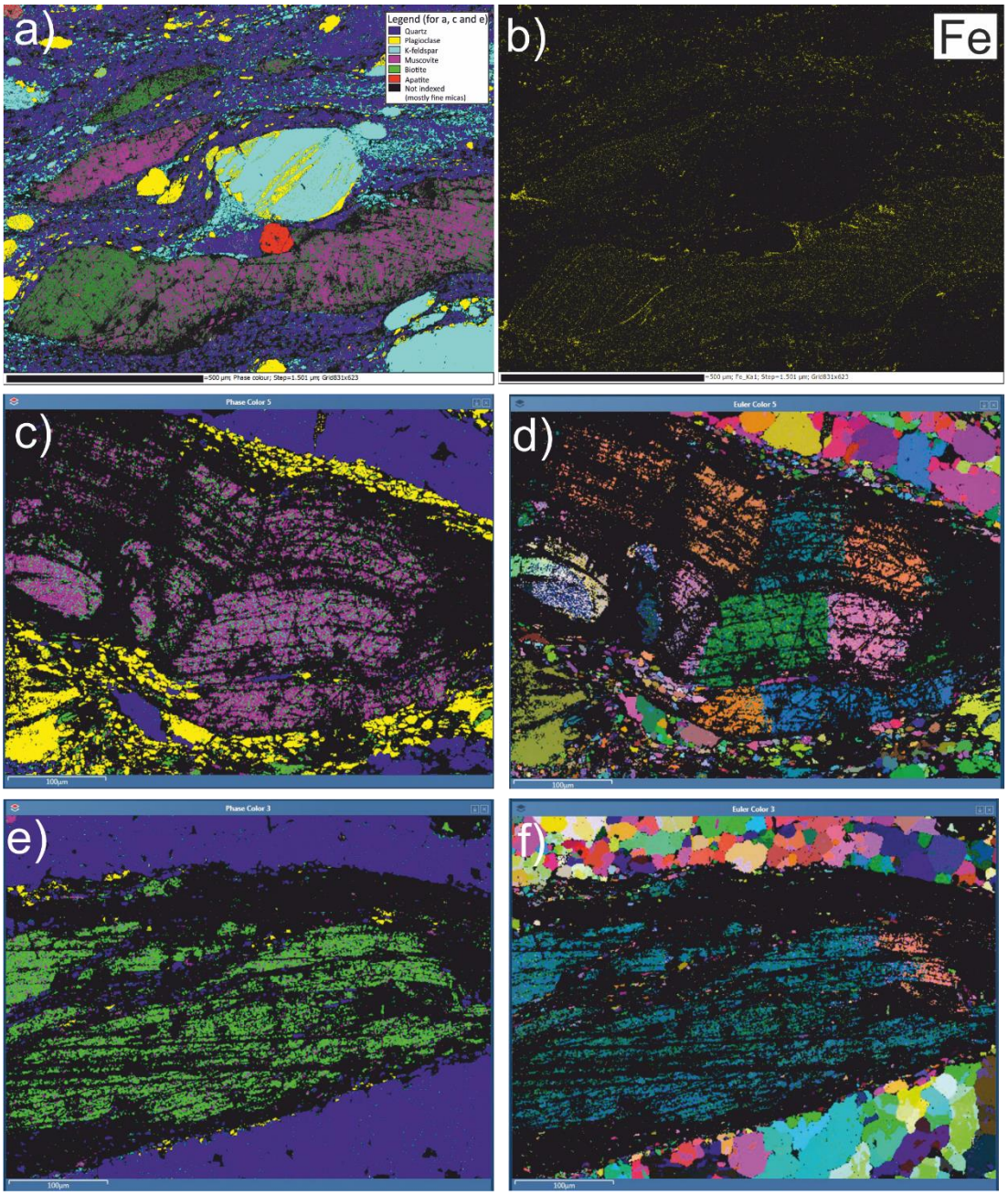


***Figure 4.5:*** *Selection of EBSD maps illustrating the issues associated with indexing mica minerals from samples POG3 (a and b) and POG22 (c,d,e and f). a) Phase colour map showing several muscovite (pink) grains which are partially mis-indexed as biotite (green) due to the similarity in the crystal structures of the two micas. b) EDS map of Fe from the same area as (a) showing that the mica is relatively low in Fe and is a muscovite grain. This image also shows that are abundant fine-grained micas within the matrix of this sample which are not indexed and show up black in (a). c) phase colour map of a muscovite grain which is partially mis-indexed as biotite but also very poorly indexed in general with a large amount of unindexed pixels particularly around its edges. The indexing quality stands in contrast to the good indexing of plagioclase (yellow) and quartz (blue). d) All Euler colour map of the same area as (c) showing that within the muscovite grain there are multiple segments with apparently very different orientations (different colours) due to systematic mis-indexing. e) Phase colour map of a biotite grain with poor indexing quality, especially at the edges of the grain where very fine biotite is present (see chapter 6 for discussion of the process with forms this). f) All Euler colour map of the same are as (e) displaying systematic mis-indexing within the biotite grain.*

appear very similar and are sometimes mistaken for one another by the program. These artefacts can be removed by identifying the angle-axis pair required to reorient the data to the true orientation of the crystal. However, in many cases within mica grains in this study, this was not possible as the extent of systematic mis-indexing was so great that the true orientation could not be reliably distinguished from the false one(s).

After each data set had been sufficiently cleaned, a grain list was calculated, also within the Tango application of Channel 5. Grain boundaries are defined where two neighbouring pixels belong to different phases or where they are mis-oriented with respect to one another by 10° or more. Twinning is a true intragranular misorientation which should not be corrected against (as this would replace correct data with incorrect data) but must be accounted for when defining the boundaries of grains. For this purpose, known common twin laws within the phases of the sample were defined as misorientations across which no grain boundary should be interpreted, despite misorientations in excess of 10°.

### 4.4.6. Transmission Kikuchi diffraction

Transmission Kikuchi diffraction (TKD), or transmission EBSD, is a SEM based EBSD technique which enables the acquisition of EBSD data at very high spatial resolution (Trimby, 2012; Jacob *et al.*, 2016). This is made possible by using electron transparent samples such as those prepared for transmission electron microscopy (see section 4.6) through which the focussed electron beam is transmitted, with the diffraction patterns collected on the other side of the sample. The ultrathin sample allows the electrons to pass through, meaning that the activation volume from which the signal is returned is much smaller than in traditional EBSD of a thick sample surface (essentially just the width of the electron probe). This allows very fine grains to be analysed without interference from grain boundaries or other nearby grains. Unlike in regular EBSD, the sample surface does not need to be held at 20° with respect to the beam as the electrons are transmitted so maximising the escape volume by tilting the specimen is not required. However, as in EBSD, it is very important in TKD to place the sample exactly at the focal point of the electron beam so as to maximise the signal and spatial resolution. It is also worth noting that, in TKD, the EBSPs collected are generated from the lower surface of the specimen, hence the sample must be fully ion polished on both sides. In a standard SEM with a vertical electron column, TKD requires a dedicated sample holder, designed for electron transparent specimens, which holds the sample horizontal under the beam and over a lower mounted EBSD detector. This was not possible in the CamScan X500 SEM at Liverpool due to the electron column being mounted at 70° from vertical and a stage that does not facilitate tilting. A bespoke sample holder was designed and built for this

project which could hold an electron transparent specimen with its surface perpendicular to the electron beam and allowing transmitted diffracted electrons to be captured by the EBSD detector behind (Fig. 4.6). Unfortunately, due to geometric issues inside the sample chamber, chiefly the presence of the heat shield blocking vertical movement of the sample holder, the specimen could not be placed at the optimum working distance for the electron beam focal point, prohibiting the collection of useful diffraction patterns.

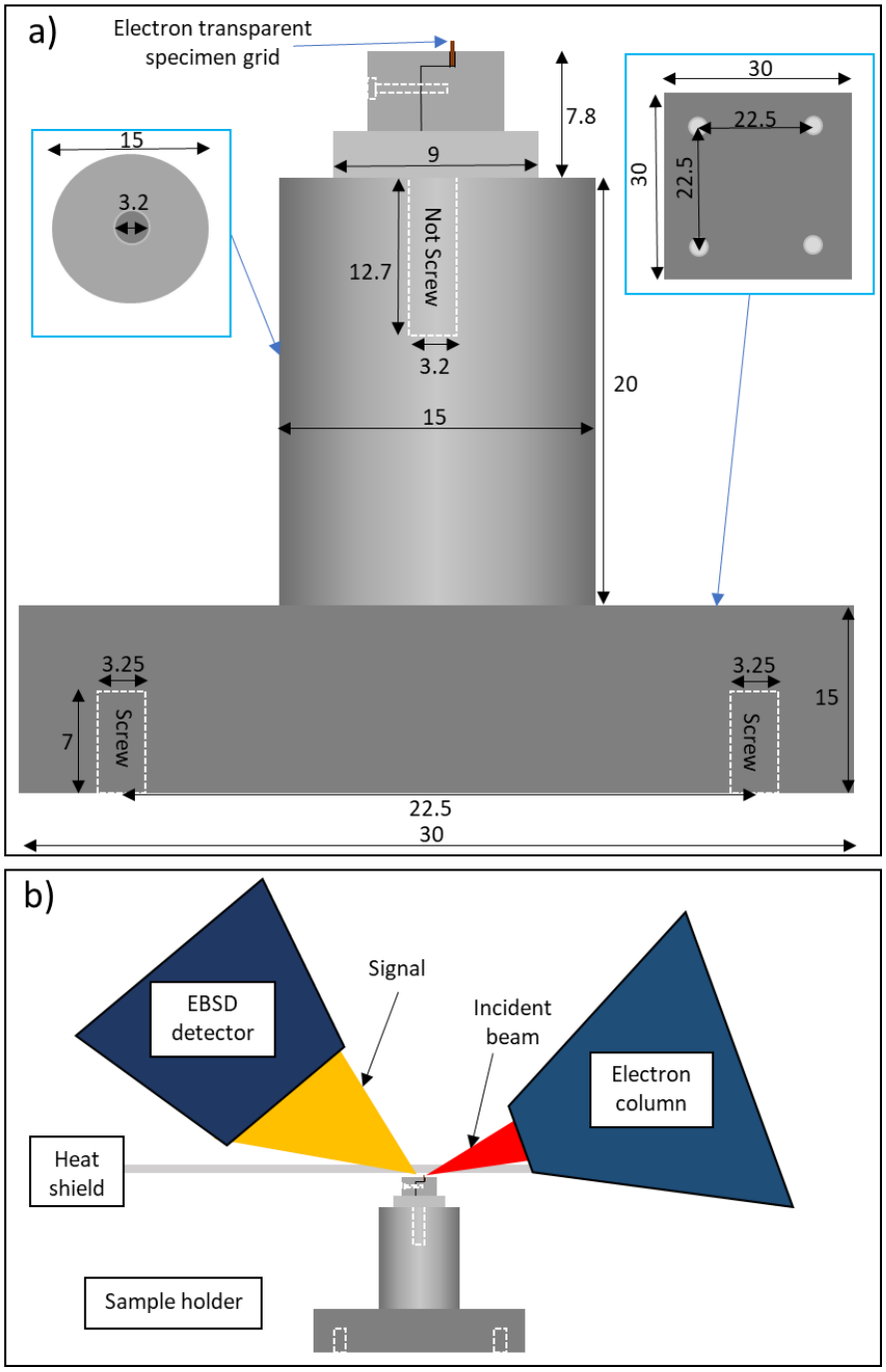


**Figure 4.6:** a) Design of the sample holder developed and built during this project to enable transmission Kikuchi diffraction (TKD) to be conducted on an electron transparent specimen using a Camscan X500 crystal probe SEM. The upper part is a 12.7 mm small FIB grid holder purchased from Agar Scientific. All measurements are in mm. b) The geometry within the sample chamber.

## 4.5. Electron probe microanalysis

### 4.5.1. The electron microprobe

Electron probe microanalysis (EPMA) enables the quantitative determination of chemical composition and elemental abundance within samples using a specially adapted SEM known as an electron probe microanalyser (or electron microprobe). The basic body of an electron microprobe is the same as that of a SEM but with several wavelength dispersive spectrometers (WDS) attached around the sample chamber. As the names suggest, WDS differentiates X-rays according to their wavelength whereas EDS does so according to their energy. The energy and wavelength of an X-ray are related by De Broglie's equation:

$$E = {}^{hc}/_{\lambda} \tag{4.2}$$

Where E is the energy, λ is the wavelength, h is Planck's constant ($6.626 \times 10^{-34}$Js) and c is the speed of light in a vacuum ($3.0 \times 10^{8}$ms$^{-1}$). As h and c are both constants this means that energy and wavelength are directly correlated, with an increase in energy corresponding to a decrease in wavelength and vice versa. EDS detectors measure the energy of each X-ray that they receive which produces a spectrum with peaks that correspond to each element. A WDS detector, by contrast, is tuned to determine the concentration of a single element at a time, requiring several detectors and/or several runs to scan a sample for all constituent elements but giving an order of magnitude better resolution for the purposes of quantification.

WDS detectors filter incoming X-rays using a diffraction crystal, which is simply a crystal (usually synthetic) with a perfectly defined lattice spacing. Incoming X-rays reflect off the lattice planes according to Bragg's equation:

$$n\lambda = 2d\ sin\theta \tag{4.3}$$

where n is an integer, λ is the wavelength, d is the lattice spacing and θ is the incidence angle. This means that when the distance between two lattice planes in line with the path of a reflected wave equals exactly a multiple of their wavelength, that particular wavelength will be amplified by constructive interference while all other wavelengths will be diminished. Changing the angle of the crystal relative to the incident X-rays changes the incidence angle (θ), enabling the filter to be tuned to amplify a chosen wavelength; that of the X-rays generated from a particular element. In practice, θ can only be varied between 10° and 70° meaning no single crystal has the range to cover all required wavelengths. As a result, most spectrometers contain 2 or 3 crystals with different d spacings, and most microprobes possess several spectrometers with different sets of crystals to ensure all major, minor and

some trace elements can be analysed for. The filtered X-rays then travel towards the detector, which must be placed at exactly the same angle and distance from the diffraction crystal as the source of the X-rays (the sample) as this is where the effective focus of the X-rays lies. This is a point on a circle which is equidistant from the diffraction crystal known as a Rowland circle. Several types of detector can be used to complete the spectrometer. The instruments used for this study employed the common gas flow proportional counter type whereby atoms of a gas within a chamber are ionised by incoming X-rays, producing ions and liberated electrons. This generates a current across the chamber (between an anode and a cathode) which is proportional to the energy of the X-ray.

### 4.5.2. EPMA Techniques

Two electron microprobe instruments were used to collect compositional data for this thesis, located at the School of Environment, Earth and Ecosystem Sciences at the Open University and at the School of Earth and Environmental Sciences at the University of Manchester. In both cases the instruments operated were Cameca SX100 electron probe microanalysers fitted with 5 WDS spectrometers (Fig. 4.7). A combination of standard lithium fluoride (LIF), pentaerythritol (PET) and thallium acid phthalate (TAP) crystals were used as the diffracting crystals as well as some large versions (LLIF, LPET, LTAP) where greater count values were desired due to expected low abundance of an element, or where this was the optimum setup for the instrument. On the instrument at Manchester, F was measured in addition to the other major elements, requiring the use of a PC0 crystal to enable light element analysis. The full setups for each instrument during analytical runs are detailed in Table 4.1 and Table 4.2. At the University of Manchester an accelerating voltage of 15 kV was used and a 15 µm de-focused beam to avoid damage to the beam sensitive micas, which were the target of EPMA analyses in all samples except for POG3 in which feldspars were analysed. At the Open University a 1 µm beam diameter was used in order to target finer grains with the accelerating voltage reduced to 10 kV to limit damage from the focussed beam. Monte Carlo simulations of the beam conditions used within a biotite substrate show the activation volume to be a region about 3 µm deep in the case of the 15 kV beam and 1.5 µm deep in the case of the 10 kV beam (Fig. 4.8). In both cases the interaction volume does not extend far beyond the beam diameter used. As the samples were cut perpendicular to foliation (and therefore perpendicular to most biotite basal planes), biotite grains that are greater than 15 µm at the surface can be reasonably assumed to extend beyond 3 µm into the sample. K was

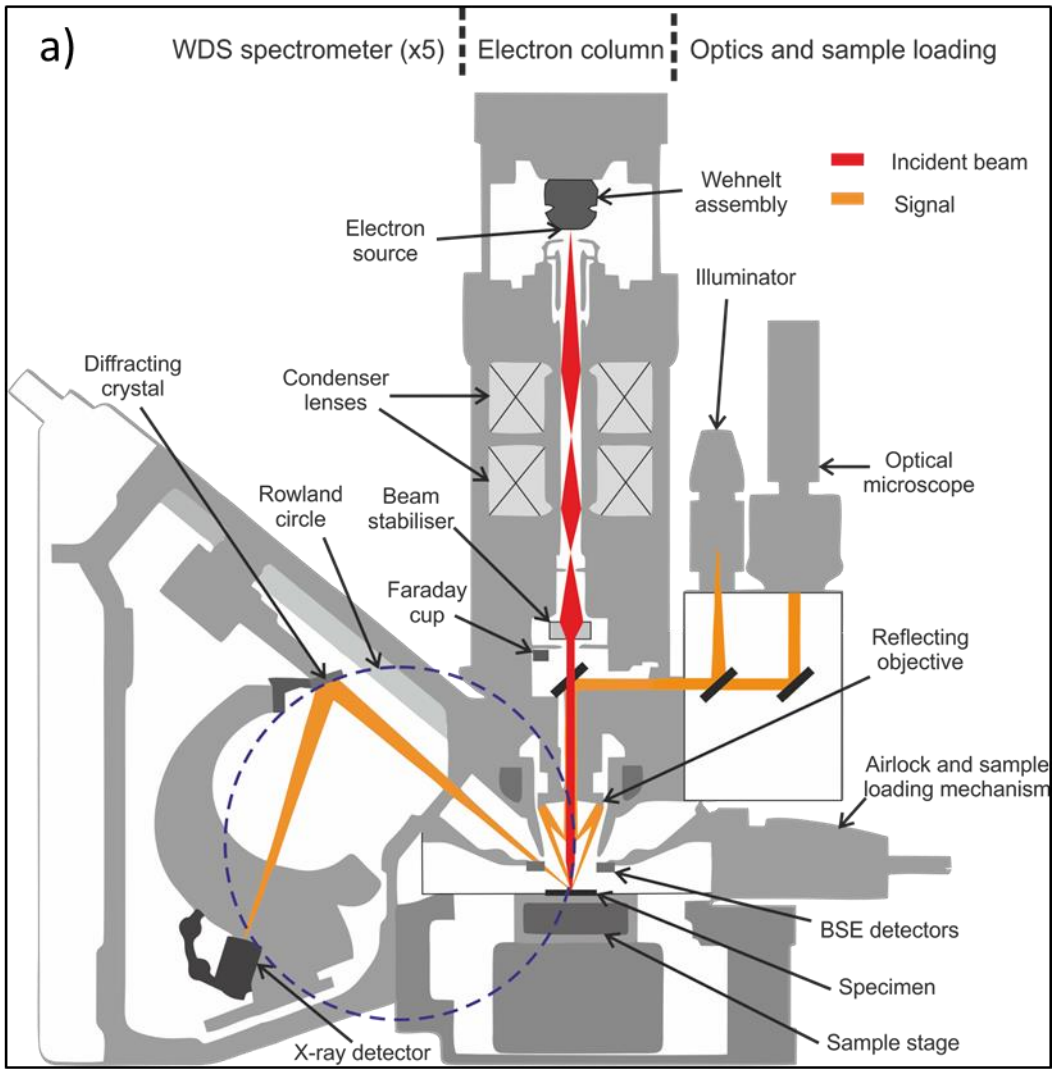


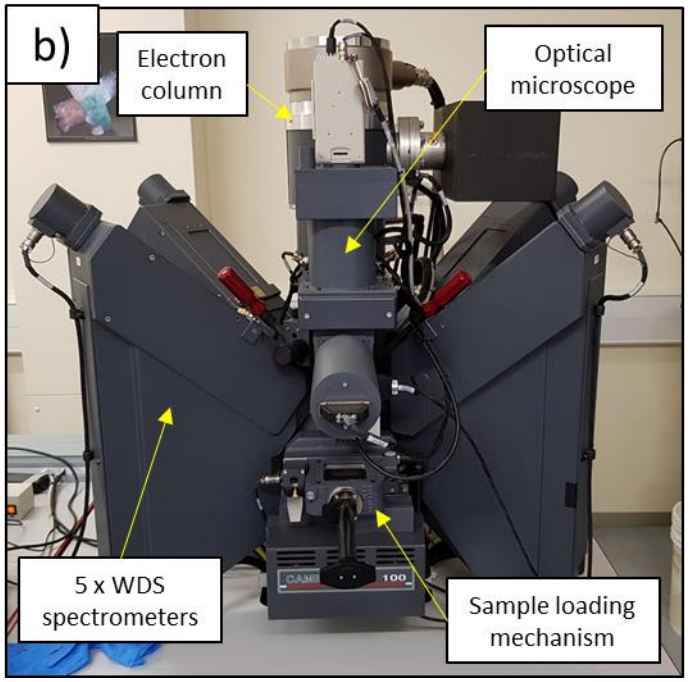


**Figure 4.7:** a) Schematic cutaway of a Cameca SX100 electron probe microanalyser including one of 5 WDS spectrometers. To satisfy the Bragg equation the point of incidence on the specimen surface, the diffracting crystal and the X-ray detector must all sit on the edge of an imaginary circle named the Rowland circle. b) Photograph of the Cameca SX100 electron probe microanalyser in the school of Environment, Earth and Ecosystem Sciences at the Open University.

*Table 4.1*

**OU Analysis parameters**
**Column Conditions: 10 keV, 10 nA. Beam size: 1 µm**

| Spectrometer | Element/Line | Crystal | Standard used | Peak Position | Hi-Off Position | Lo-Off Position | Bias | Gain | Dtime |
|---|---|---|---|---|---|---|---|---|---|
| 4 | K Ka | LPET | fspr-In5 | 42754 | 44054 | 41654 | 1859 | 824 | 3 |
| 3 | Fe Ka | LLIF | Haematite | 48061 | 51461 | 45561 | 1856 | 376 | 3 |
| 3 | Mn Ka | LLIF | Bustamite | 52179 | 55249 | 49179 | 1857 | 479 | 3 |
| 5 | Ca Ka | PET | Bustamite | 38386 | 40586 | 36811 | 1290 | 996 | 3 |
| 2 | Na Ka | LTAP | jad-BM4 | 46387 | 48687 | 44387 | 1290 | 2193 | 3 |
| 2 | Mg Ka | LTAP | for-BM4 | 38517 | 40817 | 35637 | 1290 | 2193 | 3 |
| 1 | Si Ka | TAP | fspr-In5 | 27735 | 29735 | 25235 | 1302 | 2359 | 3 |
| 1 | Al Ka | TAP | fspr-In5 | 32467 | 34447 | 29967 | 1290 | 2193 | 3 |
| 4 | Ti Ka | LPET | rut-BM4 | 31418 | 33918 | 30178 | 1867 | 1091 | 3 |

**Table 4.2**

**Manchester Analysis parameters**
**Column Conditions: 15 keV, 5 nA. Beam sise: 15 µm**

| Spectrometer | Element/Line | Crystal | OnPeak Time | Off Peak Time | Standard | Analytical Error(rel%) | Detection Limit(99%) | On-Peak Position | Hi-Off Position | Lo-Off Position | Baseline | Window | Gain | Bias | Inte/Diff | Dtime |
|---|---|---|---|---|---|---|---|---|---|---|---|---|---|---|---|---|
| 1 | Fe ka | LLIF | 20 | 20 | fay | 0.932734 | 0.051977 | 48039 | 48988.5 | 46911.6 | 0.5 | 3 | 380 | 1835 | DIFF | 3.3 |
| 2 | F ka | PC0 | 60 | 60 | flu | 6.58255 | 0.050744 | 39722 | 45611.2 | 32753.9 | 0.56 | 4 | 600 | 1490 | DIFF | 3.3 |
| 3 | K ka | LPET | 20 | 20 | ksp | 0.76034 | 0.015975 | 42752 | 43452 | 41922 | 0.75 | 3.7 | 800 | 1840 | DIFF | 3.3 |
| 4 | Al ka | TAP | 40 | 40 | ksp | 0.628666 | 0.015443 | 32453 | 34189.7 | 30648.4 | 0.93 | 3.22 | 2500 | 1320 | DIFF | 3.3 |
| 5 | Na ka | TAP | 20 | 20 | jad | 76.7691 | 0.032256 | 46428 | 47375.2 | 44747.7 | 1 | 3.5 | 2500 | 1300 | DIFF | 3.3 |
| 1 | Mn ka | LLIF | 40 | 40 | teph | 8.8456 | 0.03118 | 52146 | 52794.9 | 51497.1 | 0.5 | 3 | 380 | 1835 | DIFF | 3.3 |
| 3 | Ca ka | LPET | 20 | 20 | wol | -18.15 | 0.016141 | 38380 | 39104.3 | 37503.1 | 0.75 | 3.7 | 800 | 1840 | DIFF | 3.3 |
| 4 | Si ka | TAP | 20 | 20 | wol | 0.617187 | 0.02301 | 27733 | 28558.5 | 25687.2 | 1 | 3.5 | 2500 | 1320 | DIFF | 3.3 |
| 5 | Mg ka | TAP | 45 | 40 | per | 0.985591 | 0.015192 | 38572 | 39972.1 | 36790.2 | 1 | 4.02 | 2500 | 1300 | DIFF | 3.3 |
| 3 | Ti ka | LPET | 20 | 20 | rut | 1.74592 | 0.019815 | 31418 | 32431.9 | 30774.4 | 0.75 | 3.7 | 800 | 1840 | DIFF | 3.3 |

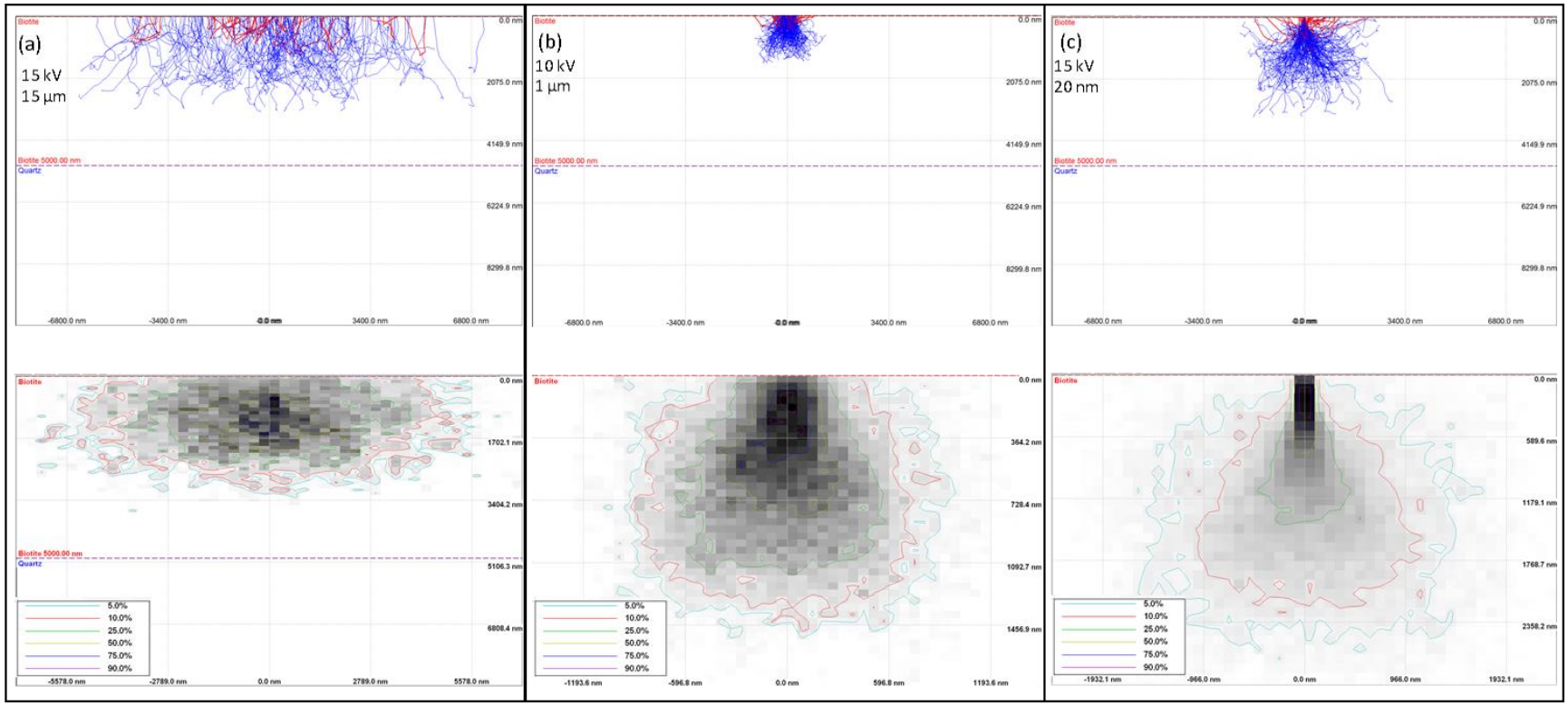


***Figure 4.8:*** *Monte Carlo simulations of the electron interaction volumes generated within a 5 µm thick biotite grain, showing a comparison between a defocussed 15 kV beam with a diameter of 15 µm (a), a focussed 10 kV beam with a diameter of 1 µm (b) and a very focused 15 kV beam with a diameter of 20 nm (c). In both cases with 15 kV beams the interaction volume reaches maximum depths of around 3 µm, while the lower energy 10 kV beam interacts with material within 1.5 µm of the surface. Interaction with a second phase therefore becomes an issue only if the target grain extends less than 3 µm below the sample surface (or less than 1.5 µm in the case of the 10 kV beam). The lower parts of each panel shows the contoured energy distribution of the respective simulation. In the case of the defocused beam the energy is distributed very widely, reducing the effects of beam damage, while in the more focused beams the increased spatial resolution is traded against very high energy concentrations which can accelerate beam damage and lead to erroneous results. (a) and (b) represent conditions employed in this study while (c) is a hypothetical extreme example.*

measured in all cases during the first pass of the beam in order to mitigate the effect of beam induced K diffusion, a well-established phenomenon in electron beam microanalysis (Van der Pluijm et al., 1988). The spectrometers were calibrated for each element prior to data acquisition by running analyses on standards with appropriate and known composition, held by the respective laboratories. Additionally, further standards were analysed intermittently between and during sample runs to identify and enable the correction of any instrument drift. Lists of the standards used, and their compositions are given in Table 4.3 and Table 4.4. Matrix corrections are required for quantitative EPMA in order to account for the effects of X-rays passing through the sample material before leaving the surface and reaching the detector. In this study, Phi-Rho-Z·f matrix corrections were applied to the raw WDS data using the PAP analytical model (Pouchou and Pichoir, 1991). These corrections were applied using the Probe for EPMA software package from Probe Software Inc.

***Table 4.3:*** *OU Standard Compositions*

| Standard name | Mineral | Composition |
|---|---|---|
| fspr-In5 | K-feldspar | Na : 0.85%, Al : 9.83%, Si : 30.1%, K : 12.39%, O : 46.03%, Ba : 0.73%, H : 0.01%, Rb : 0.03%, Sr : 0.03% |
| Haematite | Haematite | O : 30.06%, Mg : 0.03%, Al : 0.1%, V : 0.04%, Fe : 69.86% |
| Bustamite | Bustamite | O : 38.39%, Na : 0.04%, Mg : 0.13%, Al : 0.02%, Si : 22.46%, K : 0.05%, Ca : 13.56%, Mn : 18.83%, Fe : 6.32%, Zn : 0.2% |
| jad-BM4 | Jadeite | Al : 13.28%, Ca : 0.06%, Fe : 0.05%, Na : 11.2%, O : 47.64%, Si : 27.77% |
| for-BM4 | Forsterite | Ca : 0.04%, Fe : 14.64%, Mg : 25.52%, Mn : 0.14%, O : 41.33%, Si : 18.33% |
| rut-BM4 | Rutile | Ti : 59.95%, O : 40.05% |

***Table 4.4:*** *Manchester Standard Compositions*

| Standard name | Mineral | Composition |
|---|---|---|
| 28 (albite) | albite | O : 48.76%, Si : 32.1%, Al : 10.32%, Na : 8.71%, K : 0.11% |
| 46 (flu) | fluorite | Ca : 51.335%, F : 48.665% |
| 47 (jad) | jadeite | O : 47.49%, Si : 27.789%, Al : 13.348%, Na : 11.373% |
| 50 (cor) | corundum | Al : 52.926%, O : 47.074% |
| 52 (wol) | wollastonite | O : 41.22%, Ca : 34.12%, Si : 24.08%, Fe : 0.58% |
| 55 (rut) | rutile | Ti : 59.95%, O : 40.05% |
| 49 (per) | periclase | Mg : 60.311%, O : 39.689% |
| 54 (ksp) | K-feldspar | O : 45.8%, Si : 30.75%, K : 13.02%, Al : 9.32%, Na : 0.64%, Fe : 0.47% |
| 58 (teph) | tephrite | Mn : 54.405%, O : 31.688%, Si : 13.07% |
| 59 (fay) | fayalite | Fe : 54.812%, O : 31.405%, Si : 13.783% |

Element maps were produced at Manchester by analysing a grid of points within an area of the sample and visualising this on an intensity map for each element or oxide. The length of time for which each point is analysed is much shorter than during point analyses making this a less quantitative tool but very powerful for visualising spatial variations in composition. WDS element maps were input as bitmaps into imageJ, where the colour scales were optimised to reveal subtle compositional variation.

## 4.6. Transmission electron microscopy

All transmission electron microscopy work and sample preparation was performed at the University of Liverpool's Imaging Centre at Liverpool (ICaL) with the expertise and assistance of Dr Karl Dawson (University of Liverpool, ICaL).

### 4.6.1. The transmission electron microscope

Transmission electron microscopes (TEMs) are similar to SEMs in that they involve the targeting of an electron beam onto a sample and provide information about that sample based on its interaction with the beam. However, the fundamental difference is that TEM relies on the transmission of electrons through the sample rather than detecting signals reflected or diffracted back from the surface. In this way, a TEM is more similar to an optical microscope which utilises the transmission of photons through sample material before being viewed by the observer. TEM samples must therefore be prepared so as to be thin enough to achieve electron transparency. An advantage of the transmission of electrons rather than their backscattering or reflection is that the resolution of a TEM is limited only by the wavelength of the electrons whereas the signal received by the detectors of an SEM originates within an activation volume (Goodhew *et al.*, 2014).

In a TEM, an electron beam is generated at the top of the column by the electron source or electron gun. It is then focussed through a series of apertures and lenses until it reaches the specimen in the middle of the column. After this, the electrons which have been transmitted through the sample then pass through an objective lens, among others, which re-focusses these electrons to form an image. Sample material will diffract and scatter electrons in the beam, making sample material appear dark against a bright background where there is no sample and therefore no interaction with the electron beam. This type of imaging is called brightfield imaging (McLaren, 1991). Crystalline samples will diffract the beam differently depending on their lattice orientation with respect to the beam. In lattice resolution images, regions with a higher density of atoms (or a 'column' of atoms) will appear darker than those with a lower density of atoms, sometimes allowing individual lattice planes to be resolved,

as in the case of micas. Diffraction effects in a TEM also allow an assessment of the degree of crystallinity of a specimen and the generation of selected area diffraction (SAD) patterns which can be used to determine the lattice parameters of a crystal (Goodhew *et al.*, 2014).

Two different instruments were used for TEM analyses during the course of this thesis. Both were located at the ICaL facility. High magnification lattice resolution imaging and all scanning transmission electron microscopy (STEM) work was conducted using a CEOS GmbH "CESCOR" probe side aberration corrected JEOL 2100 FCs transmission electron microscope, operating at 200keV. The resolution offered by the microscope is 1.4Å using conventional TEM illumination and sub-Angstrom using aberration corrected STEM. Lower magnification imaging and chemical analysis of samples was conducted using a tungsten filament JEOL 2000FX TEM operating at 200keV and equipped with a liquid nitrogen cooled EDAX energy dispersive X-ray (EDX) detector. The 2100FCs instrument was operated by Dr Karl Dawson of ICaL while the 2000FX instrument was operated by the author.

### 4.6.2. TEM sample preparation

TEM samples must be prepared at a thickness that enables electron transparency in the specific material and must be very well polished on both sides as the electron beam passes across both surfaces. As a result, TEM samples undergo more extensive sample preparation procedures than other analytical samples. Most TEM sample preparation techniques utilise ion milling or polishing to reduce sample thickness and produce a very high-quality polish. The samples used in this thesis were prepared using two different techniques: Ar ion milling, and a Ga focussed ion beam.

#### *Ar ion milling*

Samples prepared using Ar ion milling were taken from 3 mm cores drilled into hand specimens. These cores were then encased in brass tubes to maintain rigidity and strength using Crystalbond adhesive and sliced into ~0.5 mm thick discs with a low powered diamond bladed saw. The discs were then reduced to a thickness of ~100 µm by polishing with 600 and 1200 grit papers on a water based automatic polisher and finished to a high quality using 2500 and 4000 grit papers on the same machine. The polished 100 µm thick discs were removed from their protective brass rings and cleaned of Crystalbond by immersion in acetone for several hours. Finally, selected discs were placed in a Gatan precision ion polishing system (PIPS) at ICaL and milled on the upper and lower faces with dual Ar ion beams until a perforation was formed within or bordering a biotite grain. The PIPS achieves a small central perforation by rotating the sample disc through two Ar ion beams directed at

a low angle to the upper and lower sample surfaces. Due to the angle, the region in the centre is usually milled fastest producing a central circular perforation with a gradually thickening rim around its edge. In the samples used in this study, heterogeneous mineral milling rates, due to the multiphase nature of the samples, complicated this process, with the initial perforation sometimes not occurring in a target biotite grain, meaning that further milling was required.

### *Ga focused ion beam*

Samples prepared using the focused ion beam (FIB) technique were produced either from standard polished petrographic thin sections, in which an area of interest was selected using optical and scanning electron microscopy, or from the polished surface of a disc prepared by the method detailed above but not thinned to 100 µm, and polished only on one side. The instrument used for the ion milling was a FEI Helios Nanolab™ 600 I DualBeam™ Ga ion FIB SEM at ICaL, utilising the ex-situ FIB lift out technique detailed by Giannuzzi *et al.*, (2005). This involves laying down a protective Pt strip across a region of interest on the sample surface (Fig. 4.9a), milling trenches either side of it with the focused Ga ion beam and then lifting out the cross section preserved under the Pt strip (Fig. 4.9b). This section is then secured to a copper sample holder using Pt deposition (Fig. 4.9c), further milled down to electron transparency and polished with a 5.00 kV low energy surface wipe to remove surface amorphisation features (Fig. 4.9d, e).

FIB sections produced from biotite grains and polymineralic rocks have a tendency to bend while undergoing thinning to electron transparency (Fig. 4.9f). The bending and flexing of samples once they reach thicknesses of under 1 µm (or sometimes even thicker) makes the process of thinning the whole specimen to the same degree very challenging and increases the risk of over thinning certain regions to produce specimens with holes and variable thicknesses. Bending of samples during FIB preparation is not uncommon and has been attributed to the accommodation of residual stresses in the sample or the differing physical and mechanical properties of phases in the case of polyphase materials (Gasser *et al.*, 2004). Despite this being a common problem, biotite and polyphase rocks appear to bend to an excessive degree and, as a result, the samples used in this study were usually not thinned across their entire length, leaving only a small electron transparent region available for study. All FIB sample preparation detailed in this thesis was conducted by Dr Karl Dawson of ICaL.

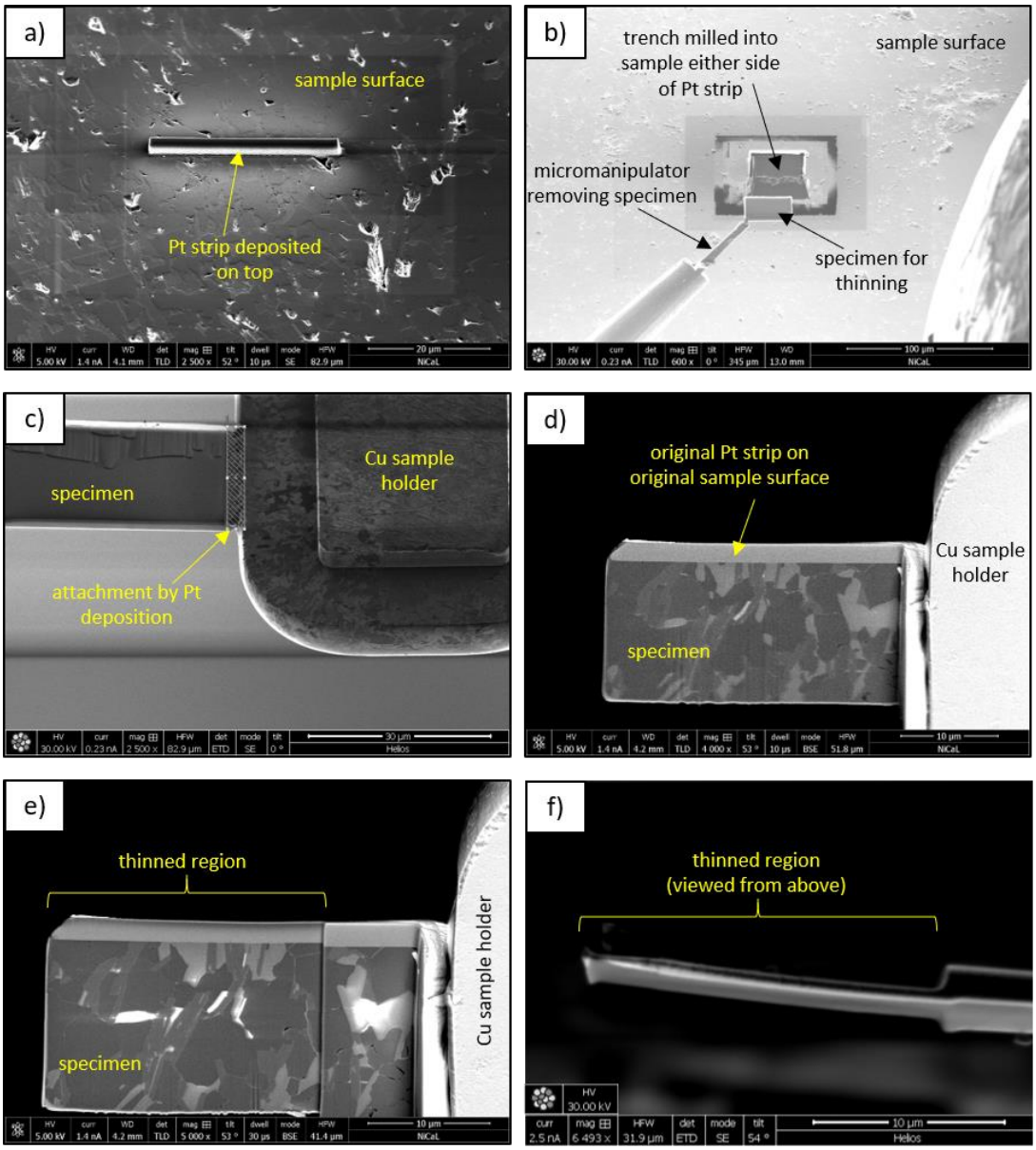


***Figure 4.9:*** *TEM sample preparation in the FIB SEM. a) SE image of a sample surface with a protective Pt strip deposited over the target site. b) Thin film being removed on a micromanipulator after Ga ion trenching either side of the protective strip. c) SE image of a thin film after attachment (by Pt deposition) to the copper sample holder. d) BSE image of a specimen prior to thinning, the lighter strip at the top is the initial protective Pt strip. e) BSE image of the same specimen during thinning, the section closest to the sample holder is kept thicker for stability. f) SE image of the top view of a specimen film showing excessive bending during thinning.*

## 4.6.3. TEM techniques

TEM work in this thesis was focused on analysing the intracrystalline structure and fine scale intergranular microstructure of biotite grains from the studied mylonite samples. Biotite is a beam sensitive species which is regularly observed to become amorphous when exposed to a focussed electron beam for extended periods of time. The composition of biotite can also be affected by beam exposure through the diffusion of $K^+$ cations (Van der Pluijm *et al.*, 1988).

To minimise these effects, once a sample had been loaded into the TEM, care was taken to avoid any unnecessary exposure of the sample to the electron beam. Beam alignment and initial focussing was conducted on regions at the edges of the foil which did not contain biotite. Low magnification sweeps of the sample were necessary in order to locate suitable biotite grains. These grains were then studied in more detail at higher magnification, with care being taken to note which regions had already been studied when moving back over the sample. Images were taken of regions of biotite grains which had only undergone minimal beam exposure from low magnification navigation around the sample. Focussing of the electron beam was carried out on different regions so as to avoid unnecessary exposure of target grains. All observations and images were carried out at 200 kV. Details of TEM based chemical analysis techniques are provided in Chapter 5 section 5.5.2.

# 5. Ripplocations provide a new mechanism for the deformation of phyllosilicates in the lithosphere

*Joe Aslin, Elisabetta Mariani, Karl Dawson and Michel Barsoum*
Published in the journal Nature Communications

## 5.1. Abstract

Deformation in Earth's lithosphere is localised in narrow, high-strain zones. Phyllosilicates, strongly anisotropic layered minerals, are abundant in these rocks where they accommodate much of the strain and play a significant role in inhibiting or triggering earthquakes. Until now it was understood that phyllosilicates could deform only by dislocation glide along layers and could not accommodate large strains without cracking and dilation. Here we show that a new class of atomic-scale defects known as ripplocations explain the development of layer-normal strain without brittle damage. We use high-resolution transmission electron microscopy (TEM) to resolve nano-scale bending characteristic of ripplocations in the phyllosilicate mineral biotite. We demonstrate that conjugate delamination arrays are the result of elastic strain energy release due to the accumulation of layer-normal strain in ripplocations. This work provides the missing mechanism necessary to understand phyllosilicate deformation with important rheological implications for phyllosilicate bearing seismogenic faults and subduction zones.

## 5.2. Introduction

Layered phyllosilicate minerals (or sheet silicates) include clays, serpentine and micas and are important constituents of Earth's lithosphere, occurring in a range of rock types and tectonic settings. Laboratory studies show that interconnected layers of phyllosilicates are weak (Wintsch *et al.*, 1995; Bos and Spiers, 2001), while in the field these minerals are observed to be ubiquitous in plate bounding faults and shear zones (Boulton *et al.*, 2012; Hunter *et al.*, 2016). Due to their weakness, phyllosilicates are recognised to localise deformation and their rheology has a strong influence on the nucleation and propagation of earthquakes in seismogenic faults (Collettini *et al.*, 2009; Faulkner *et al.*, 2011; Niemeijer, 2018) and on the dynamics of subduction zones and zones of shear in the viscous lower-crust (Dempsey *et al.*, 2011; Hunter *et al.*, 2016). The mechanical response of phyllosilicates is due primarily to the strongly layered, and therefore anisotropic structure of their crystal lattice. This consists of layers of silicon-oxygen tetrahedra (T) and octahedrally coordinated cations (M) referred to as TMT layers (Fig. 5.1). In micas and most clays these layers are bound

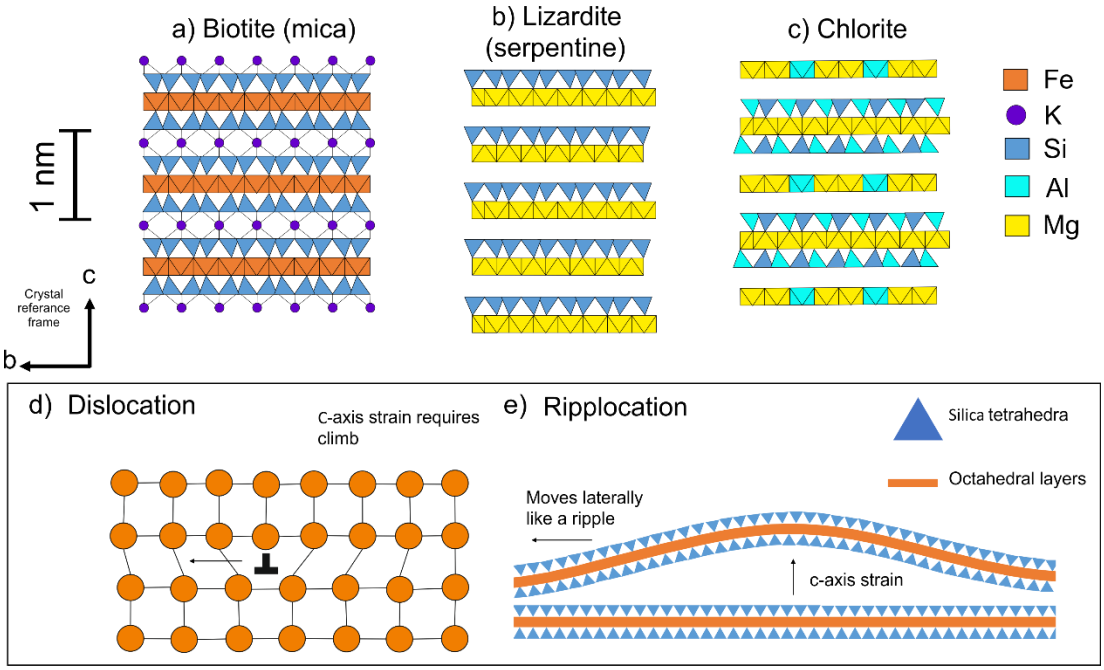


***Figure 5.1:*** *Phyllosilicate structures and ripplocation morphology. (a) – (c) Atomic structure models of some common phyllosilicates with valences identified by polygons. The indices of these polygons are occupied by O atoms or OH groups. (a) Biotite, like other micas, requires an interlayer cation (I) to balance the overall negative charge of its tetrahedral (T) and octahedral (M) layers. In the cases of biotite and muscovite this cation is predominantly K whereas in paragonite, and others, it is Na. (b) Lizardite, like the other serpentine minerals antigorite and chrysotile has a 1:1 ratio of T to M layers which possess a neutral charge resulting in no interlayer cations. (c) The structure of chlorite is similar to biotite except that the interlayer cations are replaced by individual octahedral layers, so called brucite like sheets. (d) and (e) Comparison between a dislocation (d) and a ripplocation in a generic phyllosilicate lattice (e). Both enable the movement of one plane of atoms over another. However, while dislocation climb is required to deform out of this plane in (d), ripplocations intrinsically contain an element of c-axis parallel strain due to bending and more crucially are attracted to each other rather than repelled.*

together by charge-balancing interlayer cations (such as K in biotite - Fig. 5.1a) and possess an overall negative charge. In serpentines and most chlorites tetrahedral-octahedral layers are linked by Van der Waals and hydrogen bonding and their charge is neutral (Fig. 5.1b and c). The layering described makes phyllosilicates particularly weak when sheared parallel to layers (the basal or 'c' planes) (Kronenberg, Kirby, *et al.*, 1990) and gives them a disproportionately large influence on the strength of the rocks in which they occur (Shea and Kronenberg, 1992, 1993; Holyoke and Tullis, 2006b; Mariani *et al.*, 2006; Hirth and Guillot, 2013; Hunter *et al.*, 2016).

Currently, viscous deformation in most minerals is understood to occur by the motion of defects called dislocations through a process known as dislocation creep. This process is a combination of dislocation glide, where the defects move along specific layers and directions in the crystal lattice (known as slip systems) and dislocation climb, or cross-slip whereby

dislocations are able to step between planes in a crystal lattice to avoid obstacles such as impurities. The strongly layered structure of phyllosilicates, however, limits dislocation glide to the basal plane with no facility for dislocation motion on other planes (Kronenberg, Kirby, *et al.*, 1990). As a result, dislocation creep is not a viable deformation mechanism in phyllosilicates and the means by which strain is accommodated parallel to the c-axis (perpendicular to the layering) remain ambiguous. In addition to this, the work of Noe and Veblen (Noe and Veblen, 1999a) questions the viability of dislocation defects within the (001) biotite interlayer (the cleavage plane) altogether, on the basis of energy considerations. These authors show that instead, basal dislocations are found only within the (001) oxygen layer between the octahedral and tetrahedral sheets, thus highlighting that it is a misconception to assume that cleavage planes are glide planes for dislocations.

In layered minerals kinking is observed to be the dominant process of shortening parallel to basal planes (Supp Fig. S5.1 and S5.2). However, kink bands cannot be explained using glide of basal dislocations alone. The most comprehensive models invoke the formation of complex arrays of dislocation walls at kink band boundaries (KBBs) which impart curvature of the lattice over a finite region (Etheridge *et al.*, 1973; Bell *et al.*, 1986). While these models determine basal slip as the primary mechanism for kinking, they recognise that another mechanism is necessary to account for the c-axis parallel strain required to form kink bands (Etheridge *et al.*, 1973) (KBs) (Supplementary Note 5.1). To date this c-axis strain has been explained through the brittle damage mechanisms of dilation or cleavage when basal glide is inhibited (Behrmann, 1984; Bell *et al.*, 1986). The importance of phyllosilicates with regard to the strength and dynamics of the lithosphere demands a proper understanding of their behaviour. Despite this, existing mechanisms fail to fully explain commonly observed structures and processes associated with phyllosilicate deformation, suggesting an important piece of the puzzle is missing.

Recently, a new fundamental defect type, named ripplocations, has been proposed which takes the form of atomic-scale ripples in the basal layer (Kushima *et al.*, 2015). They have so far been studied and modelled in $MoS_2$ (Kushima *et al.*, 2015), $Ti_3SiC_2$ (Gruber *et al.*, 2016; Griggs *et al.*, 2017) and graphite (Gruber *et al.*, 2016; Freiberg *et al.*, 2018) but are theoretically applicable to phyllosilicates and other layered solids (Barsoum and Tucker, 2017). Ripplocations have a similar effect to dislocations in that they allow the motion of one plane of atoms over another and may be more favourable in certain crystallographic directions (Kushima *et al.*, 2015; Fabbri *et al.*, 2016), but differ because they do not require the breaking and re-building of in-plane bonds (Figs. 5.1d and e) and result in an expanded

unit cell dimension normal to the weak layer. Another fundamental difference is that ripplocations attract each other and may merge, in contrast to same-sign dislocations, which repel and pile-up (Kushima *et al.*, 2015; Gruber *et al.*, 2016). Ripplocations on different layers are also capable of aligning to form a through-going bend in the lattice, i.e. a kink band boundary (KBB) (Gruber *et al.*, 2016; Barsoum and Tucker, 2017). Crucially, ripplocations involve a ripple in the basal layers, giving them a component of c-axis parallel strain that is absent in basal dislocations. They have been visualized in transmission electron microscope (TEM) observations of experimentally deformed $MoS_2$ (Kushima *et al.*, 2015) and $Ti_3SiC_2$ (Gruber *et al.*, 2016; Griggs *et al.*, 2017), while ripplocation behaviour has been tested through numerical modelling (Kushima *et al.*, 2015; Gruber *et al.*, 2016). However, prior to this study, ripplocations have not been reported in any naturally occurring mineral. The geological implications of the presence of ripplocations in phyllosilicates are substantial.

They provide a previously unrecognised mechanism to account for the geometric problems associated with deforming such anisotropic minerals. Phyllosilicates are increasingly seen as fundamental players in the localisation of strain in the lithosphere, with a controlling effect on the rheology of many crustal rocks (Dempsey *et al.*, 2011; Hunter *et al.*, 2016; Niemeijer, 2018). Our current understanding of the deformation of these important minerals is hindered by the lack of a mechanism for geometrically necessary c-axis strain. Ripplocation motion and their interactions may be that missing mechanism. In this study we use high resolution TEM to examine the nano-scale structure of naturally deformed biotite mica from a regional scale shear zone in the Ivrea-Verbano area of North-West Italy (Supplementary Note 5.2), and show that ripplocations are essential to account for the lattice bending and basal delaminations we observe.

## 5.3. Results

### 5.3.1. TEM observations of ripplocations in biotite

TEM samples were prepared using the focussed ion beam (FIB) in situ lift out technique (Giannuzzi and Stevie, 2005) (see methods). All biotite grains analysed contained regions of lattice expansion parallel to the basal plane, these were up to 0.2 µm in length and visible as bright streaks in brightfield images (Fig. 5.2 and Supp. Fig. 5.3). The width of biotite interlayers expands from 3 Å in the undisturbed lattice to up to 60 Å in the regions of greatest lattice expansion. The TMT layers by contrast remain at 7 Å width but form ripples deflecting around regions of lattice expansion (Fig. 5.3). Expanded regions, transitioning to delaminations in the brightest areas, are often asymmetrical, lozenge shaped and occur in

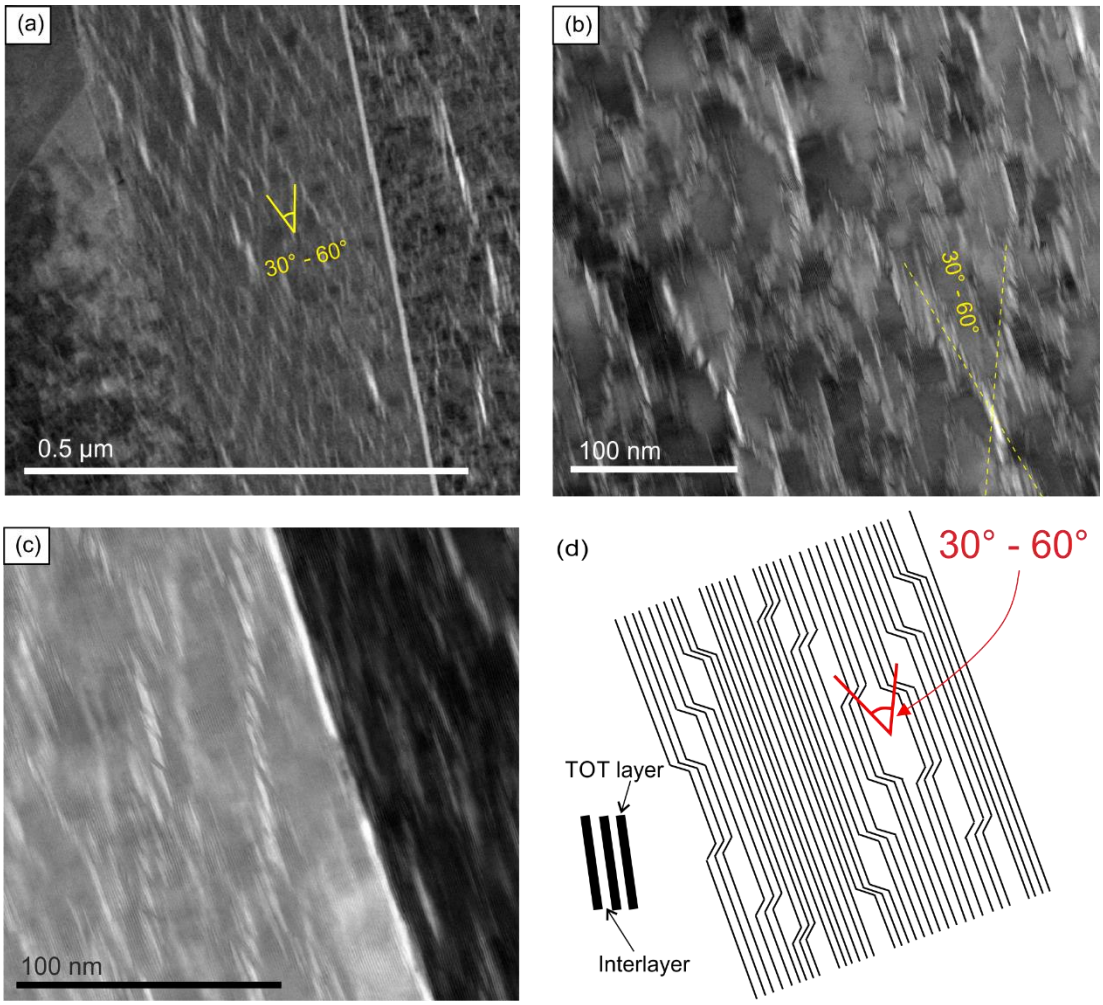


***Figure 5.2:*** *Diamond shaped expansion structure arrays. Brightfield TEM micrographs of FIB-prepared biotite specimens from mylonitic orthogneiss. (a) Bright streaks parallel to the basal plane, but stacked in two principle orientations, produce elongated, diamond-shaped arrays across the entirety of biotite grains. The acute angles of these diamonds measure between 30° and 60°. (b) At higher magnifications, these streaks are revealed to be up to 60 Å wide, lozenge-shaped lattice expansion (or delamination) structures of the biotite basal planes. (c) Detail of expansion structures/delaminations stacked in en-echelon arrays. (d) Schematic of the features observed in (a), (b) and (c) showing the en-echelon stacking of lozenge shaped expansion structures/delaminations offsetting TMT layers and producing diamond shaped arrays.*

en-echelon stacks, which are aligned in two principal directions, 30°-60° apart and bisected by the basal plane (Fig. 5.2a-d). This geometry produces an elongated diamond-shaped pattern across entire biotite grains (Fig. 5.2a, Supp. Fig. 5.4). Expansion structures have the appearance of waves (Fig. 5.3) and exist at multiple scales, from delamination of two TMT layers, along the interlayer, visible at the micron-scale, to ripples that increase interlayer distances at the nano-scale (arrows in Fig. 5.3a). Such large rotations of layers forming ripples are orders of magnitude greater than those which could be produced by individual

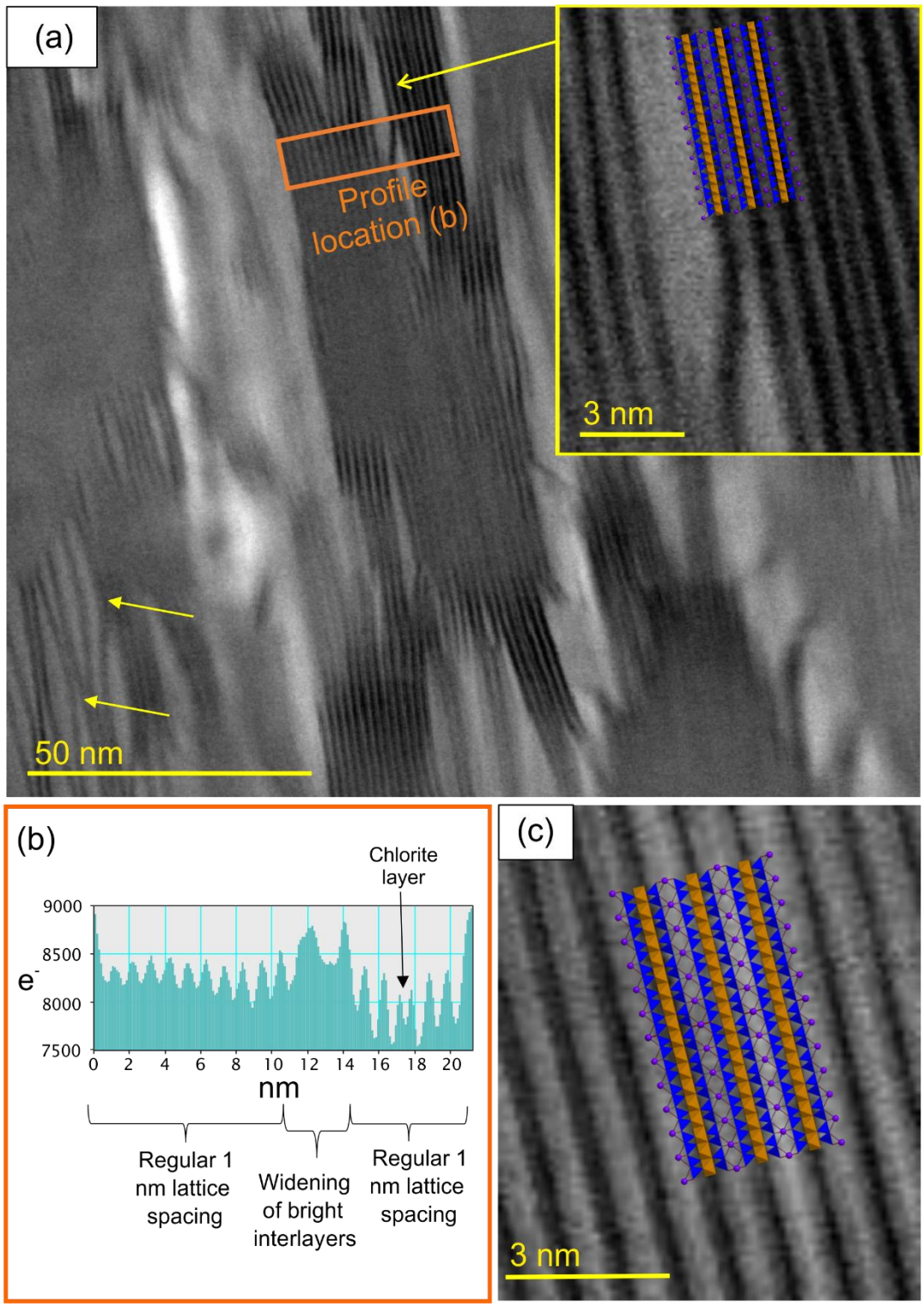


***Figure 5.3:*** *Lattice curvature and interlayer expansion. (a) Lattice curvature is visible at the scale of individual TMT layers which bend up to 30° within as little as 3 nm forming ripples (indicated by arrows in bottom left). Inset shows detail of the region indicated by the attached arrow overlain with a biotite atomic structure model showing how the lattice expansion occurs within the interlayer. (b) Profile integrated from the region defined in (a) showing a widening of brighter contrast interlayers within the regular 1 nm lattice spacing of pristine biotite. The double peak to the right represents an individual chlorite layer. (c) High magnification TEM lattice fringe image with biotite atomic structure model overlain. Dark regions centre on octahedral layers, intermediate (grey) regions show tetrahedral layers and light regions demonstrate the location of interlayers.*

dislocations or complex arrays of dislocation walls, which can result in bending of the (001) plane only within a broader finite region on the order of 1-2 µm (Etheridge *et al.*, 1973; Bell *et al.*, 1986). Bending of (001) within individual KBBs has been described on the scale of 40° in 0.2 µm (Bell *et al.*, 1986) and was interpreted to have been achieved by the rotation accumulated across numerous dislocation walls. However, we observe rotation of very low numbers of (or in some cases individual) biotite TMT layers on the order of 30° across just 3 or 4 nm (Fig. 5.3). According to the above studies, individual dislocation walls are capable of rotating (001) by up to 2°, this would mean our observations require around 15 individual dislocation walls within the space of 3 or 4 nm, a distance of less than 8 unit cells in the a direction and around 4 unit cells in the b direction. This degree of rotation cannot be physically accommodated by means of dislocation walls but can be explained by elastic bending of basal layers as in existing models of ripplocations (Kushima *et al.*, 2015; Gruber *et al.*, 2016). Profiles drawn across expansion structures concur that regular 10 Å spacings (the c-axis dimension of a biotite unit cell) increase, and that this expansion occurs within the interlayer regions (Fig. 5.3a, b and c).

Most previous studies on interlayer delaminations in phyllosilicates did not utilise the FIB sample preparation method but rather used ion milling systems which involve polishing until a perforation is produced in the centre of the sample (See Methods). Therefore, for direct comparison with previous work, and to eliminate the FIB method as a potential source of delamination structures, we also prepared foils from 3 samples using an Ar precision ion polishing system (PIPS). At the ultra-thin edges of the central perforation of PIPS specimens, voids could occasionally be seen to grow during observation. They often became much wider than delaminations in FIB specimens or within the thicker regions of PIPS samples and had lower aspect ratios. In contrast, thicker regions further away from the perforation edge contained smaller expansion structures and delaminations closely resembling those of the FIB specimens in size, aspect ratio and their arrangement in diamond-like arrays (Supplementary Figure 5). To examine the relationship between these arrays and the degree of strain a biotite grain has experienced, samples were prepared (using both FIB and PIPS methods) from undeformed Westerly granite (WG) specimens to be compared directly to those from mylonitic biotite described above and shown in Fig. 5.2 and Fig. 5.3 (Supplementary Table 5.1). Diamond-shaped arrays of expansion structures and delaminations were present in all the biotite samples analysed (Supplementary Figures 4-6) but were more clearly observed and more abundant in biotite from naturally deformed mylonite samples. Evidence for ripplocations in nominally undeformed granitic biotite is not

entirely surprising and might be linked to two possible causes: 1) Ripplocations are a form of crystal defect and might therefore develop during crystal growth, due for example to layer mismatch, much like the way growth-related lattice mismatch forms dislocations (Matthews and Blakeslee, 1974); 2) An undeformed granite, during intrusion through the Earth's crust, could develop local grain-scale differential stresses due to crystal impingement during growth or differential thermal expansion/contraction.

It must be noted that we did not observe kinking in biotite grains from Westerly granite, suggesting that, while ripplocations are present in this biotite, no motion or interaction of ripplocations have occurred. This observation may support the idea of ripplocations as growth defects (point 1). The evident increased abundance of lattice expansion and delaminations in biotite from mylonites is indicative of the intense deformation experienced by these rocks relative to granites.

The best explanation for the geometric arrangement of conjugate lattice expansion arrays we show in this study is an overall expansion parallel to the c-axis (perpendicular to the basal plane) of the biotite grain. The fact that the edges of these 'diamond' geometries are 30°-60° apart and are bisected by the basal plane is not a coincidence, it is a clue to the stress field in which these structures formed. The clear conceptual comparison is to conjugate normal faulting, which occurs under extensional stresses, where $\sigma_1$ is vertical and $\sigma_3$ is horizontal and parallel to extension (Fig. 5.4a). The acute angle between faults is commonly 60° but can vary and the effect on the rock mass is an extension perpendicular to the plane that bisects this angle (Anderson, 1951). In our diamond-shaped arrays, the bisecting plane is the basal plane and the extension (and $\sigma_3$) would therefore be parallel to the c-axis (Fig. 5.4b). These conjugate arrays are therefore likely to have formed during expansion parallel to the c-axis (normal to the basal planes).

Since, in order to achieve electron transparency, TEM specimens are exceptionally thin (< 100 nm) the possibility arises that the delaminations form to relieve stored c-axis strain once the grain becomes completely unconfined during thinning (Barsoum and Tucker, 2017). Basal dislocations are not a viable mechanism for storing this strain energy as they possess no component of c-axis strain. We propose that this c-axis strain could initially be stored in the form of bulk ripplocations, which originate from compression parallel to the basal planes (as a component of the overall stress field) and their strain energy is released to form conjugate arrays of expansion structures on thinning for TEM analysis. This interpretation is supported

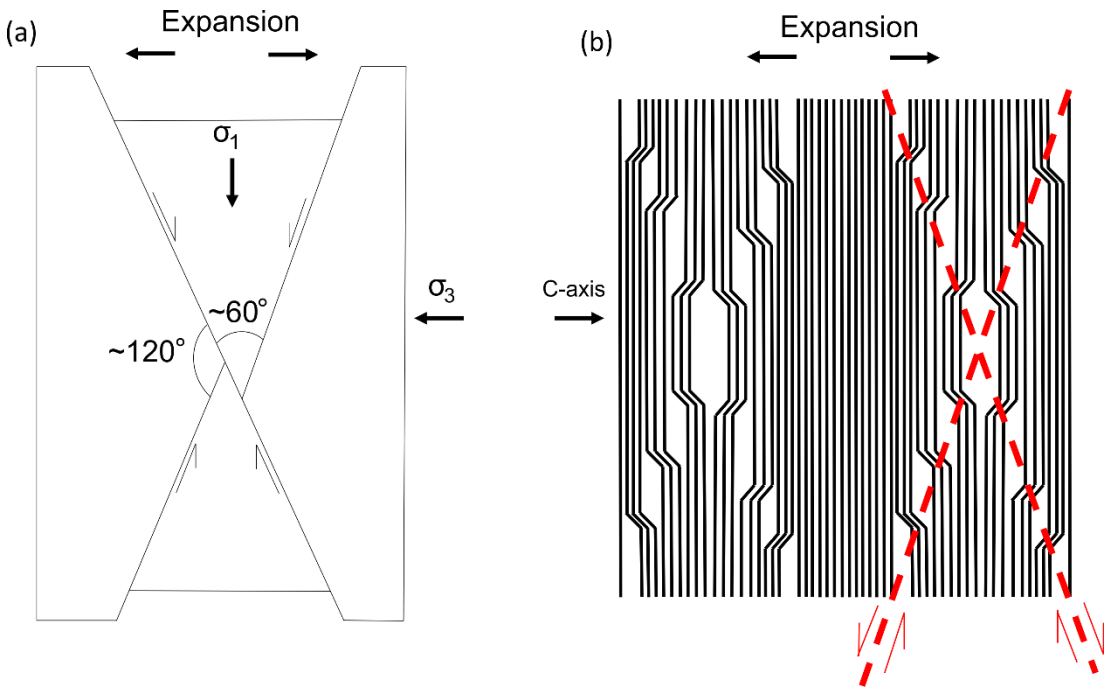


***Figure 5.4:*** *Formation of conjugate arrays of expansion structures. Analogy between (a) the Anderson model of conjugate faulting and (b) a schematic representation of the conjugate arrays of expansion structures and delaminations we observe in biotite. In both cases structures (faults in (a) expansion structures in (b)) form in two principal orientations which are up to 60° apart and display opposite shear sense. The obtuse angle between the two orientations is bisected by $\sigma_3$ in (a) and the c-axis in (b). In both cases this is the orientation along which expansion (or extension) occurs. In this way the diamond shaped expansional arrays are crystallographically controlled as is evidenced by the fact that they have different orientations in different grains, being always aligned with the c-axis of each grain. Conjugate delamination arrays represent the most efficient way to relieve stored grain-scale c-axis strain energy, just as conjugate normal faults result from extension on a larger scale. The orientations of principal stresses in this figure are therefore representative of the time when stored elastic strain energy is released (during thinning for TEM), not necessarily the time during which strain was being accumulated (deformation within the viscous shear zone).*

by substantial flexing of the TEM films observed during FIB preparation (Supp. Fig. S5.7), indicating elastic energy release.

Delaminations have been previously observed in TEM studies of deformed micas (Iijima and Zhu, 1982; Ahn *et al.*, 1986; Merriman *et al.*, 1990; Shau *et al.*, 1990) and attributed to electron beam damage (Ahn *et al.*, 1986). However, the extensive, ordered diamond-shaped arrays described here have not been reported before. To assess whether the structures seen are caused, or extenuated by beam damage, we analysed regions previously unexposed to the electron beam. The first evidence that abundant delaminations are not beam damage artefacts is the fact that they are visible at the outset of observations in the TEM and cover grains extensively and uniformly (Supp. Fig. S5.8a). Beam effects were observed during our experiments, but took the form of progressive mottling and amorphisation, eventually obscuring or destroying the lattice structure (Supp. Fig. S5.8a, b). Beam damage effects are

expected and observed to be localised to areas where the beam has been held and should not occur uniformly across a whole grain.

The principal mechanism previously provided for the formation of basal delaminations is the diffusion of alkali interlayer cations (Na in paragonite) due to beam exposure (Ahn *et al.*, 1986), with layer separations forming to counteract the resulting volume decrease. This was supported by a rapid decrease in the Na peak in sequential X-ray spectra of paragonite collected during progressive beam exposure. Interactions between alkali elements and an electron beam result in a depletion of the element's concentration at the sample surface and higher concentrations immediately below (Morgan VI and London, 1996; Humphreys *et al.*, 2006). This must be accounted for during electron microprobe analysis of geological materials (Craw, 1981; Van der Pluijm *et al.*, 1988). In our study, K is the interlayer cation in biotite, it is heavier than Na and, under the same beam conditions, is also less mobile due to its lower diffusivity (Humphreys *et al.*, 2006). Despite this, the delamination arrays we document are more extensive than those reported in paragonite (Fig. 1a of Ahn *et al.*, 1986) suggesting that diffusion of alkali cations may not be the cause. Energy dispersive X-ray (EDX) spectroscopy of our specimens in the TEM shows a decrease in K relative to Si over periods of up to 16 minutes, as could be expected from cation diffusion (Van der Pluijm *et al.*, 1988), however the rate of decrease slows over time and stabilises asymptotically around values of 0.33 K/Si (Supp. Figs. 5.8c, 5.9-5.13). This is in contrast to the rapid and near-total loss of Na in the paragonite analysed by Ahn and co-workers (Ahn *et al.*, 1986). In addition, in our observations K loss cannot be linked with a simultaneous nucleation or growth of delaminations because these are present before any K loss occurs. While the beam damage mechanism (Ahn *et al.*, 1986) does not therefore explain our structures, the delamination of basal planes must indeed have been driven by some degree of c-axis parallel strain. As basal dislocations cannot impart c-axis strain we propose ripplocations as the defects governing the observed (001) interlayer plane bending and associated expansion.

## 5.4. Discussion

Our model for the formation of conjugate expansional arrays is in agreement with numerical modelling of ripplocations in $Ti_3SiC_2$ and graphite (Gruber *et al.*, 2016), which suggests ripplocations, when confined, nucleate as multiple small ripples, but when unconfined, fewer, larger undulations are energetically favoured. This is analogous to the production of delaminations in our samples when the 'confinement' is removed during thinning. In other words, the energy of the ripplocations is unable to delaminate the layers around them until

the confining energy is sufficiently reduced. Multiple small ripplocations build up whilst the rock containing the biotite is experiencing differential stress (Fig. 5.5a-b). If these stresses continue, or increase, then eventually the ripplocations gain enough energy to overcome the constraining force (lithostatic pressure) and may migrate, interact or accumulate across layers to form KBBs, hence the kinking of phyllosilicates in deformed rocks (Fig. 5.5c). If the

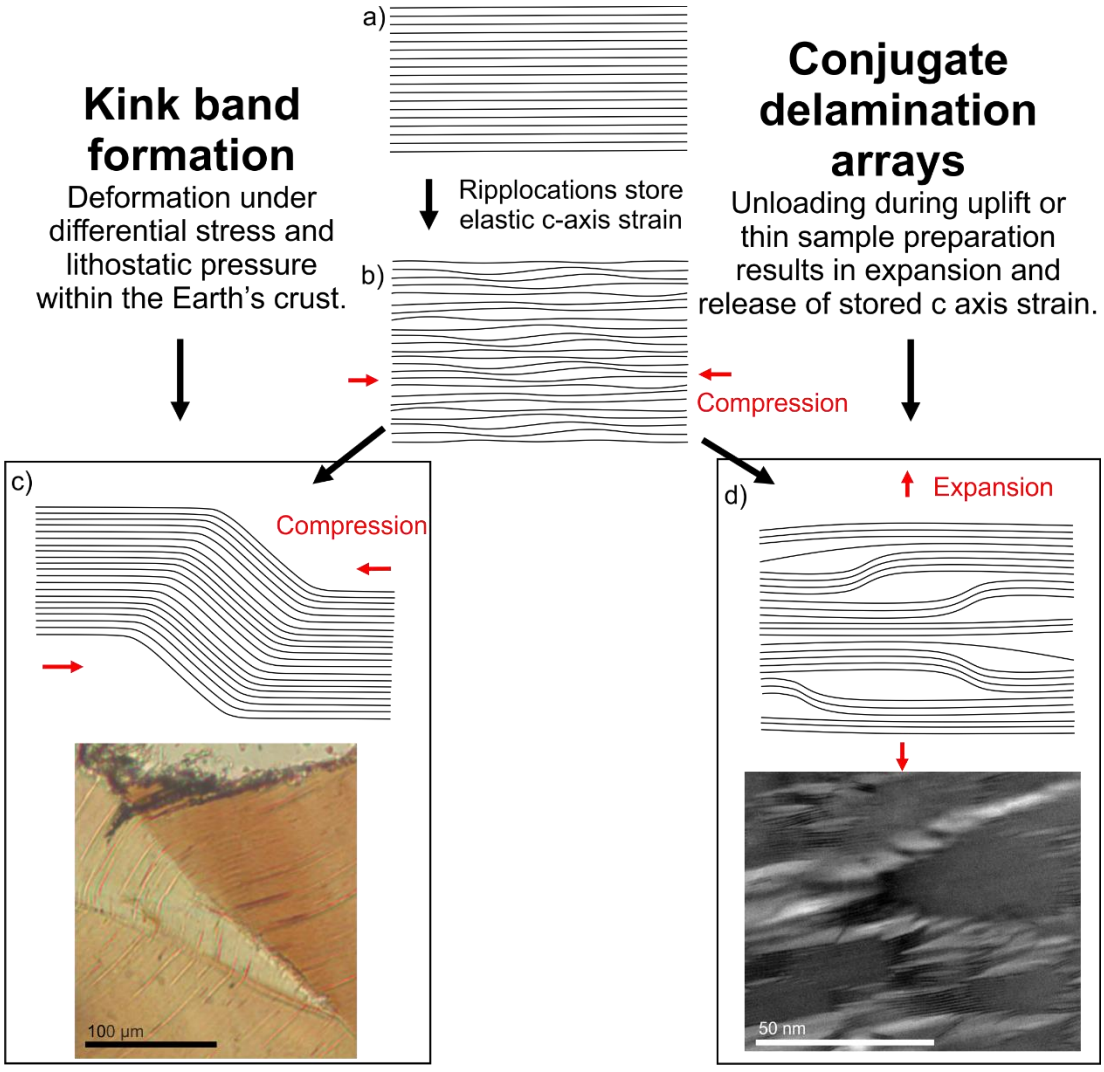


***Figure 5.5:*** *Conceptual model showing how ripplocations lead to kink bands or conjugate expansion structure arrays. A pristine undeformed biotite lattice (a) experiences differential stress with some component of compression parallel to the basal planes. As the lattice is confined this induces numerous small bulk ripplocations which store the resulting c-axis parallel strain energy (b). Continued basal plane parallel compression imparts enough energy for ripplocations on different layers to migrate and merge to form a kink band between two kink band boundaries of opposite sign (c). The elastic c-axis strain energy becomes permanent strain on the formation of mature through-going kink bands. This may produce the kinked microstructures common in micas from viscously deformed rocks. Parts of a biotite lattice that have experienced a stress field similar to (b) but in which kinking has not been induced still contain stored elastic c-axis strain energy in the form of ripplocations. This energy is released on thinning for TEM analysis in the form of conjugate arrays of expansion structures and delaminations which facilitate a grain-scale c-axis parallel expansion (d). This is represented by the structures shown in Fig. 5.2 of this study.*

ripplocations do not exceed the required energy to become mobile and form kinks, then they continue to store that strain energy until the confining energy is reduced, for example during TEM sample preparation. They then release c-axis strain energy with many small ripplocations on the same plane merging to produce fewer, larger expansion structures or delamination features which form in conjugate extensional arrays (Fig. 5.5d). Through this model, ripplocations provide the c-axis driving force necessary to produce the basal delaminations observed in our samples and reported in previous studies. The model also provides the c-axis strain necessary to explain the pressure sensitivity measured in phyllosilicate-rich rocks (whereby their yield strength increases proportionally to the applied lithostatic pressure) up to their dehydration temperature (Mariani *et al.*, 2006). In Phyllosilicates both viscous (dislocation glide) and brittle (cracks associated with kinking and dilation) deformation mechanisms are seen to occur through a large range of conditions in the Earth (from the Earth's surface to the middle and lower crust (Meike, 1989; Christoffersen and Kronenberg, 1993; Mares and Kronenberg, 1993; Mariani *et al.*, 2006)). In addition to this, while pressure sensitivity might traditionally be associated with brittle deformation, it occurs in micas even when no obvious microstructural evidence for classic brittle deformation can be observed (Mariani *et al.*, 2006). Essentially, micas might deform by a pressure sensitive but non-brittle mechanism at a range of conditions. This has to date been a poorly understood phenomenon. Ripplocations resolve this conflict by providing a pressure sensitive mechanism of deformation that does not result in fracturing or other characteristic brittle microstructures (see also Supplementary Note 5.3).

In PIPS prepared samples, exposure to the beam did appear to initiate further distortion and growth of voids in ultrathin regions close to the perforation edge. It is possible that the small amount of energy imparted by the electron beam was enough to release further elastic strain from existing ripplocations in these regions, especially where a free sample edge could be exploited. This still requires the storage and release of some degree of c-axis strain which cannot be explained by basal dislocations. The fact that these effects are only observed at ultrathin perforation edges and not in thicker regions or in FIB specimens, could explain why previous studies, which utilise PIPS-style methods, have reported large delaminations that grow under the beam (Ahn *et al.*, 1986) and have not reported conjugate expansion structure arrays.

This work demonstrates the existence of ripplocations within the phyllosilicate mineral biotite and highlights the fact that ripplocations may be a ubiquitous deformation mechanism in all types of phyllosilicates as they are applicable to all layered solids (Barsoum

and Tucker, 2017). In particular, serpentine minerals and chlorite may be even more susceptible to the nucleation and motion of ripplocations than micas. Their structures do not incorporate interlayer cations and their interlayer bonding relies on weak Van der Waals forces and hydrogen bonds (Bish and Giese, 1981) (Fig. 5.1b and c). In clay minerals the impact of ripplocations may be enhanced by lower lithostatic pressures in the upper crust, where clays are important constituents of fault gouges, as the size and mobility of ripplocations is likely a function of confinement (Gruber *et al.*, 2016).

The existence of ripplocations has fundamental implications for our understanding of phyllosilicate deformation. Existing models of kink band formation struggle to explain c-axis parallel strain without invoking brittle mechanisms. KBBs display a range of rotation angles and radii of curvature, and may be partially elastic, as shown by reversible experimental hysteresis curves (Basu *et al.*, 2009). Such 'incipient' kink bands appear to be entirely reversible, up to a point where they are pinned and transition into permanent kink bands. This process of recoverable plasticity is better explained by the formation and destruction of ripplocations than by the motion of basal dislocations or dislocation walls. The ability of ripplocations to store extensive elastic strain energy raises questions on how this strain may be distributed to other phases or released under changing conditions in the Earth. It is worth noting that, while studies of natural rocks represent a 'frozen in' microstructure in which the contribution, or impact, of elastic strain is difficult to quantify post-mortem, elastic strains are likely to play an important role in the development of locally high stresses with a significant effect on recrystallisation and mineral reactions (Wheeler, 2014, 2018). It remains unclear whether ripplocations should be defined as either brittle or viscous defects (see also Supplementary Note 5.3). They are defined as waves in atomic layers[18-20] and can form at different scales, involving few to several interlayer bonds. Ripplocations may stretch interlayer bonds (visco-elastic behaviour), but larger scale ripplocations may cause these bonds to break (delaminations as lenticular micro-cracks). If lenticular micro-cracks form, the motion of ripplocations might drive micro-crack migration in a continuous cycle of cracking and healing, thus accommodating deformation via a combination of visco-elastic and transient brittle processes. The behaviour we describe here would have considerable implications for fluid transport in deep shear zones where ripplocations would provide the transient porosity waves needed to move fluids through the crust. This idea is not dissimilar to the model proposed by Phipps Morgan and Holtzman, (2005) where vug waves are defined as a combined deformation and fluid migration mechanism whereby migration of fluid-filled cracks is driven by the release of elastic strain energy. Fluids in faults, shear zones and

subduction zones can weaken the mineral components of these structures, increase the rate of diffusive mass transfer, or generate overpressures. While the applicability of a vug wave-type model to ripplocations must be tested carefully with further work, the implications for the strength of faults, shear zones and subduction zones are significant. As the properties of ripplocation defects are clearly important for understanding the rheology of micas in mylonites of the middle and lower crust, so they may also prove a critical consideration for the frictional behaviour of phyllosilicates within seismogenic faults and subduction zones (Heaton, 1990; Brune *et al.*, 1993). Now that ripplocations have been identified in natural phyllosilicates, these defects must be accounted for in microphysical modelling of the mechanical properties of phyllosilicate-rich faults, shear zones and subduction zones as they are likely to have a crucial influence on the rheology of these tectonic lineaments and on the nucleation and propagation of large magnitude earthquakes (Heaton, 1990; Brune *et al.*, 1993; Niemeijer and Spiers, 2007; Collettini *et al.*, 2009; Faulkner *et al.*, 2011).

## 5.5. Methods

### 5.5.1 Preparation of TEM samples

Electron transparent TEM specimens were produced by both focused ion beam (FIB) and Ar ion milling in order to identify and compare any effects of sample preparation procedure on the distribution and morphology of delaminations. This comparison is important as FIB is a popular and effective method of TEM sample preparation however the majority of previous studies on deformed phyllosilicates utilised ion milling techniques. The FIB specimens were produced using the lift out method using a FEI Helios Nanolab™ 600 I DualBeam™ Ga focused ion beam (FIB) scanning electron microscope (SEM). Target biotite grains were identified in standard petrographic thin sections of mylonitic samples using optical and scanning electron microscopy. Site specific specimens were prepared using the FIB, with sections cut perpendicular to cleavage via the in-situ trenching and lift out technique (Giannuzzi and Stevie, 2005) (Supplementary Figure 5.7a). Once prepared, thin lamellae received a 5.00 kV low energy surface wipe, to reduce the thickness of amorphized surface damaged layers. During this thinning process, all samples were observed to bend and flex extensively, which we interpret to result from the release of stored elastic strain energy (Supp. Fig. S5.7b and c).

Samples prepared using Ar ion milling were taken from 3mm cores drilled into hand specimens. These cores were then encased in brass tubes using Crystalbond adhesive and sliced into ~0.5 mm thick discs with a low powered diamond bladed saw. The discs were then

reduced to a thickness of ~100 µm by polishing with 600 and 1200 grit papers on a water based automatic polisher and finished to a high quality using 2500 and 4000 grit papers on the same machine. The polished 100 µm thick discs were removed from their protective brass rings and cleaned of Crystalbond by immersion in acetone for several hours. Finally, selected discs were placed in a Gatan precision ion polishing system (PIPS) and milled with dual Ar ion beams until a perforation was formed within or bordering a biotite grain. Heterogeneous milling rates, due to the multiphase nature of the samples, complicated this process, with the first perforation sometimes not occurring in a biotite grain, meaning that further milling was required.

### 5.5.2. TEM analysis

Transmission electron microscopy experiments were performed using a CEOS GmbH "CESCOR" probe side aberration corrected JEOL 2100FCs instrument, operating at 200keV. The resolution offered by the microscope is 1.4Å using conventional TEM illumination and sub-Ångstrom using aberration corrected STEM.

Low resolution imaging and EDX measurements were performed using a tungsten filament JEOL 2000FX TEM operating at 200keV. Extra care was taken during TEM analysis due to the nature of micas as beam sensitive materials and the fact that the delamination features of interest were initially hypothesized to be a result of beam damage. Beam exposure was kept to a minimum in areas of interest; alignments and focusing were carried out in sacrificial areas of the sample and critical regions exposed only during image capture. Some areas were imaged at multiple magnifications meaning they were exposed to the beam for longer. In these instances, beam damage was often observed but as described in the main text, this took the form of amorphisation and a loss of contrast. The expansion structures on which this study is focused were not observed to grow or form during extended exposure to the beam except in some regions in close proximity to the perforation edge of PIPS prepared samples.

Chemical analysis including beam induced K loss measurements, were performed using an EDAX energy dispersive X-ray (EDX) detector attached to the JEOL 2000FX TEM. Previously unexamined regions of biotite were selected for measurements to ensure no prior diffusion of K from beam exposure. Spectra were taken from target regions using collection times of either 90 live seconds or 120 live seconds, an amp time constant of 102.4 µs, detector area of 30mm$^2$ and a detector energy resolution of 136eV at FWHM Mn k-alpha. Measurements were repeated at the same location using a constant live time to investigate the loss of K

between each spectrum. During this period the beam was not moved from its position to ensure all spectra were collected from the same spot. Spectra were mathematically filtered to remove background data. K/Si ratios were used as described by Van der Pluijm et al.(Van der Pluijm *et al.*, 1988) so as to normalise the loss of K to that of Si.

## 5.6. Supplementary information

### 5.6.1. Supplementary notes

*Supplementary Note 5.1: Kink band morphology and formation*

As described in the main text of this article, previous studies of kink bands have attributed their formation to the development of complex arrays of dislocation walls, which result in bending of the (001) plane within a finite region on the order of 1-2 μm (Etheridge *et al.*, 1973; Bell *et al.*, 1986). However such a mechanism is unable to account for the degree of lattice curvature that we report in this study. In addition basal dislocations alone struggle to explain observed kink band asymmetry. Etheridge *et al.*, (1973) lay out a detailed description of kink band morphology and constitution. They define kink band asymmetry as:

$$|\phi - \phi_K| \tag{5.1}$$

Where ϕ is the angle between (001) in the limb outside the kink band and the axial plane of the KBB and $\phi_K$ is the angle between (001) in the limb inside the kink band and the axial plane of the KBB. The angle between the basal planes of the undeformed limb of the kink band and the deformed limb is known as the angle of bending (ω). According to Etheridge *et al.*, (1973) kink asymmetry is dependent on temperature and orientation with greater amounts of asymmetry in specimens deformed along [010] and in those deformed at higher temperatures, however, asymmetric kink bands occur at all conditions. This asymmetry of kink bands is the most difficult aspect of their morphology to explain through basal slip alone as it, by necessity, results in an expansion of the basal plane spacing in the region contained within the kink band. Previous authors (Etheridge *et al.*, 1973; Behrmann, 1984; Bell *et al.*, 1986) agree that this asymmetry, and the resultant c-axis parallel strain, requires some other deformation mechanism in addition to basal dislocation glide, and invoke non-basal slip and/or fracturing to account for this, despite little unequivocal evidence. Ripplocations as a recently recognised defect (Kushima *et al.*, 2015) are directly characterised by such an expansion in the basal plane spacing and, consequently, perfectly describe this phenomenon. Descriptions of kink bands on the scale of both optical microscopy (Etheridge *et al.*, 1973) and TEM (Bell *et al.*, 1986) report basal delaminations around and across KBBs. These

delaminations possess variable symmetry and curvature and are similar in form to those described in this study and associated with the release of stored c-axis parallel strain. The distribution of these structures along KBBs is also in strong agreement with the computational models of Gruber *et al.*, (2016) (supplementary movie 4 of Gruber *et al.*, 2016) which model kink band formation using ripplocations instead of basal dislocations.

### *Supplementary Note 5.2: Sample locations and geological background*

The three naturally deformed samples used in this study were collected from viscously deformed granitic orthogneiss rocks of the Cossatto-Mergozzo-Brissago (CMB) line and the associated Pogallo line shear zones in north western Italy. The CMB line is a vertical tectonic discontinuity which separates the lower crustal Ivrea-Verbano zone to the NW from the mid-upper crustal Serie dei Laghi to the SE. It was active at lower amphibolite facies conditions during the Permian and accounts for several tens of km of lateral displacement (Siegesmund *et al.*, 2008). The Pogallo line is a slightly younger amphibolite to upper greenschist facies shear zone which cuts the CMB line at a very low angle (Boriani, Burlini, *et al.*, 1990). The orthogneiss samples used were composed primarily of quartz and both plagioclase feldspar and K-feldspar. Micas constituted between 15% and 20% of the samples with biotite usually comprising just over half of this with the remainder being muscovite.

The undeformed sample was a block of Westerly granite from Rhode Island, USA, which is a medium grained, relatively biotite-rich (5-10%) intrusive igneous rock. It is a useful standard material used extensively for deformation experiments in rock mechanics as it is homogeneous and has undergone very limited natural deformation.

### *Supplementary Note 5.3: Brittle v viscous character of ripplocations and the pressure sensitivity of micas*

It is not clear whether deformation by ripplocations falls under the category of a brittle or a viscous mechanism. Unlike a brittle fracture they do not represent the permanent breaking of bonds but nor do they occur through in plane motion of one plane of atoms relative to another as in dislocation glide. In addition, their effects, such as kinking, are prevalent in phyllosilicates across the entire range of conditions within the Earth's crust and occur alongside both classically brittle and viscous processes. A key effect of ripplocations is the expansion of the unit cell parallel to the c-axis. Where this occurs in a recoverable manner, which essentially consist of stretching the interlayer bonding, it may be that this can be considered a viscous mechanism. However, once the unit cell expansion is too great, and the bonding is broken rather than stretched, a true delamination is formed, and the mechanism

is better described as brittle. In reality, the boundary between these two states may be somewhat blurred, micro-scale delaminations may exist in a transient form that are small enough to heal and leave behind a regular lattice.

Viscous dislocation glide is possible in micas even at the pressure and temperature conditions of the Earth's surface (Meike, 1989), where brittle mechanisms dominate in most minerals. Brittle behaviour is characterised by a proportional increase in yield strength with increasing lithostatic pressure, as higher pressures increase the energy required to break bonds. This response is observable in mica rich rocks up to their dehydration temperature (Mariani *et al.*, 2006) but is often coupled with a lack of microstructural evidence for brittle deformation. This unusual pressure sensitivity of phyllosilicates can now be explained by ripplocations. Gruber *et al.*, (2016) showed that the nucleation and motion of ripplocations is strongly dependent on their confinement (or the lithostatic pressure). At the same time, they do not result in fractures or other brittle features but rather produce a bending of lattice planes and kinking. Such observations strongly suggest that ripplocations are the mechanism responsible for this, until now, poorly understood mechanical response of phyllosilicates.

## 5.6.2. Supplementary figures and tables

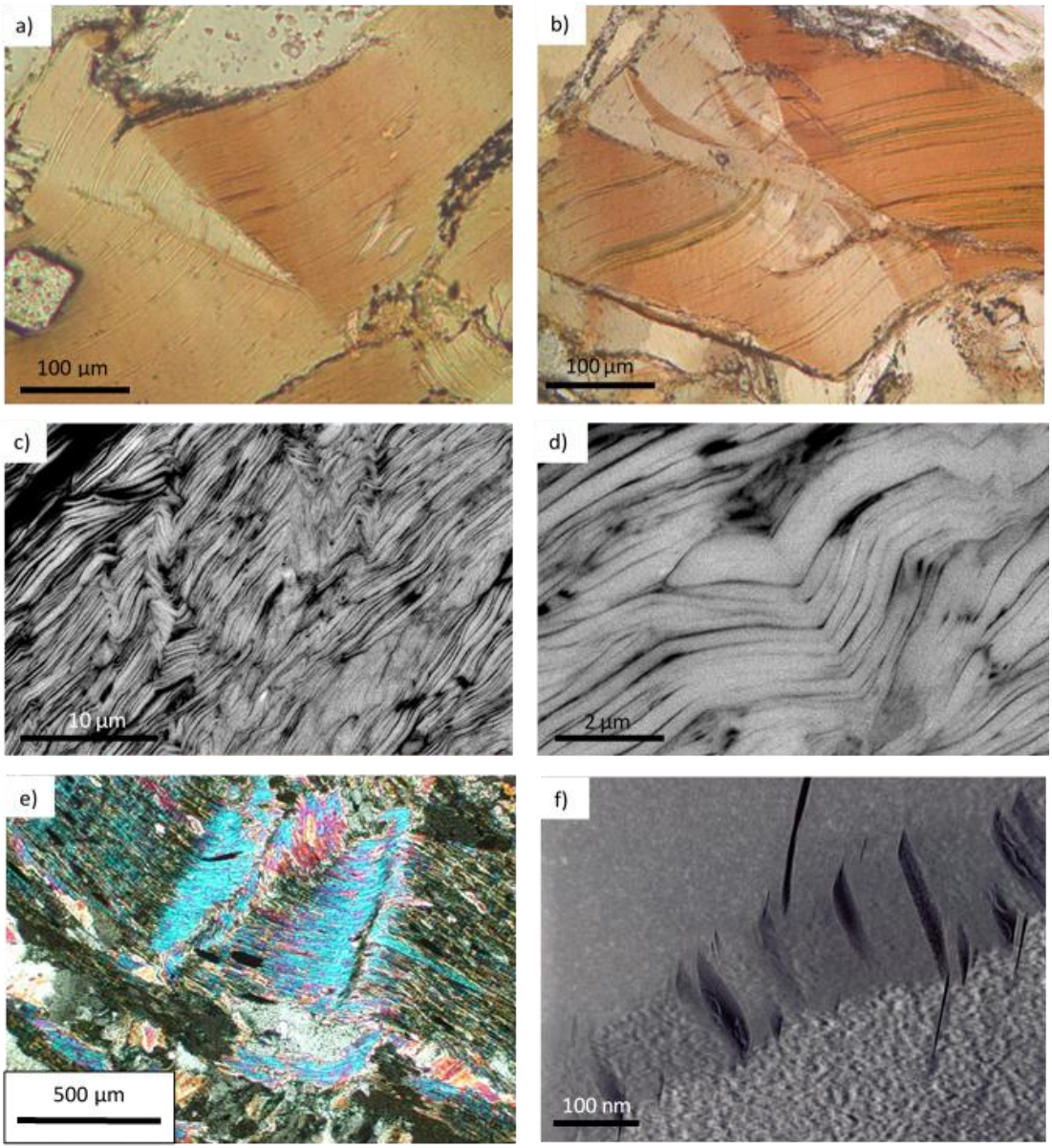


***Supplementary Figure S5.1:*** *Examples of various forms of kinking and folding in micas from different conditions and at a range of scales demonstrating its importance as a ubiquitous process of deformation in phyllosilicates. (**a**) and (**b**) Optical micrographs (plane polarized light) of biotite from sample CMB5A, an amphibolite facies mylonite from the Cossatto-Mergozzo-Brisaggo line used in this study. Note how the sharpness of individual kink band boundaries often varies along their length with sharp kinks sometimes grading into more gentle bends. (**a**) A simple single kink band which serves to locally increase the width of the grain and decrease its length. The two (possibly three) kink band boundaries either side of the kink band meet and annihilate towards the bottom of the grain. (**b**) A more complex network of kink bands which facilitates greater basal plane parallel compression and c-axis parallel expansion of the grain. (**c**) and (**d**) Back scattered electron images of muscovite deformed experimentally under conditions of simple shear (**c**) and torsion (**d**). Kinks are abundant and accompanied by basal layer delaminations. In simple shear (**c**) the kinks show a vergence towards the direction of shear. Scale bars are (**e**) Optical micrograph (crossed polarized light) of kinked metamorphic muscovite. (**f**) TEM micrograph of a simple kink band in biotite from sample POG 7 Showing that kinking occurs even at the nano-scale and demonstrating that where kink band asymmetry is substantial, widening of the basal spacing or delamination is geometrically necessary. (**c**) and (**d**) are from Mariani (2002), (**e**) courtesy of Dr Giles Droop.*

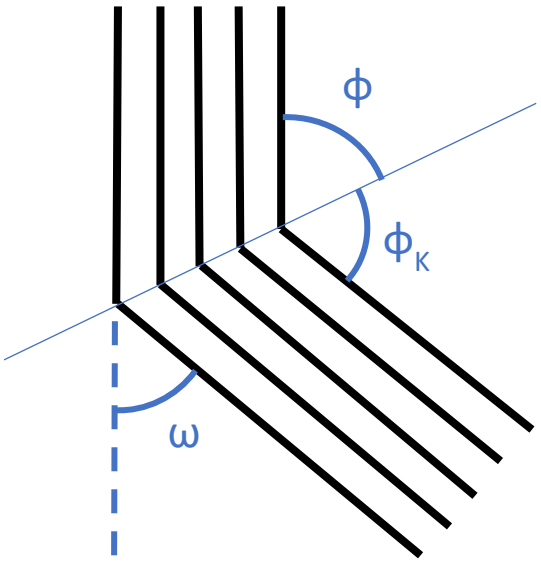


***Supplementary Figure S5.2:*** *Kink band morphology. Designation of angles within a kink band boundary as defined by Etheridge et al. (1973). ω is the angle of bending, φ is the angle between (001) in the limb outside the kink band and the axial plane of the KBB and $\varphi_K$ is the angle between (001) in the limb inside the kink band and the axial plane of the KBB.*

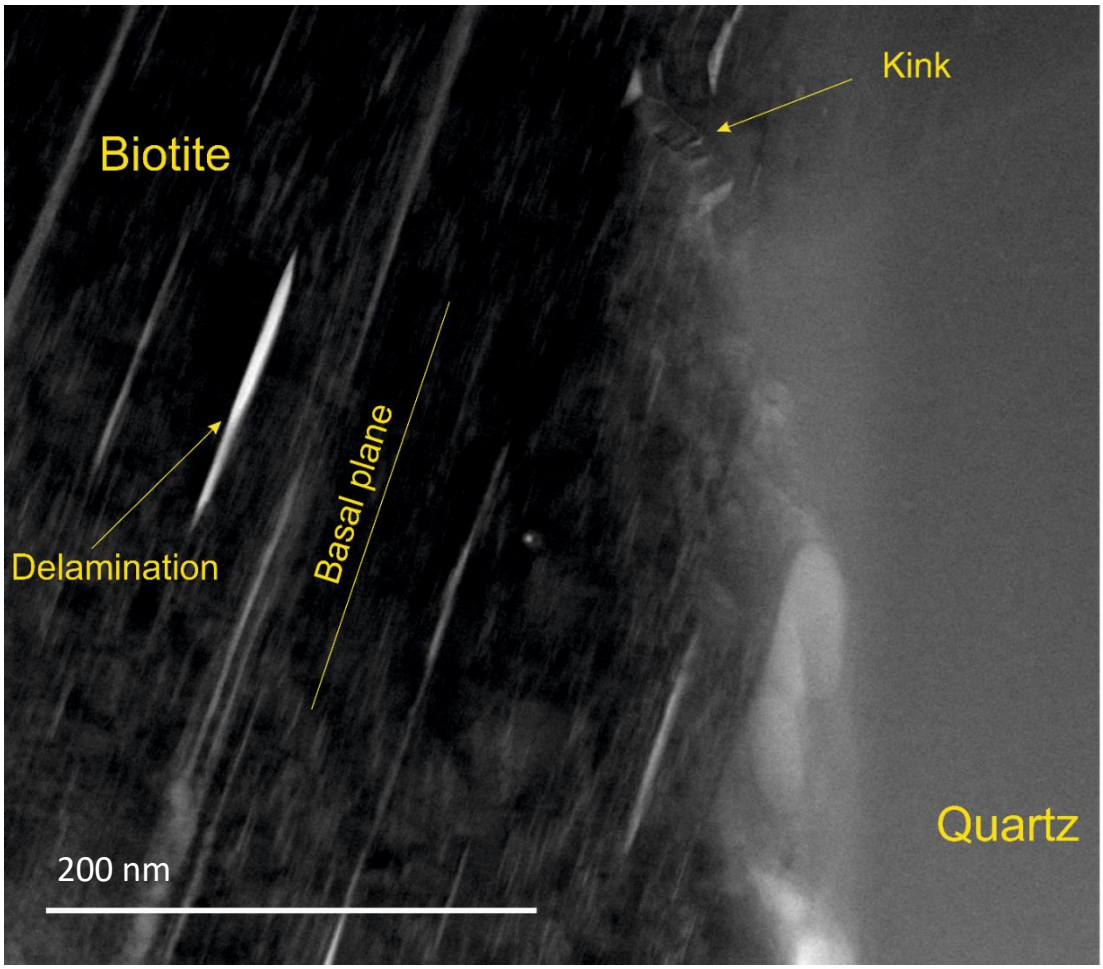


***Supplementary Figure S5.3:*** *Brightfield TEM image from sample CMB5A prepared by FIB, showing delamination and expansion structures of variable scales within biotite as well as a nanometer-scale kink band (indicated in the upper part of the image) which may be related to local differential stresses associated with the proximity of a biotite-quartz phase boundary.*

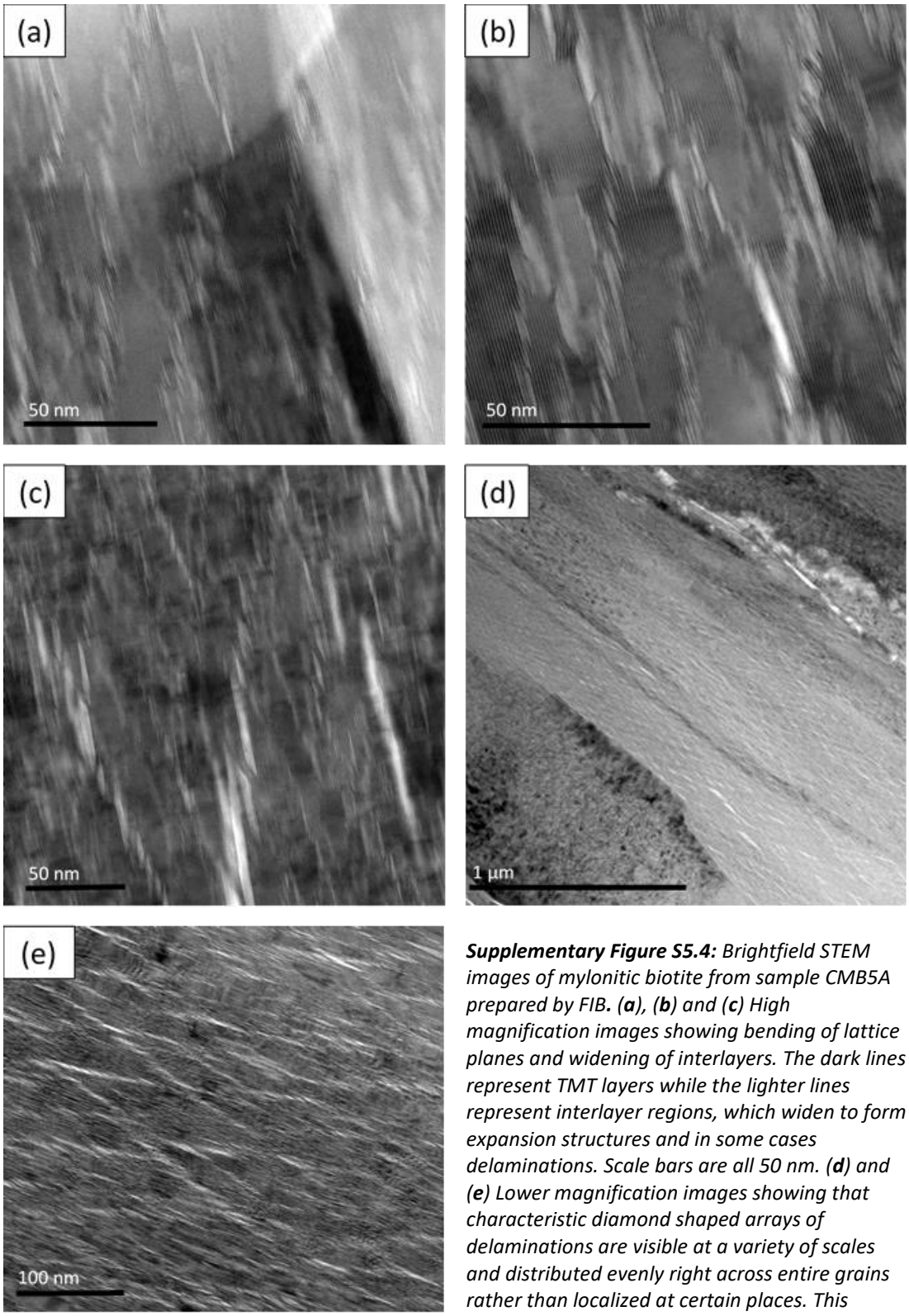


***Supplementary Figure S5.4:*** *Brightfield STEM images of mylonitic biotite from sample CMB5A prepared by FIB. (**a**), (**b**) and (**c**) High magnification images showing bending of lattice planes and widening of interlayers. The dark lines represent TMT layers while the lighter lines represent interlayer regions, which widen to form expansion structures and in some cases delaminations. Scale bars are all 50 nm. (**d**) and (**e**) Lower magnification images showing that characteristic diamond shaped arrays of delaminations are visible at a variety of scales and distributed evenly right across entire grains rather than localized at certain places. This supports the idea that the structures are formed through grain scale c-axis expansion rather than beam damage.*

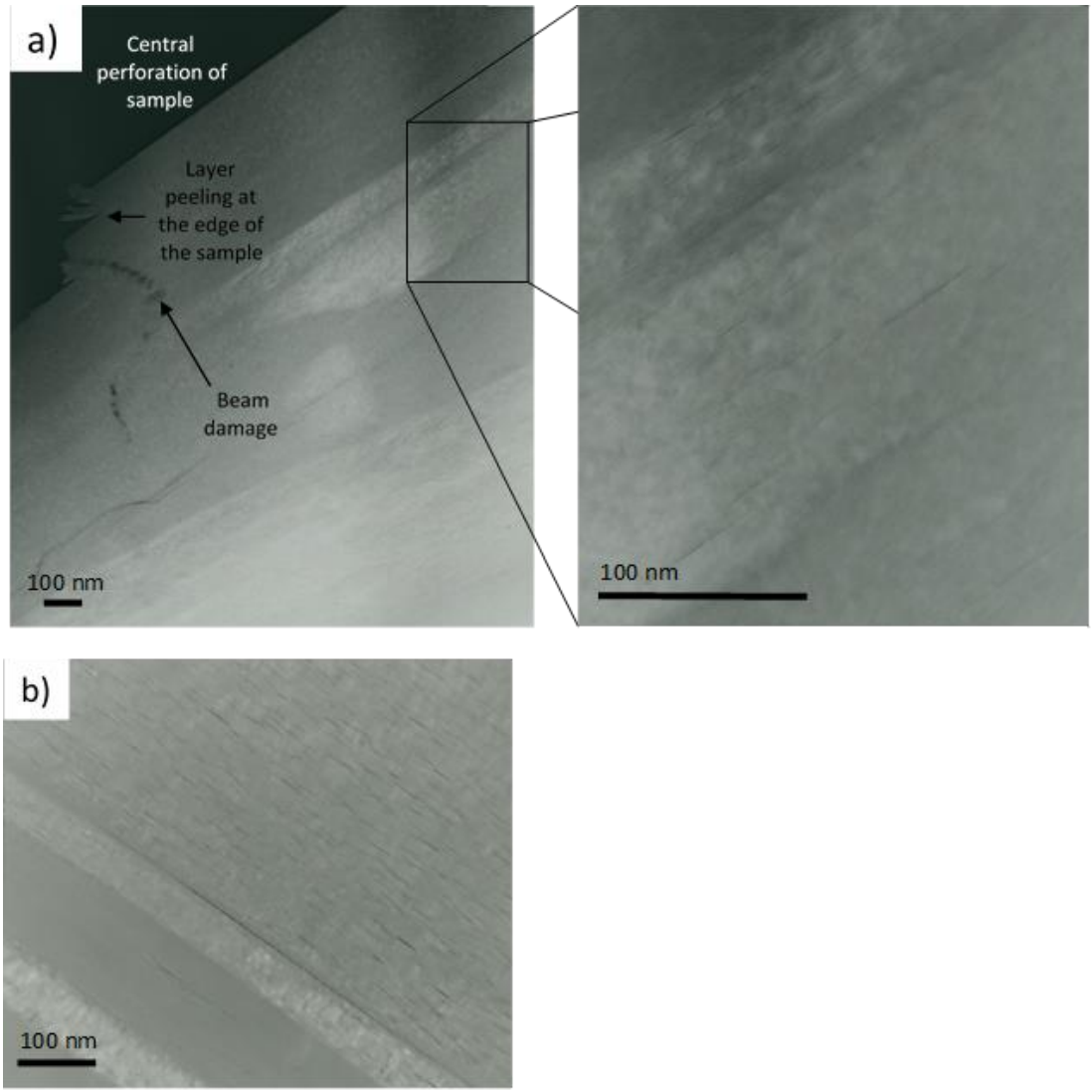


***Supplementary Figure S5.5:*** *Negatives of brightfield TEM micrographs of biotite grains from Westerly granite samples prepared using: (**a**) Ar ion polishing system and (**b**) Ga FIB. In the Ar ion beam prepared sample, (**a**) layers can be seen peeling along the (001) plane at the edge of the central perforation. In the thicker parts of the sample, narrow delaminations are present and oriented parallel to (001) as shown in the cut-away. The FIB prepared sample (**b**) also displays narrow delaminations similar to in the thicker regions of the sample shown in a. In both cases, the diamond shaped arrays of abundant delaminations are less clear in these nominally undeformed granite samples than in the mylonitic samples described and shown in the rest of this study.*

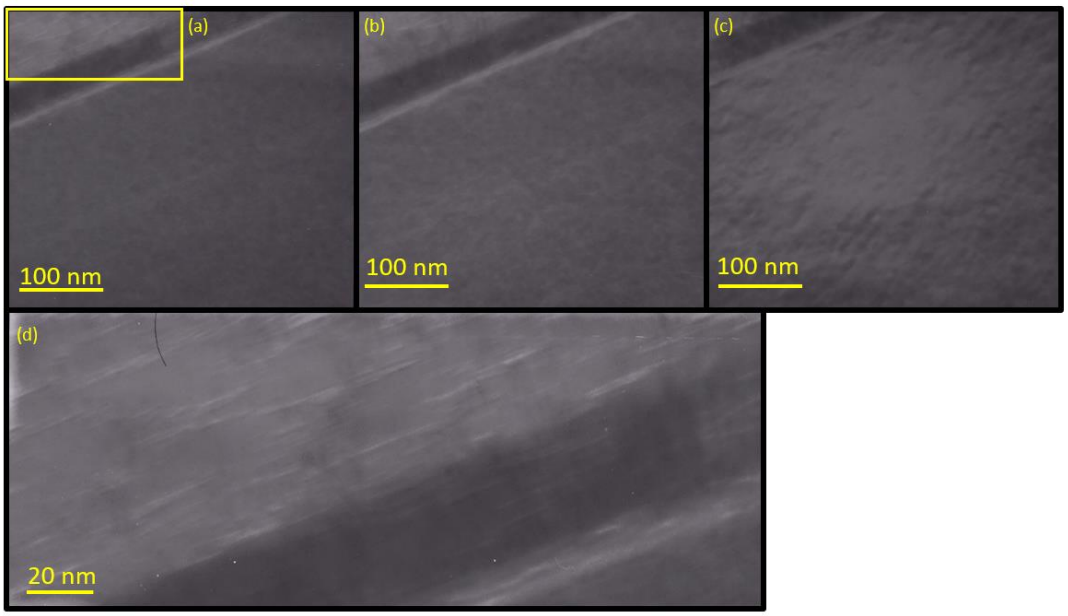


***Supplementary Figure S5.6:*** *Sequential inverted colour TEM images of the same region of sample POG 3 (FIB) taken after (**a**) no previous exposure (**b**) 8 minutes exposure and (**c**) having been viewed at higher magnification for a further 7 minutes. Delaminations are present in the upper left part of the image even after no previous beam exposure (**d**). These delaminations do not appear to grow or form with increased exposure to the beam. Extensive beam exposure does however result in amorphisation, increased mottling and a loss of contrast.*

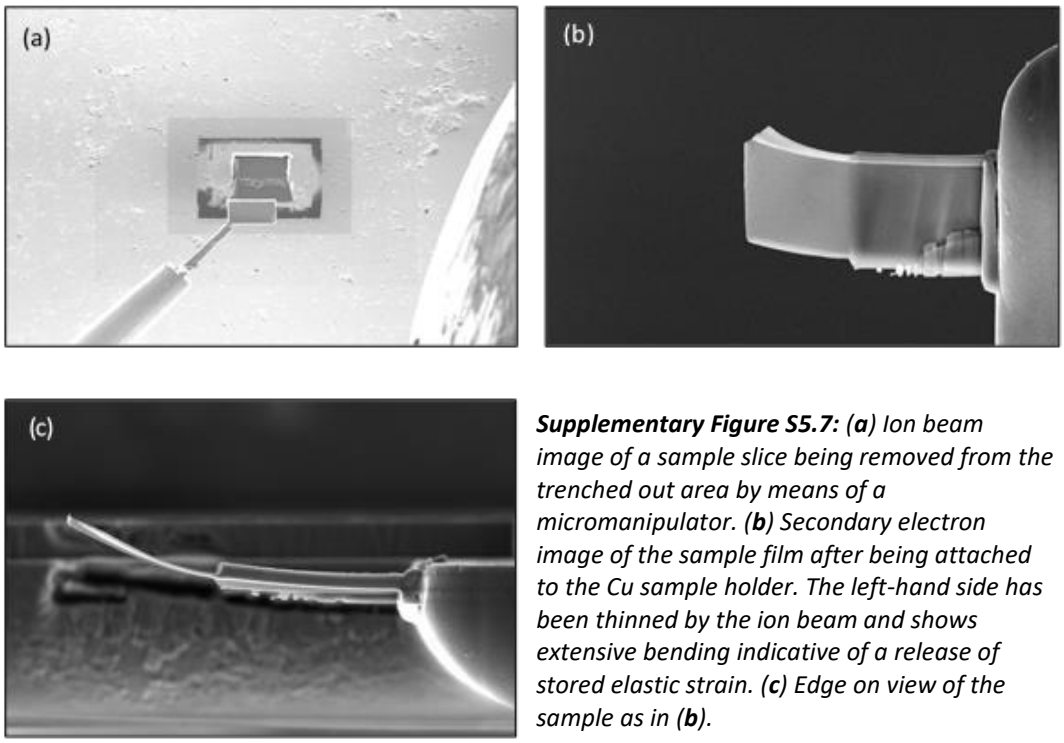


***Supplementary Figure S5.7:*** *(**a**) Ion beam image of a sample slice being removed from the trenched out area by means of a micromanipulator. (**b**) Secondary electron image of the sample film after being attached to the Cu sample holder. The left-hand side has been thinned by the ion beam and shows extensive bending indicative of a release of stored elastic strain. (**c**) Edge on view of the sample as in (**b**).*

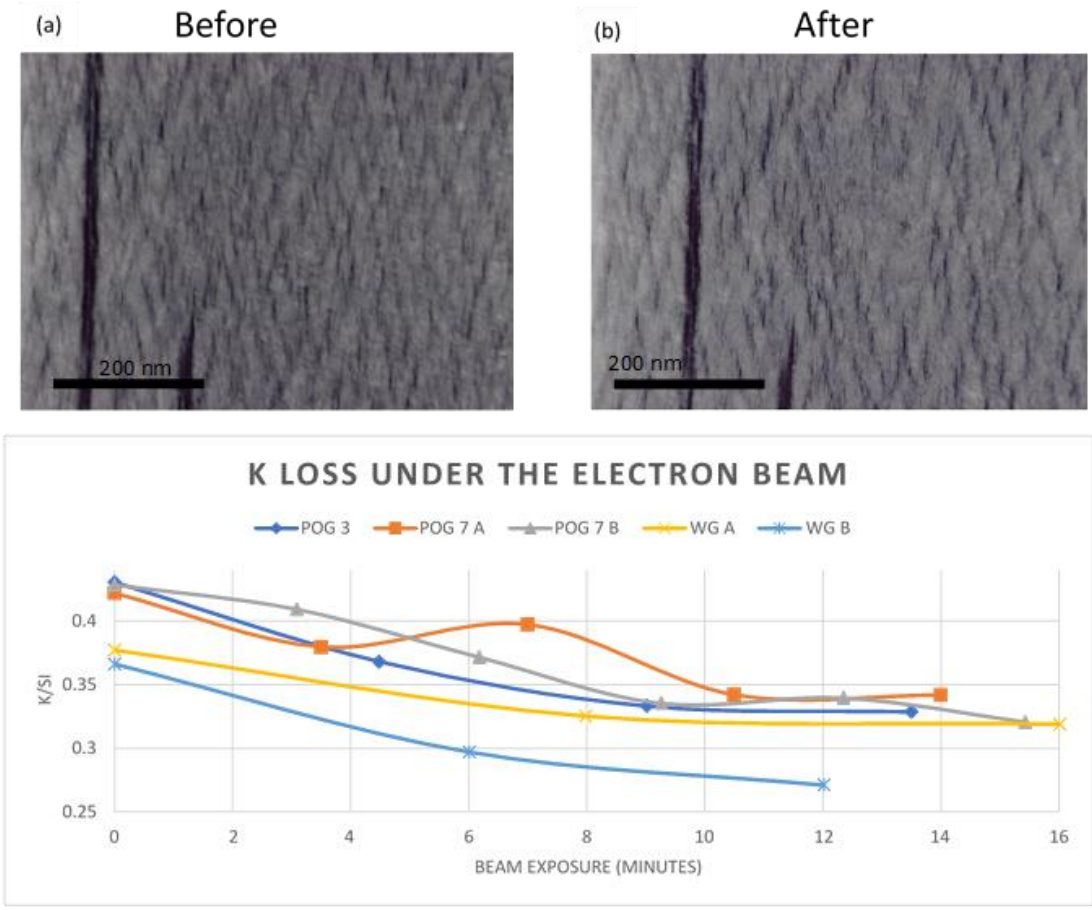


***Supplementary Figure S5.8:*** *(**a**) and (**b**) TEM micrographs of a region of biotite from sample POG 7 from which EDX spectra were collected. En-echelon arrays of delaminations were present both before and after EDX analysis using a focussed beam. Beam effects are visible and highlighted in (**b**) as amorphisation and removal of material around the beam spot. (**c**) Plot of K/Si ratio v time spent exposed to the beam as recorded in biotite from two different samples, POG 3, an ultramylonite and POG 7, a protomylonite. K is lost but the rate of decrease reduces over time and considerable K is retained in the biotite even after 15 minutes or more exposure. This is in contrast to the rapid and near total loss of Na previously reported in paragonite over a shorter timescale[28].*

# POG 3 FIB

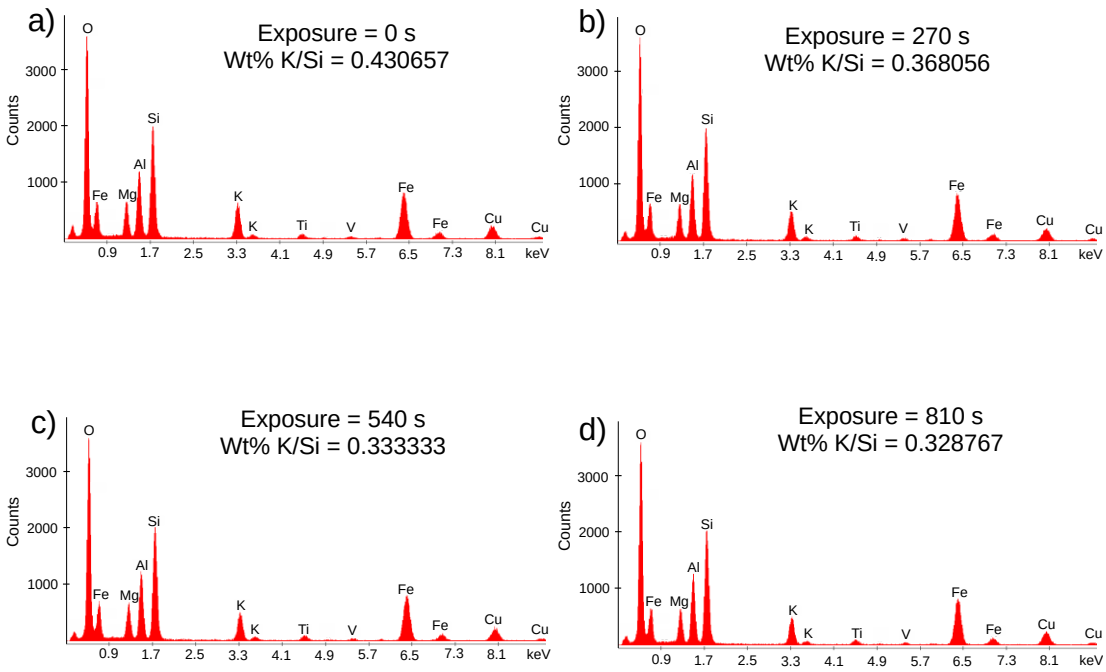


***Supplementary Figure S5.9:*** *EDX spectra acquired from a biotite in sample POG 3, an ultramylonite. The exposure value indicates the amount of time the point had been exposed to the beam prior to beginning the acquisition, this increases from 0 s in (a) to 270 s in (b), 540 s in (c) and 810 s in (d). A small decrease in the height of the K peak at approximately 3.3 keV occurs over time. Acquisition time was 90 live seconds per spectrum,*

# POG 7 (grain A)

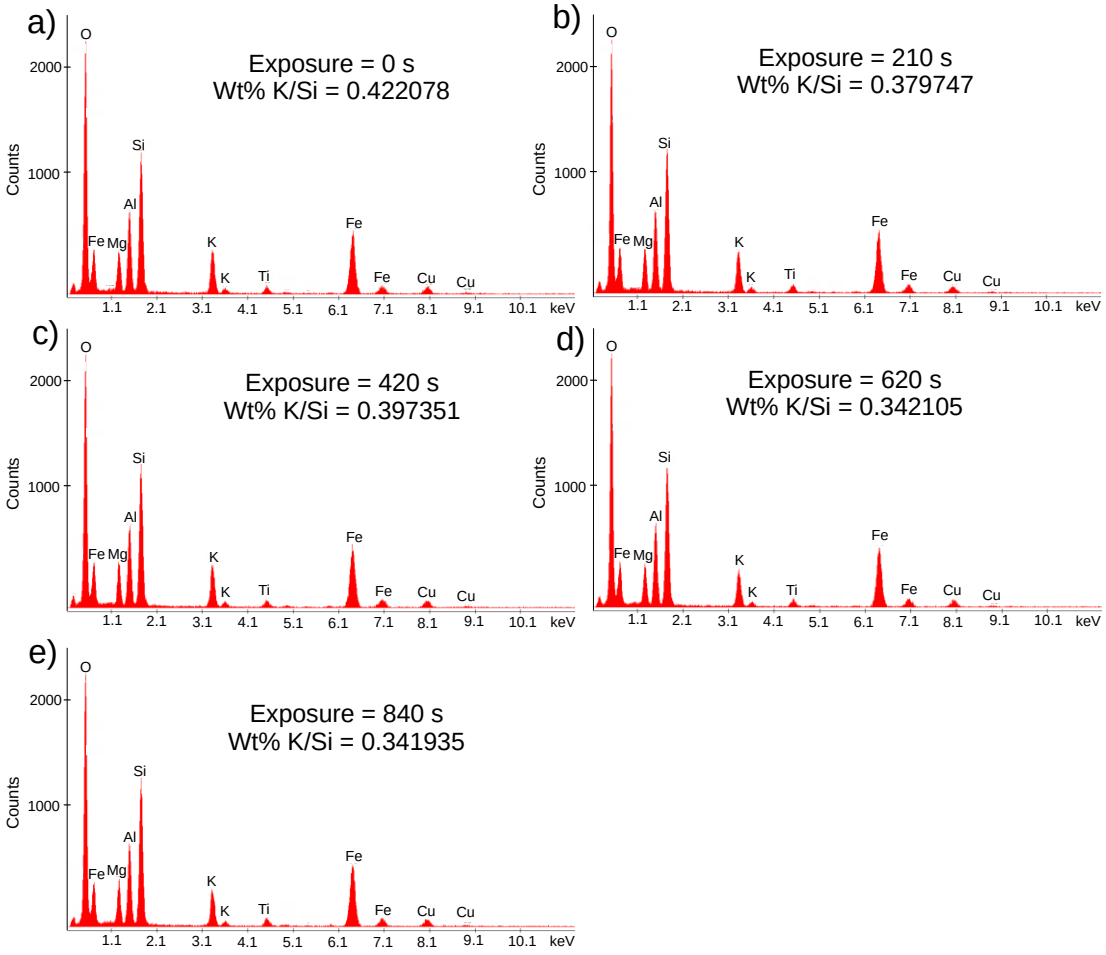


***Supplementary Figure S5.10:*** *EDX Spectra acquired from a biotite in sample POG 7, a Protomylonite. This is the region that is imaged in Supplementary Figure S5.8 (a) and (b) before and after these spectra were collected. The exposure value indicates the amount of time the point had been exposed to the beam prior to beginning the acquisition (in this case the first spectra was collected after the site had been exposed to the beam briefly for around 15 seconds in order to collect the image used in Supplementary Figure S5.8a). The time increases from 0 s in (a) to 210 s in (b), 420 s in (c), 620 s in (d) and 840 s in (e). A small decrease in the height of the K peak at approximately 3.3 keV occurs over time. Acquisition time was 60 live seconds per spectrum, accelerating voltage used was 200 keV.*

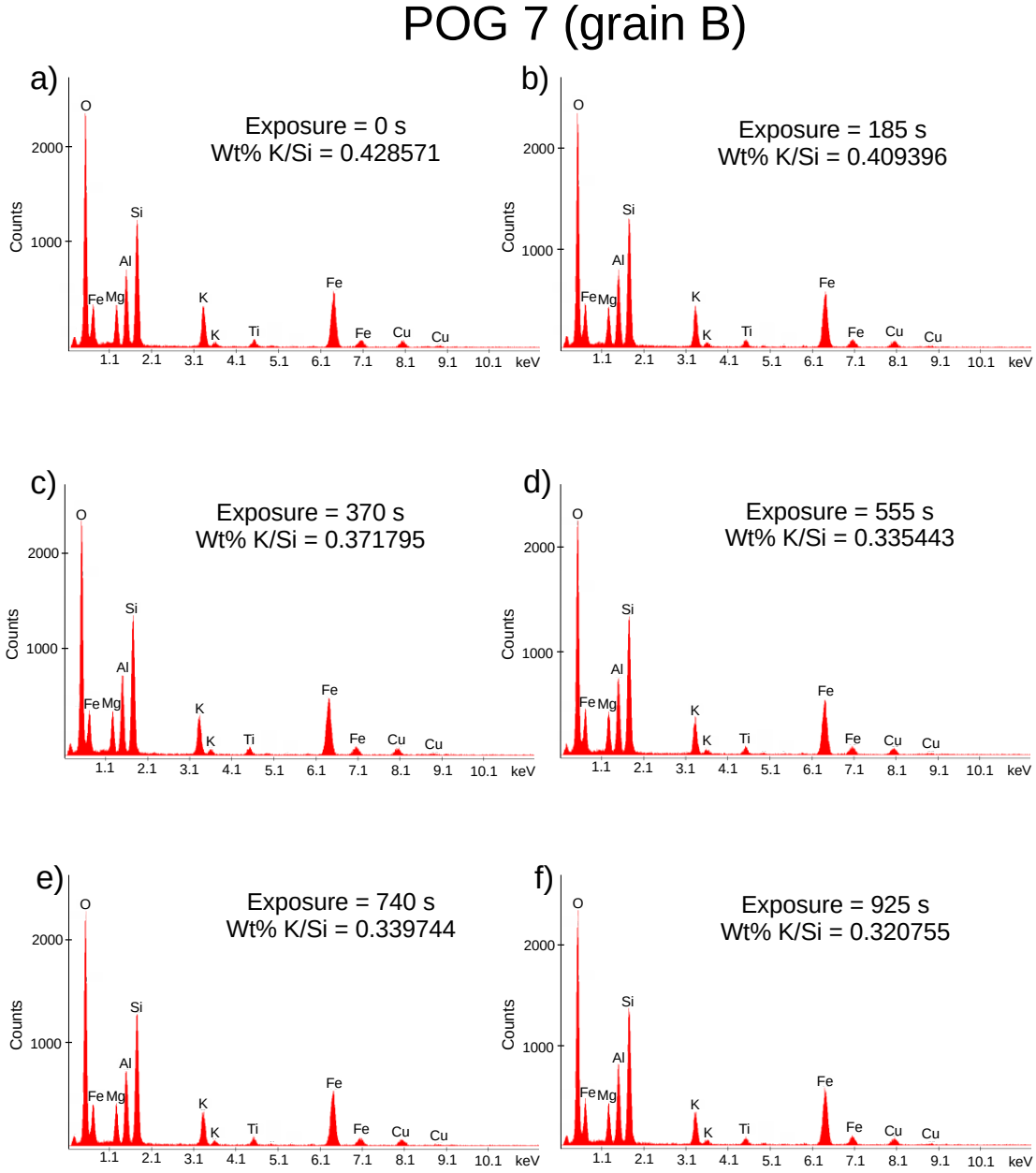


***Supplementary Figure S5.11:*** *EDX Spectra acquired from a biotite in sample POG 7, a Protomylonite. The exposure value indicates the amount of time the point had been exposed to the beam prior to beginning the acquisition, this increases from 0 s in (a) to 185 s in (b), 370 s in (c), 555 s in (d), 740 s in (e) and 925 s in (f). A small decrease in the height of the K peak at approximately 3.3 keV occurs over time. Acquisition time was 60 live seconds per spectrum, accelerating voltage used was 200 keV.*

# Westerly granite (grain A)

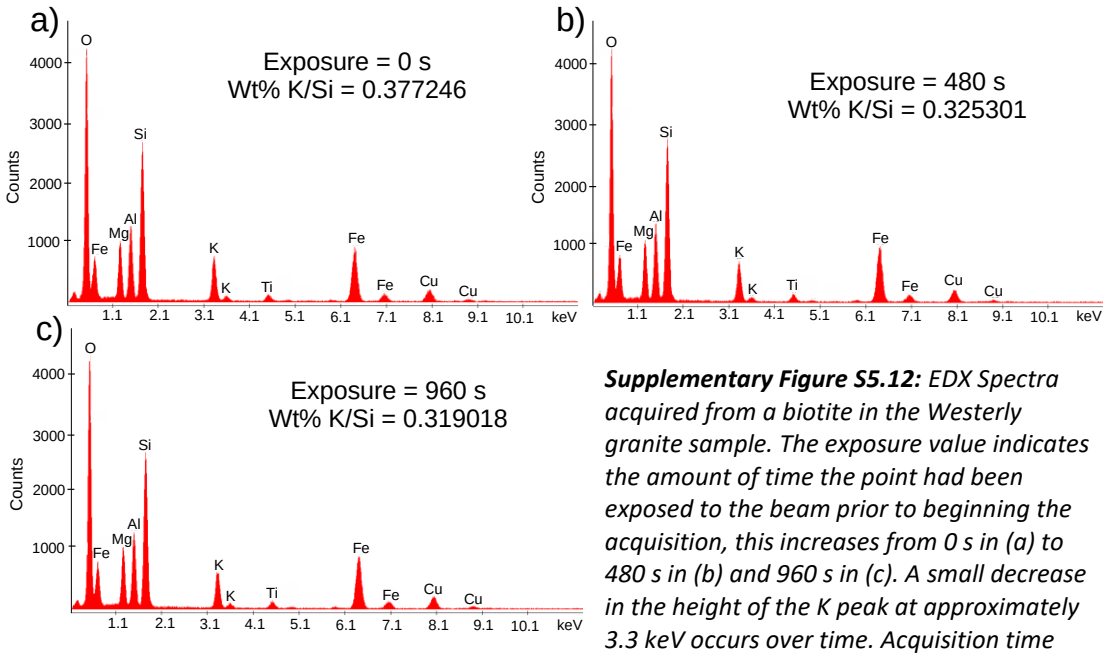


***Supplementary Figure S5.12:*** *EDX Spectra acquired from a biotite in the Westerly granite sample. The exposure value indicates the amount of time the point had been exposed to the beam prior to beginning the acquisition, this increases from 0 s in (a) to 480 s in (b) and 960 s in (c). A small decrease in the height of the K peak at approximately 3.3 keV occurs over time. Acquisition time was 120 live seconds per spectrum, accelerating voltage used was 200 keV.*

# Westerly granite (grain B)

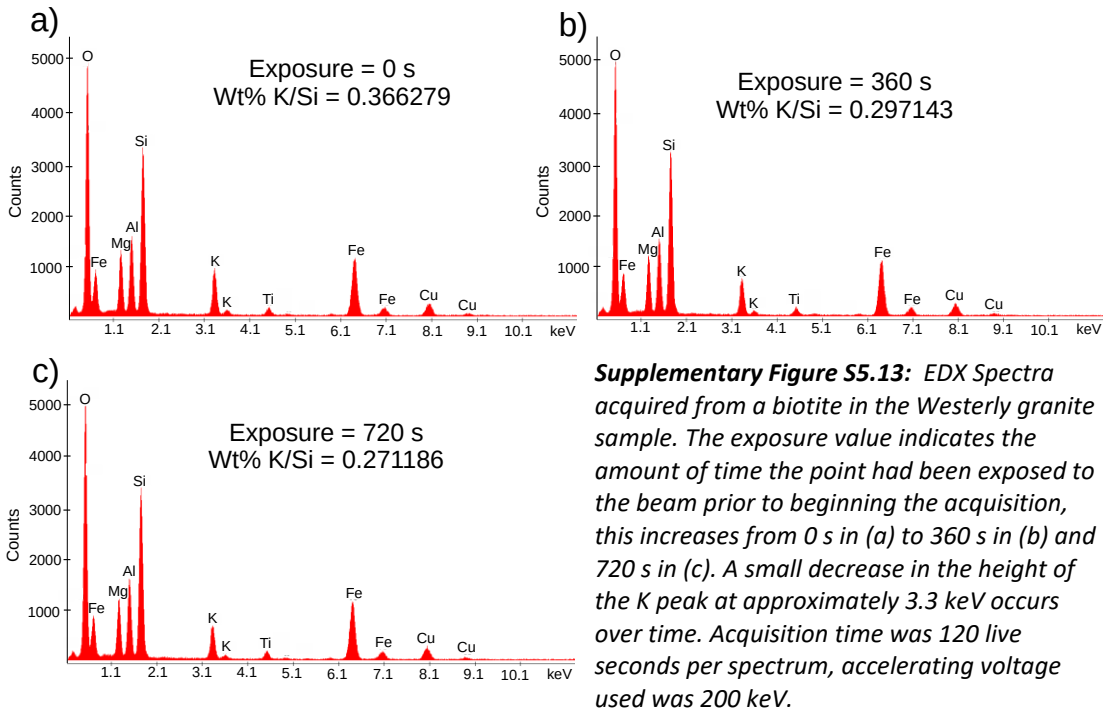


***Supplementary Figure S5.13:*** *EDX Spectra acquired from a biotite in the Westerly granite sample. The exposure value indicates the amount of time the point had been exposed to the beam prior to beginning the acquisition, this increases from 0 s in (a) to 360 s in (b) and 720 s in (c). A small decrease in the height of the K peak at approximately 3.3 keV occurs over time. Acquisition time was 120 live seconds per spectrum, accelerating voltage used was 200 keV.*

***Supplementary Table S5.1:*** *List of samples and TEM foils used. Within the instrument column, 2100 refers to a CEOS GmbH "CESCOR" probe side aberration corrected JEOL 2100FCs TEM while 200FX refers to a tungsten filament JEOL 2000FX TEM.*

| Sample | TEM foil name | Location | Lithology | Location in sample | Preparation | Instrument (accelerating voltage) | TEM mode | EDX? |
|---|---|---|---|---|---|---|---|---|
| CMB5A | CMB5A 1 | CMB line (Mte. Cerano) | Orthogneiss mylonite | Recrystallized halo of coarse biotite | FIB | 2100 (200KeV) | Scanning | No |
| CMB5A | CMB5A 2 | CMB line (Mte. Cerano) | Orthogneiss mylonite | Centre of coarse biotite | FIB | 2100 (200KeV) | Scanning | No |
| CMB5A | CMB5A 3 | CMB line (Mte. Cerano) | Orthogneiss mylonite | Matrix | FIB | 2100 (200KeV) | Scanning | No |
| POG 3 | POG 3 FIB | Pogallo line (Val Pogallo) | Orthogneiss ultramylonite | Matrix | FIB | 2000FX (200KeV) | Imaging | Yes |
| POG 3 | POG 3 PIPS | Pogallo line (Val Pogallo) | Orthogneiss ultramylonite | Matrix | PIPS | 2000FX (200KeV) | Imaging | No |
| POG 7 | POG 7 FIB | Pogallo line (Val Pogallo) | Orthogneiss protomylonite | Matrix biotite grain | FIB | 2000FX (200KeV) | Imaging | Yes (x2) |
| POG 7 | POG 7 PIPS | Pogallo line (Val Pogallo) | Orthogneiss protomylonite | Matrix | PIPS | 2000FX (200KeV) | Imaging | No |
| WG | WG FIB | Rhode island, USA | Granite | Coarse biotite grain | FIB | 2000FX (200KeV) | Imaging | Yes (x2) |
| WG | WG PIPS | Rhode island, USA | Granite | Groundmass biotite grain | PIPS | 2000FX (200KeV) | Imaging | No |

# 6. Grain size reduction of biotite in mid-crustal mylonites: implications for shear zone rheology

## 6.1. Abstract

Despite their importance for strain accommodation in the mid crust, the processes and mechanisms of deformation and grain size reduction in micas are still not fully understood. In predominantly quartzo-feldspathic lithologies, micas contribute to strain localisation by two main processes; 1) by forming interconnected networks of strongly aligned weak micas, 2) by pinning grain boundaries of other dominant phases such as quartz, inhibiting grain growth and thus favouring grain size-sensitive rheologies. However, due to the ambiguity surrounding the deformation mechanisms responsible for intracrystalline deformation within micas, the processes which enable interconnection and grain size reduction are not clearly determined. In this study, analysis was conducted on a suite of mylonites from the amphibolite to upper-greenschist facies Cossato-Mergozzo-Brissago line and the Pogallo line in North West Italy, with compositions between approximately 10% and 25% mica. With increasing strain in these rocks, biotite undergoes a dramatic grain size reduction. This process occurs initially at the tips of biotite grains and along kink band boundaries, with new, fine biotite forming preferentially along C and C' shear surfaces where it is found in association with fine-grained quartz, feldspar and Ti-oxide phases. Muscovite notably does not undergo the same process, with muscovite fish persisting in high strain samples. Optical microscopy was utilised alongside backscattered electron (BSE) imaging, electron backscatter diffraction (EBSD), energy dispersive x-ray spectroscopy (EDS) and transmission electron microscopy (TEM) to examine the microstructures associated with this grain size reduction process. Deformed biotite grains were also targeted for chemical analysis, utilising electron probe microanalysis (EPMA). TEM images reveal that grain size reduction occurs via a single step, with 1-5 µm grains forming directly from coarse biotite fish, while EPMA analyses show that the fine-grained biotite possesses subtly but consistently lower Ti content than coarser parent grains. The microstructures and compositional data suggest the biotite has broken down via disequilibrium reactions in a form of dissolution and reprecipitation. Once nucleated, the fine biotite pins grain growth of other phases within an interconnected network of C and C' shear bands and facilitates a transition in deformation mechanism from grain size-insensitive to grain size-sensitive creep. In this study we show that biotite can play an important role in the rheological evolution of mid-crustal mylonites, even where it is present in relatively low quantities.

## 6.2. Introduction

Mica minerals are abundant and widespread constituents of the Earth's middle and upper crust. They are found within igneous rocks of a range of compositions, from mafic through to felsic, and commonly occur as products of metamorphic reactions, especially in Al-rich systems. Their ubiquity means they are regular constituents of faults and shear zones and have a substantial influence on the rheology of the rocks and structures in which they are found (Shea and Kronenberg, 1993; Handy *et al.*, 1998; Mariani *et al.*, 2006; Hunter *et al.*, 2016). While the deformation behaviour of other common minerals in the middle crust, such as quartz, have been widely studied (e.g. Schmid and Casey, 1986; Stipp *et al.*, 2002; Law, 2014; Rahl and Skemer, 2016) there is a much smaller body of work detailing the deformation mechanisms that govern mica deformation in mid-crustal mylonites and important questions remain.

### 6.2.1. Mica deformation in experiments

Experimental studies on intracrystalline plasticity within micas have established that dislocation glide is only possible on the basal plane, with the easy slip directions within (001) being [100] and <110> (Etheridge *et al.*, 1973; Meike, 1989). As a result, they are mechanically very anisotropic minerals, which are weak when (001) is oriented at 45°, to $\sigma_1$ under conditions of pure shear (Kronenberg, Kirby, *et al.*, 1990). In other orientations, kinking or fracturing is observed rather than crystal plasticity, with no evidence of a contribution from cross-slip or dislocation climb (Kronenberg, Kirby, *et al.*, 1990). This has a substantial effect on the anisotropy of the rocks in which micas occur (Shea and Kronenberg, 1993). The slip systems of micas do not appear to be affected by temperature (Christoffersen and Kronenberg, 1993) while their strength is temperature and strain-rate insensitive at least up to 700°C (Mares and Kronenberg, 1993; Mariani *et al.*, 2006). Unlike most other minerals deforming at high temperatures, experimental testing has shown the strength of micas to be dependent on normal stress at temperatures up to their dehydration temperature (Mariani, 2002). This could be explained by frictional and brittle processes playing a role at unusually high temperatures or by the motion of ripplocations, a confining pressure sensitive deformation mechanism exclusively applicable to layered solids such as micas (Aslin *et al.*, 2019).

### 6.2.2. Mica deformation in natural rocks

Existing studies of mica deformation in natural rocks have focussed principally on the intracrystalline structures and deformation mechanisms within mica (Etheridge and Hobbs,

1974; Bell, 1978; Wilson and Bell, 1979; Bell and Wilson, 1981; Bell *et al.*, 1986; Goodwin and Wenk, 1990) or on the role of micas within deforming polyphase rocks (Goodwin and Wenk, 1995; Wenk *et al.*, 2010; Hunter *et al.*, 2016). In deformed rocks, coarse to medium-grained micas often display kink bands or disaggregation along the basal plane. Such microstructures are characteristic of phyllosilicates and other minerals with very few slip systems. Kinking enables shortening parallel to (001) and can serve to rotate sections of the mica lattice into orientations which are more favourable for shear. Within higher strain mylonites it is common to observe mica in the form of mineral fish, which behave as stable, rigid bodies within a viscously deforming matrix. It is notable that muscovite fish are a far more common occurrence than biotite fish (ten Grotenhuis *et al.*, 2003) owing to the apparently greater propensity for biotite to 'recrystallise' relative to muscovite under the same conditions (Passchier, 1985).

The mechanism (and meaning) of 'recrystallisation' in micas is contentious. The observation of fine, new grains in and around coarser, deformed micas has been reported in several studies (Etheridge and Hobbs, 1974; Bell, 1978; Wilson and Bell, 1979; Bell and Wilson, 1981; Passchier, 1985; ten Grotenhuis *et al.*, 2003). However, in the case of micas, such microstructures are not produced by classic dynamic recrystallisation mechanisms as described by Doherty *et al.*, (1998), which are not feasible in micas due to their inherent anisotropy (Etheridge and Hobbs, 1974; Bell, 1978; Wilson and Bell, 1979; Bell and Wilson, 1981). Bell and Wilson, (1981) proposed a grain size reduction mechanism (termed segmentation) by which smaller grains were formed through a series of misorientations across boundaries parallel and subnormal to (001). This process involved a physical break up of coarse grains into smaller grains which are not newly recrystallized but rather rotated pieces of older grains. As a process, segmentation appears to be favourable only in minerals with a limited number of slip systems, such as micas, in which dynamic recrystallisation is inhibited. The product grains are elongate and locally parallel to (001) of the parent grain. Segmentation is analogous to, but differs from, classical recovery recrystallisation process in that while small, slightly misoriented grains are formed, they are not internally strain free and normal grain growth does not appear to apply to them (Wilson and Bell, 1979). Bell, (1978) put forward a mechanism to explain the formation of fine, new biotite grains which formed along the hinges of kink bands and individually within the interiors of large grains. These grains are sometimes smaller than the critical nucleus size required for the growth of new grains within a host biotite by means of a classical nucleation mechanism (Etheridge and Hobbs, 1974). Segmentation and associated mechanisms suggest a purely mechanical origin

for fine biotite grains, however Etheridge and Hobbs, (1974) identified that chemical driving forces, as well as strain, play a role in the nucleation of new mica grains, and that such recrystallisation may involve disequilibrium reactions and the nucleation of micas with subtly different composition to their parent grains. Intracrystalline cataclasis has also been proposed as a mechanism for grain size reduction in micas, caused by bending of lattice planes and the opening of intracrystalline cavities (Goodwin and Wenk, 1990). Despite (or perhaps because of) the variety of mechanistic interpretations, new, fine-grained micas in natural, deformed rocks are commonly referred to simply as 'recrystallised micas' without explicit definition of the mechanism by which grain size reduction proceeded.

Recently, a new type of defect called a ripplocation has been proposed for layered materials (Kushima *et al.*, 2015; Barsoum *et al.*, 2019). The first evidence of ripplocations in naturally deformed micas was reported from the same samples used in this study (Aslin *et al.*, 2019 see Chapter 5 of this thesis). Ripplocations have a similar character to basal dislocations but involve a bending of the basal planes and a localised expansion of the interlayer region (Griggs, 1967; Gruber *et al.*, 2016; Barsoum and Tucker, 2017). Additionally, ripplocations occur within the interlayer region of phyllosilicates whereas basal dislocations are most likely to nucleate and move between the octahedral and tetrahedral sheets of a phyllosilicate structure (Noe and Veblen, 1999a). The build-up and movement of ripplocations can facilitate the intracrystalline deformation of micas when not oriented favourably for basal glide and is likely responsible for the development of kink bands (Aslin *et al.*, 2019).

### 6.2.3. Deformation of polyphase aggregates

While studies of deformation mechanisms in single crystals and single phase aggregates have been invaluable to our understanding of the rheology of minerals, the behaviour of polyphase aggregates must be considered when extrapolating to natural systems, with numerous studies highlighting the additional complexity this introduces (Handy, 1990; Wheeler, 1992; Herwegh and Berger, 2004; Holyoke and Tullis, 2006a; Oliot *et al.*, 2014; Czaplińska *et al.*, 2015; Andrew J. Cross *et al.*, 2017). This is particularly important when considering micas, which rarely dominate lithologies but often form an abundant second phase. The presence of a second phase can have significant implications for the rheology of an aggregate, primarily through second phase pinning (or Zener pinning) (Smith, 1948; Olgaard and Evans, 1988; Evans *et al.*, 2001; Herwegh *et al.*, 2011). The presence of a fine secondary phase distributed within a single-phase matrix has the effect of pinning grain boundaries that would otherwise move through the primary framework phase. This impedes grain growth through recovery and results in a finer grained overall aggregate (Warren and

Hirth, 2006; Little *et al.*, 2015). The extent of this effect is dependent not only on the amount of secondary phase but, at least in the case of mica in quartz, also requires the secondary phase to be widely distributed rather than clustered (Song and Ree, 2007). If the pinned grain size is fine enough, this can promote the feasibility of grain boundary sliding (GBS) and grain size sensitive creep mechanisms resulting in a switch from dislocation creep to diffusion creep and GBS (Warren and Hirth, 2006), with implications for the bulk rock rheology. There is evidence that this process is particularly important in phyllosilicate bearing mylonites (Olgaard and Evans, 1988; Herwegh and Jenni, 2001).

### 6.2.4. Mica interconnectivity

Micas almost invariably define the foliation of the polyphase rocks in which they occur. Where a foliation becomes well developed – such as in schists and mylonites – micas often occur in through-going micaceous layers forming an interconnected network of mica (Wintsch *et al.*, 1995; Holyoke and Tullis, 2006a, 2006b; Goncalves *et al.*, 2015). This is an important development in granitic rocks as the mica component in the initial microstructure is usually distributed throughout as isolated grains or groups of grains within a quartzofeldspathic, load-bearing framework. Such a microstructural transition, from a load-bearing framework to interconnected weak layers, is understood to have a significant weakening effect on the rheology of a bulk aggregate (Handy, 1990, 1994). In this way, micas can have a disproportionately large effect on the rheology of rocks in which they are not the most dominant phase (Shea and Kronenberg, 1992, 1993; Handy *et al.*, 1998). It is therefore critically important to understand the mechanisms responsible for grain size reduction and interconnectivity of mica within non-mica dominated lithologies as these rocks are abundant in the Earth's crust.

The mechanisms of mica interconnection were investigated experimentally by Holyoke and Tullis, (2006a, 2006b) who conducted shear experiments on natural fine-grained paragneiss with 13% biotite which was aligned but dispersed. They found that the mica grains behaved like weak pockets, generating high stresses at their tips and initiating localised semi-brittle flow and grain scale faulting in the surrounding quartz and feldspar, which made up a load bearing framework. They stipulate that this localised fracturing around biotite tips enables the interconnection of mica grains via easy slip on (001) (Holyoke and Tullis, 2006b). The biotite then underwent a dehydration reaction, due to the high temperatures (800°C) of the experiments, which was localised within portions of biotite grains that were highly strained. The fine-grained and well mixed reaction products then deformed by grain size-sensitive creep mechanisms resulting in weakening and further localisation (Holyoke and Tullis,

2006a). While this specific dehydration reaction is not common in the Earth's crust and the temperatures are elevated above those characteristic of mid-crustal shear zones, the experimental microstructure is reminiscent of natural mica-bearing mylonites.

This study aims to examine the processes by which micas contribute to the weakening of predominantly quartzofeldspathic rocks during viscous deformation along a major shear zone. A suite of samples of naturally deformed rocks, with mica contents between 10% and 25%, from an amphibolite to upper-greenschist facies shear zone in north-western Italy, have been examined. The mechanisms of grain size reduction and interconnectivity of mica (predominantly biotite) in these natural examples have been investigated and placed in the context of previous studies on naturally and experimentally deformed rocks with similar mica content.

### 6.2.5. Geologic context

The Cosatto-Mergozzo-Brissago (CMB) line and the associated Pogallo line in north-western Italy are amphibolite to upper greenschist facies shear zones which form the south-eastern edge of the Ivrea Verbano zone (IVZ), one of the best exposed sections of the Earth's lower crust. The CMB and Pogallo faults are important tectonic discontinuities which bring the IVZ into contact with the middle to upper crustal rocks of the Serie dei Laghi (SdL) (Boriani, Burlini, *et al.*, 1990; Handy and Streit, 1999; Rutter *et al.*, 2007; Siegesmund *et al.*, 2008). Together these faults form a sub-vertical tectonic lineament striking NNE which has been inferred by separate researchers to represent either a predominantly strike-slip, trans-tensional shear zone uplifted from the middle crust (Boriani, Burlini, *et al.*, 1990; Boriani and Giobbi, 2004) or a low angle normal fault, later rotated to the present orientation (Hodges and Fountain, 1984; Handy *et al.*, 1999; Siegesmund *et al.*, 2008). The CMB line is of Permian age, extends for 80 km and has a width of 100 m on average. Deformation along this fault involves different lithologies including granitic and granodioritic orthogneiss, metasedimentary schists and gneisses, amphibolite and the phyllosilicate-rich mica-schists of the Kinzigite Formation, which constitutes most of the SE part of the IVZ (Fig. 6.1). The Pogallo line is younger in age, having been active between 180 and 230 Ma (Hodges and Fountain, 1984; Handy, 1987) and cross-cuts the mylonites of the CMB line between Lago d'Orta and Valle Cannobina, incorporating the same lithologies. The Pogallo mylonite belt strikes NNE and dips at 80° towards the WNW (Boriani, Burlini, *et al.*, 1990). This orientation

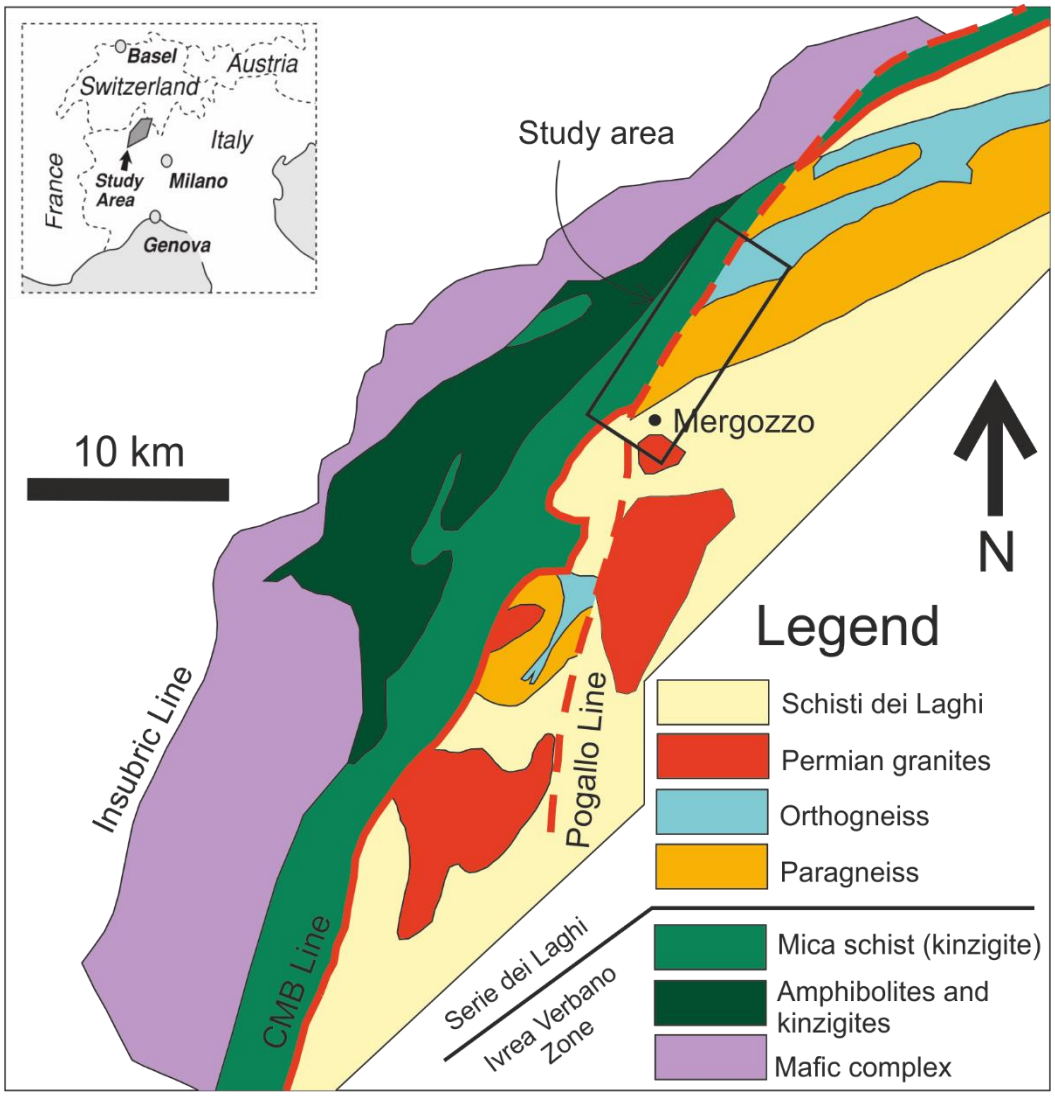


***Figure 6.1:*** *Simplified geological map of the region in the vicinity of the Cossatto-Mergozzo-Brissago (CMB) line and Pogallo line. The CMB line forms the SE boundary of the Ivrea Verbano zone (IVZ) which is interpreted to be a lower crustal section bound to the NW by the alpine age Insubric line. The SdL on the SE side of the CMB line is composed of metasedimentary schists and gneisses as well as granitic orthogneiss, which is the protolith of the Pogallo line samples used in this study, and Permian granites, (adapted from Rutter et al. 2007 and Siegesmund et al. 2008).*

is concordant with the attitude of the IVZ rocks but discordant by 25° to 30° with those of the SdL (Boriani, Burlini, *et al.*, 1990). To the North of Valle Cannobina, the Pogallo fault widens to become a region of distributed deformation within the Kinzigite Formation. The focus of this study are protomylonites, mylonites and ultramylonites derived from granitic orthogneisses and one micaschist of the SdL (Fig. 6.1). The effect of deformation along the CMB and Pogallo fault on the mica-rich Kinzigites of the IVZ is examined in Chapter 7.

## 6.3. Methods

### 6.3.1. Samples

The samples used in this study are composed predominantly of quartz, plagioclase, K-feldspar, biotite and muscovite. A list of the samples used with their locations, mineralogy and characteristics is given in Table 6.1. Samples POG3, POG5 and POG7 were collected from an exposure of the Pogallo line mylonites in Val Pogallo (see Figs. 7.1 and 7.5 from Chapter 7 of this thesis). They likely all represent the same orthogneiss protolith from the SdL but have been deformed to different degrees of strain, increasing from a protomylonite (POG7) to an ultramylonite (POG3). They are light coloured, massive rocks with dark banding. In the protomylonites this banding is discontinuous, wavy and approximately 5 mm in width. With increasing strain, the banding becomes straighter, more continuous and narrows to approximately 1 mm in width. The ultramylonites show compositional banding on the cm scale but otherwise are light to dark grey, massive, very fine-grained rocks spotted with 1 mm feldspar porphyroclasts and occasional larger feldspar porphyroclasts up to 3 mm in diameter. Sample CMB18 originates from an exposure of the CMB line south of the town of Ornavasso. It has a similar composition to the samples collected in Val Pogallo and likely also formed from a granitic protolith. Sample CMB5A was part of an existing collection but was sampled from the same area as sample CMB18. Unlike the other samples it represents a metasedimentary protolith but is included in this study as it has a relatively low mica content (15% biotite 7% muscovite).

***Table 6.1:*** *List of samples used in this study along with the location they were collected, approximate mineralogy and inferred protolith. CMB5A has a higher biotite content than the others and a composition that indicates metasedimentary protolith. * Sample CMB5A was collected separately to this study by Elisabetta Mariani. The coordinates of the sampling site are not known.*

| Sample number | Area | Location (long - lat) | Degree of strain | Approximate mineralogy | Protolith |
|---|---|---|---|---|---|
| POG 3 | Val Pogallo | 8°29'31.052"E 46°1'30.336"N | Ultramylonite | 50% Qtz, 15% Plag, 15% Ksp, 12% Musc, 5% Bio, 3% other | Orthogneiss |
| POG 5 | Val Pogallo | 8°29'33.324"E 46°1'26.004"N | Mylonite | 35% Qtz, 30% Plag, 15% Ksp, 7% Musc, 10% Bio, 3% other | Orthogneiss |
| POG 7 | Val Pogallo | 8°29'33.994"E 46°1'23.901"N | Protomylonite | 30% Qtz, 40% Plag, 10% Ksp, 6% Musc, 10% Bio, 4% other | Orthogneiss |
| CMB 18 | Ornavasso | 8°25'11.928"E 45°57'29.819"N | Mylonite | 40% Qtz, 25% Plag, 20% Ksp, 5% Musc, 7% Bio, 3% other | Granitoid |
| CMB5A | Camponi | Monte Cerano* | Mylonite | 40% Qtz, 30% Plag, 5% Ksp, 7% Musc, 15% Bio, 3% other | Micaschist |

### 6.3.2. Optical Microscopy

Single polished 30 µm thin sections were prepared from hand specimens by cutting the samples perpendicular to foliation and parallel to lineation. Initial observations and characterisation were carried out by optical microscopy using a Meiji Techno MT9000 polarised binocular microscope. Plane and crossed polarised light images were taken using a Lumenera Infinity 4 camera. Whole thin section scans in both plane and crossed polarised light were collected using a Plustek OpticFilm OF8200i Ai 35 mm film and slide scanner and SilverFast acquisition software. All mineral abbreviations used are based on the recommendations laid out by Siivola and Schmid (2007).

### 6.3.3. EBSD and EDS in the SEM

Thin section samples were prepared for SEM analyses by polishing for two hours with 0.05 µm colloidal silica SYTON solution before receiving a light carbon coat. Backscattered electron images were collected in a Phillips XL30 SEM at the electron microscopy laboratory at the University of Liverpool (Department of Earth, Ocean and Ecological Sciences) operating at an accelerating voltage of 20 kV, a beam current of 43-44 nA and a spot size of 5 nm. Quartz c-axis CPOs were measured using electron backscatter diffraction (EBSD) in a CamScan X500 CrystalProbe field emission gun (FEG) SEM at the same laboratory and plotted in lower hemisphere pole figures to enable comparison with the experimental samples of Heilbronner and Tullis (2006). Operating conditions for the Camscan X500 were: 20.00 kV accelerating voltage, 20-30 nA beam current and a spot size of 5.5 nm. Step sizes used for the maps varied according to the sample grain size and dimensions of the map being collected. EBSD orientation and phase maps were produced using CHANNEL 5 HKL software or using the MTEX Matlab toolbox. Pole figures and M-index (Skemer *et al.*, 2005) values were calculated using the MTEX Matlab toolbox. Energy dispersive X-ray spectroscopy (EDS) element maps were collected using the same Camscan X500 instrument simultaneously with the collection of EBSD data. Large area phase maps were collected using a FEI WellSite QEMSCAN SEM at the University of Liverpool, Department of Earth, Ocean and Ecological Sciences, with phases defined by matching EDS spectra to database standards using the iDiscover software package.

### 6.3.4. EPMA

Grains from 7 sites in 3 different samples were analysed by EPMA in Cameca SX-100 microprobes at the Open University and the University of Manchester. At each site, between 24 and 74 (totalling 347) point analyses were collected from one or a small number of large

grains and from 6 - 35 fine grains in the immediate vicinity to increase the potential for the sampled fine grains to have been derived from the sampled larger grains. The regions used for point analyses are shown in Supplementary Figure S6.1. The instruments were set up to measure major elements; Si, Fe, Mg, Al, K, Ti, Na, Ca and Mn with F additionally measured at Manchester. Full details of the experimental setup are given in Chapter 4 of this thesis. At the University of Manchester an accelerating voltage of 15 kV was used and a 10 µm de-focused beam to avoid damage to the beam sensitive micas. At the Open University a 1 µm beam diameter was used in order to target finer grains with the accelerating voltage reduced to 10 kV to limit damage from the concentrated beam. K was measured in all cases during the first pass of the beam in order to mitigate the effect of beam induced K diffusion, a well-established phenomenon in electron beam microanalysis (Van der Pluijm *et al.*, 1988). In order to avoid, as much as possible, the effects of grain boundaries, the fine grains selected for analysis were generally the larger of the fine grains (however, as mentioned above, a 1 µm beam diameter was used in some analyses for samples with particularly fine grains). This is an important consideration as erroneous results can be recorded if the beam interacts across a grain boundary, especially if that is a contact with a different phase. Monte Carlo simulations of the beam conditions used show the activation volume to be a region about 3 µm deep in the case of the 15 kV beam and 1.5 µm deep in the case of the 10 kV beam (Chapter 4, Fig. 4.8). In both cases the interaction volume does not extend far beyond the beam diameter used. As the samples were cut perpendicular to foliation (and therefore perpendicular to most biotite basal planes), biotite grains that are greater than 10 µm at the surface can be reasonably assumed to extend beyond 3 µm into the sample. Nevertheless, dealing in such small grain sizes did result in occasional erroneous results which were easily identifiable by drastically higher Si or Na/Ca content (caused by beam interaction with part of a quartz or plagioclase grain respectively) or by significantly low closing totals suggesting interaction with grain or phase boundaries. These clearly anomalous results were removed from the data set prior to plotting and interpretation. Phi-Rho-Z·f matrix corrections were applied to the data using the PAP analytical model (Pouchou and Pichoir, 1991). This processing and analysis was performed using the Probe for EPMA software package by Probe Software.

Data from EPMA point analyses of coarse and fine biotite grains were assessed for statistical significance using a t-test. The purpose of this test is to determine whether the difference between the means of two populations, in this case the compositional results of coarse and fine biotite, is statistically significant. To perform the test the means and standard deviations

for the weight percent oxide of each of the major components of biotite (K, Fe, Mg, Si, Al and Ti) were input into the formula:

$$t = \frac{(x_1 - x_2)}{\sqrt{\frac{(S_1)^2}{n_1} + \frac{(S_2)^2}{n_2}}} \quad (6.1)$$

where $x_1$ and $x_2$ are the means of populations 1 and 2 respectively, $S_1$ and $S_2$ are the standard deviations of populations 1 and 2 respectively and $n_1$ and $n_2$ are the sample sizes of populations 1 and 2 respectively. This calculated t-value was then compared to the critical t value for the corresponding degrees of freedom (degrees of freedom = $n_1 + n_2 - 2$). If the calculated t-value is greater than the critical t-value then the difference between the two populations can be considered statistically significant.

### 6.3.5. TEM

Specimens were prepared for TEM analysis using a FEI Helios Nanolab™ 600 I DualBeam™ Ga focused ion beam (FIB) SEM to cut sections perpendicular to the surface of a regular petrographic thin section (sample CMB5A). The standard ex-situ FIB lift out technique detailed by Giannuzzi *et al.*, (2005) was used to trench the specimen and remove a sample. The sample was then thinned down to electron transparency before being given a final 5.00 kV low energy surface wipe. Samples were analysed using a CEOS GmbH "CESCOR" probe side aberration corrected JEOL 2100FCs instrument, operating at 200 keV in both imaging and scanning TEM (STEM) modes.

## 6.4. Results

### 6.4.1. Microstructural evolution

The microstructural characteristics of the mylonites evolve with increasing strain from protomylonites to ultramylonites. Figure 6.2 displays the phase distribution and mineralogy of 4 key samples: POG7 (protomylonite), POG5 and CMB18 (mylonites), and POG3 (ultramylonite). Optical thin section scans of the same samples showing the microstructural evolution with increasing strain are given in Supplementary Figure S6.2. POG7, POG5 and POG3 are interpreted to represent the same orthogneiss protolith deformed to different degrees of strain. In the cases of POG7 and POG5 this is a very confident assumption. The interpretation is extended to POG3 as it was collected in the same transect as POG7 and POG5 and it contains a very different assemblage to that of the kinzigites (rich in quartz and

bearing K-feldspar). However, according to the results of QEMSCAN phase mapping (Fig. 6.2) it is distinctly richer in quartz and poorer in plagioclase than both POG7 and POG5, leaving open the possibility that its protolith is instead a granitoid of different composition. It should be noted that the apparent compositional disparity may be a result of the QEMSCAN technique, as the 20 µm step size used may not give an accurate representation of the modal abundance of POG3, which is predominantly composed of very fine 1-3 µm grains within a quartz dominated matrix. The assumption that POG3 developed from the same protolith as POG5 and POG7 could be better supported by additional analytical techniques, such as X-ray fluorescence analysis, if time and resources allowed.

The microstructure of the protomylonites is characterised by discontinuous bands of mica defining a foliation approximately 5 mm wide. The micas are set within a load bearing framework of quartz, plagioclase and K-feldspar which comprise approximately 30%, 40% and 10% of the rock respectively, with micas contributing a further 15%. In the higher strain mylonite samples the foliation is finer – down to 1 mm – and a pervasive S-C fabric is apparent as well as C' shear bands. Along these microstructural planes there is a notable development of fine-grained biotite-dominated bands, connecting coarser biotite grains which would otherwise be isolated from each other. This makes the foliation more pervasive and greatly increases the connectivity of the mica phases, though a load-bearing framework of quartz and feldspar ultimately persists. As well as biotite, the fine-grained bands contain quartz, plagioclase, K-feldspar and some Ti oxides (rutile and ilmenite). In the highest strain samples collected, the majority of the rock is composed of a fine-grained polymineralic matrix similar to that present along C and C' surfaces in the mylonites. Within the matrix are abundant porphyroclasts of K-feldspar, plagioclase and muscovite mostly of <1 mm in diameter. The mineralogy of the matrix itself is a mixture of quartz, plagioclase, biotite, K-feldspar, muscovite and apatite in proportions that vary locally in foliation parallel compositional bands as well as in the vicinity of porphyroclasts. Compositional banding within the matrix is also reflected in the porphyroclast mineralogy, with K-feldspar porphyroclasts abundant within (though not entirely limited to) regions of quartz-rich matrix, while plagioclase porphyroclasts are more abundant in the bands which have higher biotite content. This may reflect some degree of deformation induced compositional banding or a pre-existing compositional banding in the protolith.

### 6.4.2. Microstructural evolution of the mica phases.

In the lowest strain protomylonites, micas (both biotite and muscovite) have grain sizes of ~200 µm to 3 mm and occur as mineral fish either isolated or in clusters defining the foliation

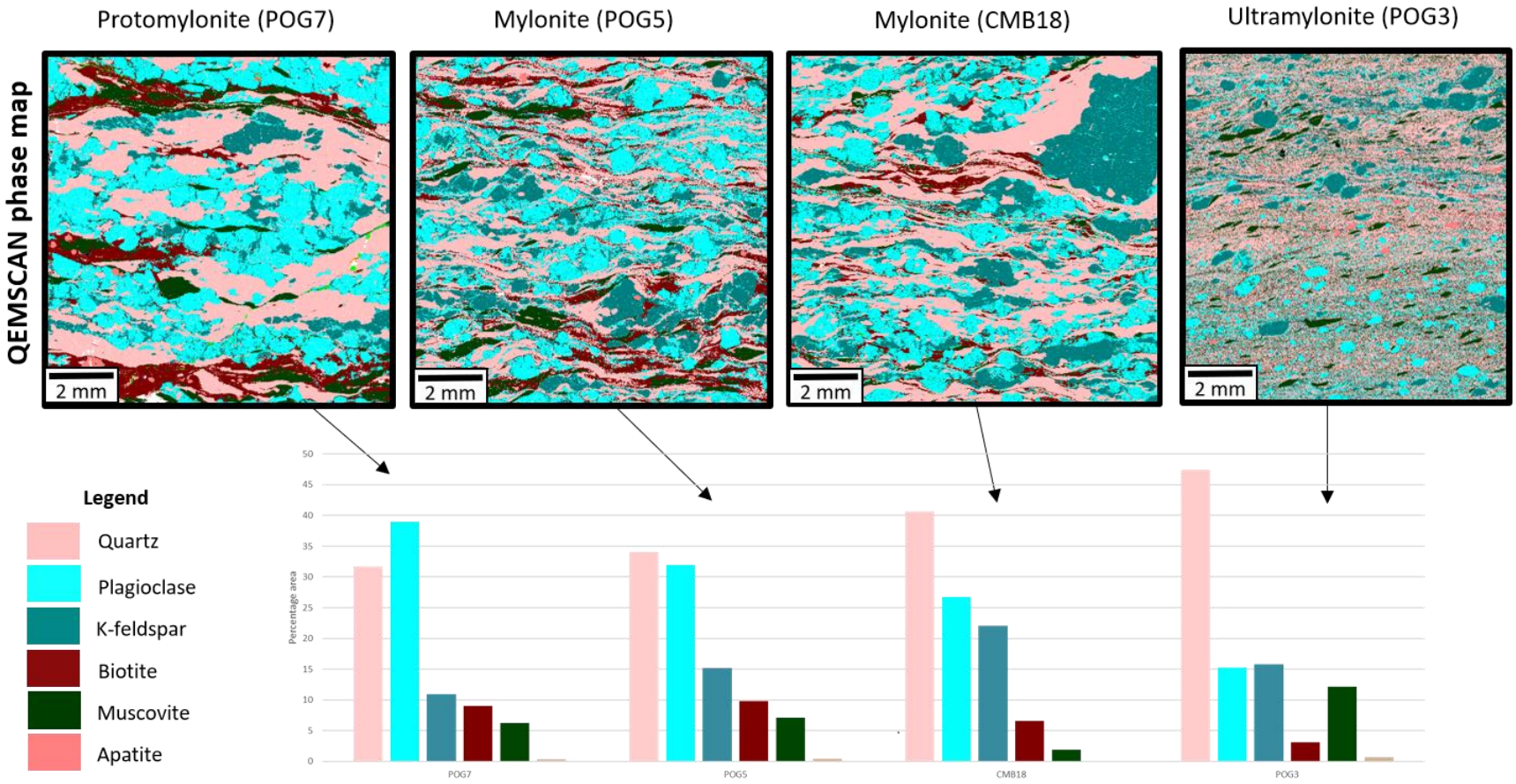


***Figure 6.2:*** *QEMSCAN phase maps and modal abundance data displaying the phase distribution and percentage area of thin sections from 4 of the key samples used in this study. Sample CMB18 is a deformed granitoid mylonite from the CMB line with very low mica content. POG3, POG5 and POG7 are an ultramylonite, mylonite and protomylonite respectively collected from a transect across the Pogallo line and share a felsic orthogneiss protolith. Increasing strain from POG7 through POG5 to POG3 produces a reduction in grain size of all phases, although the mechanisms are different (see text). There also appears to be a change in mineralogy with increasing quartz and muscovite and decreasing plagioclase and biotite.*

and forming discontinuous bands. Intracrystalline deformation within these coarse grains is evidenced by the presence of kink bands and some disaggregation along the basal planes (Fig. 6.3a). A small proportion of the biotite exists as finer grains (3 – 10 μm) within fine mixed phase domains which occur in narrow bands along foliation, usually connecting coarser mica grains. Despite this, the mica component does not form a fully interconnected network in these protomylonites. At higher strain (POG5, CMB5A, CMB18) there is a notable change in the distribution of biotite. Fine-grained biotite-rich regions are localised predominantly around the edges and especially at the tips of coarser biotite grains and extend along foliation to form a penetrative interconnected network (Fig. 6.3b-d). The fine-grained polyphase regions that were incipient in the protomylonites are far more prevalent in the mylonites and a significant proportion of the biotite in the mylonite occurs as part of these regions. In sample POG5 the fine grains are around 5 – 15 μm in diameter although in CMB5A they are only 1 – 3 μm in size. Relict biotite fish are finer grained than in lower strain samples (<1 mm) and consistently surrounded by fine grains (Fig. 6.3). There is no gradual transition from parent grain to fine new grains, and no subgrains or classic dynamic recrystallisation structures are observed (e.g. De Bresser *et al.*, 1998; Stipp *et al.*, 2002). The narrow regions of fine-grained material, while dominated by biotite, are also composed of quartz, feldspar, muscovite and titanium oxides. EDS element maps (Fig. 6.4) reveal that Ti-rich phases, (rutile and ilmenite) are distributed throughout the fine-grained domains and are especially concentrated around the margins of large biotite grains in association with fine-grained biotite. In samples CMB5A and CMB18, grain size reduction of biotite is notably enhanced within C’ shear bands (Fig. 6.5). Muscovite in the mylonite samples does not show evidence of undergoing as extensive grain size reduction and exists in the form of mica fish (Fig. 6.3c-f) and a small component of fine fragments detached from coarser grains along the basal planes. Muscovite porphyroclasts within the fine-grained shear bands display sharp, clear boundaries which appear to be stable in the fine-grained matrix. By contrast relict fragments of coarser biotite within the shear bands have irregular, diffuse boundaries with the matrix (Fig. 6.6). In the ultramylonites, biotite exists solely as a component of the fine matrix with no surviving coarser clasts. Muscovite similarly forms a component of this matrix however muscovite fish on the order of 1 mm in length are also common. These fish are bent or kinked but display no evidence of subgrains and often possess tails rich in fine, elongate muscovite flakes. Backscattered electron images from ultramylonite sample POG3 show that the muscovite fish tails become disaggregated by flaking along (001) cleavage planes, and that small amounts of biotite exist in places in between these cleavage surfaces (Fig. 6.7a). Biotite and muscovite grains within the ultramylonite matrix display a shape preferred orientation

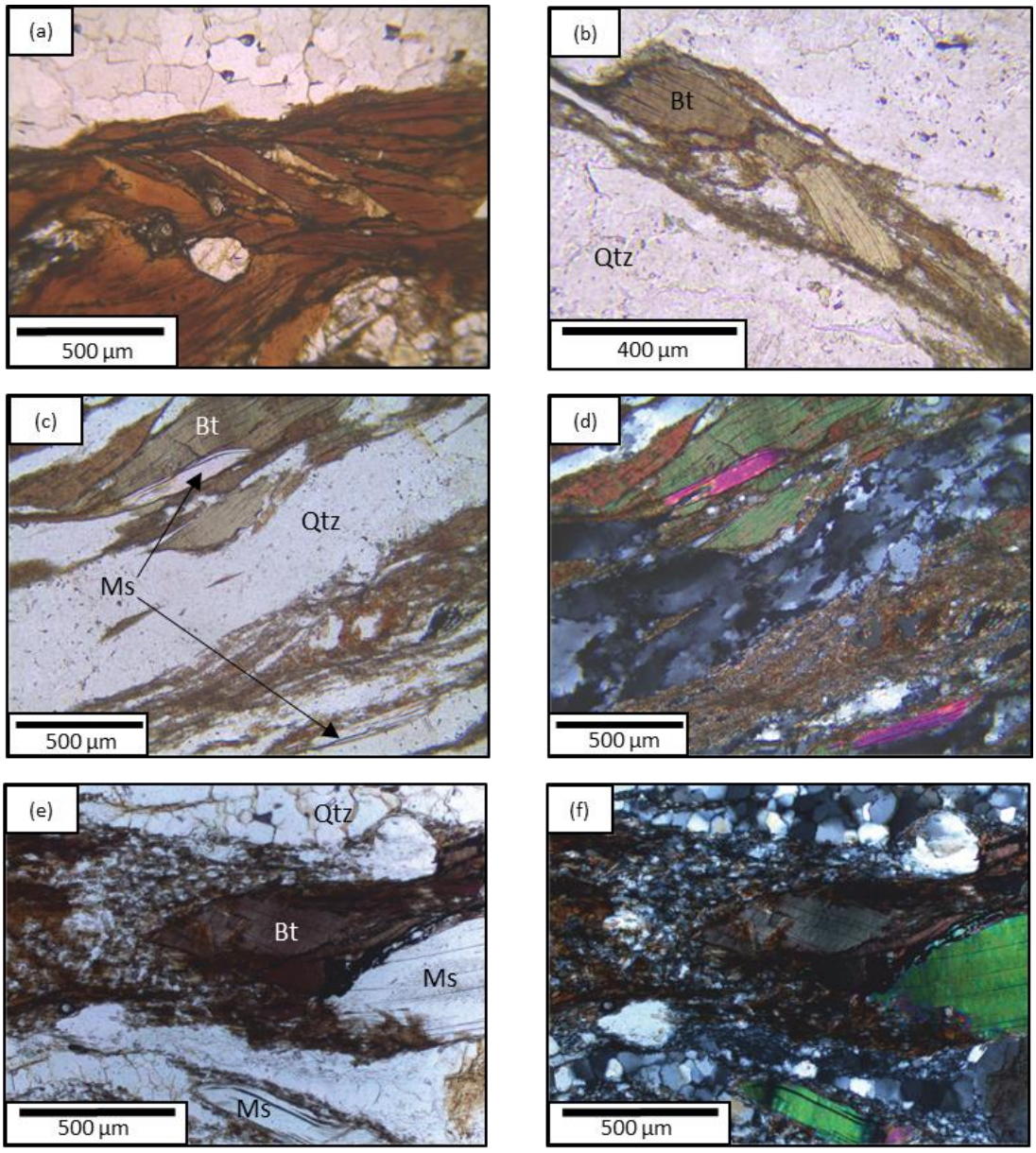


***Figure 6.3:*** *Optical micrographs of microstructures from mylonite samples. a) Plane polarised light image of a region from protomylonites sample POG7 showing a cluster of coarse biotite grains, some containing kink bands. b), Plane polarised light image of a region of sample CMB18 showing a coarse biotite grain which has undergone dramatic grain size reduction around its margins. The new biotite grains are 1-5µm in diameter, substantially finer than both the parent grain and the recrystallised quartz surrounding it and extend along the mylonitic foliation connecting otherwise isolated coarser grains. c) and d), Plane- and crossed-polarised light images respectively of a region of sample CMB18 showing a cluster of coarse old biotite (top left) in close proximity to a band of fine-grained new biotite within a higher strain shear band (bottom). Note the muscovite grains - pink interference colours in (d) - which are coarse in both regions. e) and f), Plane- and crossed-polarised light images respectively of a region of sample POG5 showing a coarse biotite grain bordered to the left by a mixture of fine biotite and quartz. Note the difference in grain size between the recrystallised quartz in the monomineralic band at the top of the image and that of the quartz where it is mixed with biotite. As in c) and d), muscovite grains show no evidence of the same grain size reduction process.*

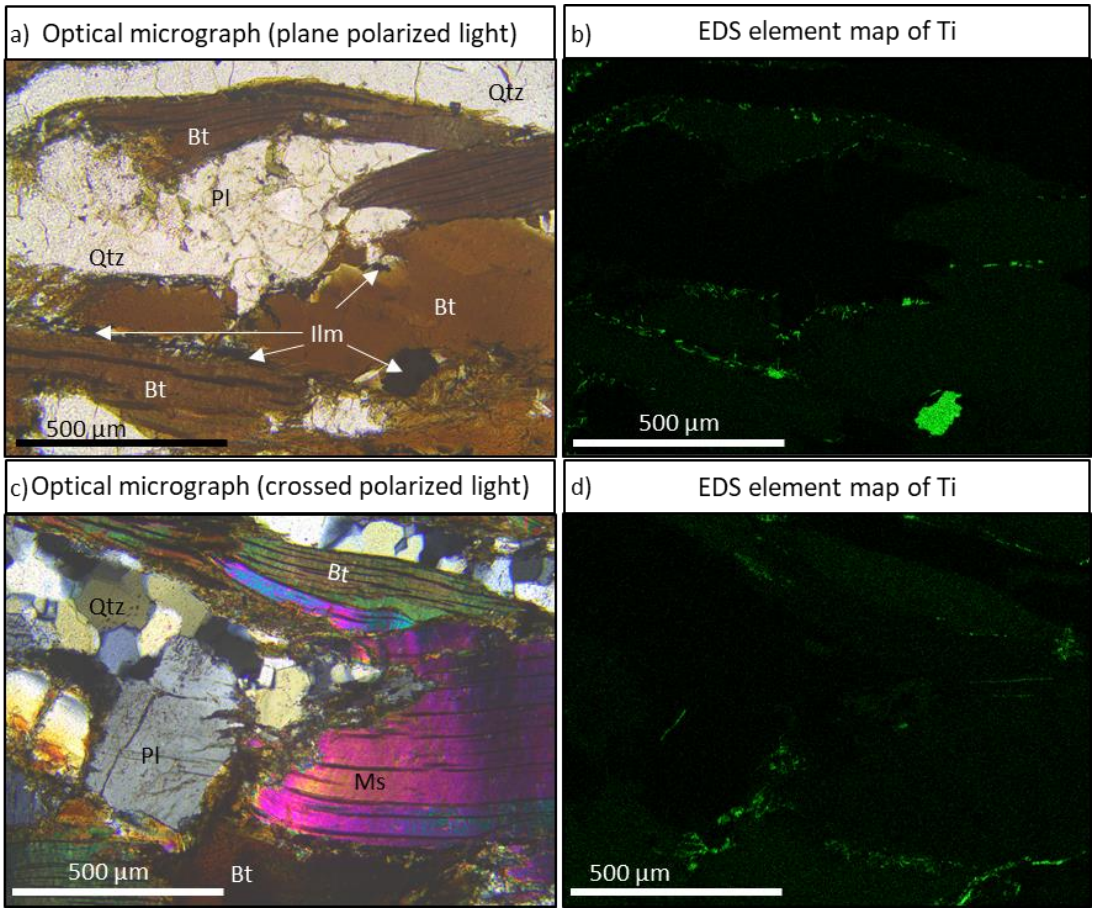


***Figure 6.4:*** *Optical micrographs (a and c) and SEM EDS Ti element maps (b and d) of two regions of sample POG7 where coarse biotite grains have started to undergo grain size reduction. The Ti maps reveal the presence of Ti-rich phases concentrated around the margins of coarse biotite grains and coinciding with the regions where fine-grained biotite has formed. Fine grains of other phases are also present in these regions including muscovite, plagioclase and quartz.*

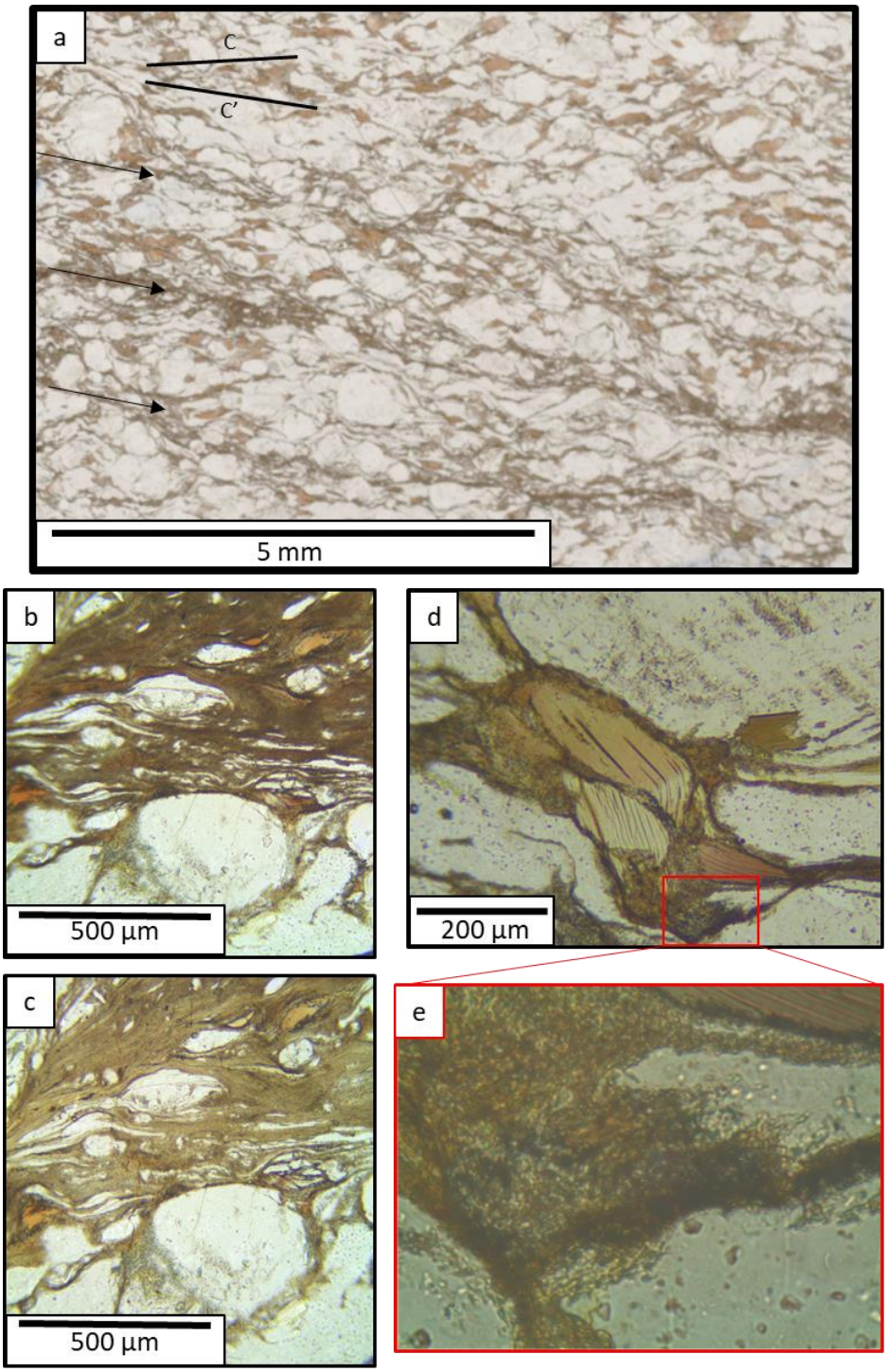


***Figure 6.5:*** *Plane polarised light optical micrographs of sample CMB5A. a) Low magnification image showing the general microstructure of the mylonite with isolated coarse biotite grains connected by narrow bands of very fine biotite. The three arrows indicate localised high strain zones comprised primarily of very fine-grained biotite and quartz and defining the C' surfaces of an overall C-C' fabric. b) and c) Detail of a region within the shear band indicated by the middle arrow in (a) with 90° difference in the orientation of the polariser. The fine biotite in the shear band displays a strong uniform pleochroism. d) Detail of a biotite grain from outside of the shear bands. The old biotite grain is kinked and displays rounded boundaries. Very fine biotite has formed along the margins of the grain, especially at the tips, and is distributed away from the grain along quartz and feldspar grain boundaries. e) Detail of the fine-grained material from the region highlighted in (d). While the main constituent of this fine-grained region is biotite, there is also quartz and oxide minerals.*

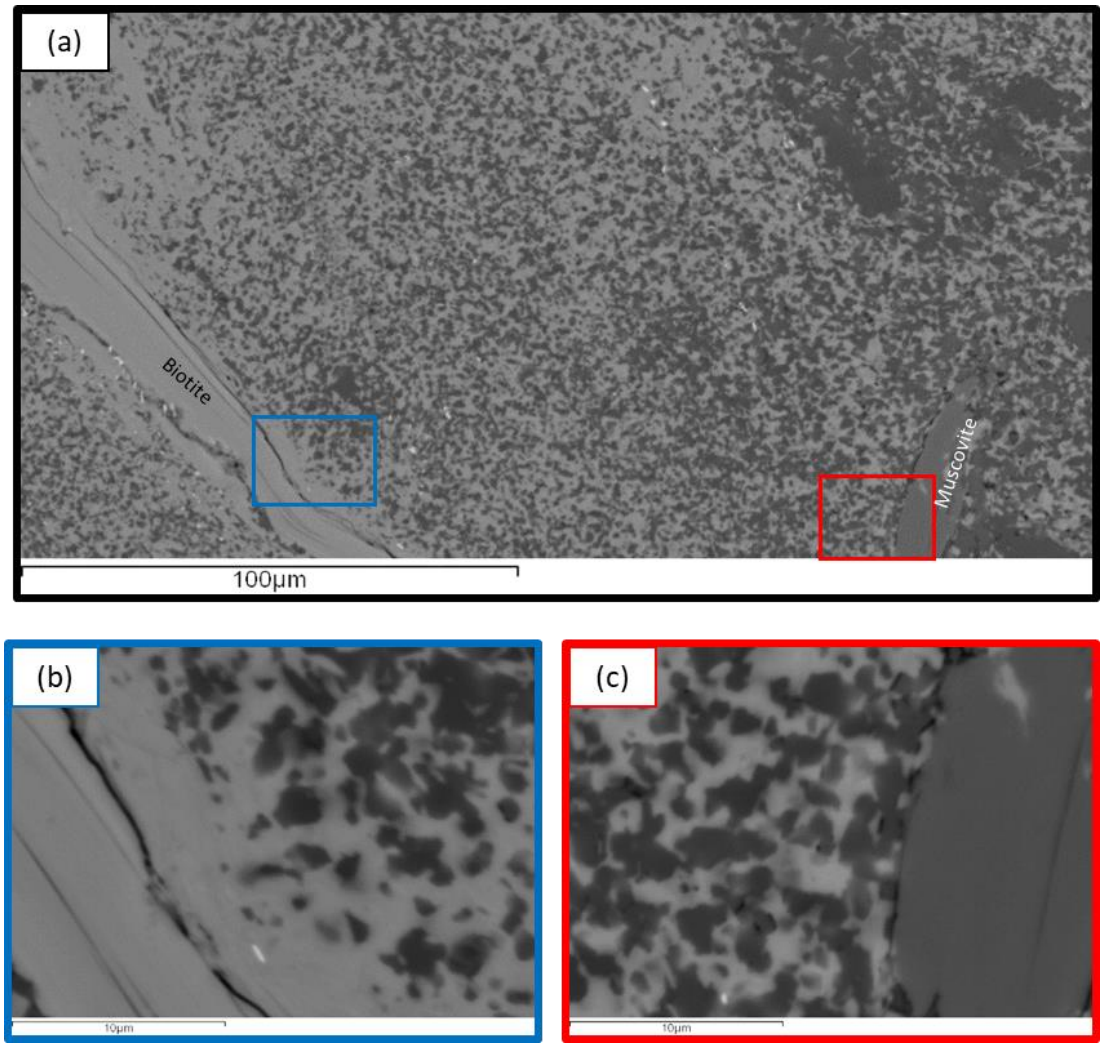


***Figure 6.6:*** *a) SEM backscattered electron image from one of the fine grained shear bands in sample CMB5A highlighting the extremely fine grain size. The shear band is composed primarily of biotite (light grey) and quartz (darkest grey) with both phases widely distributed throughout. b) and c), detail of the areas indicated in (a) showing the contrast between the diffuse, poorly defined margin of a coarse biotite grain with the fine shear band matrix (b) and the sharp boundary of a muscovite grain (c).*

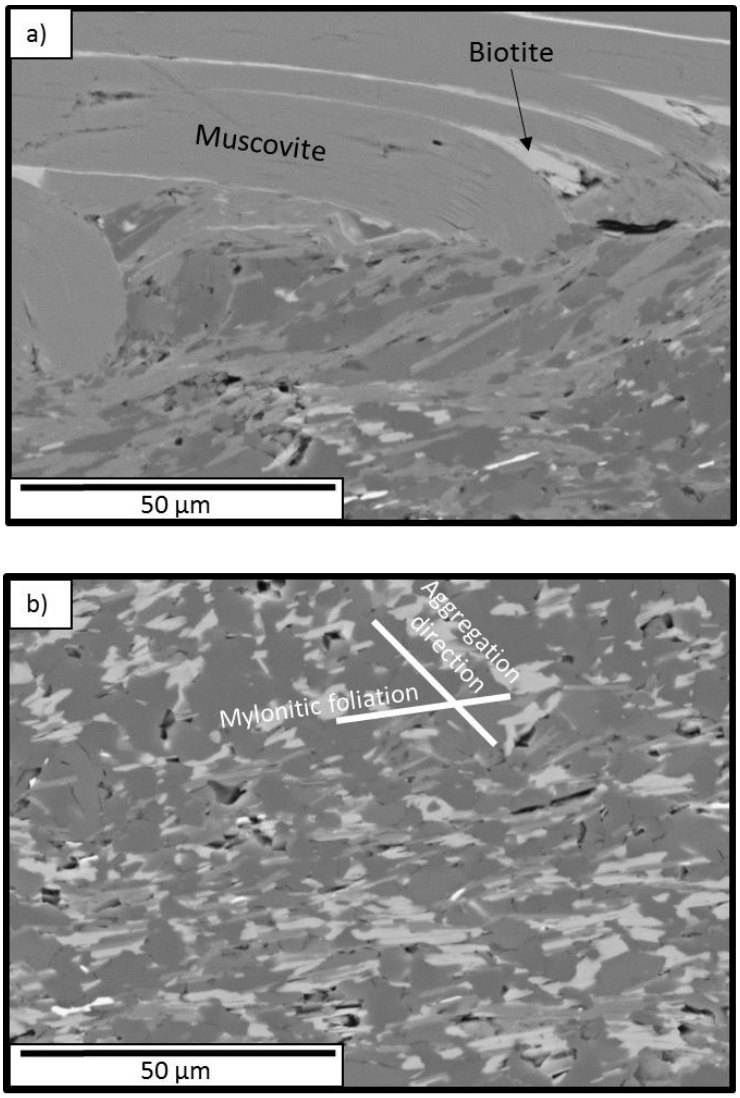


***Figure 6.7:*** *SEM backscatter electron images from sample POG3. a) Fine flakes of muscovite (medium grey) become part of the matrix by peeling off from larger muscovite fish along the basal planes. Small amounts of biotite (light grey) can be seen filling the cleavage spaces produced by this peeling. b) The fine-grained matrix of the ultramylonite is composed of multiple phases including quartz, plagioclase, biotite, K-feldspar and muscovite. The biotite and muscovite grains are elongate and aligned parallel to the mylonitic foliation. On a fine scale, like phases (particularly quartz) can be seen to aggregate together forming one grain wide bands of individual phases aligned at a high angle to mylonitic foliation. Such aggregation has been proposed to form as a result of deformation by grain size sensitive mechanisms such as diffusion creep (Miyazaki et al. 2013).*

and are elongated parallel to shear (Fig. 6.7b). The fine biotite grains in the matrix and in shear bands of the mylonites display uniform pleochroism indicative of a strong CPO.

### 6.4.3. Microstructural evolution of quartz

Quartz in the protomylonites (POG7) exists in monomineralic domains of polygonal grains of approximately 100 µm to 700 µm diameter (the finer grain sizes are typically associated with narrower domains). This is smaller than the grain size of feldspars and most of the micas in the protomylonites. The quartz grains are polygonal in shape with straight grain boundaries.

Some larger grains display undulose extinction, but this is absent in the smaller grains (Fig. 6.8a). The mylonite samples also exhibit monomineralic domains of quartz, however these are more elongate, forming foliation-parallel bands which wrap around feldspar porphyroclasts and have a finer grain size at ~50 µm. Most of the quartz in these moderate strain samples occurs in these dynamically recrystallised bands, with very few coarse grains with undulose extinction remaining. Quartz in the mylonites is also present within the fine-grained biotite dominated domains described in section 6.4.2. The grain size of this quartz is 1-10 µm, in stark contrast to the coarser grains in the monomineralic bands of dynamically recrystallised quartz (Fig. 6.3e, f). In the ultramylonites, quartz occurs solely as part of the fine-grained matrix with grain sizes of 1-5 µm, with no coarser monomineralic domains. Grains of quartz (and biotite) within the fine matrix display phase aggregation at high angles of approximately 45° to the foliation (Fig. 6.7b). This is similar to the aggregation of like phases in a fine matrix described by Miyazaki et al. (2013).

### 6.4.4. Microstructural evolution of feldspars

The lowest strain orthogneiss protomylonites (POG7) are characterised by coarse (~1-3 mm) plagioclase and, to a lesser extent K-feldspar, porphyroclasts surrounded by ribbons of finer recrystallized quartz. The feldspar porphyroclasts are sub-angular, occur in foliation parallel bands of grains and show strong evidence for brittle fracturing as well as limited undulose extinction (Fig 6.8b). The grain size of feldspar porphyroclasts in the mylonite samples (POG5, CMB18, CMB5A) is generally <1 mm however larger porphyroclasts up to 5 mm are present in sample CMB18. In these samples many of the fractured feldspar porphyroclasts contain fine feldspar grains within fractures and between porphyroclasts. These fine grains are not necessarily of the same phase as the porphyroclast, with both plagioclase and K-feldspar associated with both types of porphyroclasts. These microstructures are analysed and discussed at length in Chapter 8 of this thesis. In the ultramylonites, feldspar also forms abundant porphyroclasts. The largest porphyroclasts are composed of k-feldspar and range in size up to 3 mm in the thin section. However, the majority of K-feldspar porphyroclasts are <1 mm and rounded. The plagioclase porphyroclasts are smaller, with the largest at 1 mm and the majority <500 µm, and well-rounded in shape. Both K-feldspar and plagioclase are also present in abundance as part of the matrix with grain sizes of 1-5 µm.

### 6.4.5. Quartz c-axis orientations and CPO evolution from EBSD

Though the samples analysed in this study are polymineralic rocks, their load bearing framework is composed predominantly of quartz and the extent of recrystallisation and

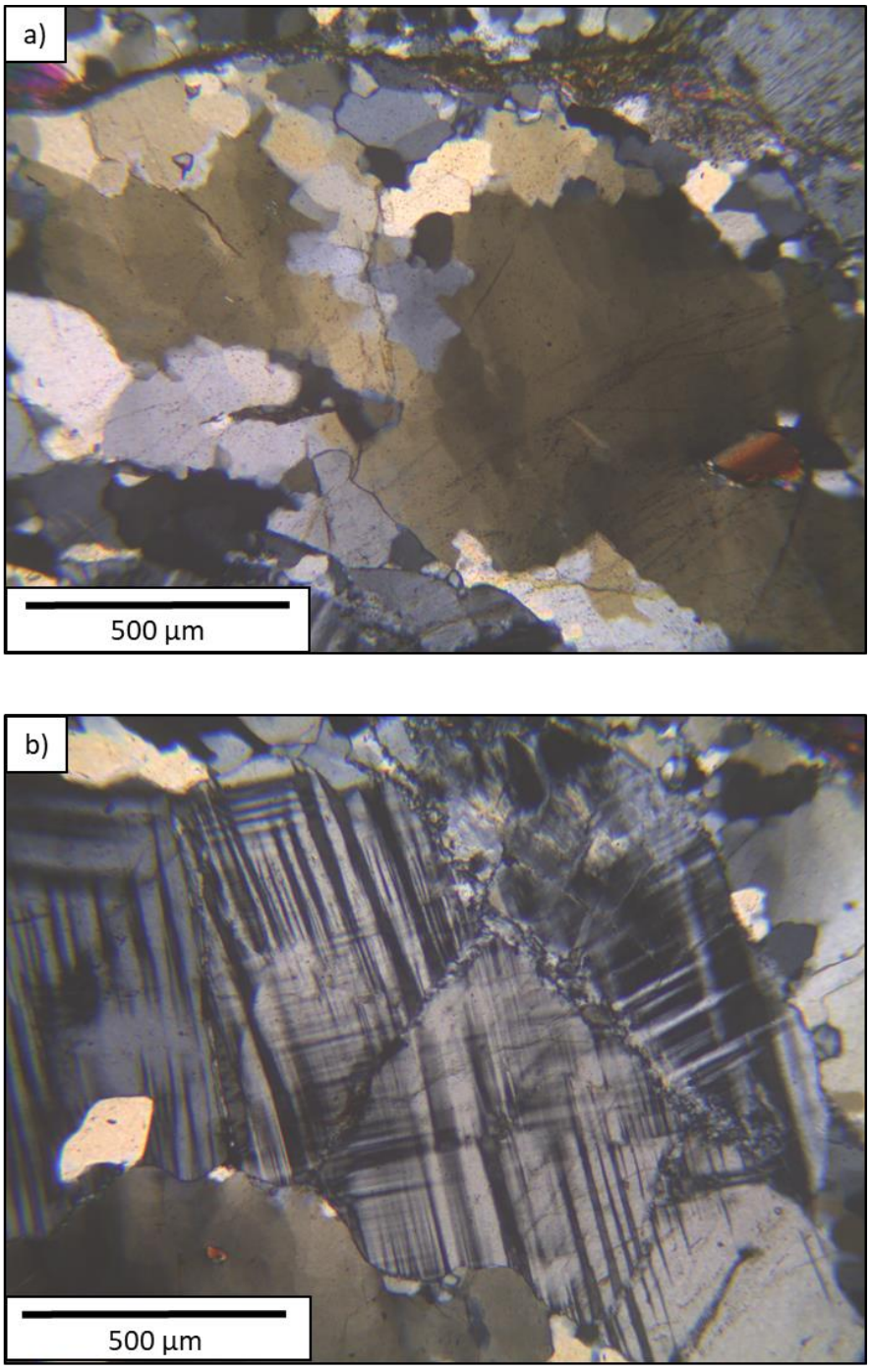


***Figure 6.8:*** *Crossed polarised light optical micrographs from protomylonite sample POG7. a) Large distorted quartz grain displaying undulose extinction throughout as well as subgrains and strain free new grains at the edges. b) Fractured microcline grain.*

undulose extinction within monomineralic quartz regions indicates that the quartz component has accommodated significant strain. Fig. 6.9a displays a quartz c-axis pole figure and corresponding quartz IPF colour orientation map taken from a 7 mm by 3.5 mm region of sample POG7 (the lowest strain sample of orthogneiss protomylonites). The quartz c-axis pole figure is dominated by a single girdle with weak elements of a type II crossed girdle. The fabric strength is very weak with a m-index of 0.0318.

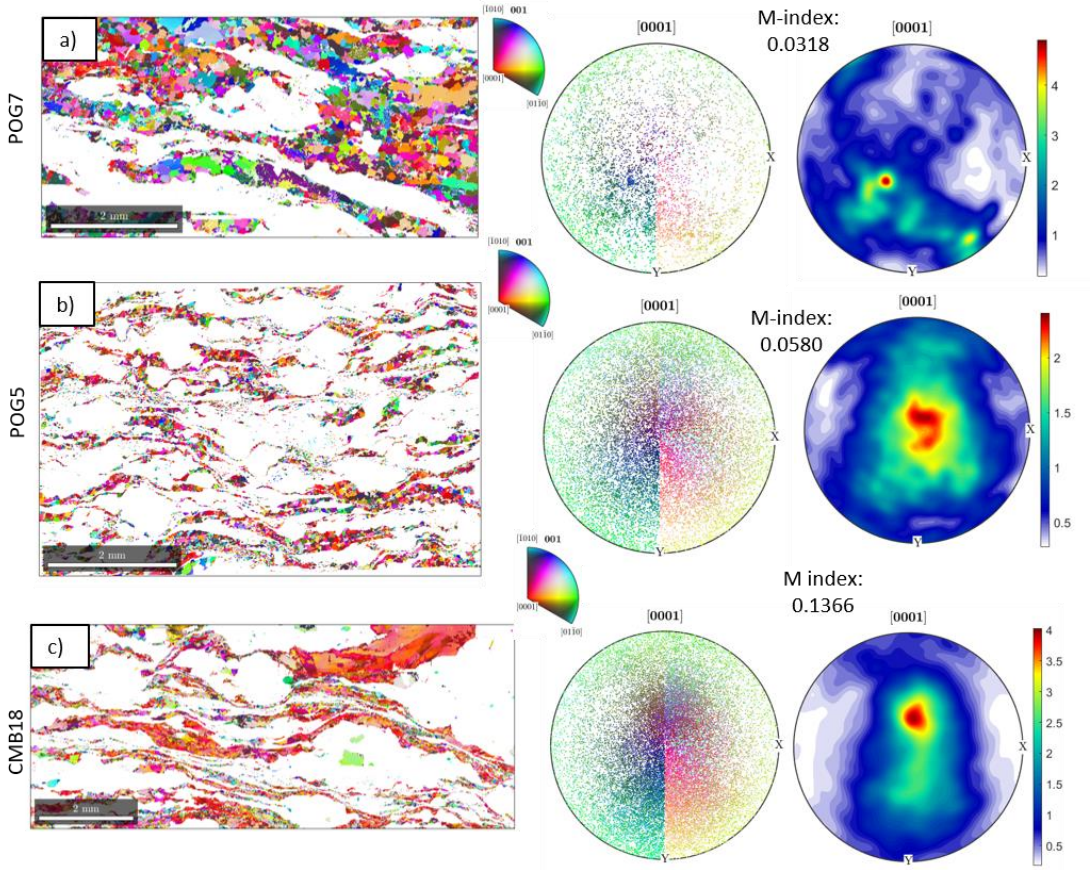


***Figure 6.9:*** *EBSD IPF colour orientation maps of the quartz phase within large regions of samples POG7 (a), POG5 (b) and CMB18 (c) with accompanying quartz c-axis pole figures produced using a single point to represent the mean orientation of each grain. The colours in the scattered pole figures also correspond to the IPF colours in the maps. POG7, a protomylonite, is characterised by large monophase areas recrystallised quartz and a relatively coarse grain size. The quartz c-axis pole figure for this region displays a weak crossed girdle distribution and has a relatively low M-index. Localised peaks on the pole figure are caused by large undulose grains associated with numerous slightly misoriented grains and subgrains. Quartz in the mylonite samples, POG5 and CMB18, occurs within narrow recrystallised ribbons with a much finer grain size than POG7. The quartz c-axis pole figures for POG5 and CMB18 both display central maxima with elements of a single girdle, indicative of higher strain. They also have stronger quartz CPOs with M-indexes of 0.0580 and 0.1366 respectively. EBSD orientation maps were collected using a 5 µm step size.*

The mylonites of POG5 and CMB18 display a finer grain size and narrower recrystallised ribbons. The quartz c-axis pole figures of these samples are characterised by the development of a central maximum with weak elements of a single girdle (Fig 6.9b, c). When individual recrystallised quartz ribbons from within the larger analysed area are selected as subsets, the c-axis pole figures possess more of a girdle shape than a central maximum although the orientations and strength of these girdles vary (Fig. 6.10). When quartz in regions of mixed phases (as opposed to monomineralic bands) are analysed separately, the fabric strength drops notably and the presence of girdles is generally less apparent (Fig. 6.10).

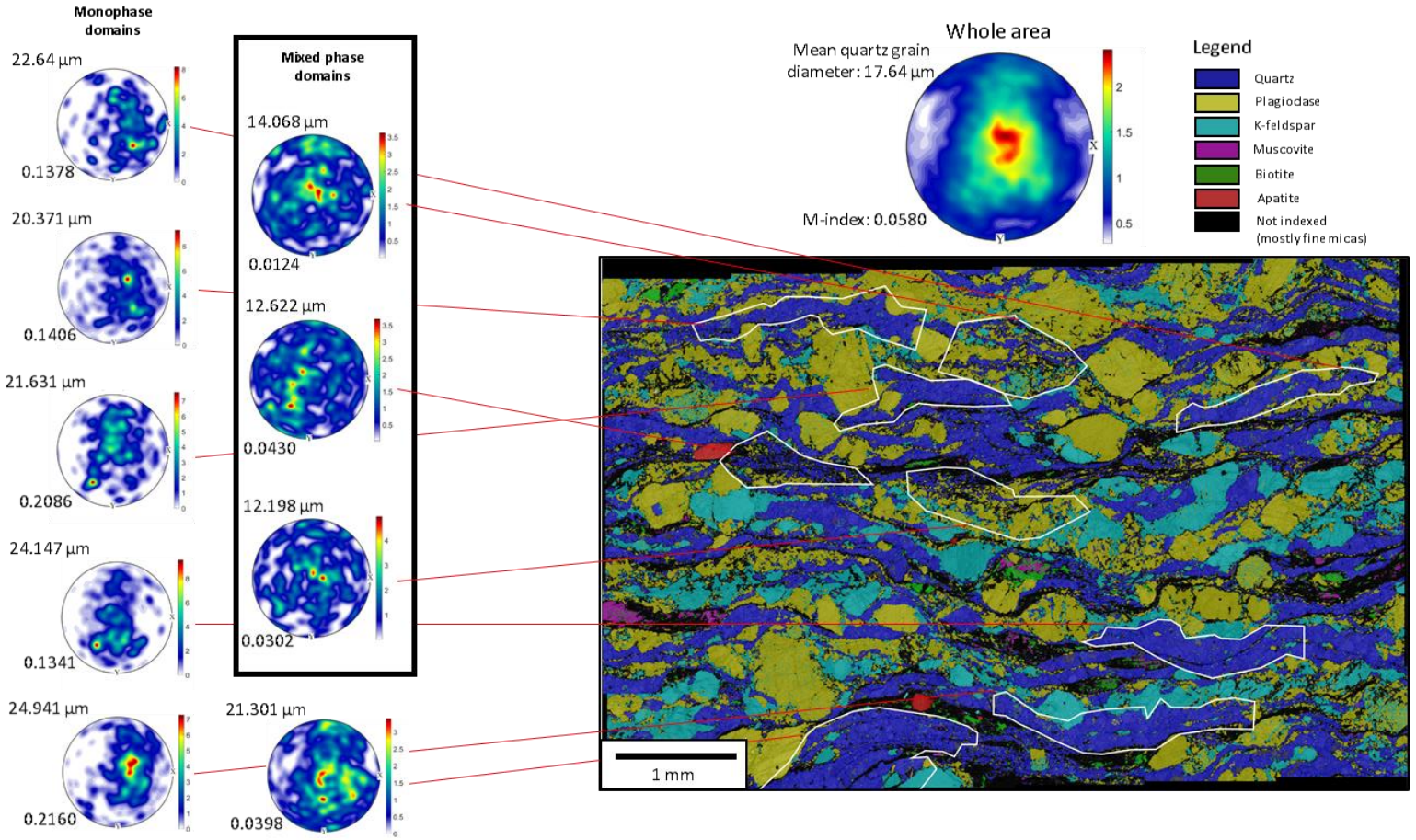


***Figure 6.10:*** *Lower hemisphere contoured quartz c-axis pole figures from sample POG5 and EBSD phase map of the same area. Individual subsets of monophase quartz ribbons and mixed phase domains are highlighted and attached to their corresponding pole figures. Top pole figure displays the data for the whole area. Monophase quartz ribbons display strong CPOs in the form of single girdles. By contrast, quartz c-axis pole figures taken from regions of mixed phases display much weaker CPOs indicated by lower M-index values and present less clear girdle patterns. Mixed phase domains are also characterised by a finer quartz grain size than monophase quartz ribbons. Pole figures incorporate one data point per grain (mean orientation). The step size is 5 µm.*

This is coupled with a finer grain size and fewer quartz-quartz grain boundaries within the polyphase regions. The quartz c-axis pole figures for POG3, which is the highest strain, ultramylonitic sample, display a weaker CPO than the lower strain samples, although the strength of this varies between sites of different mineralogy produced by compositional banding in the matrix (Fig. 6.11a). EBSD data taken from parts of the matrix that are quartz rich (45.23% quartz) (Fig. 6.11b) and parts that are relatively quartz poor (29.11% quartz) (Fig. 11c) display M-indexes of 0.0128 and 0.0048 respectively. The fabric strength is therefore higher in parts of the matrix with a greater density of quartz-quartz boundaries and lower where interphase boundaries are more common. In both cases this fabric is around an order of magnitude weaker than that expected within an aggregate in which the dominant deformation mechanism was dislocation creep.

Misorientation angle distributions (Wheeler *et al.*, 2001) of quartz orientation data from the same EBSD maps described above (and presented in Figs. 6.9 and 6.11) is plotted in Figure 6.12. The correlated misorientation angle distributions in the protomylonite (POG7) and mylonite (POG5, CMB18) samples display high peaks at low misorientation values and divert substantially from the theoretical random distribution at higher misorientation values. This is most pronounced in POG7 and CMB18. In contrast, the two datasets collected from the matrix of ultramylonite sample POG3 have less substantial peaks at low misorientation values and more closely follow the theoretical random distribution at higher misorientation values. In all plots there is a spike at 60° which is an artefact of dauphine' twinning relationships in quartz grains.

### 6.4.6. Chemical variation between coarse and fine biotite grains measured by EPMA

The grain size reduction of biotite may be facilitated by a predominantly mechanical process (dynamic recrystallisation or brittle fracturing) or by one that involves a chemical component (dissolution-precipitation and reactions). In deforming rocks, physical and chemical deformation and comminution mechanisms are not mutually exclusive. Dissolution precipitation reactions, for example, are greatly enhanced where fracturing provides abundant fluid pathways and sites of dilation. However, where chemical driving forces are involved, grain-size reduction can often be accompanied by a variation in mineral composition between parent and product grains which is not present in purely mechanical comminution mechanisms such as classic dynamic recrystallisation. To test whether chemical driving forces played a role in the grain size reduction of biotite in the studied mylonites,

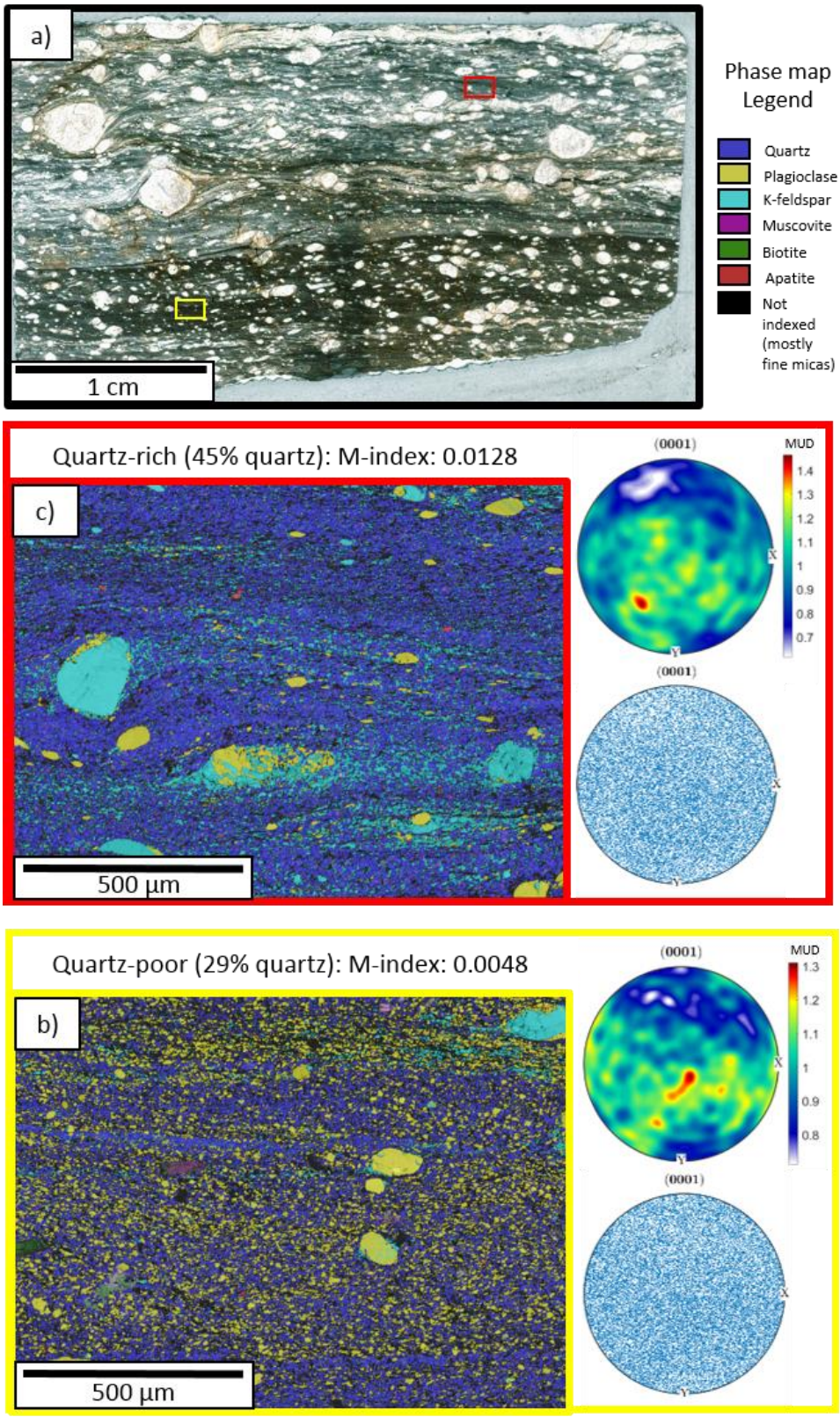


***Figure 6.11:*** *a) Optical thin section scan (plane polarized light) of sample POG3 showing compositional banding within the matrix. b) EBSD phase map of the region highlighted in (a) in a quartz rich domain within the matrix. Quartz composes 45% of the map. The quartz c-axis pole figure displays a very weak CPO with a M-index of 0.0128. c) EBSD phase map of the region highlighted in (a) within a quartz poor, biotite-rich section of the matrix. Quartz comprises 29% of the map and is well mixed with other phases. The CPO is even weaker than that of (b) with a M-index of 0.0048. Phase maps were collected using a 1 µm step size.*

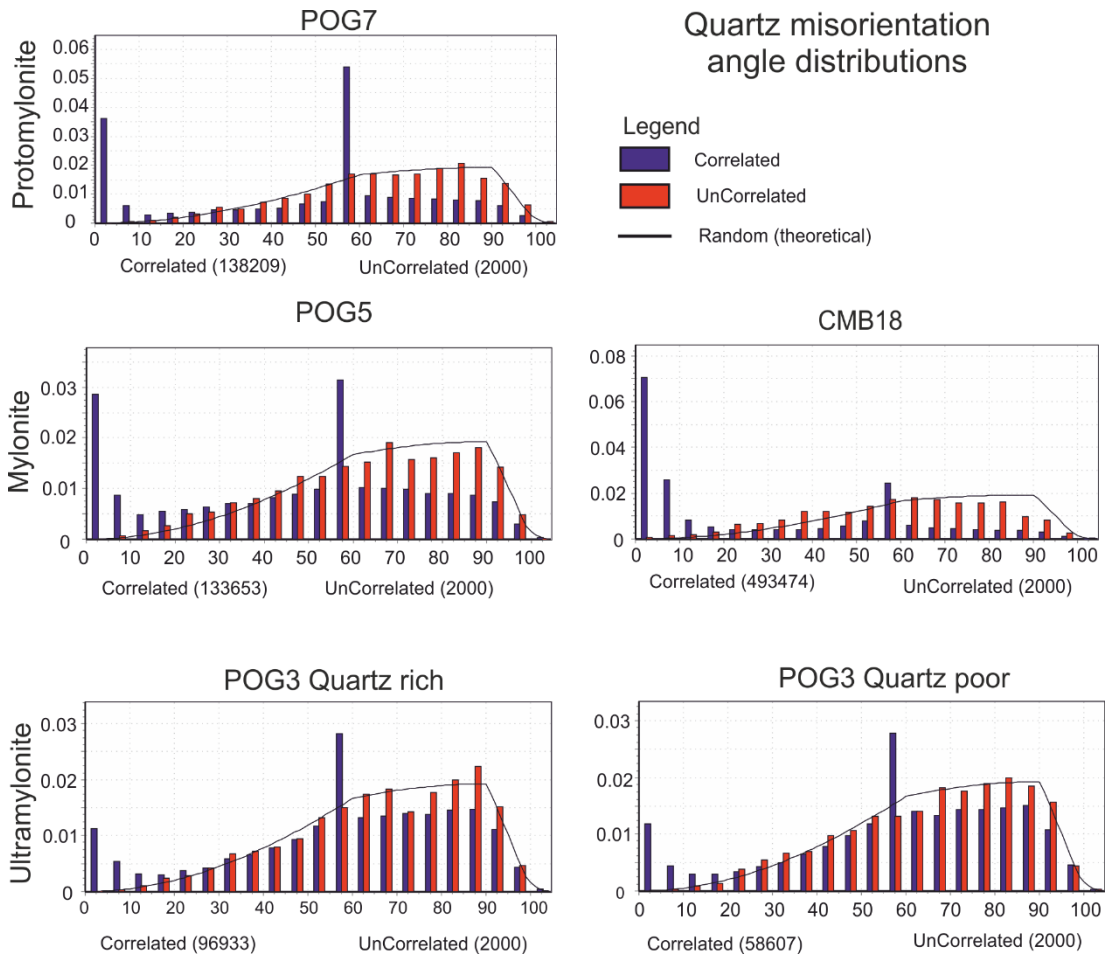


***Figure 6.12**: Misorientation angle distributions of quartz from the areas displayed in EBSD maps in Figs. 6.9 and 6.11. X-axis labels are in degrees. Misorientation angles below 2° were excluded from the data set to avoid error and the inclusion of correlated pairs within the same undeformed grain. Bin size is 5°.*

electron probe micro analysis (EPMA) was conducted on populations of both old and new biotite grains. If the process of grain size reduction was solely mechanical, then there should be no difference in the chemical composition of coarse grains relative to fine grains. However, as biotite exists in solid solution, new populations of biotite that have nucleated separately may exhibit regular and measurable differences in composition to that of the parent grains. The compositions of grains from 7 sites in 3 different samples were analysed. The samples chosen were all moderate strain mylonites as they needed to contain both coarse parent biotite grains and fine new grains. These samples are summarised in Table 6.2 and the areas used for acquisition are shown in Supplementary Figure S6.1. Tables 6.3 and 6.4 display the averaged results of microprobe analyses on each of these 7 sites in terms of wt% oxides and atoms per formula unit respectively. All measured wt% oxide values used to calculate these averages are available in Digital Appendix 1. Statistical t-tests using the mean values and the standard deviations of the wt% oxide data for each site were used to test for

***Table 6.2:*** *List of samples and sites within samples used for EPMA analyses of coarse and fine biotite grains along with the instrument conditions used. In both the University of Manchester and the Open University (OU) the instrument used was a Cameca SX-100 microprobe. Full wt% oxide data are available in Digital Appendix 1.*

| Sample | Site number | Strain level | Mineral analysed | Coarse grain data points | Fine grain data points | Total data points | Analysed at: | Beam diameter | Accelerating voltage | F measured (Y/N) |
|---|---|---|---|---|---|---|---|---|---|---|
| CMB18 | 0 | Mylonite | Biotite | 43 | 20 | 63 | Manchester | 10 µm | 15 kV | Y |
| CMB18 | 2 | Mylonite | Biotite | 31 | 36 | 67 | OU | 1 µm | 10 kV | N |
| CMB18 | 3 | Mylonite | Biotite | 30 | 29 | 59 | OU | 1 µm | 10 kV | N |
| CMB5A | 1 | Mylonite | Biotite | 14 | 22 | 36 | OU | 1 µm | 10 kV | N |
| CMB5A | 2 | Mylonite | Biotite | 17 | 7 | 24 | OU | 1 µm | 10 kV | N |
| POG5 | 1 | Mylonite | Biotite | 18 | 6 | 24 | Manchester | 10 µm | 15 kV | Y |
| POG5 | 2 | Mylonite | Biotite | 45 | 29 | 74 | OU | 1 µm | 10 kV | N |

a statistically significant difference between coarse and fine biotite populations. The results of this analysis is given in Supplementary Table 1. At a coarse scale, the composition of the two populations is very similar in all the samples. The Mg:Fe ratio does not show significant variation between the two populations (Fig. 6.13). However, when Al content is plotted against Ti content, for each site, two broadly distinct populations can be identified (Fig. 6.14). In 5 out of the 7 sites, the coarse grains display higher TiO2 wt% and lower Al2O3 wt% than associated fine grains. Although the mean wt% oxide values of coarse and fine populations sometimes fall within error of each other (Fig. 6.15), the drop in TiO2 is statistically significant in 6 of the 7 sites while the increase in Al2O3 is statistically significant in 5 out of 7 (Supp. Table S6.1). When the analyses are averaged for each site, TiO2 wt% reduces from coarse to fine grains in every site, SiO2 wt% increases in every site except CMB18 site 3, where a small decrease is observed, and Al2O3 increases in every site except POG5 site 1 where the values are almost equal (Table 6.3).

There is a potential, with spots collected in small grains, for the electron beam to interact with grain boundaries and produce lower than accurate values of all components, which could lead to a source of error when compared directly to measurements taken from large grains. This effect may be identified if fine grains give both low $TiO_2$ values and low closing totals along a linear trend. However, when Wt% $TiO_2$ of these analyses is plotted against the closing totals, fine grains give lower Wt% $TiO_2$ values than coarser grains irrespective of their closing total (Fig. 6.16). The overall compositional variation is best visualised when the EPMA data are plotted in terms of atoms per formula unit (apfu) (Table 6.4) (Fig. 6.17). Coarse biotite grains have average Ti concentrations ranging from 0.39 apfu to 0.28 apfu while Ti in fine grains ranges from 0.31 apfu to 0.22 apfu. Ti content decreases (ΔTi) from coarse to fine

***Table 6.3:*** *Results of microprobe analyses of coarse and fine biotite grains. Displayed are mean Wt% oxide values and standard deviations (SD) for the sites analysed. The numbers of analyses taken in coarse and fine grains at each site are given in Table 2. Analyses of coarse grains are highlighted in blue rows while those of fine grains are highlighted in orange rows.*

| Sample | Site | Coarse /Fine | FeO Wt% | SD | F Wt% | SD | K2O Wt% | SD | Al2O3 Wt% | SD | Na2O Wt% | SD | MnO Wt% | SD | CaO Wt% | SD | SiO2 Wt% | SD | MgO Wt% | SD | TiO2 Wt% | SD | Closing Total | SD |
|---|---|---|---|---|---|---|---|---|---|---|---|---|---|---|---|---|---|---|---|---|---|---|---|---|
| CMB 18 | 0 | C | 23.55 | 0.62 | 0.22 | 0.04 | 9.29 | 0.26 | 17.38 | 0.65 | 0.09 | 0.04 | 0.37 | 0.05 | 0.03 | 0.02 | 33.41 | 0.53 | 6.35 | 0.19 | 3.24 | 0.34 | 93.93 | 0.95 |
| | | F | 23.22 | 1.12 | 0.16 | 0.04 | 8.89 | 0.76 | 17.69 | 0.48 | 0.25 | 0.43 | 0.34 | 0.04 | 0.19 | 0.22 | 34.20 | 1.03 | 6.24 | 0.33 | 2.58 | 0.45 | 93.76 | 0.89 |
| | 2 | C | 24.60 | 1.00 | | | 9.22 | 0.55 | 17.61 | 1.01 | 0.06 | 0.02 | 0.33 | 0.09 | 0.06 | 0.09 | 34.99 | 0.61 | 6.89 | 0.33 | 2.74 | 0.29 | 96.51 | 1.47 |
| | | F | 23.91 | 0.98 | | | 9.34 | 0.42 | 18.17 | 0.48 | 0.03 | 0.03 | 0.30 | 0.06 | 0.05 | 0.09 | 35.19 | 0.77 | 6.81 | 0.22 | 2.47 | 0.25 | 96.28 | 0.96 |
| | 3 | C | 24.21 | 0.84 | | | 9.64 | 0.12 | 17.73 | 0.43 | 0.07 | 0.03 | 0.39 | 0.08 | 0.01 | 0.09 | 35.28 | 0.52 | 6.86 | 0.26 | 2.89 | 0.40 | 97.10 | 0.78 |
| | | F | 24.25 | 1.18 | | | 8.77 | 0.80 | 18.56 | 0.71 | 0.04 | 0.03 | 0.33 | 0.07 | 0.13 | 0.25 | 34.87 | 0.92 | 6.94 | 0.42 | 1.92 | 0.51 | 95.84 | 1.26 |
| CMB 5A | 1 | C | 20.27 | 0.91 | | | 9.52 | 0.41 | 18.13 | 0.49 | 0.11 | 0.02 | 0.27 | 0.05 | 0.03 | 0.09 | 35.28 | 0.37 | 8.50 | 0.26 | 2.88 | 0.29 | 95.00 | 0.92 |
| | | F | 20.52 | 1.12 | | | 8.97 | 0.40 | 18.38 | 0.42 | 0.06 | 0.02 | 0.21 | 0.04 | 0.05 | 0.10 | 35.35 | 1.41 | 8.64 | 0.46 | 2.22 | 0.46 | 94.42 | 1.08 |
| | 2 | C | 20.03 | 0.97 | | | 9.58 | 0.18 | 18.18 | 0.47 | 0.11 | 0.03 | 0.25 | 0.07 | 0.00 | 0.05 | 35.62 | 0.31 | 8.61 | 0.17 | 2.82 | 0.26 | 95.23 | 1.07 |
| | | F | 19.39 | 0.94 | | | 9.28 | 0.21 | 18.07 | 0.78 | 0.04 | 0.03 | 0.22 | 0.03 | 0.05 | 0.11 | 35.91 | 1.14 | 8.41 | 0.35 | 2.32 | 0.34 | 93.71 | 0.48 |
| POG 5 | 1 | C | 23.12 | 0.46 | 0.50 | 0.04 | 9.32 | 0.36 | 17.42 | 0.34 | 0.06 | 0.03 | 0.30 | 0.02 | 0.07 | 0.08 | 34.20 | 0.43 | 7.12 | 0.17 | 2.35 | 0.16 | 94.46 | 1.07 |
| | | F | 22.99 | 0.80 | 0.47 | 0.04 | 8.77 | 0.34 | 17.41 | 0.39 | 0.04 | 0.02 | 0.30 | 0.06 | 0.06 | 0.04 | 34.62 | 1.09 | 6.89 | 0.14 | 2.24 | 0.41 | 93.80 | 1.30 |
| | 2 | C | 23.18 | 1.00 | | | 9.70 | 0.26 | 17.71 | 0.38 | 0.05 | 0.02 | 0.30 | 0.06 | 0.05 | 0.11 | 35.60 | 0.46 | 7.50 | 0.22 | 2.40 | 0.15 | 96.50 | 1.10 |
| | | F | 22.54 | 1.30 | | | 9.30 | 0.50 | 18.23 | 0.64 | 0.06 | 0.03 | 0.27 | 0.06 | 0.11 | 0.16 | 35.80 | 0.67 | 7.41 | 0.35 | 2.19 | 0.22 | 95.94 | 1.15 |

***Table 6.4:*** *Average compositional data for coarse and fine biotite grains expressed as atoms per formula unit (apfu). The change in each element from coarse to fine grains is given in the 'Δ' columns. The 'Total Cations' column should sum to 16 as this is the amount of cations which exist in the biotite unit formula. The deficiency can be related partly to low closure values of the analyses and the existence of $Fe^{3+}$ in octahedral sites, which is not analysed by EPMA. Also, as $Al^{3+}$ and $Fe^{3+}$ increasingly substitute for $Mg^{2+}$ and $Fe^{2+}$ in octahedral sites, the biotite becomes less trioctahedral and more dioctahedral, which will also reduce the total number of cations.*

| Sample | Site | Coarse /Fine | Fe (apfu) | ΔFe | F (apfu) | ΔF | K (apfu) | ΔK | Al (apfu) | ΔAl | Na (apfu) | ΔNa | Mn (apfu) | ΔMn | Ca (apfu) | ΔCa | Si (apfu) | ΔSi | Mg (apfu) | ΔMg | Ti (apfu) | ΔTi | Total Cations | ΔTotal |
|---|---|---|---|---|---|---|---|---|---|---|---|---|---|---|---|---|---|---|---|---|---|---|---|---|
| CMB 18 | 0 | C | 3.14 | | 0.11 | | 1.89 | | 3.27 | | 0.03 | | 0.05 | | 0.00 | | 5.33 | | 1.51 | | 0.39 | | 15.72 | |
| | | F | 3.08 | -0.06 | 0.08 | -0.03 | 1.80 | -0.09 | 3.31 | 0.04 | 0.08 | 0.05 | 0.05 | 0.00 | 0.03 | 0.03 | 5.42 | 0.10 | 1.48 | -0.03 | 0.31 | -0.08 | 15.63 | -0.09 |
| | 2 | C | 3.19 | | | | 1.83 | | 3.23 | | 0.02 | | 0.04 | | 0.01 | | 5.37 | | 1.59 | | 0.32 | | 15.62 | |
| | | F | 3.10 | -0.09 | | | 1.85 | 0.02 | 3.32 | 0.10 | 0.01 | -0.01 | 0.04 | -0.01 | 0.01 | 0.00 | 5.39 | 0.02 | 1.58 | -0.02 | 0.29 | -0.03 | 15.59 | -0.03 |
| | 3 | C | 3.13 | | | | 1.90 | | 3.23 | | 0.02 | | 0.05 | | 0.00 | | 5.38 | | 1.58 | | 0.34 | | 15.63 | |
| | | F | 3.16 | 0.03 | | | 1.74 | -0.16 | 3.41 | 0.18 | 0.01 | -0.01 | 0.04 | -0.01 | 0.02 | 0.02 | 5.36 | -0.02 | 1.61 | 0.03 | 0.22 | -0.11 | 15.59 | -0.04 |
| CMB 5A | 1 | C | 2.62 | | | | 1.88 | | 3.31 | | 0.03 | | 0.04 | | 0.01 | | 5.39 | | 1.96 | | 0.34 | | 15.58 | |
| | | F | 2.67 | 0.04 | | | 1.78 | -0.10 | 3.36 | 0.05 | 0.02 | -0.01 | 0.03 | -0.01 | 0.01 | 0.00 | 5.42 | 0.03 | 2.00 | 0.04 | 0.26 | -0.08 | 15.54 | -0.03 |
| | 2 | C | 2.61 | | | | 1.88 | | 3.29 | | 0.03 | | 0.03 | | 0.00 | | 5.42 | | 1.98 | | 0.32 | | 15.57 | |
| | | F | 2.53 | -0.08 | | | 1.85 | -0.04 | 3.32 | 0.03 | 0.01 | -0.02 | 0.03 | -0.01 | 0.01 | 0.01 | 5.52 | 0.10 | 1.95 | -0.03 | 0.27 | -0.05 | 15.48 | -0.09 |
| POG 5 | 1 | C | 3.06 | | 0.25 | | 1.88 | | 3.25 | | 0.02 | | 0.04 | | 0.01 | | 5.41 | | 1.68 | | 0.28 | | 15.88 | |
| | | F | 3.05 | -0.01 | 0.24 | -0.01 | 1.77 | -0.11 | 3.25 | 0.00 | 0.01 | 0.00 | 0.04 | 0.00 | 0.01 | 0.00 | 5.48 | 0.07 | 1.63 | -0.05 | 0.27 | -0.01 | 15.75 | -0.13 |
| | 2 | C | 3.00 | | | | 1.91 | | 3.23 | | 0.02 | | 0.04 | | 0.01 | | 5.43 | | 1.73 | | 0.28 | | 15.64 | |
| | | F | 2.91 | -0.09 | | | 1.83 | -0.08 | 3.32 | 0.09 | 0.02 | 0.00 | 0.04 | 0.00 | 0.02 | 0.01 | 5.46 | 0.02 | 1.71 | -0.02 | 0.25 | -0.02 | 15.56 | -0.08 |

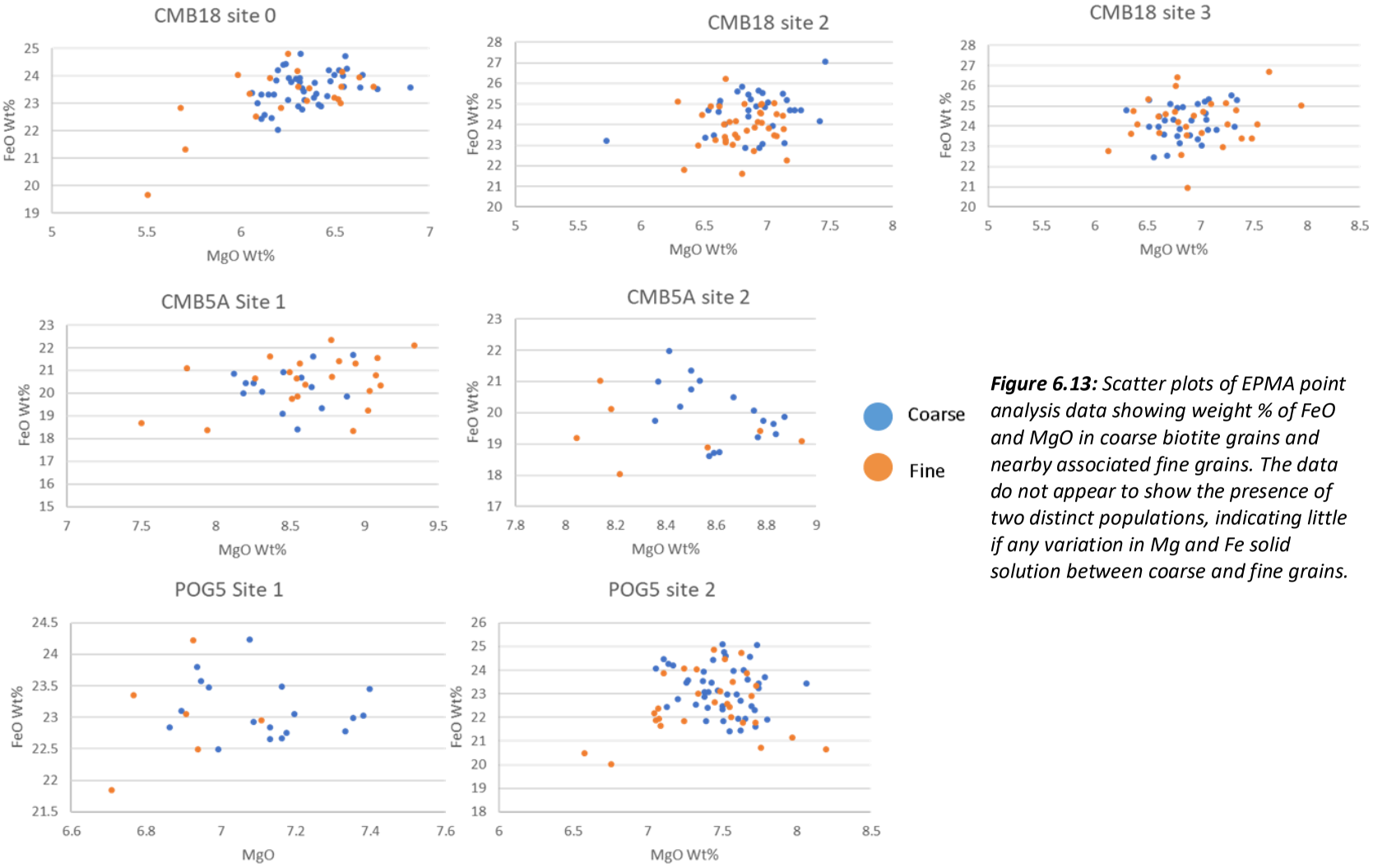


***Figure 6.13:*** *Scatter plots of EPMA point analysis data showing weight % of FeO and MgO in coarse biotite grains and nearby associated fine grains. The data do not appear to show the presence of two distinct populations, indicating little if any variation in Mg and Fe solid solution between coarse and fine grains.*

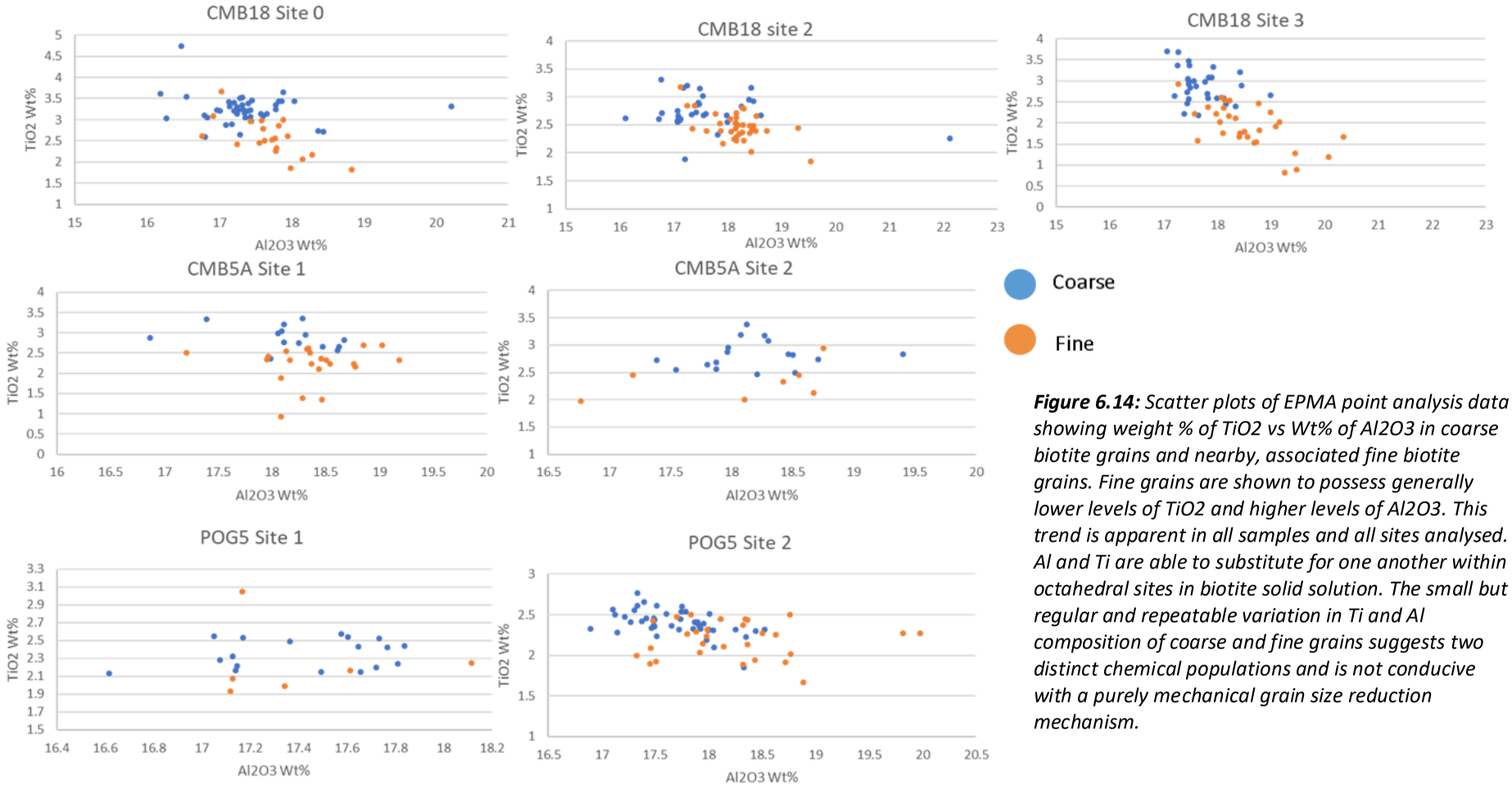


***Figure 6.14:*** *Scatter plots of EPMA point analysis data showing weight % of TiO2 vs Wt% of Al2O3 in coarse biotite grains and nearby, associated fine biotite grains. Fine grains are shown to possess generally lower levels of TiO2 and higher levels of Al2O3. This trend is apparent in all samples and all sites analysed. Al and Ti are able to substitute for one another within octahedral sites in biotite solid solution. The small but regular and repeatable variation in Ti and Al composition of coarse and fine grains suggests two distinct chemical populations and is not conducive with a purely mechanical grain size reduction mechanism.*

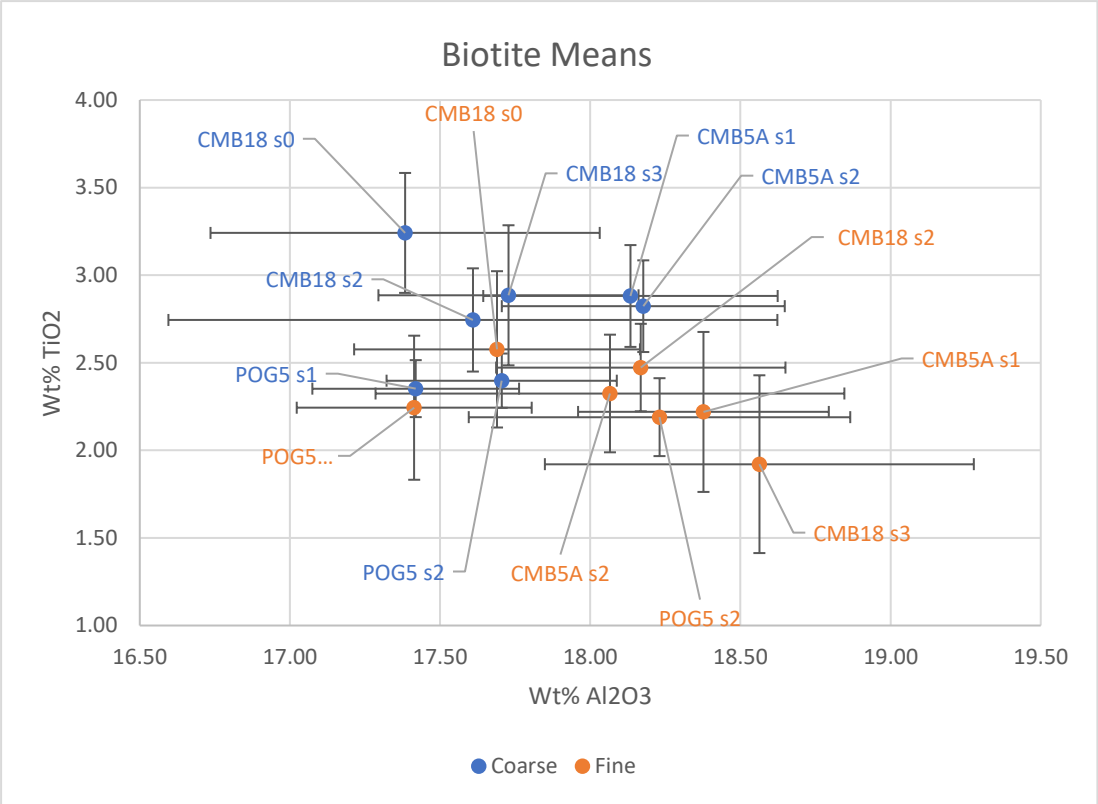


***Figure 6.15:*** *Plot of mean wt% $TiO_2$ against mean wt% $Al_2O_3$ for fine and coarse biotite grain at 7 sites in 3 samples. Error bars represent one standard deviation either side of the value.*

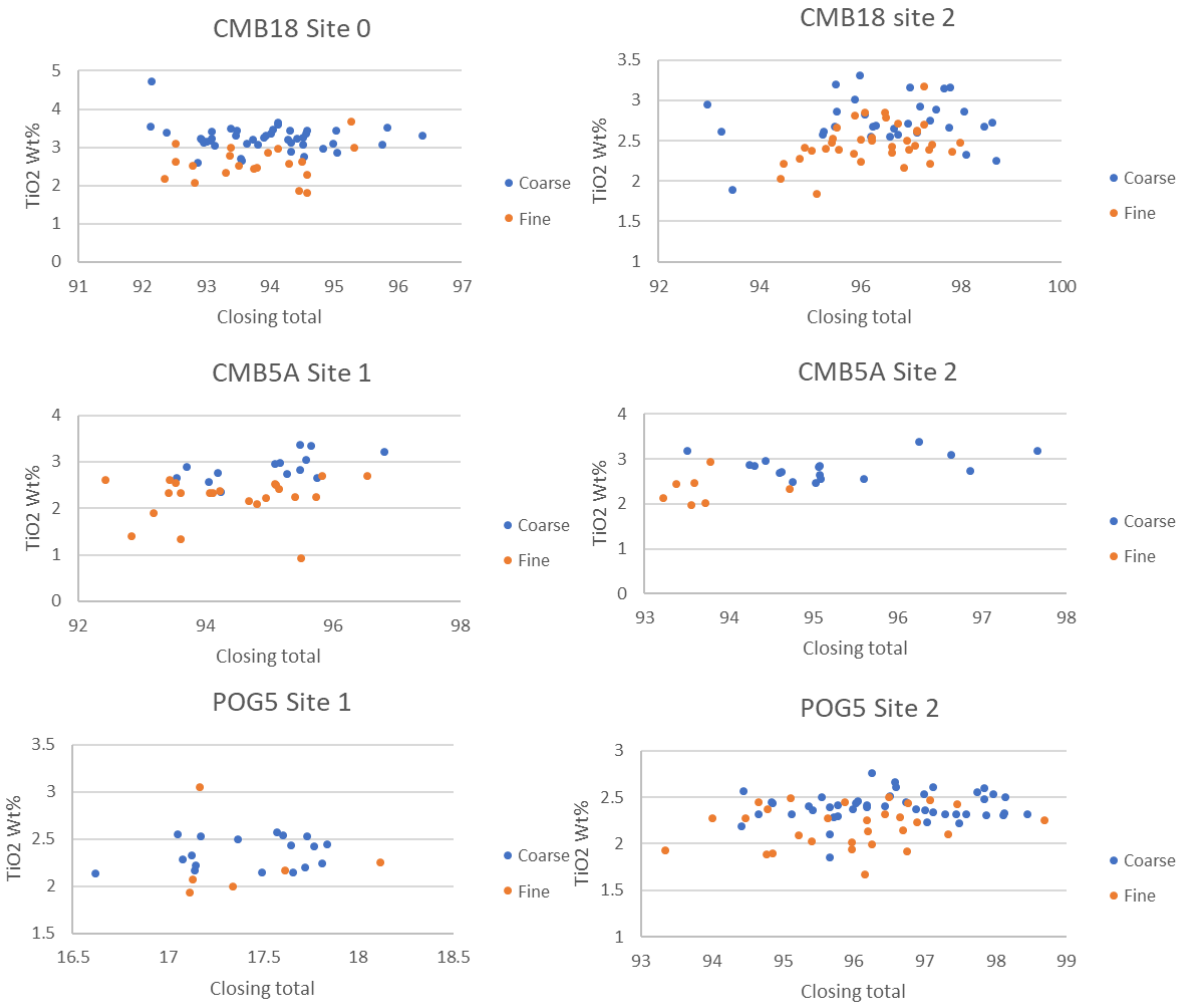


***Figure 6.16**: Scatter plots of EPMA point analysis data showing weight % of TiO2 vs the overall closing total of the analysis. In the majority of these plots the Ti content of fine grains plots below that of coarse grains even when the closing total is the same or even higher. This is evidence that the lower Ti content of fine biotite is not an artefact of overall lower closing totals in the analyses.*

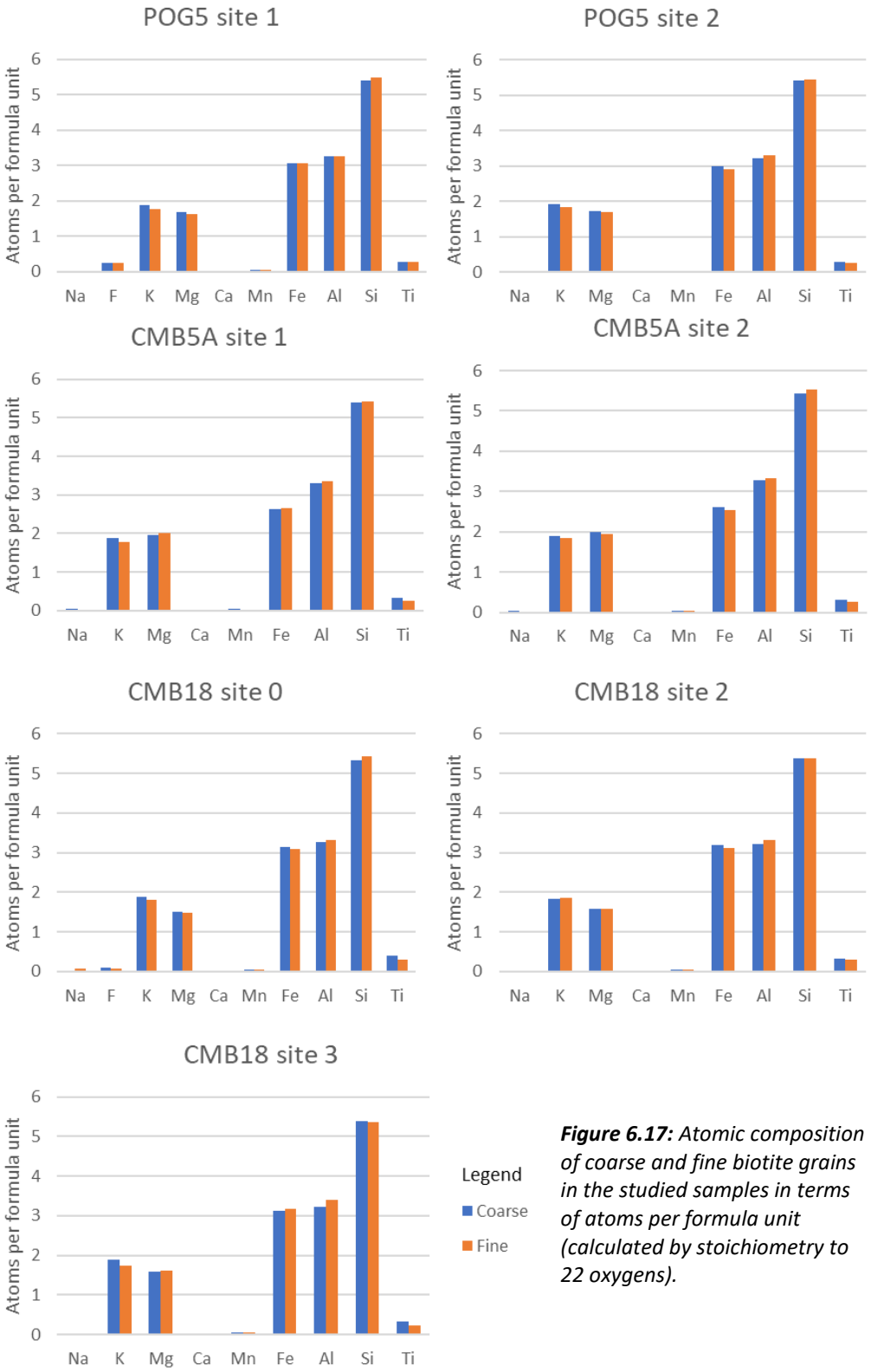


***Figure 6.17:*** *Atomic composition of coarse and fine biotite grains in the studied samples in terms of atoms per formula unit (calculated by stoichiometry to 22 oxygens).*

grains in all samples by degrees varying from 0.11 apfu in CMB18 site 3 to 0.01 apfu in POG5 site 1. The range in Al is from 3.23 to 3.31 apfu in coarse biotite grains and from 3.25 to 3.41 apfu in fine biotite grains with increases (ΔAl from coarse to fine grains) in individual sites of up to 0.18 apfu. Si increases from coarse to fine grains in all but one site, however the magnitude of these variations is in most cases not statistically significant (Supp. Table S6.1). There is also a small but statistically significant reduction in K from coarse to fine grains across all sites except for CMB18 site 2.

### 6.4.7. The transition between biotite porphyroclasts and new, fine-grained biotite

Microstructural analysis of the area of transition between the coarse and fine grains of biotite is critical to interpreting the mechanism responsible for grain size reduction. Due to the complex nature of this transition, and the fine grain sizes involved, the best method for these observations is transmission electron microscopy (TEM). The sample used for TEM analysis was CMB5A. In total, 3 TEM specimens were prepared from this sample (Fig. 6.18), one from the centre of a coarse biotite grain (specimen 1), one from a corner of that grain where fine grains had started to form (specimen 2), and one from the fine grained biotite rich matrix nearby (specimen 3) (Fig. 6.18a). The sample taken from the interior of the large grain is composed of a single grain of biotite with no evidence of subgrain formation or segmentation (Fig. 6.18c). In contrast, brightfield TEM images from the transition region clearly show euhedral, straight-sided biotite grains (Fig. 6.18d). These grains are interlocking with high angle boundaries and a pronounced shape preferred orientation (Fig. 6.18d, e). In a typical microstructure formed by dynamic recrystallisation, one would expect to observe core and mantle structures with subgrains gradually rotating to form new grains (subgrain rotation recrystallisation) or serrated grain boundaries if grain boundary migration recrystallisation was active (Stipp *et al.*, 2002; Passchier and Trouw, 2005). However, in the TEM specimen taken from the matrix there can be observed many euhedral biotite grains interlocking with quartz grains with which they are relatively well mixed (Fig. 6.18b). The boundaries between quartz and biotite grains are in places very irregular and lobate, with both phases curving into one another. These grains are of a very similar size to those observed in the transitional section, indicating that grain size reduction has occurred in one step, across a very sharp transition between specimens 1 and 2, followed by a further distribution of the new, fine grains amongst the quartz matrix between specimens 2 and 3. The biotite grains in the matrix possess a shape preferred orientation which is also evident from uniform pleochroism, displayed in optical micrographs (Fig. 6.5b, c).

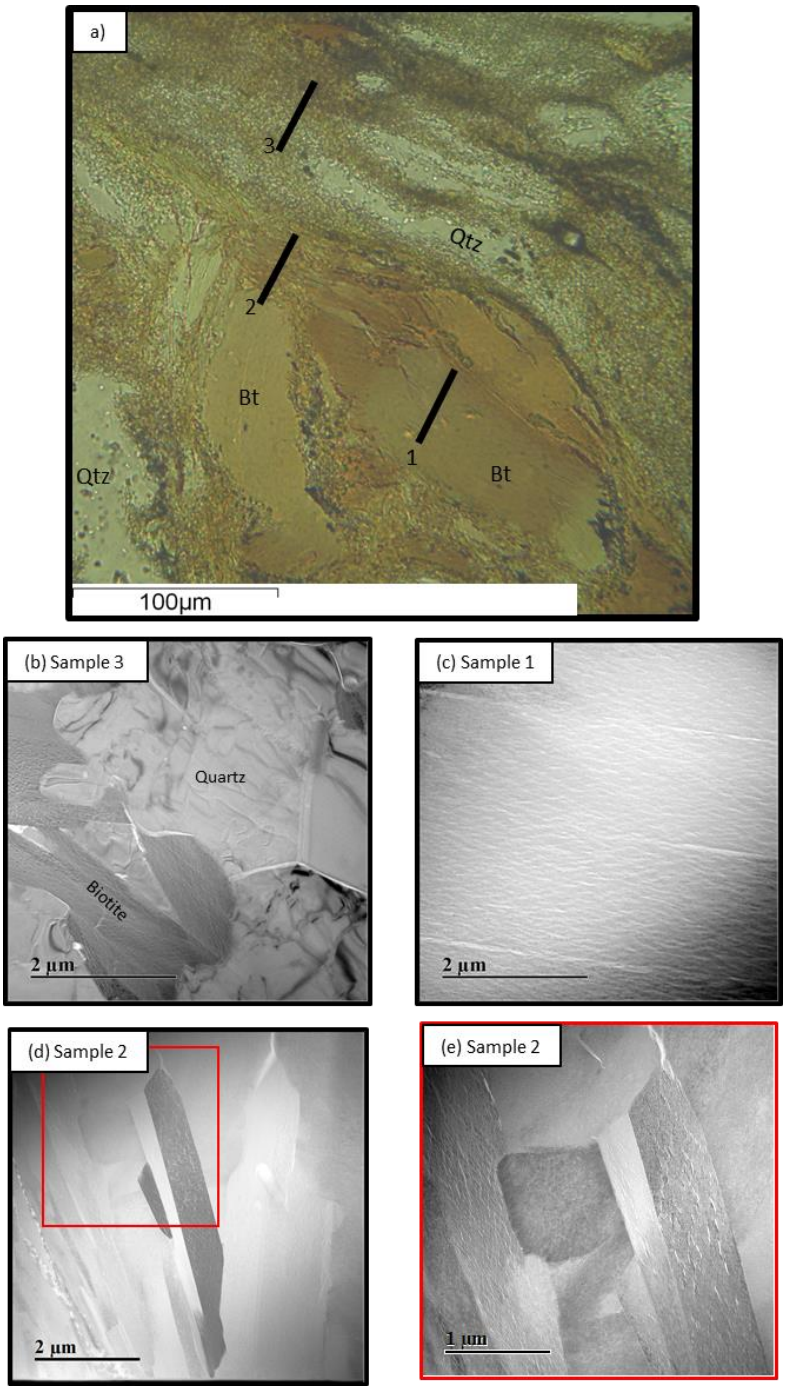


***Figure 6.18:*** *a) Optical micrograph (plane polarized light) of a region of sample CMB5A at which three TEM samples were prepared using a Ga ion FIB. The site was selected as it contains the three main stages of the biotite grain size reduction process in close proximity; sample 1 was taken from within a coarse biotite grain, sample 2 was taken from a region of fine biotite at the tip of the coarse grain and sample 3 was taken from a fine-grained domain composed predominantly of biotite and quartz. b) Brightfield TEM micrograph of sample 3 showing euhedral biotite mixed with anhedral quartz within the fine-grained matrix. c) Brightfield TEM micrograph of sample 1 showing the interior of the coarse biotite grain which is devoid of subgrains. d) and e) Brightfield TEM micrographs of sample 2 showing fine euhedral, interlocking and overlapping grains of biotite with high angle boundaries to one another as indicated by the variation in diffraction contrast. The variously oriented biotite grains are of approximately the same size as those observed in sample 3 indicating no further grain size reduction between the formation of fine biotite and its incorporation into a fine matrix.*

## 6.5. Discussion

### 6.5.1. The biotite grain size reduction mechanism

The biotite microstructures in the orthogneiss mylonites of the CMB line and Pogallo line are characterised by a dramatic grain size reduction from coarse, kinked parent grains in low strain protomylonites, to <3 μm components of a fine-grained matrix in the ultramylonites. The growth of fine grains is concentrated at the margins of parent biotite grains and especially at their tips and along kink band boundaries. In this section, the mechanisms responsible for this grain size reduction of biotite will be discussed based on the microstructural and chemical evidence outlined in section 6.4.

#### *Mechanical comminution*

The formation of fine biotite grains may be related to either a mechanical process (such as fracturing or dynamic recrystallisation), a chemical breakdown (as in the case of metamorphic reactions) or a combination of the two (a stress-driven reaction or dissolution-precipitation process). Dynamic recrystallisation in the classic sense (Urai *et al.*, 1986; De Bresser *et al.*, 1998, 2001; Stipp *et al.*, 2002) is not a feasible deformation mechanism in micas owing to the inability of dislocations to move outside of the basal plane (Kronenberg, Kirby, *et al.*, 1990; Christoffersen and Kronenberg, 1993). That said, it is possible that the biotite grain size reduction mechanism is governed by similar principles of mechanical rotation of subgrains to produce new grains, as in the segmentation model proposed by Wilson and Bell (1979). However, there is a distinct lack of evidence for subgrains in the parent biotites observed in this study and the grain size of the new grains is much finer than that which would be expected with these processes. Fracturing is likely to play some role, particularly in the early stages of biotite deformation involving the disaggregation of mica fish. However, the uniform grain size of the new biotite and the lack of intermediate grain sizes suggests another process is responsible for the generation of the fine-grained biotite.

#### *Chemical breakdown*

Reaction-weakening — in which reactions produce a weaker mineral or a fine-grained aggregate of reaction products — has been proposed to be an important process for microstructural evolution and strain localisation in mid-crustal mylonites (Brodie and Rutter, 1986; Wheeler, 1992; Wintsch *et al.*, 1995; Handy and Stunitz, 2002; Wintsch and Yi, 2002; Oliot *et al.*, 2010). Similar microstructures involving replacement of coarse biotite grains by

fine-grained polyphase aggregates have been observed in naturally deformed rocks and attributed to deformation catalysed reactions (Kerrich *et al.*, 1980; Fusseis, 2007). Experimental studies of quartzofeldspathic rocks with relatively low biotite content have also found that fine-grained reaction products nucleate at the highly strained tips of biotite grains and go on to localise deformation (Holyoke and Tullis, 2006a, 2006c, 2006b), although the reaction in this case is a dehydration of biotite due to elevated experimental temperatures. Mariani *et al.*, (2006) observed dehydroxilation reactions in muscovite experimentally deformed at 700 °C, but the extent of this reaction was small and widespread interconnected regions of reaction products were not observed.

### *The inter-relation of stress-related and chemical driving forces*

Previous studies have highlighted the potential for chemical- as well as stress-related driving forces in the recrystallisation of biotite (Etheridge and Hobbs, 1974; Kerrich *et al.*, 1980; Holyoke and Tullis, 2006c; Fusseis, 2007). This can occur when chemical reactions take place preferentially in sites where higher internal strain energy supplements a chemical driving force (Etheridge and Hobbs, 1974) and results in the formation of biotite of a subtly different composition than its parent, as well as several other phases, at the expense of the parent grain (Etheridge and Hobbs, 1974; Kerrich *et al.*, 1980; Fusseis, 2007). These studies are particularly pertinent to the results of this work as the biotite grain size reduction process in the CMB and Pogallo line orthogneiss mylonites used in this study is characterised by a subtle change in biotite composition highlighted by a reduction in Ti and an increase in Al. Ti is a particularly sensitive indicator of two distinct compositional populations as it has a strongly temperature dependent solubility in biotite. Ti becomes less soluble in biotite at lower temperatures (Henry *et al.*, 2005) such that biotite with lower Ti content (and higher Al content) represents equilibrium at lower temperatures (Douce, 1993). $Ti^{4+}$ substitutes for $Mg^{2+}$ and $Fe^{2+}$, with the charge being balanced either by $Al^{3+}$ substituting for $Si^{4+}$ in tetrahedral sites, or by the production of octahedral vacancies (leading to a structure that is intermediate between a trioctahedral and dioctahedral mica). In this study, while the differences in composition are subtle, the reduction in $TiO_2$ and increase in $Al_2O_3$ in fine grains relative to coarse grains are clear trends, producing statistically significant differences between the two populations in most of the samples analysed (Fig. 6.17, Supp. Table 6.1). This substitution and chemical change cannot be explained by mechanical grain size comminution or dynamic recrystallisation, as it implies substantial compositional re-arrangement, but instead suggests that new grains have nucleated and grown after a break down or dissolution of coarse parent grains.

### 6.5.2. A new model for dissolution and precipitation in biotite

As previously described, the fine-grained biotite occurs in association with fine-grained quartz, feldspar and Ti oxide minerals (Fig. 6.4) suggesting either that several different phases are growing at the expense of the parent biotite, or that fine grains of other phases are precipitating alongside the new biotite. The reduced concentration of Ti in the new biotite can be balanced by the growth of fine rutile and ilmenite to act as sinks for Ti, while small amounts of new quartz, feldspar and muscovite may also be involved in such a reaction. For example, the reaction of quartz with biotite of approximately the composition of the parent grains can produce new biotite with increased Si content and decreased Ti content along with approximately 1 mole of rutile for every 10 moles of reacting biotite:

$$10K_2(Mg_{1.5}Fe_3)(Al_{0.6}Ti_{0.4})[Si_{5.3}Al_{2.7}O_{20}](OH)_4 + SiO_2 \rightarrow$$
$$10K_2(Mg_{1.5}Fe_3)(Al_{0.7}Ti_{0.3})[Si_{5.4}Al_{2.6}O_{20}](OH)_4 + TiO_2 \quad (6.2)$$

Ilmenite could be formed by a more complex reaction involving small amounts of muscovite and feldspar as well as an increase in the Al composition of the new biotite:

$$10K_2(Mg,Fe)_{4.5}(Al_{0.6}Ti_{0.4})[Si_{5.3}Al_{2.7}O_{20}](OH)_4 + KAl_2(Si_3AlO_{10})(OH)_2 \rightarrow$$
$$10K_2(Mg,Fe)_{4.4}(Al_{0.8}Ti_{0.3})[Si_{5.3}Al_{2.7}O_{20}](OH)_4 + KAlSi_3O_8 + (Mg,Fe)TiO_3 + H_2O \quad (6.3)$$

Other reactions are possible involving the other constituent phases in the rock and resulting in subtle variations in new biotite composition. As biotite is by far the principle reactant and product in these reactions, they are best viewed as a form of dissolution and reprecipitation of a mineral that exists in solid solution, with compositions affected by local disequilibrium conditions.

Dissolution-precipitation of micas is a contentious issue. The deformation mechanism of dissolution-precipitation creep is well documented in other minerals (e.g. Cox and Paterson, 1991; Wintsch and Yi, 2002; Menegon, Pennacchioni and Spiess, 2008) but has not been invoked for phyllosilicates due to their apparent insolubility relative to other phases (Hickman and Evans, 1995; Bos and Spiers, 2001, 2002). Indeed, phyllosilicates are observed to accelerate dissolution of other minerals with which they are in contact whilst not themselves dissolving (Renard *et al.*, 1997, 2001; Gratier *et al.*, 2013). However, evidence of dissolution and subsequent nucleation of biotite, and to a much lesser extent, muscovite, has been reported in naturally deformed rocks, evidenced by irregular and serrated grain

boundaries (Wilson and Bell, 1979; Bell and Wilson, 1981). In these studies, as in this one, dissolution of biotite was concentrated within regions of high internal strain energy, such as kink band boundaries, and along grain boundaries where fluids are able to come into contact with grains. Wilson and Bell, (1979) suggest this dissolution occurs within a metamorphic fluid and results in the nucleation and growth, by diffusional processes, of fine-grained, strain-free biotite at the expense of deformed parent grains. This process shares many similarities with the chemically-driven recrystallisation of Etheridge and Hobbs, (1974) and is essentially the same as mineral replacement by dissolution-precipitation (Putnis, 2002; Putnis and Putnis, 2007; Ruiz-Agudo *et al.*, 2014), which usually encompasses a compositional change between the parent and product grains.

As well as the chemical variation between coarse and fine biotite (Tables 6.3 and 6.4, Figs. 6.13-6.17), there is abundant microstructural evidence supporting the dissolution and precipitation of biotite within the mylonites examined in this study. Firstly, the fine-grained biotite is associated with similarly fine grains of other phases, notably quartz, feldspars and Ti oxides. The growth of a mixture of phases such as this is indicative of mineral replacement reactions (Putnis, 2002) and cannot be achieved by mechanical disaggregation or subgrain formation. TEM analysis of the fine biotite product grains shows that the grain size reduction has occurred in one stage, with no intermediate-sized subgrains between the parent biotite and the fine matrix grains (Fig. 6.18). Within the matrix itself, biotite-biotite and quartz-quartz boundaries are generally straight, producing euhedral grains but some biotite-quartz phase boundaries have irregular lobate shapes which could not be produced without the dissolution and precipitation of both phases (Fig. 6.18b). In addition, biotite is observed within expanded cleavage cracks of muscovite fish, forming wedge-shaped grains that can only be explained by the precipitation of biotite during peeling along the muscovite basal planes (Fig. 6.7a).

### *Difference in the behaviour of muscovite*

It is important to note that the grain size reduction process does not affect muscovite in the same samples to the same extent as biotite, and that muscovite exists as coarse mica fish even in the highest strain ultramylonite samples. If the process of grain size reduction in biotite was purely mechanical, it may be expected that a similar process would affect the coarse muscovite grains due to the structural similarities between the two minerals. This is evidently not the case, while biotite entirely breaks down to a component of the fine-grained mylonitic matrix, muscovite undergoes more modest grain size reduction through brittle disaggregation into fine slithers by peeling along the cleavage planes. Evidence of this process

is shown in Fig. 6.7a and the result is a gradual reduction in the size of muscovite fish while adding fine muscovite to the matrix. However, it is clearly a fundamentally different and slower process than that which affects biotite in the same rocks. This apparent stability of muscovite, relative to biotite, serves as further evidence for dissolution-precipitation reactions as the cause of the grain size reduction in biotite. This is because biotite exists in solid solution, so there is a chemical driving force for the replacement of old biotite with new biotite of a subtly different composition. As muscovite is not a solid solution — except for up to 20% substitution of K for Na (paragonite) at very high homologous temperatures (Deer *et al.*, 1980) — this chemical driving force would probably be negligible. Such a disparity in the stability of biotite relative to muscovite has been described previously and related to differences in solubility (Wilson and Bell, 1979). The implications of this are that biotite and muscovite, though both weak micas, cannot be considered to behave similarly and have similar effects on bulk rock rheology, in quartzofeldspathic mylonites, as they react very differently during progressive deformation.

### *Association of dissolution-precipitation with sites of higher strain and the importance of fluids*

An important observation in the mylonites used in this study is the positive correlation between the extent of this reaction and the degree of strain. Etheridge and Hobbs (1974) showed that the nucleation of new, fine biotite with different composition was likely dependent on both stored strain energy and a local chemical driving force. In parent grains the reaction is initially favoured along kink band boundaries, fractures or along grain boundaries. These locations are also the sites where fluids could be in contact with the biotite grain, accelerating diffusive processes. Within through-going C' shear bands where strain has been localised, the breakdown of parent biotite to form fine-grained reaction products is substantially more advanced than in other regions within the same thin section (Fig. 6.5). This could be due to locally higher strain within the shear bands but also potentially a result of significant permeability and fluid flow within these deforming zones (Fusseis *et al.*, 2009; Menegon *et al.*, 2015; Leclère *et al.*, 2016). Evidence of abundant dissolution and precipitation processes in the feldspar phases of the same ultramylonite sample (POG3) are presented in Chapter 8 of this thesis and support the assertion that deformation occurred in the presence of fluids. The localisation of this dissolution reaction at sites of high strain in biotite grains and its occurrence to a greater extent within shear bands, suggests a strong relationship between strain energy, fluid availability and the reaction driving force. The apparent strain energy dependence of this reaction, coupled with the presence of biotite as

both the primary reactant and most abundant product, suggest it is a dissolution-precipitation process where a weak chemical driving force is supplemented in sites of high strain energy to enable localised reaction and nucleation to occur (Etheridge and Hobbs, 1974; Kerrich *et al.*, 1980; Holyoke and Tullis, 2006c). The initial stress heterogeneities exploited by this reaction are provided by the high phase strength contrast between biotite and the surrounding quartz and feldspar framework at amphibolite facies conditions.

### 6.5.3. Transition from dominant dislocation creep to fluid assisted grain size sensitive creep

The development and evolution of a quartz c-axis fabric during dynamic recrystallisation is known to be an effective way of assessing the degree of strain and conditions of deformation in quartz-dominated viscous shear zones (Heilbronner and Tullis, 2006; Law, 2014). Undeformed igneous rocks should contain no quartz CPO, or in the case of metamorphic rocks, a weak CPO. During dislocation creep and dynamic recrystallisation of quartz, the c-axis CPO increases in strength with the degree of strain, while the maxima on pole figures evolve from the periphery through a crossed girdle and single girdle, to a central maximum. This represents the progression of dominant slip system from basal <a> slip to rhomb <a> slip and then prism <a> slip with increasing strain and degree of recrystallisation (Heilbronner and Tullis, 2006). During grain size sensitive (GSS) creep, rotation of grains has typically been inferred to destroy existing CPOs (Law, 1990; Fliervoet *et al.*, 1999). However, more recent work has shown that CPOs from a previous episode of dislocation creep can be partially retained during GSS creep although in a substantially weaker form (Wheeler, 2009). In some cases weak CPOs can be formed during diffusion creep (Miyazaki *et al.*, 2013) and dissolution-precipitation creep (Heidelbach *et al.*, 2000). However, in general, the weakening of a CPO can be taken as evidence of a transition in dominant deformation mechanism away from dislocation creep and towards grain size sensitive creep mechanisms such as diffusion or dissolution-precipitation accommodated grain boundary sliding and viscous granular flow (Kilian *et al.*, 2011; Menegon *et al.*, 2013; Viegas *et al.*, 2015; Goncalves *et al.*, 2016; Peters *et al.*, 2016).

The monomineralic quartz bands within the moderate strain mylonites of this study display strong quartz c-axis CPOs which take the form of central maxima with elements of single girdles (Fig. 6.9b, c and Fig. 6.10). This fabric is conducive with the dominance of dislocation creep within these monomineralic domains. The CPO strength drops considerably in the finer grained quartz within polyphase regions (Fig. 6.10) and is very weak to non-existent in quartz

from the ultramylonite matrix of POG3 (Fig. 6.11). As discussed above, such a change in CPO strength is indicative of a significant reduction in the importance of dislocation creep as a deformation mechanism in the quartz phase in the fine-grained polyphase matrix relative to the monomineralic bands (Kilian *et al.*, 2011; Menegon *et al.*, 2013; Viegas *et al.*, 2015; Goncalves *et al.*, 2016; Peters *et al.*, 2016). Where quartz is more abundant in the ultramylonite matrix (meaning a higher proportion of quartz-quartz grain boundaries) the quartz c-axis CPO is slightly stronger (Fig. 6.11c), indicating dislocation creep processes may still be active but significantly hindered by the presence of secondary phases. A caveat here is the fact that experimental studies which relate quartz c-axis fabric evolution to the conditions of deformation and degree of strain (e.g. Heilbronner and Tullis, 2006) are focussed on monomineralic quartzites which are not representative of the polyphase natural rocks used in this study. Even the data collected in this study which pertain to monomineralic quartz domains are subject to the effects of strain distribution into other neighbouring phases and microstructural domains (Menegon, Pennacchioni, Heilbronner, *et al.*, 2008; Kilian *et al.*, 2011). As such, the analyses of quartz c-axis distribution detailed here is used only to give an indication of the samples in which dislocation creep of quartz is most important and not to infer deformation conditions or the absolute strain accommodated.

The correlated misorientation angle distributions (Fig. 6.12) for quartz in the ultramylonite matrix (POG3) follows a theoretical random distribution much more closely than in the mylonite and protomylonite samples (POG7, POG5, CMB18) which also display peaks at low misorientation angles. These distributions in the protomylonite and mylonite resemble those expected in an aggregate deforming by dislocation creep with a large proportion of low angle boundaries and fewer high angle boundaries (Wheeler *et al.*, 2001). The more random distributions in the ultramylonites are indicative of a greater influence of GSS creep mechanisms (Wheeler *et al.*, 2001).

As in previous studies of polyphase deformation, (Wheeler, 1992; Kruse and Stünitz, 1999; Herwegh and Berger, 2004; Warren and Hirth, 2006; Song and Ree, 2007; Herwegh *et al.*, 2011; Little *et al.*, 2015; Andrew J. Cross *et al.*, 2017) the effect of fine grains of other phases may be to limit (through pinning) the recrystalising quartz grains to a much finer size than they would otherwise be (Herwegh *et al.*, 2011; Little *et al.*, 2015; Andrew J. Cross *et al.*, 2017). This would prohibit the growth of quartz grains that are newly precipitated within polyphase domains. The development of well mixed and equigranular polyphase aggregates can be explained by the dissolution and precipitation of multiple phases. With increasing strain, quartz in the monomineralic bands is dissolved and precipitated within polyphase

domains where its fine grain size is maintained, and dislocation creep is inhibited by abundant phase boundaries. This ultimately results in the absence of monomineralic bands within the ultramylonite (POG3) and the growth of fine-grained polymineralic domains with increasing strain.

Deformation in the polyphase aggregates, in contrast to the monomineralic domains, is inferred to be dominated by GSS creep mechanisms such as granular flow facilitated by dissolution-precipitation and grain boundary sliding of all phases. While quartz CPO strength has decreased substantially, fine-grained biotite within the polyphase domains and the ultramylonitic matrix displays a strong SPO, identifiable from uniform pleochroism, with long axes of biotite grains oriented parallel to the elongation direction (Fig. 6.5b, c). This is further evidence of grain boundary sliding as the rotation of elongate grains (such as micas) in a diffusion or dissolution assisted GBS regime slows as they become aligned with the flow direction in a rotational steady state (Wheeler, 2009). In addition, the matrix of POG3 displays weak aggregation of like phases at a high angle to foliation which has been proposed by Hiraga *et al.*, (2013) to characterise polyphase mixtures deforming by grain boundary sliding. The presence of fluids within the system would serve to increase the rate of diffusive mass transfer and lead to substantial weakening in these polyphase regions (Rybacki and Dresen, 2000; Menegon, Pennacchioni and Spiess, 2008; Viegas *et al.*, 2015; Ceccato *et al.*, 2018). The apparent weakness of these fine grained domains (which form along high strain surfaces and C' shear bands) relative to the surrounding quartzofeldspathic framework, can therefore be explained by a disparity in dominant deformation mechanism, from dislocation creep in quartz and brittle fracture in feldspar, to fluid assisted GSS creep in the polyphase aggregates. The microstructural change and the switch in dominant deformation mechanism could be expected to lead to strain weakening and the formation of localised ultramylonites (Behrmann and Mainprice, 1987; Kilian *et al.*, 2011; Menegon *et al.*, 2013). This is an important rheological change in the mylonite that is brought about, at least initially, by the dissolution, reaction and precipitation of biotite, with phase mixing, pinning and an increased prevalence of grain size sensitive creep ultimately stemming from this process.

### 6.5.4. Model of microstructural evolution with increasing strain

From the observations and results laid out above, we can produce a model for the influence of micas on the accommodation of strain within the orthogneiss and paragneiss mylonites of the CMB and Pogallo line. In the lowest strain protomylonites, the microstructure is characterised by a load-bearing framework of quartz and feldspar which accommodates the majority of the strain. Throughout the up-strain evolution of the mylonites all phases

undergo grain size reduction to some degree. The dominant quartz phase is the first to experience significant grain size reduction and appears to do so through SGR and GBM recrystallisation, steadily forming ~20 μm grains by the mechanical rotation of subgrains and the motion of grain boundaries (Fig. 6.8a) (Fig. 6.19a). The feldspar phases by contrast undergo comminution through brittle fracturing as porphyroclasts are broken apart and their fragments dispersed along C planes (Figs. 6.2, 6.8b). Such a microstructural development concurs with the findings of Stunitz and Fitz Gerald, (1993) in granitoid mylonites at similar conditions. At this point the strength of the rock is likely to approximate that of quartz deforming viscously by dislocation creep. Intracrystalline deformation within the coarse biotite and muscovite grains is likely to be facilitated by basal dislocation glide and, where micas are not oriented favourably for shear, by a significant build-up of ripplocations and the motion of these ripplocations to form kink bands (Aslin *et al.*, 2019). The deformed mica grains exhibit kinking and slip along basal planes (Fig. 6.3a) but cannot account for significant strain as they do not form a fully interconnected network, with the microstructure approximating the 'type 1' load bearing framework of Handy, (1990).

However, this microstructure changes with increasing strain from the protomylonites (POG7) to the mylonites (POG5, CMB18) as biotite undergoes a dramatic grain size reduction by the stress-induced reactions described in section 6.5.1. The resulting fine grains then become distributed along grain boundaries not just of biotite, but also of quartz and feldspar (Fig. 6.5d, 6.19b). The previously stronger framework minerals (quartz and feldspar) also increasingly deform by dissolution and precipitation as fracturing of feldspar porphyroclasts increases the reactive surface area and dynamically recrystalising quartz becomes pinned by fine-grained secondary phases. This process facilitates the connection of isolated biotite grains via narrow channels of fine-grained biotite and other reaction products along C and C' surfaces, forming a penetrative, interconnected network in which dissolution-precipitation and diffusion accommodated viscous grain boundary sliding are the dominant deformation mechanisms (Fig. 6.19c). Such a switch in dominant deformation mechanism has been widely interpreted to result in rheological weakening at the conditions of the mid-crust (Behrmann and Mainprice, 1987; Stunitz and Fitz Gerald, 1993; Holyoke and Tullis, 2006a; Menegon *et al.*, 2006, 2013; Kilian *et al.*, 2011; Ceccato *et al.*, 2018). These fine-grained biotite-dominated bands are weaker than the load bearing framework and serve to localise strain, becoming small scale shear bands which widen and interconnect, with increasing strain, to ultimately form a widespread ultramylonitic matrix (POG3). This continued evolution, with increasing strain, towards a polyphase, ultramylonitic matrix deforming by grain-size creep, supports

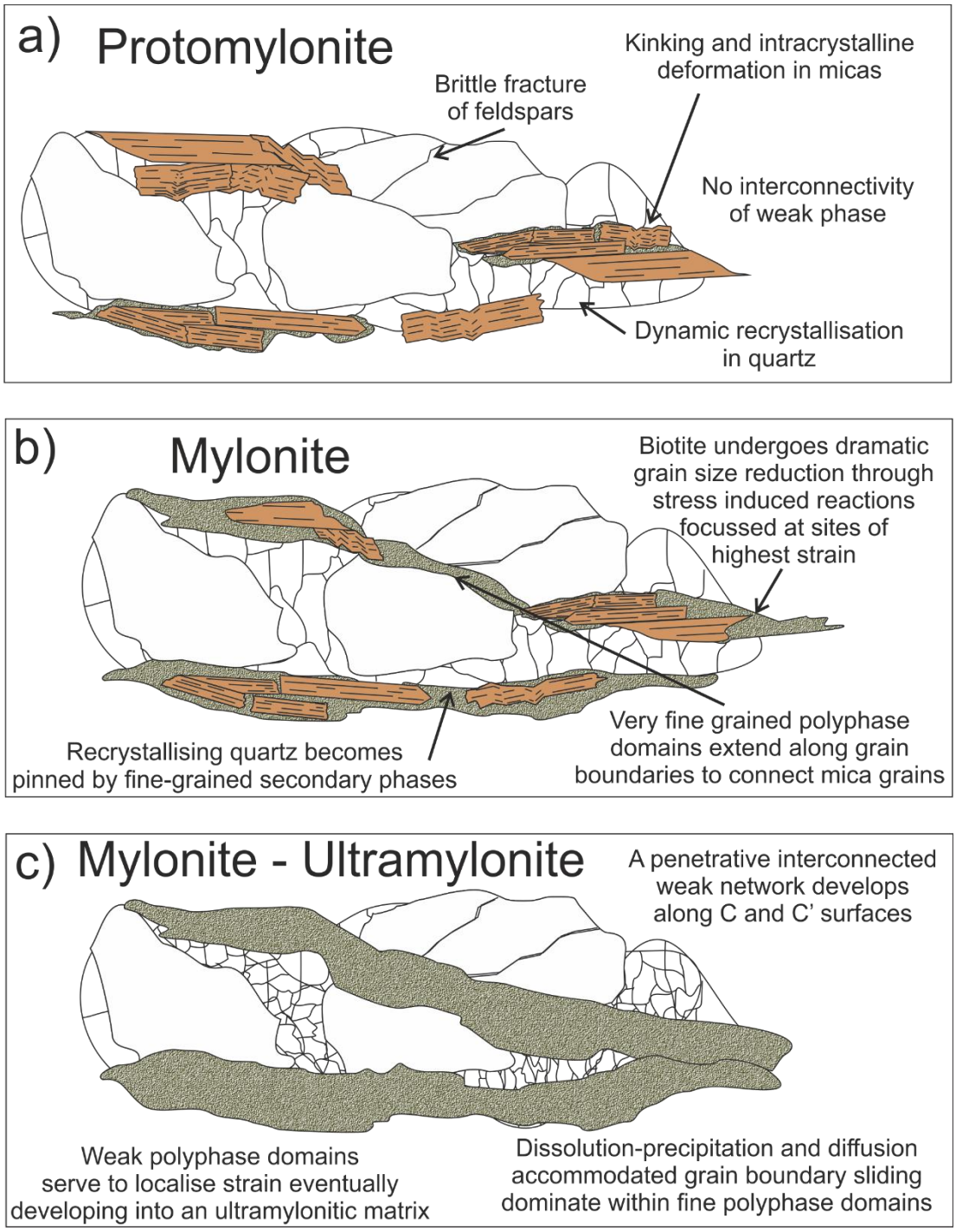


***Figure 6.19:*** *Schematic diagram illustrating the microstructural evolution interpreted within the orthogneiss samples of this study. a) In the protomylonites strain is accommodated predominantly by intracrystalline deformation within micas (kinking and the motion of ripplocations), by dynamic recrystallisation in quartz and by brittle fracture in the feldspar phases. b) At higher strains, biotite undergoes dramatic grain size reduction through stress induced dissolution-precipitation focussed initially at sites of highest stress such as kink band boundaries and grain boundaries. Fine grained biotite and other reaction products then form domains along grain boundaries of other phases which enable the interconnection of formerly separate mica grains. c) Eventually all original biotite grains are consumed and replaced by fine-grained polyphase ultramylonitic domains which deform predominantly by grain size sensitive creep and grain boundary sliding.*

the recent suggestion, put forward by Stenvall *et al.* (2019), that such fine-grained mixtures are likely to be even weaker than mylonites dominated by interconnected networks of phyllosilicates. This is because the shear bands continue to widen even after they become interconnected. The importance of this microstructural evolution for the rheology of the mylonite lies in the transition from a load bearing framework to an interconnected weak layer microstructure (Handy, 1990, 1994). This is similar to the microstructural evolution observed in the experiments of Holyoke and Tullis, (2006b, 2006a). The implication of the dramatic grain size reduction of biotite is therefore not just in producing small regions of fine new grains but also in reducing the recrystalising grain size of the quartz that forms the mylonite framework and facilitating a transition to an interconnected weak layer microstructure dominated by grain size-sensitive creep.

As discussed in section 6.2.5. the CMB line and Pogallo line shear zones have been interpreted variously to represent either a mid-crustal trans-tensional shear zone (Boriani, Burlini, *et al.*, 1990; Boriani and Giobbi, 2004) or a low angle normal fault (Hodges and Fountain, 1984; Handy *et al.*, 1999; Siegesmund *et al.*, 2008). In either case, the system represents a very large-scale shear zone which accommodated displacements of at least 10s of km and potentially 1000s of km (Boriani *et al.*, 2016). The global paucity of examples of such large-scale middle/lower-crustal shear zones makes this an invaluable source of information relating to the processes which control crustal deformation on a continental scale. The findings of this Chapter suggest that the presence of biotite – even in relatively low abundances such as those of a granitoid – significantly weakens mid-crustal mylonites, not only by creating an interconnected network of weak phyllosilicates but more fundamentally by assisting and accelerating the transition from dislocation creep to grain-size sensitive creep as the dominant deformation mechanism.

## 6.6. Conclusions

In summary, we have examined a suite of mylonites with mica modal abundances between 10% and 25% from the CMB line and Pogallo line, which border the Ivrea-Verbano Zone in North West Italy, with the aim of determining the role that biotite, as a secondary component of these rocks, plays in influencing the rheology of the shear zone. From this study, the following conclusions can be drawn:

- With increasing strain, biotite in the studied samples undergoes a dramatic grain size reduction, forming very fine-grained, biotite-dominated regions which connect mica grains predominantly along C and C’ surfaces.

- These very fine-grained polyphase regions deform principally by a combination of dissolution-precipitation creep and grain boundary sliding, making them weaker than the quartzofeldspathic framework and enabling them to localise strain.
- The mechanism responsible for the biotite grain size reduction is unlike classical dynamic recrystallisation mechanisms as it does not involve subgrain formation but is instead characterised by the nucleation of very small, euhedral new grains which have a subtle but regular difference in composition compared to the parent grains. This is best described as fluid-facilitated, stress-induced dissolution-reprecipitation reaction.
- Through this process biotite becomes a fine-grained, widely distributed phase which, even in relatively low abundances, has significant implications for the rheology of the polyphase aggregate. Muscovite, by contrast, is less affected by this process and consequently has far less influence on the microstructural evolution and rheology of these shear zones.

This work has shown that small amounts of biotite can have a substantial influence on the strength and behaviour of amphibolite facies mylonites in the mid-crust. In particular, biotite appears capable of accelerating the transition to the weaker rheology of grain size sensitive creep, thereby facilitating strain localisation. This challenges existing assumptions that the more abundant phases completely control deformation and suggests that models and studies which imagine the mid-crust as a pure quartz or quartzofeldspathic rheology may be overestimating the strength of this region as biotite is a ubiquitous, if rarely dominant, component of mid-crustal lithologies.

## 6.7. Supplementary figures

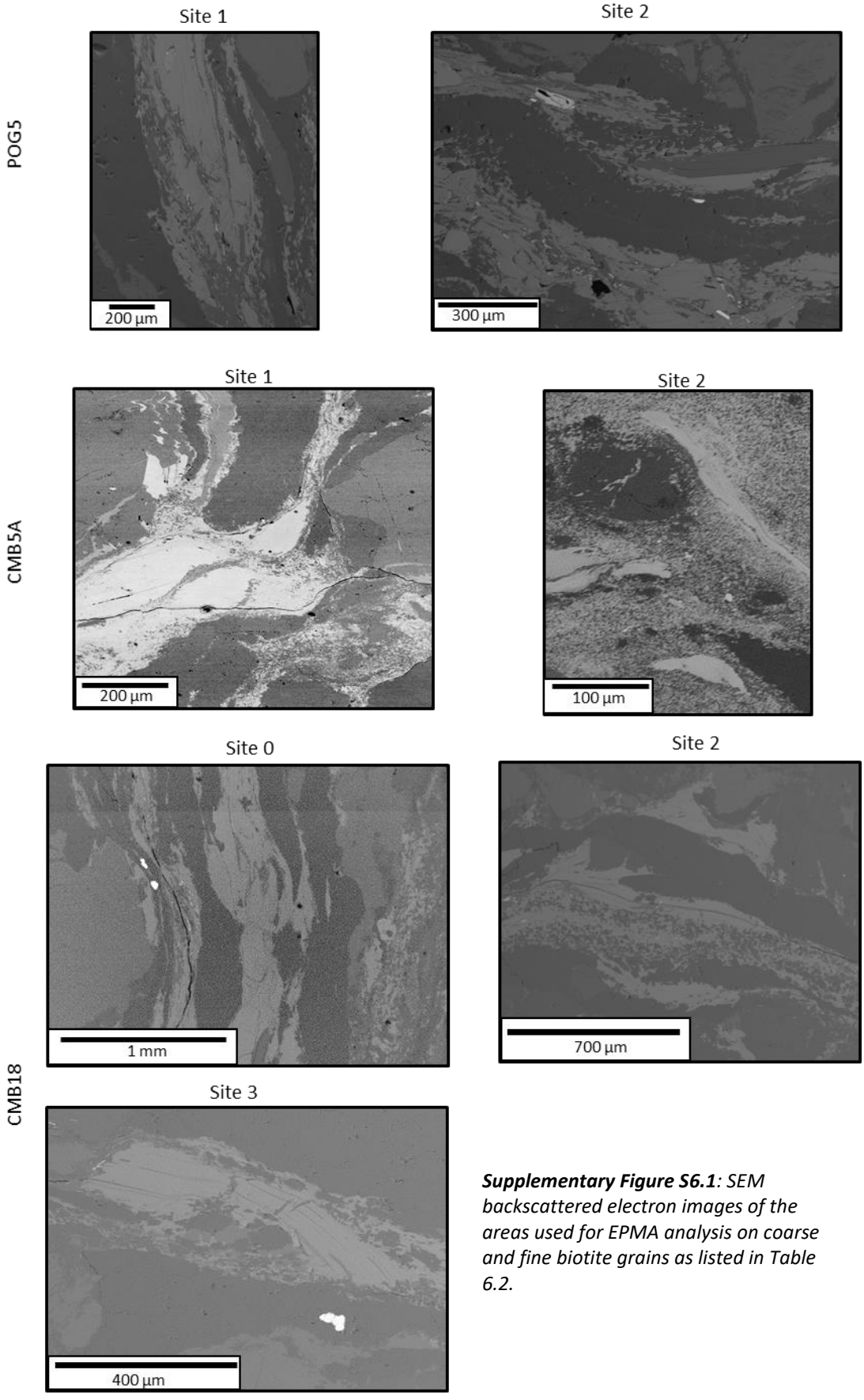


***Supplementary Figure S6.1****: SEM backscattered electron images of the areas used for EPMA analysis on coarse and fine biotite grains as listed in Table 6.2.*

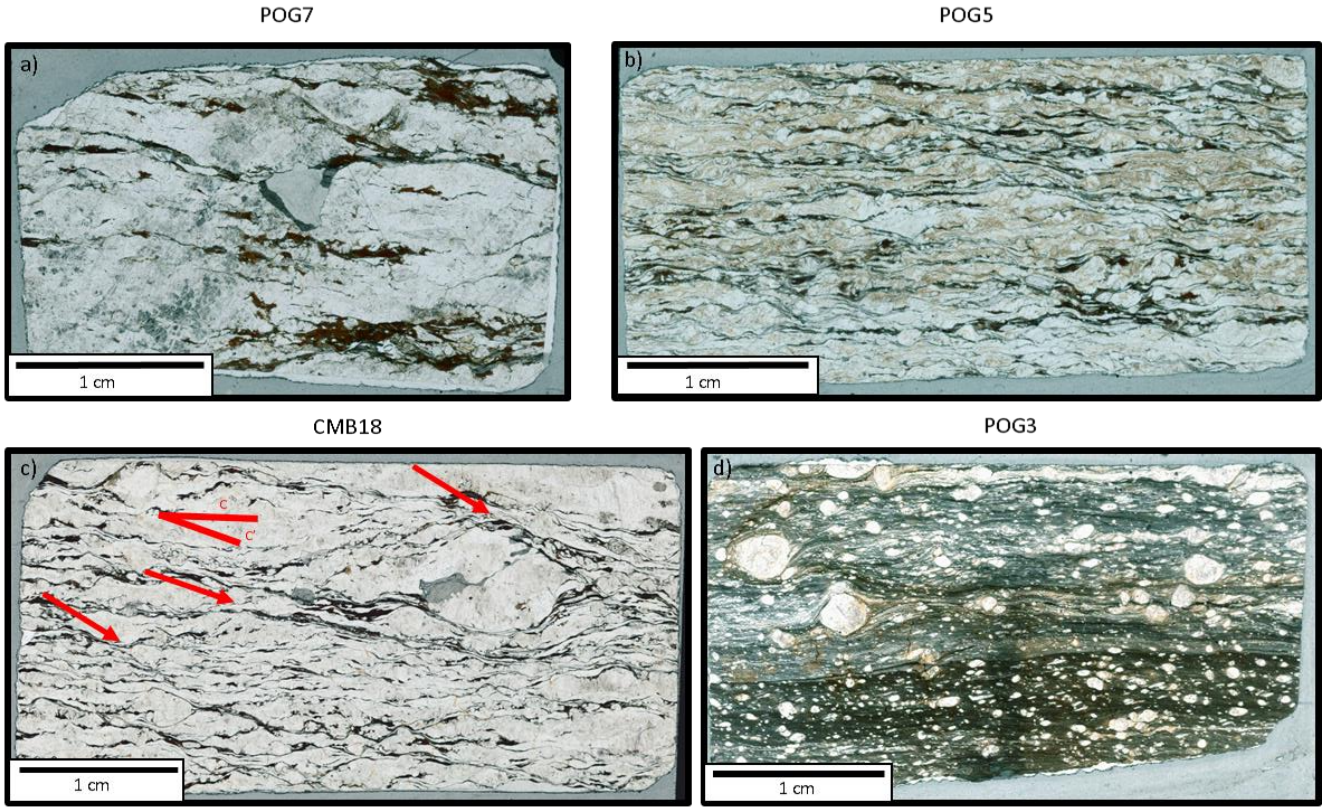


***Supplementary Figure S6.2:*** *Optical plane polarized light thin section scans of the 4 samples detailed in Fig. 6.2. a) POG7, an orthogneiss protomylonite with coarse biotite and muscovite occurring as individual grains or clusters which, while aligned with the foliation, do not form a penetrative, interconnected network. b) POG5, an orthogneiss mylonite displaying a finer grain size in all phases, fine biotite occurs along grain boundaries and facilitates the connection of larger mica grains along foliation to produce an interconnected network. c) CMB18, a granitic mylonite from the CMB line in which fine biotite has produced an interconnected mica network (as in POG5) and defines several higher strain shear bands along C' (arrows). d) POG3, a high strain orthogneiss ultramylonite composed predominantly of a very fine matrix of quartz, biotite, plagioclase, K-feldspar and muscovite and incorporating generally well rounded porphyroclasts of K-feldspar, plagioclase and muscovite fish. All five main phases are present throughout the matrix, however clear foliation parallel compositional banding is apparent, producing darker biotite and plagioclase-rich domains and lighter quartz and k-feldspar-rich domains.*

***Supplementary Table S6.1:*** *Results of statistical t-tests for the mean oxide weight % values of the principle constituents of biotite, determining whether there is a statistically significant difference between the results for coarse and fine grains. If the calculated t-value is greater than the critical t-value then there is a statistically significant difference between the populations (coloured green). If the calculated t-value is lower than the critical t-value then the difference is not statistically significant (coloured red).*

| Sample site | Degrees of freedom | Critical t-value | TiO2 t-value | Al2O3 t-value | SiO2 t-value | FeO t-value | MgO t-value | K2O t-value |
|---|---|---|---|---|---|---|---|---|
| **CMB18 site 0** | 61 | 2.000 | 10.693 | 2.635 | 3.364 | 2.092 | 3.211 | 5.848 |
| **CMB18 site 2** | 65 | 1.997 | 4.972 | 4.928 | 1.475 | 3.389 | 1.305 | 1.536 |
| **CMB18 site 3** | 57 | 2.002 | 11.774 | 6.015 | 3.330 | 0.166 | 1.017 | 19.409 |
| **CMB5A site 1** | 34 | 2.032 | 7.594 | 2.290 | 0.240 | 0.869 | 1.410 | 4.709 |
| **CMB5A site 2** | 22 | 2.074 | 6.263 | 0.551 | 0.663 | 1.752 | 3.466 | 6.149 |
| **POG5 site 1** | 22 | 2.074 | 1.638 | 0.047 | 0.915 | 0.625 | 5.344 | 5.293 |
| **POG5 site 2** | 72 | 1.993 | 8.399 | 4.336 | 1.550 | 3.088 | 2.354 | 8.239 |

***Digital Appendix 1:*** *Excel Workbook with Wt% oxide values measured by EPMA, used to calculate the mean values for each site which are reported in this chapter, and used to plot Figures 6.13, 6.14 and 6.16. CMB18-Site 2, CMB18-Site3, CMB5A-Site1, CMB5A-Site2 and POG5-Site2 were collected at the Open University. CMB18-Site0 and POG5-Site1 were collected at the University of Manchester.*

# 7. Effect of mica content on strain localisation and deformation mechanisms in mylonites of the CMB and Pogallo shear zones.

## 7.1. Abstract

Micas are common secondary constituents of many lithologies in which they play the role of the weaker phase alongside stronger framework minerals. The presence of mica in crustal rocks is often associated with strain localisation during both brittle and viscous deformation. This chapter examines how the quantity of mica affects the role it plays in deformation and strain localisation. Samples were taken from two transects across the Cossatto-Mergozzo-Brissago (CMB) line and the Pogallo line which border the Ivrea-Verbano Zone in North West Italy and incorporate a range of different lithologies, from metapelites with mica contents of up to 57%, to orthogneiss mylonites containing as little as 5% mica. Optical microstructural analysis and fabric determination using electron backscatter diffraction (EBSD) are combined with outcrop scale observations and mapping in the field to build a picture of how strain is distributed across different rock types within the shear zone and between the various minerals of each lithology. It is found that mica-rich metapelites, which possess an interconnected micaceous network from the outset, develop distributed S-C mylonitic fabrics in which the critical S and C surfaces are defined by well-oriented mica basal planes. By contrast, rocks with lower mica content develop C' shear bands and localised high strain zones earlier in their microstructural evolution in order to transform isolated mica grains and domains into an interconnected weak network. This pattern of heterogeneous strain localisation in mica-poor rocks and a more spatially homogenous distribution of strain in mica-rich rocks is also shown to be true at the shear zone scale. Where mica-content is low (but still present), strain is accommodated in numerous, narrow, high strain shear zones delimiting regions of lower strain rocks, whereas, where mica content is high, moderate strain S-C mylonites prevail over a wider region. It is proposed that a small amount of mica in quartzofeldspathic rocks enhances strain localisation and the formation of high strain shear bands, while large quantities of mica result in more widely distributed strain. An important consideration is the phase strength contrast (PSC) between the weak mica phase and the dominant framework phase, be it quartz, feldspar or mica, with high PSC enhancing strain localisation and low PSC limiting it.

## 7.2. Introduction

Mica minerals are common and important constituents of the Earth's crust. As well as being primary components of igneous rocks across a wide compositional range, they occur abundantly as products of metamorphic reactions, especially where fluids and Al-rich phases are involved (Deer *et al.*, 1980). Metapelites in particular, often contain abundant micas up to and including amphibolite facies metamorphic conditions. This means that micas are ubiquitous in the middle crust at conditions associated with the brittle-viscous transition, where the principal mode of deformation switches from brittle, generally localised failure in the upper crust, to viscous generally more distributed deformation at greater depths (Kohlstedt *et al.*, 1995). In the brittle regime, strength increases linearly with confining pressure and therefore with depth. However, in the viscous regime, strength decreases exponentially with depth as the temperature increases. This results in rocks of the brittle-viscous transition being some of the strongest in the crust (e.g. Scholz, 1988). In the continental crust the situation is complicated by the distribution of very different rock types and the influence of different phases. This is because both brittle and viscous mechanisms can occur under the same conditions in different rock types and within different minerals of the same rock, presenting a complex picture of strength contrasts and leading to strain localisation (e.g. Schrank *et al.*, 2008; Fagereng *et al.*, 2014). In this context, the rheology of metapelites and other foliated schists and gneisses may be dominated by the rheology of mica minerals, which are commonly reported to be weak phases throughout the range of crustal conditions (Wintsch *et al.*, 1995; Mariani *et al.*, 2006).

The influence of micas on rock strength has been studied through fieldwork, microstructural observations and laboratory experiments (Kronenberg, Kirby, *et al.*, 1990; Shea and Kronenberg, 1992, 1993; Mares and Kronenberg, 1993; Holyoke and Tullis, 2006b; Mariani *et al.*, 2006; Song and Ree, 2007). Under most conditions, including those of the mid-crust, micas are found to be weaker than other common minerals (Mares and Kronenberg, 1993; Shea and Kronenberg, 1993; Mariani *et al.*, 2006). This is due primarily to their strong mechanical anisotropy and the ease with which they deform parallel to the basal plane (Kronenberg, Kirby, *et al.*, 1990). In addition, the coefficient of friction applicable to micas is anomalously low relative to other common silicate minerals (Byerlee, 1978; Scruggs and Tullis, 1998; Mariani *et al.*, 2006). This means that when oriented favourably for shear, they almost invariably represent the weakest phase in a given rock. A critical development in the rheology of a mica-bearing rock is the formation of an interconnected network of mica, as this can facilitate the localisation of strain away from the stronger phases (Handy, 1990,

1994; Shea and Kronenberg, 1993; Wintsch *et al.*, 1995; Holyoke and Tullis, 2006a; Hunter *et al.*, 2016). As isolated, randomly oriented grains, micas have a limited influence on bulk rock rheology. In metapelites and mica-schists, micas define a foliation which represents a continuous connected network of mica grains in which their basal planes are strongly aligned.

To date, many studies have focussed on the rheology, structure and microstructure of quartzo-feldspathic rocks with low mica content (Berthe *et al.*, 1979; Canova *et al.*, 1992; ten Grotenhuis *et al.*, 2003; Holyoke and Tullis, 2006b, 2006a; Song and Ree, 2007; Menegon, Pennacchioni and Spiess, 2008; Sullivan *et al.*, 2013). Mica dominated lithologies, by contrast, are studied less frequently (Shea and Kronenberg, 1992, 1993), potentially due to the complex anisotropic structure of mica minerals, which sets them apart from other silicate phases. This chapter compares and contrasts the microstructural evolution of mica-rich metapelites, known as Kinzigites, with that of mica-bearing, but not mica-dominated lithologies (the rocks described in detail in Chapter 6) deformed along the Cossatto-Mergozzo-Brissago (CMB) and the Pogallo fault zones, an associated pair of upper greenschist to amphibolite facies viscous shear zones exposed in north western Italy. These different lithologies were deformed at the same locations along the same shear zone, providing a natural laboratory in which to determine how variations in mica content affect the degree and mechanisms by which mica influences strain localisation and rheology. The following section gives an overview of the shear zones and geological context.

### 7.2.1. Geological context

The CMB line and the Pogallo line are upper greenschist to mid-amphibolite facies mylonitic shear zones located in North West Italy (Hodges and Fountain, 1984; Boriani, Giobbi Origoni, *et al.*, 1990; Handy and Streit, 1999) (Fig. 7.1). The CMB line is a late Variscan, steeply dipping, NE/SW trending tectonic discontinuity which defines the boundary between the Ivrea Verbano Zone (IVZ) to the NW and the Serie dei Laghi (SdL) to the SE (Boriani, Burlini, *et al.*, 1990; Boriani, Giobbi Origoni, *et al.*, 1990) (Fig. 7.2). The Pogallo line is slightly younger (160 – 240 Ma) (Zingg, 1983) and coincides with the CMB line for a distance of approximately 20 km within the Val Grande National park. Along this section, which is a principal focus of this study, the shear zone has been termed the Pogallo ductile fault zone (PDFZ) by Handy (1987) and is characterised by an approximately 1 km wide region of distributed deformation within the IVZ, delimited along its south eastern edge by the Pogallo line itself (Handy, 1987). The deformation on the PDFZ and on the Pogallo line are concordant and believed to be related to the same deformational event (Handy, 1987).

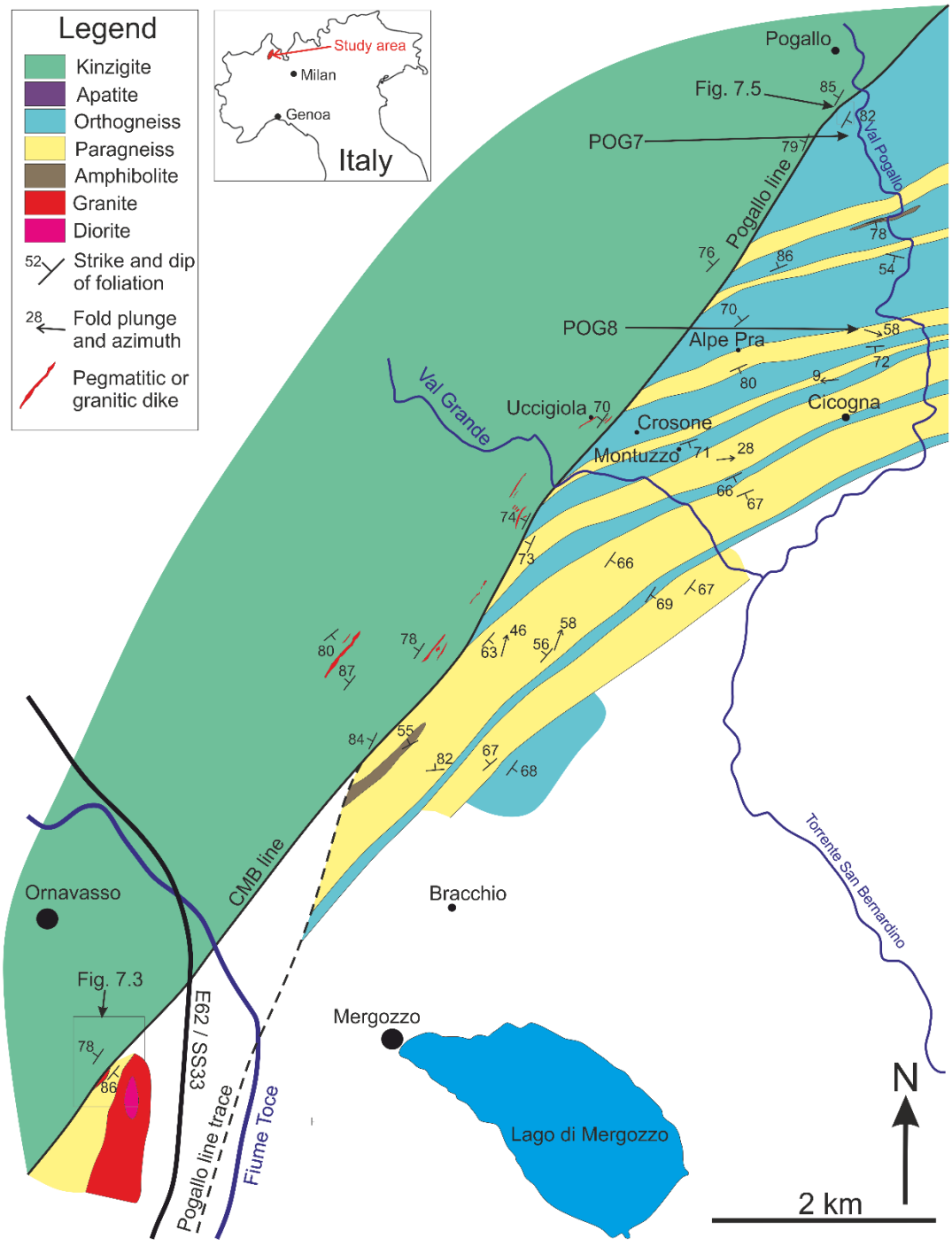


***Figure 7.1:*** *Geological map of the study area NW of Lago Maggiore. The Kinzigites crop out along the length of the North western side of the CMB and Pogallo line while the Serie dei Laghi to the SE is composed of intercalated orthogneiss and paragneiss with occasional discontinuous bands of amphibolite. Granitic pegmatites intrude the Kinzigite while the large granitic body in the south is associated with the Permian age Graniti dei Laghi.*

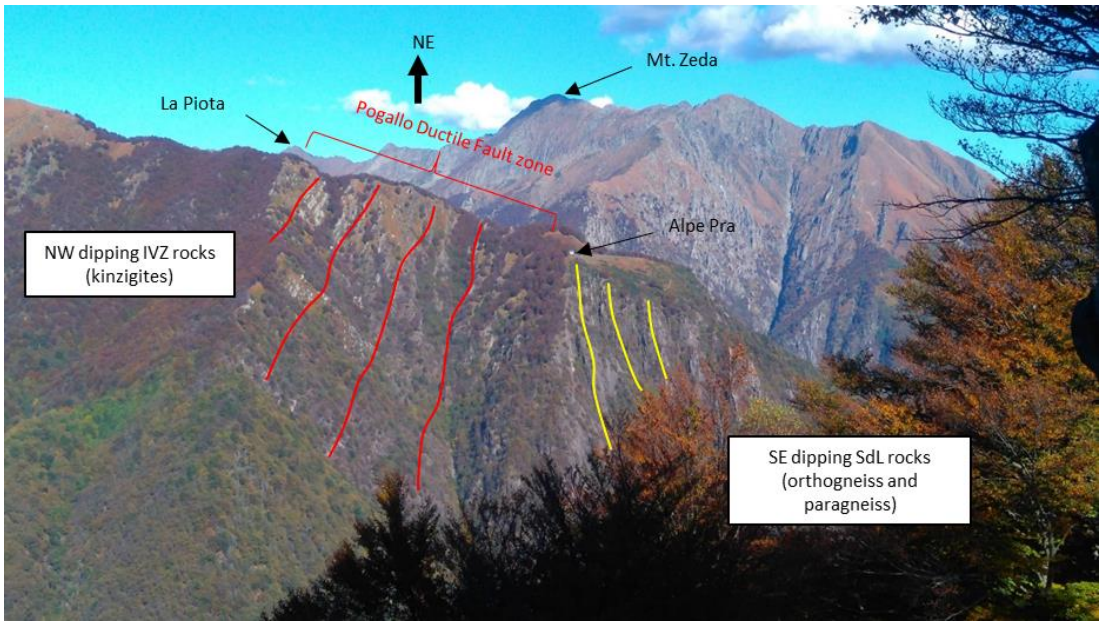


***Figure 7.2:*** *Photograph of the Pogallo fault zone taken looking NE across Val Grande from Casarecce. There is a subtle difference in the dip of foliations across the tectonic discontinuity of the Pogallo line. The Pogallo line continues across Val Pogallo cropping out at La Piota in the North East.*

On the other side of the Pogallo line, deformation in the SdL is characterised by a very narrow, complex zone of anastomosing, high strain mylonites and ultramylonites (Handy, 1987). To the north east of this stretch, near the peak of Mte. Piota, the Pogallo line breaks away from the CMB line and becomes a wide region of distributed deformation within the IVZ. The deformational grade of the Pogallo line increases slightly along strike from the south west to the north east (from upper-greenschist to amphibolite facies) as the structural level of the fault's activity becomes deeper (Hodges and Fountain, 1984; Boriani, Giobbi Origoni, *et al.*, 1990).

Along the length of its outcrop, the CMB line juxtaposes deep crustal rocks (the IVZ) against mid-crustal rocks (the SdL) (Boriani, Giobbi Origoni, *et al.*, 1990) (Fig. 7.1). The part of the IVZ in contact with the CMB line and Pogallo line is composed of medium grade, mica-rich metapelites termed the Kinzigite Formation(Boriani, Burlini, *et al.*, 1990; Handy *et al.*, 1999; Rutter *et al.*, 2007) (Fig. 7.1). The metapelites are mica-rich with as much as 45% biotite and 20% muscovite although compositional variation is common. Other important phases are quartz, plagioclase and sillimanite, while garnet, staurolite and kyanite can also be present in low abundances. On the south eastern side of the boundary the rocks of the SdL include quartz-rich, mica-bearing paragneisses (the schisti dei laghi and the gneiss minuti) and granitic and granodioritic orthogneisses (Boriani, Giobbi Origoni, *et al.*, 1990; Boriani, Origoni, *et al.*, 1995). The sites detailed in this study were within a section of the SdL known as the Strona Ceneri zone which is an amphibolite facies, predominantly metaspammitic

sequence including many intercalations of orthogneiss (Boriani and Giobbi, 2004) (Fig. 7.1). These rocks have variable mica contents, but in all cases significantly less than in the metapelitic Kinzigites of the IVZ.

## 7.3. Methods

Two transects were chosen for this study based on their relative continuity of exposure across the shear zone, however, it should be noted that even in these locations, continuous reliable outcrop could not be found and gaps in exposure were common. Other locations along the CMB line and Pogallo line were visited, but detailed microstructural analyses were focused on the two areas which represented transects across large parts of the shear zone. The first transect crosses the CMB line at the foot of the north eastern spur of Mte Cerano, south of the town of Ornavasso, from approximately 45°57'27" 8°25'16" (UTM 32 N 455141 5089488) to approximately 45°57'38" 8°24'59" (UTM 32 N 454778 5089831). The second transect crosses the Pogallo line within Val Pogallo just south of the village of Pogallo itself, from approximately 46°01'26" 8°29'34" (UTM 32 N 460742 5096827) to approximately 46°01'30" 8°29'32" (UTM 32 N 460699 5096950). 1:1000 scale mapping was conducted at these sites and samples were collected at points along the transect where compositional or strain related changes occurred.

30 µm thick, single polished thin sections were cut from these hand specimens in orientations perpendicular to foliation and parallel to lineation. Optical microscopy was conducted using a Meiji Techno MT9000 polarised binocular microscope. Plane and crossed polarised light images were taken using a Lumenera Infinity 4 camera. All mineral abbreviations used are based on the recommendations laid out by Siivola and Schmid (2007). Whole thin section scans in both plane- and crossed-polarised light were collected using a Plustek OpticFilm OF8200i Ai 35 mm film and slide scanner and SilverFast acquisition software. Large area phase maps were collected using a FEI WellSite QEMSCAN SEM at the University of Liverpool with phases defined by matching EDS spectra to database standards using the iDiscover software package.

Electron backscatter diffraction (EBSD) analysis of the transect samples was conducted using a CamScan X500 CrystalProbe field emission gun (FEG) SEM at the University of Liverpool. Samples were first polished to a high quality using 0.05 µm colloidal silica solution (SYTON) for 2 hours, before a light carbon coat (~5-15 nm thick) was applied. Large representative areas of each thin section measuring approximately 10 mm x 5 mm but varying for some samples, were mapped using the Oxford Instruments Aztec automation procedure followed

by stitching of multiple frames. A magnification of 100x was used for each frame and step size varied according to sample grain size (usually 4 µm or 5 µm). More details on the EBSD method and the instrument used can be found in Chapter 4 of this thesis. The data was cleaned using a noise reduction procedure in the Channel 5 software package (detailed in Chapter 4 of this thesis) and pole figures were produced using the MTex MATLAB toolbox. Quartz pole figures in this chapter display one data point per grain which represents the mean orientation of that grain. While the volume occupied by large grains with a given orientation in a rock is an important characteristic of the rock itself, representing one data point per grain helps to reduce the effect of a few large grains on the statistically significant crystallographic preferred orientation (CPO) of a rock. Biotite pole figures by contrast, plot every data point. This was necessary as the poor polishing quality of biotite regularly produces incomplete indexing of grains and therefore an inaccurate estimation of grain boundaries. This means that a 'one point per grain' data set is even more skewed towards large but poorly indexed grains which become divided into many 'pseudo-grains' each represented by a point in the data set. In this case, plotting all the available data minimises this effect and is especially important in samples containing a large number of very fine biotite grains.

Quartz data sets were separated into recrystallised and relict grain fractions in order to plot these two populations separately in pole figures and consider the fabric strength of each population separately. This was done using the method detailed by Cross *et al.*, (2017) which discriminates between recrystallised and relict grains based on the degree of intracrystalline lattice distortion. This is calculated in the MTex MATLAB toolbox using the m'is2mean' property which is defined as the misorientation angle between each pixel in a grain and the mean orientation of that grain. Grains with a higher mis2mean contain a larger degree of intracrystalline distortion and are classified as relict grains using this methodology, whereas grains with lower values are less internally distorted, as would be expected of newly recrystallised grains (Cross *et al.*, 2017). Each EBSD orientation map of quartz in this chapter is accompanied by a map showing which grains were classified as relict and which were classified as recrystallised. These are the grain sets which were then used to plot the corresponding pole figures for each of these two populations.

Fabric strength in quartz was measured using the misorientation index (M-index) of Skemer *et al.*, (2005). The M-index is defined as the difference between the observed distribution of uncorrelated misorientation angles and the distribution of uncorrelated misorientation angles for a random fabric and is given by:

$$M \equiv \frac{1}{2}\int |R^T(\theta) - R^0(\theta)|d\theta \quad (7.1)$$

Where *M* is the misorientation index, $R^T(\theta)$ is the theoretical distribution of misorientation angles for a random fabric and $R^0(\theta)$ is the observed distribution of misorientation angles normalised for the number of data (Skemer *et al.*, 2005). The result of the M-index calculation is a number between 0 and 1 where 0 is a random fabric and 1 is a single crystal.

## 7.4. Results

### 7.4.1. Outcrop-scale characteristics of the transect sites

The outcrops around the CMB line at Ornavasso pass from regular, unsheared Kinzigite in the NW, through to granite and gabbrodiorite of the graniti dei laghi in the SE (Fig. 7.3). Varying degrees of strain are apparent across this transect with generally lower strain protolith rocks and protomylonites towards the peripheries and higher strain mylonites in the centre. Notably, there are no observed exposures of ultramylonites in this section of the CMB line. Strain is accommodated within a ~300 m wide mylonitic band. Across the CMB fault from the IVZ to the SdL there is an abrupt compositional transition from dark, banded rocks with quartz veins and very high mica content (the Kinzigites) in the IVZ, to quartz and feldspar dominated gneisses derived from granitoid and sedimentary protoliths in the SdL. This transition occurs between samples CMB 17 (Kinzigite mylonite) and CMB 18 (orthogneiss mylonite) defining the mappable trace of the CMB line and, by extension, the boundary between the IVZ and the SdL. Pegmatites up to 3 m wide are common in the deformed Kinzigites NW of the CMB line, these are sub-concordant with foliation but cut it at low angles in places and are well foliated to lightly foliated themselves. Finer grained felsic and mafic appinites are present along the CMB line itself and are interpreted to be related to Permian age intrusions that exploited the CMB line during the large scale intrusion events that produced the granitic batholiths of the Graniti dei Laghi (Boriani, Burlini, *et al.*, 1990; Boriani, Origoni, *et al.*, 1995).

The picture is more complicated along the section of the Pogallo line exposed in Val Pogallo, where the numerous different lithologies in the Serie dei Laghi have been incorporated into the shear zone, producing alternating compositional bands (Fig. 7.4). The predominant rock type in the southern part of the transect is granitic orthogneiss, with sections of more mafic granodioritic orthogneiss identified by the presence of hornblende. Intermittent bands of mylonites and protomylonites with higher mica content become more common and wider further northwards (Fig. 7.5). Boudinaged appinites are present but rare. This part of the

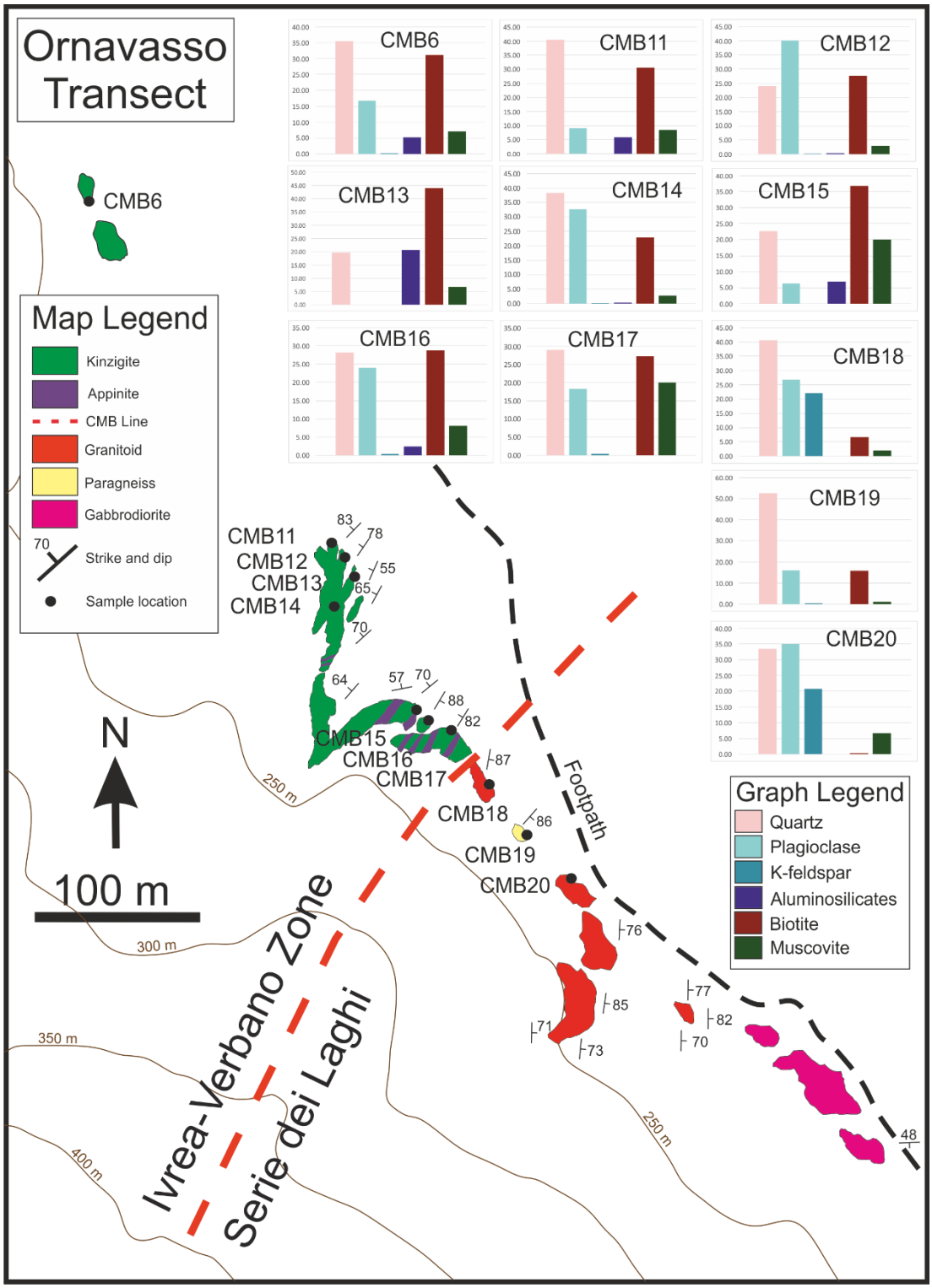


***Figure 7.3:*** *Outcrop map of the Ornavasso transect across the CMB line (location shown in Fig. 7.1) with sample locations indicated along with modal abundance data for the main minerals collected using EDS mapping of whole thin sections in a QEMSCAN SEM. The CMB line marks the boundary between the Ivrea Verbano zone and the Serie dei Laghi and its trace is clearly defined by a compositional divide between very mica-rich Kinzigites devoid of K-feldspar in the NW and granitic or metaspammitic rocks to the SE with much lower mica content. The shear zone is also associated with a high density of syntectonic appinite intrusions on the IVZ side as described in Boriani et al. (1990). Grid references of all samples are given in Table 7.1.*

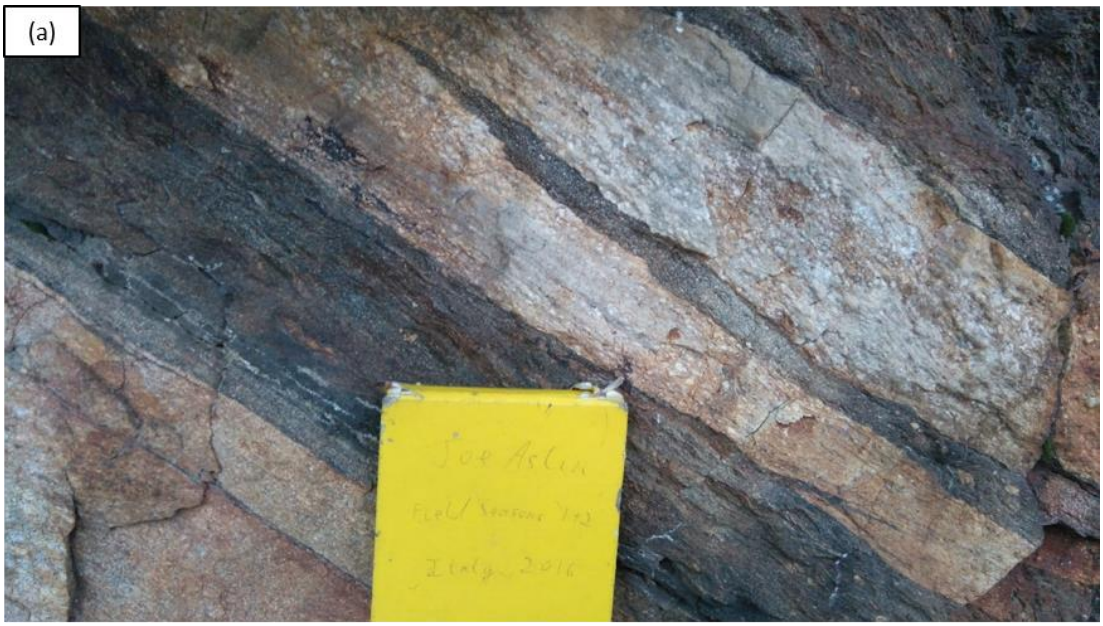


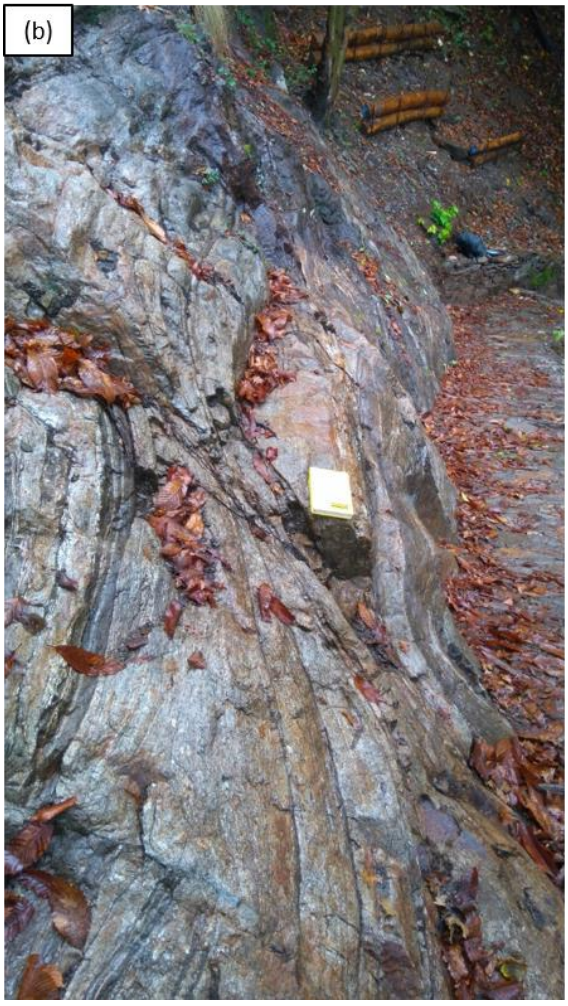


***Figure 7.4:*** *(a) Intercalated bands of mica-rich (dark) and mica poor (light) mylonites within mylonites of the Pogallo shear zone in Val Pogallo. (b) Localised shear zone within orthogneiss of the SdL close to the contact with the IVZ in Val Grande. This is to illustrate nearby structures. Samples were not taken from this locality.*

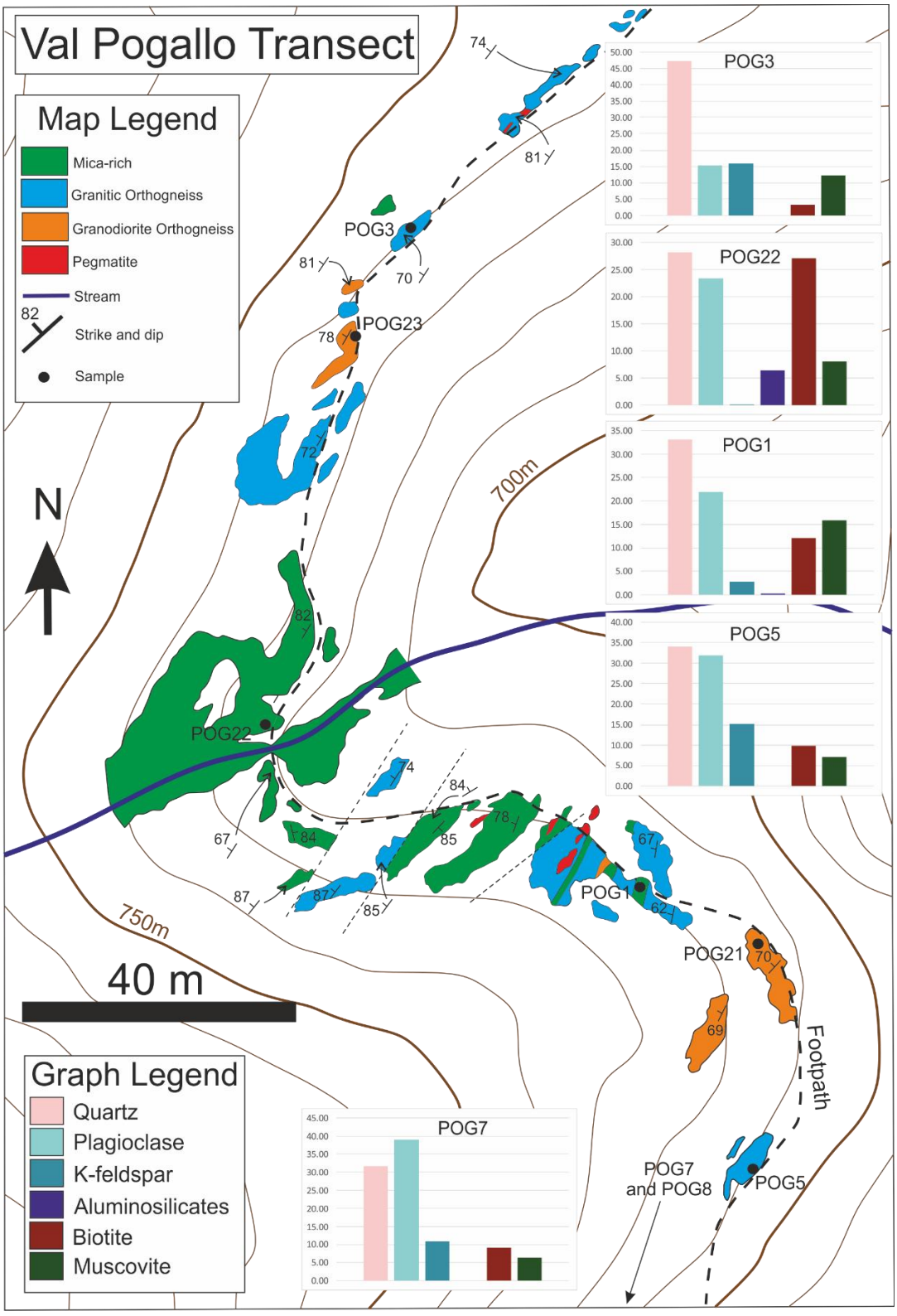


***Figure 7.5:*** *Outcrop map of the Pogallo line transect in Val Pogallo (location is shown in Fig. 7.1) with sample locations indicated, as well as modal abundance data for the main minerals, collected using EDS mapping of whole thin sections in a QEMSCAN SEM. POG7 and POG8 were collected further south and their locations are given in Fig. 7.1. The shear zone structure in Val Pogallo is complex and the exact trace of the boundary between rocks of the IVZ and SdL is difficult to determine. Mica-rich mylonites are interspersed with granitic and granodioritic orthogneiss mylonites, with narrow, high strain bands at compositional contacts as well as zones of granitic ultramylonites such as the one sampled in POG3. Grid references of all samples are given in Table 7.1.*

transect is also characterised by high strain bands intercalated with sections of lower strain rocks, with the highest strain zones occurring regularly, but not always, along the lithological boundaries between rocks of different compositions. A complex spatial and temporal relationship between the high strain zones is evidenced by cross cutting relationships with foliation and variations in shear sense (Fig. 7.6). This results in an anastomosing or multiple-branched nature to the shear zone here, with shear bands delimiting tectonic blocks which have internally experienced lower strain. Shortly before the point where the transect crosses a small stream, the outcrops become consistently mica-rich along with more prominent quartz veins which are folded or boudinaged. The degree of strain is difficult to determine in these dark rocks but remains fairly constant for ~50 m, without the complexity and heterogeneity observed south of the stream. The northern part of the transect culminates in a narrow but continuous band of very high strain, fine grained ultramylonites of granitic composition. Beyond this there is a paucity of reliable outcrop for several hundred metres before coarse-grained, unsheared Kinzigites are encountered close to the village of Pogallo. The complex mixture of lithologies prohibits an exact delineation of the contact between the SdL and the IVZ at this location. The rocks transition from mostly orthogneiss with elements of mica-rich rocks, to predominantly mica-rich rocks with bands of orthogneiss, from SE to NW. The lack of exposure of sheared Kinzigites north of the ultramylonite band also means the finite width of the shear zone cannot be estimated, although the mylonites that are exposed give a lower bound of ~200 m. This mesoscale structure of the Pogallo line in Val Pogallo concurs with previous work, which describes a wide zone of distributed deformation in the SE part of the IVZ (the PDFZ) juxtaposed against a complex zone of anastomosing or conjugate high strain bands of mylonites and ultramylonites at the contact and within the north easternmost part of the SdL (Handy, 1987). Examples of the Kinzigite and orthogneiss mylonites in outcrop and hand specimen are given in Figure 7.7.

### 7.4.2. Microstructural characteristics of Kinzigites in the CMB line

A list displaying details of the samples used in this study is given in Table 7.1. Sample CMB6 (Supp. Fig. S7.1) is a Kinzigite collected approximately 500 m from the trace of the CMB line near Ornavasso. It represents the coarse grained, mica-rich protolith of the variously strained Kinzigites taken from closer to the CMB line. It is composed of approximately 35% quartz, 30% biotite, 17% plagioclase, 10% muscovite and 5 % sillimanite along with minor amounts of apatite. The sample bears evidence of viscous deformation in as much as it is strongly foliated and displays abundant undulose extinction in quartz and biotite grains. The foliation in the Kinzigites is at a low angle to that related with the shearing that formed the CMB line

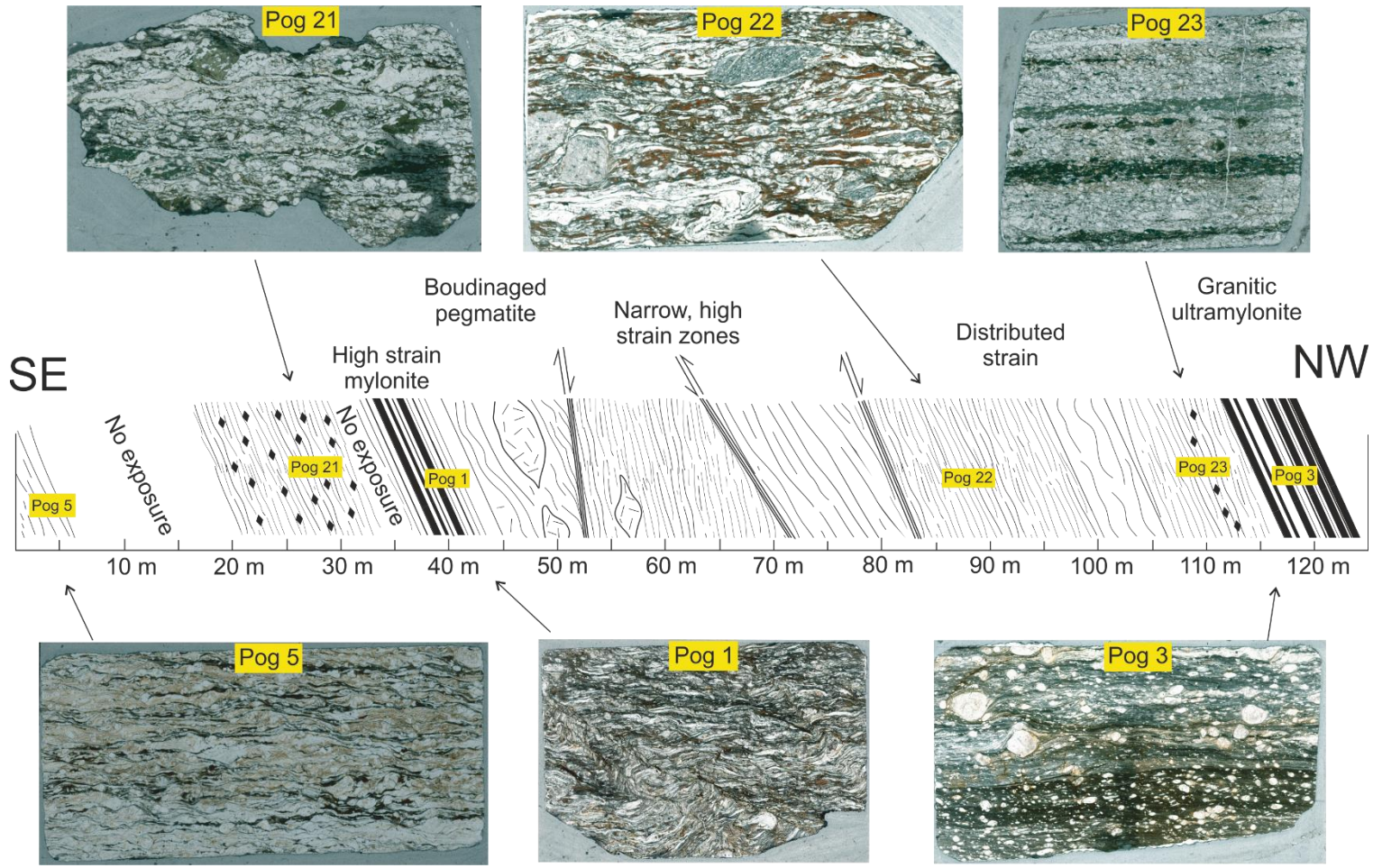


***Figure 7.6:*** *Schematic cross section across the exposed part of the Pogallo line shear zone in Val Pogallo. Strain is distributed heterogeneously with several narrow high strain zones and ultramylonites within wider regions of lower strain mylonites and protomylonites. The higher strain bands are often located at the boundaries between different lithologies. The mylonitic foliation bends sharply into the high strain bands which do not all have the same shear sense indicating they share an anastomosing or conjugate relationship.*

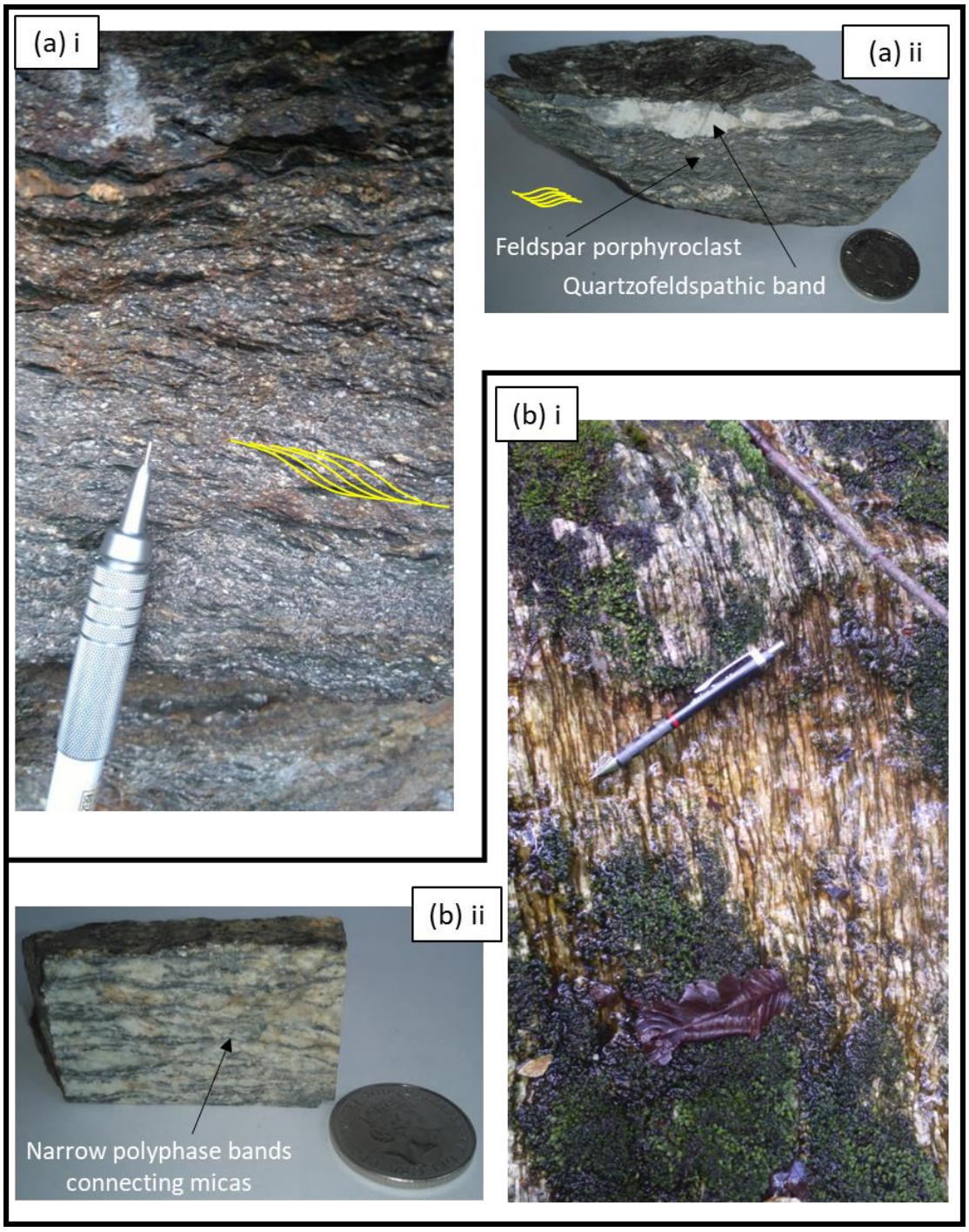


***Figure 7.7:*** *Field photographs and cut hand specimens of mylonites from a) Kinzigite and b) orthogneiss protoliths. The Kinzigite is dark from the very high abundance of biotite and muscovite but with fine porphyroclasts of plagioclase feldspar which appear as white specs on fresh and broken surfaces. Occasional boundinaged bands much richer in quartz and plagioclase are present. Wavy or S/C mylonitic fabrics are evident and defined by the curved basal planes of micas. The Orthogneiss displays narrow (1-5 mm wide) dark, mica-rich banding across the predominantly quartzo-feldspathic framework, producing an augen texture which becomes elongate at higher strain.*

***Table 7.1***

| Sample number | Transect | Location | Degree of deformation | Probable protolith | Modal Abundance |
|---|---|---|---|---|---|
| POG8 | Val Pogallo | 8°29'42.8"E 46°0'32.4"N | Protolith | Paragneiss | ~50% Qtz, ~20% Pl, ~20% Bt, ~8% Ms, ~2% other |
| POG7 | Val Pogallo | 8°29'34.0"E 46°1'23.9"N | Protomylonite | Orthogneiss (granitic) | 32% Qtz, 39% Pl, 11% Kfs, 9% Bt, 6% Ms, <1% Ap 3% other |
| POG5 | Val Pogallo | 8°29'33.3"E 46°1'26.0"N | Mylonite | Orthogneiss (granitic) | 34% Qtz, 32% Pl, 15% Kfs, 10% Bt, 7% Ms, <1% Ap 2% other |
| POG21 | Val Pogallo | 8°29'33.4"E 46°1'27.0"N | Mylonite | Orthogneiss (granodiorite) | ~30% Qtz, ~35% Pl, ~18% Am, ~13% Bt, ~4% other |
| POG1 | Val Pogallo | 8°29'32.6"E 46°1'27.3"N | Mylonite | Mica schist (possible kinzigite) | 33% Qtz, 22% Pl, 16% Ms, 12% Bt, 8% Chl, 3% Kfs, <1% Sil, 5% other |
| POG22 | Val Pogallo | 8°29'30.0"E 46°1'28.0"N | Mylonite | Mica schist (possible kinzigite) | 28% Qtz, 27% Bt, 23% Pl, 8% Ms, 6% Ky, 8% other |
| POG23 | Val Pogallo | 8°29'30.4"E 46°1'29.4"N | Mylonite | Orthogneiss (granodiorite) | ~35% Qtz, ~35% Pl, ~20% Am, ~7% Bt, ~3% other |
| POG3 | Val Pogallo | 8°29'31.1"E 46°1'30.3"N | Ultramylonite | Orthogneiss (granitic) | 47% Qtz, 16% Kfs, 15% Pl, 12% Ms, 3% Bt, 1% Ap, 6% other |
| | | | | | |
| CMB6 | Ornavasso | 8°25'1.0"E 45°57'41.0"N | Protolith | Kinzigite | 35% Qtz, 30% Bt, 17% Pl, 10% Ms, 5% Sil, 3% other |
| CMB11 | Ornavasso | 8°25'7.7"E 45°57'34.5"N | Protomylonite | Kinzigite | 41% Qtz, 31% Bt, 9% Pl, 8% Ms, 6% Sil, 5% other |
| CMB12 | Ornavasso | 8°25'8.1"E 45°57'34.1"N | Protomylonite | Kinzigite | 24% Qtz, 40% Pl, 28% Bt, 3% Ms, <1% Sil, 5% other |
| CMB13 | Ornavasso | 8°25'8.3"E 45°57'33.9"N | Protomylonite | Kinzigite | 20% Qtz, 44% Bt, 21% Sil, 7% Ms, 5% St, 3% other |
| CMB14 | Ornavasso | 8°25'7.8"E 45°57'33.1"N | Protomylonite | Kinzigite | 38% Qtz, 33% Pl, 23% Bt, 3% Ms, <1% Sil, 3% other |
| CMB15 | Ornavasso | 8°25'9.9"E 45°57'31.3"N | Mylonite | Kinzigite | 23% Qtz, 37% Bt, 20% Ms, 7% Sil, 6% Pl, 2% St, 3% Grt, 2% other |
| CMB16 | Ornavasso | 8°25'10.2"E 45°57'31.1"N | Mylonite | Kinzigite | 28% Qtz, 29% Bt, 24% Pl, 8% Ms, 2% Sil, <1% Kfs, 7% other |
| CMB17 | Ornavasso | 8°25'11.0"E 45°57'30.8"N | Mylonite | Kinzigite | 29% Qtz, 27% Bt, 20% Ms, 18% Pl, <1% Kfs, 5% other |
| CMB18 | Ornavasso | 8°25'11.9"E 45°57'29.8"N | Mylonite | Orthogneiss (granitic) | 40% Qtz, 25% Pl, 20% Kfs, 5% Ms, 7% Bt, 3% other |
| CMB19 | Ornavasso | 8°25'13.0"E 45°57'28.9"N | Mylonite | Paragneiss | 53% Qtz, 16% Pl, 16% Bt, 1% Ms, <1% Kfs, <1% Ilm, <1 Ap, <1% Rt |
| CMB20 | Ornavasso | 8°25'14.1"E 45°57'28.0"N | Protomylonite | Orthogneiss (granitic) | 34% Qtz, 35% Pl, 21% Kfs, 7% Ms, <1% Bt, 2% Chl |

mylonites and is interpreted to be metamorphic, pre-dating deformation along the CMB shear zone. The grain size and the foliation are coarse, with quartz grains up to 6 mm in size and major foliation spacings of up to 10 mm. No mylonitic fabrics are apparent. The abundant mica (mostly biotite but also muscovite) forms wide, foliation-parallel bands but also occurs as individual grains within quartzofeldspathic domains. The biotite grains are predominantly oriented with their c-axes perpendicular to foliation although there is some variation, particularly in grains hosted within predominantly quartzofeldspathic domains. CMB11-14 (Supp. Figs. S7.2-S7.5) represent four protomylonite samples collected from an outcrop between 120 m and 150 m NW of the trace of the CMB line. They possess different mineral modal abundances reflecting the variation within the Kinzigite unit, with CMB11 and CMB13 possessing significant sillimanite (~5% - ~20%) but very little plagioclase (<10%) and CMB12 and CMB14 containing a large amount of plagioclase (~30% - ~40%) and little if any sillimanite. The quartz content varies from ~20% (CMB13) to ~40% (CMB11), biotite from ~23 % (CMB14) to ~44% (CMB13) while muscovite constitutes <10% in all four samples. All four samples contain minor apatite and CMB 13 also contains ~5% staurolite (Fig. 7.3).

In the plagioclase poor samples (CMB11 and CMB13), there are several key differences relative to the Kinzigite protolith CMB6 (Supp. Fig. 7.1). Firstly, the grain size of all phases is smaller, at between 0.5 mm and 3 mm, producing a finer foliation and a finer grained rock overall. Biotite grains are more elongate and are also more strongly aligned parallel to foliation. In CMB11 this results in a greater number of narrower mica bands, separated by quartz-rich domains, while in CMB13 there are large bands of very elongate, well aligned mica grains (Supp. Figs. S7.2, S7.4). Fibrous sillimanite lathes commonly occur in association with biotite domains in these samples and are aligned with their long axes parallel to lineation. Quartz is confined to bands separated by mica domains and commonly containing further individual mica grains. The quartz is partly recrystallised, with sub-grains and some fine new grains formed around and within coarse, elongate grains which possess a high degree of internal deformation shown by strong undulose extinction (Supp. Figs. S7.2, S7.4). A second important development is the presence of a gentle S-C mylonitic fabric, defined by the curvature of biotite basal planes. The few feldspar grains that are present possess angular boundaries and do not display undulose extinction.

The plagioclase rich Kinzigite protomylonites (CMB12 and CMB14) were collected within a few metres of CMB11 and CMB13 (see Fig. 7.3) but possess a different microstructure. Biotite and muscovite grains define both a primary mylonitic foliation and several C’ shear bands, giving a dextral sense of shear. In the case of CMB12, between these shear bands the

mylonitic foliation is curved into a small fold structure delineated by the orientations of biotite basal planes (Supp. Fig. S7.3). Biotite throughout CMB14 is less elongate and less interconnected than in the plagioclase poor samples although a subtle, wavy foliation plane is still defined by the basal planes (Supp. Fig. S7.5). Quartz shows undulose extinction and internal distortion of grains but recrystallisation and subgrain formation is not as developed as within CMB11 and CMB13. Plagioclase feldspars show little evidence of viscous deformation and are fractured and angular in shape.

Three further Kinzigite samples were collected from outcrops within 50 m of the trace of the CMB line. The furthest from the line is CMB15 (Supp. Fig. S7.6) which has a low plagioclase content (~6%) and is dominated by micas, with ~ 37% biotite and ~20% muscovite. The remaining major minerals are quartz (~23%) and sillimanite (~7%) with a small amount of garnet and staurolite. The microstructure is dominated by thick bands (up to 10 mm wide) of biotite and muscovite and narrower, discontinuous bands of quartz with some feldspar. The boundaries of the mica and quartz domains define a S/C mylonitic fabric although at least one C' shear band is also present at the thin section-scale. The quartz is mostly recrystallised by subgrain rotation, producing an overall finer quartz grain size than in the previously described protomylonites sampled further from the CMB line. This recrystallisation has occurred to the greatest extent in the narrowest bands of quartz confined within or between mica domains. Where coarser quartz grains remain, in the larger, quartz-rich domains, they are very elongate with strong undulose extinction. Occasional garnet and staurolite grains within mica domains show brittle fracture and boudinage. Coarse, apparently randomly oriented, metamorphic biotite and muscovite occur in two clusters either side of the C' shear band. However, aside from these, mica grains are aligned with their basal planes parallel to the mylonitic foliation (Supp. Fig. S7.6).

CMB16 is the first true mylonite (as opposed to a protomylonite) encountered along the transect (Supp. Fig. S7.7). It can be described as such due to an abundance of fine-grained (<500 μm) recrystallised quartz and fine biotite. It has a bulk mineralogy composed of ~29% biotite, ~8% muscovite, ~24% plagioclase and ~28% quartz, with <5% sillimanite and minor apatite. There is a strong, pervasive C' fabric in which the wavy mylonitic foliation is cut regularly by narrow C' shear bands (Fig. 7.8). This offsets otherwise continuous alternating bands of biotite and quartz/feldspar, producing small, individual, inclined sigmoidal shaped domains. While the through-going bands of quartz and feldspar are broken by the shear bands, the C' surfaces themselves are composed of further biotite grains or the extended tails of S shaped biotite domains (Fig. 7.8). This means that the mylonite retains an

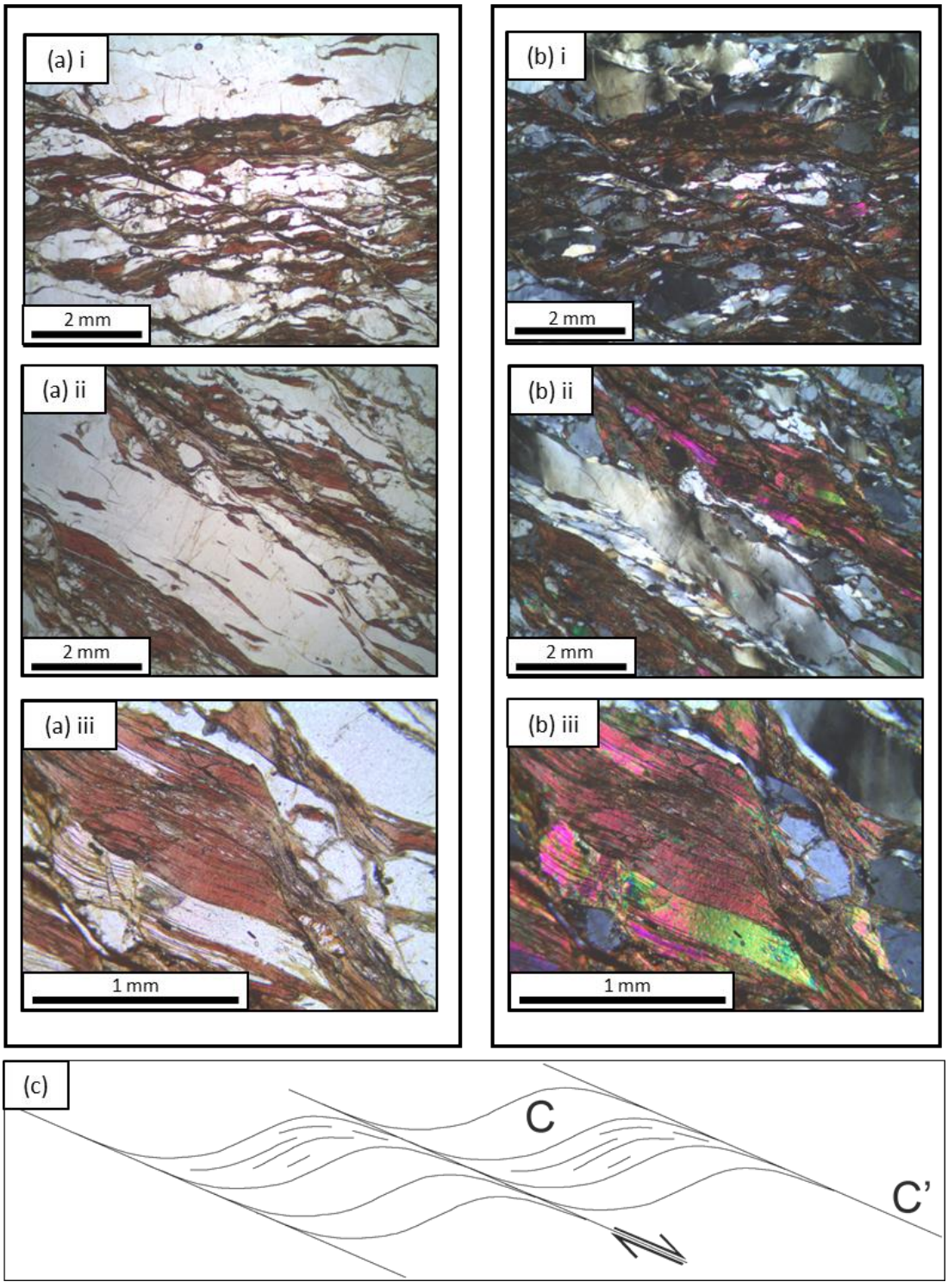


***Figure 7.8:*** *Optical micrographs from sample CMB16 showing the typical microstructures of mica interconnection within the Kinzigites. The bent basal planes of mica grains define the S, C and C' surfaces along which deformation is accommodated. Quartz ribbons and grains display extensive undulose extinction but are markedly less recrystallised than quartz in rocks with low mica content. a) Plane polarised light optical micrographs. b) Crossed polarised light optical micrographs. c) Schematic representation of the relation between C and C' surfaces with a top to the right shear sense. This sketch is in approximately the same orientation as the upper images of panels (a) and (b).*

interconnected mica network with basal planes aligned along important S, C and C' slip surfaces. Quartz has also accommodated strain, as evidenced by severe undulose extinction and recrystallisation, which facilitates the shape change required to form sigmoidal domains surrounded by mica. However, the C' shear bands which represent regions of localised higher strains are dominated by mica (Fig. 7.8, Supp. Fig. S7.7).

CMB17 (Supp. Fig. S7.8) is the last sample of Kinzigite composition taken before the transition to rocks of the SdL across the CMB line. It was sampled within 10 m of CMB16 and is also a relatively high strain mylonite but has a modal composition with less plagioclase (18%) and significantly more muscovite (20%). The quartz and biotite contents are similar at ~30% and ~27% respectively. Microstructurally the two mylonites share some similarities but also have important differences. CMB17 displays a well-developed S-C fabric but has a lower abundance of pervasive C' shear bands than CMB16. It contains wide domains (1 – 4 mm) of relatively coarse (up to 2 mm) biotite and muscovite, which is strongly kinked, while plagioclase grains are finer (<1 mm) and more isolated, regularly surrounded by recrystallised quartz. These quartz grains are very elongate and distorted with serrated boundaries suggesting a prevalence of grain boundary migration recrystallisation. Mica basal planes are aligned parallel to S surfaces except within the large regions of coarse grains where unfavourably oriented biotite and especially muscovite have accommodated a significant amount of strain through complex kinking (Supp. Fig. 7.8).

As an overall picture, the Kinzigite samples collected near Ornavasso display an increasing degree of strain as they approach the trace of the CMB line and the switch to rocks associated with the SdL. With increasing strain, large bands and clusters of mica grains transition into a network which is fully interconnected across S and C' surfaces. Sections with low plagioclase feldspar content have higher total mica content and only a small amount of deformation across quartz and feldspar-rich domains is required to bridge them and produce a fully interconnected, mica network. In higher strain rocks of similar modal abundances, such as CMB17 (Supp Fig. S7.8), strain is distributed throughout the micaceous S and C surfaces with quartz grains recrystalising to satisfy the shape change of their mica-bounded domains. By contrast, sections with high plagioclase content, such as CMB12 and CMB14, more commonly display localised, high strain C' shear bands. At higher strains, C' bands become more abundant, resulting in a pervasive C' fabric which focusses deformation within mica phases and around feldspar rich domains. Whilst variations in modal abundance within the Kinzigite influences the microstructural evolution and distribution of strain to some extent, strain always appears to be accommodated principally by the mica phases which dominate these

rocks. Spatially, however, strain is quite evenly distributed across the samples within and throughout the well-connected micaceous networks. It is worth noting that, despite careful and detailed fieldwork, no high strain ultramylonites of Kinzigite composition were observed in association with the CMB line.

### 7.4.3. Microstructural characteristics in samples derived from the Serie dei Laghi

Samples collected on the south eastern side of the CMB line do not share the mica-rich metapelitic composition of the Kinzigites from the north western side, being instead derived from the orthogneisses and paragneisses of the Serie dei Laghi. These mylonites have reduced mica content and substantial differences in microstructure relative to those on the IVZ side, as micaceous layers or grains are subordinate features in an initial microstructure which is dominated by quartz and feldspar. CMB20 (Supp. Fig. S7.9) was sampled from an outcrop 100 m SE of the trace of the CMB line. Despite this, the degree of quartz recrystallisation is comparable to, if not greater than, that of the most highly deformed Kinzigite samples (CMB16 and CMB17). It has a granitic protolith with a high quartz content (~34%), both plagioclase (~35%) and K-feldspar (~21%), some muscovite (~7%) but very little biotite (<1%) (although there is almost 2% chlorite which has likely replaced biotite). The muscovite that is present occurs as coarse, isolated grains which are kinked and sheared. Discontinuous bands of muscovite (and chlorite) aligned with foliation are present but are not pervasive and do not form any degree of interconnected network. Instead, most muscovite grains appear to have been rotated and bent by the brittle-viscous flow of the quartzofeldspathic load-bearing framework. Dislocation creep is the dominant deformation mechanism in quartz with SGR recrystallisation producing elongate domains of equant ~20 µm sized grains. These domains, along with mica basal planes, define a pervasive S-C mylonitic foliation (Supp. Fig. S7.9). Both plagioclase and K-feldspar show evidence of brittle fracturing and possibly some degree of dissolution precipitation creep (see Chapter 8) but show no evidence of dynamic recrystallisation.

CMB19 (Supp. Fig. S7.10) has a biotite content (~16%) that is higher than CMB20 and is devoid of K-feldspar, giving it a likely metasedimentary protolith. However, a very high quartz content (~53%) and the lack of sillimanite identifies it as a paragneiss or mica-schist of the SdL rather than a mica dominated metapelite of the Kinzigite formation. It has a plagioclase content of ~16%, approximately 1% muscovite and minor amounts of apatite, ilmenite and rutile. The biotite content allows a degree of interconnection between fine (<500 µm) mica

grains which define a wavy S-C foliation. The angle between S and C planes is small (approximately 30°), indicating a mature microstructure that has accommodated substantial strain (Vitale and Mazzoli, 2010). Quartz forms fine (~100 μm) recrystallised grains but also coarse distorted elongate grains whose boundaries help to define the foliation. A prominent pseudotachylite or ultracataclasite zone abruptly cuts the mylonitic fabric without evidence of fault drag.

CMB18 (Supp. Fig. S7.11) represents a return to a granitoid protolith dominated by quartz (~40%), plagioclase (~27%) and K-feldspar (~22%). The mica component is similar to that of CMB20 however in CMB18 it is predominantly biotite (~7%) rather than muscovite (~2%). CMB18 was collected within a few metres of the CMB line trace and possesses the finest recrystallised quartz grain size of any sample on this transect (10 μm – 50 μm). Despite only comprising around 7% by volume, biotite forms a fine-grained, interconnected network in this sample. This is interpreted to have occurred through a dramatic grain size reduction in much of the biotite and the distribution of this very fine biotite, along with similarly sized quartz and other phases, along grain boundaries connecting the coarse parent grains (Fig. 7.9). This process, and its influence on the microstructural evolution of mica-bearing, but quartz and feldspar dominated, mylonites, is described in detail in Chapter 6 of this thesis. The widest regions of this very fine-grained material occur along penetrative C' shear bands.

### 7.4.4. Microstructural characteristics of the Pogallo line transect

Unlike the CMB line transect at Ornavasso, the transect studied across the Pogallo line in Val Pogallo runs predominantly through rocks of the SdL, with very limited exposure within the Kinzigites (Fig. 7.5). The shear zone here is characterised by intercalations of multiple lithologies and a heterogeneous distribution of strain, producing a more complex transect than at Ornavasso. Granitic orthogneiss predominates in the south east (POG7 and POG5) with several bands of more amphibole bearing granodiorite orthogneiss (POG23 and POG21) across the transect. These rocks have a relatively low mica content (especially the granodiorites) and their microstructural evolution with increasing strain is similar to that of the orthogneiss mylonites at Ornavasso, with abundant shear bands and zones of very fine-grained polyphase material. The quartz, which, along with feldspar, constitutes the load bearing framework of these rocks, is highly recrystallised.

POG8 is the most southerly sample from the Pogallo transect and represents an un-sheared paragneiss of the SdL. It is composed predominantly of quartz (~50%), plagioclase (~20%), biotite (~20%) and muscovite (~8%) along with minor amounts of apatite, ilmenite, staurolite

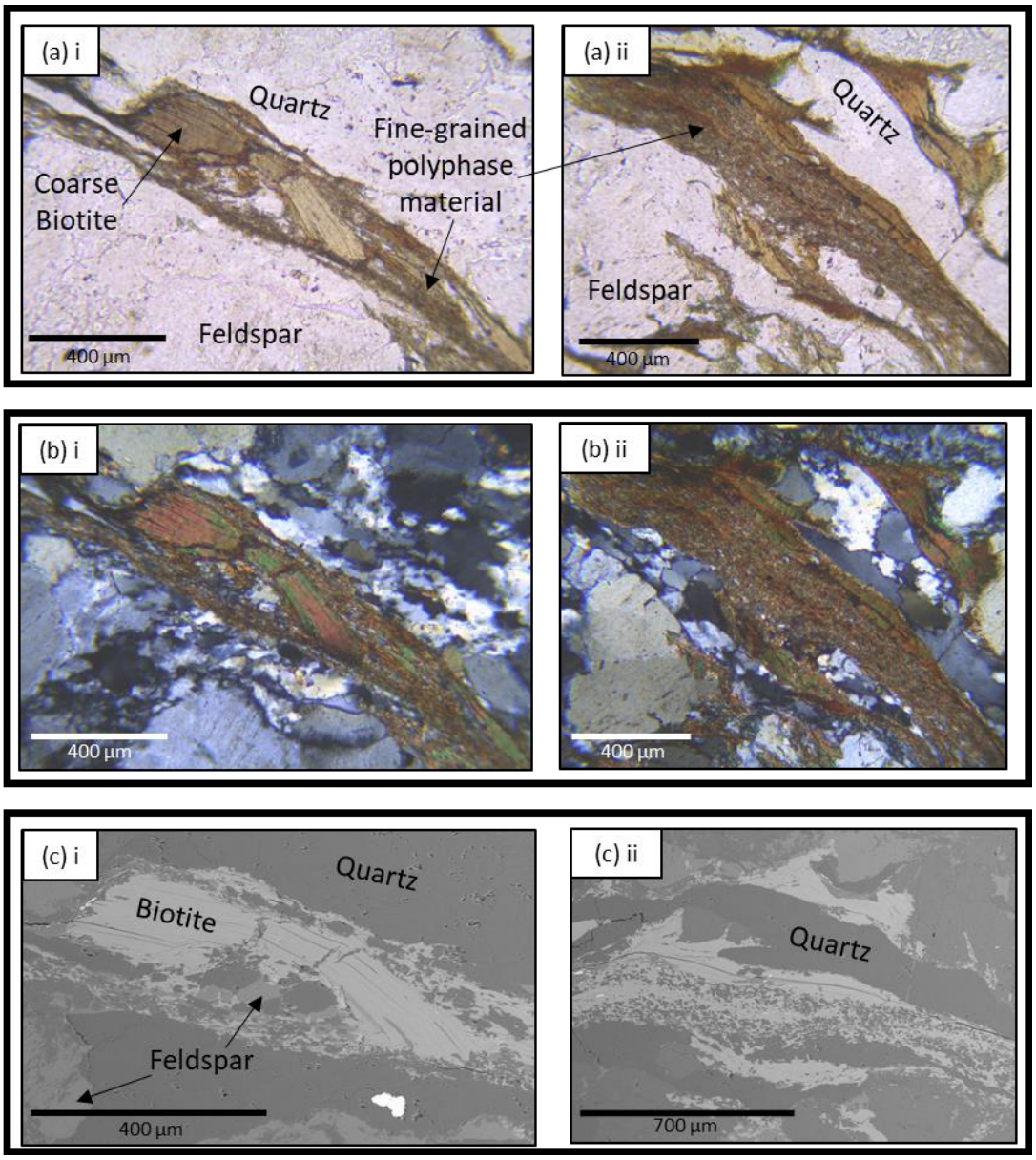


***Figure 7.9:*** *Examples (from sample CMB18) of the fine-grained biotite microstructures which facilitate the production of an interconnected weak network in orthogneiss mylonites (see Chapter 6 of this thesis) linking coarse biotite grains through fine-grained polyphase bands. a) plane polarised light optical micrographs. b) Crossed polarised light optical micrographs of the same areas as in (a) showing recrystallised quartz and porphyroclasts of feldspar surrounding the biotite. c) Backscattered electron SEM images of roughly the same areas as in (a) and (b).*

and zircon. The grain size is uniformly fine, at between 100 µm and 300 µm. The mica phases, whilst abundant, occur as isolated grains surrounded by a load-bearing framework of quartz and feldspar. The quartz grains display a small amount of undulose extinction while the mica grains are strongly aligned, with their basal planes defining the foliation.

The samples of granitic orthogneiss mylonites from this transect, represented by samples POG7, POG5 and POG3, contain abundant quartz (30% -50%), both plagioclase (15% -40%) and K-feldspar (10% -16%), a mica content of just over 15% (biotite and muscovite) and minor amounts of apatite, rutile and ilmenite. The microstructure of these samples has been discussed in detail in Chapter 6 but is summarised below. The protomylonites (POG7) are dominated by bands of coarse-grained (up to 700 µm) polygonal quartz and 1 – 3 mm feldspar porphyroclasts. The feldspars show evidence of brittle fracturing while the quartz bands have undergone a degree of dynamic recrystallisation and show undulose extinction in the larger grains. Mica grains are predominantly coarse (0.5 – 3 mm), kinked, mineral fish which occur in clusters, discontinuous bands or as isolated grains aligned with foliation. A small amount of 3 – 10 µm biotite is present around the peripheries of larger grains. In the higher strain sample (POG5), the grain size of all phases has reduced significantly. The quartz component is entirely recrystalised into monomineralic bands of ~50 µm grains while feldspar porphyroclasts are <1 mm in size and are angular, with clear evidence of fracturing and some dissolution and precipitation of finer grains (see Chapter 8). Micas are present as mica fish but also to a much greater extent as very fine-grained components of polymineralic bands which connect coarser mica grains along foliation or in C’ shear bands. In the Ultramylonite sample (POG3) almost the entire sample is composed of a very fine-grained (1 – 5 µm) polymineralic matrix containing all component minerals of the rock. The exceptions are muscovite mica fish up to 1 mm in length and porphyroclasts of plagioclase and K-feldspar up to 3 mm in size but generally <1 mm. The fine-grained biotite in this matrix displays strong uniform pleochroism, suggesting it is well aligned with foliation.

The granodiorite orthogneiss mylonite samples, represented by POG21 and POG23, also contain mica in low abundances (~10%) and share many microstructural characteristics with the granitic orthogneiss mylonites. Quartz, which constitutes ~30% modal abundance, forms elongate, highly recrystallised domains while plagioclase occurs as either coarse porphyroclasts with evidence of brittle fracturing, or very fine precipitated grains. Amphibole is abundant (~20%) and appears to behave as a rigid porphyroclast, similar to the feldspars. As in other sampled orthogneiss mylonites, biotite occurs as very fine grains (1 – 5 µm) distributed within polyphase domains.

Mica-rich mylonites are also present along this transect, interspersed with the mylonites derived from orthogneisses. POG1 was sampled from a narrow intercalation of high strain, mica-rich mylonite within an otherwise orthogneiss dominated part of the transect. It has a modal abundance of ~33% quartz, ~22% plagioclase, ~16% muscovite, ~12% biotite and <5% K-feldspar. There is also a significant amount of retrogressive chlorite after biotite suggesting a true syntectonic biotite content of ~20%. It is not clear whether POG1 was originally part of the Kinzigite formation, or a paragneiss unit within the SdL (such as POG8), however the small thickness, lack of obvious tectonic contacts with the orthogneiss and differences in composition relative to Kinzigites suggests the latter is more likely. POG22 is part of a larger section of moderate strain mica-rich mylonites in the central part of the transect and has a composition similar to that of Kinzigite samples from the transect at Ornavasso, except for the fact that aluminosilicates take the form of kyanite instead of the fibrolitic sillimanite common to the Kinzigites. The composition of POG22 is ~28% quartz, ~27% biotite, ~23% plagioclase, ~8% muscovite and ~6% kyanite. Again, it is uncertain whether POG22 represents a Kinzigite of the IVZ or a paragneiss of the SdL although in this case the compositional similarities and its presence within a wide section of mica-rich mylonites suggest POG22 may be of Kinzigite origin.

In both POG1 and POG22, biotite is present both as coarse grains and within very fine polyphase domains similar to those seen in granitic orthogneiss mylonites of both this transect and the one studied at Ornavasso. This is unlike the Kinzigite mylonites from the Ornavasso transect which did not display evidence of the same dramatic grain size reduction in biotite. POG1 displays a particularly high strain mylonitic microstructure with very elongate monomineralic domains of highly recrystallised quartz interspersed with mica-rich layers composed of coarse muscovite and biotite (in part replaced by chlorite) and fine-grained mixtures of phases. These layers are folded and bent around coarse porphyroclasts of plagioclase which are fractured but mostly sub-rounded in shape. Several localised shear bands cut the microstructure, folding the foliation and in some cases resulting in a brittle fracture plane. POG22 has a similar microstructure to POG1 with respect to quartz, forming elongate recrystalised domains and ribbon grains, and plagioclase, behaving as rigid porphyroclasts. The kyanite porphyroclasts in POG22 are very coarse-grained (up to 5 mm), are generally euhedral to subhedral and are strongly fractured. Much of the biotite exists in the form of coarse grains which are aligned to form an interconnected network. A subtle low-angle (high strain) S-C fabric is retained within the foliation but larger-scale folding is also present. Some biotite occurs as very fine grains similar to those in polymineralic domains

described previously, but this grain size reduction has occurred to a lesser extent than in POG1.

Overall, the Pogallo line transect displays a very different microstructural progression to the CMB line transect at Ornavasso. The southern part in particular is characterised by a heterogeneous distribution of strain, with lithological boundaries and narrow bands of different lithology serving as sites of localised high strain. POG1 is an example of a narrow section of mica-rich rocks within mostly quartzofeldspathic orthogneiss which contains high strain, highly recrystallised microstructures. The mixing of different lithologies both within the SdL at this location and tectonically within the Pogallo shear zone itself produces a complex picture of narrow, high strain bands interspersed with larger sections of moderate or lower strain. Unfortunately, the nature of strain evolution from the shear zone leading into the IVZ to the north is obstructed by a lack of outcrop here.

### 7.4.5. Fabric analyses using EBSD

#### *Quartz fabric: Ornavasso transect*

Quartz C-axis pole figures produced from large area EBSD maps of the samples from the Ornavasso transect display an evolution in CPO across the strain gradient for both recrystallised and relict grain fractions (Fig. 7.10). The quartz c-axis fabric in the pole figures for the Kinzigite protolith sample (CMB6) are heavily influenced by the presence of a small number of large grains, which, despite plotting a single mean orientation for each grain, produces single crystal data clusters that affect the data multiple of uniform density in the pole figures. The quartz c-axis fabrics in pole figures of the protomylonites CMB11 and CMB12, take the form of weakly defined cross girdles with low fabric strength. This is true of both the recrystallised and relict grain populations with M-indexes (Skemer *et al.*, 2005) in recrystallised grains of 0.0108 and 0.0196 for CMB11 and CMB12 respectively and in relict grains of 0.0160 and 0.0320 respectively. In CMB13 and CMB14 the c-axis distributions transition towards a single girdle (Fig. 7.10). The M-indexes for CMB13 are noticeably greater, at 0.0332 (recrystallised) and 0.0588 (relict) while for CMB14 they are in line with those of CMB11 and CMB12 at 0.0239 (recrystallised) and 0.0283 (relict). CMB15 is anomalous, not only in composition, with very high mica content as described in section 7.4.2, but also in the fact that the quartz c-axes for this sample are clustered at the top and bottom of the pole figures for both recrystallised and relict populations, rather than producing a girdle distribution (Fig. 7.10). The quartz c-axis pole figures for the highest strain Kinzigite samples in this transect, CMB16 and CMB17, take the form of single girdle distributions with increased

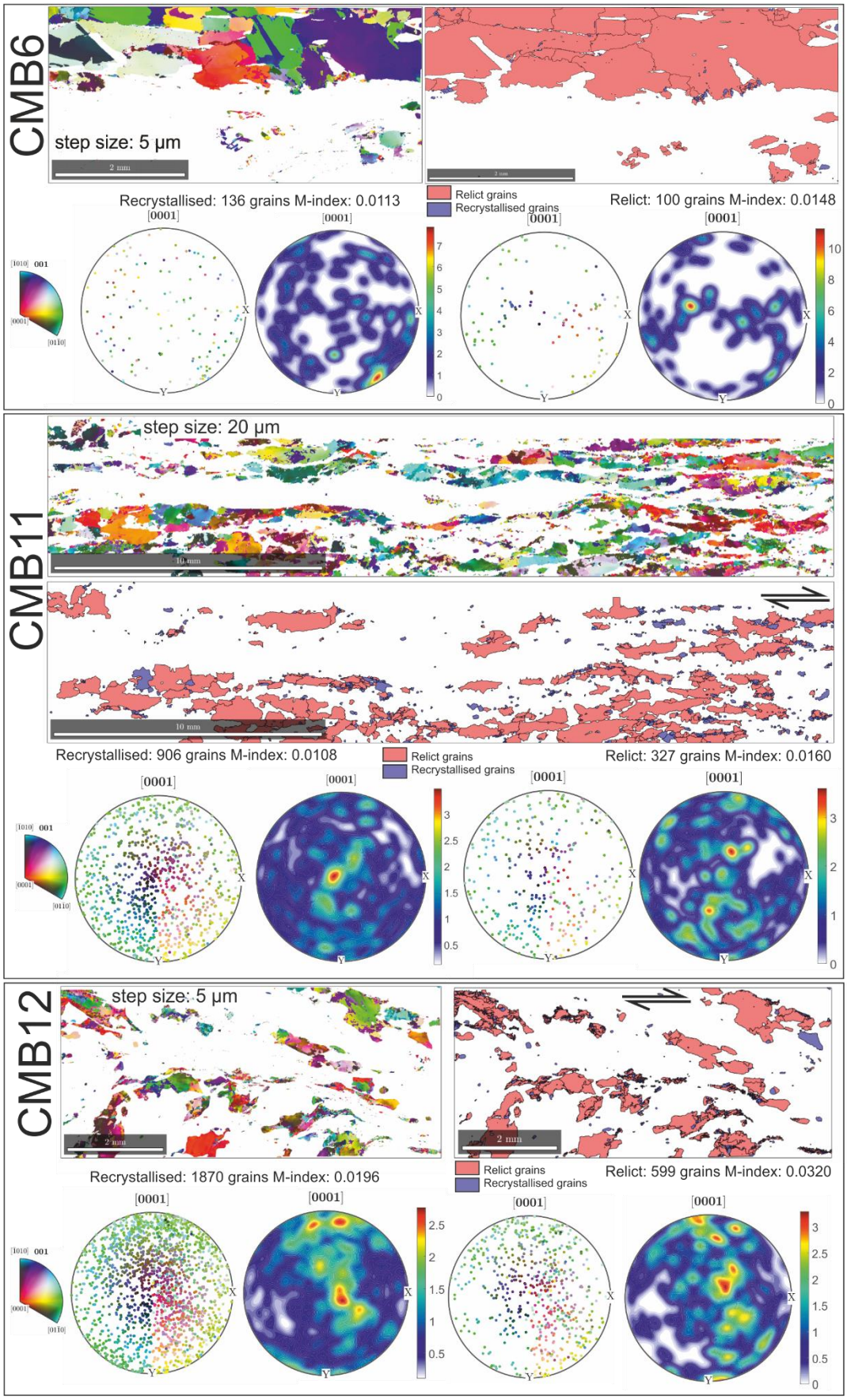


***Fig: 7.10:*** *caption overleaf.*

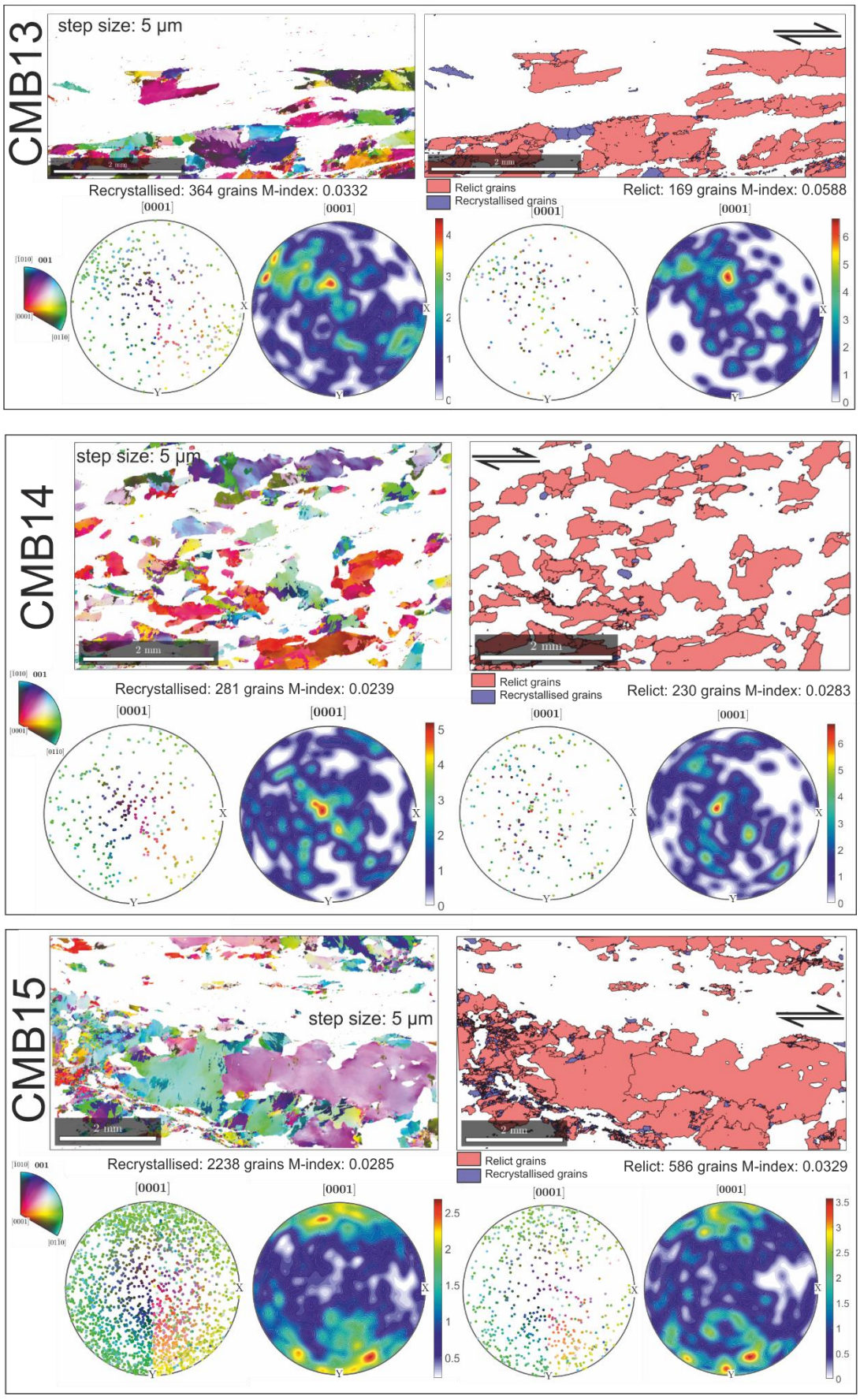


***Fig: 7.10:*** *caption overleaf.*

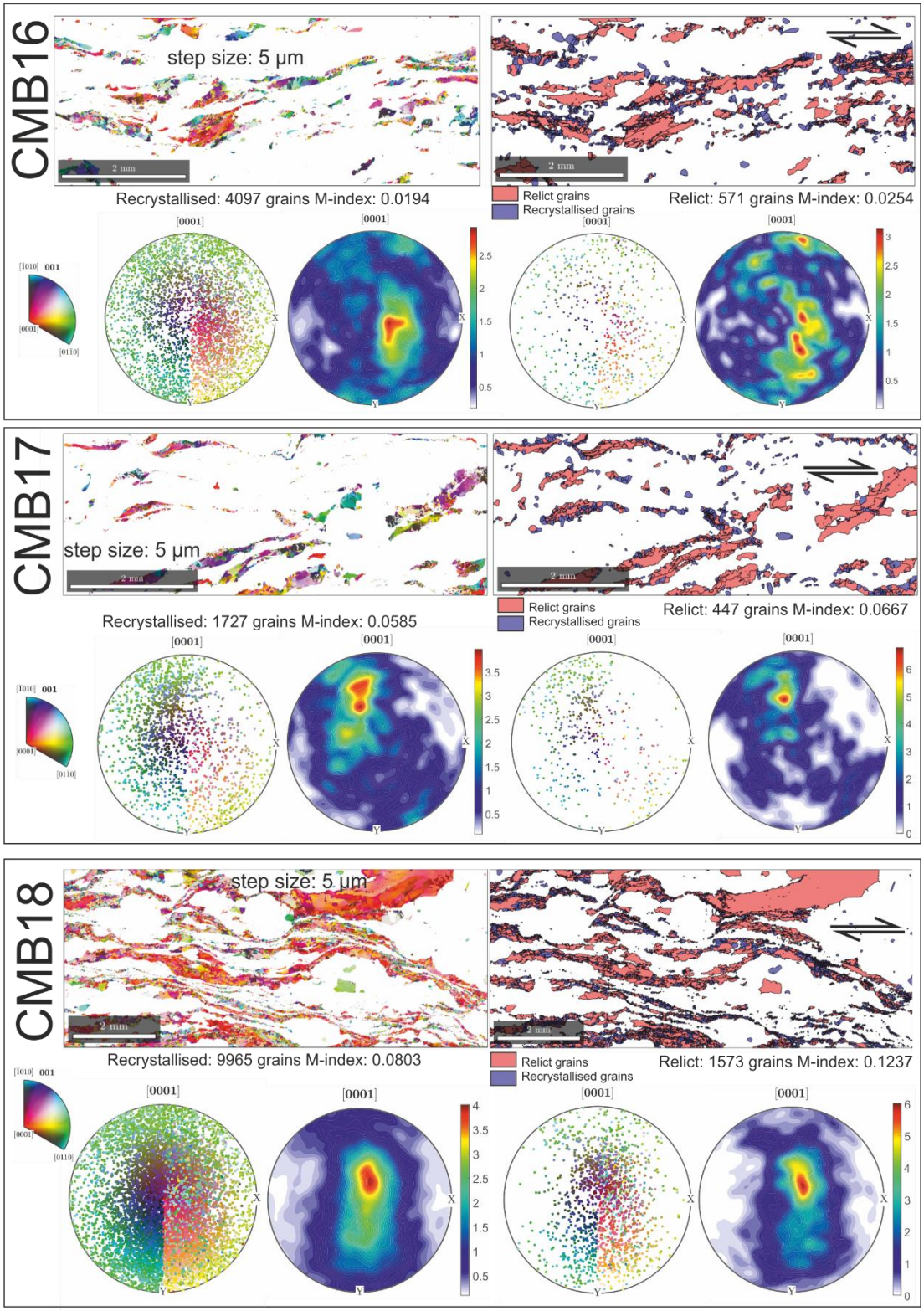


***Figure 7.10:*** *Lower hemisphere, contoured quartz c-axis pole figures and corresponding IPF colour orientation maps for the samples of the CMB line transect near Ornavasso along with calculated M-index values of fabric strength. The second map for each sample displays the recrystallised (blue) and relict (red) grain populations as calculated using the methodology of Cross et al. (2017). The pole figures are plotted separately for recrystallised and relict grains. Plots were made using one data point per grain. Samples are displayed in the order they occur along the transect.*

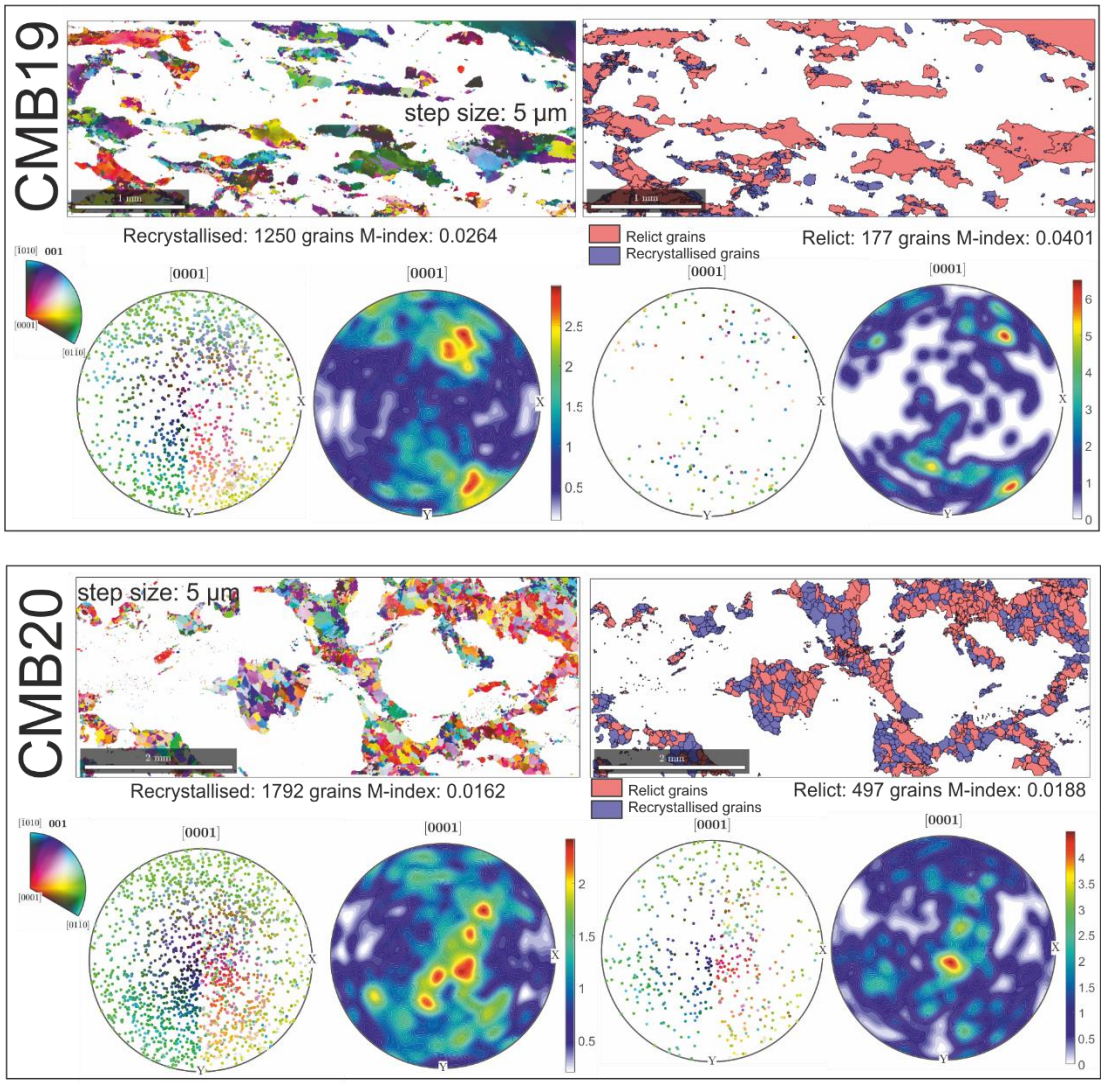


***Fig: 7.10:*** *caption on previous page.*

prominence of a single central maximum. In these samples this trend towards a single maximum and a clear girdle is more pronounced within the recrystallised grain fraction with the relict grain data set more affected by disparate clusters.

On the SdL side of the CMB line, the orthogneiss mylonite CMB18 displays a strong quartz CPO with a single girdle distribution but dominated by a central maximum in both the recrystallised and relict grain sets (Fig. 7.10). This is coupled with very strong M-indexes (relative to the other studied samples) of 0.0803 and 0.1237 for recrystallised and relict grains respectively. With increasing distance from the CMB line, CMB19 displays weak upper and lower maxima in the c-axis pole figures while CMB20 displays weak elements of a crossed-girdle distribution. This reduction in fabric strength is also shown by the low M-indexes of 0.0264 and 0.0162 (recrystallised), and 0.0401 and 0.0188 (relict) for CMB19 and CMB20 respectively. (Fig. 7.10).

### *Biotite fabric: Ornavasso transect*

Biotite pole figures from the same data sets as the quartz pole figures from the CMB line transect at Ornavasso, all display c-axis peripheral maxima at the top and bottom of pole figures and lateral girdles for the a and b axes (Fig. 7.11). This is to be expected due to the strong crystallographic and morphological anisotropy of biotite grains whose c-planes define the foliation (Lloyd *et al.*, 2009; Dempsey *et al.*, 2011). That being said, there is some variation in the strength and distribution of the biotite pole figures. The peripheral maximum is strongest in c-axis pole figures of CMB13 which has the highest content of biotite and is also strong in the other mica- rich samples. The pattern is weakest in CMB12 which is a low strain protomylonite with a relatively low mica content and a large component of plagioclase (Fig. 7.11). The a- and b-axis pole figures display a smearing in the data which is caused by internal continuous distortion where biotite grains bend from an S surface to a C or C' surface. This is also responsible for the broad nature of the upper and lower maxima in the c-axis pole figures. Across the pole figures there is no clear evidence that either the a or b direction is preferentially aligned with lineation (E-W in pole figures).

### *Quartz fabric: Pogallo transect*

Quartz c-axis pole figures for the Pogallo transect present a different evolution to those of the Ornavasso transect. The paragneiss protolith sample, (POG8) displays a weak CPO with a cross girdle distribution, compatible with the microstructural observations (described in section 7.4.4) which indicate little shear strain (Fig. 7.12). In the granitic orthogneiss protomylonite, (POG7) the quartz c-axis CPO develops a weak cross-girdle character in both the recrystallised and relict grains. Microstructurally, the orthogneiss mylonite samples POG5, POG21 and POG23 are similar in that they all record significant dynamic recrystallisation of quartz, in conjunction with the dramatic grain size reduction of the small quantities of biotite they contain. This similarity is reflected in the quartz c-axis pole figures which all display strong central maxima and weak elements of a single girdle. This is true of both the recrystallised and relict grain fractions in all three of these samples and is strongest in POG23 (Fig. 7.12). The recrystallised quartz fabric strength for these mylonite samples is given by M-indexes of 0.0362 (POG5), 0.0187 (POG21) and 0.0438 (POG23) and the relict quartz fabric strength is shown by M-indexes of 0.0876 (POG5), 0.0512 (POG21) and 0.0953 (POG23). Interestingly, the two mica-rich samples which also come from the high strain central part of the transect, POG1 and POG22, possess distributions that are closer to single girdles than central maxima. Two large area maps were taken from the high strain ultramylonite sample POG3, from quartz-rich and quartz-poor parts of the matrix. Both

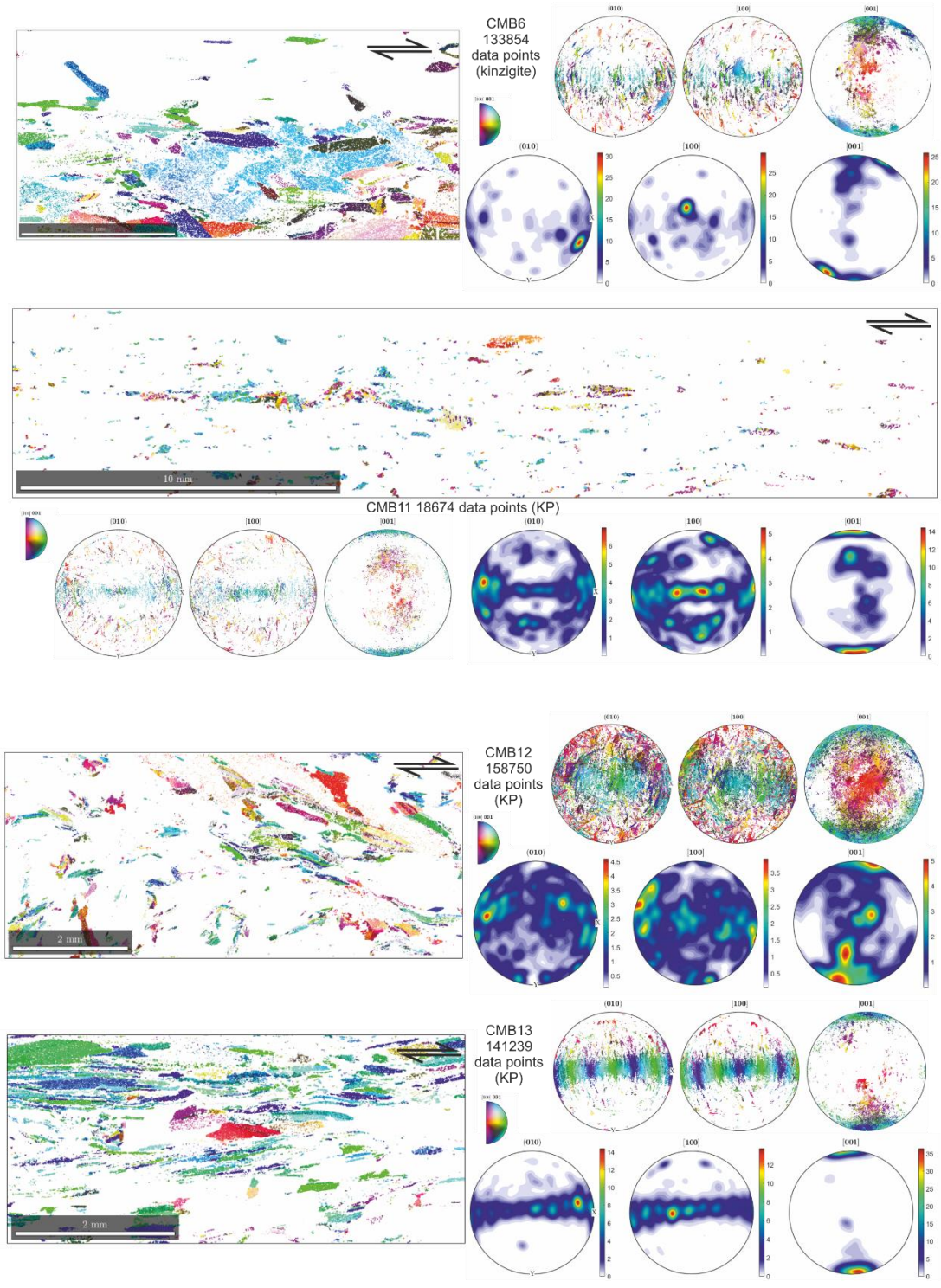


***Fig: 7.11:*** *caption overleaf.*

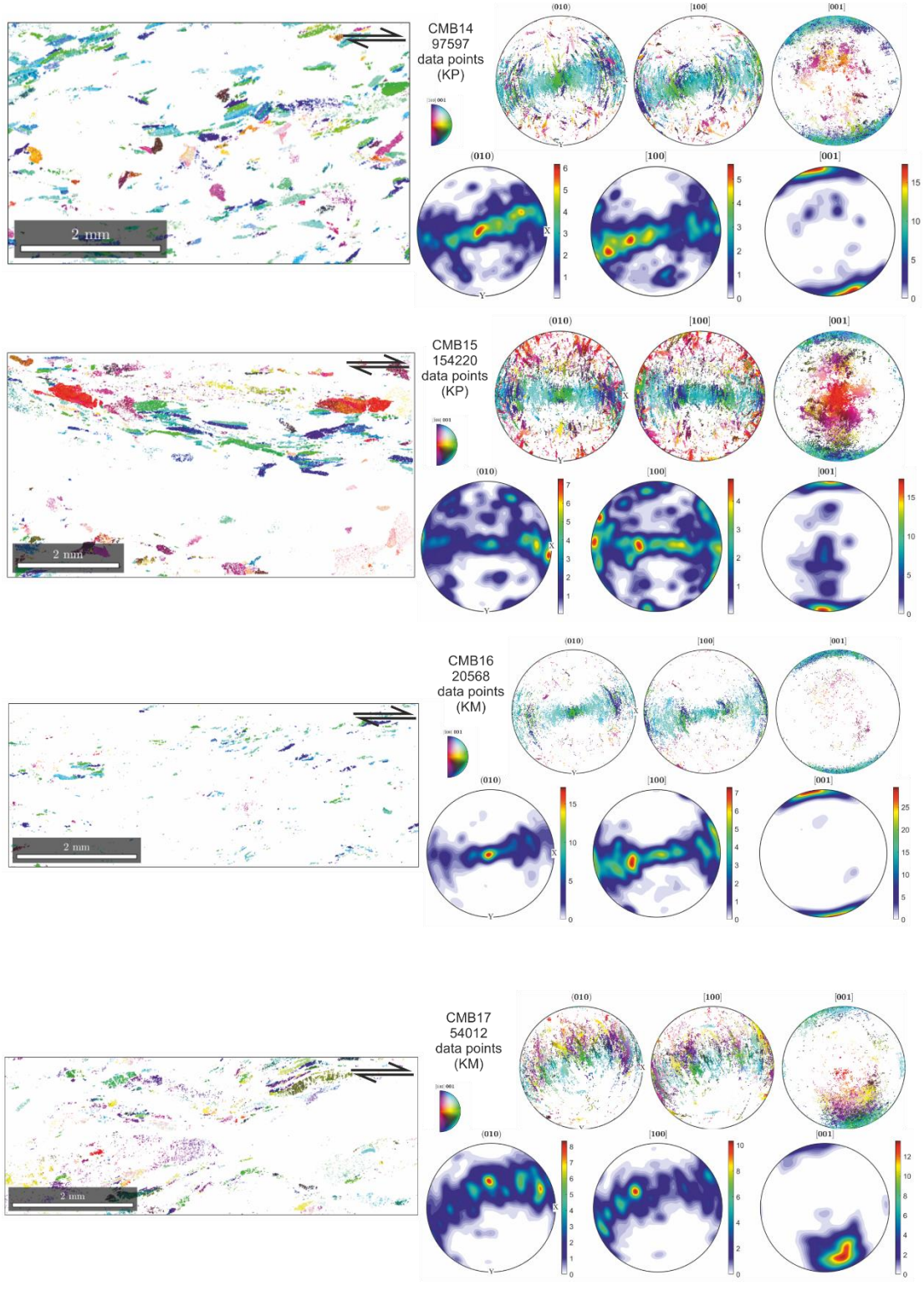


***Fig: 7.11:*** *caption overleaf.*

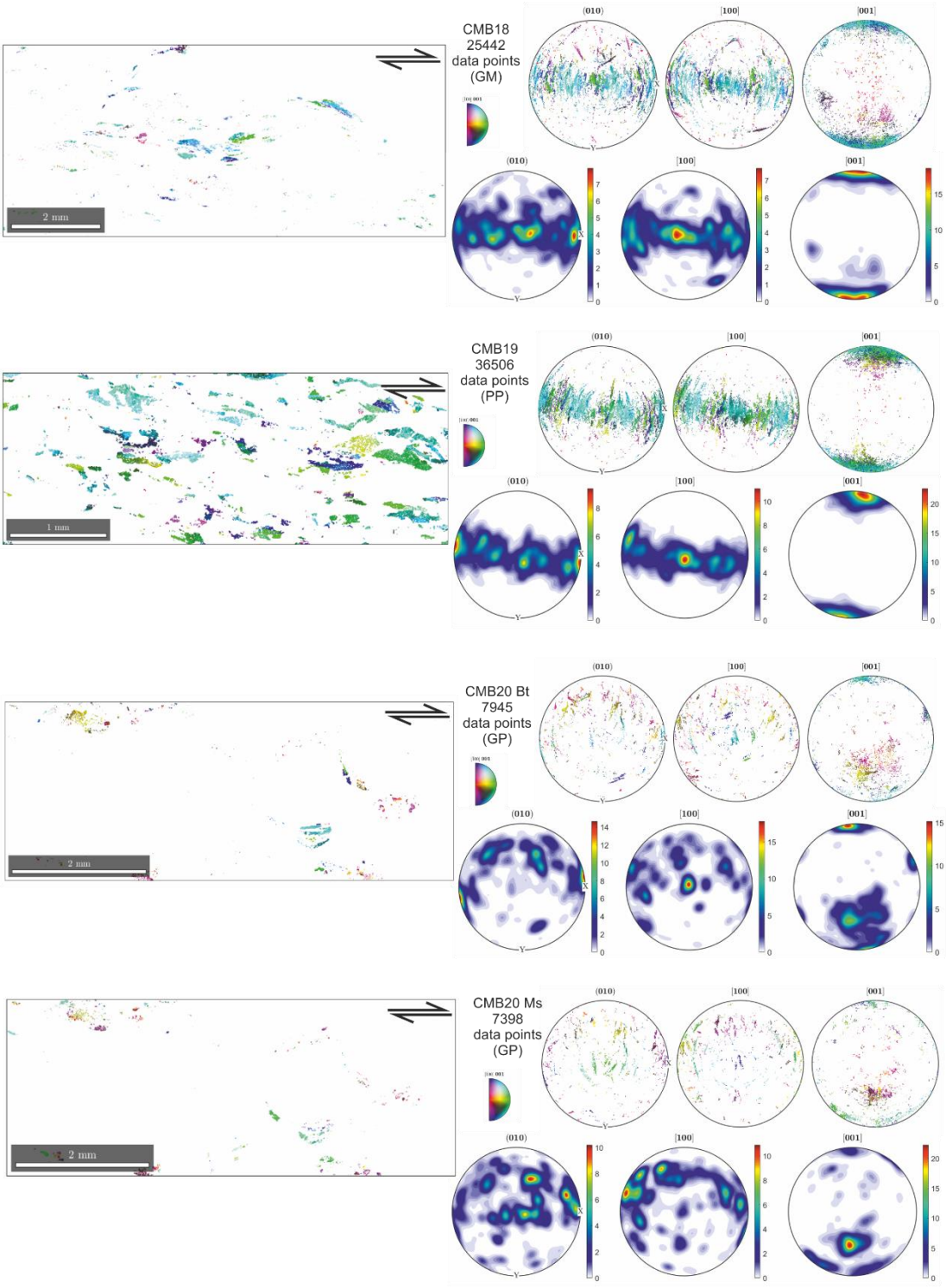


***Figure 7.11:*** *Lower hemisphere pole figures of biotite for each of the samples from the Ornavasso transect along with biotite IPF colour orientation maps of the areas used to collect the data (which are the same as those used for the quartz data displayed in Fig. 7.10). Initials indicate the lithology: KP – Kinzigite protomylonite; KM – Kinzigite mylonite; GM – granitic orthogneiss mylonite; PP – paragneiss protomylonite; GP – granitic orthogneiss protomylonite. All measured data points are shown. Samples are displayed in the order they occur along the transect.*

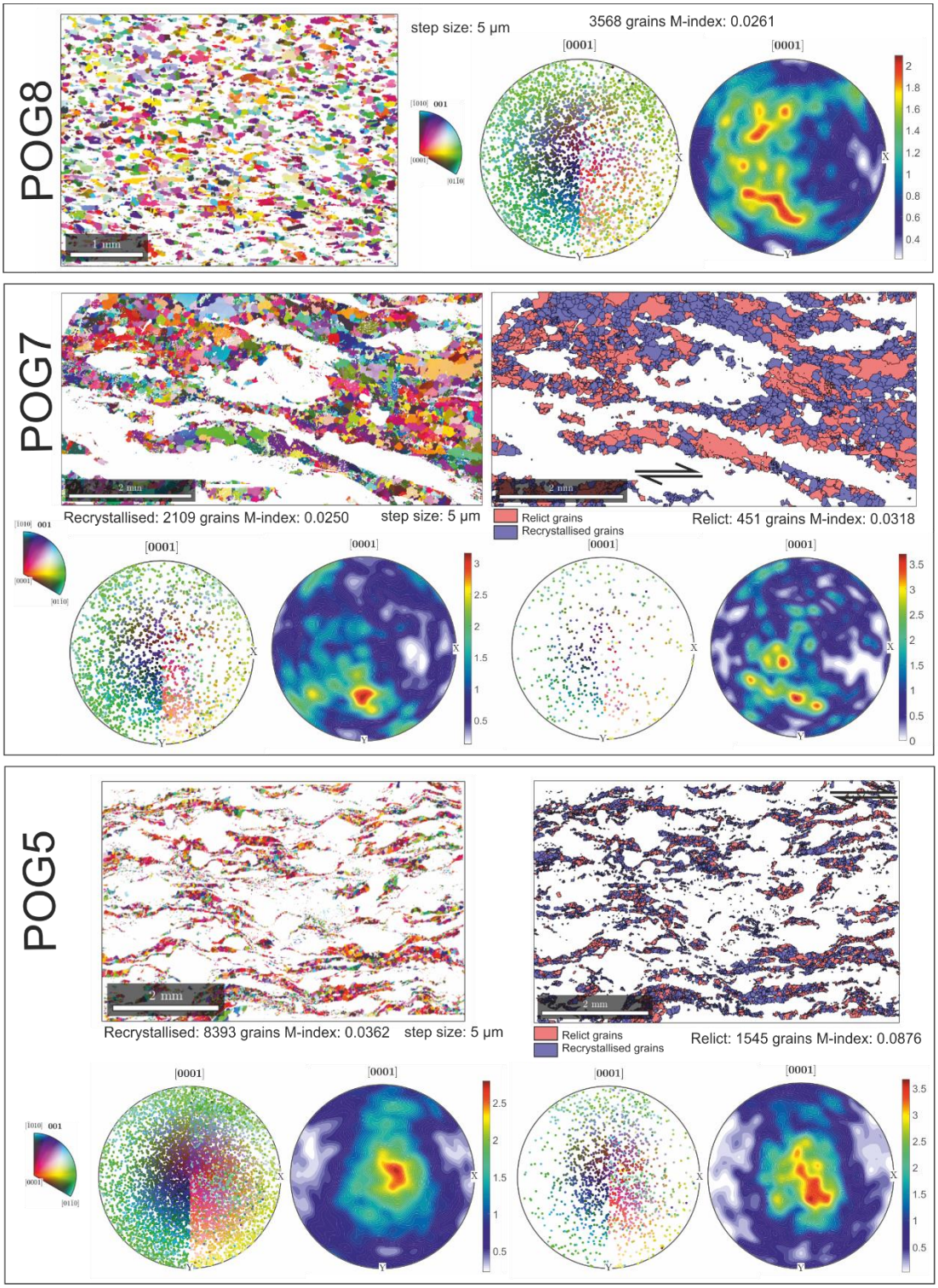


***Figure 7.12:*** *Lower hemisphere, contoured quartz c-axis pole figures and corresponding IPFcolour maps for the samples of the Pogallo line transect, along with calculated M-index values of fabric strength. The second map for each sample displays the recrystallised (blue) and relict (red) grain populations as calculated using the methodology of Cross et al. (2017). The pole figures are plotted separately for recrystallised and relict grains. Plots were made using one data point per grain. Two areas were used in the POG3 ultramylonite matrix, one which was Quartz rich and one which was quartz poor. Samples are displayed in the order they occur along the transect.*

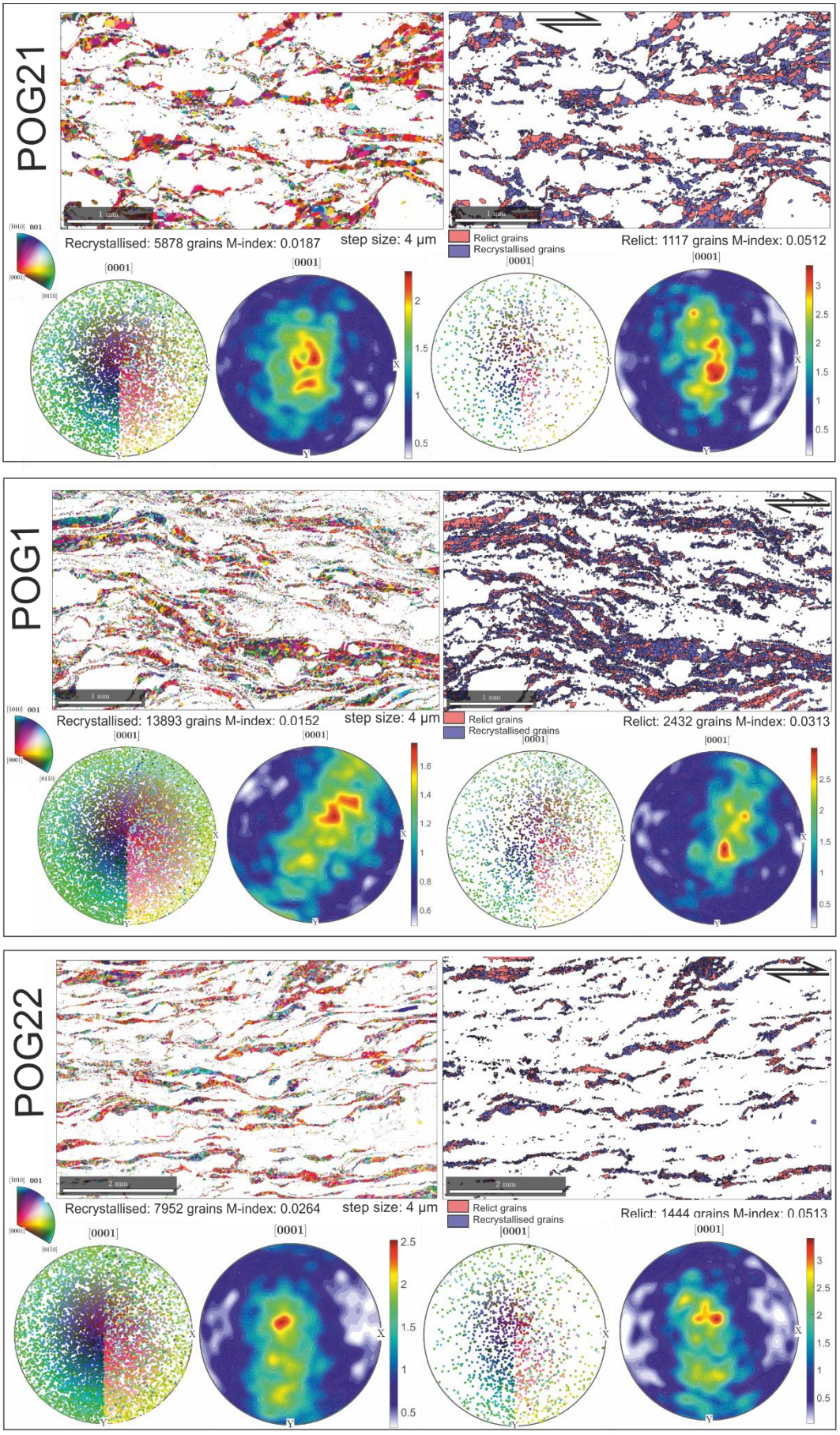


***Fig: 7.12:*** *caption on previous page.*

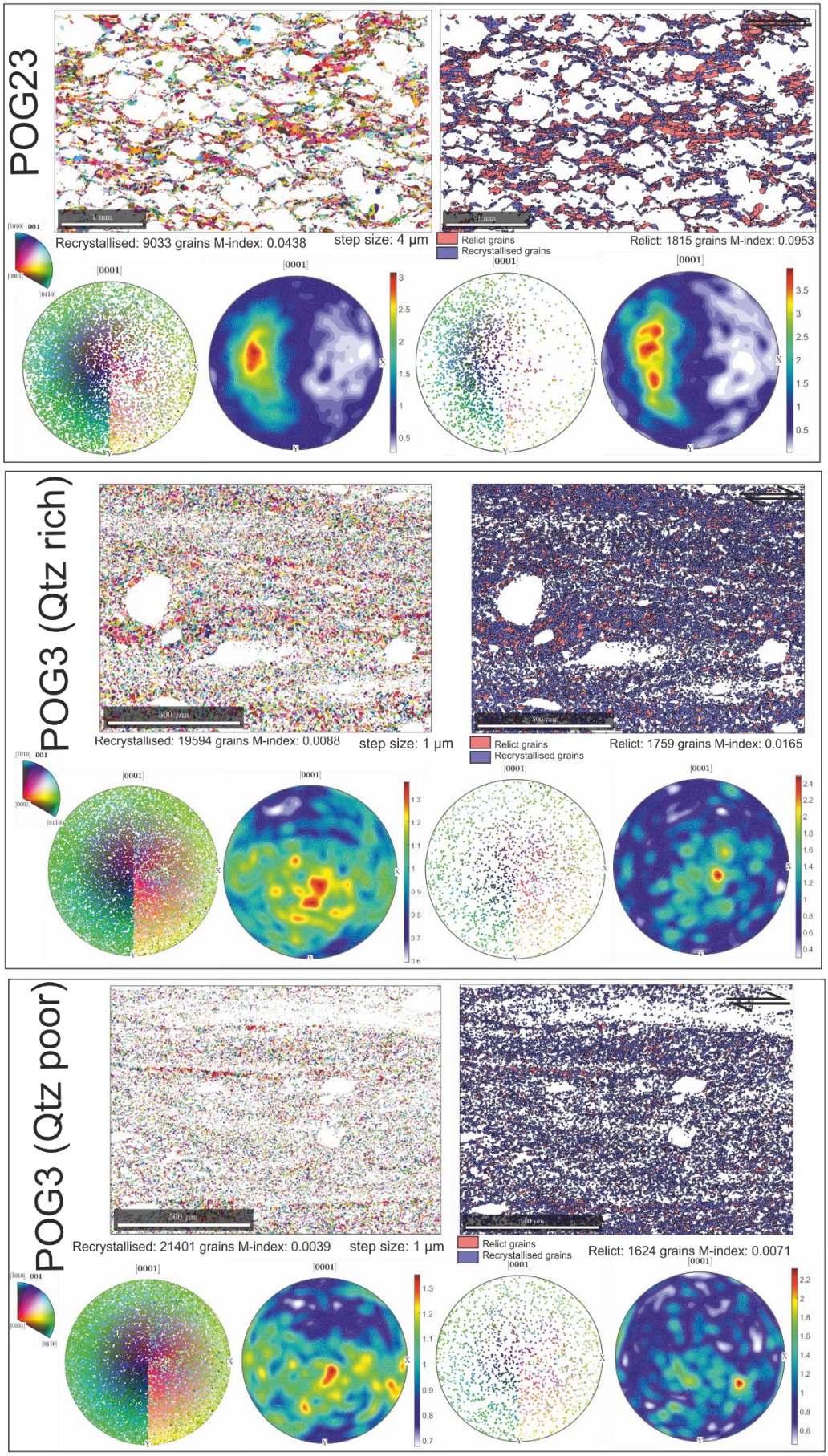


***Fig: 7.12:*** *caption on previous page.*

display weak CPO strengths (recrystallised M-indexes of 0.0088 and 0.0039 respectively, relict M-indexes of 0.0165 and 0.0071 respectively) and a scattered distribution of quartz c-axes (Fig. 7.12). This weakening of quartz CPO strength in the ultramylonites was reported in Chapter 6 of this thesis and given as evidence of a shift in the principal deformation mechanism of quartz from dislocation creep in lower strain mylonites to fluid assisted grain size sensitive creep within the matrix of this high strain ultramylonite.

### *Biotite fabric: Pogallo transect*

Biotite pole figures for the same EBSD maps of the Pogallo line samples, which are predominantly orthogneiss mylonites, display some important differences to those produced from the Ornavasso transect, which are mostly from samples of Kinzigite. The dominant feature of the c-axis distributions, like in the Ornavasso samples, is a peripheral maximum at the top and bottom of the pole figures, produced by biotite basal planes aligned with the foliation (Fig. 7.13). In the Pogallo transect, this distribution is strongest in the undeformed paragneiss sample POG8 however it is also very dominant in the protomylonite POG7 and the mica-rich mylonite sample POG22 (Fig. 7.13). The peripheral maximum and the CPO, while present in all samples, becomes much weaker in samples where biotite has undergone a degree of significant grain size reduction, with both remnant coarse grains and very fine new grains present. This weakening of the CPO is most apparent in the mylonite samples POG5, POG21 and POG23 but also occurs to a much lesser extent in the mica-rich sample POG1, which has a weaker CPO and wider c-axis distribution than the other mica-rich sample POG22, but also displays a greater degree of biotite grain size reduction in its microstructure (Fig. 7.13). The CPO and peripheral maxima strengthen slightly again in the high strain ultramylonite POG3, in which the grain size reduction process has run to completion and no coarse, older biotite grains remain. That being said, the limitations associated with successfully indexing micas, and fine-grained micas in particular, when using EBSD means that this is a tentative interpretation as the data could be significantly affected by misindexing.

### *M-index variation across the transects*

The values of the M-index (Skemer *et al.*, 2005) calculated from the quartz orientation data displayed in Figures 7.10 and 7.12 shows variation in the strength of the recrystallised and relict quartz fabrics across the two transects studied (Fig. 7.14). In the Ornavasso transect the highest values fall either side of the CMB line trace with quartz dominated CMB18 showing the highest values, with a gradual reduction towards the IVZ side and a sharper reduction into the SdL. The transect in Val Pogallo is more complicated with generally lower values and

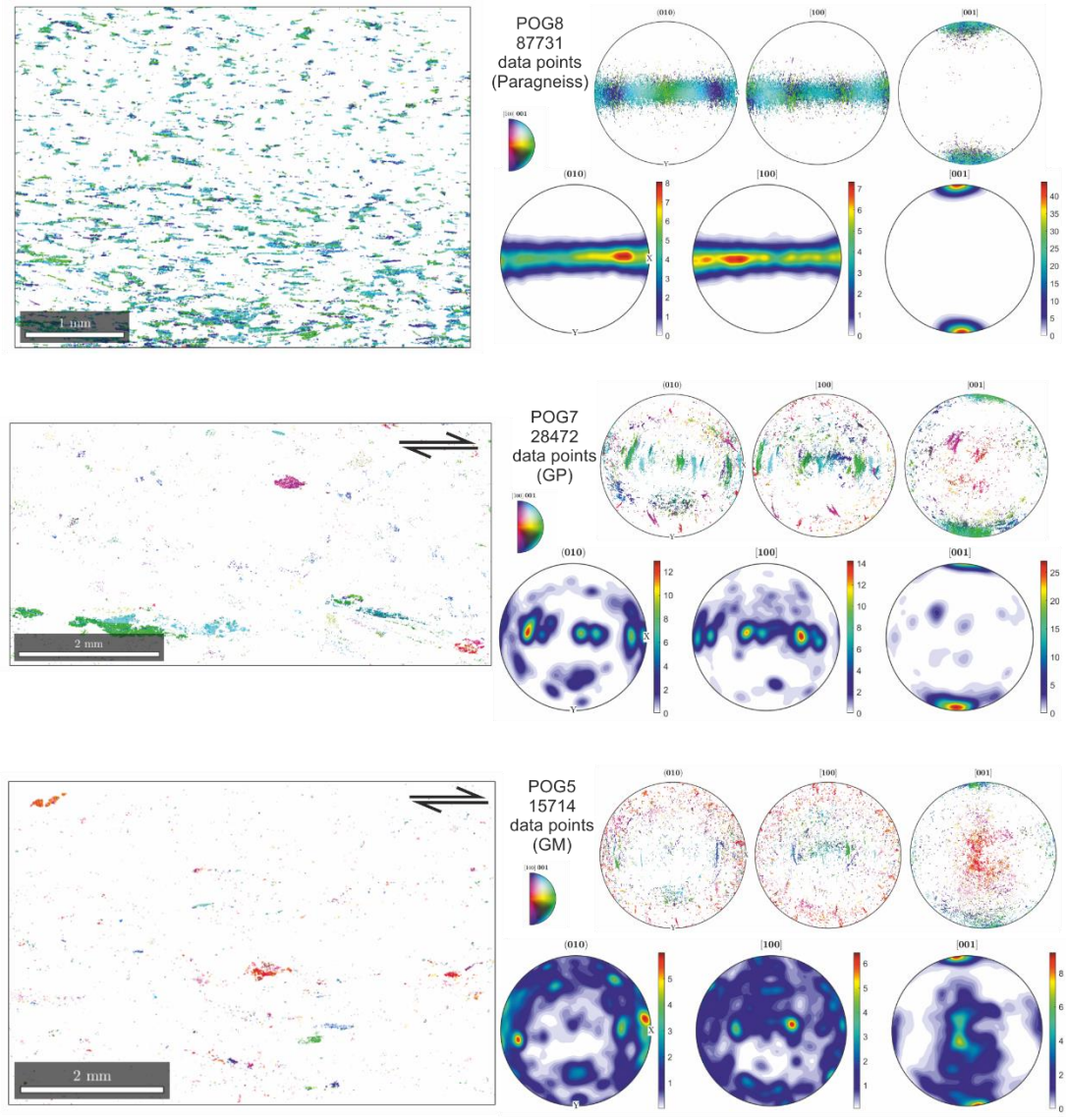


***Fig: 7.13:*** *caption overleaf.*

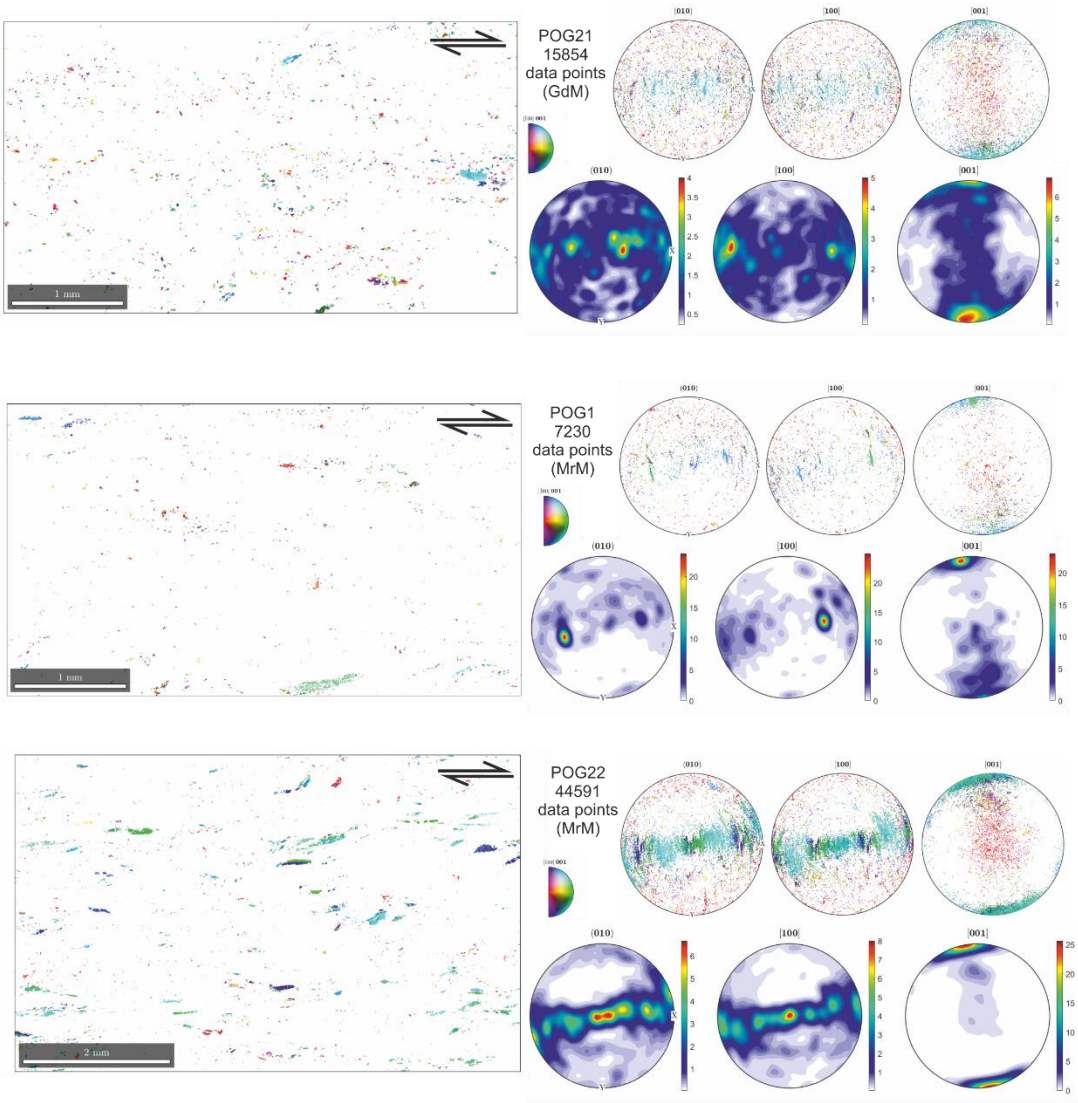


***Fig: 7.13:*** *caption overleaf.*

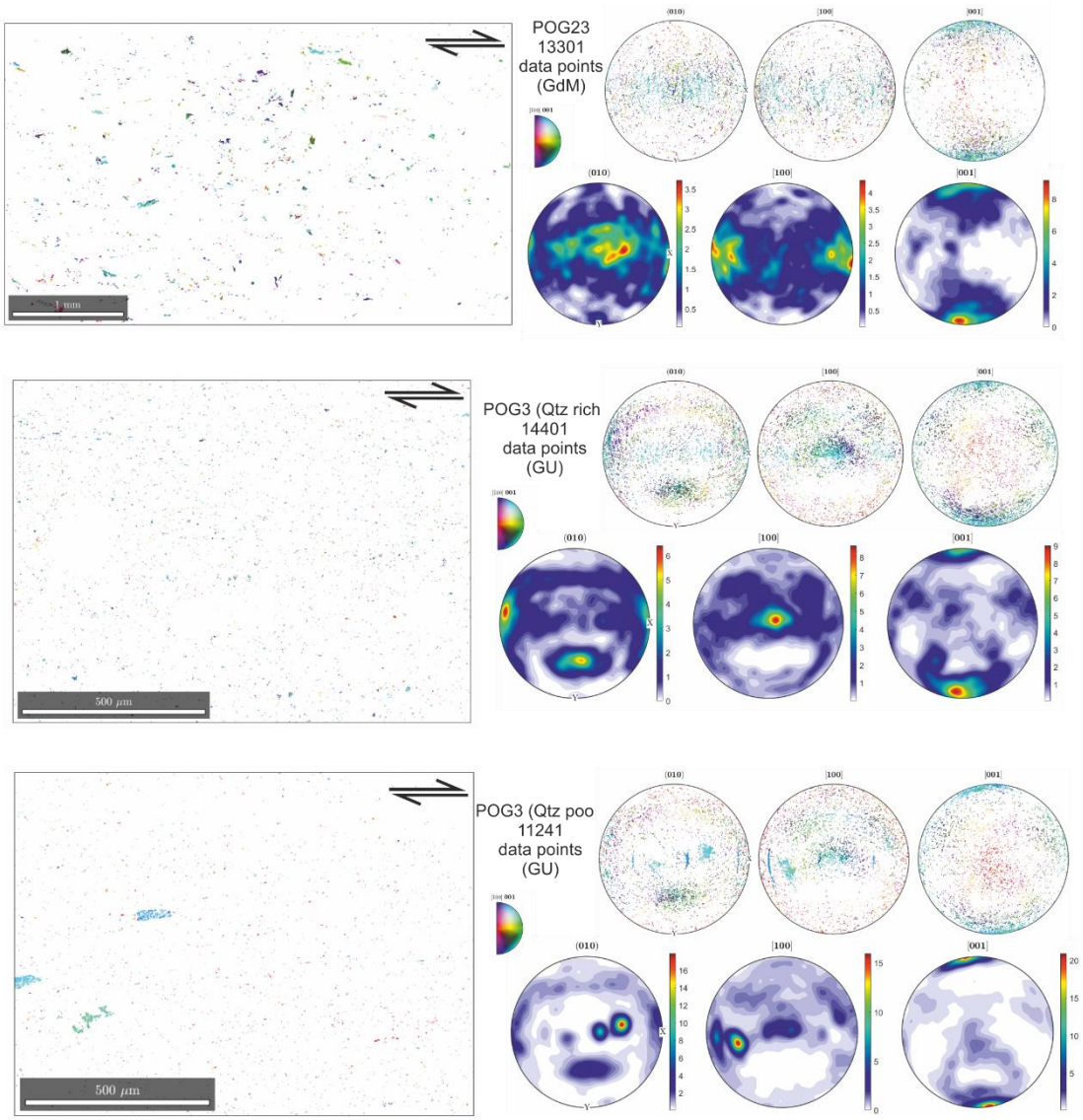


***Figure 7.13:*** *Lower hemisphere pole figures of biotite for each of the samples from Val Pogallo transect along with biotite IPF colour orientation maps of the areas used to collect the data (which are the same as those used for the quartz data displayed in Fig. 7.12). Initials indicate the lithology: GP – granite orthogneiss protomylonite; GM – granitic orthogneiss mylonite; GdM – granodiorite orthogneiss mylonite; MrM – Mica-rich mylonite; GU – granite orthogneiss ultramylonite. All measured data points are shown. Samples are displayed in the order they occur along the transect.*

two peaks in fabric strength in POG5 and POG23 both of which are high strain mylonites but not ultramylonites like POG3. The ultramylonites (POG3) and mica rich samples (POG1 and POG22) have very low M-indexes. In both transects, the recrystallised and relict grain fabric strengths follow the same trends, with consistently higher values and more pronounced changes recorded in the relict grains and a less pronounced reflection of this within the recrystallised grains (Fig. 7.14).

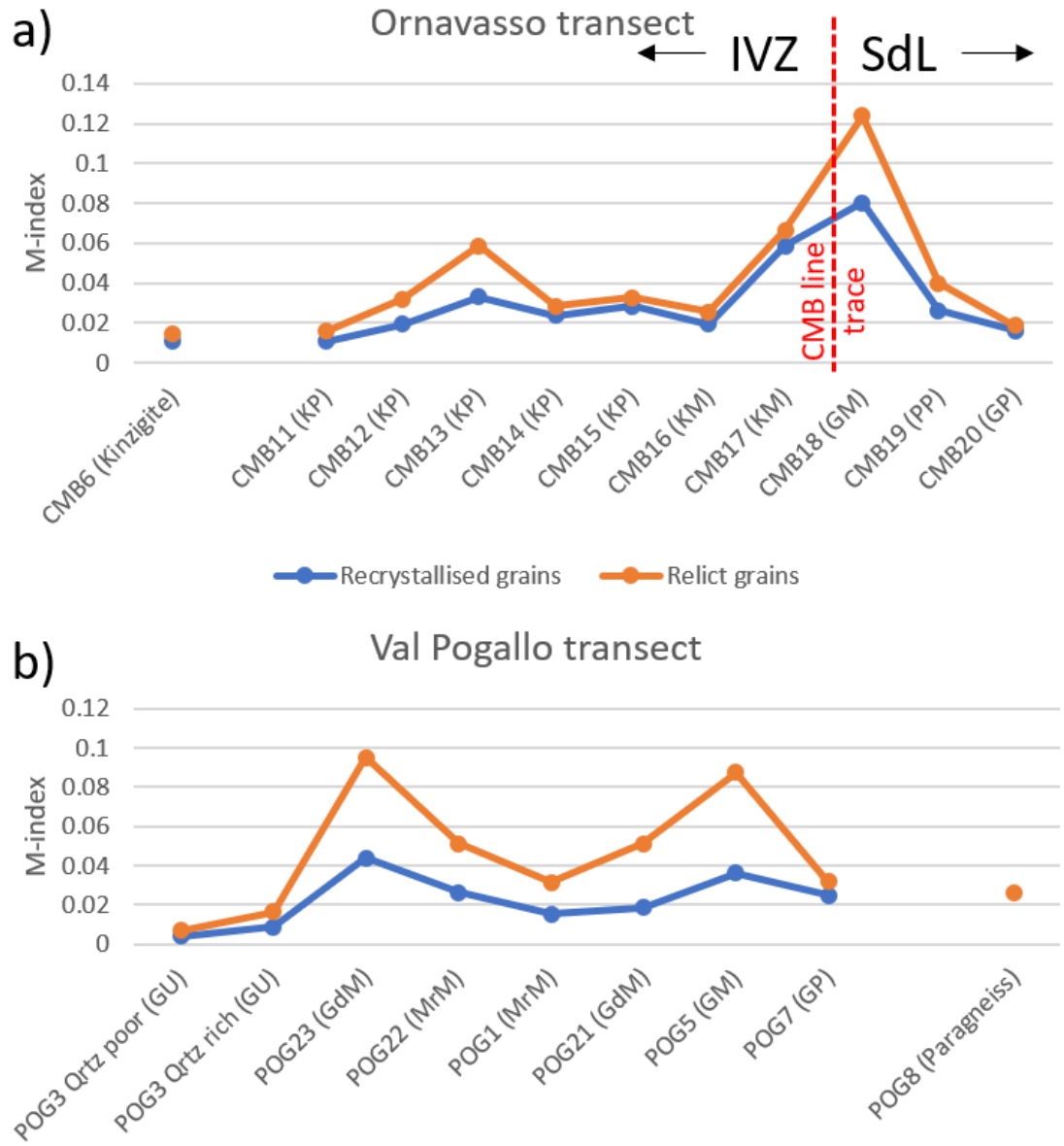


***Figure 7.14:*** *M-index values of quartz orientation data from each transect. CMB6 and POG8 are protolith samples collected away from the shear zones, so are shown separate from the other values.*

## 7.5. Discussion

### 7.5.1. Interpretations of optical microstructure and EBSD analyses

According to previous studies of quartz c-axis distributions resulting from deformation by dislocation creep, active quartz slip systems transition, with increasing strain and/or temperature of deformation, from dominantly basal <a> slip, through rhomb <a> slip and prism <a> slip, to <c> slip (Stipp *et al.*, 2002; Passchier and Trouw, 2005; Heilbronner and Tullis, 2006). This manifests (in c-axis pole figures plotted in the kinematic plane) as a transition from a peripheral maximum at the upper and lower edges of the pole figure, through a cross girdle and single girdle distribution towards a single central maximum and ultimately, when <c> slip dominates, a peripheral maximum at a low angle to the lineation direction (Stipp *et al.*, 2002; Passchier and Trouw, 2005; Heilbronner and Tullis, 2006). However, these studies were conducted in monomineralic quartz systems and the applicability of these transitions – and the resulting evolution of maxima within c-axis pole figures – within polymineralic rocks is complex. This is due principally to the fact that strain is partitioned differently when second or third phases are present relative to monomineralic systems, even where monomineralic domains exist (as in the samples analysed in this study) (Menegon, Pennacchioni, Heilbronner, *et al.*, 2008; Kilian *et al.*, 2011). In addition, the protoliths of the mylonites used in this study are all metamorphic rocks which may have possessed initial CPOs within the quartz phase and cannot be assumed to have had random (granitic) fabrics at the initiation of deformation within the CMB line and Pogallo line systems. The c-axis distributions and quartz fabric strengths reported and analysed in this study are therefore used as an indication of the degree of strain accommodated within the quartz phase of each sample. They are compared relative to each other to give an idea of how strain may be partitioned between different phases at different points within the shear zone and within the various lithologies analysed. They are not used to give definitive evidence of the slip systems active within quartz in each sample, to infer the deformation conditions or to quantify the absolute strain accommodated.

#### *Ornavasso transect*

The quartz c-axis distributions in pole figures of the protomylonites CMB11 and CMB12, are characterised by weak cross girdles and low fabric strengths (Fig. 7.10). The transition towards a single girdle, in samples CMB13 and CMB14 may represent an increasing degree of strain accommodated with the quartz phase. The anomalous quartz c-axis distribution in

CMB15, with maxima at the upper and lower peripheries of the pole figure may indicate that strain in this sample is accommodated more substantially within the wide mica bands, reducing the amount of strain accommodated by the stronger quartz phase. The highest strain Kinzigite samples (CMB16 and CMB17) display single girdles and central maxima. This is indicative of higher strain in the quartz phase than the other Kinzigite samples and is evident within both the recrystallised and relict grain fractions. On the SE side of the CMB line the quartz c-axis fabric of CMB20 and CMB19 display weak fabric strengths suggesting relatively low strain. This contrasts with the c-axis distribution of CMB18 which is characterised by a strong central maximum and the strongest fabric strength within the transect. This indicates a much higher degree of strain in agreement with the field and microstructural observations across these samples (described in sections 7.4.1 and 7.4.3), particularly the fact that CMB18 displays the most advanced dynamic recrystallisation of quartz of any sample in this transect.

Overall, the quartz c-axis distribution across the CMB line at the Ornavasso transect (with the exception of CMB15) evolves from a cross girdle in the most distal sheared samples, through a single girdle and towards a central maximum in the samples immediately adjacent to the CMB line itself. However, CMB17 and CMB16 give distinctly lower quartz M-indexes than CMB18 despite being in similarly close proximity to the CMB line itself. A possible explanation for this could be that CMB16 and CMB17 have well developed mica dominated S-C and C' mylonitic fabrics, with different quartz domains separated by micaceous foliation and slip surfaces. This could reduce the fabric strength within the quartz phase as strain is localised away from the quartz and into the weaker layers and shear bands (Wintsch *et al.*, 1995; Holyoke and Tullis, 2006b; Menegon, Pennacchioni, Heilbronner, *et al.*, 2008; Fagereng *et al.*, 2014; Hunter *et al.*, 2016). The general pattern within quartz c-axis fabrics in the samples analysed in this study suggests a lower degree of strain is accommodated by quartz in samples with higher mica content. This concurs with the findings of Hunter *et al.*, (2016) and supports the hypothesis that higher mica content reduces the amount of strain accommodated within the stronger phases.

Within the Kinzigites of the CMB line transect near Ornavasso, there is a disparity in microstructure between those samples with higher mica content and those with significant plagioclase components. In Kinzigites which contain an abundance of strong, rigid plagioclase (CMB12: Supp. Fig. S7.3, CMB14: Supp. Fig. S7.5), biotite appears to have formed discrete shear bands, which localise higher degrees of strain, while the more rigid framework accommodates less strain. By contrast, in the mica-rich and plagioclase poor samples

(CMB11: Supp. Fig. S7.2, CMB13: Supp. Fig. S7.4), strain is more distributed due to fewer rigid feldspar grains and well aligned, through-going bands of mica. In these mica-rich samples, the majority of strain is accommodated through intracrystalline deformation of micas within this network. Basal dislocation glide may account for some of this intracrystalline deformation where mica grains are favourably aligned. a- and b-axis pole figures of biotite (Figs. 7.11 and 7.13) suggest this is likely to take place within the (001) [110] and (001) $[\bar{1}10]$ slip systems as neither the a- or b- axis is clearly and regularly aligned with lineation. The presence of kinked and bent mica grains (e.g. Figs. 7.8 and 7.9) however, suggests ripplocations also play an important role. As discussed in Chapter 5 of this thesis (Aslin *et al.*, 2019), the motion of ripplocations is a newly identified deformation mechanism that is best able to describe the formation of kink bands and facilitates intracrystalline strain parallel to the c-axis in phyllosilicates. A combination of basal dislocation glide and ripplocation motion is therefore proposed to account for the intracrystalline deformation within micas.

The difference in microstructure between Kinzigites of different composition is also apparent in the higher strain examples of Kinzigite collected close to the CMB line trace, through-going C' shear bands are more prevalent in CMB16 (higher plagioclase content) than in CMB17 (higher mica content). In both samples the microstructure is dominated by a widespread interconnected mica network within which strain is accommodated, however, in CMB16 this network has developed through the formation of numerous C' shear bands and the localisation of strain along these features, whereas strain is more evenly distributed throughout sample CMB17. The high mica content of CMB17 means that biotite and muscovite together compose a fully interconnected network, without requiring the development of regular pervasive C' shear bands to increase mica connectivity. This means that higher mica content results in a more homogeneous distribution of strain, while localisation of strain into C' shear bands is more prominent in lithologies with a greater proportion of strong phases. In contrast, the quartz and feldspar rich and mica poor SdL derived mylonites on the south eastern side of the CMB line at Ornavasso are characterised by abundant evidence of dislocation creep in quartz and a smaller dependence on intracrystalline deformation within micas relative to the Kinzigite mylonites of the IVZ. Overall, strain is distributed more heterogeneously in this set of samples both on the shear zone scale, with a strong distinction in the degree of strain across the three samples (CMB20, CMB19 and CMB18), and on the microstructural scale as evidenced by the development of high strain C' shear bands in CMB18.

### *Pogallo transect*

In the Pogallo line mylonites, an abundance of fine-grained, dynamically recrystallised quartz and generally strong quartz c-axis CPOs suggest that quartz has accommodated a large amount of strain. Quartz-rich orthogneiss mylonites (POG5, POG21 and POG23) display central maxima indicative of high strains and most likely facilitated by dislocation creep. This is not true of the two high strain mica-rich samples (POG1 and POG22). Pole figures of quartz c-axes from both POG1 and POG22 display single girdles indicative of moderate strain and the associated fabric strengths are lower. It is proposed that dislocation creep of quartz plays less of a role in the accommodation of strain in these samples relative to the orthogneiss samples, with a greater proportion accommodated by mica (as in the Kinzigite samples at the Ornavasso transect). As described in Chapter 6 of this thesis, the distinct drop in quartz c-axis fabric strength in the highest strain sample (POG3) is interpreted to represent a change in dominant deformation mechanism in the quartz phase from dislocation creep to grain size sensitive creep and viscous grain boundary sliding. This is inferred to result in this fine-grained polyphase matrix being weaker than the former framework and serving to localise strain.

### *Biotite fabrics*

The biotite fabrics in samples from both transects display strong c-axis maxima at the upper and lower peripheries of the pole figures, as is to be expected in highly foliated mica bearing rocks (Wenk *et al.*, 2008; Lloyd *et al.*, 2009; Dempsey *et al.*, 2011), with some spread of these maxima associated with the variation in orientation between biotites in S and C planes (Lloyd *et al.*, 2009). In addition to this first order distribution, the biotite fabrics from samples of the Pogallo line transect display an interesting correlation between the strength of biotite c-axis peripheral maxima and the extent of biotite grain size reduction (Fig. 7.13). Where larger proportions of biotite exist as fine grains, such as in moderate strain orthogneiss mylonites with low mica content (POG5, POG21 and POG23), the fabric strength is lower, and the biotite c-axes are more distributed away from the upper and lower peripheries of the pole figures. The peripheral maxima are stronger in biotite-rich samples (POG1 and POG22). Interestingly the peripheral maxima are also greater in the very high strain ultramylonites (POG3) where the grain size reduction process is complete, and biotite is only present as very fine grains. Optical observation of POG3 reveals uniform biotite pleochroism across the matrix (Chapter 6, Fig. 6.5), also suggesting a strong CPO of (001) (see also Fig. 7.13). Such a CPO can result in micas from deformation by grain rotation and grain boundary sliding in which elongate grains rotate towards, and then remain oriented parallel to, foliation because

this is the most energetically favourable orientation (Wheeler, 2009; Kilian *et al.*, 2011). This produces a CPO as, in phyllosilicates, the shape of grains is highly influenced by their crystallography. This variation in the distribution of biotite orientations and strengths of biotite CPOs within the mylonites of the Pogallo line transect therefore highlights a key feature of the biotite grain size reduction process; when coarse grains deform by basal slip along S and C foliations they define a very strong CPO, however, as fine new grains nucleate and precipitate in variable orientations, the CPO is weakened. Once all biotite occurs as very fine grains within a more microstructurally mature ultramylonitic matrix, grain boundary sliding and grain rotation serves to strengthen a shape preferred orientation and, by relation, a CPO.

### 7.5.2. Differences in strain distribution and microstructural evolution between mica-rich and mica-bearing mylonites.

From the microstructural evidence presented in the above section it is apparent that the mica content of the rocks studied has a strong influence on the distribution of strain, both spatially and between phases.

#### *Mica-rich Kinzigites*

In the mica-rich Kinzigites the presence of a pre-existing, extensive framework of mica means that strain is predominantly accommodated by basal slip and ripplocation motion within the weak mica phases throughout the evolution of the mylonite. The degree of interconnection of different mica layers increases with increasing strain through the development of pervasive mylonitic fabrics. Quartz also accommodates a degree of strain in these rocks, with undulose extinction across large ribbon grains as well as dynamic recrystallisation indicating dislocation creep within the quartz bands. Plagioclase feldspar grains however act as rigid bodies deforming predominantly by brittle processes. Plagioclase-rich and (relatively) mica-poor sections of Kinzigite, develop narrow C’ shear bands more readily and at lower strain than samples with high mica content (Supp. Figs. S7.3, S7.5, S7.7). This provides a mechanism by which mica-rich bands interconnect across plagioclase-rich domains, facilitating the accommodation of strain within the weakest phase. The effect of this is to increase the degree of strain localisation within the microstructure and produce a more heterogeneous distribution of strain across the mylonite as a whole (Wintsch *et al.*, 1995). By contrast, strain in the mica-rich samples is distributed more evenly throughout the well-connected mica network, without the need for abundant high strain C’ shear bands.

The presence of C' shear bands in the plagioclase-rich samples also highlights the importance of brittle deformation alongside the dominant viscous processes in these rocks (Viegas *et al.*, 2015). The development and evolution of shear bands in C' fabrics has been hypothesised to involve 3 key stages (Bukovska *et al.*, 2016). Initiation occurs in stage 1 through the formation of micro-cracks, in the case of our samples this would be represented by localised fracture of feldspar grains. Slip along these micro-cracks leads to subgrain rotation recrystallisation in quartz and the widening of the shear band during stage 2. Stage 3 takes hold through the interconnection of weak phases such as micas with strain becoming localised into intracrystalline deformation within mica (Bukovska *et al.*, 2016).

### *Mica-bearing orthogneiss*

A heterogeneous distribution of strain is observed to a greater extent when the quartzofeldspathic rocks of the SdL are compared to the Kinzigites. The granitic orthogneiss mylonites have mica contents of <10% but display some very high strain microstructures (CMB18, POG3, POG5). The small amount of biotite in these samples is involved in the development of weak, fine-grained shear bands into which strain is localised (See Chapter 6 of this thesis). Further evolution towards a microstructural steady state eventually leads to the formation of ultramylonite bands alongside lower strain rocks producing a shear zone of anastomosing high strain bands and low strain lozenges (Rennie *et al.*, 2013). This heterogeneous distribution of strain in mica bearing, but not dominated, lithologies is true at scales ranging from the thin section to the outcrop and is clearest in the transect at Val Pogallo (Figs. 7.5 and 7.6). A contrasting picture of structural evolution and strain distribution is observed on either side of the CMB and Pogallo lines, with the IVZ side characterised by a wide region of low to moderate strain protomylonites and mylonites, and the SdL side characterised by a narrower deformed region where strain is heterogeneously localised into ultramylonitic bands. Ultimately, the onset of strongly heterogeneous strain localisation is aided by the presence, but low abundance, of biotite and is hindered in lithologies which are dominated by a pre-existing network of mica and lack a strong load-bearing framework.

## 7.5.3. Models of strain localisation

A significant microstructural difference in strain localisation similar to this was produced in experiments by Holyoke and Tullis, (2006b) who observed strain localisation and C' shear bands or distributed, pervasive S-C fabric development based on differences in phase strength contrast. They performed shear experiments on samples of the Gneiss Minuti (which is part of the Strona Ceneri zone described in this study and has a similar composition

to sample CMB19) at varying temperatures and strain rates, and found that the difference in the strength of biotite relative to the quartz framework under different conditions resulted in the development of very different fabrics and degrees of strain localisation. The important factor is the magnitude of the phase strength contrast (PSC), particularly in relation to the framework phase and the weakest phase (Holyoke and Tullis, 2006b). This can be viewed in the context of the distinct types of mechanical behaviour of polymineralic rocks outlined by Handy, (1990, 1994). In granitoid rocks, small quantities of mica act as a weak phase within a load bearing framework of stronger minerals, whereas rocks with higher mica content present an interconnected weak layer microstructure containing 'clasts' of stronger minerals (Fig. 7.15a). These microstructures can then evolve with increasing strain, for example when a weak phase (such as mica) in low abundance becomes interconnected, it is able to accommodate a greater proportion of strain as the microstructure has evolved away from isolated weak grains in a load bearing framework — Type 1 in the model of Handy, (1994) — and towards an interconnected weak layer microstructure (Fig. 7.15b). In the orthogneiss rocks of this study, this transition takes place through the interconnection of isolated mica grains by means of the development of fine-grained polyphase domains. This material deforms by GSS creep and is likely to be weaker than the framework. As the volume proportion of this weak, fine-grained material increases, the microstructure evolves more towards that of an ultramylonite with strong clasts surrounded by a weak, fine-grained matrix. In the Kinzigite rocks with much higher mica content, the mica phase is already interconnected, giving a microstructure representative of Type 3 in the model of Handy, (1994).

In this model, the deformation microstructures of an idealised two-phase system are a function of the magnitude of the viscous strength contrast between the two phases and the volume proportion of the weak phase (Fig. 7.15a). This viscous strength contrast is essentially the same as the phase strength contrast of Holyoke and Tullis (2006b), however, it should be noted that the important factor is the difference in strength between the weakest phase and the phase that makes up the framework, rather than simply the difference in strength between the two phases of the rock. This is the reason for the inclusion of the volume proportion of the weak phase in the model of Handy (1994). For example, in a hypothetical rock composed of 70% mica and 30% plagioclase (resembling microstructure Type 3 in Figure 7.14), the viscous strength contrast (Handy, 1990, 1994) would be high, but, as the mica represents the weakest phase *and* the framework phase, there would be less strain localisation than if the mica was present in low abundance, as the strain is distributed

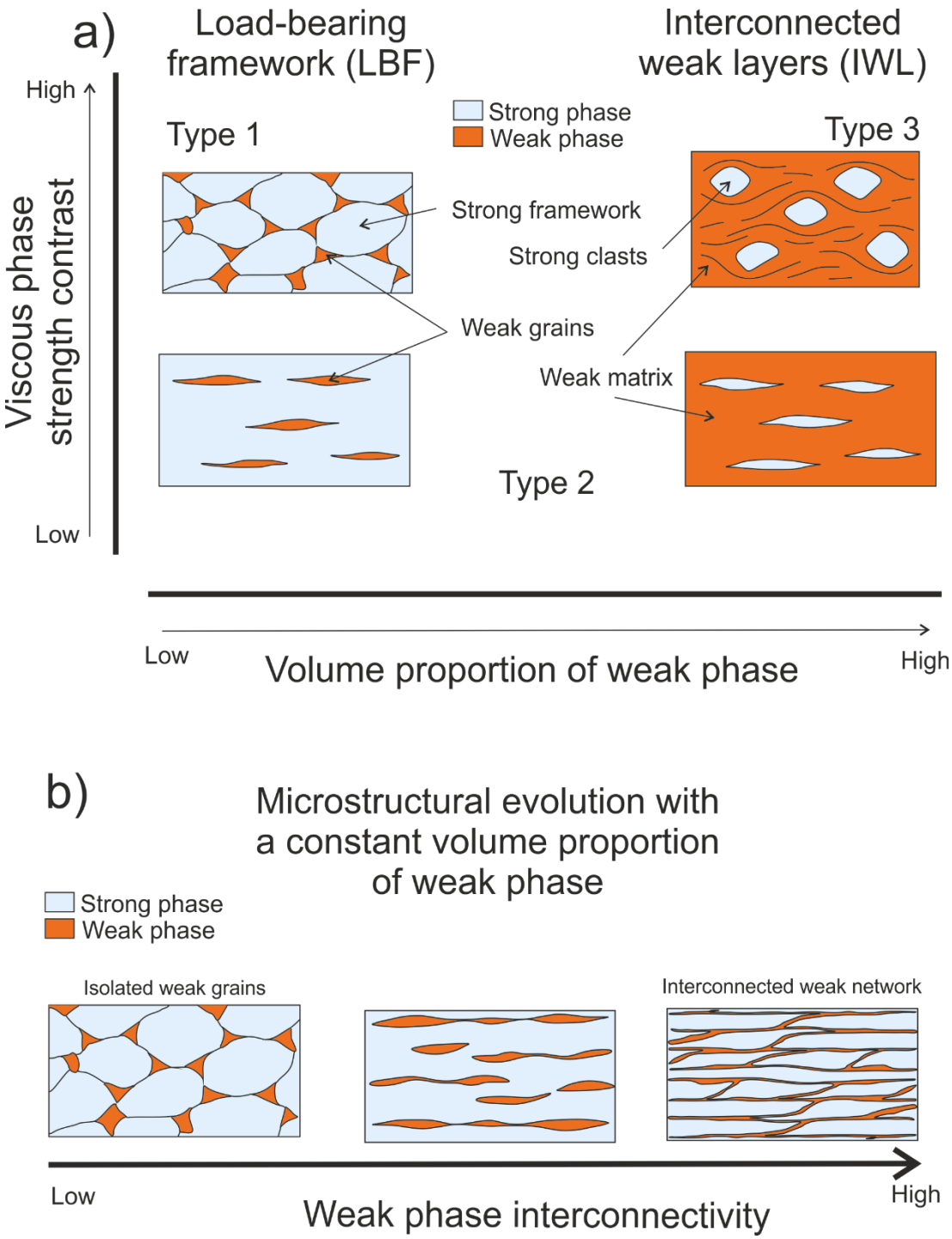


***Figure 7.15:*** *a) Schematic diagram of deformation microstructures in idealised two phase rocks based on the magnitude of the viscous strength contrast between the stronger and the weaker phase and on the volume proportion of the weak phase. Adapted from Handy (1994). b) Schematic diagram of microstructural evolution in a rock with a low volume proportion of weak phase. Initially, weak minerals are isolated, and the rheology is dominated by the strong framework phase (i.e. biotite in a granite or the orthogneisses of this study). With increasing deformation however, this microstructure changes, the weak phase becomes interconnected, and the rheology of the rock becomes controlled to a greater extent by the weak phase*

throughout the interconnected weak layers. This type of relationship was not considered by Holyoke and Tullis, (2006b) as their experiments varied the deformation conditions but not the starting material, so initial microstructure and phase proportions were constant.

### 7.5.4. Implications for the CMB and Pogallo line and other large-scale shear zones

In the rocks examined for this study, the weak phases are micas and the strong phases are quartz and feldspars. The rocks either side of the shear zone are deformed by the same event under the same P/T conditions so the magnitude of the viscous strength contrast between the minerals should not change significantly between different samples. The difference is therefore in the volume proportion of weak micas, producing different microstructures for orthogneiss and for Kinzigites. On the thin section scale this results in mica-rich C' shear bands in mica-bearing but not dominated rocks, such as orthogneiss, and distributed S-C fabrics in mica-rich rocks, such as Kinzigites. This disparity is also present within the Kinzigite Formation as shown by the different microstructures displayed by the most mica-rich Kinzigites (producing S-C fabrics) compared to those with less mica and a higher plagioclase content (a greater tendency to develop C' shear bands).

On the larger scale of the CMB and Pogallo line shear zones, the result is a narrow, heterogeneously deformed region on the SdL side composed of high strain ultramylonites alongside lower strain mylonites and protomylonites, and a wider, more diffuse region of more homogeneous S-C mylonites on the IVZ side (Handy, 1987) (Fig. 7.16). The interpretation that micas facilitate strain localisation in mylonites must therefore be handled carefully. It appears true that, where possible, strain is localised into a mica phase, as favourably oriented mica grains are weaker than most other minerals at a range of conditions (Shea and Kronenberg, 1993; Mariani *et al.*, 2006). This produces high strain shear bands in most mica-bearing rocks. However, the results of this chapter suggest that in mica-dominated systems the presence of large quantities of micas does not result in extensive strain localisation but leads to distributed strain throughout the micas which form the major framework phase. This relationship extends over the scale of kilometres producing distinct patterns of strain distribution within the different lithologies on either side of the shear zone.

As the CMB line and Pogallo line system (the field area used in this study) potentially represents an exposed example of a deep-crustal, low-angle detachment fault (e.g. Hodges and Fountain, 1984), these results are pertinent to understanding the dynamics of other large mid- and lower-crustal shear zones and their influence on crustal rheology. The apparent lack

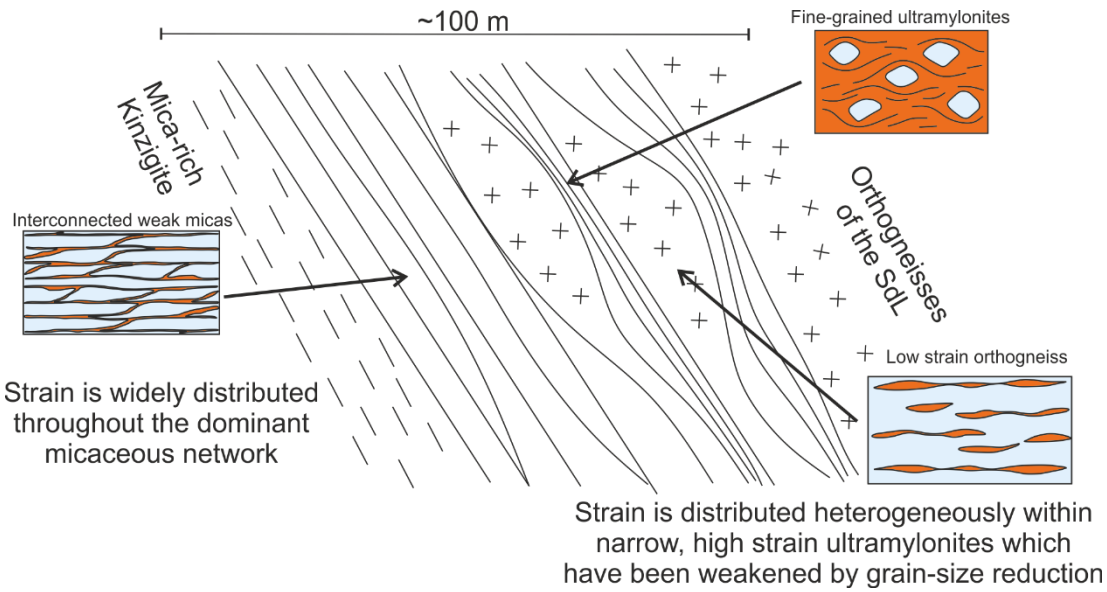


***Figure 7.16:*** *Schematic diagram illustrating how different parts of the CMB and Pogallo line shear zone accommodate strain in different ways, with mica content being a crucial factor. In the Mica-rich Kinzigites of the Ivrea Verbano zone strain is distributed within a wide band of mylonites in which the interconnected mica network accommodates the bulk of the strain. In the Orthogneisses of the Serie dei Laghi the strain is accommodated heterogeneously within narrow high strain bands and ultramylonites.*

of formation of localised high strain zones within mica-rich rocks and their tendency to accommodate strain within an existing weak network of micas, suggests narrow high strain shear zones are less likely to nucleate within regions of the mid-crust in which micas dominate the lithology. By contrast, quartzofeldspathic dominated but mica-bearing sections of crust may be more susceptible to the development and propagation of clearly defined narrow shear zones bearing ultramylonites and accommodating substantial strain. When such shear zones propagate into mica dominated sections of crust, it is possible that they may dissipate into a broader region of more moderate deformation as, occurs in the North Eastern portion of the CMB line and Pogallo line system within the Kinzigites of Valle Cannobina (Boriani, Giobbi Origoni, *et al.*, 1995). If this was the case, the widening of crustal-scale shear zones, and dissipation of strain, may occur not just due to increased temperatures at depth but also when substantial lithological changes are encountered, if those changes involve a variation in the abundance of mica.

## 7.6. Conclusions

This chapter has reported the microstructural evolution and fabric development of mylonites with varying mica content with the aim of understanding how mica content affects strain localisation in mid-crustal mylonites.

Deformation within the Serie dei Laghi on the SE side of the CMB line at Ornavasso consists of a narrow region, ~100 m wide, of relatively high strain mylonites, derived principally from granitic orthogneiss as well as psammitic paragneiss. By contrast, in the mica-rich metapelites of the Kinzigite Formationto the NW, deformation is distributed across a wider band (~200 m) of moderate strain S-C mylonites. At the Pogallo line in Val Pogallo, strain in the orthogneisses of the SdL is accommodated heterogeneously within narrow, high strain shear zones and ultramylonites alongside lower strain protomylonites. The Kinzigite side of the shear zone is very poorly exposed, however, mica-rich mylonites incorporated into the shear zone may have originated in the Kinzigite formation.

Small variations in mineral abundances within the Kinzigite Formationhave a strong influence on the microstructural evolution with increasing strain. Localised, high strain C' shear bands develop more readily in samples with high plagioclase feldspar content and relatively lower mica content and develop only at higher strains in samples with a very high mica content and very little plagioclase. This is likely due to the fact that very mica-rich rocks possess an extensive interconnected network of mica from the outset of deformation, whereas those with a greater feldspar component possess a load-bearing framework which must be disrupted through C' shear bands in order for the weak mica grains to form a fully interconnected network. Brittle deformation of plagioclase is interpreted to be an important factor in the initiation of these C' shear bands.

Quartz c-axis CPOs reveal a general pattern of increasing strain towards the centre of the shear zone in both transects and that dislocation creep of quartz plays an important role in strain accommodation within the studied mylonites. This role is however reduced in rocks with higher mica content with apparent lower strains in quartz from mica-rich rocks relative to similarly located mica-poor rocks.

Biotite possesses a very strong foliation parallel CPO in all samples, but this is weakened during precipitation of very fine new grains during the dramatic grain size reduction that takes place in orthogneiss mylonites and is reported in detail in Chapter 6 of this thesis. The important consideration for strain localisation is the strength contrast between the weakest phase (mica) and the framework phase. In mica-bearing but quartz or feldspar dominated rocks the strength contrast is high, and strain is very localised, whereas in mica-dominated lithologies the mica represents the framework as well as the weakest phase and strain is distributed more homogeneously throughout. Ultimately, strain localisation is enhanced by

small or moderate amounts of mica, whereas strain is more evenly distributed in rocks with very high mica content.

## 7.7. Supplementary figures

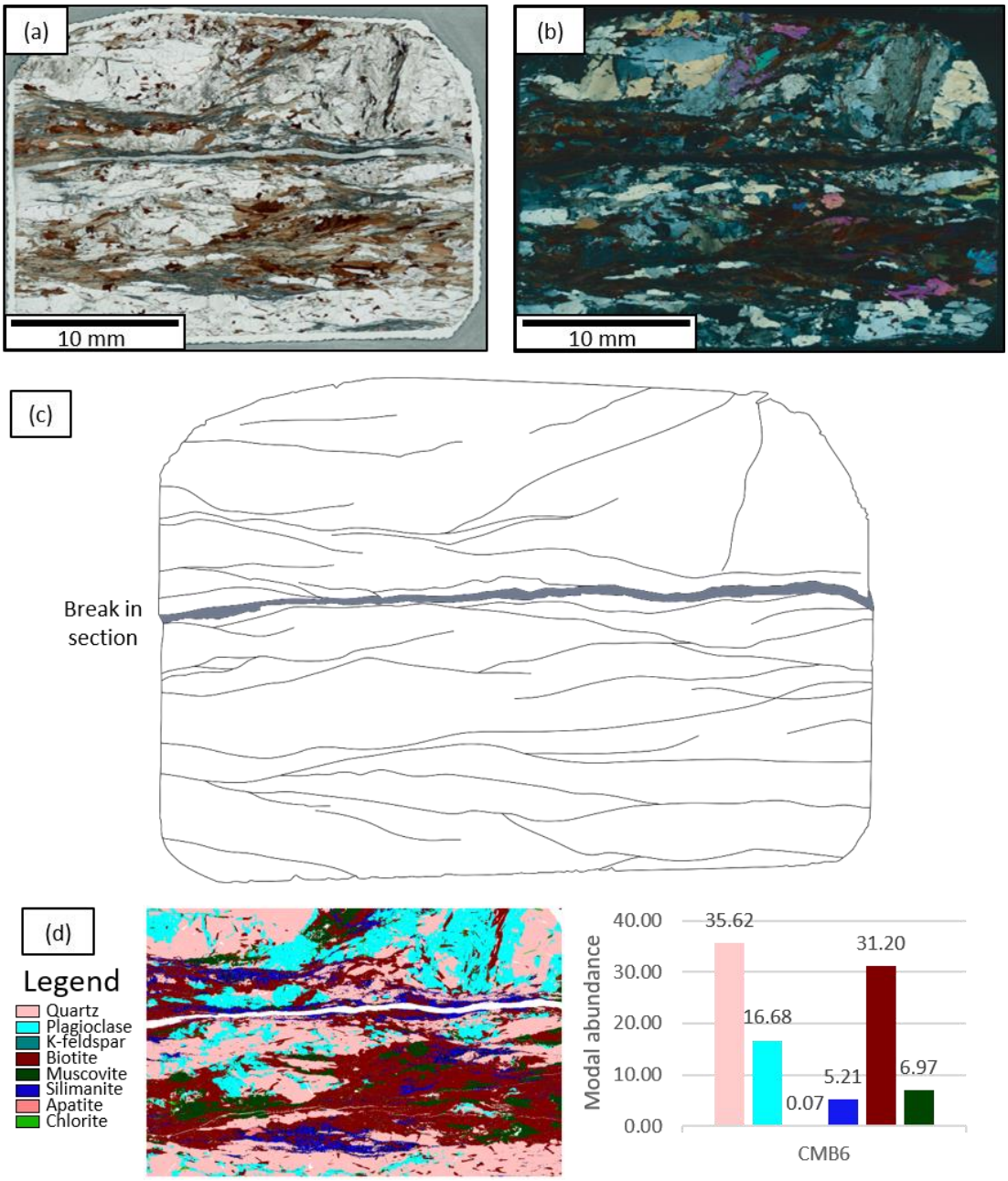


***Supplementary Figure S7.1:*** *Sample CMB6 a) in plane polarised light, b) in crossed polarised light. c) Sketch of major foliations and fabric features, d) QEMSCAN phase map and plot of modal abundances of major minerals; quartz, plagioclase, K-feldspar, sillimanite, biotite and muscovite. This sample represents the Kinzigite protolith essentially unaffected by the CMB line shear zone and was collected c. 500 m from the trace of the CMB.*

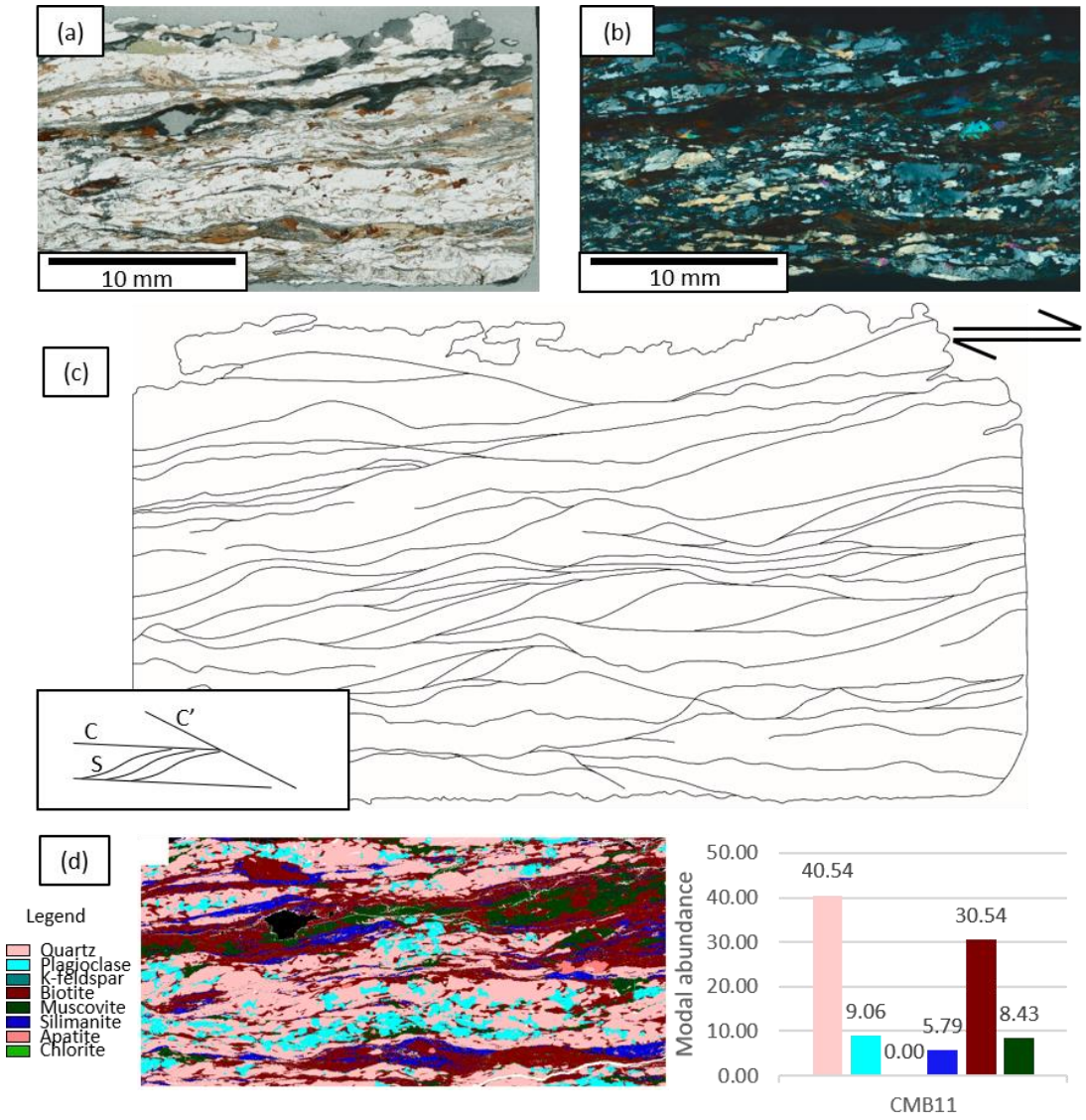


**Supplementary Figure S7.2:** Sample CMB11 a) in plane polarised light, b) in crossed polarised light. c) Sketch of major foliations and fabric features. d) QEMSCAN phase map and plot of modal abundances of major minerals; quartz, plagioclase, K-feldspar, sillimanite, biotite and muscovite. This sample is a mica-rich Kinzigite protomylonite with a primitive mylonitic foliation defined predominantly by mica basal planes and silimanite lathes and undulose extinction and limited dynamic recrystallisation of quartz.

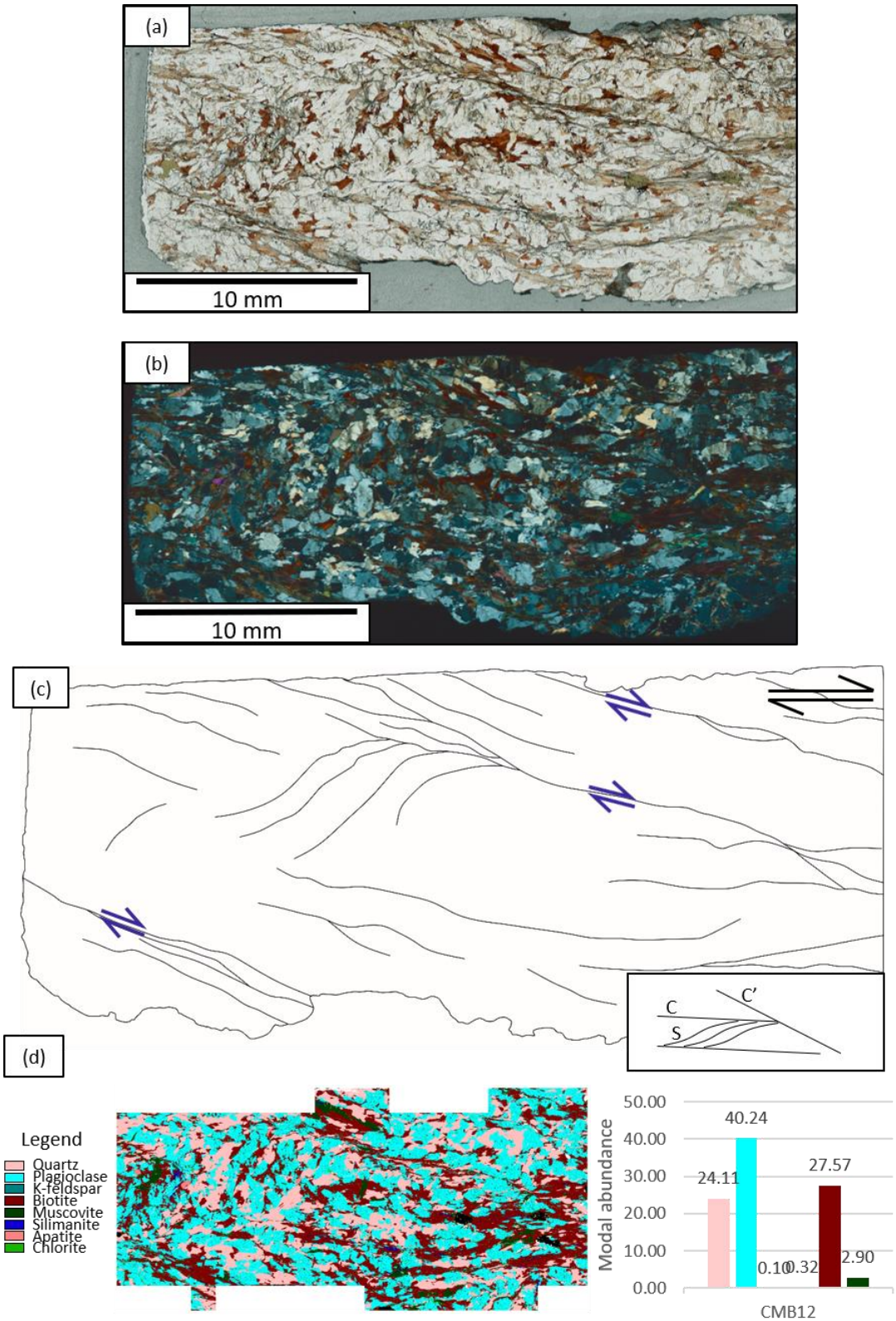


***Supplementary Figure S7.3:*** *Sample CMB12 a) in plane polarised light, b) in crossed polarised light. c) Sketch of major foliations and fabric features, C' shear bands are highlighted by blue shear sense indicators. d) QEMSCAN phase map and plot of modal abundances of major minerals; quartz, plagioclase, K-feldspar, sillimanite, biotite and muscovite. This sample is a Kinzigite which is relatively poor in mica content*

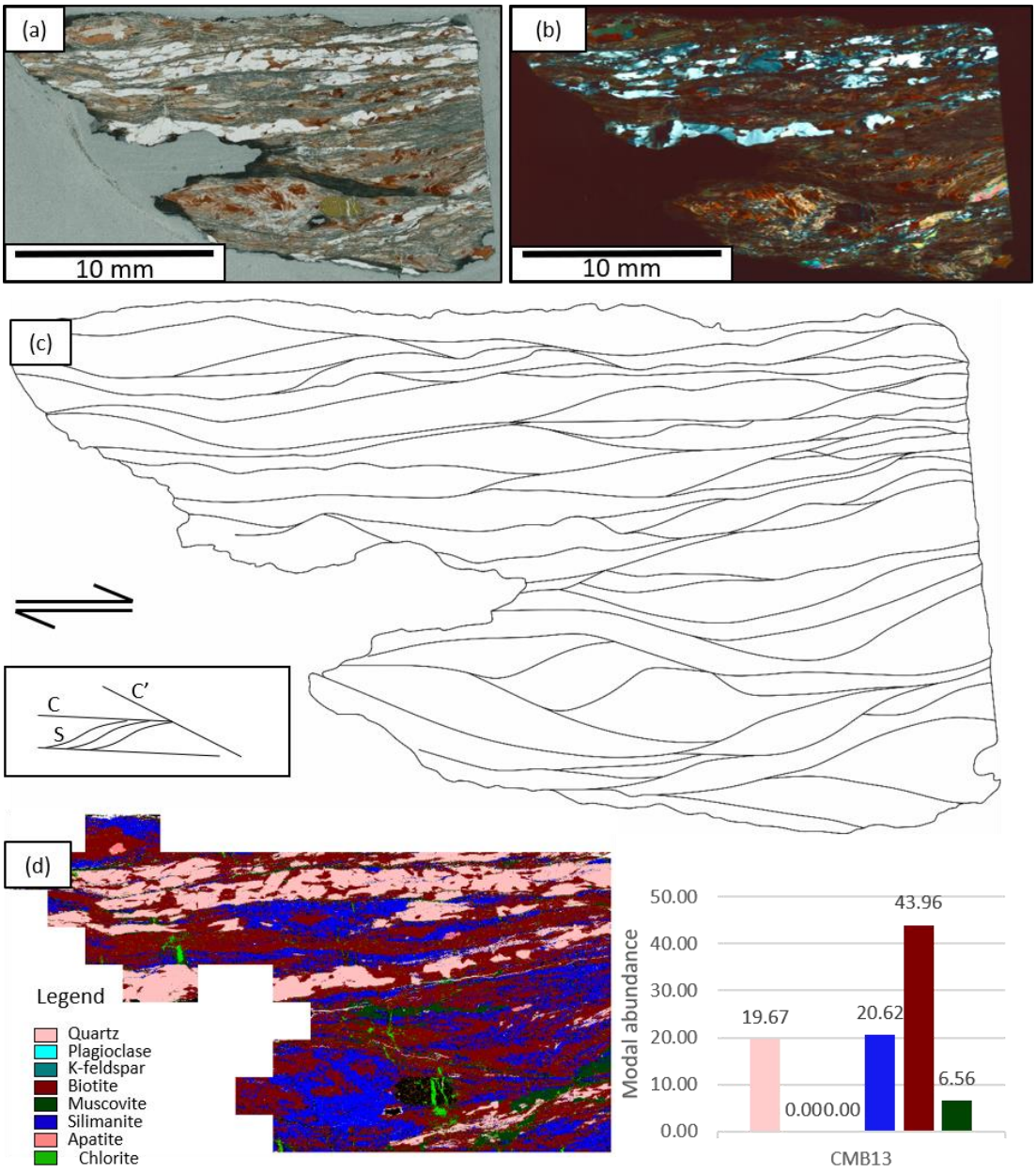


***Supplementary Figure S7.4:*** *Sample CMB13 a) in plane polarised light, b) in crossed polarised light. c) Sketch of major foliations and fabric features. d) QEMSCAN phase map and plot of modal abundances of major minerals; quartz, plagioclase, K-feldspar, sillimanite, biotite and muscovite. The large black grain cut by chlorite veins is staurolite.*

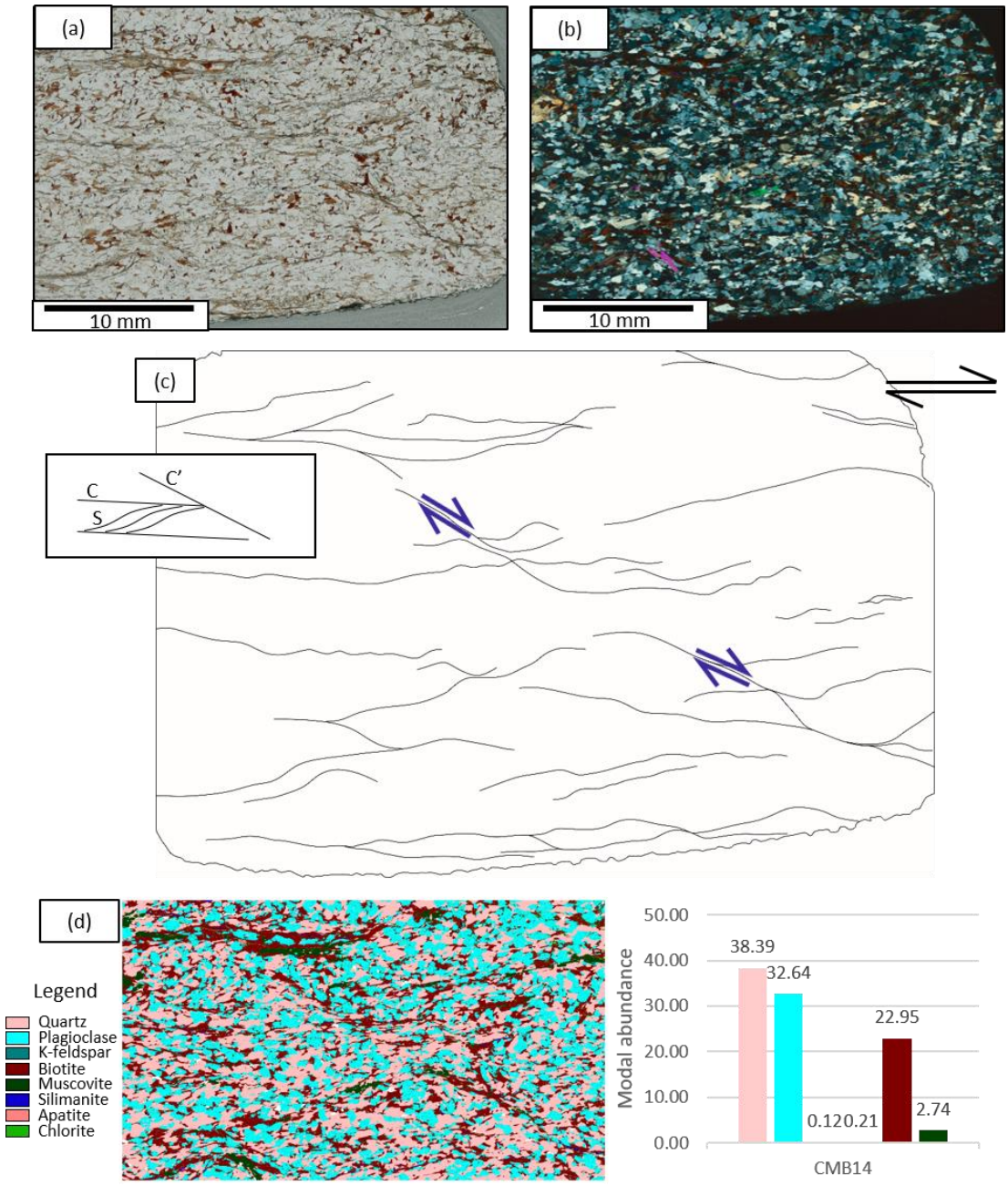


***Supplementary Figure S7.5:*** *Sample CMB14 a) in plane polarised light, b) in crossed polarised light. c) Sketch of major foliations and fabric features, C' shear bands are highlighted by blue shear sense indicators. d) QEMSCAN phase map and plot of modal abundances of major minerals; quartz, plagioclase, K-feldspar, sillimanite, biotite and muscovite.*

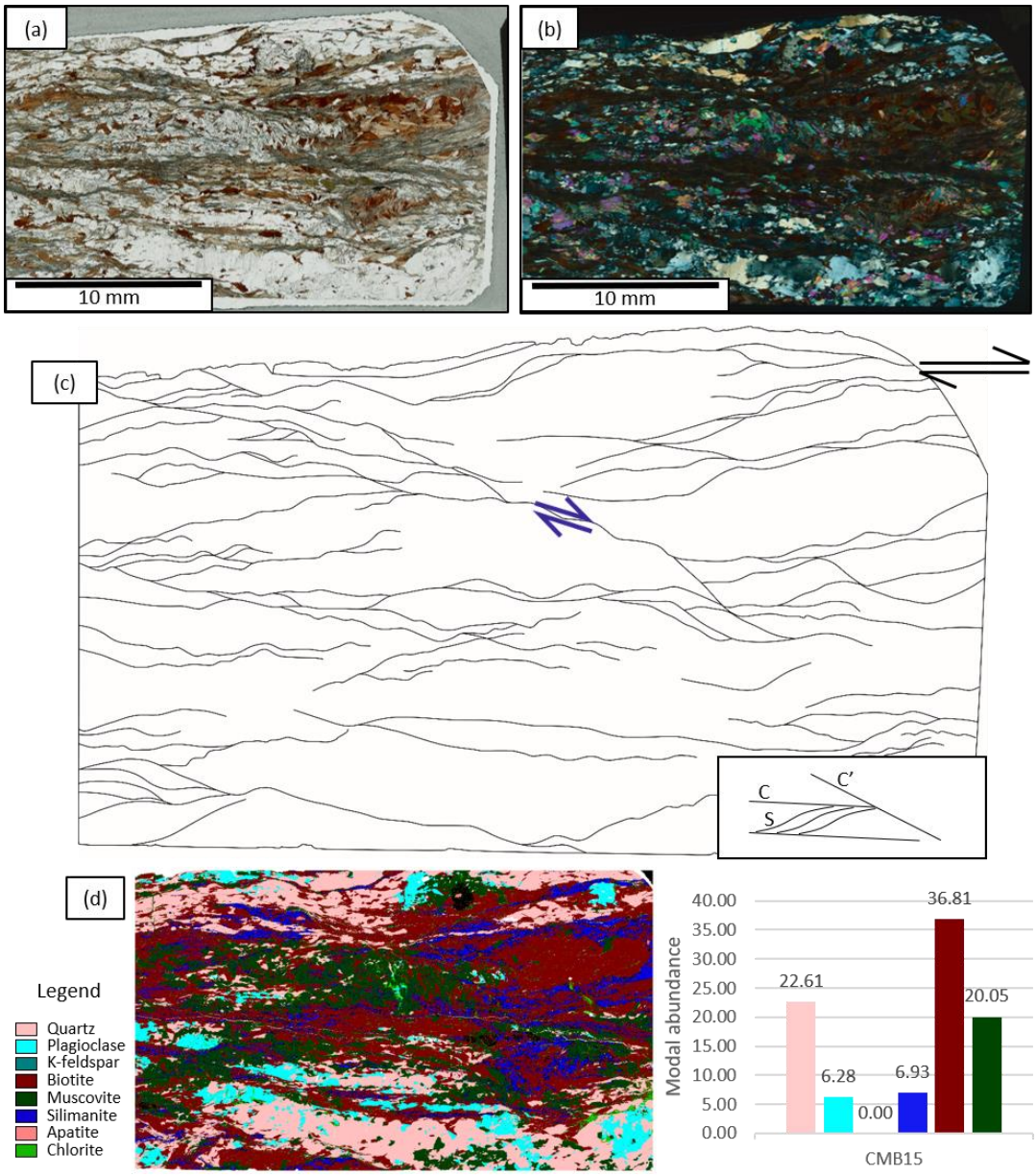


***Supplementary Figure S7.6:*** *Sample CMB15 a) in plane polarised light, b) in crossed polarised light. c) Sketch of major foliations and fabric features, with C' shear bands highlighted by blue shear sense indicators. d) QEMSCAN phase map and plot of modal abundances of major minerals; quartz, plagioclase, K-feldspar, sillimanite, biotite and muscovite. The un-indexed black grains are staurolite and garnet.*

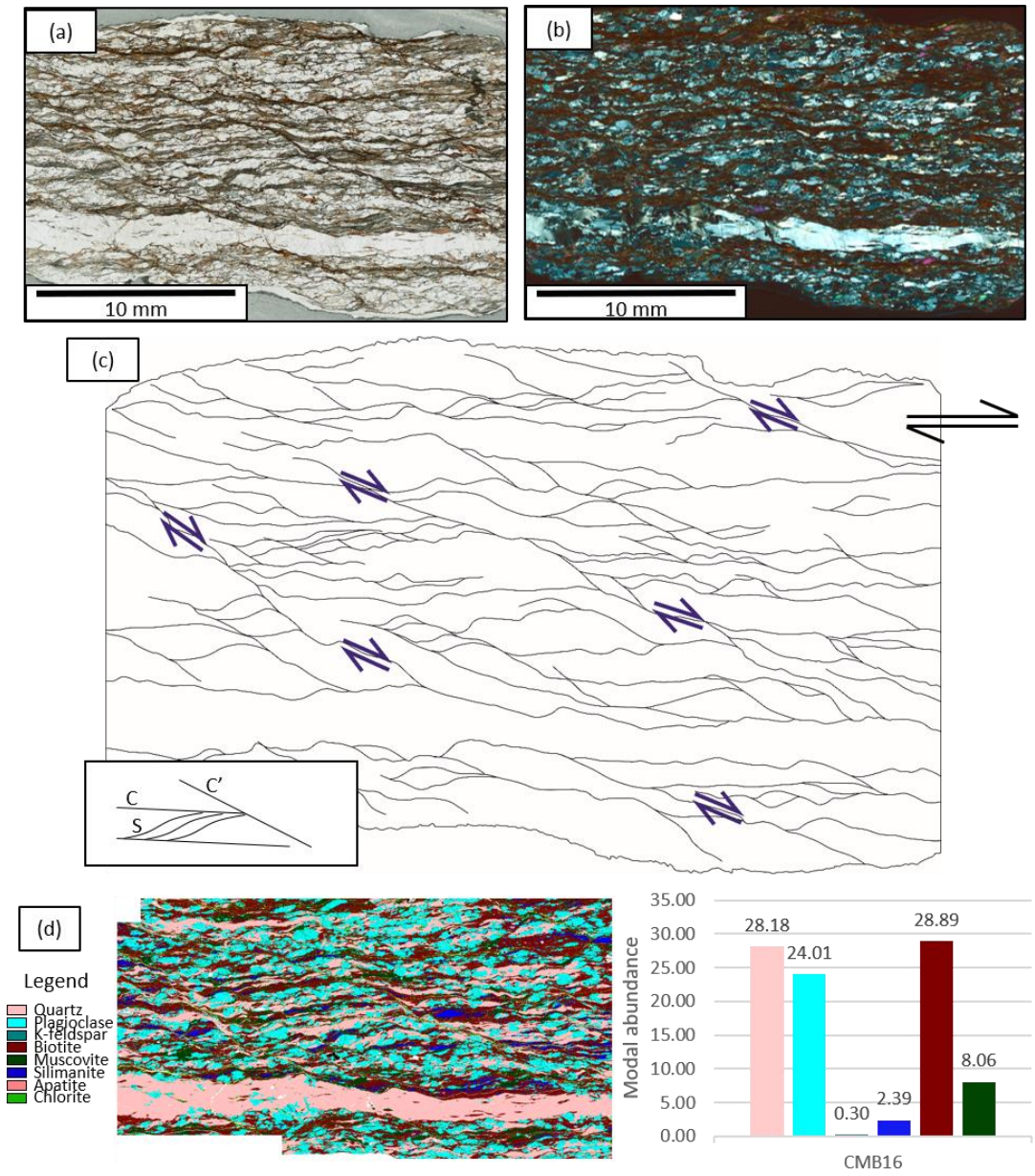


***Supplementary Figure S7.7:*** *Sample CMB16 a) in plane polarised light, b) in crossed polarised light. c) Sketch of major foliations and fabric features, C' shear bands are highlighted by blue shear sense indicators. d) QEMSCAN phase map. and plot of modal abundances of major minerals; quartz, plagioclase, K-feldspar, sillimanite, biotite and muscovite. CMB16 is a high strain Kinzigite mylonite with multiple C' shear bands cutting a high strain, low angle S-C fabric.*

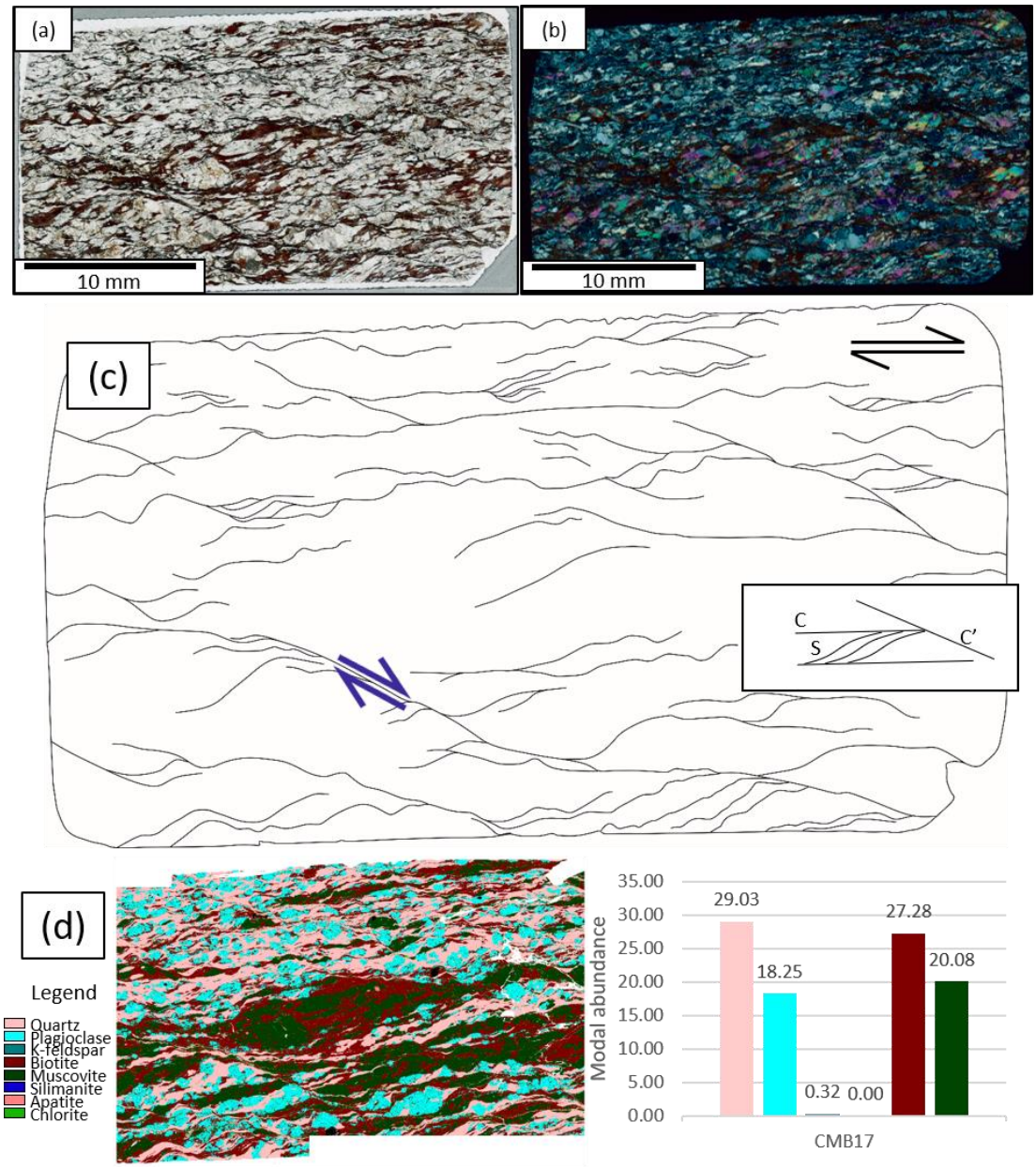


***Supplementary Figure S7.8**: Sample CMB17 a) in plane polarised light, b) in crossed polarised light. c) Sketch of major foliations and fabric features, C' shear bands are highlighted by blue shear sense indicators. d) QEMSCAN phase map. and plot of modal abundances of major minerals; quartz, plagioclase, K-feldspar, sillimanite, biotite and muscovite. CMB17 is a high strain Kinzigite mylonite with a well-developed S-C fabric.*

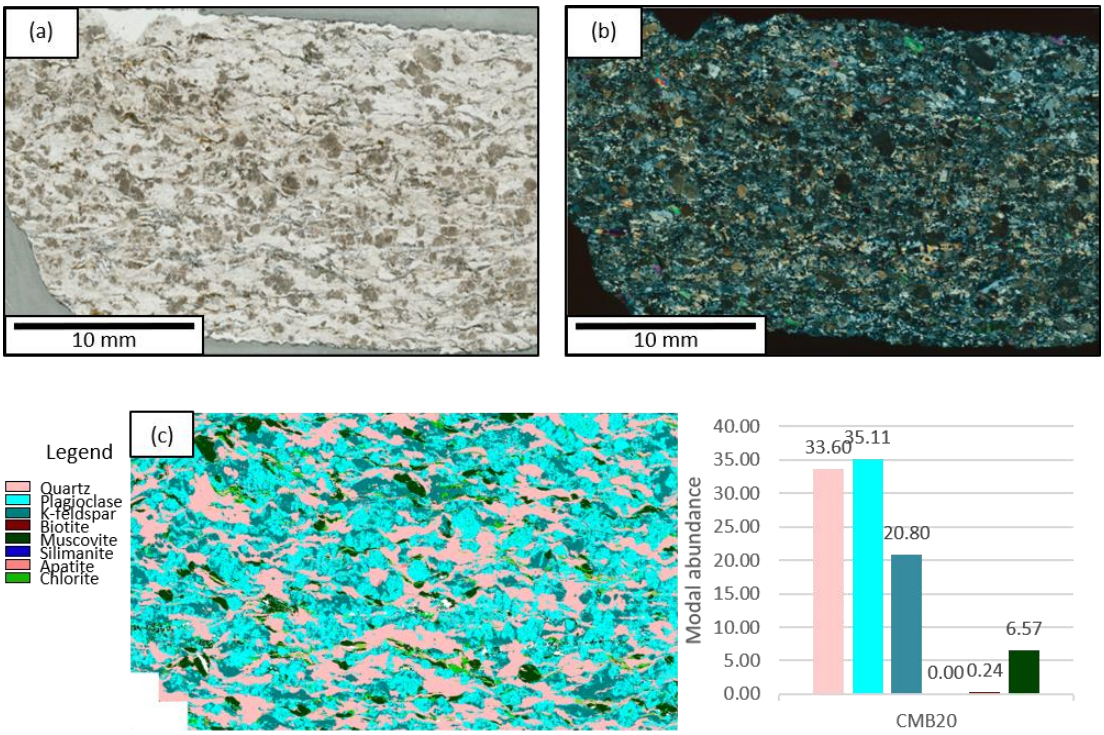


***Supplementary Figure S7.9:*** *Sample CMB20 a) in plane polarised light, b) in crossed polarised light. c) QEMSCAN phase map and plot of modal abundances of major minerals; quartz, plagioclase, K-feldspar, sillimanite, biotite and muscovite.*

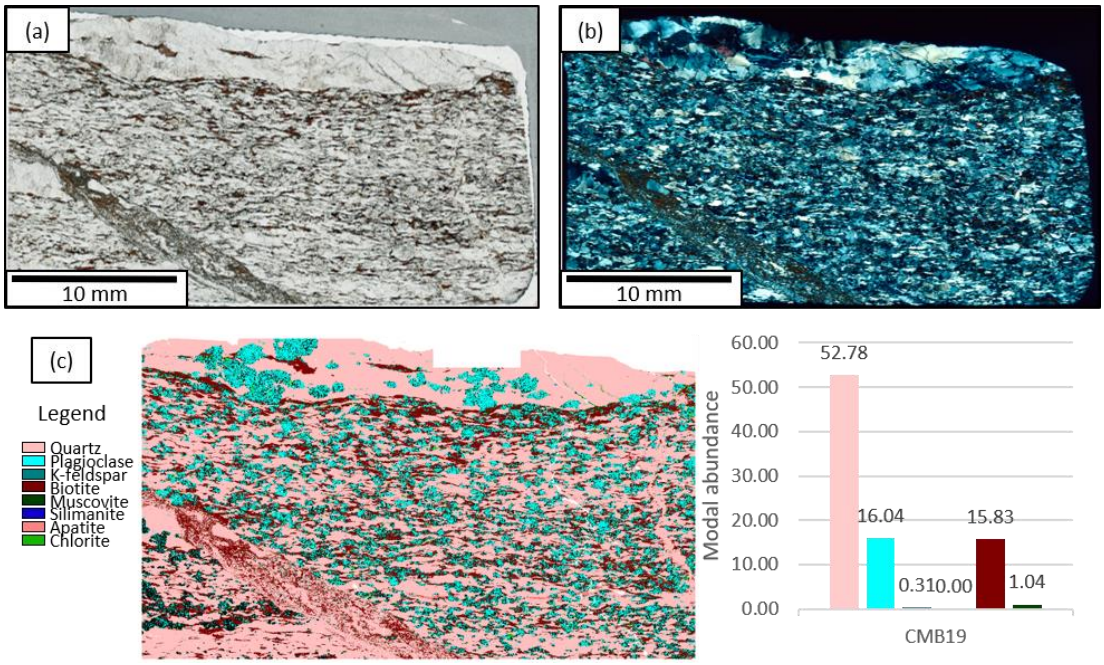


***Supplementary Figure S7.10:*** *Sample CMB19 a) in plane polarised light, b) in crossed polarised light. c) QEMSCAN phase map and plot of modal abundances of major minerals; quartz, plagioclase, K-feldspar, sillimanite, biotite and muscovite.*

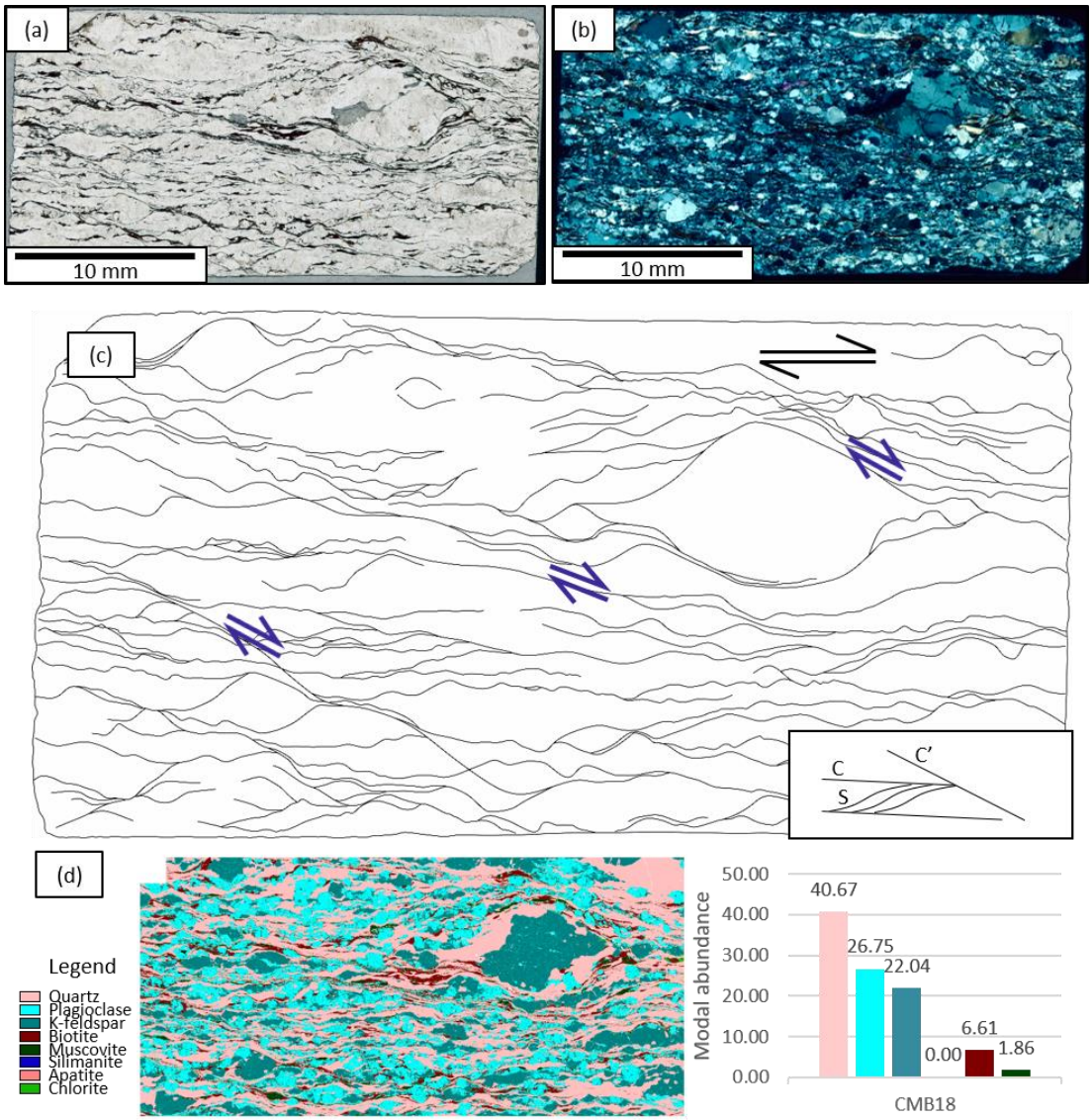


***Supplementary Figure S7.11:*** *Sample CMB18 a) in plane polarised light, b) in crossed polarised light, c) sketch of major foliations and fabric features, d) QEMSCAN phase map and plot of modal abundance. CMB18 is a granitic mylonite which has developed predominantly a C-C' mylonitic fabric although S surfaces are evident in places. The C and S planes are defined by the basal planes of coarse mica grains and the boundaries of highly recrystallised monomineralic quartz domains. The high strain C' planes are however dominated by very fine-grained mixed phases, predominantly biotite, quartz and plagioclase. Major C' shear bands are indicated with blue shear sense markers.*

# 8. Incongruent pressure solution of feldspars in granitic orthogneiss mylonites

## 8.1. Abstract

The heterogeneous distribution of fine-grained plagioclase and K-feldspar along the boundaries of feldspar porphyroclasts in amphibolite to upper-greenschist facies orthogneiss mylonites from the Pogallo line shear zone in north western Italy is examined in the context of stress-dependent fluid-facilitated reactions and incongruent pressure solution. Plagioclase grains decorate the surfaces of K-feldspar porphyroclasts facing the direction of maximum principle stress ($\sigma_1$) while fine-grained K-feldspar fills pressure shadows and fractured regions of porphyroclasts. Electron backscatter diffraction (EBSD) analyses suggest a strong similarity between the orientations of feldspar porphyroclasts and the associated fine grains of plagioclase and K-feldspar present along their boundaries, indicative of a topotactic relationship. Electron probe microanalysis (EPMA) indicates the fine plagioclase grains represent a separate population to the plagioclase porphyroclasts, with compositions of $Ab_{81}$ and $Ab_{76}$ respectively. A set of stress-driven, fluid-facilitated reactions are proposed to explain these observations. K-feldspar porphyroclasts react with fluids, bearing $Na^+$ and $Ca^{2+}$ cations, at high stress interfaces to precipitate plagioclase, resulting in a volume decrease at sites of high stress. This increases the activity of $K^+$ ions in solution, which is balanced by the precipitation of K-feldspar at the expense of plagioclase, or other matrix phases, within pressure shadows and dilatant sites elsewhere in the mylonite. This process is greatly enhanced by brittle fracturing of the feldspar porphyroclasts which provides fluid pathways, increases the reactive surface area and produces dilatant regions where K-feldspar can form. This amounts to a redistribution of volume from sites of high stress to sites of low stress, via coupled ionic exchange reactions with an intergranular fluid, and constitutes a form of incongruent pressure solution. Critically, unlike in regular pressure solution, only highly mobile $K^+$, $Na^+$ and $Ca^{2+}$ cations need be transported significant distances by diffusive mass transfer. Other constituents of the solid phases (such as Si and Al) are utilised in situ as one feldspar forms at the direct expense of another. The implications of this process are significant with regard to the microstructural evolution of the mylonite, accelerating the grain size reduction of feldspar from coarse, rigid porphyroclasts to a component of a fine-grained polymineralic matrix.

## 8.2. Introduction

Pressure solution is the process by which material deforms by diffusion around grain boundaries in response to applied stresses, facilitated by an aqueous intergranular film which can support shear stress (Rutter, 1983). The deformation mechanism of pressure solution creep has also been referred to as stress induced solution transfer or, more commonly, dissolution-precipitation creep (Menegon, Pennacchioni and Spiess, 2008; Mukai *et al.*, 2014). It is similar to the process of Coble creep in dry rocks (Wheeler, 1992) but faster due to the increased rate of diffusive mass transfer within a fluid. The driving force is stress, which induces chemical potential gradients, leading to diffusion and local chemical reactions (Rutter, 1983) with the typical process consisting of the dissolution of material in sites of high stress combined with diffusive mass transfer and precipitation of material in sites of lower stress (Shimizu, 1995). In compacting sandstones for example this manifests as the dissolution of quartz at grain to grain contacts orthogonal to the orientation of maximum stress ($\sigma_1$), and the precipitation of material within pore spaces. In mylonites and other fault lithologies the equivalent process is responsible for the nucleation and growth of certain phases within the pressure shadows of porphyroclasts, which can be used as effective shear sense indicators (Passchier and Trouw, 2005). Dissolution-precipitation creep is typically assumed to be most important at low temperatures due to the dominance of dislocation creep at higher temperatures, such as within the mid-lower crust and lithospheric mantle. However, as dissolution-precipitation creep involves the diffusion of material in intergranular fluids, it is dependent on the length of diffusion pathways and is inversely proportional to grain size (Klinge *et al.*, 2015), making it important in certain fine grained or highly fractured rocks even at higher temperatures (Rutter and Brodie, 1988; Wheeler, 1992; Wintsch and Yi, 2002).

Dissolution-precipitation creep of single phases has been discussed in many different minerals including quartz (eg. Cox and Paterson, 1991; Niemeijer, Spiers and Bos, 2002), salt (Renard *et al.*, 2001; Spiers *et al.*, 2008), K-feldspar (Menegon, Pennacchioni and Spiess, 2008; Fukuda *et al.*, 2012; Giuntoli *et al.*, 2018) plagioclase (Fukuda and Okudaira, 2013) and possibly within mantle peridotites (Dick and Sinton, 1979). Dissolution-precipitation creep is distinguished from dissolution-precipitation in mineral replacement reactions (Putnis, 2002; Plumper and Putnis, 2009; Putnis and John, 2010; Ruiz-Agudo *et al.*, 2014) by the fact that the former is induced by differential stresses and results in a change in shape of the rock volume via diffusive mass transfer (Rutter, 1976, 1983; Bons and den Brok, 2000; Gratier *et al.*, 2013), while the latter involves a phase (or assemblage) change and is a reaction

mechanism rather than a deformation mechanism. Despite this, the microstructures produced can be very similar, in particular, dissolution-precipitation reactions can produce apparently deformed microstructures which have undergone limited if any deformation (Spruzeniece *et al.*, 2017; Gardner, 2019). Both the replacement reaction and the deformation mechanism require the presence of an aqueous intergranular film to facilitate dissolution and reprecipitation of material.

Where stress-induced dissolution, diffusive mass transfer and precipitation is accompanied by a reaction and a resulting phase change, the process can be termed incongruent pressure solution (Fry, 1982). It can be viewed as the pressure solution of one mineral only if suitable other minerals are available (Fry, 1982), just as metamorphic reactions occur only if a suitable assemblage exists. In a metamorphic reaction a reactant mineral, or group of minerals, which becomes chemically unstable due to a change in pressure and/or temperature conditions, is directly replaced by a product mineral, or set of minerals, which are stable at the new conditions. In incongruent pressure solution, the phases on one side of the reaction are more stable under higher stresses while those on the other side are more stable under lower stresses. This results in a reversible reaction which moves in one direction at sites of high stress (such as the $\sigma_1$ facing edges of grains) and the other direction in sites of low stress (such as pressure shadows) (Beach, 1979; Fry, 1982). The phases from both sides of the reaction will therefore be present in the rock's assemblage but their distributions will be strongly influenced by microstructural stress heterogeneities.

Importantly, incongruent pressure solution serves as evidence of how deformation and metamorphic reactions can be interlinked and, more fundamentally, of the connection between stress and chemistry in geological systems (Paterson, 1973; Vaughan *et al.*, 1984; Schmid *et al.*, 2009; Wheeler, 2014, 2018). As the microstructures produced by incongruent pressure solution do not entirely resemble those of congruent pressure solution due to the involvement of multiple phases, it is possible that evidence of incongruent pressure solution has, in the past, been overlooked and its importance within deforming polyphase rocks may have been underestimated. While there are very few existing studies invoking incongruent pressure solution in the tectonic and metamorphic literature, those that do cover a range of systems and conditions. Simpson and Wintsch, (1989) describe an example of deformation-induced replacement of K-feldspar by oligoclase and quartz in the form of myrmekite, within the Santa Rosa mylonite of Southern California, which they define as a form of incongruent pressure solution. Similar replacement of K-feldspar by oligoclase and quartz myrmekite during deformation is described by Menegon *et al.*, (2006), Ceccato *et al.*, (2018) and

Cisneros-Lazaro *et al.*, (2019), although in these cases the term incongruent pressure solution is not used. Wassmann and Stöckhert, (2013) provide evidence of incongruent pressure solution of garnet under low stress conditions whereby dissolution of garnet poikiloblasts along edges where they approach one another was accompanied by precipitation of a mixture of chlorite, white mica and quartz in pressure shadows. Moore *et al.*, (2019) show that different assemblages, representative of distinct local equilibrium conditions, form along grain boundaries of plagioclase during granulite hydration, and that their distribution is dependent on the orientation of that boundary with respect to the principle stress axes. While the explicit discussion of incongruent pressure solution has been limited, there is a growing body of literature highlighting how heterogeneous stress distributions and grain-scale perturbations can produce locally distinct thermodynamic equilibria (Tajčmanová *et al.*, 2013; Wheeler, 2014, 2018; Vrijmoed and Podladchikov, 2015). Further microstructural evidence of incongruent pressure solution playing a role in the deformation of natural rocks is now required to validate these theoretical developments.

This chapter aims to add microstructural evidence from natural rocks to this under-explored field by detailing the relationship between K-feldspar and plagioclase within orthogneiss mylonites of the amphibolite to upper-greenschist facies Pogallo line in North Western Italy (see Chapter 1 section 1.3). It will describe the heterogeneous distribution of these phases and how this relates to the orientations of principle stress axes during deformation, before explaining the microstructures in the context of incongruent pressure solution. It is then proposed that such a mechanism could potentially work much faster than congruent pressure solution of a single feldspar (without a phase change) and how this, coupled with brittle fracturing, is the principal mechanism of feldspar grain size reduction and deformation in granitoid mylonites at the conditions associated with mid-crustal shear zones.

## 8.3. Methods

The samples used in this study were oriented orthogneiss mylonites collected from the Pogallo line, an amphibolite to upper-greenschist facies mylonitic shear zone in North West Italy. The principle sample (POG3) is an ultramylonite with modal abundances of approximately 50% quartz, 15% plagioclase, 15% K-feldspar, 12% muscovite, 5% biotite and 3% other phases including apatite, zircon and oxide minerals. The other two samples used (POG7 and POG5) are lower strain protomylonites and mylonites collected on the same transect of the Pogallo line as the ultramylonite and are interpreted to represent lower strain examples of the same orthogneiss protolith (see Chapter 6 of this thesis for full descriptions

of the samples). 30 µm single polished thin sections of these rocks were prepared with surfaces perpendicular to foliation and parallel to lineation. Optical observations and characterisation were conducted using a Meiji Techno MT9000 polarised binocular microscope. Plane and crossed polarised light images were taken using a Lumenera Infinity 4 camera. All mineral abbreviations used are based on the recommendations laid out by Siivola and Schmid (2007).

Backscattered electron (BSE) images were collected using the Phillips XL30 tungsten filament scanning electron microscope (SEM) in the electron microscopy laboratories at the University of Liverpool, Department of Earth, Ocean and Ecological Sciences. Operating conditions were 20 kV accelerating voltage, 43-4 nA beam current and a 5 nm spot size. Electron backscatter diffraction (EBSD) was used to determine the crystallographic orientation of K-feldspar and plagioclase grains and to identify the presence and nature of any intracrystalline distortion. This was done using orientation maps, pole figures and misorientation analyses generated using CHANNEL 5 HKL software. Samples were prepared for EBSD analysis by polishing for 2 hours using 0.05 µm colloidal silica before a very thin carbon coat was applied to mitigate charging within the SEM. EBSD data were collected using a CamScan X500 CrystalProbe field emission gun (FEG) SEM at the same laboratory, operating at 20 KV accelerating voltage, 20-30 nA beam current, a spot size of 5.5 nm and a working distance of 25 mm. Simultaneous acquisition of element maps was conducted using a silicon drift detector (SDD) for energy dispersive spectroscopy (EDS) analyses mounted on the X500 CrystalProbe SEM. QEMSCAN phase maps were produced using a FEI WellSite Qemscan SEM in the department of Earth, Ocean and Ecological Sciences at the University of Liverpool.

Quantitative chemical datasets were collected using a Cameca SX-100 Electron Probe Microanalyser (EPMA) at the University of Manchester. Point analyses were collected within both new and old plagioclase grains and new and old K-feldspar grains. The instrument was set up to measure major elements; Si, Fe, Mg, Al, K, Ti, Na, Ca and Mn using an accelerating voltage of 15 kV and a 10 µm de-focused beam. Analyses were taken from the coarser of the fine grains (>10 µm) in order to avoid introducing errors due to grain boundary effects. A small number of anomalous data points with low closing values or high Si values due to beam interaction with quartz were removed from the data set prior to plotting and interpretation. One EPMA map was collected using the same beam settings detailed above. The colour scale was adjusted using ImageJ software in order to visualise subtle chemical variation. Phi-Rho-Z·f matrix corrections were applied to the data using the PAP analytical model (Pouchou and

Pichoir, 1991). Data were processed and analysed using the Probe for EPMA software package from Probe Software Inc.

## 8.4. Results

### 8.4.1. Distribution and texture of plagioclase and K-feldspar

Optical observations of the ultramylonite sample POG3 reveal that it is composed predominantly of a very fine-grained polymineralic matrix containing primarily quartz, biotite, muscovite, feldspar and apatite. Within this matrix are numerous well-rounded porphyroclasts of both plagioclase and K-feldspar, which form delta and sigma clasts giving a dextral sense of shear, as well as muscovite mica-fish. While all these phases are present throughout the sample their distribution on the thin section scale is not homogeneous. Analysis using a petrographic microscope (Fig. 8.1a-c) and QEMSCAN phase mapping (Fig. 8.2a) reveals two distinct regions, one with a quartz-rich matrix bearing predominantly K-feldspar porphyroclasts and one with a more biotite-rich matrix associated with a greater abundance of plagioclase porphyroclasts. K-feldspar porphyroclasts are up to 3 mm in diameter although the majority are <1 mm, while plagioclase porphyroclasts are smaller with the largest at 1 mm and the majority <500 μm. The thin section-scale compositional banding may be due to pre-existing compositional variation in the protolith, or to lithological mixing during deformation. A heterogeneous distribution of phases is also seen at a finer scale in relation to both types of feldspar porphyroclasts, with many K-feldspar porphyroclasts decorated by fine plagioclase grains along two opposite boundaries (Fig. 8.1d, e, Fig. 8.2b). These boundaries are the parts of the porphyroclasts which face the direction of the greatest principal stress ($\sigma_1$), taking into account the dextral shear sense of the section. In addition, the strain shadows of both K-feldspar and plagioclase porphyroclasts contain a high concentration of fine-grained K-feldspar.

BSE images were taken to examine the nature of the phase and grain contacts in the rims of feldspar porphyroclasts. Figure 8.3a shows a K-feldspar porphyroclast with K-feldspar in the pressure shadows in the upper right and lower left corners and plagioclase accompanied by some quartz along most of the rest of the porphyroclast's periphery. The boundaries of the plagioclase and quartz grains are lobate and curve into the K-feldspar porphyroclast forming an irregular boundary (Fig. 8.3b). A notable amount of grain boundary porosity is present within the plagioclase and quartz aggregates. Dilated grain boundaries in quartz and plagioclase terminate at the seamless contact with K-feldspar. By contrast, the boundary of the porphyroclast adjacent to the pressure shadow is quite sharply defined, with K-feldspar

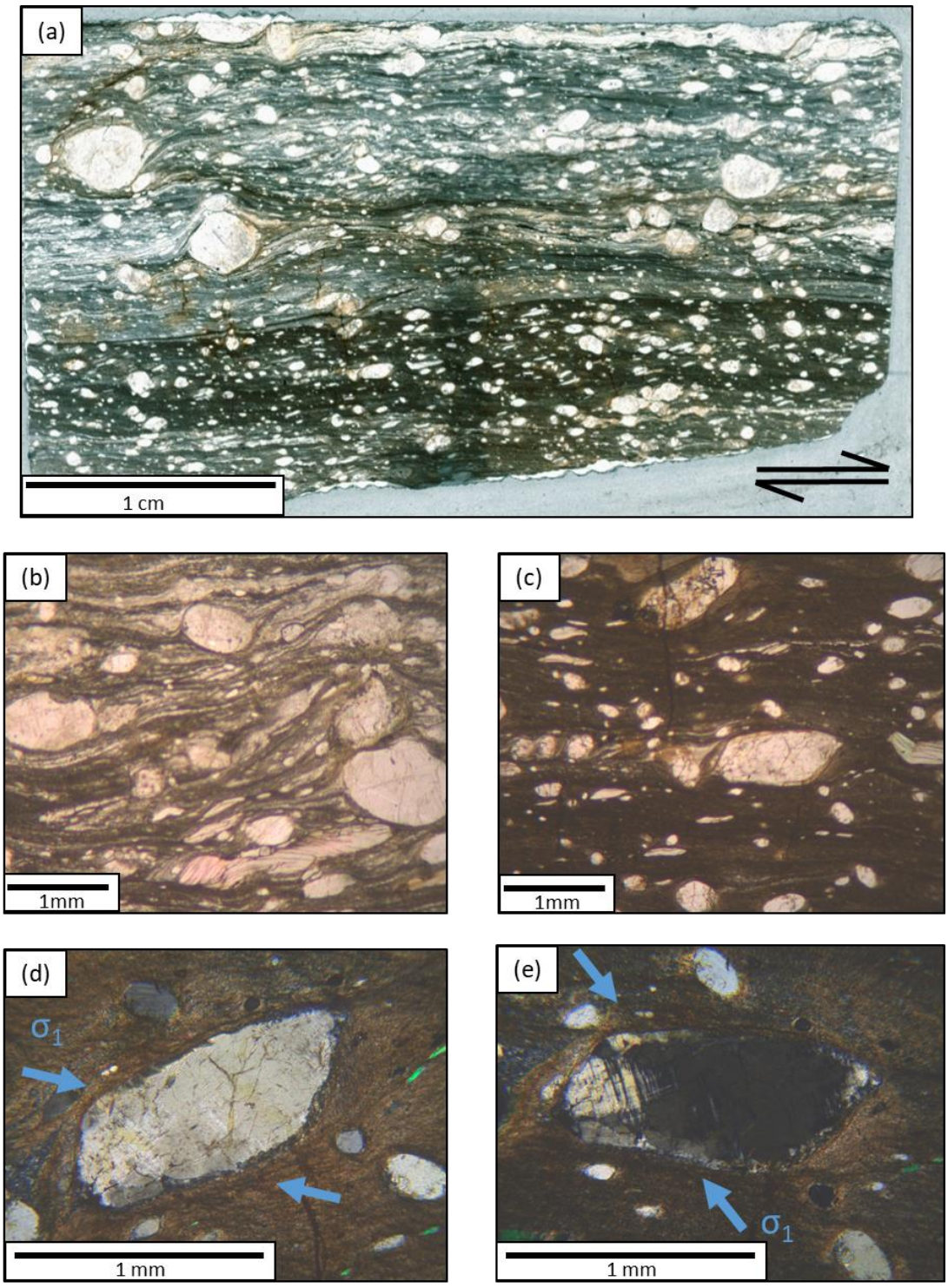


***Figure 8.1:*** *a) Plane polarised light full thin section scan of sample POG3 showing foliation parallel bands of different composition. Shear sense is dextral (top to the right). b) Plane polarised light optical micrograph of part of POG3 with a quartz-rich matrix. c) Plane polarised light optical micrograph of part of POG3 with a biotite-rich matrix. d) and e) Cross polarised light optical micrographs of a K-feldspar porphyroclast with partial rims of plagioclase at edges facing* $\sigma_1$.

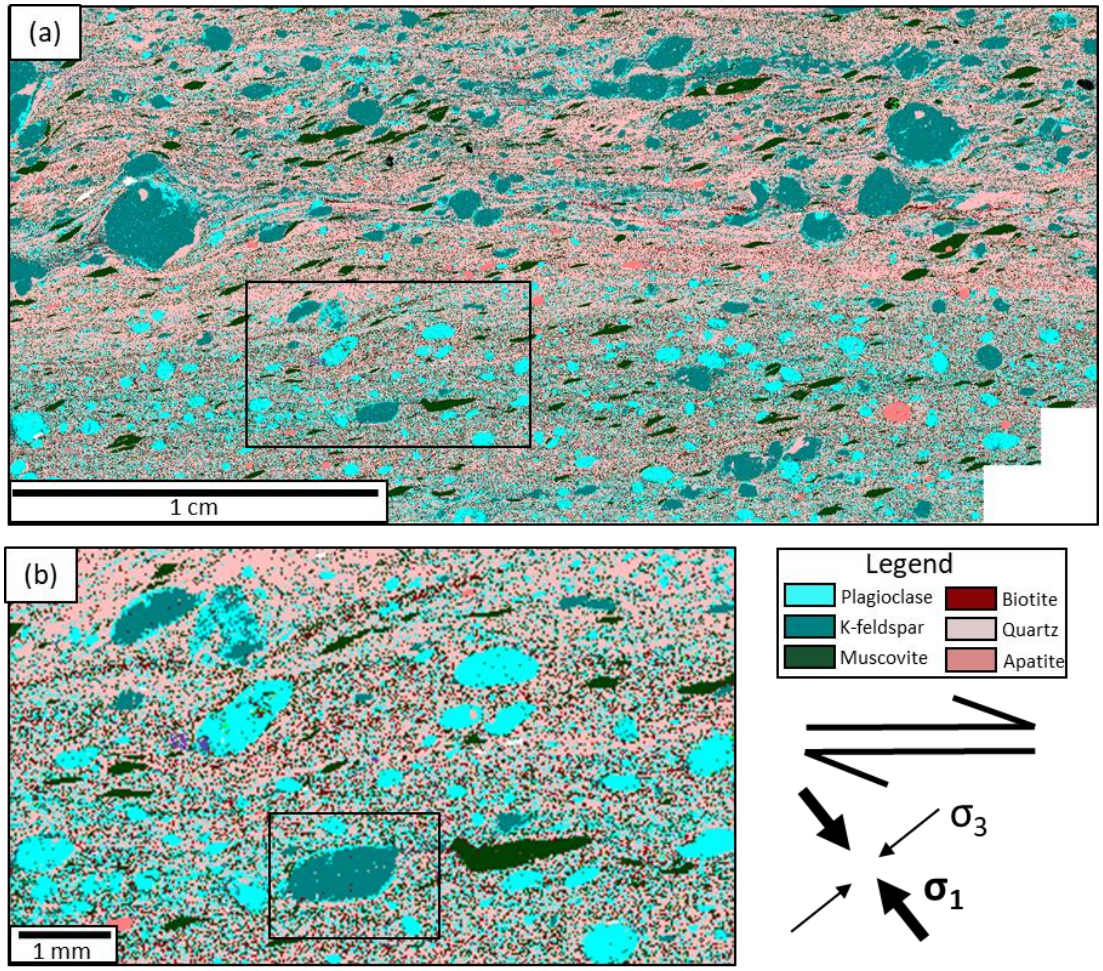


***Figure 8.2:*** *a) QEMSCAN phase map of the same sample showing the presence of plagioclase along high strain edges of K-feldspar grains and K-feldspar in the pressure shadows of porphyroclasts. b) Detail of the area highlighted in (a). Box in (b) defines the area shown in Fig. 8.3 (a). Shear sense is dextral (top to the right).*

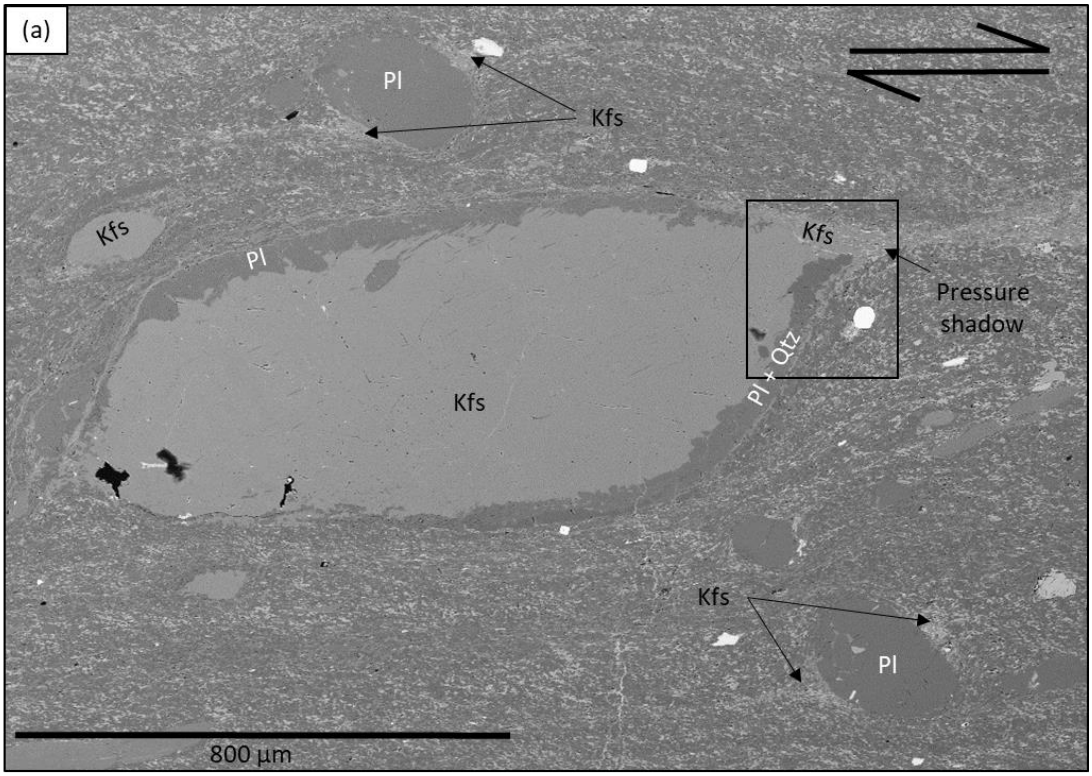


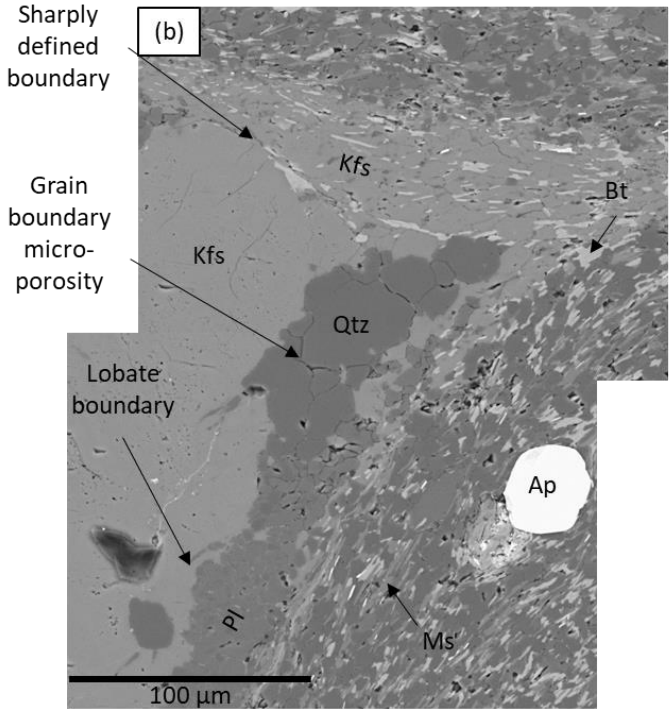


***Figure 8.3:*** *a) SEM BSE image of a K-feldspar porphyroclast with K-feldspar pressure shadows to the upper right and lower left and plagioclase grains along with some quartz decorating the upper left and lower right edges, which are facing the direction of maximum principle stress. Nearby plagioclase porphyroclasts also have K-feldspar dominated pressure shadows. The bright, generally rounded grains are apatite. b) Detail of the upper right part of the porphyroclast. The boundary between the porphyroclast and the plagioclase/quartz is irregular and, in some cases, lobate. Micro-porosity along grain boundaries in the plagioclase and quartz terminates at this boundary with the K-feldspar. By contrast the boundary between the porphyroclast and the K-feldspar in the pressure shadow is sharply defined. Biotite occurs with K-feldspar in the pressure shadow but in approximately the same concentration as in the rest of the matrix, whereas muscovite and quartz are highly depleted in the pressure shadow and K-feldspar is very strongly concentrated.*

grains within the pressure shadow forming part of the matrix rather than appearing to develop at the expense of the K-feldspar porphyroclast. While the pressure shadow is composed predominantly of K-feldspar, other minerals are also present, particularly biotite, in approximately the same abundance as it occurs in the rest of the matrix, and a small amount of fine-grained, isolated quartz. A similar distribution is apparent around the K-feldspar porphyroclast in Figure 8.4 except that in this case fine plagioclase grains extend down the entire left side of the porphyroclast where it is in close proximity to a plagioclase porphyroclast, and occur only in a small section in the lower right, immediately opposite a muscovite mica fish. The plagioclase porphyroclast itself has K-feldspar rich pressure shadows, like the K-feldspar porphyroclast, but does not display the same distribution of finer plagioclase along the opposing surfaces.

### 8.4.2. Microstructural analysis of feldspar generations using EBSD

The microstructural relationship between the populations of fine feldspar grains and the porphyroclasts, was examined quantitatively and in detail using electron backscatter diffraction (EBSD) and simultaneous EDS. EBSD data is presented in the form of all Euler colour orientation maps, phase maps and texture component maps overlain onto band contrast images of feldspar porphyroclasts and their local vicinities. In texture component maps, pixels of the phase in question are coloured according to their misorientation with respect to a reference orientation (chosen in the centre of each porphyroclast). The step size and map size are given in the caption for each figure. In particular, EBSD was used to measure intracrystalline distortion within feldspar porphyroclasts and identify whether topotactic relationships existed between porphyroclasts and the new, fine feldspar grains associated with them. This was done to identify the provenance of the fine feldspar grains and determine the relative importance of different mechanisms (dynamic recrystallisation, brittle fracturing and incongruent/congruent pressure solution) in the deformation and grain size reduction of the feldspar porphyroclasts.

Figure 8.5 and Figure 8.6 show plagioclase porphyroclasts characterised by clustering of fine-grained K-feldspar in pressure shadows and at dilatant sites where plagioclase porphyroclasts have fractured. In Figure 8.5, fine grained quartz is also associated with dilatant sites and fractures within the plagioclase porphyroclast. These sites represent locations of lower stress during deformation. This distribution of K-feldspar around the plagioclase porphyroclasts is most clearly discerned in the EDS element maps of K (Fig. 8.5c, 8.6c). The plagioclase porphyroclasts show strong evidence of brittle fracturing especially around the peripheries (Fig 8.5a, b, 8.6a, b), with disaggregated angular plagioclase grains on the order of 10s of μm

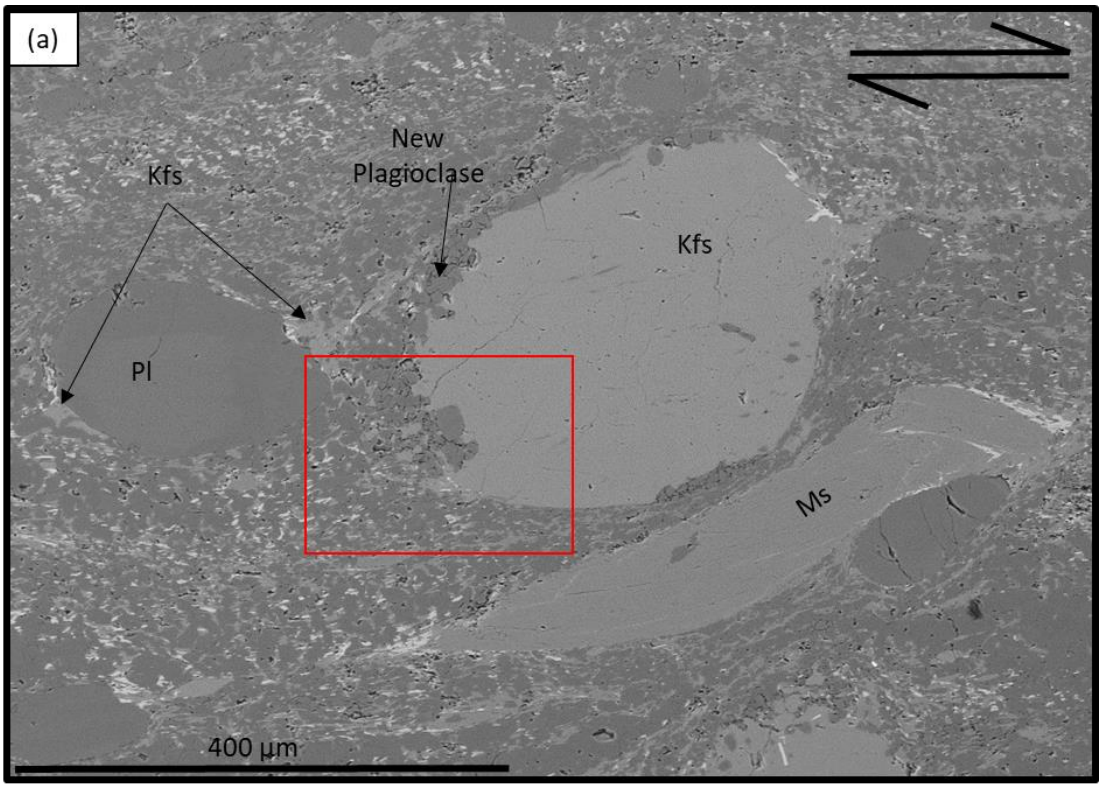


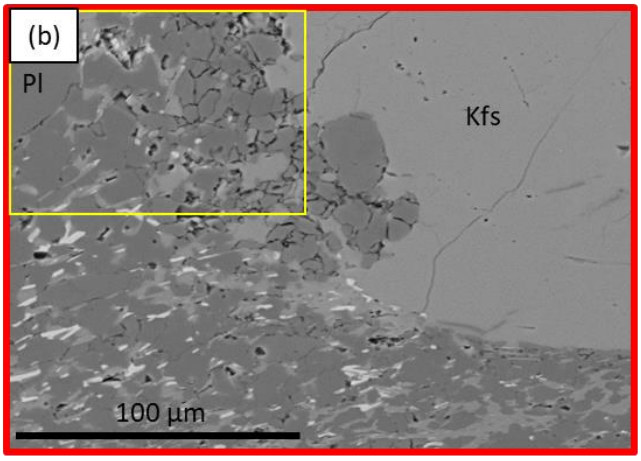


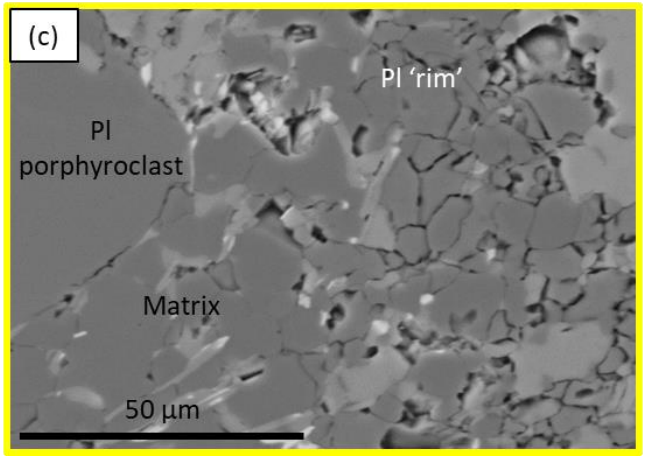


***Figure 8.4:*** *SEM BSE images of porphyroclasts in POG3. a) K-feldspar porphyroclast with plagioclase at the bottom right and along the left and upper left edges along with a small amount of K-feldspar in the pressure shadows. The plagioclase porphyroclast to the left also produces K-feldspar dominated pressure shadows. b) Detail of the red box in a) showing the irregular lobate boundaries of plagioclase grains within the K-feldspar porphyroclast. c) Detail of the yellow box in b) showing the abundance of grain boundary porosity apparent in the plagioclase 'rim' grains relative to that of the regular matrix.*

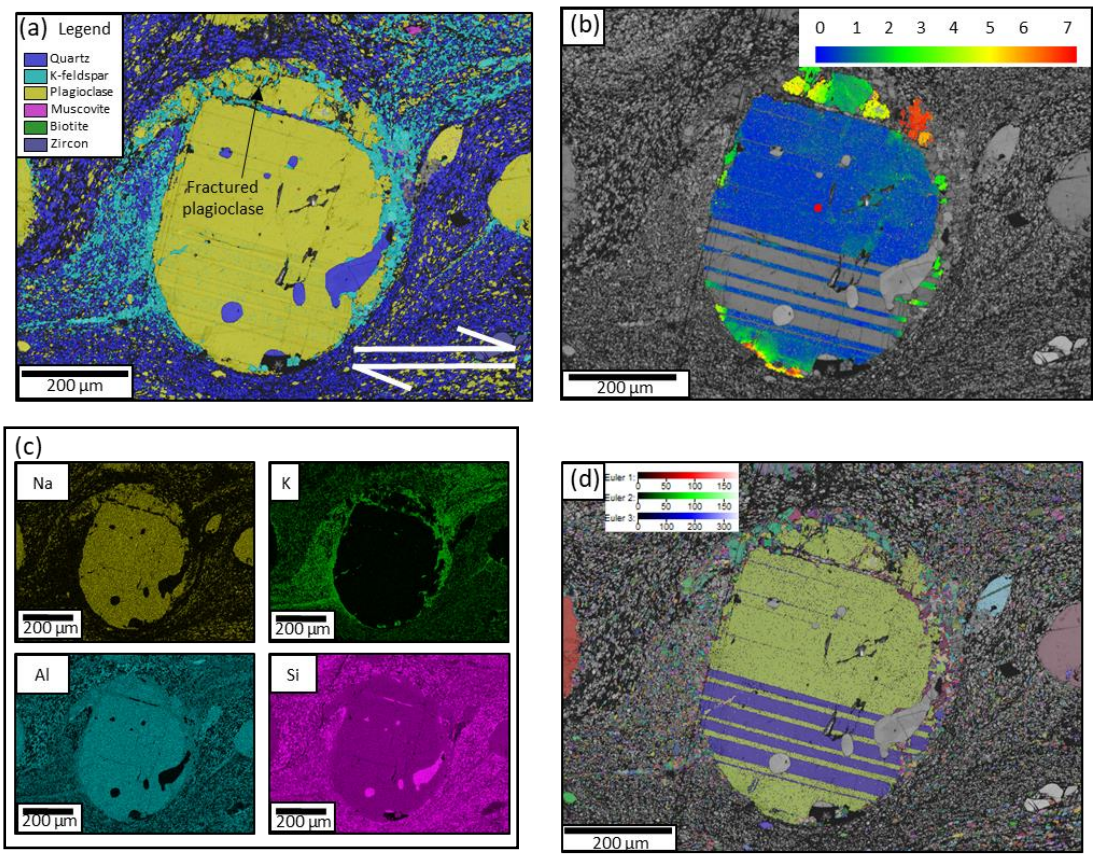


***Figure 8.5:*** *EBSD data of a plagioclase porphyroclast. (a) EBSD phase map showing abundant K-feldspar within the pressure shadows of the porphyroclast, the concentration is greatest along the contact with the grain, especially on the right side of the porphyroclast, especially on the right side, where some K-feldspar appears to have formed within the edge of the porphyroclast. K-feldspar is also associated with fractures in the upper part of the plagioclase grain, alongside some quartz. (b) Texture component map showing the misorientation in degrees across the plagioclase porphyroclast. The majority of the clast contains <1° misorientation, however at the lower periphery of the porphyroclast the lattice is more distorted, with misorientations of up to 5°. The plagioclase grains in the fractured upper part are separated from the porphyroclast and are misoriented by up to and above 7° with respect to the main porphyroclast due to rotation in the matrix. The reference point for misorientations is given by the red spot. (c) EDS element maps of the area giving the relative distribution of Na, K, Al and Si. The concentration of K (as part of the K-feldspar phase) within pressure shadows, fractures and sites of dilation is clearly displayed. (d) All Euler orientation map of feldspars (both plagioclase and K-feldspar). Step size in the maps is 1 µm and the grid is 960 x 720 pixels.*

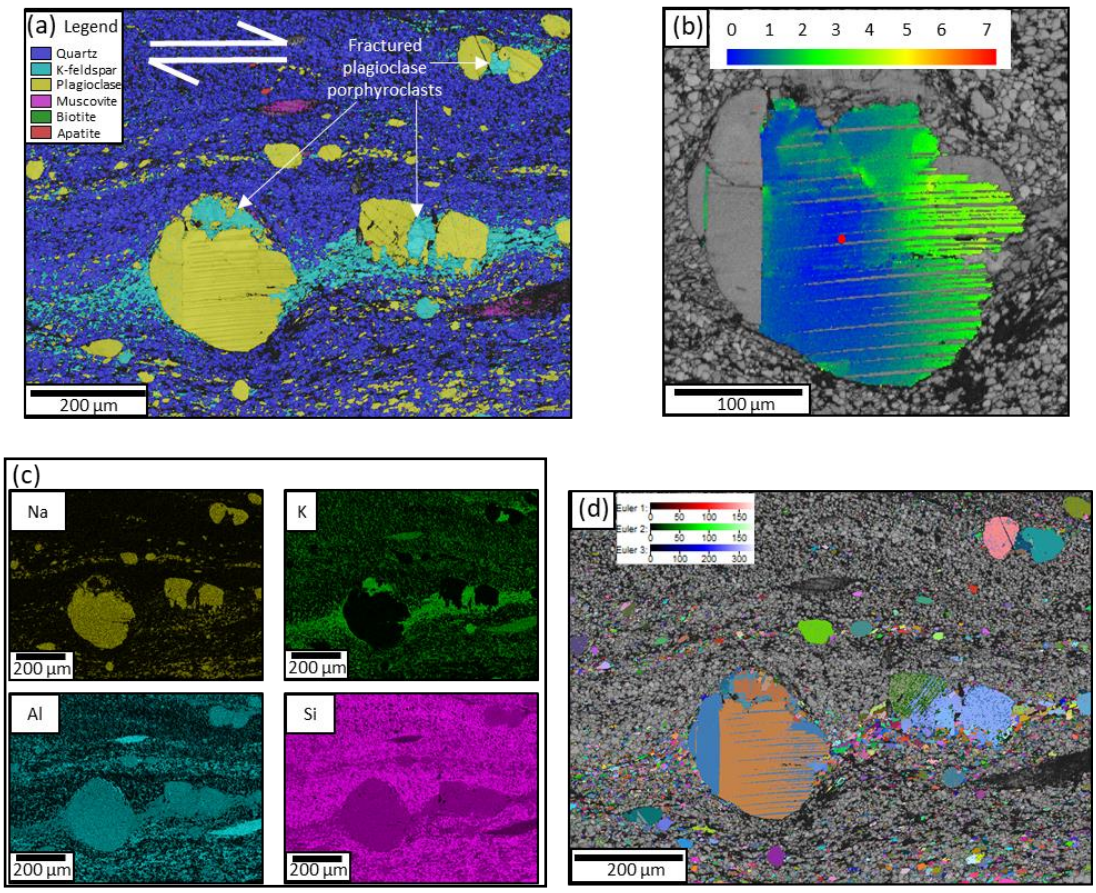


***Figure 8.6:*** *EBSD data of several plagioclase porphyroclasts. (a) EBSD phase map showing the presence of K-feldspar within the pressure shadows of Plagioclase porphyroclasts as well as dilatant sites in association with fractures of the porphyroclasts. (b) Texture component map showing the misorientation across the largest porphyroclast in (a), indicating a small amount of intracrystalline strain in the form of gentle bending of approximately 3° across the porphyroclast but no apparent sub grains. The reference point for misorientations is given by the red spot. (c) EDS element maps of the same area as in (a), giving the relative distribution of Na, K, Al and Si. (d) All Euler colour orientation map of the feldspar phases (both plagioclase and K-feldspar). The K-feldspar associated with the fractured part section at the top of the largest plagioclase grain has an almost identical orientation to the porphyroclast itself. This is also true of the K-feldspar associated with other plagioclase porphyroclasts where they have fractured. Step size in the maps is 1 µm and the grid is 960 x 720 pixels.*

in diameter. Texture component maps of the porphyroclasts (Fig. 8.5b, 8.6b) reveal intracrystalline distortion of up to 5° associated with these fractured regions, with disaggregated grains displaying greater misorientations relative to the porphyroclast. The intracrystalline distortion takes the form of either grain scale gradual bending (Fig. 8.6b) or localised misorientations of 1-5° across straight low-angle boundaries. K-feldspar and quartz are present within the plagioclase porphyroclasts along lines of pre-existing fractures, suggesting that these phases could have precipitated at sites of fluid infiltration.

In Figure 8.6d, where K-feldspar is associated with fractured parts of plagioclase it forms larger grains than those in the pressure shadows and possesses a similar crystallographic orientation to the fractured plagioclase porphyroclast, even inheriting the twinning relationships of the parent grain (Fig. 8.6d). This is shown when pole figures of K-feldspar grains in fractured sections of plagioclase porphyroclasts are compared to pole figures representing the porphyroclasts themselves (Fig. 8.7, 8.8). It is worth noting that although the unit cells of plagioclase and K-feldspar are different, in these cases the a, b and c axes of the two minerals are oriented almost identically. As a result, they are described here as having similar crystallographic orientations. K-feldspar in the pressure shadows is characterised by largely equant grains of around 5 μm in diameter, although they are larger (up to 30 μm) where they are in direct contact with the plagioclase porphyroclast or where they occur in a shared pressure shadow between two plagioclase porphyroclasts. These pressure shadow K-feldspar grains do not show as strong a correlation with the orientation of the plagioclase porphyroclast as those which occur within fractured regions (Fig. 8.7, 8.8).

Figures 8.9 and 8.10 (and Supplementary Figure S8.1) display EBSD and EDS data of K-feldspar porphyroclasts. The phase maps show the presence of plagioclase at the high stress boundaries of the porphyroclasts, along with fine K-feldspar in the pressure shadows. As previously mentioned, all K-feldspar porphyroclasts are also associated with K-feldspar-rich pressure shadows, the porphyroclast in Figure 8.9 in particular, shows a large number of new K-feldspar grains in the lower left. Texture component maps show intracrystalline distortion of up to around 5° within the porphyroclasts, concentrated predominantly around the boundaries and forming straight, subgrain walls. In Figure 8.9b the greatest degree of intracrystalline distortion occurs along the lower left boundary, coinciding with the location of abundant new fine K-feldspar grains. This boundary is angular and irregular, in contrast to the rest of the porphyroclast surface. Contoured pole figures of the K-feldspar grains in the pressure shadow (Fig. 8.9c) reveal that the population is strongly related to the orientation of the porphyroclast although the scattered data shows that many other orientations are also

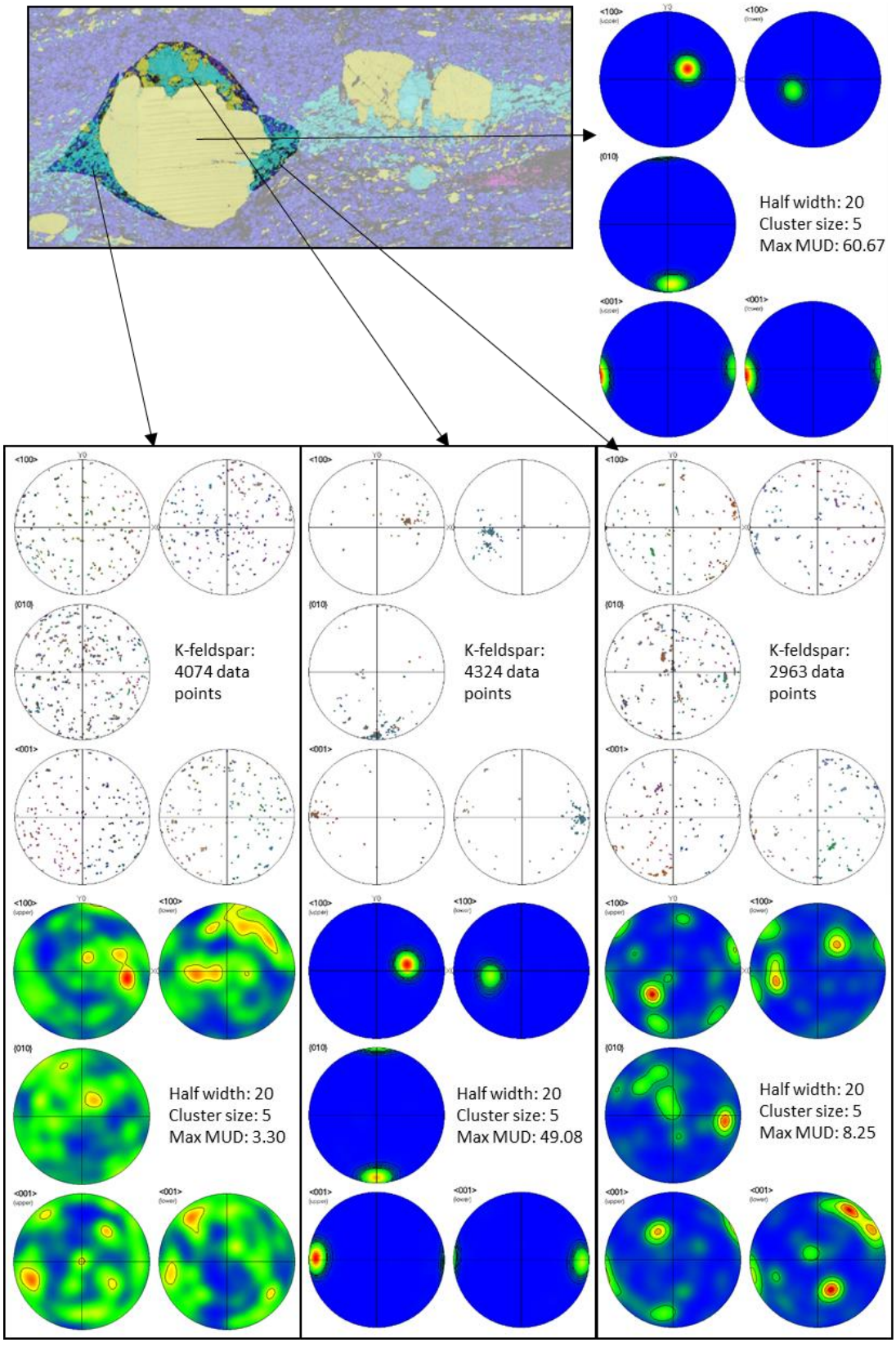


***Figure 8.7:*** *EBSD phase map and lower hemisphere equal area pole figures generated from the plagioclase porphyroclast and the associated fine-grained K-feldspar shown. The K-feldspar from the fractured upper part of the porphyroclast has an almost identical crystallographic orientation to that of the plagioclase porphyroclast itself. The K-feldspar grains in the pressure shadows have more distributed orientations which are not as clearly related to that of the porphyroclast. Half widths and cluster sizes used for contouring are given in degrees.*

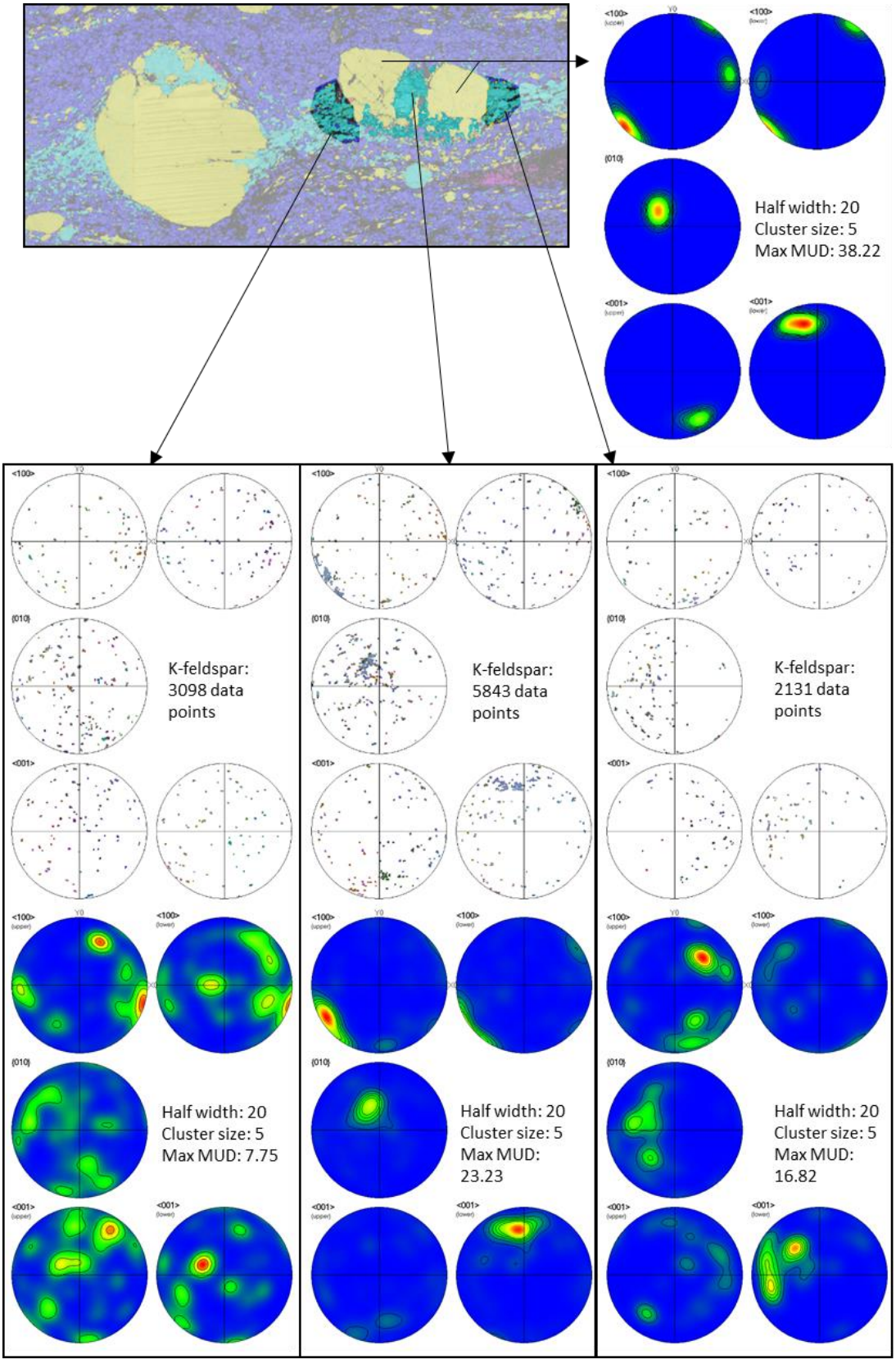


***Figure 8.8:*** *EBSD phase map and lower hemisphere equal area pole figures from a plagioclase porphyroclast and associated fine-grained K-feldspar shown. The K-feldspar from the central section along the fracture between two pieces of porphyroclast has an almost identical crystallographic orientation to that of the two sections of plagioclase porphyroclast. The K-feldspar grains in the pressure shadows either side of the two porphyroclast fragments display much less similarity to the plagioclase orientation. Half widths and cluster sizes used for contouring are given in degrees.*

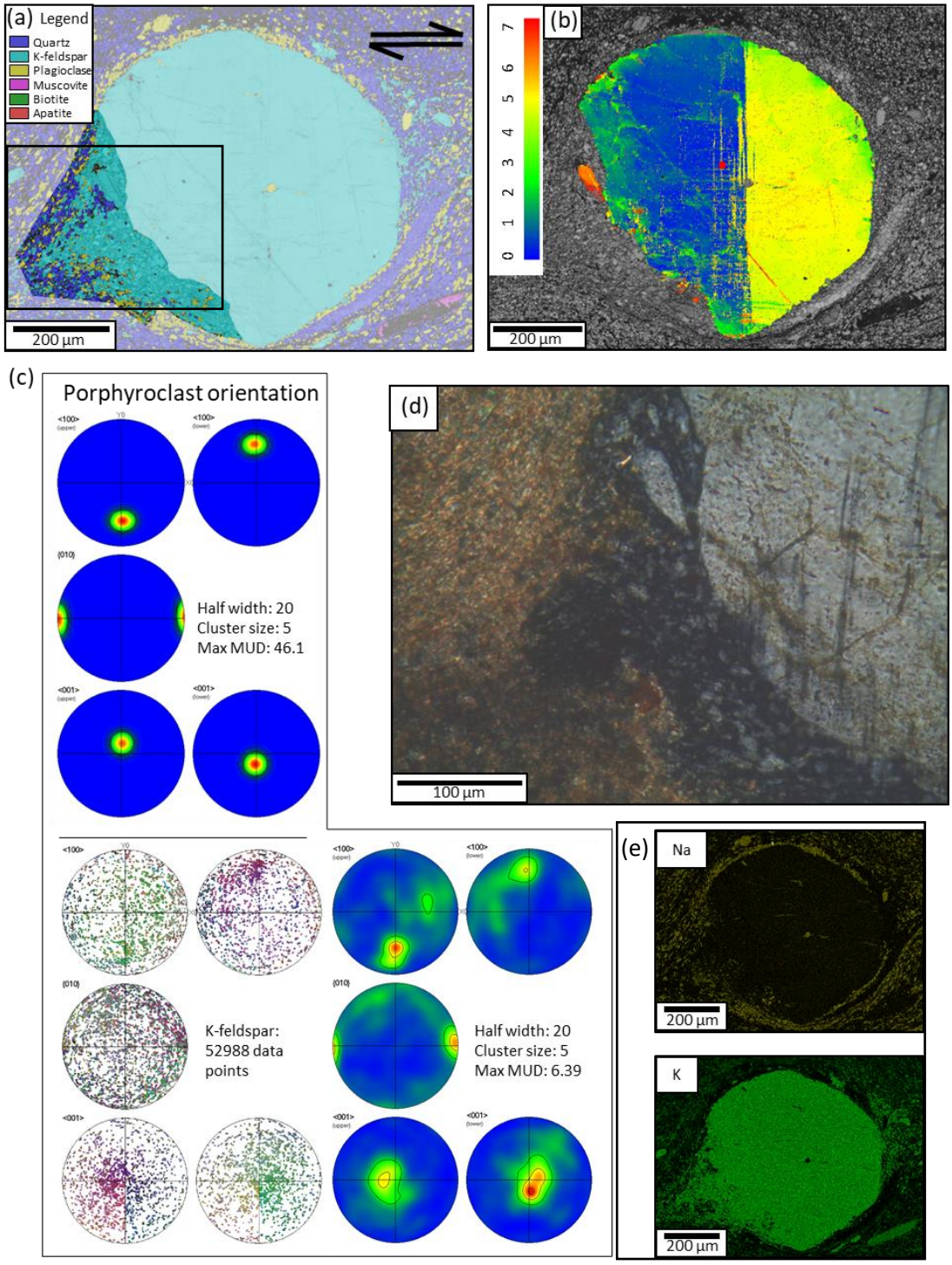


***Figure 8.9:*** *(a) EBSD phase map showing an increased presence of plagioclase along the upper and lower parts of the grain as well as new, fine K-feldspar within the pressure shadows especially at the lower left of the grain. (b) Texture component map revealing a sharp, angular boundary and an increased degree of intracrystalline distortion along the left edge of the porphyroclast with misorientations of up to 5°. The reference point for misorientations is given by the red spot. (c) Lower hemisphere equal area pole figures of the K-feldspar porphyroclast orientation and of the K-feldspar grains in the pressure shadow to the lower left of the porphyroclast. Although there is a spread of different orientations represented by grains in the pressure shadow, their orientations are dominated by that of the porphyroclast. (d) Cross polarised light optical micrograph of the region indicated by the box in (a) showing angular, fractured fragments of K-feldspar in the pressure shadow. (e) EDS element maps of the area giving the relative distribution of Na and K. Step size in the maps is 1 µm and the grid is 960 x 720 pixels. Half widths and cluster sizes used for contouring are given in degrees.*

present within the pressure shadow. Several of the K-feldspar grains in the pressure shadow are larger and more elongate than the majority of the pressure shadow grains (up to 80 µm x 20 µm) and also possess irregular, angular boundaries (Fig. 8.9d). EDS element maps of Na and K show that the pressure shadow at the opposite boundary of the porphyroclast also contains fine K-feldspar grains but in lower abundance, while fine plagioclase grains are most abundant at high stress interfaces (upper left and lower right) (Fig. 8.9e).

Figure 8.10c displays pole figures which show a strong relationship between the orientation of new plagioclase grains decorating the high stress boundaries of a K-feldspar porphyroclast and the orientation of the porphyroclast itself. The majority of these plagioclase grains are in contact with, or very close to the porphyroclast, with a small number protruding into the porphyroclast itself. Na and K EDS element maps of the area (Fig. 8.10d) show how the distribution of fine grains of plagioclase and K-feldspar around the porphyroclast is strongly influenced by the inferred stress field. There is a faint linear boundary between fine-grained plagioclase (Na-rich phase) and fine-grained K-feldspar (K-rich phase) evident within the tails of the porphyroclast (Fig. 8.10d).

Fine K-feldspar is concentrated in all pressure shadows within the sample, as shown in Figure 8.11, regardless of the mineral phase that constitutes the porphyroclast. The K-feldspar porphyroclast in Figure 8.11 is decorated along half of its surface with fine plagioclase grains, including within part of a pressure shadow. In this case a K-feldspar rich pressure shadow is still present but it is on the outer side of the polycrystalline plagioclase rim, forming a microstructure that is unusual in this ultramylonite, where a band of fine-grained plagioclase is bordered on one side by the porphyroclast and on the other by fine-grained K-feldspar. The pole figures of the fine-grained new plagioclase grains show a weak association with the orientation of the K-feldspar porphyroclast (Fig. 8.12). The K-feldspar grains in the left-side pressure shadow – those separated from the porphyroclast by the plagioclase grains – also display only a small correlation with the orientation of the porphyroclast itself. However, the orientations of the fine-grained K-feldspar in the right-side pressure shadow and tail possess a stronger similarity to the orientation of the porphyroclast (Fig. 8.12).

### 8.4.3. Composition of coarse and fine feldspar

In order to further test the hypothesis that the fine grains of plagioclase and K-feldspar formed predominantly by precipitation rather than dynamic recrystallisation via crystal plastic processes, electron probe microanalysis (EPMA) was conducted to determine the chemical compositions of the new and old feldspar populations. The locations of EPMA point

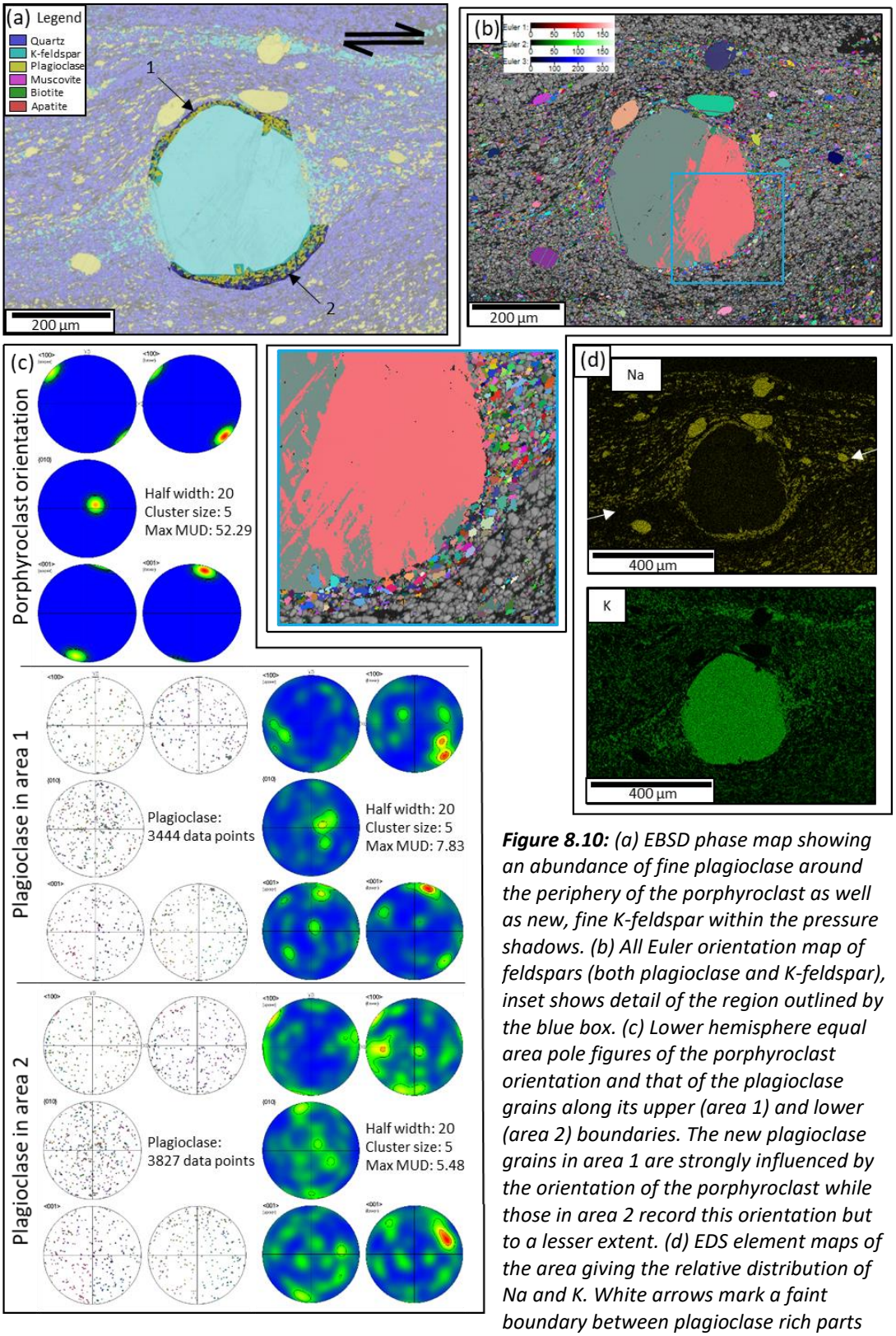


***Figure 8.10:*** *(a) EBSD phase map showing an abundance of fine plagioclase around the periphery of the porphyroclast as well as new, fine K-feldspar within the pressure shadows. (b) All Euler orientation map of feldspars (both plagioclase and K-feldspar), inset shows detail of the region outlined by the blue box. (c) Lower hemisphere equal area pole figures of the porphyroclast orientation and that of the plagioclase grains along its upper (area 1) and lower (area 2) boundaries. The new plagioclase grains in area 1 are strongly influenced by the orientation of the porphyroclast while those in area 2 record this orientation but to a lesser extent. (d) EDS element maps of the area giving the relative distribution of Na and K. White arrows mark a faint boundary between plagioclase rich parts and K-feldspar rich parts of the porphyroclast tails. Step size in the maps is 1 µm and the grid is 960 x 720 pixels. Half widths and cluster sizes used for contouring are given in degrees.*

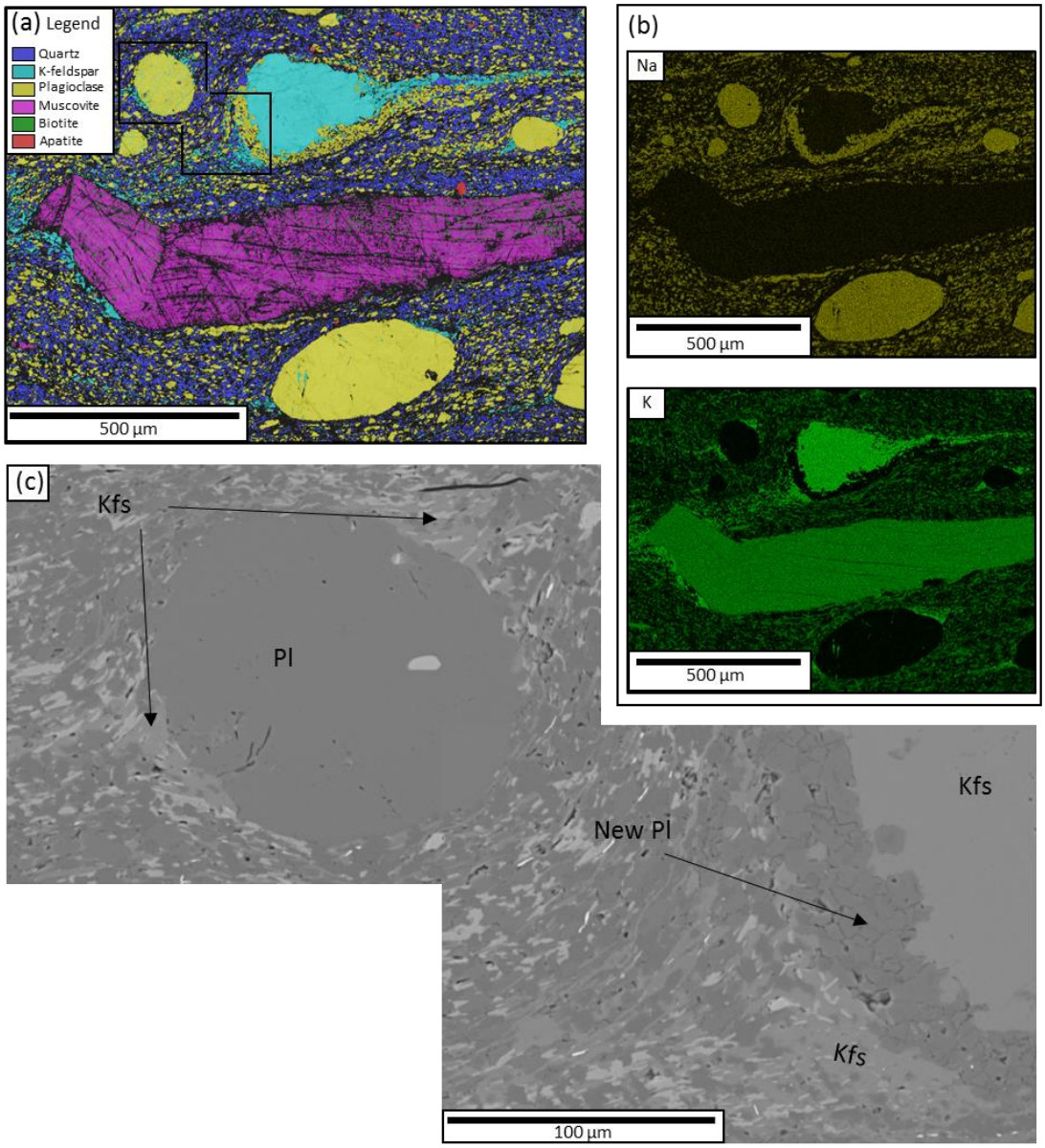


***Figure 8.11:*** *(a) EBSD phase map in which K-feldspar is seen in the pressure shadows of all porphyroclasts regardless of porphyroclast mineralogy. The K-feldspar porphyroclast towards the top of the area is interesting in that plagioclase is present across the entire bottom part even though in the lower left K-feldspar is still the main phase in the pressure shadow. Step size in the map is 0.75 µm and the grid is 1664 x 1248 pixels (b) EDS element maps of the area giving the relative distribution of Na and K. The distribution of plagioclase around the K-feldspar porphyroclast and the presence of K-feldspar in all the pressure shadows is evident in the maps of Na and K respectively. (c) SEM BSE image of the area specified in (a) showing concentrations of fine-grained K-feldspar in pressure shadows as well as a 'rim' of fine-grained plagioclase around the lower left part of the K-feldspar porphyroclast separating the K-feldspar in the pressure shadow here from the boundary of the porphyroclast itself.*

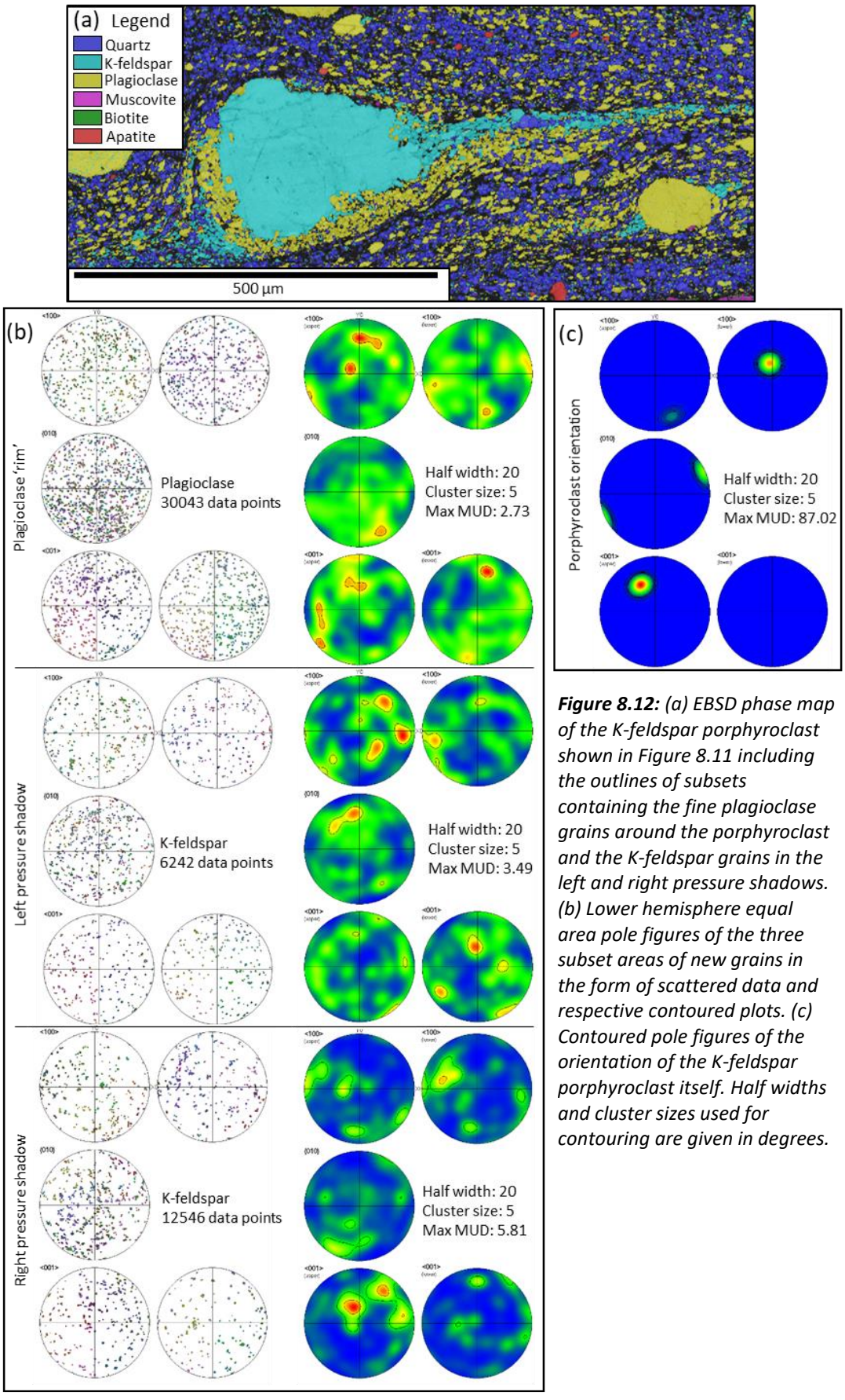


***Figure 8.12:*** *(a) EBSD phase map of the K-feldspar porphyroclast shown in Figure 8.11 including the outlines of subsets containing the fine plagioclase grains around the porphyroclast and the K-feldspar grains in the left and right pressure shadows. (b) Lower hemisphere equal area pole figures of the three subset areas of new grains in the form of scattered data and respective contoured plots. (c) Contoured pole figures of the orientation of the K-feldspar porphyroclast itself. Half widths and cluster sizes used for contouring are given in degrees.*

analyses are shown in Supplementary Figure S8.2 with the results given in Supplementary Tables S8.1, S8.2, S8.3 and S8.4. These results are plotted on a feldspar ternary diagram in Figure 8.13. The average compositions of each population (old K-feldspar, new K-feldspar, old plagioclase and new plagioclase) are given in Table 8.1. From these data it can be seen that both old and new K-feldspar populations have an average composition of approximately $Or_{95}$ $Ab_{5}$ although on average there is a ~1% increase in the purity of new K-feldspar grains which possess an albite content ~1% lower than the older porphyroclasts. While the spread of compositions for old K-feldspar is relatively large (from $Or_{88.2}$ to $Or_{98.1}$) the range of measured compositions for new K-feldspar is clustered between $Or_{92.4}$ and $Or_{96.5}$. In the case of plagioclase, the new grains form a compositional population that is clearly distinct from analyses taken within old plagioclase porphyroclasts. The porphyroclasts have a mean composition of $Ab_{76}$ $An_{23}$ with a range from $Ab_{74.7}$ to $Ab_{77.1}$ whereas the new plagioclase grains are more albitic with a mean composition of $Ab_{81}$ $An_{18}$ and a range from $Ab_{79.6}$ to $Ab_{82.9}$. An EPMA element map of Wt% CaO covering the same area in which many of the point analyses

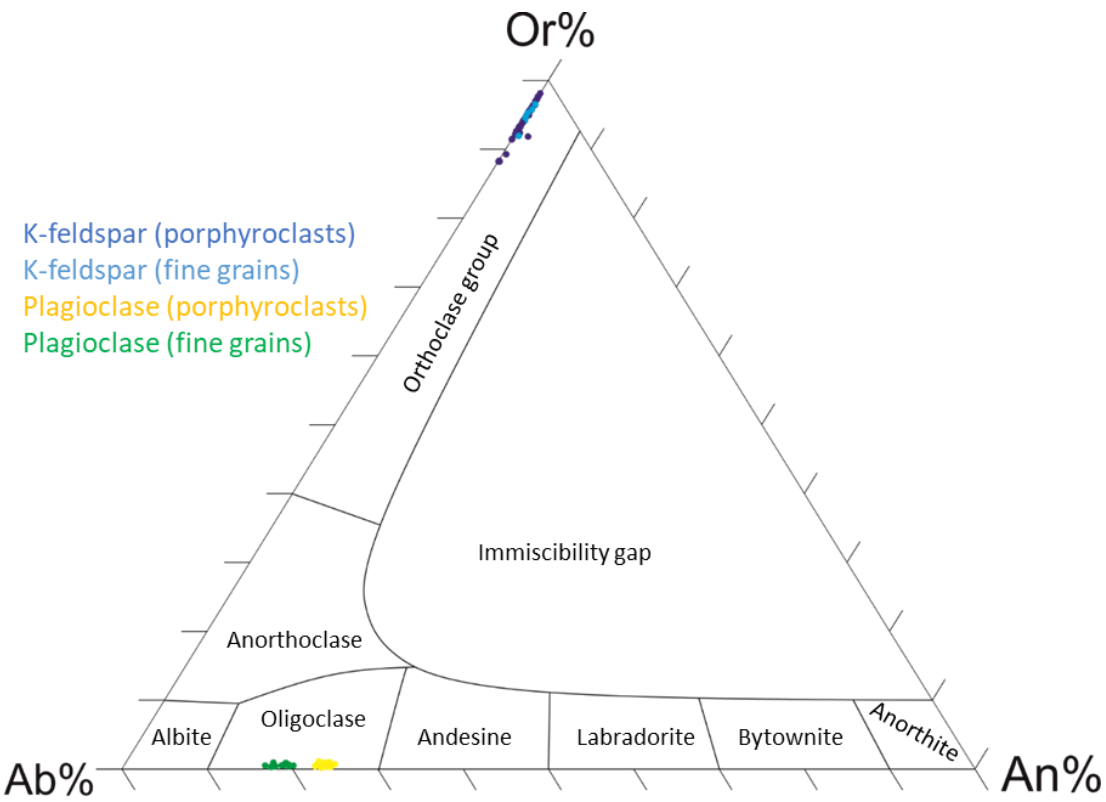


***Figure 8.13:*** *Feldspar ternary diagram displaying the EPMA point analysis data recorded in tables 1-4 and colour coded by type of feldspar grain. Kfs porphyroclasts show a spread in composition between approximately 2% to 12% Ab. New, fine grained Kfs are characterised by a more homogeneous composition clustering around 5% Ab. The plagioclase on the other hand records two distinct populations of old and new grains. Whilst both populations plot within the oligoclase field, the new grains have compositions between 16% and 20% An, while the older porphyroclast grains have compositions between 22% and 25% An. This plot was produced using the TRI-POLT template of Graham and Midgley (2000).*

***Table 8.1:*** *Mean Compositions*

| Wt% | K-feld OLD | K-feld NEW | Plag OLD | Plag NEW |
|---|---|---|---|---|
| FeO | 0.10 | 0.76 | 0.03 | 0.53 |
| $K_2O$ | 15.50 | 14.54 | 0.11 | 0.08 |
| $Al_2O_3$ | 18.64 | 17.71 | 23.73 | 19.62 |
| $Na_2O$ | 0.63 | 0.48 | 8.99 | 8.21 |
| MnO | 0.00 | 0.01 | 0.00 | -0.01 |
| CaO | 0.01 | 0.05 | 4.98 | 3.30 |
| $SiO_2$ | 63.62 | 64.59 | 61.78 | 67.10 |
| MgO | 0.01 | 0.26 | 0.01 | 0.01 |
| $TiO_2$ | 0.00 | 0.08 | 0.00 | 0.00 |
| Total | 98.38 | 98.40 | 99.50 | 98.72 |
| n | 53 | 6 | 24 | 14 |
| Number of cations on the basis of eight oxygens | | | | |
| Fe | 0.00 | 0.03 | 0.00 | 0.02 |
| K | 0.93 | 0.87 | 0.01 | 0.00 |
| Al | 1.03 | 0.98 | 1.25 | 1.03 |
| Na | 0.06 | 0.04 | 0.78 | 0.71 |
| Mn | 0.00 | 0.00 | 0.00 | 0.00 |
| Ca | 0.00 | 0.00 | 0.24 | 0.16 |
| Si | 2.98 | 3.03 | 2.75 | 3.00 |
| Mg | 0.00 | 0.02 | 0.00 | 0.00 |
| Ti | 0.00 | 0.00 | 0.00 | 0.00 |
| Total | 5.01 | 4.97 | 5.02 | 4.93 |
| An% | 0.07 | 0.25 | 23.31 | 18.11 |
| Ab% | 5.83 | 4.73 | 76.07 | 81.37 |
| Or% | 94.10 | 95.02 | 0.61 | 0.53 |

were collected and overlapping with the area shown in Figure: 8.11, displays a subtle variation in the composition of plagioclase porphyroclasts relative to finer plagioclase grains (Fig. 8.14).

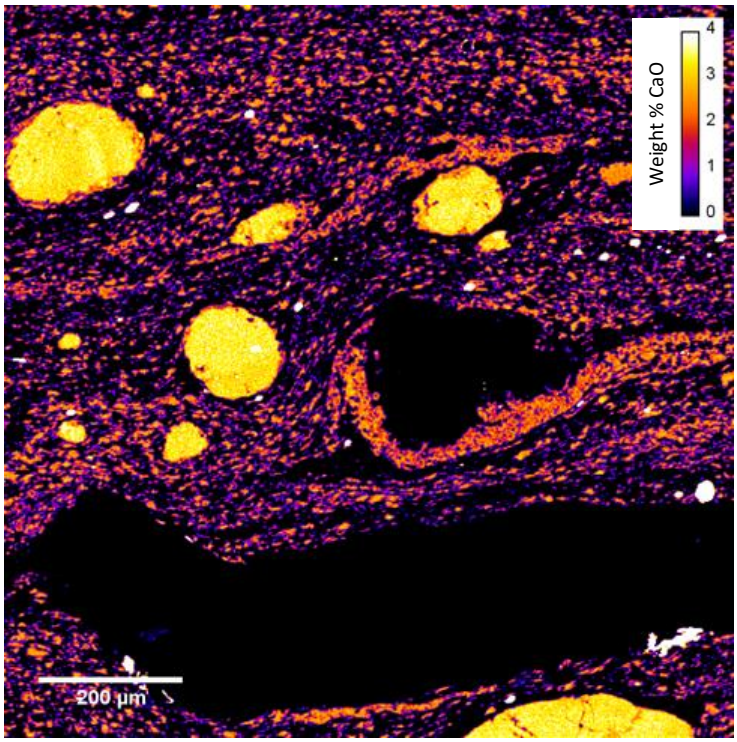


***Figure 8.14:*** *EPMA element map of weight % CaO. There is a subtle difference in the Plagioclase compositions with the porphyroclasts possessing slightly higher CaO content than the finer grained plagioclase associated with the K-feldspar porphyroclast and within the matrix.*

### 8.4.4. Association of Plagioclase and K-feldspar in lower strain samples

Samples POG5 and POG7 represent lower strain specimens from the same transect of the Pogallo shear zone and are of similar orthogneiss protolith to the main subject of this study, sample POG3. EBSD maps collected from these samples (Figs. 8.15 and 8.16) highlight a close association between coarse and fine grains of plagioclase and K-feldspar throughout the up-strain evolution of this mylonite. In both cases coarse grains which have undergone brittle fracturing are rimmed and, in some cases, surrounded by fine grains of both plagioclase and K-feldspar. This is especially evident in the EDS element maps of Na and K (Figs 8.15c and 8.16c) which highlight the distribution of plagioclase and K-feldspar respectively. Fine grains are less common than in POG3 and there is less of a clear spatial relationship between the distribution of plagioclase and K-feldspar, and the orientation of principle stress axes. However, the presence of fine grains of one feldspar in association with porphyroclasts of another hints at the role of chemical reactions and dissolution precipitation processes in addition to the brittle deformation that is evident from the angular shape of fractured feldspar grains.

## 8.5. Discussion

### 8.5.1. Interpretation of microstructural observations

The distribution of fine-grained plagioclase and K-feldspar around porphyroclasts of both feldspar phases in the samples used in this study is strongly related to the orientations of the principle stress axes acting on the mylonite during deformation. Where fine grained K-feldspar is present in pressure shadows of K-feldspar porphyroclasts (e.g. Fig. 8.9) it's formation could potentially be explained by brittle fracture or dynamic recrystallisation of the parent clast, with subsequent fine grains becoming dispersed into the matrix via the porphyroclast tails. However, this explanation does not address the occurrence of K-feldspar in the pressure shadows of plagioclase grains nor for the formation of plagioclase along the high stress boundaries of K-feldspar porphyroclasts. The intracrystalline distortion observed within K-feldspar porphyroclasts (Figs. 8.9 and 8.10) is not indicative of dynamic recrystallisation and extensive dislocation motion. It is however compatible with significant brittle fracturing of the porphyroclasts (particularly in the porphyroclast in Fig. 8.9). Some of the fine grains in this instance likely represent fragments of the parent grain as suggested by the strong correlation in orientation of these grains with the porphyroclast (Fig. 8.9c). This interpretation is supported by abundant microstructural evidence for brittle fracturing in

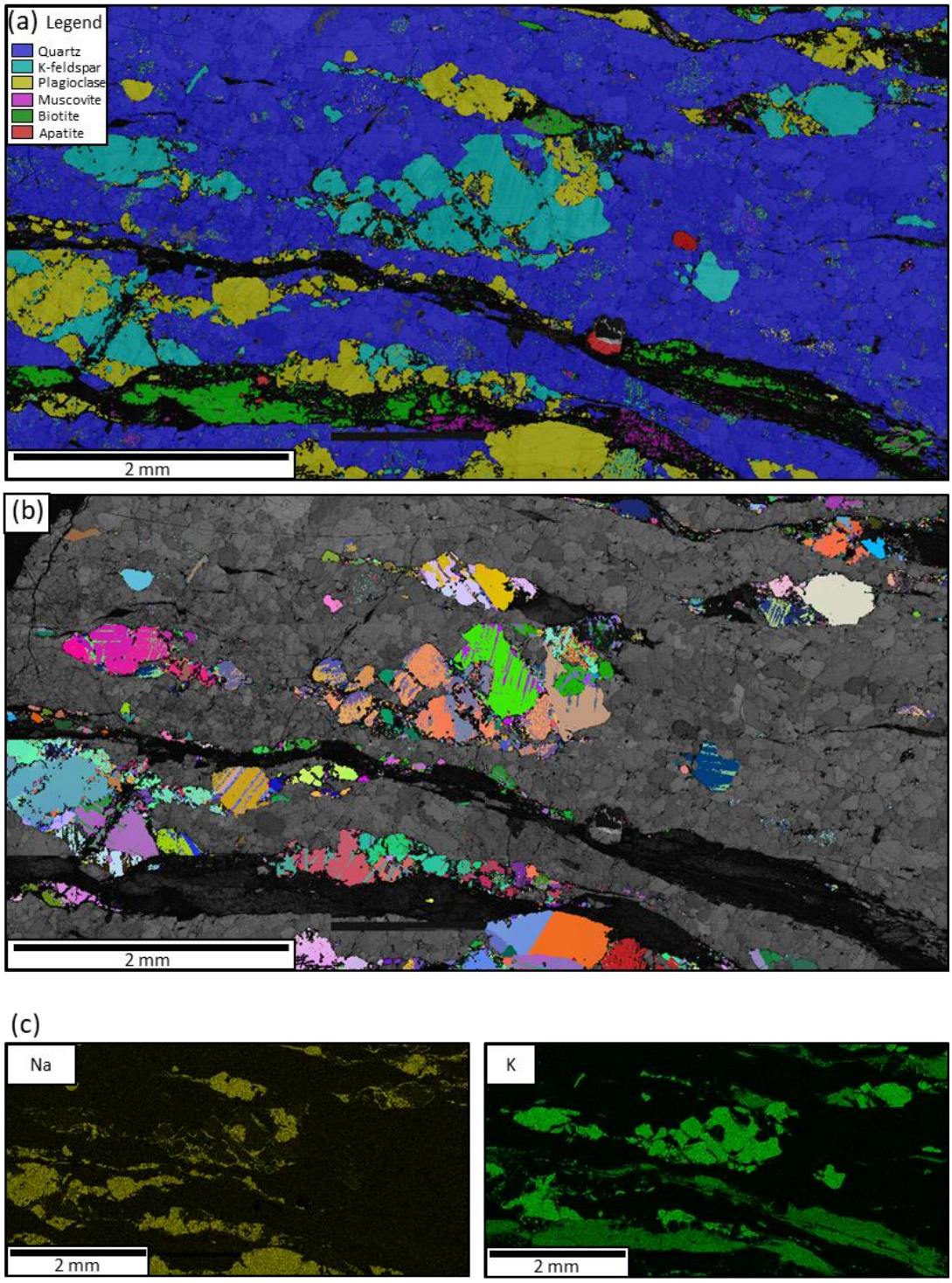


***Figure 8.15:*** *EBSD data from sample POG7, a granitic protomylonite from the same section of the Pogallo line as POG3, showing a close association between plagioclase and K-feldspar in equivalent lower strain versions of POG3. (a) EBSD phase map. (b) All Euler colour orientation map of feldspar phases. (c) EDS element maps. The Na map, when compared to the K map, shows a clear presence of fine plagioclase grains associated with the boundaries of K-feldspar porphyroclasts. Step size in the maps is 5 µm and the grid is 1372 x 692 pixels.*

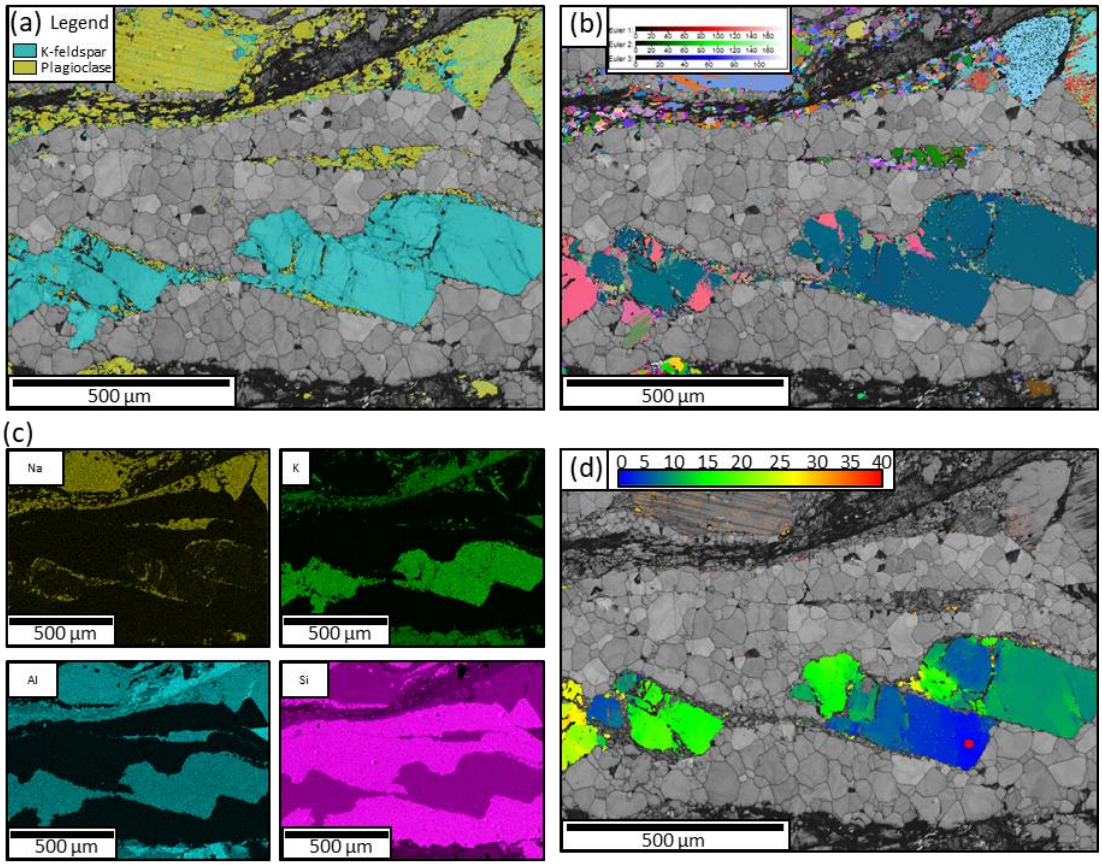


***Figure 8.16:*** *EBSD data from sample POG5, a lower strain granitic mylonite from the same section of the Pogallo line as POG3, showing a close association between plagioclase and K-feldspar in equivalent lower strain versions of POG3. (a) EBSD phase map of showing feldspar phases. (b) All Euler colour orientation map of feldspar phases. (c) EDS element maps. The Na map, when compared to the K map, highlights the presence of fine plagioclase grains associated with the boundaries of K-feldspar porphyroclasts. (d) Texture component map showing a high degree of intracrystalline strain associated with brittle fracturing of K-feldspar porphyroclasts within a viscously deforming quartz domain. The reference point for misorientations is given by the red spot. Step size in the maps is 1.5 µm and the grid is 832 x 624 pixels.*

both feldspar phases in all studied samples. However, the equant nature and uniform fine grain size of most pressure shadow grains, coupled with the presence of K-feldspar in pressure shadows of other phases, strongly suggests that precipitation at sites of low stress is an important mechanism for the formation of fine K-feldspar grains in these mylonites. Indeed dissolution-precipitation creep would be greatly enhanced by the simultaneous action of brittle fracturing as the latter creates fluid pathways and increases the surface area available for reaction. In the lower-strain, earlier stages of deformation fracturing is likely to have been the principle way in which fluids were able to infiltrate the system and enable dissolution-precipitation processes to occur. The close association of fine plagioclase within clear fractures in K-feldspar porphyroclasts, (and vice-versa) shown in Figs. 8.15 and 8.16, is evidence that dissolution-precipitation was limited to these fluid-bearing fractures within the lower strain mylonites and protomylonites. Thus, the two processes of brittle fracturing and dissolution-precipitation creep are likely to work in tandem to produce fine-grained K-feldspar not just in pressure shadows but also within highly fractured regions of K-feldspar and plagioclase porphyroclasts where fracturing forms dilatant sites at which K-feldspar precipitates. This is supported by the strong relationship between the orientation of fine K-feldspar grains and the K-feldspar porphyroclast in Figure 8.9 which suggests epitaxial growth of new K-feldspar nucleating at the boundaries of fractured fragments of the porphyroclast or of the porphyroclast itself (Menegon, Pennacchioni and Spiess, 2008; Ceccato *et al.*, 2018). A similarly strong correlation exists between the orientation of fine K-feldspar and plagioclase porphyroclasts in fractured sites (Figs. 8.7 and 8.8). Here, this is indicative of topotaxy, whereby the K-feldspar has grown directly at the expense of plagioclase or nucleated around plagioclase fragments with similar orientations to the host porphyroclast. This relationship is evident to varying extents in the K-feldspar grains formed in pressure shadows. This may be due either to new grains rotating, via granular flow in the matrix, away from the orientation in which they nucleated, or to the precipitation of K-feldspar within pressure shadows but not directly at the porphyroclast interface. New K-feldspar which topotactically replaces plagioclase in fractured sites within porphyroclasts and that which forms between two close porphyroclasts, is also generally coarser grained than the K-feldspar precipitated in other pressure shadows (e.g. Fig. 8.6). This may occur due to these sites being more protected from the deforming matrix, enabling a small number of nuclei to grow larger, whereas grains in the tails are dragged out of the pressure shadows, via granular flow in the matrix, before significant growth can take place. A topotactic relationship is also evident where plagioclase grains decorate the $\sigma_1$ facing boundaries of K-feldspar porphyroclasts (Fig.

8.10) strongly supporting growth of the plagioclase via a reaction at the expense of K-feldspar in these sites (Ceccato *et al.*, 2018).

The EPMA results reinforce the interpretations, drawn from microstructural observations that the fine-grained plagioclase, present along the boundaries of K-feldspar porphyroclasts, has nucleated as new grains and does not represent mechanically disaggregated pieces of coarser plagioclase porphyroclasts. The fact that the composition of fine feldspars is different to that of the coarser porphyroclasts adds weight to the argument for dissolution and precipitation processes (Fukuda *et al.*, 2012; Fukuda and Okudaira, 2013). If the finer grains were produced by formation and rotation of subgrains from a porphyroclast, then the composition should not have changed. Furthermore, the approximately 5% higher albite content suggests the new grains grew at lower temperature than the porphyroclasts, although the retention of substantial Ca within the plagioclase lattice precludes growth of new grains at greenschist facies conditions (Carpenter, 1994). The increase in Ab% recorded in the plagioclase populations may be associated with the similar (but smaller) decrease in Ab% within the K-feldspar populations which may represent a transfer of Na from K-feldspar into plagioclase across the feldspar miscibility gap (Fig. 8.13). That said, these results are inconclusive with regard to the origin of the fine K-feldspar grains as the populations are different but not clearly distinct.

### 8.5.2. Constituent reactions for incongruent pressure solution

Similar microstructures to the ones described here were reported in granitoid mylonites recently by Ceccato *et al.*, (2018) and Cisneros-Lazaro, Miller and Baumgartner, (2019), and less recently by Simpson and Wintsch, (1989), who proposed a model in which myrmekite formed at the expense of K-feldspar along the $\sigma_1$ facing grain boundaries of K-feldspar porphyroclasts by means of cation exchange. Similar to this study they observed plagioclase along the high stress boundaries of K-feldspar megacrysts in granitic mylonites, as well as the precipitation of K-feldspar in pressure shadows. However, they did not observe replacement of plagioclase by K-feldspar (though they speculated that this may occur). Simpson and Wintsch (1989) introduced three key reactions which can explain the replacement and precipitation of feldspars at different places around porphyroclasts and within the matrix, based on the model of Becke, (1908) and modifications by Phillips, (1980). In the following sections these reactions are used and expanded upon to produce a model of incongruent pressure solution that explains the microstructures described earlier in this study. Advancing beyond the work of Simpson and Wintsch, (1989) the driving forces for these reactions and their relationship with stress will be examined. Critically the reactions all require the

presence of aqueous cations within a fluid phase. They are shown here using albite (Ab) and anorthite (An) end-members of plagioclase for simplicity although the actual reactions will involve a combination of the two based on the plagioclase composition. They are:

1) The reaction of K-feldspar with $Na^+$ and $Ca^{2+}$ ions to form plagioclase, $K^+$ ions and quartz;

$$Na^+ + KAlSi_3O_8 = NaAlSi_3O_8 + K^+$$

and

$$Ca^{2+} + 2KAlSi_3O_8 = CaAl_2Si_2O_8 + 2K^+ + 4SiO_2 \quad (8.1)$$

2) The reaction of $K^+$ ions with muscovite and quartz in the matrix to form K-feldspar;

$$2K^+ + KAl_2[Si_3AlO_{10}](OH)_2 + 6SiO_2 = 3KAlSi_3O_8 + 2H^+ \quad (8.2)$$

3) The reaction of $Na^+$ and $Ca^{2+}$ ions with matrix muscovite and quartz to form plagioclase;

$$3Na^+ + KAl_2[Si_3AlO_{10}](OH)_2 + 6SiO_2 = 3NaAlSi_3O_8 + K^+ + 2H^+$$

and

$$3Ca^{2+} + 2KAl_2[Si_3AlO_{10}](OH)_2 = 3CaAl_2Si_2O_8 + 2K^+ + 4H^+ \quad (8.3)$$

Reaction 1 is the reaction that accounts for the growth of plagioclase at the expense of K-feldspar. This reaction has been cited for the formation of myrmekite at the expense of K-feldspar previously (Simpson and Wintsch, 1989; Menegon *et al.*, 2006) and requires the presence of a fluid phase to transport cations. This reaction is responsible for the formation of plagioclase along the $\sigma_1$ facing edges of k-feldspar porphyroclasts (Figs. 8.3, 8.4, and 8.9-8.12). In this reaction quartz is only produced by the reaction of $Ca^{2+}$ ions so the role of quartz in the reaction is proportional to the anorthite content of the product plagioclase. This is known as the quartz proportionality (Phillips and Ransom, 1968; Ashworth, 1972). Reaction 1 consumes aqueous $Na^+$ and $Ca^{2+}$ ions but increases the activity of $K^+$ ions in solution. There is evidence that the reverse of reaction 1 occurs along the $\sigma_3$ facing edges of plagioclase porphyroclasts, with the generation of fine K-feldspar at the expense of plagioclase within pressure shadows (Figs. 8.5 and 8.6). This is also likely to be the process responsible for the topotactic growth of K-feldspar within fractures and dilatant sites of plagioclase porphyroclasts (Figs. 8.5 and 8.6). Reaction 2 is different to reaction 1 in that it enables the production of K-feldspar without requiring the consumption of any plagioclase. This may be

the process by which K-feldspar precipitates within pressure shadows away from the surfaces of porphyroclasts and requires aqueous $K^+$ ions to react with quartz and muscovite in the matrix. An example of this is the pressure shadow in Fig. 8.3b which contains biotite in the same abundance (and texture) as the rest of the matrix and has a sharply defined boundary with the porphyroclast rather than a reactive one. This is evidence that the K-feldspar in this pressure shadow has grown at the expense of the other matrix phases excluding biotite (namely quartz, muscovite and plagioclase). The edges of the K-feldspar occurrence in this pressure shadow can be viewed as the region in which the activity of aqueous $K^+$ ions perturbed the local equilibrium sufficiently to precipitate K-feldspar at the expense of quartz and muscovite via reaction 2. This reaction is seen within the pressure shadows of the majority of porphyroclasts in the sample, regardless of the porphyroclast mineralogy (as seen in Fig. 8.11). $Na^+$ and $Ca^{2+}$ ions play no role either as reactants or products in this reaction. Reaction 3 is the means by which fine plagioclase grains could precipitate from the matrix phases at sites where the activity of $Na^+$ and $Ca^{2+}$ ions rise above that of the local equilibrium. Importantly, while reaction 3 does not involve the consumption of K-feldspar, it would nevertheless increase the activity of aqueous $K^+$ ions due to the consumption of muscovite. There is, however, a paucity of evidence for reaction 3 within the studied microstructure, the potential reason for this is discussed below.

### 8.5.3. Molar volume considerations and chemical potentials

Table 8.2 displays molar volume calculations for the reactions discussed above using mineral molar volumes from Robie et al. (1967). In both reactions in which K-feldspar is formed (reaction 2 and the reverse of reaction 1), the molar volume of the solid products is greater than that of the solid reactants, resulting in a volume increase. This is part of the explanation for why these reactions (and therefore the precipitation of K-feldspar) appear to be favourable within low stress sites, such as pressure shadows, fractures and sites of dilation, throughout the microstructure. In the forward version of reaction 1 in which plagioclase is

***Table 8.2.*** *Molar volume calculations*

| Phase | K-spar | Albite | Anorthite | Quartz | Muscovite |
|---|---|---|---|---|---|
| **Molar Volume (V)** | 10.893 | 10.043 | 10.079 | 2.269 | 14.081 |

(kJ $kbar^{-1}$) from Robie et al. (1967)

| Reaction | 1 (Ab) | 1 (An) | 2 | 3 (Ab) | 3 (An) |
|---|---|---|---|---|---|
| **V of Reactants** | 10.893 | 21.786 | 27.695 | 27.695 | 28.162 |
| **V of Products** | 10.043 | 19.155 | 32.679 | 30.129 | 30.237 |
| **ΔV** | -0.85 | -2.631 | 4.984 | 2.434 | 2.075 |

produced, the overall molar volume change from reactants to products is negative and the reaction may therefore be favoured in sites of high normal stress. However, as this reaction requires the consumption of K-feldspar, it is limited to the high normal stress regions of K-feldspar porphyroclasts. As a result, plagioclase is observed growing at the expense of K-feldspar at the edges of porphyroclasts facing $\sigma_1$ (Figs. 8.3, 8.4, and 8.9-8.12). Menegon et al. (2006) also identified a volume decrease in this reaction as an important factor in its distribution. The precipitation of plagioclase from quartz and muscovite in the matrix (reaction 3), by contrast, results in a volume increase, and is therefore not favourable at sites of high normal stress. This explains why fine, new plagioclase will decorate the σ1-facing edges of K-feldspar porphyroclasts (through reaction 1) but does not necessarily occur in all high normal stress sites around all porphyroclasts, while K-feldspar is present in all pressure shadows regardless of the minerals (as it can precipitate either directly from plagioclase or from other phases in the matrix).

Reaction 1 can also be expressed in terms of the chemical potentials of the components of the reaction. If we assume a plagioclase composition that is representative of the values measured in this study ($Ab_{80}$ $An_{20}$) then reaction 1 would take the form:

$$4Na^+ + Ca^{2+} + 6KAlSi_3O_8 \rightarrow 4NaAlSi_3O_8 + CaAl_2Si_2O_8 + 4SiO_2 + 6K^+ \quad (8.4)$$

The chemical potentials ($\mu^x$) can then be written as:

$$4\mu^{Na^+} + \mu^{Ca^{2+}} + 6\mu^{Ksp} = 4\mu^{Alb} + \mu^{An} + 4\mu^{Qtz} + 6\mu^{K^+} \quad (8.5)$$

To find whether there is a driving force for the forward reaction (removing $Na^+$ and $Ca^{2+}$ ions from solution and putting $K^+$ ions into solution) under high normal stress, this can first be rearranged with the aqueous components on one side and the solid components on the other:

$$4\mu^{Na^+} + \mu^{Ca^{2+}} - 6\mu^{K^+} = 4\mu^{Alb} + \mu^{An} + 4\mu^{Qtz} - 6\mu^{Ksp} \quad (8.6)$$

The chemical potential at the surface of a grain under anisotropic stress is given by:

$$\mu = F + \sigma_n \cdot V \quad (8.7)$$

Where μ is the chemical potential in an adjacent fluid or grain boundary, F is the specific Helmholtz free energy of the solid, $\sigma_n$ is the component of normal stress across the boundary and V is the specific volume of the solid (McLellan, 1980; Wheeler, 1992). Therefore, to find the chemical potential of cations in the fluid at the boundary of a porphyroclast undergoing reaction 1, we can use the molar volume of the solid phases involved in the reaction:

$$4\mu^{Na^+} + \mu^{Ca^{2+}} - 6\mu^{K^+} = F + \sigma_n \cdot \left(4V^{Alb} + V^{An} + 4V^{Qtz} - 6V^{Ksp}\right)$$

$$= F + \sigma_n \cdot (\{4 \cdot 10.043\} + 10.079 + \{4 \cdot 2.269\} - \{6 \cdot 10.893\})$$

$$= F - 6.031\sigma_n \quad (8.8)$$

The negative value of V means that at high values of $\sigma_n$ (at the grain boundaries facing $\sigma_1$), μ will be lower than at low values of $\sigma_n$ (at grain boundaries facing $\sigma_3$). Therefore, the reaction will proceed forwards down a chemical potential gradient, precipitating plagioclase at the expense of K-feldspar at high stress interfaces. The molar volume calculations presented in Table 2 show that all the other reactions involve an increase in molar volume, and hence, would not proceed forwards under conditions of high normal stress.

### 8.5.4. Driving forces and ionic activities

The mechanism of the reactions described above is essentially ion exchange between solid phases and cations in aqueous solution (Simpson and Wintsch, 1989; Menegon *et al.*, 2006). The fact that the direction of reaction 1 is reversed at locations as little as tens of microns apart, is evidence of significant gradients in the activities of the respective cations locally within the fluid and around grains. The forward or backward direction of reactions 1 and 2 is influenced by the activities of the relevant cations in solution. The equilibrium constant of the reaction 1 for the Albite end member ($K_1$) is given by:

$$K_1 = \frac{(a_{Alb})\cdot(a_{K^+})}{(a_{Ksp})\cdot(a_{Na^+})} \quad (8.9)$$

The forward reaction (forming plagioclase at the expense of K-feldspar) can be driven by an increase in $a_{Na}^+$ (and $a_{Ca}^{2+}$ when the anorthite component is considered) while the reverse (forming K-feldspar at the expense of plagioclase) is driven by an increase in $a_K^+$.

The gradients in these activities is likely to be related to differences in chemical potential. The chemical potential of phase A ($\mu_A$) is a function of the activity of that phase ($a_A$) such that:

$$\mu_A = \mu_0 + RTln(a_A) \quad (8.10)$$

where $\mu_0$ is the standard chemical potential for the pure phase, R is the gas constant (8.314 $JKmol^{-1}$) and T is temperature in degrees Kelvin. Combining this with the equation relating μ with V (eqn. 7) gives:

$$\mu_A = F_A + \sigma_n \cdot V_A = \mu_0 + RTln(a_A) \quad (8.11)$$

As we are dealing with an aqueous solution it is best to separate the activity into that of individual component ions. The chemical potentials and activities of K-feldspar and albite can therefore be expressed as:

$$\mu_{Ksp} = F_{Ksp} + \sigma_n \cdot V_{Ksp} = \mu_0 + RT \cdot ln(a_{K^+} \cdot a_{Al^{3+}} \cdot (a_{Si^{4+}})^3 \cdot (a_{O^{2-}})^8) \quad (8.12)$$

$$\mu_{Alb} = F_{Alb} + \sigma_n \cdot V_{Alb} = \mu_0 + RT \cdot ln(a_{Na^+} \cdot a_{Al^{3+}} \cdot (a_{Si^{4+}})^3 \cdot (a_{O^{2-}})^8) \quad (8.13)$$

If we consider the albite end-member form of reaction 1 whereby albite grows at the expense of K-feldspar then:

$$\mu_{Alb} - \mu_{Ksp} = (F_{Alb} - F_{Ksp}) + \sigma_n(V_{Alb} - V_{Ksp}) = RT \cdot ln\left(\frac{a_{Na^+}}{a_{K^+}}\right) \quad (8.14)$$

Which can be rearranged to:

$$ln\left(\frac{a_{Na^+}}{a_{K^+}}\right) = F + \frac{\Delta V}{RT} \cdot \sigma_n \quad (8.15)$$

As ΔV for this reaction is negative, this means that at interfaces where $\sigma_n$ is high (i.e. grain boundaries at high angles to $\sigma_1$) $a_{K^+}$ is also high and $a_{Na^+}$ is low, whereas in sites where $\sigma_n$ is low (i.e. grain boundaries at high angles to $\sigma_3$) $a_{K^+}$ is low and $a_{Na^+}$ is high, relatively speaking (and assuming local equilibrium at the boundary). This concept is visualised in Fig. 8.17a. This may at first glance seem contrary to the microstructural observations, $a_{K^+}$ is higher at the sites where albite is precipitating and $a_{Na^+}$ is higher at the sites where K-feldspar is precipitating. However, what is actually being described is the fact that the activity of the aqueous cations is higher at these sites because they are being released from the solid phase by the reaction, while the other species of cation is being drawn out of the aqueous phase to form the precipitating feldspar. Furthermore, this produces a gradient in the activities of aqueous $K^+$ and $Na^+$ and therefore a driving force for the diffusion of these ions down these activity gradients; $K^+$ moves from sites of high stress (high $a_{K^+}$) towards sites of low stress (low $a_{K^+}$), $Na^+$ moves in the opposite direction. This flux of aqueous cations driven by stress heterogeneities around porphyroclasts would perturb the local equilibria at the respective high or low stress sites and enable the reactions in the respective direction. In the case of low stress sites for example, though $a_{K^+}$ is lower in these sites than at high stress K-feldspar interfaces, the flux of aqueous $K^+$ towards these regions means that $a_{K^+}$ increases above the local equilibrium levels, leading to the precipitation of K-feldspar.

These interactions enable the reaction to be seen as a closed system on the scale of a thin section in which both K-feldspar and plagioclase are abundant (Menegon *et al.*, 2006).

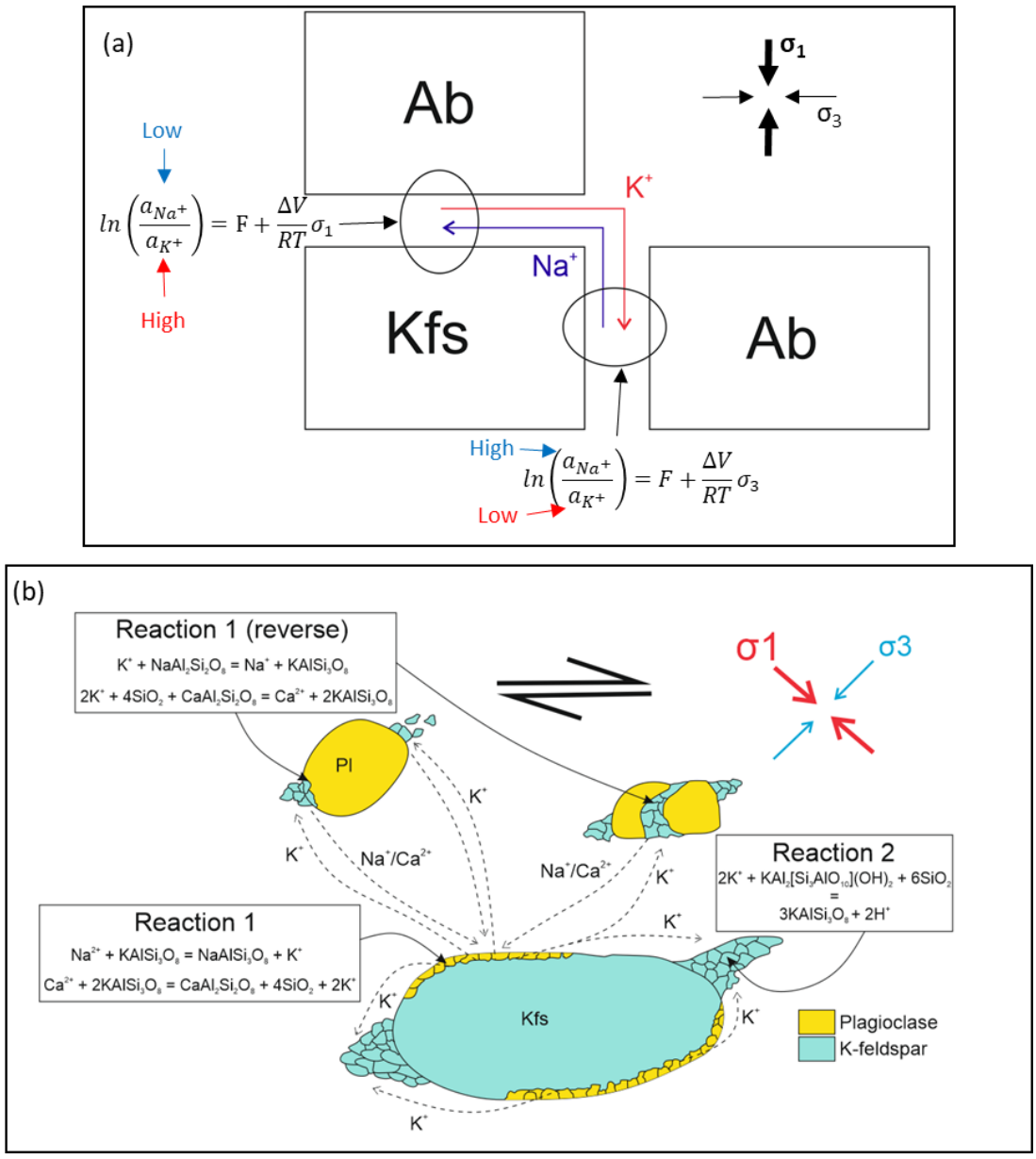


***Figure 8.17:*** *a) Schematic block diagram of the relation between ionic activities and driving forces for reaction 1 at σ1 and σ3 facing edges of K-feldspar and albite porphyroclasts. As ΔV is negative for reaction 1, in order to balance these expressions, $a_{K^+}$ must be high at high stress sites and low at low stress sites while the opposite is true of $a_{Na^+}$. This creates the gradient required for diffusion of these species. b) Conceptual model for the stress dependent distribution of plagioclase and K-feldspar in the studied mylonite. Reaction 1 takes place at the σ1 facing edges of porphyroclasts driven by a molar volume decrease. The activity of $K^+$ ions in solution then increases at these sites producing a gradient and a diffusion of $K^+$ ions into the surrounding matrix. The increase in $a_{K^+}$ drives the precipitation of K-feldspar either by reaction 2, where quartz and muscovite in the matrix react, or by the reverse of reaction 1 at the expense of plagioclase porphyroclasts. Both of these reactions produce a volume increase and so they occur preferentially within sites of low stress such as pressure shadows and dilational fractures. The occurrence of the reverse of reaction 1 liberates $Na^+$ and $Ca^{2+}$ cations which then diffuse down an activity gradient towards σ1 facing edges of K-feldspar porphyroclasts, supplying reactants for the continuation of reaction 1 at these sites.*

However, on the scale of a single K-feldspar porphyroclast, transfer of $K^+$ away from high stress interfaces would lead to an increase in $a_{K^+}$ at the pressure shadows which could not be balanced by K-feldspar precipitation as there is no plagioclase present with which to react (a caveat to this is that fine plagioclase grains in the matrix would provide reactants for this reaction but not to form the almost pure K-feldspar pressure shadows observed). This highlights the importance of reaction 2, which facilitates the reaction of quartz and muscovite in the matrix with $K^+$-bearing fluids to precipitate K-feldspar in the pressure shadows. The equilibrium constant of this reaction ($K_2$) is given by:

$$K_2 = \frac{(a_{Ksp})^3 \cdot (a_{H^+})^2}{(a_{mus}) \cdot (a_{K^+})^2 \cdot (a_{Qtz})^6} \quad (8.16)$$

Reaction 2 (in combination with reaction 1) therefore explains how K-feldspar porphyroclasts display a pattern of both fine plagioclase and fine K-feldspar around their peripheries, distributed depending on the orientation of principle stresses. It is notable however that this is not true of plagioclase porphyroclasts which have K-feldspar rich pressure shadows but do not display 'caps' of fine plagioclase along high stress interfaces. This can be explained by considering the fact that while reaction 2, and the reverse of reaction 1, are feasible to produce K-feldspar from plagioclase or quartz and muscovite in the presence of increased $a_{K^+}$ in pressure shadows, reaction 3 would need to occur to precipitate plagioclase at the expense of quartz and muscovite in the corresponding regions of high stress around plagioclase porphyroclasts. However, reaction 3 results in an increase in molar volume, and it is therefore inhibited in these high normal stress regions. Thus, molar volume considerations make it favourable for plagioclase to be formed at the expense of K-feldspar, where it is present (via reaction 1 and a reduction in molar volume), but not through the consumption of other matrix phases at high stress interfaces of other porphyroclasts.

A stepwise model can be proposed for the driving forces behind these stress-driven dissolution-precipitation reactions and the transport of cations. We will work with the albite end member for simplicity and assume a system which contains both sodic- and potassic-feldspar as well as an aqueous phase with a certain equilibrium concentration of both $K^+$ and $Na^+$ cations. When this system is placed in a shear zone with high differential stress:

1) Plagioclase starts to form via reaction 1 at the high stress interfaces of K-feldspar porphyroclasts driven by the molar volume reduction inherent in this reaction.
2) This locally reduces $a_{Na^+}$ and locally increases $a_{K^+}$ in the aqueous phase, producing a gradient in both activities relative to $a_{Na^+}$ and $a_{K^+}$ in the rest of the system.

3) Aqueous $Na^+$ diffuses down this gradient towards the high stress interfaces of K-feldspar porphyroclasts while aqueous $K^+$ diffuses away into other parts of the system. At this point, all over the system, except for at high stress sites of K-feldspar porphyroclasts, $a_{K^+}$ is higher than its equilibrium concentration and $a_{Na^+}$ is lower.
4) This means there is a driving force for the precipitation of K-feldspar and the consumption of plagioclase (reverse of reaction 1) or quartz and muscovite (reaction 2). However, as these reactions result in a volume increase, they are inhibited by lithostatic pressure and so occur only in sites of lowest stress such as pressure shadows and dilation sites or fractures.

This explains why K-feldspar is abundant in pressure shadows throughout the thin section, and how wherever plagioclase grains fracture they readily react with the $K^+$ primed fluid phase to form K-feldspar. The topotactic relationship of new K-feldspar with respect to fractured plagioclase porphyroclasts provides evidence for this within the microstructure (Figs. 8.5-8.8). The dissolution of low stress sections of plagioclase grains is particularly important as this is the source of $Na^+$ and $Ca^{2+}$ ions which diffuse towards the K-feldspar porphyroclasts and enable reaction 1 to continue. This process would be self-sustaining, as when more plagioclase is precipitated it is balanced by the consumption of plagioclase elsewhere through the reversal of reaction 1. It is also reasonable to expect that reaction 2 occurs in reverse in order to balance the system. For example, if a K-feldspar grain grows in a pressure shadow by means of reaction 2 but is then transported outside of that pressure shadow through grain-boundary sliding or the rotation of the nearby porphyroclast, it will be exposed to higher stresses which drive the reaction in the direction of negative ΔV (i.e. the reverse of reaction 2). The boundaries of the pressure shadows (such as in Fig. 8.3b) therefore represent the line along which the driving force from ΔV is equal to the driving force from increased $a_{K^+}$, with one driving force or the other prevailing either side. This model, including the relative transport of cations and the locations at which the reactions discussed occur, is illustrated in Fig. 8.17b.

### 8.5.5. Feldspar cation exchange as a form of incongruent pressure solution

The fluid-assisted, cation exchange process detailed above, particularly the parts of it regarding reaction 1 and its reversal, are best described as a form of incongruent pressure solution. This is demonstrated by the fact that the reversible reactions result in a molar volume reduction at sites of high stress and a 'redistribution' in effect, of that volume to sites

of lower stress. The result is a shape change via dissolution and precipitation of different phases in different microstructural locations as well as an overall grain size reduction as fine new grains grow at the expense of coarse porphyroclasts. Where this process differs from conventional pressure solution, or dissolution-precipitation creep, is that it does not require the diffusive mass transfer of all components of a phase. Rather, in the case of the feldspars in this study, only the $K^+$, $Na^+$ and $Ca^{2+}$ cations need diffuse significant distances in the aqueous phase. Al is likely to be fairly immobile in terms of diffusivity relative to monovalent cations such as $K^+$ and $Na^+$ (Carlson, 2002). However, in the example we have discussed, the Al (and indeed the Si and O) from the feldspars need not be redistributed but simply switched from being hosted in one feldspar phase to another, as in the mineral replacement reactions of Putnis, (2002). The Al in the high strain margins of K-feldspar porphyroclasts becomes the Al in fine new plagioclase grains at the same location via a mineral replacement reaction (Mukai *et al.*, 2014; Ruiz-Agudo *et al.*, 2014). The redistribution of $K^+$ in aqueous solution can be achieved much faster than if the transport of all components was required and K-feldspar can be precipitated in low stress sites from the reaction of these fluids with plagioclase, or with other components in the matrix which are encountered at that site. The samples studied by Simpson and Wintsch, (1989) displayed little evidence for replacement of plagioclase by K-feldspar though this seems necessary in order to provide $Na^+$ and $Ca^{2+}$ cations for reaction 1, unless the reaction is metasomatic with external fluids. In addition, their mylonites were ostensibly devoid of muscovite meaning reaction 2 would not be possible.

The mylonites in the present study are intensely deformed, with a very fine grained, banded matrix as well as sigma and delta porphyroclasts and mica fish. Therefore, the effect of incongruent dissolution-precipitation reactions on plagioclase porphyroclasts, as well as within the muscovite bearing matrix at pressure shadows can be observed clearly. An unusual example, which highlights the reversibility of these reactions, the influence of the orientation of principal stress axes and the influence of local gradients in cation activity is captured in Fig. 8.11. Here, plagioclase has formed around the entire lower half of a K-feldspar porphyroclast with a K-feldspar pressure shadow then forming on the other side of this 'rim' of plagioclase. Fig. 8.18 presents a conceptual model of how this microstructure probably formed and how this provides strong evidence of stress induced reaction of the feldspars. As the shear sense in the thin section is dextral, the porphyroclast can be back rotated in an anticlockwise direction to give an initial orientation. The wide base of the porphyroclast is now in close proximity to the muscovite fish below, producing high stresses along the lower boundary and extensive precipitation of plagioclase at the expense of K-feldspar via reaction

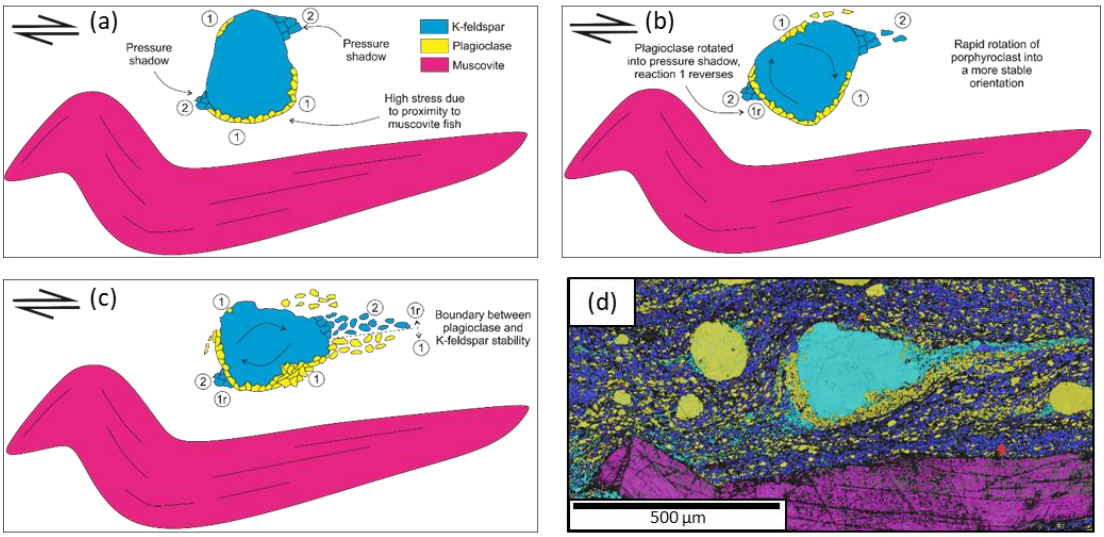


***Figure 8.18:*** *Conceptual model explaining the distribution of plagioclase around the K-feldspar clast in Fig. 8.11 in the context of stress induced reactions of feldspars and clast rotation. The locations of reactions 1, 2 and the reverse of reaction 1 (1r) are shown. (a) K-feldspar clast displays plagioclase along high stress boundaries including the lower periphery which experiences elevated normal stress due to its proximity to a large muscovite fish. K-feldspar is precipitated in the pressure shadows. (b) The irregularly shaped clast rotates clockwise to reach a more stable orientation within the deforming matrix. As it does so it rotated the plagioclase grains at its base through the pressure shadow leading some to revert to K-feldspar via the reverse of reaction 1. The sites of the forward reaction 1 also change slightly due to the clast's rotation through the stress field. (c) Once the porphyroclast has rotated into a more stable position some of the plagioclase has survived the rotation and is now beyond the pressure shadow on the left side of the porphyroclast, whilst more plagioclase is formed on the high stress lower right edge by reaction 1. A divide is present in the tail from the upper right corner, with K-feldspar in the pressure shadow and an abrupt change to plagioclase in the lower part of the tail outside of the pressure shadow. This can be viewed as a boundary across which reaction 1 runs either forwards or in reverse. (d) EBSD phase map of the site represented by the model in a, b and c, abundant plagioclase porphyroclasts nearby have K-feldspar pressure shadows and may be a source of $Na^{+}$ / $Ca^{2+}$ ions as well as a potential further sink for $K^{+}$ ions via the reverse of reaction 1.*

1 (Fig.8.18a). The irregular shape of the porphyroclast would make it unstable in this orientation within a deforming matrix, so it can be expected to rotate clockwise relatively rapidly to its present stable position (Passchier and Trouw, 2005) (Fig. 8.18b). This rotation brings the newly formed plagioclase lower rim around through the lower left pressure shadow and up to form the left side of the porphyroclast in its new orientation. A new pressure shadow forms in the lower left which is observed in the present microstructure and is composed of K-feldspar formed via reaction 2 but also potentially the reverse of reaction 1 (consuming the plagioclase grains of the rim) (Fig. 8.18b). There is now a new lower boundary to the porphyroclast, in close proximity to the mica fish, along which reaction 1 again occurs extensively, forming the fine plagioclase grains along the lower right side of the porphyroclast. The pressure shadow in the upper right facilitates the precipitation of fine K-feldspar grains, however a distinct boundary between K-feldspar and plagioclase is evident

in the tail and defines the line across which reaction 1 runs either forwards or in reverse (Fig. 8.18c).

As described, the reaction of plagioclase to form K-feldspar (reaction $1_r$) occurs in the pressure shadows of plagioclase porphyroclasts not just in highly fractured, dilatant sites. Here the K-feldspar neoblasts are pulled off into the porphyroclast tails by grain boundary sliding and grain size sensitive creep mechanisms in the matrix. This removal of new grains results in this reaction seeming less prominent than the formation of plagioclase along boundaries of K-feldspar porphyroclasts (reaction 1), however, its effects may be underestimated. It is proposed here that the well-rounded shape of all plagioclase porphyroclasts in the sample is testament to the activity of this reaction. A model is laid out in Fig. 8.19 to show how dissolution of plagioclase at pressure shadows and it's reprecipitation as fine K-feldspar, coupled with continuous rotation of the porphyroclast as would be expected under conditions of non-coaxial strain (Passchier and Trouw, 2005) would lead to rounding, and a reduction in size of the porphyroclast over time. This process of 'reaction rounding' can be thought of as similar to a pencil sharpener in which the static regions of low stress which exist in the pressure shadows, act like the blade, eroding off plagioclase from the edge of the porphyroclast by dissolution and precipitation as fine K-feldspar. As the porphyroclast rotates through the stress field, the part of the boundary in contact with the pressure shadow also moves. In this way, an irregularly shaped porphyroclast would become both rounder and smaller over time. The same is true of K-feldspar porphyroclasts but with the reverse reaction occurring at the interfaces facing $\sigma_1$, meaning the plagioclase neoblasts are less easily removed from the porphyroclast in the tails.

### 8.5.6. Implications

There are important implications of this incongruent pressure solution process for the microstructure and rheology of the mylonite and the shear zone as a whole. The most important effect in this regard is the widespread grain size reduction achieved by the dissolution of coarse porphyroclasts and the precipitation of fine, new feldspar grains. This accelerates a transition in the role of feldspar from that of rigid porphyroclasts, which undergo brittle fracture but in general do not accommodate significant strain, to a constituent of the fine-grained matrix which deforms by diffusion creep and grain boundary sliding (see Chapter 6 of this thesis). Ultimately at the conditions of the mid-crust this could result in an overall weakening of the mylonite (Behrmann and Mainprice, 1987; Menegon *et al.*, 2006, 2013; Kilian *et al.*, 2011), which would be self-sustaining as phase mixing by dissolution precipitation inhibits dynamic recrystallisation by dislocation creep. Brittle

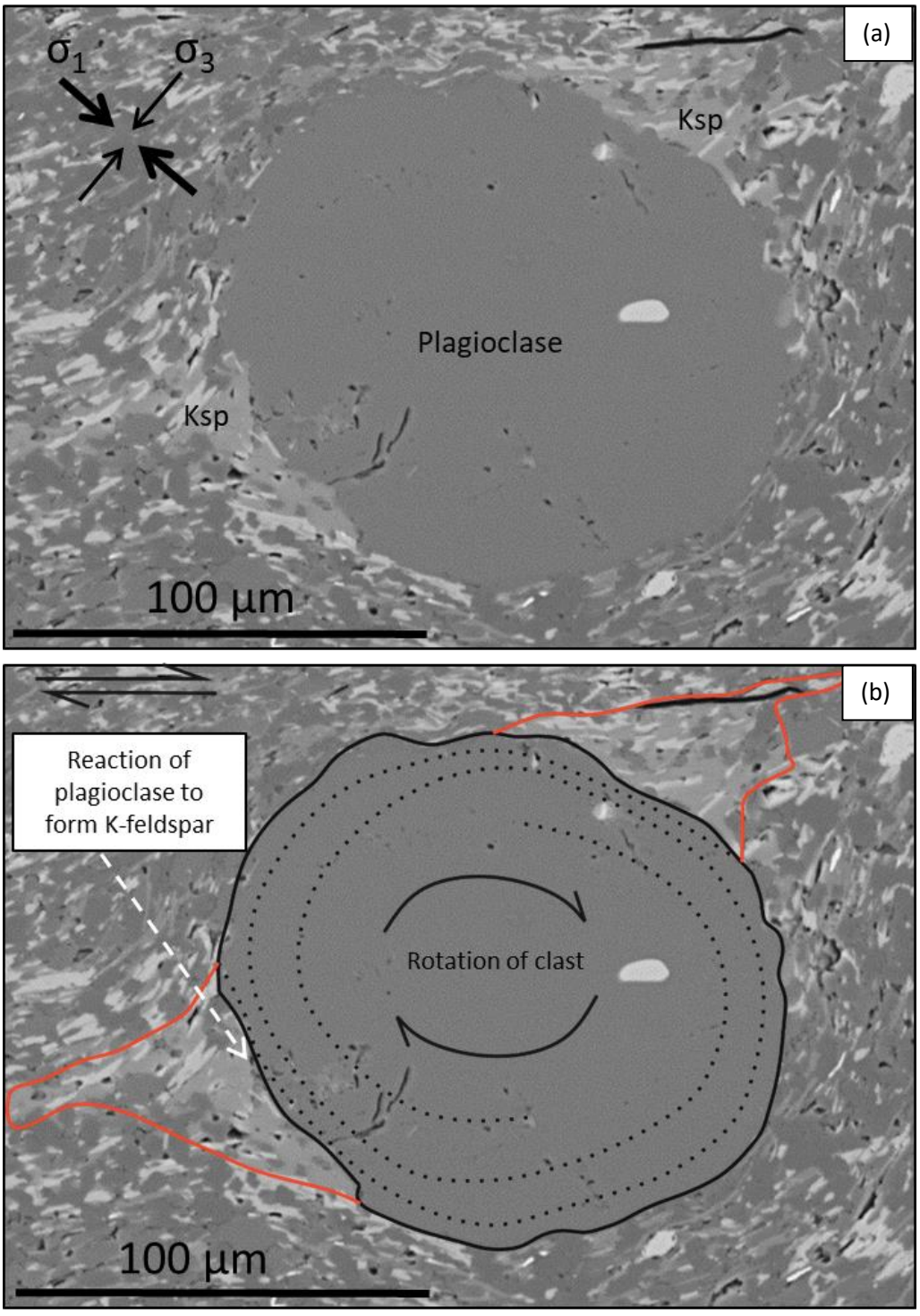


***Figure 8.19:*** *Model for the progressive rounding of porphyroclasts via rotation coupled with the precipitation of new grains at the expense of the porphyroclast. Such 'reaction rounding' is facilitated by the sites of reaction remaining stationary with respect to the orientations of applied stresses while the porphyroclast rotates through this field. In the case of plagioclase porphyroclasts (the vast majority of which within the sample POG3 are very well rounded as in (a)) the reaction which depletes the mass of the porphyroclast is the reverse of reaction 1, which involves the formation of K-feldspar at the expense of plagioclase. This occurs along the edges of the porphyroclast in the vicinity of the pressure shadows (indicated by red outlines in (b)) with the product K-feldspar then moving away from the porphyroclast within the tails. The dotted lines in (b) represent the possible future boundaries of the porphyroclast if rotation and reaction were to continue. Through this process, the clast would become smaller and, in the case of an originally angular clast, rounder over time.*

fracturing is an integral part of this process as it creates fluid pathways and dilation sites and increases the reactive surface area of the feldspars. The paucity of evidence for substantial dynamic recrystallisation of feldspars indicates that brittle fracture, coupled with incongruent dissolution and precipitation is the principle mechanism by which grain size reduction of the feldspar phases is achieved. This is supported by the EPMA results which confirm that fine plagioclase grains have distinct compositions to the coarse porphyroclasts and therefore do not represent dynamically recrystallised grains. Indeed, if the feldspars were deforming more readily by dynamic recrystallisation, and only minimally or not at all by brittle fracture, then the progress of dissolution and precipitation may be inhibited by a lack of fractures within plagioclase grains, producing fewer places where reaction 1 could reverse and resulting in a limited availability of $Na^{+}$ and $Ca^{2+}$ ions to facilitate the forward reaction.

There are relatively few examples of incongruent pressure solution in the existing literature (e.g. Simpson and Wintsch, 1989; Wassmann and Stöckhert, 2013), although the relationship between stress and chemistry is becoming more widely discussed (Schmid *et al.*, 2009; Wheeler, 2014, 2018; Wolterbeek *et al.*, 2018) and there is mounting evidence that reactions and/or phase changes can occur heterogeneously within microstructures based on the orientations of the principle stress axes, both from experimental studies (e.g. Richter, Stünitz and Heilbronner, 2016) and in observations of natural rocks (e.g. Moore *et al.*, 2019). It is possible that incongruent pressure solution processes, such as the one described in this study, are more common than this record suggests but have not been recognised due to the subtlety of the microstructures produced. The precipitation of one phase at the expense of another means that the microstructures only partially resemble those of regular, congruent pressure solution. Despite this, incongruent pressure solution may be a faster process, in some instances, than congruent pressure solution, as only some of the components of each phase are transported by diffusive mass transfer. This could result in strain rates even greater than those of dissolution-reprecipitation creep. In the case of the mylonite discussed, the implications of this are to make the otherwise strong, rigid feldspar phases break down significantly faster than they otherwise would and to accelerate their integration within the polyphase ultramylonitic matrix. This highlights the importance of these reactions in affecting grain size reduction and strain weakening within these mylonites.

The presence of fluids and brittle fracturing are both critical to the action of incongruent pressure solution as a deformation mechanism in these rocks. Fluid infiltration was likely facilitated initially by fracturing and later sustained by creep cavitation and along grain boundaries once a fine-grained ultramylonitic matrix became widespread. Fluids are required

to provide the aqueous medium for cation exchange while fractures and grain boundaries enable this fluid to react with a greater surface area of the porphyroclasts. Indeed, in this study the microstructures indicative of the dissolution precipitation reactions were far more prevalent in the highly deformed, fine-grained ultramylonite than they were in coarser grained lower strain samples in which feldspar porphyroclasts were surrounded by monomineralic quartz domains deforming viscously by dislocation creep.

## 8.6. Conclusions

This study has focussed on describing and explaining the distribution of fine feldspar grains in association with coarse feldspar porphyroclasts, within an amphibolite facies orthogneiss mylonite, in the context of incongruent pressure solution. The distribution of fine-grained feldspars around porphyroclasts in the studied mylonites is strongly related to the orientations of principle stresses during deformation. Fine plagioclase decorates the $\sigma_1$ facing boundaries of K-feldspar porphyroclasts, while new K-feldspar occurs within the pressure shadows of all types of porphyroclast as well as around fractures and sites of dilation.

EBSD data reveals little evidence for dynamic recrystallisation in the feldspar porphyroclasts, but significant evidence of brittle fracturing. There is a topotactic relationship between new feldspars and the associated porphyroclasts. This is especially evident in the case of K-feldspar in fractured regions and in plagioclase present along the boundaries of K-feldspar porphyroclasts and strongly suggests the new grains formed by topotactic replacement of the porphyroclasts. EPMA analyses indicate that new plagioclase grains are more albitic than the plagioclase porphyroclasts, supporting microstructural evidence that the fine grains represent a different population and have not been produced by dynamic recrystallisation processes.

It is proposed that dissolution-precipitation processes and ion exchange reactions involving substantial ionic transfer with an aqueous phase are responsible for the microstructures observed via the stages outlined below.

Stage 1) At high stress interfaces of K-feldspar porphyroclasts, the negative ΔV associated with the formation of plagioclase at the expense of K-feldspar drives this reaction (1) forward, drawing $Na^+$ and $Ca^{2+}$ ions out of the fluid phase and releasing $K^+$ ions into the fluid phase in the local vicinity.

Stage 2) This locally alters the activities of $K^+$, $Na^+$ and $Ca^{2+}$ in solution, producing a chemical gradient in these species across the system: $K^+$ therefore diffuses away from sites of high stress while $Na^+$ and $Ca^{2+}$ diffuse towards them.

Stage 3) As $a_{K^+}$ increases and $a_{Na^+}$ and $a_{Ca^{2+}}$ reduces in the fluid elsewhere in the system it is balanced by the precipitation of K-feldspar at the expense of plagioclase or quartz and muscovite. This occurs preferentially at sites of low stress due to the molar volume increase associated with these reactions.

Stage 4) These reactions are aided by brittle fracturing in the feldspar phases which create fluid pathways and sites of dilation and increase the reactive surface area of porphyroclasts.

This process is important in the context of the mylonite as a whole as it (along with brittle fracturing which is critical in producing fluid pathways for the initial infiltration of fluids) is the principle mechanism of grain size reduction in the feldspars, producing fine grains at the expense of coarse porphyroclasts. The fine grains form part of a polymineralic matrix which deforms by grain size sensitive creep mechanisms and is substantially weaker than monomineralic quartz deforming by dynamic recrystallisation or the brittle deformation of feldspars. The process is best described as a fluid-facilitated, stress-driven set of reactions which result in a shape change and grain size reduction. It constitutes a form of dissolution precipitation creep as volume is redistributed away from sites of high stress towards sites of low stress via the dissolution and precipitation of feldspars, however, it is incongruent as it locally involves a phase change.

It is suggested that the importance of incongruent dissolution-precipitation creep in natural mylonites may have, in the past, been overlooked. Despite this, processes such as the one outlined in this study may be faster than regular congruent pressure solution or dissolution-precipitation creep as they only require the diffusive mass transfer of low valency cations such as $K^+$ and $Na^+$ through the intergranular medium, rather than the diffusion of all components in a phase. The implication of this is that rocks with two feldspars may be weaker than those with a single feldspar which cannot undergo these stress-induced reactions due to a lack of the required reactant phases. In addition, previous studies which overlook incongruent pressure solution as a viable deformation mechanism within feldspar-bearing rocks may have missed a key process by which feldspars are comminuted and deformed in mid-crustal granitic mylonites.

## 8.7. Supplementary figures and tables

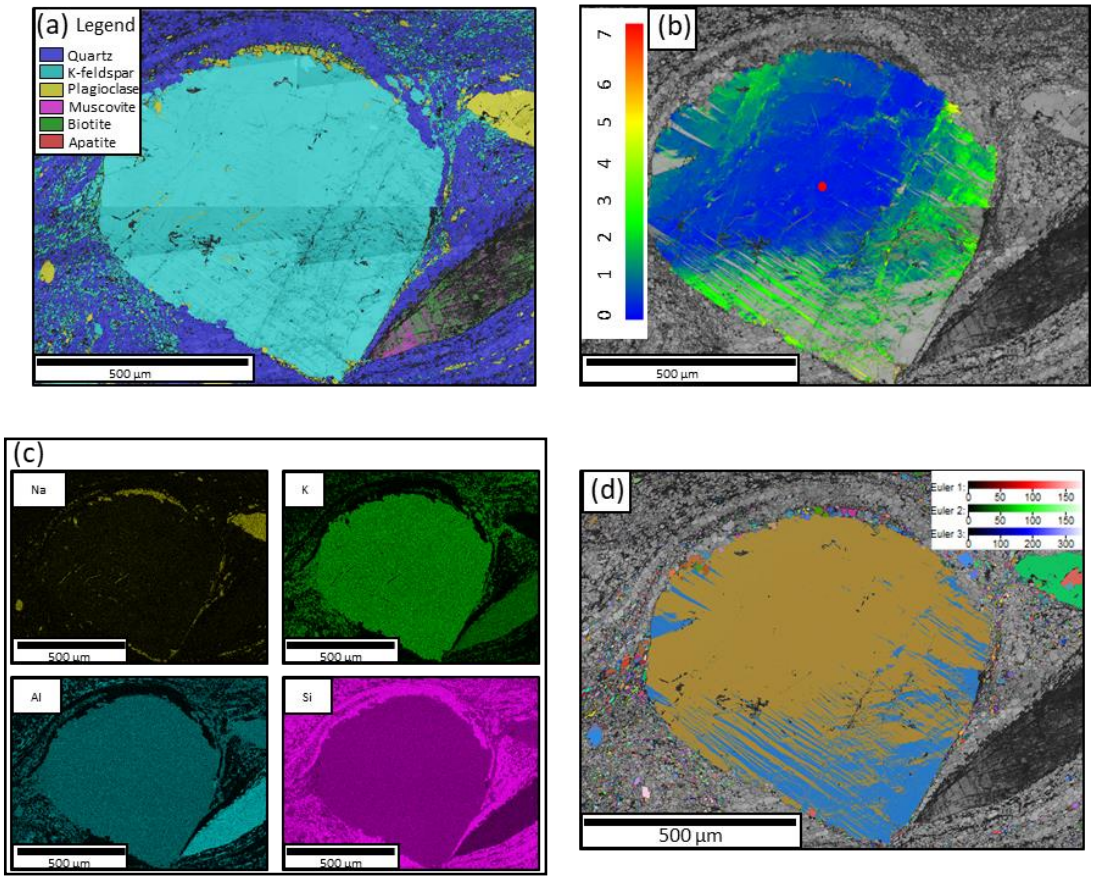


***Supplementary Figure S8.1:*** *EBSD data of a K-feldspar porphyroclast. (a) EBSD phase map showing an increased presence of plagioclase along the upper and lower parts of the grain as well as new, fine K-feldspar within the pressure shadows. (b) Texture component showing limited intracrystalline strain in the form of a gentle bending of around 5° across the width of the porphyroclast. The reference point for misorientations is given by the red spot. (c) EDS element maps of the area giving the relative distribution of Na, K, Al and Si. (d) All Euler orientation map of feldspars (both plagioclase and K-feldspar). Step size in the maps is 0.7 µm and the grid is 1693 x 1270 pixels.*

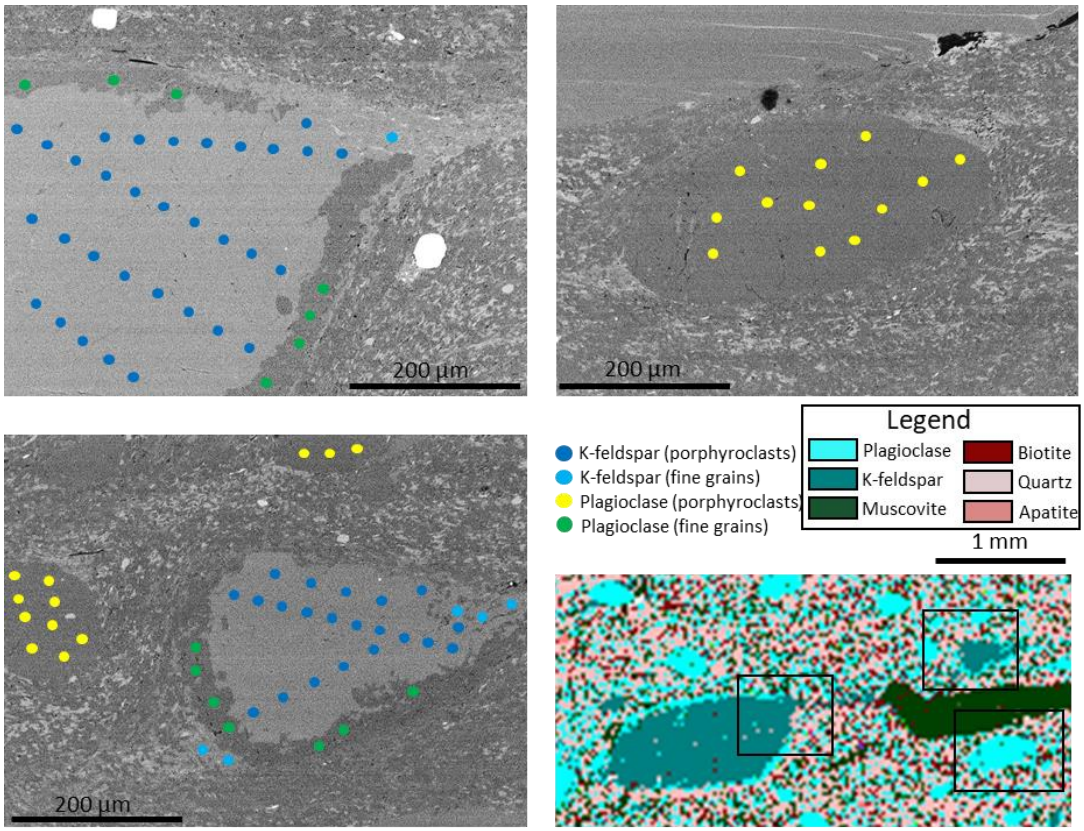


***Supplementary Figure S8.2:*** *Electron microprobe BSE images of the sights used for EPMA spot analyses. The individual analysis sites are indicated by points which are colour coded in terms of the type grain that analysis is used to represent. Points in large porphyroclasts were chosen to provide wide coverage across the porphyroclast while those of fine grains were located in order to avoid interference from other phases and grain boundaries as best as possible. The lower right panel is a low resolution QEMSCAN phase map of the area concerned.*

***Supplementary Table S8.1:*** *EPMA point analyses of K-feldspar porphyroclasts*

| Analysis number | 385 | 386 | 387 | 388 | 389 | 390 | 391 | 392 | 393 | 394 | 395 | 396 | 397 | 398 | 399 | 400 | 401 | 402 |
|---|---|---|---|---|---|---|---|---|---|---|---|---|---|---|---|---|---|---|
| **Wt% Oxides** | | | | | | | | | | | | | | | | | | |
| **FeO** | 0.02 | -0.01 | -0.02 | -0.08 | 0.02 | 0.04 | -0.03 | 0.00 | 0.07 | 0.00 | 0.06 | 0.01 | -0.01 | -0.03 | -0.06 | 0.05 | 0.08 | 0.06 |
| **$K_2O$** | 15.63 | 15.70 | 15.71 | 15.52 | 15.45 | 15.88 | 15.59 | 15.57 | 15.55 | 16.00 | 15.67 | 15.74 | 15.71 | 15.04 | 16.04 | 16.10 | 14.51 | 15.56 |
| **$Al_2O_3$** | 18.61 | 18.42 | 18.89 | 19.00 | 19.08 | 18.75 | 18.81 | 18.93 | 18.77 | 18.98 | 18.91 | 18.64 | 18.59 | 19.14 | 18.94 | 18.76 | 18.44 | 19.04 |
| **$Na_2O$** | 0.55 | 0.67 | 0.60 | 0.64 | 0.50 | 0.50 | 0.49 | 0.64 | 0.58 | 0.51 | 0.38 | 0.65 | 0.56 | 1.14 | 0.46 | 0.62 | 1.25 | 0.66 |
| **MnO** | 0.01 | 0.00 | 0.00 | -0.01 | 0.00 | 0.01 | 0.00 | 0.05 | 0.01 | -0.01 | 0.00 | -0.01 | 0.00 | 0.01 | -0.01 | 0.01 | -0.01 | 0.00 |
| **CaO** | 0.00 | 0.01 | 0.00 | 0.00 | -0.01 | 0.00 | 0.01 | 0.00 | 0.01 | 0.00 | 0.00 | 0.01 | 0.01 | 0.09 | 0.00 | 0.01 | 0.04 | 0.00 |
| **$SiO_2$** | 65.15 | 64.15 | 64.48 | 64.07 | 64.15 | 64.22 | 64.80 | 64.57 | 63.91 | 64.12 | 63.71 | 64.32 | 63.78 | 65.21 | 63.91 | 63.56 | 64.50 | 63.33 |
| **MgO** | 0.01 | 0.01 | 0.00 | 0.01 | 0.02 | 0.01 | 0.01 | 0.01 | 0.00 | 0.00 | 0.02 | 0.00 | 0.00 | 0.01 | 0.00 | 0.01 | 0.01 | 0.01 |
| **$TiO_2$** | 0.01 | 0.00 | 0.01 | 0.01 | 0.00 | 0.02 | 0.00 | 0.00 | 0.00 | 0.03 | 0.02 | 0.01 | 0.01 | 0.02 | -0.01 | 0.01 | 0.00 | 0.00 |
| **Total** | 99.92 | 98.81 | 99.53 | 99.06 | 99.06 | 99.35 | 99.53 | 99.64 | 98.86 | 99.52 | 98.63 | 99.30 | 98.54 | 100.46 | 99.17 | 99.03 | 98.69 | 98.53 |
| **Cations on the basis of 8 Oxygens** | | | | | | | | | | | | | | | | | | |
| **Fe** | 0.00 | 0.00 | 0.00 | 0.00 | 0.00 | 0.00 | 0.00 | 0.00 | 0.00 | 0.00 | 0.00 | 0.00 | 0.00 | 0.00 | 0.00 | 0.00 | 0.00 | 0.00 |
| **K** | 0.92 | 0.94 | 0.93 | 0.92 | 0.92 | 0.94 | 0.92 | 0.92 | 0.93 | 0.95 | 0.94 | 0.93 | 0.94 | 0.88 | 0.95 | 0.96 | 0.86 | 0.93 |
| **Al** | 1.01 | 1.01 | 1.03 | 1.04 | 1.05 | 1.03 | 1.03 | 1.03 | 1.03 | 1.04 | 1.04 | 1.02 | 1.03 | 1.03 | 1.04 | 1.03 | 1.01 | 1.05 |
| **Na** | 0.05 | 0.06 | 0.05 | 0.06 | 0.04 | 0.05 | 0.04 | 0.06 | 0.05 | 0.05 | 0.03 | 0.06 | 0.05 | 0.10 | 0.04 | 0.06 | 0.11 | 0.06 |
| **Mn** | 0.00 | 0.00 | 0.00 | 0.00 | 0.00 | 0.00 | 0.00 | 0.00 | 0.00 | 0.00 | 0.00 | 0.00 | 0.00 | 0.00 | 0.00 | 0.00 | 0.00 | 0.00 |
| **Ca** | 0.00 | 0.00 | 0.00 | 0.00 | 0.00 | 0.00 | 0.00 | 0.00 | 0.00 | 0.00 | 0.00 | 0.00 | 0.00 | 0.00 | 0.00 | 0.00 | 0.00 | 0.00 |
| **Si** | 3.01 | 3.00 | 2.99 | 2.98 | 2.99 | 2.99 | 3.00 | 2.99 | 2.98 | 2.98 | 2.98 | 2.99 | 2.99 | 2.99 | 2.98 | 2.97 | 3.00 | 2.97 |
| **Mg** | 0.00 | 0.00 | 0.00 | 0.00 | 0.00 | 0.00 | 0.00 | 0.00 | 0.00 | 0.00 | 0.00 | 0.00 | 0.00 | 0.00 | 0.00 | 0.00 | 0.00 | 0.00 |
| **Ti** | 0.00 | 0.00 | 0.00 | 0.00 | 0.00 | 0.00 | 0.00 | 0.00 | 0.00 | 0.00 | 0.00 | 0.00 | 0.00 | 0.00 | 0.00 | 0.00 | 0.00 | 0.00 |
| **Total** | 4.99 | 5.01 | 5.00 | 5.00 | 5.00 | 5.00 | 4.99 | 5.00 | 5.00 | 5.01 | 5.00 | 5.00 | 5.01 | 5.00 | 5.01 | 5.02 | 5.00 | 5.01 |
| | | | | | | | | | | | | | | | | | | |
| **Or%** | 94.91 | 93.85 | 94.50 | 94.14 | 95.39 | 95.41 | 95.42 | 94.15 | 94.55 | 95.38 | 96.40 | 94.06 | 94.81 | 89.26 | 95.86 | 94.42 | 88.21 | 93.94 |
| **An%** | -0.01 | 0.04 | 0.01 | -0.01 | -0.03 | 0.01 | 0.07 | 0.00 | 0.04 | 0.00 | 0.01 | 0.07 | 0.04 | 0.42 | -0.01 | 0.03 | 0.19 | 0.02 |
| **Ab%** | 5.10 | 6.10 | 5.49 | 5.88 | 4.65 | 4.58 | 4.51 | 5.85 | 5.40 | 4.62 | 3.59 | 5.87 | 5.15 | 10.32 | 4.15 | 5.55 | 11.60 | 6.04 |

| Analysis number | 403 | 431 | 432 | 433 | 434 | 435 | 436 | 437 | 438 | 439 | 440 | 441 | 442 | 443 | 444 | 445 | 446 | 447 |
|---|---|---|---|---|---|---|---|---|---|---|---|---|---|---|---|---|---|---|
| **Wt% Oxides** | | | | | | | | | | | | | | | | | | |
| **FeO** | 0.07 | 0.01 | 0.67 | 1.97 | 0.02 | 0.34 | 0.08 | 0.04 | 0.03 | -0.03 | 0.11 | 0.04 | 0.32 | 0.06 | 0.08 | 0.02 | -0.01 | -0.01 |
| **$K_2O$** | 15.59 | 15.27 | 15.29 | 15.27 | 15.24 | 15.45 | 15.80 | 15.67 | 16.05 | 15.86 | 16.26 | 15.15 | 15.04 | 15.31 | 15.55 | 15.23 | 15.57 | 15.40 |
| **$Al_2O_3$** | 18.61 | 18.46 | 18.71 | 18.08 | 18.53 | 18.47 | 18.36 | 19.00 | 18.10 | 18.58 | 18.65 | 18.38 | 18.48 | 18.52 | 18.44 | 18.81 | 18.54 | 18.50 |
| **$Na_2O$** | 0.54 | 0.71 | 0.73 | 0.44 | 0.81 | 0.53 | 0.50 | 0.42 | 0.29 | 0.26 | 0.21 | 0.66 | 0.73 | 0.93 | 0.82 | 0.71 | 0.87 | 0.53 |
| **MnO** | 0.00 | 0.00 | -0.02 | 0.01 | -0.01 | 0.00 | 0.01 | -0.01 | 0.00 | 0.01 | 0.01 | 0.01 | 0.00 | -0.02 | -0.01 | 0.01 | 0.00 | 0.01 |
| **CaO** | 0.00 | 0.02 | 0.02 | 0.03 | -0.01 | 0.01 | 0.00 | 0.00 | 0.01 | -0.01 | 0.00 | 0.01 | 0.01 | 0.01 | 0.00 | 0.34 | 0.01 | 0.00 |
| **$SiO_2$** | 64.77 | 63.78 | 62.94 | 61.49 | 62.28 | 62.12 | 62.87 | 62.57 | 62.27 | 63.55 | 62.93 | 63.70 | 64.03 | 63.85 | 63.08 | 63.08 | 63.45 | 63.63 |
| **MgO** | 0.00 | 0.00 | 0.01 | 0.01 | 0.01 | 0.01 | 0.00 | 0.02 | 0.01 | 0.01 | 0.01 | 0.00 | 0.01 | 0.01 | 0.01 | 0.01 | 0.01 | 0.01 |
| **$TiO_2$** | 0.01 | 0.01 | -0.02 | -0.02 | -0.01 | 0.01 | 0.00 | 0.00 | 0.00 | 0.00 | 0.00 | 0.01 | -0.01 | 0.01 | 0.02 | 0.00 | -0.01 | 0.02 |
| **Total** | 99.46 | 98.14 | 98.21 | 97.14 | 96.68 | 96.80 | 97.54 | 97.62 | 96.64 | 98.11 | 98.07 | 97.85 | 98.43 | 98.55 | 97.81 | 98.09 | 98.30 | 97.94 |
| **Cations on the basis of 8 Oxygens** | | | | | | | | | | | | | | | | | | |
| **Fe** | 0.00 | 0.00 | 0.03 | 0.08 | 0.00 | 0.01 | 0.00 | 0.00 | 0.00 | 0.00 | 0.00 | 0.00 | 0.01 | 0.00 | 0.00 | 0.00 | 0.00 | 0.00 |
| **K** | 0.92 | 0.91 | 0.92 | 0.93 | 0.93 | 0.94 | 0.96 | 0.95 | 0.98 | 0.95 | 0.98 | 0.91 | 0.90 | 0.91 | 0.94 | 0.91 | 0.93 | 0.93 |
| **Al** | 1.02 | 1.02 | 1.04 | 1.02 | 1.04 | 1.04 | 1.03 | 1.06 | 1.02 | 1.03 | 1.04 | 1.02 | 1.02 | 1.02 | 1.03 | 1.04 | 1.03 | 1.03 |
| **Na** | 0.05 | 0.06 | 0.07 | 0.04 | 0.07 | 0.05 | 0.05 | 0.04 | 0.03 | 0.02 | 0.02 | 0.06 | 0.07 | 0.08 | 0.08 | 0.06 | 0.08 | 0.05 |
| **Mn** | 0.00 | 0.00 | 0.00 | 0.00 | 0.00 | 0.00 | 0.00 | 0.00 | 0.00 | 0.00 | 0.00 | 0.00 | 0.00 | 0.00 | 0.00 | 0.00 | 0.00 | 0.00 |
| **Ca** | 0.00 | 0.00 | 0.00 | 0.00 | 0.00 | 0.00 | 0.00 | 0.00 | 0.00 | 0.00 | 0.00 | 0.00 | 0.00 | 0.00 | 0.00 | 0.02 | 0.00 | 0.00 |
| **Si** | 3.00 | 3.00 | 2.96 | 2.95 | 2.97 | 2.97 | 2.98 | 2.96 | 2.98 | 2.99 | 2.97 | 3.00 | 3.00 | 2.99 | 2.98 | 2.97 | 2.98 | 3.00 |
| **Mg** | 0.00 | 0.00 | 0.00 | 0.00 | 0.00 | 0.00 | 0.00 | 0.00 | 0.00 | 0.00 | 0.00 | 0.00 | 0.00 | 0.00 | 0.00 | 0.00 | 0.00 | 0.00 |
| **Ti** | 0.00 | 0.00 | 0.00 | 0.00 | 0.00 | 0.00 | 0.00 | 0.00 | 0.00 | 0.00 | 0.00 | 0.00 | 0.00 | 0.00 | 0.00 | 0.00 | 0.00 | 0.00 |
| **Total** | 5.00 | 5.00 | 5.01 | 5.02 | 5.02 | 5.01 | 5.01 | 5.01 | 5.01 | 5.00 | 5.01 | 5.00 | 5.00 | 5.01 | 5.02 | 5.01 | 5.02 | 5.00 |
| | | | | | | | | | | | | | | | | | | |
| **Or%** | 95.01 | 93.30 | 93.15 | 95.68 | 92.60 | 94.97 | 95.45 | 96.05 | 97.28 | 97.59 | 98.11 | 93.79 | 93.06 | 91.48 | 92.53 | 91.83 | 92.18 | 95.00 |
| **An%** | 0.01 | 0.09 | 0.09 | 0.17 | -0.06 | 0.06 | -0.02 | 0.02 | 0.03 | -0.04 | -0.01 | 0.05 | 0.07 | 0.04 | 0.01 | 1.70 | 0.04 | 0.01 |
| **Ab%** | 4.99 | 6.62 | 6.76 | 4.15 | 7.46 | 4.98 | 4.57 | 3.93 | 2.69 | 2.45 | 1.89 | 6.16 | 6.87 | 8.48 | 7.45 | 6.47 | 7.78 | 4.99 |

| Analysis number | 448 | 449 | 450 | 451 | 452 | 453 | 454 | 455 | 456 | 457 | 458 | 459 | 460 | 461 | 406 | 407 | 462 |
|---|---|---|---|---|---|---|---|---|---|---|---|---|---|---|---|---|---|
| **Wt% Oxides** | | | | | | | | | | | | | | | | | |
| **FeO** | -0.04 | 0.60 | 0.09 | 0.07 | 0.04 | 0.08 | 0.02 | 0.05 | 0.01 | 0.01 | -0.01 | 0.04 | 0.01 | 0.01 | 0.04 | 0.05 | 0.00 |
| **$K_2O$** | 15.43 | 15.21 | 15.26 | 14.80 | 14.82 | 15.42 | 14.63 | 15.32 | 15.72 | 15.65 | 15.92 | 16.09 | 15.61 | 15.47 | 14.88 | 15.51 | 15.57 |
| **$Al_2O_3$** | 18.79 | 18.22 | 18.66 | 18.53 | 18.27 | 18.78 | 18.90 | 18.79 | 18.22 | 18.80 | 18.20 | 18.40 | 18.64 | 18.33 | 18.91 | 18.83 | 18.47 |
| **$Na_2O$** | 0.73 | 0.62 | 0.94 | 1.29 | 0.72 | 0.81 | 1.26 | 0.45 | 0.50 | 0.49 | 0.32 | 0.50 | 0.58 | 0.24 | 0.80 | 0.67 | 0.52 |
| **MnO** | 0.01 | 0.00 | 0.00 | 0.02 | 0.00 | 0.01 | 0.02 | 0.00 | -0.01 | 0.01 | 0.02 | 0.01 | -0.01 | -0.01 | 0.01 | 0.00 | 0.00 |
| **CaO** | -0.01 | 0.01 | 0.00 | 0.01 | -0.01 | 0.01 | 0.02 | 0.00 | 0.00 | 0.00 | 0.00 | 0.00 | 0.00 | 0.00 | 0.11 | 0.01 | -0.01 |
| **$SiO_2$** | 63.96 | 62.66 | 64.01 | 63.87 | 62.76 | 63.20 | 63.43 | 62.45 | 63.06 | 64.35 | 63.17 | 63.86 | 63.92 | 62.32 | 64.47 | 64.03 | 63.84 |
| **MgO** | 0.01 | 0.00 | 0.01 | 0.01 | 0.02 | 0.01 | 0.00 | 0.01 | 0.03 | 0.00 | 0.01 | 0.02 | 0.00 | 0.01 | 0.00 | 0.01 | 0.00 |
| **$TiO_2$** | -0.01 | -0.01 | 0.01 | 0.01 | 0.01 | -0.01 | 0.01 | 0.01 | 0.01 | 0.00 | 0.00 | 0.01 | -0.01 | -0.01 | 0.01 | 0.01 | 0.00 |
| **Total** | 98.76 | 97.19 | 98.84 | 98.46 | 96.52 | 98.24 | 98.20 | 96.94 | 97.41 | 99.20 | 97.47 | 98.81 | 98.60 | 96.27 | 99.13 | 99.02 | 98.28 |
| **Cations on the basis of 8 Oxygens** | | | | | | | | | | | | | | | | | |
| **Fe** | 0.00 | 0.02 | 0.00 | 0.00 | 0.00 | 0.00 | 0.00 | 0.00 | 0.00 | 0.00 | 0.00 | 0.00 | 0.00 | 0.00 | 0.00 | 0.00 | 0.00 |
| **K** | 0.92 | 0.92 | 0.91 | 0.88 | 0.90 | 0.92 | 0.87 | 0.93 | 0.95 | 0.93 | 0.96 | 0.96 | 0.93 | 0.95 | 0.88 | 0.92 | 0.93 |
| **Al** | 1.03 | 1.02 | 1.03 | 1.02 | 1.03 | 1.04 | 1.04 | 1.05 | 1.02 | 1.03 | 1.02 | 1.01 | 1.03 | 1.04 | 1.03 | 1.03 | 1.02 |
| **Na** | 0.07 | 0.06 | 0.09 | 0.12 | 0.07 | 0.07 | 0.11 | 0.04 | 0.05 | 0.04 | 0.03 | 0.05 | 0.05 | 0.02 | 0.07 | 0.06 | 0.05 |
| **Mn** | 0.00 | 0.00 | 0.00 | 0.00 | 0.00 | 0.00 | 0.00 | 0.00 | 0.00 | 0.00 | 0.00 | 0.00 | 0.00 | 0.00 | 0.00 | 0.00 | 0.00 |
| **Ca** | 0.00 | 0.00 | 0.00 | 0.00 | 0.00 | 0.00 | 0.00 | 0.00 | 0.00 | 0.00 | 0.00 | 0.00 | 0.00 | 0.00 | 0.01 | 0.00 | 0.00 |
| **Si** | 2.99 | 2.98 | 2.99 | 2.99 | 3.00 | 2.97 | 2.97 | 2.97 | 2.99 | 2.99 | 3.00 | 2.99 | 2.99 | 2.99 | 2.99 | 2.98 | 3.00 |
| **Mg** | 0.00 | 0.00 | 0.00 | 0.00 | 0.00 | 0.00 | 0.00 | 0.00 | 0.00 | 0.00 | 0.00 | 0.00 | 0.00 | 0.00 | 0.00 | 0.00 | 0.00 |
| **Ti** | 0.00 | 0.00 | 0.00 | 0.00 | 0.00 | 0.00 | 0.00 | 0.00 | 0.00 | 0.00 | 0.00 | 0.00 | 0.00 | 0.00 | 0.00 | 0.00 | 0.00 |
| **Total** | 5.00 | 5.01 | 5.01 | 5.01 | 5.00 | 5.01 | 5.01 | 5.00 | 5.01 | 5.00 | 5.01 | 5.01 | 5.00 | 5.00 | 4.99 | 5.00 | 5.00 |
| | | | | | | | | | | | | | | | | | |
| **Or%** | 93.32 | 94.14 | 91.41 | 88.23 | 93.16 | 92.59 | 88.31 | 95.75 | 95.42 | 95.49 | 97.00 | 95.51 | 94.63 | 97.67 | 91.92 | 93.77 | 95.25 |
| **An%** | -0.04 | 0.04 | 0.00 | 0.05 | -0.05 | 0.05 | 0.09 | 0.01 | -0.01 | -0.02 | -0.01 | 0.00 | 0.02 | -0.01 | 0.56 | 0.03 | -0.06 |
| **Ab%** | 6.71 | 5.83 | 8.59 | 11.73 | 6.89 | 7.36 | 11.60 | 4.24 | 4.59 | 4.53 | 3.01 | 4.49 | 5.35 | 2.35 | 7.52 | 6.20 | 4.81 |

***Supplementary Table S8.2:*** *EPMA point analyses of fine K-feldspar grains*

| Analysis number | 463 | 404 | 405 | 408 | 409 | 410 |
|---|---|---|---|---|---|---|
| **Wt% Oxides** | | | | | | |
| **FeO** | 1.28 | 0.10 | 0.04 | 0.03 | 1.71 | 1.40 |
| **K2O** | 13.90 | 15.36 | 15.53 | 15.40 | 13.65 | 13.40 |
| **Al2O3** | 18.04 | 18.37 | 18.42 | 18.42 | 16.89 | 16.14 |
| **Na2O** | 0.71 | 0.35 | 0.62 | 0.51 | 0.38 | 0.30 |
| **MnO** | 0.01 | 0.01 | 0.02 | 0.00 | 0.02 | 0.00 |
| **CaO** | 0.08 | 0.04 | 0.03 | 0.05 | 0.03 | 0.03 |
| **SiO2** | 61.95 | 64.59 | 64.36 | 63.70 | 66.10 | 66.86 |
| **MgO** | 0.49 | 0.02 | 0.01 | 0.02 | 0.55 | 0.48 |
| **TiO2** | 0.13 | 0.01 | 0.00 | -0.01 | 0.21 | 0.13 |
| **Total** | 96.51 | 98.73 | 98.89 | 98.02 | 99.52 | 98.73 |
| **Cations on the basis of 8 Oxygens** | | | | | | |
| **Fe** | 0.05 | 0.00 | 0.00 | 0.00 | 0.07 | 0.05 |
| **K** | 0.85 | 0.92 | 0.92 | 0.92 | 0.81 | 0.80 |
| **Al** | 1.02 | 1.01 | 1.01 | 1.02 | 0.92 | 0.89 |
| **Na** | 0.07 | 0.03 | 0.06 | 0.05 | 0.03 | 0.03 |
| **Mn** | 0.00 | 0.00 | 0.00 | 0.00 | 0.00 | 0.00 |
| **Ca** | 0.00 | 0.00 | 0.00 | 0.00 | 0.00 | 0.00 |
| **Si** | 2.97 | 3.02 | 3.00 | 3.00 | 3.07 | 3.12 |
| **Mg** | 0.03 | 0.00 | 0.00 | 0.00 | 0.04 | 0.03 |
| **Ti** | 0.00 | 0.00 | 0.00 | 0.00 | 0.01 | 0.00 |
| **Total** | 4.99 | 4.98 | 5.00 | 5.00 | 4.94 | 4.92 |
| | | | | | | |
| **Or%** | 92.37 | 96.42 | 94.13 | 94.94 | 95.75 | 96.50 |
| **An%** | 0.47 | 0.23 | 0.18 | 0.27 | 0.18 | 0.20 |
| **Ab%** | 7.16 | 3.35 | 5.70 | 4.80 | 4.07 | 3.30 |

***Supplementary Table S8.3:*** *EPMA point analyses of plagioclase porphyroclasts*

| Analysis number | 411 | 412 | 413 | 414 | 415 | 416 | 417 | 418 | 419 | 428 | 429 | 430 |
|---|---|---|---|---|---|---|---|---|---|---|---|---|
| **Wt% Oxides** | | | | | | | | | | | | |
| **FeO** | 0.08 | 0.09 | 0.06 | 0.09 | 0.07 | 0.04 | 0.11 | 0.07 | -0.05 | 0.03 | 0.06 | 0.02 |
| **K2O** | 0.09 | 0.10 | 0.05 | 0.09 | 0.06 | 0.12 | 0.07 | 0.07 | 0.11 | 0.11 | 0.06 | 0.04 |
| **Al2O3** | 24.14 | 24.20 | 23.81 | 24.17 | 24.21 | 23.91 | 24.19 | 23.26 | 23.72 | 23.99 | 23.33 | 23.61 |
| **Na2O** | 9.08 | 9.01 | 8.91 | 9.26 | 8.81 | 8.47 | 9.11 | 9.01 | 8.83 | 9.15 | 8.86 | 9.09 |
| **MnO** | 0.01 | 0.01 | 0.00 | 0.00 | 0.01 | -0.01 | -0.01 | 0.02 | -0.01 | 0.00 | -0.01 | 0.01 |
| **CaO** | 5.04 | 5.04 | 5.21 | 5.10 | 5.08 | 5.05 | 4.80 | 4.96 | 4.69 | 5.02 | 4.97 | 4.99 |
| **SiO2** | 61.92 | 61.50 | 61.51 | 62.16 | 61.73 | 62.76 | 62.54 | 61.62 | 61.91 | 62.18 | 61.72 | 62.08 |
| **MgO** | 0.01 | 0.02 | 0.01 | 0.01 | 0.01 | 0.02 | 0.01 | 0.01 | 0.01 | 0.01 | 0.00 | 0.01 |
| **TiO2** | 0.01 | 0.01 | 0.01 | 0.00 | 0.00 | 0.01 | 0.00 | -0.01 | -0.01 | 0.00 | -0.02 | 0.00 |
| **Total** | 100.24 | 99.84 | 99.42 | 100.80 | 99.83 | 100.25 | 100.64 | 98.85 | 99.10 | 100.44 | 98.81 | 99.72 |
| **Cations on the basis of 8 Oxygens** | | | | | | | | | | | | |
| **Fe** | 0.00 | 0.00 | 0.00 | 0.00 | 0.00 | 0.00 | 0.00 | 0.00 | 0.00 | 0.00 | 0.00 | 0.00 |
| **K** | 0.01 | 0.01 | 0.00 | 0.00 | 0.00 | 0.01 | 0.00 | 0.00 | 0.01 | 0.01 | 0.00 | 0.00 |
| **Al** | 1.26 | 1.27 | 1.25 | 1.25 | 1.27 | 1.25 | 1.25 | 1.23 | 1.25 | 1.25 | 1.23 | 1.24 |
| **Na** | 0.78 | 0.78 | 0.77 | 0.79 | 0.76 | 0.73 | 0.78 | 0.78 | 0.76 | 0.78 | 0.77 | 0.78 |
| **Mn** | 0.00 | 0.00 | 0.00 | 0.00 | 0.00 | 0.00 | 0.00 | 0.00 | 0.00 | 0.00 | 0.00 | 0.00 |
| **Ca** | 0.24 | 0.24 | 0.25 | 0.24 | 0.24 | 0.24 | 0.23 | 0.24 | 0.22 | 0.24 | 0.24 | 0.24 |
| **Si** | 2.74 | 2.73 | 2.74 | 2.73 | 2.74 | 2.77 | 2.75 | 2.76 | 2.76 | 2.74 | 2.77 | 2.76 |
| **Mg** | 0.00 | 0.00 | 0.00 | 0.00 | 0.00 | 0.00 | 0.00 | 0.00 | 0.00 | 0.00 | 0.00 | 0.00 |
| **Ti** | 0.00 | 0.00 | 0.00 | 0.00 | 0.00 | 0.00 | 0.00 | 0.00 | 0.00 | 0.00 | 0.00 | 0.00 |
| **Total** | 5.02 | 5.02 | 5.02 | 5.02 | 5.02 | 4.99 | 5.02 | 5.02 | 5.00 | 5.02 | 5.01 | 5.02 |
| | | | | | | | | | | | | |
| **Or%** | 0.51 | 0.53 | 0.31 | 0.47 | 0.36 | 0.70 | 0.40 | 0.42 | 0.63 | 0.59 | 0.36 | 0.24 |
| **An%** | 23.36 | 23.48 | 24.33 | 23.24 | 24.08 | 24.61 | 22.46 | 23.22 | 22.54 | 23.12 | 23.59 | 23.23 |
| **Ab%** | 76.12 | 75.99 | 75.36 | 76.29 | 75.57 | 74.68 | 77.14 | 76.37 | 76.83 | 76.28 | 76.05 | 76.54 |

| Analysis number | 479 | 480 | 481 | 482 | 483 | 484 | 485 | 486 | 487 | 488 | 489 | 490 |
|---|---|---|---|---|---|---|---|---|---|---|---|---|
| **Wt% Oxides** | | | | | | | | | | | | |
| **FeO** | 0.00 | 0.00 | -0.01 | 0.00 | 0.01 | 0.06 | -0.01 | -0.03 | -0.03 | 0.04 | 0.05 | 0.02 |
| **K2O** | 0.12 | 0.06 | 0.09 | 0.15 | 0.12 | 0.20 | 0.17 | 0.17 | 0.17 | 0.13 | 0.17 | 0.09 |
| **Al2O3** | 23.30 | 23.61 | 23.83 | 23.12 | 23.78 | 23.44 | 23.86 | 23.43 | 23.41 | 23.98 | 23.40 | 23.77 |
| **Na2O** | 9.03 | 8.85 | 8.94 | 9.02 | 8.95 | 8.91 | 8.85 | 8.64 | 9.30 | 9.12 | 9.36 | 9.09 |
| **MnO** | -0.01 | 0.01 | -0.01 | -0.03 | 0.02 | -0.01 | -0.01 | 0.00 | 0.00 | -0.02 | -0.01 | 0.00 |
| **CaO** | 4.95 | 4.96 | 4.72 | 4.94 | 5.00 | 4.76 | 4.99 | 4.96 | 5.04 | 5.13 | 5.20 | 5.00 |
| **SiO2** | 61.25 | 62.37 | 61.65 | 61.82 | 61.95 | 61.98 | 60.94 | 61.28 | 61.90 | 61.41 | 61.47 | 61.09 |
| **MgO** | 0.01 | 0.00 | 0.01 | 0.00 | 0.01 | 0.01 | 0.00 | -0.01 | 0.01 | 0.01 | 0.01 | 0.02 |
| **TiO2** | -0.02 | 0.01 | 0.02 | -0.01 | 0.00 | 0.02 | 0.00 | 0.00 | -0.02 | 0.01 | -0.01 | 0.01 |
| **Total** | 98.47 | 99.73 | 99.18 | 98.88 | 99.71 | 99.26 | 98.71 | 98.31 | 99.67 | 99.61 | 99.54 | 98.93 |
| **Cations on the basis of 8 Oxygens** | | | | | | | | | | | | |
| **Fe** | 0.00 | 0.00 | 0.00 | 0.00 | 0.00 | 0.00 | 0.00 | 0.00 | 0.00 | 0.00 | 0.00 | 0.00 |
| **K** | 0.01 | 0.00 | 0.01 | 0.01 | 0.01 | 0.01 | 0.01 | 0.01 | 0.01 | 0.01 | 0.01 | 0.01 |
| **Al** | 1.24 | 1.24 | 1.25 | 1.22 | 1.25 | 1.23 | 1.26 | 1.24 | 1.23 | 1.26 | 1.23 | 1.25 |
| **Na** | 0.79 | 0.76 | 0.77 | 0.78 | 0.77 | 0.77 | 0.77 | 0.76 | 0.80 | 0.79 | 0.81 | 0.79 |
| **Mn** | 0.00 | 0.00 | 0.00 | 0.00 | 0.00 | 0.00 | 0.00 | 0.00 | 0.00 | 0.00 | 0.00 | 0.00 |
| **Ca** | 0.24 | 0.24 | 0.23 | 0.24 | 0.24 | 0.23 | 0.24 | 0.24 | 0.24 | 0.24 | 0.25 | 0.24 |
| **Si** | 2.76 | 2.77 | 2.75 | 2.77 | 2.75 | 2.77 | 2.74 | 2.76 | 2.75 | 2.73 | 2.74 | 2.74 |
| **Mg** | 0.00 | 0.00 | 0.00 | 0.00 | 0.00 | 0.00 | 0.00 | 0.00 | 0.00 | 0.00 | 0.00 | 0.00 |
| **Ti** | 0.00 | 0.00 | 0.00 | 0.00 | 0.00 | 0.00 | 0.00 | 0.00 | 0.00 | 0.00 | 0.00 | 0.00 |
| **Total** | 5.02 | 5.01 | 5.01 | 5.02 | 5.02 | 5.01 | 5.02 | 5.01 | 5.03 | 5.03 | 5.04 | 5.03 |
| | | | | | | | | | | | | |
| **Or%** | 0.67 | 0.35 | 0.53 | 0.83 | 0.67 | 1.12 | 0.94 | 0.99 | 0.94 | 0.70 | 0.89 | 0.51 |
| **An%** | 23.08 | 23.58 | 22.44 | 23.02 | 23.44 | 22.54 | 23.54 | 23.85 | 22.83 | 23.52 | 23.26 | 23.19 |
| **Ab%** | 76.24 | 76.07 | 77.03 | 76.15 | 75.89 | 76.34 | 75.52 | 75.16 | 76.23 | 75.77 | 75.85 | 76.30 |

***Supplementary Table S8.2:*** *EPMA point analyses of fine plagioclase grains*

| Analysis number | 420 | 421 | 423 | 424 | 425 | 426 | 427 | 468 | 469 | 470 | 471 | 472 | 473 | 474 |
|---|---|---|---|---|---|---|---|---|---|---|---|---|---|---|
| **Wt% Oxides** | | | | | | | | | | | | | | |
| **FeO** | -0.02 | 0.03 | 0.04 | 0.12 | 0.06 | 0.33 | 0.43 | 1.56 | 0.74 | 0.41 | 0.88 | 1.09 | 0.19 | 1.60 |
| **K2O** | 0.06 | 0.06 | 0.04 | 0.07 | 0.15 | 0.09 | 0.08 | 0.07 | 0.08 | 0.06 | 0.06 | 0.06 | 0.16 | 0.09 |
| **Al2O3** | 19.36 | 19.69 | 19.26 | 19.16 | 19.74 | 22.69 | 20.45 | 18.24 | 18.42 | 19.18 | 19.23 | 18.25 | 22.18 | 18.87 |
| **Na2O** | 8.08 | 8.37 | 7.95 | 8.53 | 8.27 | 8.86 | 9.00 | 7.23 | 7.76 | 8.29 | 7.62 | 8.12 | 9.18 | 7.62 |
| **MnO** | -0.02 | -0.02 | -0.02 | -0.01 | -0.01 | -0.03 | -0.01 | -0.01 | 0.02 | -0.02 | -0.01 | -0.01 | 0.00 | 0.01 |
| **CaO** | 3.09 | 3.22 | 3.03 | 3.34 | 3.17 | 4.00 | 3.25 | 3.04 | 3.20 | 3.26 | 3.34 | 3.15 | 3.88 | 3.30 |
| **SiO2** | 69.69 | 68.21 | 68.42 | 66.14 | 67.52 | 63.14 | 65.31 | 68.11 | 69.38 | 67.68 | 67.95 | 68.78 | 62.44 | 66.58 |
| **MgO** | 0.02 | 0.00 | -0.01 | 0.02 | 0.00 | 0.02 | 0.02 | 0.01 | 0.01 | 0.02 | 0.01 | 0.01 | 0.01 | 0.02 |
| **TiO2** | 0.00 | -0.02 | 0.00 | 0.02 | -0.01 | -0.01 | 0.00 | -0.01 | 0.01 | -0.02 | 0.00 | 0.00 | 0.00 | -0.01 |
| **Total** | 100.10 | 99.40 | 98.57 | 97.28 | 98.84 | 98.92 | 98.39 | 98.20 | 99.49 | 98.76 | 98.96 | 99.32 | 97.89 | 97.94 |
| **Cations on the basis of 8 Oxygens** | | | | | | | | | | | | | | |
| **Fe** | 0.00 | 0.00 | 0.00 | 0.00 | 0.00 | 0.01 | 0.02 | 0.06 | 0.03 | 0.02 | 0.03 | 0.04 | 0.01 | 0.06 |
| **K** | 0.00 | 0.00 | 0.00 | 0.00 | 0.01 | 0.00 | 0.00 | 0.00 | 0.00 | 0.00 | 0.00 | 0.00 | 0.01 | 0.01 |
| **Al** | 1.00 | 1.03 | 1.01 | 1.02 | 1.04 | 1.20 | 1.08 | 0.97 | 0.96 | 1.01 | 1.01 | 0.96 | 1.18 | 1.01 |
| **Na** | 0.69 | 0.72 | 0.69 | 0.75 | 0.71 | 0.77 | 0.78 | 0.63 | 0.67 | 0.72 | 0.66 | 0.70 | 0.80 | 0.67 |
| **Mn** | 0.00 | 0.00 | 0.00 | 0.00 | 0.00 | 0.00 | 0.00 | 0.00 | 0.00 | 0.00 | 0.00 | 0.00 | 0.00 | 0.00 |
| **Ca** | 0.15 | 0.15 | 0.14 | 0.16 | 0.15 | 0.19 | 0.16 | 0.15 | 0.15 | 0.16 | 0.16 | 0.15 | 0.19 | 0.16 |
| **Si** | 3.06 | 3.02 | 3.05 | 3.00 | 3.01 | 2.82 | 2.93 | 3.07 | 3.08 | 3.02 | 3.03 | 3.06 | 2.82 | 3.02 |
| **Mg** | 0.00 | 0.00 | 0.00 | 0.00 | 0.00 | 0.00 | 0.00 | 0.00 | 0.00 | 0.00 | 0.00 | 0.00 | 0.00 | 0.00 |
| **Ti** | 0.00 | 0.00 | 0.00 | 0.00 | 0.00 | 0.00 | 0.00 | 0.00 | 0.00 | 0.00 | 0.00 | 0.00 | 0.00 | 0.00 |
| **Total** | 4.90 | 4.92 | 4.90 | 4.94 | 4.92 | 4.99 | 4.97 | 4.88 | 4.90 | 4.92 | 4.90 | 4.91 | 5.01 | 4.92 |
| | | | | | | | | | | | | | | |
| **Or%** | 0.40 | 0.38 | 0.29 | 0.45 | 0.95 | 0.52 | 0.51 | 0.52 | 0.53 | 0.41 | 0.44 | 0.40 | 0.90 | 0.65 |
| **An%** | 17.35 | 17.49 | 17.34 | 17.69 | 17.29 | 19.87 | 16.54 | 18.75 | 18.45 | 17.79 | 19.40 | 17.58 | 18.77 | 19.20 |
| **Ab%** | 82.25 | 82.13 | 82.37 | 81.86 | 81.76 | 79.62 | 82.95 | 80.72 | 81.02 | 81.80 | 80.16 | 82.02 | 80.34 | 80.14 |

# 9. Synthesis and further questions

## 9.1. Conclusions

This chapter will summarise the main conclusions of Chapters 5-8, placing the findings of each piece of work within the framework of the wider thesis and outlining their implications for our understanding of deformation mechanisms and strain localisation in mica-bearing mylonites. Finally, outstanding questions and future directions of study will be discussed.

### 9.1.1. Ripplocations as a mechanism of intracrystalline deformation

Chapter 5 reported evidence of ripplocations within biotite grains from mylonites of the CMB line and Pogallo line. This is the first record of such features in natural minerals and the first within a material that has been deformed by natural processes. The key evidence takes the form of nanoscale expansions of biotite interlayer regions parallel to the c-axis, observed in TEM micrographs. Such features cannot be explained by the motion of basal dislocations alone as basal dislocation glide contains no component of c-axis parallel strain. In addition, energy considerations suggest basal dislocation glide likely takes place between the octahedral and tetrahedral sheets (Noe and Veblen, 1999a) and therefore cannot account for displacement across biotite interlayers. The interlayer expansion nanostructures align to form en-echelon arrays in two principal, conjugate orientations, with the angle between these orientations bisected by the biotite basal plane. Such a configuration is reminiscent of conjugate normal faults at much larger scales and suggests distributed expansion parallel to the c-axis. During deformation, compression parallel to the basal planes can be accommodated by a build-up of ripplocations within a mica crystal lattice with an initially elastic character. These ripplocations are exceptionally mobile and are attracted to each other both within and across lattice planes (Gruber *et al.*, 2016). As further strain is accommodated, the ripplocations align across planes to form kink bands, enabling permanent strain via shortening parallel to the basal plane. If, however, a strained grain containing ripplocations is exhumed to the surface, sampled and then prepared as a specimen for analysis, the confining stresses are gradually removed and the ripplocations combine to form the observed delamination microstructures resulting in grain-scale c-axis expansion.

Ripplocations and their motion represent a new defect and mechanism which can explain many of the ambiguous properties of mica deformation, such as kinking, and present important implications for our understanding of mica bearing fault and shear zones. The

process of kinking, whilst well observed and documented, has thus far been poorly understood as researchers have struggled to explain it in the context of experimental evidence that dislocation motion outside of the basal planes does not occur in phyllosilicates. Ripplocations offer a new perspective on this process as a phenomenon driven by the coalescence of defects on the scale of lattice planes. Ripplocations may also serve as an explanation for the observed pressure sensitivity of micas even at very high temperatures as, in contrast to dislocations, the motion and characteristics of ripplocations are strongly influenced by confining pressure. In this way, the well documented easy slip of micas parallel to basal planes may be associated not with dislocation glide but with the motion of ripplocations. Initially, the character of ripplocations is likely to be elastic, as shown by their ability to form fully reversible hysteresis loops during compressional loading (Griggs *et al.*, 2017) and their probable association with kinking nonlinear elasticity in micas (Basu *et al.*, 2009). However, their ability to form permanent kink bands shows that initial elasticity develops into permanent deformation without the need for brittle fracture. Ripplocations also bear significant potential implications for fluid flow in crustal fault and shear zones. If large ripplocations and delaminations result in the formation of lenticular microcracks then there is the potential for substantial transient porosity during deformation of phyllosilicate-rich rocks, by a system similar to the vug wave model of Phipps Morgan and Holtzman, (2005). Syn-deformational fluid pumps have also been proposed in systems deforming by viscous grain boundary sliding, creep cavitation and dissolution precipitation processes (Fusseis *et al.*, 2009; Menegon *et al.*, 2015) but through ripplocations may be a common occurrence in phyllosilicate bearing shear zones.

### 9.1.2. Dramatic grain-size reduction of biotite through stress-induced dissolution-precipitation

Chapter 6 addresses the mechanism responsible for the dramatic grain size reduction which affects biotite in mylonites of the CMB line and Pogallo line composed of between 10% and 25% mica. With increasing strain, biotite undergoes a substantial grain size reduction which completely consumes original coarser grains. This process produces a sharp boundary between parent grains and very fine 1-5 μm new grains without intermediate grain sizes or the development of subgrains. A subtle but regular compositional change (principally in the form of a reduction in Ti content) is also evident in the biotite during this transformation, suggesting the process is not entirely mechanical but involves an element of chemical disequilibrium. The grain size reduction occurs initially at sites of high strain within biotite grains such as along kink bands and at grain tips and peripheries and, notably, does not affect

muscovite grains to same extent. From the microstructural and chemical evidence, it is proposed that the biotite has undergone a fluid-facilitated, stress-induced dissolution-precipitation reaction, whereby fine, new biotite, and other phases including Ti oxides and feldspars, precipitate at the expense of strained parent biotite grains. Dissolution-precipitation also effects the other phases in the mylonite, with plagioclase, K-feldspar and quartz undergoing dissolution-precipitation and producing bands of fine-grained polyphase material. These bands deform by fluid assisted viscous grain boundary sliding and dissolution-precipitation creep, making them weaker than the quartz and feldspar framework and enabling them to localise strain. The mixture of phases also serves to pin recrystalising quartz grain boundaries and maintain a fine grain size.

The development of weak, fine-grained polyphase domains leads to an important transition from a load-bearing framework to an interconnected weak layer microstructure. As these polyphase bands develop into wider domains and interconnect along C surfaces and C' shear bands the initial coarser grained load-bearing framework is ultimately replaced by a widespread ultramylonitic matrix. The resulting change in dominant deformation mechanism, from dislocation creep of quartz and brittle fracturing of feldspar, to fluid assisted viscous granular flow of a polyphase matrix, represents a substantial rheological weakening. This process is greatly accelerated by the dissolution-precipitation reactions of biotite as the precipitation of very fine mixed phases inhibits dynamic recrystallisation and pins the grain size of monophase quartz domains at grain sizes which favour grain size sensitive deformation mechanisms. In this way we have shown that, even when present in relatively low abundances and distributed initially in isolated grains, biotite can have a fundamental influence on the microstructural evolution of a mylonite at the conditions of the mid-crust. At the same time, muscovite is less able to influence the wider rheology of a shear zone due to its apparent stability relative to biotite under the same conditions.

### 9.1.3. The influence of mica content on strain localisation

The influence of mica on the rheology of a mylonite and at the scale of a shear zone is also the focus of Chapter 7 which compares the microstructural evolution of mica-bearing orthogneiss and paragneiss mylonites (such as those discussed in Chapter 6) with that of mica-dominated mica schists. Across the mylonites of the CMB line and Pogallo line there is a distinct difference in the distribution of strain within mica-rich rocks and those with lower mica content. The mica-rich Kinzigites (mica-schist) accommodate strain over a wide region of distributed deformation, composed predominantly of protomylonites and slightly higher strain mylonites (in closer proximity to the centre of the shear zone). By contrast, the granitic

and orthogneiss rocks of the Serie dei Laghi are deformed within a narrower region which displays highly localised deformation in high strain mylonites and ultramylonites interspersed within lower strain rocks. This type of strain distribution is mirrored at the thin section-scale. Increasing plagioclase content and decreasing mica content within Kinzigites results in a greater tendency to form localised C' shear bands while rocks with greater mica content develop pervasive S-C fabrics. We relate this to the influence of plagioclase as a rigid load-bearing framework phase. High strain shear bands are initiated by brittle failure of plagioclase grains and then serve to interconnect weaker mica layers. Conversely, in a microstructure that is dominated by mica, these layers are already well connected, and strain can be accommodated within the interconnected weak layers without the geometric requirement of forming C' shear bands. In orthogneiss rocks with low mica content, the dramatic grain size reduction process discussed in Chapter 6 produces weak domains which strongly localise strain into shear bands and enable the development of ultramylonites.

The implications of this are that ultramylonites and very high strain rocks may be less prominent in mica-rich lithologies than in those with a low to moderate mica content. Mica-rich rocks are weak — perhaps approaching the strength of mica single crystals (Wintsch *et al.*, 1995) — but distribute strain across a wide region, whereas biotite-bearing, but not biotite-dominated, lithologies promote substantial strain localisation into narrow high strain bands which undergo significant rheological weakening and changes in dominant deformation mechanism. The role of ripplocations in the deformation of micas in both these scenarios (mica-dominated and biotite-bearing) is potentially crucial. In mica-rich rocks and in muscovite — where the dissolution-precipitation mechanism is not prominent — our findings from Chapter 5 and 7 suggest ripplocations are likely to be the key mechanism facilitating the accommodation of significant strain through shape change, kinking and reorientation of non-aligned mica grains. The motion of ripplocations may also play an important role during slip on the basal plane, which has previously been considered to be entirely a result of dislocation glide. However, further understanding of the prevalence and physical properties of ripplocation motion within phyllosilicates is required to support such a statement. In these rocks there is no development of weak, fine-grained polyphase domains and strain is localised within relatively coarse-grained mica layers, with intragranular deformation of mica (facilitated by ripplocations) representing the dominant deformation mechanism in the mylonite. This is less the case in, for example, orthogneiss mylonites in which the dramatic grain size reduction of biotite occurs, and substantial strain is accommodated by fluid assisted viscous grain boundary sliding. However, ripplocations

may still be important for these processes too. The initial, coarse biotite grains are kinked and strained, indicating the role of ripplocations during early intragranular deformation. It is at these highly strained locations (kink bands, grain tips etc.) that the dissolution-precipitation reaction is initially focussed. The unique potential for ripplocation defects to carry nanoscale, transient, syn-deformational porosity may be important in making these highly strained, ripplocation-rich regions more exposed to a fluid phase. This could work in combination with a component of internal strain energy to make these highly strained regions more susceptible to dissolution processes.

### 9.1.4. Incongruent pressure solution of feldspars

Chapter 8 analyses the mechanisms affecting the feldspar clasts within a granitic orthogneiss ultramylonite of the Pogallo line, in order to evaluate the behaviour of other minerals that are common in mica-bearing rocks. Specifically, it proposes the activity of stress-induced incongruent pressure solution involving a reversible reaction between plagioclase and K-feldspar, facilitated by extensive cation exchange with an aqueous phase. This process enables shape change, volume redistribution and grain size reduction of both plagioclase and K-feldspar. This process is aided by the brittle fracturing of feldspars and is likely to be an important process in the deformation and comminution of feldspars and the development of a well-mixed, polyphase, ultramylonitic matrix. Importantly, these microstructures serve as evidence of the importance of considering the joint feedbacks between stress and chemistry in deforming rocks, especially in the presence of a fast, diffusive medium such as an aqueous phase. The evidence and model outlined in Chapter 8 are summarised below.

Fine-grained K-feldspar is present in pressure shadows of porphyroclasts and within fractures of plagioclase clasts, while K-feldspar porphyroclasts are decorated by fine-grained plagioclase along surfaces oriented perpendicular to $\sigma_1$. These fine plagioclase grains have compositions markedly more albitic than the coarser plagioclase porphyroclasts, suggesting they are not produced by brittle fragmentation of the porphyroclasts but by nucleation and growth of new plagioclase. Irregular boundaries between the new plagioclase and the K-feldspar porphyroclasts contrast with sharp, straight boundaries where both meet the matrix, indicating a direct replacement of K-feldspar with plagioclase. EBSD orientation data suggests this replacement is topotactic in nature. Similar relationships exist where fine-grained, new K-feldspar has developed in association with pressure shadows and fractures of plagioclase porphyroclasts, highlighting these as locations where the replacement reaction reverses – K-feldspar grows at the expense of plagioclase. This microstructural distribution can be summarised by the statement that plagioclase replaces K-feldspar at sites of highest

stress and K-feldspar replaces plagioclase at sites of lowest stress. The presence of fine-grained new K-feldspar within pressure shadows of porphyroclasts of all minerals indicates an inclination for K-feldspar to precipitate at sites of lower normal stress even if plagioclase is not present. However, the reverse in this case is not true, with new plagioclase only forming at high-stress interfaces of K-feldspar and not at high-stress interfaces of other types of porphyroclast.

Molar volume calculations show that the reaction of K-feldspar with aqueous $Na^+$ and $Ca^{2+}$ cations to form plagioclase and aqueous $K^+$ cations results in a molar volume decrease. This reduction in volume provides a driving force for the reaction to occur at high stress interfaces. The reaction locally increases the activity of $K^+$ in the aqueous phase while decreasing the activity of aqueous $Na^+$ and $Ca^{2+}$, introducing activity gradients in these species within the aqueous phase. The diffusion of aqueous $K^+$ away from (and aqueous $Na^+$ and $Ca^{2+}$ towards) the localised high-stress reaction sites down this gradient, results in perturbations of chemical equilibria elsewhere, where the increased activity of $K^+$ ions drives the precipitation of K-feldspar either directly at the expense of plagioclase, or by consuming quartz and muscovite from the matrix. Both of these reactions result in a volume increase meaning that they are more energetically viable (and thus principally occur) at lower stress microstructural sites, such as fractures and pressure shadows. In this way the ionic composition of the aqueous phase is locally buffered by the precipitation and consumption of plagioclase and K-feldspar, while volume is transferred away from high normal stress interfaces and towards pressure shadows and fractures. The modal abundance of each phase need not change significantly during this process, rather, plagioclase and K-feldspar are redistributed and the porphyroclasts are progressively replaced by finer-grained feldspars.

The conclusions of Chapters 6 and 8 concur that stress-induced, fluid-facilitated dissolution-reprecipitation reactions are of critical importance to the deformation and microstructural evolution of mylonites of granitoid composition in the mid crust. In the stress-induced incongruent reactions involving feldspars (discussed in Chapter 8), the requirement for only highly mobile monovalent (or divalent in the case of $Ca^{2+}$) cations to be transported intergranular distances by diffusive mass transfer without the need for transport of less mobile cations, suggests this process could be even weaker than regular, congruent, dissolution-precipitation creep as it is essentially an in situ mineral replacement reaction. In the case of both the feldspar reactions and those of biotite, not only do they weaken otherwise strong feldspar or unfavourably oriented biotite, but, crucially, such reactions are integral to the development and continued deformation of a weak, fine-grained, well-mixed,

polyphase ultramylonitic matrix. Indeed, the combined action of brittle failure and incongruent reactions initially, followed by the dominance of reactions within the more mature microstructure are the most important aspect of the microstructural evolution of these mylonites, despite the most abundant phase, quartz, taking a secondary role in these processes and deforming predominantly by dislocation creep in all but the highest strain rocks. These dissolution-precipitation reactions directly require a fluid phase, highlighting the possibility that amphibolite facies shear zones such as the ones studied may act as important conduits for the flow of fluids in the deep crust.

Figure 9.1 summarises the conceptual conclusions of this thesis and attempts to show some of the connections between the findings of each chapter.

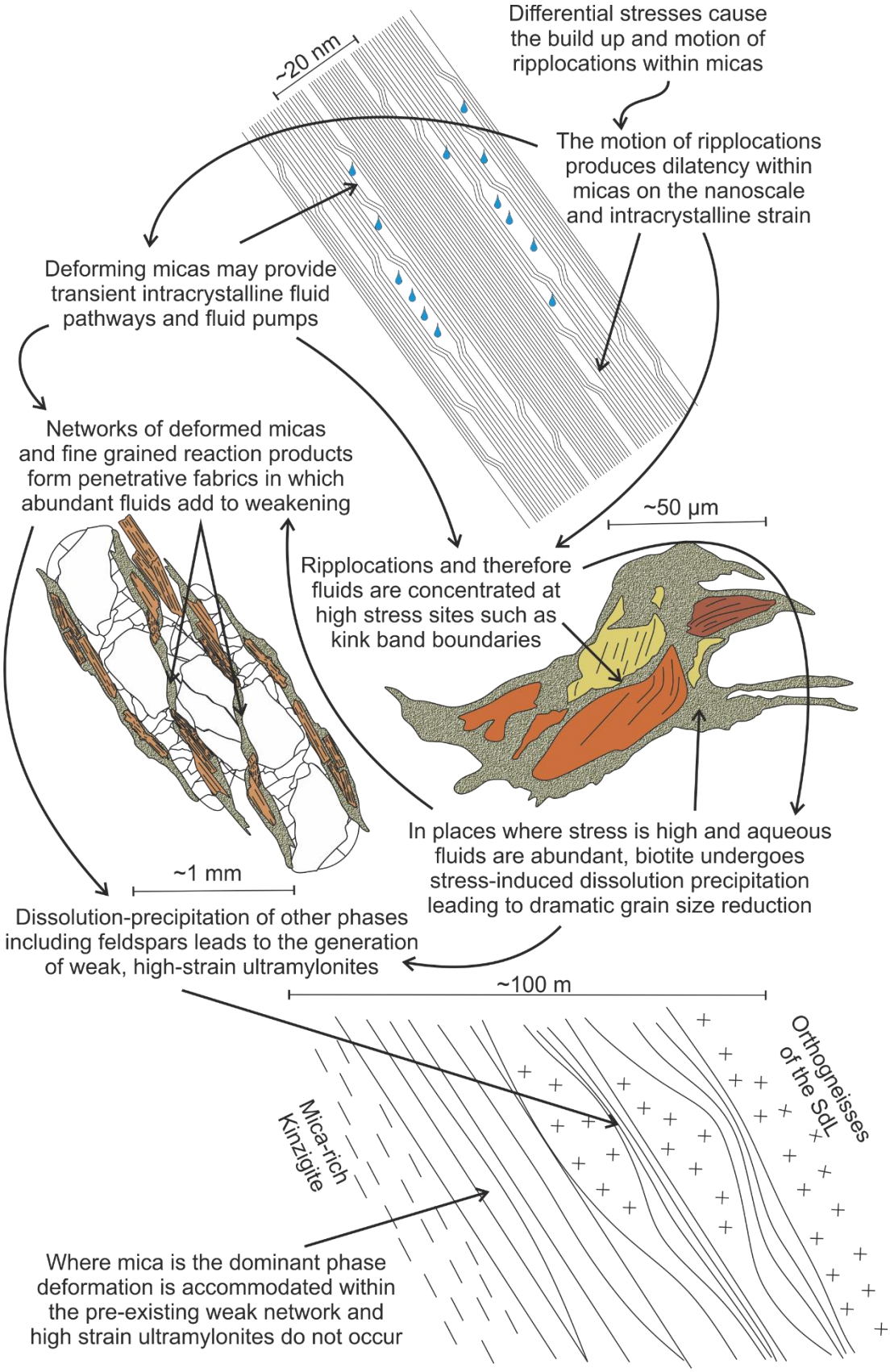


*Figure 9.1: Schematic diagrams highlighting the key conceptual findings of this thesis and the connections between the conclusions of each chapter.*

## 9.2. Remaining questions

The work outlined in this thesis has contributed to our understanding of the mechanisms and processes responsible for mica deformation under the conditions of the Earth's middle and lower crust. However, the findings also raise many important questions to be addressed by future work. This final section will discuss potential directions for future work, which arise from the conclusions of this thesis.

The most significant finding from this thesis, and also the one which requires the greatest consideration with regard to future work, is that of the presence of ripplocations as a previously unknown defect and deformation mechanism within micas. The study presented in Chapter 5 of this thesis is the first work to identify evidence of these defects in natural minerals and the scope of the study is focussed on confirming their presence. There is now a need to explore the process of ripplocation motion and its physical characteristics as a deformation mechanism. Purposely designed new experimental studies of mica deformation in the context of ripplocation theory and multi-scale microstructural analyses could address these aspects. In particular, it will be important to establish whether easy slip parallel to the basal plane (observed in many experimental studies) is, to some extent, a result of ripplocation motion and whether dislocation glide is as dominant in the deformation of micas as previously thought. If dislocation glide and ripplocation work in tandem during mica deformation, does the magnitude of the component of one mechanism relative to the other vary as a function of the orientation of principal stress axes with respect to the basal plane? For example, it may be that where micas are oriented favourably basal dislocation glide could be very important, especially at high confining pressures which inhibit the formation of ripplocations, however, where micas are oriented unfavourably, ripplocations are the mechanism which facilitates the majority of deformation through bending and kinking. Ripplocations appear to only be viable in highly anisotropic layered minerals, however, they are likely to influence neighbouring minerals across grain boundaries. It is possible, for example, that the strain accommodated in ripplocations within a biotite grain is transferred into a network of dislocations within a neighbouring quartz grain, but the dynamics of how this could occur is not clear. A major curiosity surrounding ripplocations is whether they represent a brittle or a viscous deformation mechanism. As with viscous mechanisms, they enable deformation without the permanent breaking of bonds, however, like brittle mechanisms they appear to be strongly influenced by confining-pressure. The transition from a ripplocation to a larger delamination (which is essentially a brittle lenticular micro-fracture) may be significant in this respect, although potentially very difficult to define.

The scope of this thesis has been limited to the amphibolite to upper-greenschist facies rocks of the study area. There would be value in determining the limits of the range of P/T and fluid availability conditions in which the microstructural evolution described is applicable. At higher temperatures the dehydration of micas must be considered, as in the experiments of Holyoke and Tullis, (2006), which described biotite breaking down via a dehydration reaction. At lower temperatures (and in the presence of fluid) Ca-bearing plagioclase becomes unstable and forms albite via dissolution-precipitation mineral replacement reactions which would affect the incongruent pressure solution process described in Chapter 8. In addition, all the mechanisms described in this thesis which rely on dissolution-precipitation and diffusive mass transfer would be severely hindered, if not impossible, in dry rocks deficient in an aqueous phase. The feedbacks between strain localisation and fluid availability within shear zones, and with relation to ultramylonites, are a topic of major recent interest (Oliot *et al.*, 2014; Menegon *et al.*, 2015; Finch *et al.*, 2016; Goncalves *et al.*, 2016) but remain poorly understood. It would be interesting to test if the presence of fluids is as critical in the development of ultramylonites in other lithologies as it is to those examined in this study.

It was suggested in Chapter 8 of this thesis that the incongruent pressure solution of feldspars in fluid bearing granitic mylonites may be faster than regular congruent pressure solution (or dissolution precipitation creep) as more immobile components need not diffuse over significant distances. This would be a very interesting concept to test, either experimentally or through microstructural analysis of a range of natural rocks. As well as differential stress and the presence of a fluid phase the process described requires both plagioclase and K-feldspar to be abundant within the rock, because if only a single feldspar phase were present the reaction would not be able to proceed in the way it does. This may mean that under amphibolite facies conditions and in the presence of fluids, rocks containing just one feldspar remain stronger than those bearing both plagioclase and K-feldspar, as faster incongruent pressure solution is only feasible in the latter. The importance of incongruent pressure solution may also be understated in the literature, as the microstructures produced are somewhat dissimilar to those of regular pressure solution and the process of incongruent pressure solution has not been widely reported on.

# References


Ahn, J. H., Peacor, D. R. and Essene, E. J. (1986) 'Cation-diffusion-induced characteristic beam damage in transmission electron microscope images of micas', *Ultramicroscopy*, 19(4), pp. 375–381. doi: 10.1016/0304-3991(86)90097-5.

Allen, M. J. (2017) *Physicochemical evolution of an active plate boundary fault ; the Alpine Fault , New Zealand : insight from the Deep Fault Drilling Project*. University of Liverpool.

Anderson, E. M. (1951) *The dynamics of faulting and dyke formation with applications to Britain*. Hafner Pub. Co.

Ashworth, J. R. (1972) 'Myrmekites of exsolution and replacement origins', *Geological Magazine*, 109(1), pp. 45–62. doi: 10.1017/S0016756800042266.

Aslin, J. *et al.* (2019) 'Ripplocations provide a new mechanism for the deformation of phyllosilicates in the lithosphere', *Nature Communications*, 10(1), p. 686. doi: 10.1038/s41467-019-08587-2.

Barsoum, M. W. *et al.* (2019) 'Ripplocations: A universal deformation mechanism in layered solids', *Physical Review Materials*. American Physical Society, 3(1), p. 013602. doi: 10.1103/PhysRevMaterials.3.013602.

Barsoum, M. W. and Tucker, G. J. (2017) 'Deformation of layered solids: Ripplocations not basal dislocations', *Scripta Materialia*. Acta Materialia Inc, 139, pp. 166–172. doi: 10.1016/j.scriptamat.2017.04.002.

Basu, S., Zhou, A. and Barsoum, M. W. (2009) 'On spherical nanoindentations, kinking nonlinear elasticity of mica single crystals and their geological implications', *Journal of Structural Geology*. Elsevier Ltd, 31(8), pp. 791–801. doi: 10.1016/j.jsg.2009.05.008.

Beach, A. (1979) 'Pressure solution as a metamorphic process in deformed terrigenous sedimentary rocks', *Lithos*, 12(1), pp. 51–58. doi: 10.1016/0024-4937(79)90062-8.

Becke, F. (1908) 'Uber myrmekit', *Min. Pet. Mitt*, 27, pp. 377–391.

Behrmann, J. H. (1984) 'A study of white mica microstructure and microchemistry in a low grade mylonite', *Journal of Structural Geology*, 6(3), pp. 283–292. doi: 10.1016/0191-8141(84)90052-X.

Behrmann, J. H. and Mainprice, D. (1987) 'Deformation mechanisms in a high-temperature quartz-feldspar mylonite: evidence for superplastic flow in the lower continental crust',

*Tectonophysics*, 140, pp. 297–305.

Bell, I. A. *et al.* (1986) 'Kinks in mica: Role of dislocations and (001) cleavage', *Tectonophysics*, 127(1–2), pp. 49–65. doi: 10.1016/0040-1951(86)90078-8.

Bell, I. A. and Wilson, C. J. L. (1977) 'Growth defects in metamorphic biotite', *Physics and Chemistry of Minerals*, 2(1–2), pp. 153–169. doi: 10.1007/BF00307529.

Bell, I. A. and Wilson, C. J. L. (1981) 'Deformation of Biotite and Muscovite: TEM Microstructure and Deformation Model', *Tectonophysics*, 78, pp. 201–228.

Bell, T. H. (1978) 'Syntectonic nucleation of new grains in deformed mica', *Tectonophysics*, 51(3–4). doi: 10.1016/0040-1951(78)90229-9.

Berckhemer, H. (1969) 'Direct evidence for the composition of the lower crust and the moho', *Tectonophysics*, 8(2), pp. 97–105.

Berthe, D., Choukroune, P. and Jegouzo, P. (1979) 'Orthogneiss, mylonite and non coaxial deformation of granites: the example of the South Armorican Shear Zone', *Journal of Structural Geology*, 1(1), pp. 31–42.

Bish, D. L. and Giese, R. F. (1981) 'Interlayer bonding in IIb chlorite.', *American Mineralogist*, 66(11–12), pp. 1216–1220.

Blenkinsop, T. G. (2002) *Deformation Microstructures and Mechanisms in Minerals and Rocks by Contents Acknowledgements ix*. New York, Boston, Dordrecht, London, Moscow: Kluwer Academic Publishers.

Bolognesi, F. and Bistacchi, A. (2016) 'Weakness and mechanical anisotropy of phyllosilicate-rich cataclasites developed after mylonites of a low-angle normal fault (Simplon Line, Western Alps)', *Journal of Structural Geology*. Elsevier Ltd, 83, pp. 1–12. doi: 10.1016/j.jsg.2015.11.009.

Bons, P. D. and den Brok, B. (2000) 'Crystallographic preferred orientation development by dissolution–precipitation creep', *Journal of Structural Geology*, 22(11–12), pp. 1713–1722. doi: 10.1016/S0191-8141(00)00075-4.

Boriani, A. *et al.* (1988) 'Geological and petrological studies of the Hercynian plutonism of Serie dei Laghi - Geological map of its occurrence between Valsesia and Lago Maggiore (Italy)'.

Boriani, A., Giobbi Origoni, E., *et al.* (1990) 'The evolution of the "Serie dei Laghi" (Strona-Ceneri and Scisti dei Laghi): the upper component of the Ivrea-Verbano crustal section; Southern Alps, North Italy and Ticino, Switzerland', *Tectonophysics*, 182, pp. 103–118.

Boriani, A., Giobbi Origoni, E., *et al.* (1995) 'Carta Geologica della Valle Cannobina'. Milano: Grafiche Diodoro.

Boriani, A., Burlini, L. and Sacchi, R. (1990) 'The Cossato-Mergozzo-Brissago Line and the Pogallo Line (Southern Alps, Northern Italy) and their relationships with the late-Hercynian magmatic and metamorphic events', *Tectonophysics*, 182(1–2), pp. 91–102. doi: 10.1016/0040-1951(90)90344-8.

Boriani, A., Caironi, V. and Sacchi, R. (2016) 'The CMB Line: the southern margin of the Ivrea–Verbano Zone (basement of Southern Alps, Italy): a re-appraisal', *Rendiconti Lincei*. Springer International Publishing, 27(4), pp. 673–678. doi: 10.1007/s12210-016-0548-0.

Boriani, A. and Giobbi, E. (2004) 'Does the basement of western southern Alps display a tilted section through the continental crust? A review and discussion', *Periodico di Mineralogia*, 73(2), pp. 5–22.

Boriani, A., Origoni, E. G. and Pinarelli, L. (1995) 'Paleozoic evolution of southern Alpine crust (northern Italy) as indicated by contrasting granitoid suites', *Lithos*, 35(1–2), pp. 47–63. doi: 10.1016/0024-4937(94)00043-2.

Bos, B. and Spiers, C. J. (2001) 'Experimental investigation into the microstructural and mechanical evolution of phyllosilicate-bearing fault rock under conditions favouring pressure solution', *Journal of Structural Geology*, 23(8), pp. 1187–1202. doi: 10.1016/S0191-8141(00)00184-X.

Bos, B. and Spiers, C. J. (2002) 'Frictional-viscous flow of phyllosilicate-bearing fault rock: Microphysical model and implications for crustal strength profiles', *Journal of Geophysical Research*, 107. doi: 10.1029/2001JB000301.

Boulton, C. *et al.* (2012) 'Physical properties of surface outcrop cataclastic fault rocks, Alpine Fault, New Zealand', *Geochemistry, Geophysics, Geosystems*, 13(1), pp. 1–13. doi: 10.1029/2011GC003872.

De Bresser, J. H. P. *et al.* (1998) 'On dynamic recrystallization during solid state flow: Effects of stress and temperature', *Geophysical Research Letters*, 25(18), pp. 3457–3460. doi: 10.1029/98GL02690.

De Bresser, J. H. P., Ter Heege, J. H. and Spiers, C. J. (2001) 'Grain size reduction by dynamic recrystallization: Can it result in major rheological weakening?', *International Journal of Earth Sciences*, 90, pp. 28–45. doi: 10.1007/s005310000149.

Brigatti, M. F. and Guggenheim, S. (2002) 'Mica crystal chemistry and the influence of pressure, temperature and solid solution on atomistic models', in Mottana, A. et al. (eds) *Micas:*

*Crystal Chemistry and Metamorphic Petrology*. Washington DC: Mineralogical Society of America, pp. 1–99.

Brodie, K. H. and Rutter, E. H. (1986) 'The role of transiently fine-grained reaction products in syntectonic metamorphism: natural and experimental examples', *Canadian Journal of Earth Sciences*, 24(3), pp. 556–564. doi: 10.1139/e87-054.

Brodie, K. H. and Rutter, E. H. (1987) 'Deep crustal extensional faulting in the lvrea Zone of Northern Italy', *Tectonophysics*. Elsevier Science Publishers B.V, 140, pp. 193–212.

Brune, J. N., Brown, S. and Johnson, P. A. (1993) 'Rupture mechanism and interface separation in foam rubber models of earthquakes: a possible solution to the heat flow paradox and the paradox of large overthrusts', *Tectonophysics*, 218(1–3), pp. 59–67. doi: 10.1016/0040-1951(93)90259-M.

Bukovska, Z., Jerabek, P. and Morales, L. F. G. (2016) 'Major softening at brittle-ductile transition due to interplay between chemical and deformation processes: An insight from evolution of shear bands in the South Armorican Shear Zone', pp. 7986–8011. doi: 10.1002/2015JB012061.Received.

Burke, M. M. and Fountain, D. M. (1990) 'Seismic properties of rocks from an exposure of extended continental crust-new laboratory measurements from the Ivrea Zone', *Tectonophysics*, 182, pp. 119–146.

Burov, E. B. and Watts, A. B. (2006) 'the long-term strength of continental lithosphere: "jelly sandwich" or "crème brûlée"?', *GSa ToDay GSA Today: v*, 16(4). doi: 10.1130/1052-5173(2006)016<4:tltSOc>2.0.cO;2.

Byerlee, J. (1978) 'Friction of Rocks', in *Rock friction and earthquake prediction*. Basel: Birkhauser Verlag, pp. 615–626. Available at: https://earthquake.usgs.gov/static/lfs/research/rockphysics/Friction_of_rocks.pdf.

Canova, G. R., Wenk, H. R. and Molinari, a. (1992) 'Deformation modelling of multi-phase polycrystals: case of a quartz-mica aggregate', *Acta Metallurgica et Materialia*, 40(7), pp. 1519–1530. doi: 10.1016/0956-7151(92)90095-V.

Carlson, W. D. (2002) 'Scales of disequilibrium and rates of equilibration during metamorphism.', *American Mineralogist*, 87, pp. 185–204.

Carpenter, M. A. (1994) 'Subsolidus phase relations of the plagioclase feldspar solid solution', in *Feldspars and their reactions*. Dordrecht: Springer, pp. 221–269.

Ceccato, A. *et al.* (2018) 'Myrmekite and strain weakening in granitoid mylonites', *Solid Earth*, 9(6), pp. 1399–1419. doi: 10.5194/se-9-1399-2018.

Chen, W. P. and Molnar, P. (1983) 'Focal depths of intrcontinental and intraplate earthquakes and their implications for the thermal and mechanical properties of the lithosphere.', *Journal of Geophysical Research*, 88(B5), pp. 4183–4214.

Christoffersen, R. and Kronenberg, A. K. (1993) 'Dislocation interactions in experimentally deformed biotite', *Journal of Structural Geology*, 15(9–10), pp. 1077–1095. doi: 10.1016/0191-8141(93)90157-6.

Cisneros-Lazaro, D. G., Miller, J. A. and Baumgartner, · L P (2019) 'Role of myrmekite and associated deformation fabrics in controlling development of granitic mylonites in the Pofadder Shear Zone of southern Namibia', *Contributions to Mineralogy and Petrology*, 174, p. 22. doi: 10.1007/s00410-019-1555-9.

Cole, J. *et al.* (2007) 'Localized ductile shear below the seismogenic zone: Structural analysis of an exhumed strike-slip fault, Austrian Alps', *Journal of Geophysical Research: Solid Earth*, 112(12), pp. 1–15. doi: 10.1029/2007JB004975.

Collettini, C. *et al.* (2009) 'Fault zone fabric and fault weakness', *Nature*, 462(7275), pp. 907–910. doi: 10.1038/nature08585.

Cox, S. F. and Paterson, M. S. (1991) *Experimental dissolution-precipitation creep in quartz aggregates [abs]*, *Eos, Transactions American …*.

Craw, D. (1981) 'Oxidation and microprobe-induced potassium mobility in iron-bearing phyllosilicates from the Otago schists, New Zealand', *Lithos*, 14(1), pp. 49–57. doi: 10.1016/0024-4937(81)90036-0.

Cross, A. J. *et al.* (2017) 'The recrystallized grain size piezometer for quartz: An EBSD-based calibration', *Geophysical Research Letters*, 44(13), pp. 6667–6674. doi: 10.1002/2017GL073836.

Cross, A. J., Hirth, G. and Prior, D. J. (2017) 'Effects of secondary phases on crystallographic preferred orientations in mylonites', 45(10). doi: 10.1130/G38936.1.

Curran, D. R. *et al.* (1993) 'Micromechanical model for comminution and granular flow of brittle material under high strain rate: application to penetration of ceramic targets', *International journal of impact engineering*, 13(1), pp. 53–83.

Czaplińska, D., Piazolo, S. and Zibra, I. (2015) 'The influence of phase and grain size distribution on

the dynamics of strain localization in polymineralic rocks', *Journal of Structural Geology*, 72, pp. 15–32. doi: 10.1016/j.jsg.2015.01.001.

Deer, W. A., Howie, R. A. and Zussman, J. (1980) *An introduction to the rock forming minerals*. 12th edn. London: Longman Scientific and Technology.

Dempsey, E. D. *et al.* (2011) 'Mica-controlled anisotropy within mid-to-upper crustal mylonites : an EBSD study of mica fabrics in the Alpine Fault Zone , New Zealand', pp. 33–47.

Dick, H. J. B. and Sinton, J. M. (1979) 'Compositional Layering in Alpine Peridotites: Evidence for Pressure Solution Creep in the Mantle', *The Journal of Geology*, 87(4), pp. 403–416. doi: 10.1086/628428.

Dixon, J. and Williams, G. (1983) 'Reaction softening in mylonites from the Arnaboll thrust, Sutherland', *Scottish Journal of Geology*. Geological Society of London, 19(2), pp. 157–168. doi: 10.1144/sjg19020157.

Doherty, R. D. *et al.* (1998) 'Current issues in recrystallization: A review', *Materials Today*, 1(2), pp. 14–15. doi: 10.1016/S1369-7021(98)80046-1.

Douce, A. E. P. (1993) 'Titanium substitution in biotite : an empirical model with applications to thermometry , 02 and HeO barometries , and consequences for biotite stability', 108, pp. 133–162.

Drury, M. R. and Urai, J. L. (1990) 'Deformation-related recrystallization processes', *Tectonophysics*, 172(3–4), pp. 235–253. doi: 10.1016/0040-1951(90)90033-5.

Etheridge, M. A. and Hobbs, B. E. (1974) 'Chemical and deformational controls on recrystallization of mica', *Contributions to Mineralogy and Petrology*, 43(2), pp. 111–124. doi: 10.1007/BF00572714.

Etheridge, M. A., Hobbs, B. E. and Paterson, M. S. (1973) 'Experiental deformation of single crystals of biotite', *Contributions to Mineralogy and Petrology*, 38(1), pp. 21–36. doi: 10.1007/BF00371724.

Evans, B., Renner, J. and Hirth, G. (2001) 'A few remarks on the kinetics of static grain growth in rocks', *International Journal of Earth Sciences*, 90(1), pp. 88–103. doi: 10.1007/s005310000150.

Fabbri, F. *et al.* (2016) 'Novel near-infrared emission from crystal defects in MoS 2 multilayer flakes', *Nature Communications*. Nature Publishing Group, 7, pp. 1–7. doi: 10.1038/ncomms13044.

Fagereng, Å., Hillary, G. W. B. and Diener, J. F. A. (2014) 'Brittle-viscous deformation, slow slip, and tremor', *Geophysical Research Letters*, 41(12), pp. 4159–4167. doi: 10.1002/2014GL060433.

Faulkner, D. R. *et al.* (2010) 'A review of recent developments concerning the structure, mechanics and fluid flow properties of fault zones'. doi: 10.1016/j.jsg.2010.06.009.

Faulkner, D. R. *et al.* (2011) 'Stuck in the mud? Earthquake nucleation and propagation through accretionary forearcs', *Geophysical Research Letters*, 38(18), pp. 1–5. doi: 10.1029/2011GL048552.

Finch, M. A., Weinberg, R. F. and Hunter, N. J. R. (2016) 'Water loss and the origin of thick ultramylonites', *Geology*, 44(8), p. G37972.1. doi: 10.1130/G37972.1.

Fitz Gerald, J. D. and Stunitz, H. (1993) 'Deformation of granitoids at low metamorphic grade. I: Reactions and grain size reduction', *Tectonophysics*, 221, pp. 269–297.

Fliervoet, T. F., Drury, M. R. and Chopra, P. N. (1999) 'Crystallographic preferred orientations and misorientations in some olivine rocks deformed by diffusion or dislocation creep', *Tectonophysics*, 303(1–4), pp. 1–27. doi: 10.1016/S0040-1951(98)00250-9.

Fountain, D. M. and Salisbury, M. H. (1981) 'Exposed cross-sections through the continental crust" implications for crustal structure, petrology, and evolution', *Earth and Planetary Science Letters*, 56, pp. 263–277.

Freiberg, D., Barsoum, M. W. and Tucker, G. J. (2018) 'Nucleation of ripplocations through atomistic modeling of surface nanoindentation in graphite', *Physical Review Materials*. American Physical Society, 2(5), p. 053602. doi: 10.1103/PhysRevMaterials.2.053602.

Fry, N. (1982) 'Metamorphic incongruent solution, diffusion and pressure solution stripes', *Lithos*, 15(3), pp. 183–190. doi: 10.1016/0024-4937(82)90009-3.

Fukuda, J. ichi *et al.* (2012) 'Solution-precipitation of K-feldspar in deformed granitoids and its relationship to the distribution of water', *Tectonophysics*. Elsevier B.V., 532–535, pp. 175–185. doi: 10.1016/j.tecto.2012.01.033.

Fukuda, J. and Okudaira, T. (2013) 'Grain-size-sensitive creep of plagioclase accompanied by solution–precipitation and mass transfer under mid-crustal conditions', *Journal of Structural Geology*, 51, pp. 61–73. doi: 10.1016/j.jsg.2013.03.006.

Fusseis, F. (2007) *Strain localization and shear zone formation at the brittle-viscous transition, Cap de Creus, Spain*. Freie Universitat, Berlin.

Fusseis, F. *et al.* (2009) 'Creep cavitation can establish a dynamic granular fluid pump in ductile

shear zones.', *Nature*. Nature Publishing Group, 459(7249), pp. 974–7. doi: 10.1038/nature08051.

Fusseis, F. and Handy, M. R. (2008) 'Micromechanisms of shear zone propagation at the brittle–viscous transition', *Journal of Structural Geology*, 30(10), pp. 1242–1253. doi: 10.1016/j.jsg.2008.06.005.

Gardner, J. (2019) *Links between metamorphism and deformation in feldspar at mid-crustal conditions*. University of Liverpool.

Gasser, P. *et al.* (2004) 'Site-specific specimen preparation by focused ion beam milling for transmission electron microscopy of metal matrix composites.', *Microscopy and microanalysis*, 10(2), pp. 311–316. doi: 10.1017/S1431927604040413.

Giannuzzi, L. A. *et al.* (2005) 'FIB Lift-Out Specimen Preparation Techniques', in Giannuzzi, L. A. and Stevie, F. A. (eds) *Introduction to focussed ion beams, instrumentation, theory, techniques and practice*. New York: Springer Science & Business Media, pp. 201–229.

Giannuzzi, L. a. and Stevie, F. a. (2005) *Introduction To Focused Ion Beams, Instrumentation, Theory, Techniques and Practice*, *Springer*. Edited by L. A. Giannuzzi and F. A. Stevie. New York: Springer Science & Business Media. doi: 10.1007/b101190.

Giobbi Mancini, E., Boriani, A. and Villa, I. (2003) 'Pre-Alpine ophiolites in the basement of Southern Alps: the presence of a bimodal association (LAG- Leptyno-Amphibolitic Group) in the Serie dei Laghi (N-Italy, Ticino-CH)', *Rendiconti Lincei*, 14, pp. 79–99.

Girard, J. *et al.* (2013) 'Hydrolytic weakening of olivine at mantle pressure: Evidence of [1 0 0](0 1 0) slip system softening from single-crystal deformation experiments', *Physics of the Earth and Planetary Interiors*, 216, pp. 12–20. doi: 10.1016/j.pepi.2012.10.009.

Giuntoli, F., Menegon, L. and Warren, C. J. (2018) 'Replacement reactions and deformation by dissolution and precipitation processes in amphibolites', *Journal of Metamorphic Geology*, (July), pp. 1263–1286. doi: 10.1111/jmg.12445.

Goncalves, C. C., Goncalves, L. and Hirth, G. (2015) 'The effects of quartz recrystallization and reaction on weak phase interconnection, strain localization and evolution of microstructure', *Journal of Structural Geology*. Elsevier Ltd, 71, pp. 24–40. doi: 10.1016/j.jsg.2014.11.010.

Goncalves, P. *et al.* (2016) 'How does shear zone nucleate? An example from the Suretta nappe (Swiss Eastern Alps)', *Journal of Structural Geology*. Elsevier Ltd, 86, pp. 166–180. doi: 10.1016/j.jsg.2016.02.015.

Goodhew, P. J., Humphreys, J. and Beanland, R. (2014) *Electron microscopy and analysis*. CRC Press.

Goodwin, L. B. and Wenk, H.-R. (1995) 'Development of phyllonite from granodiorite: Mechanisms of grain-size reduction in the Santa Rosa mylonite zone, California', *Journal of Srrucrural Geology*, 17(5), pp. 689–707.

Goodwin, L. B. and Wenk, H. R. (1990) 'Intrcrystalline folding and cataclasis in biotite of the Santa-Rosa mylonite: observation, TEM and HVEM', *Tectonophysics*, 172, pp. 201–215.

Gratier, J.-P., Dysthe, D. and Renard, F. (2013) 'The role of pressure solution creep in the ductility of the earth's upper crust', *Advances in Geophysics*. Elsevier, 54, pp. 47–179. doi: 10.1016/B978-0.

Griggs, D. (1967) 'Hydrolytic Weakening of Quartz and Other Silicates*', *Geophys. J. R. astr. Soc.*, 14, pp. 19–31.

Griggs, D. (1974) 'A Model of Hydrolytic Weakening in Quartz', *Journal of geophysical research*, 79(11), pp. 1653–1661. doi: 10.1029/JB079i011p01653.

Griggs, J. *et al.* (2017) 'Spherical nanoindentation, modeling and transmission electron microscopy evidence for ripplocations in Ti3SiC2', *Acta Materialia*. Elsevier Ltd, 131, pp. 141–155. doi: 10.1016/j.actamat.2017.03.055.

ten Grotenhuis, S. M., Trouw, R. A. J. and Passchier, C. W. (2003) 'Evolution of mica fish in mylonitic rocks', *Tectonophysics*, 372(1–2), pp. 1–21. doi: 10.1016/S0040-1951(03)00231-2.

Gruber, J. *et al.* (2016) 'Evidence for Bulk Ripplocations in Layered Solids', *Scientific Reports*. Nature Publishing Group, 6(August), pp. 1–8. doi: 10.1038/srep33451.

Gueydan, F. *et al.* (2003) 'Analysis of continental midcrustal strain localization induced by microfracturing and reaction-softening', *Journal of Geophysical Research: Solid Earth*, 108(B2). doi: 10.1029/2001jb000611.

Handy (1990) 'the Solid-State Flow of Polymineralic Rocks', *Journal of Geophysical Research*, 95(B6), pp. 8647–8661. doi: 10.1029/JB095iB06p08647.

Handy, M. . and Brun, J.-P. (2004) 'Seismicity, structure and strength of the continental lithosphere', *Earth and Planetary Science Letters*, 223(3–4), pp. 427–441. doi: 10.1016/j.epsl.2004.04.021.

Handy, M. R. (1987) 'The structure, age and kinematics of the Pogallo Fault zone: Southern Alps, Northwestern Italy', *Eclogae geol. Helv.*, 80, pp. 593–632. doi: 10.5169/seals-166017.

Handy, M. R. (1994) 'Flow laws for rocks containing two non-linear viscous phases: a

phenomenological approach', *Journal of Structural Geology*, 16(3), pp. 287–301.

Handy, M. R. *et al.* (1999) *Multistage accretion and exhumation of the continental crust (Ivrea crustal section, Italy and Switzerland)*, *TECTONICS*. doi: 10.1029/1999TC900034.

Handy, M. R. and Streit, J. E. (1999) 'Mechanics and mechanisms of magmatic underplating; inferences from mafic veins in deep crustal mylonite', *Earth and Planetary Science Letters*, 165(3–4), pp. 271–286. doi: 10.1016/S0012-821X(98)00272-6.

Handy, M. R. and Stunitz, H. (2002) 'Strain localization by fracturing and reaction weakening-a mechanism for initiating exhumation of subcontinental mantle beneath rifted margins', in de Meer, S. et al. (eds) *Deformation Mechanisms, Rheology and Tectonics; Current Status and Future Perspectives*. London: Geological Society of London, pp. 387–407.

Handy, M. R., Wissing, S. B. and Streit, L. E. (1998) 'Frictional-viscous flow in mylonite with varied bimineralic composition and its effect on lithospheric strength', *Tectonophysics*, 303(1–4), pp. 175–191. doi: 10.1016/S0040-1951(98)00251-0.

Heaton, T. H. (1990) 'Evidence for and implications of self-healing pulses of slip in earthquake rupture', *Physics of the Earth and Planetary Interiors*, 64(1), pp. 1–20. doi: 10.1016/0031-9201(90)90002-F.

Heidelbach, F., Post, A. and Tullis, J. (2000) 'Crystallographic preferred orientation in albite samples deformed experimentally by dislocation and solution precipitation creep', *Journal of Structural Geology*, 22(11–12), pp. 1649–1661. doi: 10.1016/S0191-8141(00)00072-9.

Heilbronner, R. and Tullis, J. (2006) 'Evolution of c axis pole figures and grain size during dynamic recrystallization: Results from experimentally sheared quartzite', *Journal of Geophysical Research: Solid Earth*, 111(10), pp. 1–19. doi: 10.1029/2005JB004194.

Henry, D. J., Guidotti, C. V. and Thomson, J. A. (2005) 'The Ti-saturation surface for low-to-medium pressure metapelitic biotites: Implications for geothermometry and Ti-substitution mechanisms', *American Mineralogist*, 90(2–3), pp. 316–328. doi: 10.2138/am.2005.1498.

Herwegh, M. *et al.* (2011) 'The role of second phases for controlling microstructural evolution in polymineralic rocks: A review', *Journal of Structural Geology*, 33, pp. 1728–1750.

Herwegh, M. and Berger, A. (2004) 'Deformation mechanisms in second-phase affected microstructures and their energy balance', *Journal of Structural Geology*, 26, pp. 1483–1498. doi: 10.1016/j.jsg.2003.10.006.

Herwegh, M. and Jenni, A. (2001) 'Granular flow in polymineralic rocks bearing sheet silicates: New

evidence from natural examples', *Tectonophysics*, 332(3), pp. 309–320. doi: 10.1016/S0040-1951(00)00288-2.

Hickman, H. and Evans, B. (1995) 'Kinetics of pressure solution at halite-silica interfaces and intergranular clay films', *Journal of Geophysical Research*, 100(13), pp. 113–132.

Hiraga, T. *et al.* (2013) 'Comparison of microstructures in superplastically deformed synthetic materials and natural mylonites: Mineral aggregation via grain boundary sliding', *Geology*, 41(9), pp. 959–962. doi: 10.1130/G34407.1.

Hirth, G. and Guillot, S. (2013) 'Signifi cance of Serpentinite', pp. 107–114. doi: 10.2113/gselements.9.2.107.

Hirth, G. and Tullis, J. (1992) 'Dislocation creep regimes in quartz aggregates', *Journal of Structural Geology*, 14(2), pp. 145–159.

Hodges, K. V and Fountain, D. M. (1984) 'Pogallo Line, South Alps, northern Italy: An intermediate crustal level, low-angle normal fault?', *Geology*, 12(3), pp. 151–155. Available at: https://pubs.geoscienceworld.org/gsa/geology/article-pdf/12/3/151/3507401/i0091-7613-12-3-151.pdf (Accessed: 21 January 2019).

Holyoke, C. W. and Tullis, J. (2006a) 'Formation and maintenance of shear zones', *Geology*, (2), pp. 105–108. doi: 10.1130/G22116.1.

Holyoke, C. W. and Tullis, J. (2006b) 'Mechanisms of weak phase interconnection and the effects of phase strength contrast on fabric development', *Journal of Structural Geology*, 28(4), pp. 621–640. doi: 10.1016/j.jsg.2006.01.008.

Holyoke, C. W. and Tullis, J. (2006c) 'The interaction between reaction and deformation: An experimental study using a biotite + plagioclase + quartz gneiss', *Journal of Metamorphic Geology*, 24(8), pp. 743–762. doi: 10.1111/j.1525-1314.2006.00666.x.

Humphreys, M. C. S., Kearns, S. L. and Blundy, J. D. (2006) 'SIMS investigation of electron-beam damage to hydrous, rhyolitic glasses: Implications for melt inclusion analysis', *American Mineralogist*, 91(4), pp. 667–679. doi: 10.2138/am.2006.1936.

Hunter, N. J. R. *et al.* (2016) 'Fabric controls on strain accommodation in naturally deformed mylonites: The influence of interconnected micaceous layers', *Journal of Structural Geology*, 83, pp. 180–193. doi: 10.1016/j.jsg.2015.12.005.

Hunziker, J. C. and Zingg, A. (1980) 'Lower Palaeozoic amphibolite to granulite facies metamorphism in the Ivrea zone (southern Alps, northern Italy).', *Schweizerische Mineralogische und*

*Petrographische Mitteilungen*, 60, pp. 181–213.

Iijima, S. and Zhu, J. (1982) 'Electron microscopy of a muscovitFbiotite interface', 67(100), pp. 1195–1205.

Jackson, J. (2002) 'Strength of the continental lithosphere: Time to abandon the jelly sandwich?', *GSA Today*, 12, pp. 4–10.

Jacob, D. E. *et al.* (2016) 'Redox-freezing and nucleation of diamond via magnetite formation in the Earth's mantle', *Nature Communications*. Nature Publishing Group, 7(May), pp. 1–7. doi: 10.1038/ncomms11891.

Kerrich, R. *et al.* (1980) 'Microstructural and chemical transformations accompanying deformation of granite in a shear zone at Miéville, Switzerland; with implications for stress corrosion cracking and superplastic flow', *Contributions to Mineralogy and Petrology*, 73(3), pp. 221–242. doi: 10.1007/BF00381442.

Kilian, R., Heilbronner, R. and Stünitz, H. (2011) 'Quartz grain size reduction in a granitoid rock and the transition from dislocation to diffusion creep', *Journal of Structural Geology*, 33(8), pp. 1265–1284. doi: 10.1016/j.jsg.2011.05.004.

Klinge, S., Hackl, K. and Renner, J. (2015) 'A mechanical model for dissolution-precipitation creep based on the minimum principle of the dissipation potential', *Proceedings of the Royal Society A: Mathematical, Physical and Engineering Sciences*, 471(2180). doi: 10.1098/rspa.2014.0994.

Kohlstedt, D. L., Evans, B. and Mackwell, S. J. (1995) 'Strength of the lithosphere: Constraints imposed by laboratory experiments', *Journal of Geophysical Research*, 100(B9), p. 17,587-17,602. doi: 10.1029/95JB01460.

Kronenberg, A. K., Kirby, S. H. and Pinkston, J. (1990) 'Basal slip and mechanical anisotropy of biotite', *Journal of Geophysical Research*, 95(B12), p. 19257. doi: 10.1029/JB095iB12p19257.

Kronenberg, A. K., Segall, P. and Wolf, G. H. (1990) 'Hydrolytic weakening and penetrative deformation within a natural shear zone.', *Geophysical Monograph*, 56, pp. 21–36.

Kronenberg, A. K. and Tullis, J. (1984) 'Flow Strengths of Quartz Aggregates: Grain Size and Pressure Effects due to Hydrolytic Weakening', *Journal of Geophysical Research*, 89(B6), pp. 4281–4297.

Kruse, R. and Stünitz, H. (1999) *Deformation mechanisms and phase distribution in mafic high-*

*temperature mylonites from the Jotun Nappe, southern Norway*, *Tectonophysics*. doi: 10.1016/S0040-1951(98)00255-8.

Kushima, A. *et al.* (2015) 'Ripplocations in van der Waals layers', *Nano Letters*, 15(2), pp. 1302–1308. doi: 10.1021/nl5045082.

Lapworth, C. (1885) 'The Highland controversy in British geology: its causes, course and consequences.', *Nature*, 32(832), pp. 558–559.

Law, R. D. (1990) 'Crystallographic fabrics: a selective review of their applications to research in structural geology', in Knipe, R. J. and Rutter, E. H. (ed.) *Deformation Mechanisms, Rheology and Tectonics*. 54th edn. Geological society special publications, pp. 335–352.

Law, R. D. (2014) 'Deformation thermometry based on quartz c-axis fabrics and recrystallization microstructures: A review', *Journal of Structural Geology*. Elsevier Ltd, 66, pp. 129–161. doi: 10.1016/j.jsg.2014.05.023.

Leclère, H. *et al.* (2016) 'Permeability control on transient slip weakening during gypsum dehydration: Implications for earthquakes in subduction zones', *Earth and Planetary Science Letters*, 442, pp. 1–12. doi: 10.1016/j.epsl.2016.02.015.

Lister, G. S. and Snoke, A. W. (1984) 'S-C Mylonites', *Journal of Structural Geology*, 6(6), pp. 617–638.

Little, T. A. *et al.* (2015) 'The link between strength of lattice preferred orientation, second phase content and grain boundary migration: A case study from the Alpine Fault zone, New Zealand', *Journal of Structural Geology*. Elsevier Ltd, 81, pp. 59–77. doi: 10.1016/j.jsg.2015.09.004.

Lloyd, G. E. (1987) 'Atomic number and crystallographic contrast images with the SEM: a review of backscattered electron techniques', *Mineralogical Magazine*, 51, pp. 3–19.

Lloyd, G. E. *et al.* (2009) 'Mica, deformation fabrics and the seismic properties of the continental crust', *Earth and Planetary Science Letters*. Elsevier B.V., 288(1–2), pp. 320–328. doi: 10.1016/j.epsl.2009.09.035.

Mancktelow, N. S. and Pennacchioni, G. (2004) 'The influence of grain boundary fluids on the microstructure of quartz-feldspar mylonites', *Journal of Structural Geology*, 26(1), pp. 47–69. doi: 10.1016/S0191-8141(03)00081-6.

Mares, V. . and Kronenberg, a. . (1993) 'Experimental deformation of muscovite', *Journal of Structural Geology*, 15(9–10), pp. 1061–1075. doi: 10.1016/0191-8141(93)90156-5.

Mariani, E. (2002) 'An Experimental Study of the Deformation of White Mica', *PhD Thesis, University of Manchester*, 52, pp. 1278–1281.

Mariani, E., Brodie, K. H. and Rutter, E. H. (2006) 'Experimental deformation of muscovite shear zones at high temperatures under hydrothermal conditions and the strength of phyllosilicate-bearing faults in nature', *Journal of Structural Geology*, 28, pp. 1569–1587. doi: 10.1016/j.jsg.2006.06.009.

Mariani, E. and Ghassemieh, E. (2010) 'Microstructure evolution of 6061 O Al alloy during ultrasonic consolidation: An insight from electron backscatter diffraction', *Acta Materialia*, 58, pp. 2492–2503. doi: 10.1016/j.actamat.2009.12.035.

Marti, S. *et al.* (2017) 'Experimental investigation of the brittle-viscous transition in mafic rocks – Interplay between fracturing, reaction, and viscous deformation', *Journal of Structural Geology*, 105, pp. 62–79. doi: 10.1016/j.jsg.2017.10.011.

Matthews, J. W. and Blakeslee, A. E. (1974) 'Defects in epitaxial multilayers I. Misfit dislocations', *Journal of Crystal Growth*, 27, pp. 118–125. doi: 10.1016/S0022-0248(74)80055-2.

McLaren, A. C. (1991) *Transmission electron microscopy of minerals and rocks*. Cambridge, UK: Cambridge University Press.

McLellan, A. G. (Alister G. (1980) *The classical thermodynamics of deformable materials*. Cambridge University Press.

Mcpherren, E. D. and Kuiper, Y. D. (2013) 'The effects of DissolutionePrecipitation Creep on quartz fabrics within the Purgatory Conglomerate, Rhode Island', *Journal of Structural Geology*, 51, pp. 105–117. doi: 10.1016/j.jsg.2013.03.002.

Means, W. D. (1981) 'The concept of steady-state foliation', *Tectonophysics*, 78, pp. 179–199.

Means, W. D. (1995) 'Shear zones and rock history', *Tectonophysics*, 247, pp. 157–160.

Meike, A. (1989) 'In situ deformation of micas: a high-voltage electron-microscope study', *American Mineralogist*, 74(7–8), pp. 780–796.

Menegon, L., Pennacchioni, G., Heilbronner, R., *et al.* (2008) 'Evolution of quartz microstructure and c-axis crystallographic preferred orientation within ductilely deformed granitoids (Arolla unit, Western Alps)'. doi: 10.1016/j.jsg.2008.07.007.

Menegon, L. *et al.* (2013) 'Transition from fracturing to viscous flow in granulite facies perthitic feldspar (Lofoten, Norway)', *Journal of Structural Geology*, 48, pp. 95–112. doi: 10.1016/j.jsg.2012.12.004.

Menegon, L. *et al.* (2015) 'Creep cavitation bands control porosity and fluid flow in lower crustal shear zones', *Geology*, 43(3), pp. 227–230. doi: 10.1130/G36307.1.

Menegon, L. *et al.* (2017) 'Earthquakes as Precursors of Ductile Shear Zones in the Dry and Strong Lower Crust', *Geochemistry, Geophysics, Geosystems*, 18(12), pp. 4356–4374. doi: 10.1002/2017GC007189.

Menegon, L., Pennacchioni, G. and Spiess, R. (2008) 'Dissolution-precipitation creep of K-feldspar in mid-crustal granite mylonites'. doi: 10.1016/j.jsg.2008.02.001.

Menegon, L., Pennacchioni, G. and Stünitz, H. (2006) 'Nucleation and growth of myrmekite during ductile shear deformation in metagranites', *Journal of Metamorphic Geology*, 24, pp. 553–568. doi: 10.1111/j.1525-1314.2006.00654.x.

Merriman, R. J., Roberts, B. and Peacor, D. R. (1990) 'A transmission electron microscope study of white mica crystallite size distribution in a mudstone to slate transitional sequence, North Wales, UK', *Contributions to Mineralogy and Petrology*, 106(1), pp. 27–40. doi: 10.1007/BF00306406.

Miyazaki, T., Sueyoshi, K. and Hiraga, T. (2013) 'Olivine crystals align during diffusion creep of Earth's upper mantle', *Nature*, 502. doi: 10.1038/nature12570.

Montemagni, C., Fulignati, P., Iaccarino, S., Marianell, P., Montomoli, C. and Sbrana, A. (2016) 'Deformation and fluid flow in the Munsiari Thrust (NW India): A preliminary fluid inclusion study', *Atti della Societa Toscana di Scienze Naturali. Memoire, Serie A,* 123, pp 67-77.

Montési, L. G. J. (2013) 'Fabric development as the key for forming ductile shear zones and enabling plate tectonics', *Journal of Structural Geology*, 50, pp. 254–266. doi: 10.1016/j.jsg.2012.12.011.

Moore, D. E. and Lockner, D. A. (1995) 'The role of microcracking in shear-fracture propagation in granite', *Journal of Structural Geology*, 17(1), pp. 95–114. doi: 10.1016/0191-8141(94)E0018-T.

Moore, J. *et al.* (2019) 'Stress orientation-dependent reactions during metamorphism', *Geology*, 47(2), pp. 151–154. doi: 10.1130/G45632.1.

Morgan VI, G. B. and London, D. (1996) 'Effect of current density on the electron microprobe analysis of alkali aluminosilicate glasses', *American Mineralogist*, 81(9–10), pp. 1176–1185. doi: 10.2138/am.2005.1769.

Morrow, C., Radney, B. and Byerlee, J. (1992) 'Frictional Strength and the Effective Pressure Law of

Montmorillonite and Illite Clays', in *International Geophysics*. Academic Press, pp. 69–88.

Mukai, H. *et al.* (2014) 'Textural evolution of plagioclase feldspar across a shear zone: Implications for deformation mechanism and rock strength', *Journal of Petrology*, 55(8), pp. 1457–1477. doi: 10.1093/petrology/egu030.

Mulch, A. *et al.* (2002) 'The age and structure of dikes along the tectonic contact of the Ivrea-verbano and Strona-Ceneri Zones (southern Alps, northern Italy, Switzerland).', *Schweiz. Mineral. Petrogr. Mitt.*, 82, pp. 55–76.

Muttoni, G., Kent, D. V. and Channell, J. E. T. (1996) 'Evolution of Pangea: Paleomagnetic constraints from the Southern Alps, Italy', *Earth and Planetary Science Letters*, 140(1–4), pp. 97–112. doi: 10.1016/0012-821X(96)00038-6.

Niemeijer, A. R. (2018) 'Velocity-dependent slip weakening by the combined operation of pressure solution and foliation development', *Scientific Reports*. Springer US, (March), pp. 1–10. doi: 10.1038/s41598-018-22889-3.

Niemeijer, A. R. and Spiers, C. J. (2007) 'A microphysical model for strong velocity weakening in phyllosilicate-bearing fault gouges', *Journal of Geophysical Research: Solid Earth*, 112(10), pp. 1–12. doi: 10.1029/2007JB005008.

Niemeijer, A. R., Spiers, C. J. and Bos, B. (2002) *Compaction creep of quartz sand at 400-600°C: Experimental evidence for dissolution-controlled pressure solution*, *Earth and Planetary Science Letters*. doi: 10.1016/S0012-821X(01)00593-3.

Noe, D. C. and Veblen, D. R. (1999a) 'HRTEM analysis of dislocation cores and stacking faults in naturally deformed biotite crystals', *American Mineralogist*, 84(11–12), pp. 1925–1931.

Noe, D. C. and Veblen, D. R. (1999b) 'Mottled contrast in TEM images of mica crystals', *American Mineralogist*, 84(11–12), pp. 1932–1938.

Olgaard, D. L. and Evans, B. (1988) 'Grain growth in synthetic marbles with added mica and water', *Contrib Mineral Petrol*, 100, pp. 246–260.

Oliot, E. *et al.* (2014) 'Mid-crustal shear zone formation in granitic rocks: Constraints from quantitative textural and crystallographic preferred orientations analyses', *Tectonophysics*. Elsevier B.V., 612–613, pp. 63–80. doi: 10.1016/j.tecto.2013.11.032.

Oliot, E., Goncalves, P. and Marquer, D. (2010) 'Role of plagioclase and reaction softening in a metagranite shear zone at mid-crustal conditions (Gotthard Massif, Swiss Central Alps)', *Journal of Metamorphic Geology*, 28(8), pp. 849–871. doi: 10.1111/j.1525-

1314.2010.00897.x.

Papeschi, S., Musumeci, G. and Mazzarini, F. (2018) 'Evolution of shear zones through the brittle-ductile transition: The Calamita Schists (Elba Island, Italy)', *Journal of Structural Geology*, 113, pp. 100–114. doi: 10.1016/j.jsg.2018.05.023.

Passchier, C. W. (1985) 'Water-deficient mylonite zones-An example from the Pyrenees', *Lithos*, 18, pp. 115–127.

Passchier, C. W. and Trouw, R. A. J. (2005) *Microtectonics*. 2nd edn. Berlin Heidelberg: Springer-Verlag Berlin Heidelberg.

Paterson, M. S. (1973) 'Nonhydrostatic thermodynamics and its geologic applications', *Reviews of Geophysics*, 11(2), pp. 355–389. doi: 10.1029/RG011i002p00355.

Paterson, M. S. (2001) 'A granular flow theory for the deformation of partially molten rock', *Tectonophysics*, 335, pp. 51–61.

Peters, M. *et al.* (2016) 'Strain localization in ductile rocks: A comparison of natural and simulated pinch-and-swell structures', *Tectonophysics*. Elsevier B.V., 680, pp. 140–154. doi: 10.1016/j.tecto.2016.04.049.

Phillips, E. R. (1980) 'On polygenetic myrmekite', *Geological magazine*, 117(1), pp. 29–36. doi: 10.1017/S0016756800033070.

Phillips, E. R. and Ransom, D. M. (1968) 'The proportionality of quartz in myrmekite', *American Mineralogist*, 53, pp. 1411–1413.

Phipps Morgan, J. and Holtzman, B. K. (2005) 'Vug waves: A mechanism for coupled rock deformation and fluid migration', *Geochemistry, Geophysics, Geosystems*, 6(8). doi: 10.1029/2004GC000818.

Pirrie, D. *et al.* (2004) 'Rapid quantitative mineral and phase analysis using automated scanning electron microscopy (QemSCAN); potential applications in forensic geoscience', *Geological society of London, Special publications*, 232, pp. 123–136.

Platt, J. P. (2015) 'Influence of shear heating on microstructurally defined plate boundary shear zones', *Journal of Structural Geology*, 79, pp. 80–89. doi: 10.1016/j.jsg.2015.07.009.

Platt, J. P. and Behr, W. M. (2011) 'Grainsize evolution in ductile shear zones: Implications for strain localization and the strength of the lithosphere', *Journal of Structural Geology*, 33(4), pp. 537–550. doi: 10.1016/j.jsg.2011.01.018.

Van der Pluijm, B., Lee, J. and Peacor, D. R. (1988) 'Analytical Electron Microscopy and the Problem

of Potassium Diffusion', *Clays and Clay Minerals*, 36(6), pp. 498–504. doi: 10.1346/CCMN.1988.0360603.

Plumper, O. and Putnis, A. (2009) 'The Complex Hydrothermal History of Granitic Rocks: Multiple Feldspar Replacement Reactions under Subsolidus Conditions', *Journal of Petrology*, 50(5), pp. 967–987. doi: 10.1093/petrology/egp028.

Poirier, J.-P. (1985) *Creep of crystals: high-temperature deformation processes in metals, ceramics and minerals*. Cambridge University Press.

Pouchou, J.-L. and Pichoir, F. (1991) 'Quantitative Analysis of Homogeneous or Stratified Microvolumes Applying the Model "PAP"', in *Electron Probe Quantitation*. Boston: Springer, pp. 31–75. doi: 10.1007/978-1-4899-2617-3_4.

Priestley, K., Jackson, J. and Mckenzie, D. (2008) 'Lithospheric structure and deep earthquakes beneath India, the Himalaya and southern Tibet', *Geophys. J. Int*, 172, pp. 345–362. doi: 10.1111/j.1365-246X.2007.03636.x.

Prior, D. J. *et al.* (1999) 'The application of electron backscatter diffraction and orientation constrast imaging in th SEM to textural problems in rocks', *American Mineralogist*, 84, pp. 1741–1759.

Prior, D. J. *et al.* (2015) 'Making EBSD on water ice routine', *Journal of Microscopy*, 259(3), pp. 237–256. doi: 10.1111/jmi.12258.

Prior, D. J., Mariani, E. and Wheeler, J. (2009) 'EBSD in the Earth Sciences: Applications, Common Practice, and Challenges', in, p. 16. doi: 10.1007/978-0-387-88136-2.

Putnis, A. (2002) 'Mineral replacement reactions: from macroscopic observations to microscopic mechanisms', *Mineralogical Magazine*, 66(5), pp. 689–708. doi: 10.1180/0026461026650056.

Putnis, A. and John, T. (2010) 'Replacement processes in the earth's crust', *Elements*, 6(3), pp. 159–164. doi: 10.2113/gselements.6.3.159.

Putnis, A. and Putnis, C. V. (2007) 'The mechanism of reequilibration of solids in the presence of a fluid phase', *Journal of Solid State Chemistry*. Academic Press, 180(5), pp. 1783–1786. doi: 10.1016/J.JSSC.2007.03.023.

Rahl, J. M. and Skemer, P. (2016) 'Microstructural evolution and rheology of quartz in a mid-crustal shear zone', *Tectonophysics*. Elsevier B.V., 680, pp. 129–139. doi: 10.1016/j.tecto.2016.05.022.

Ramsay, J. G. and Graham, R. H. (1970) 'Strain variation in shear belts', *Canadian Journal of Earth Sciences*, 7(3), pp. 786–813.

Rawling, G. C. (2002) 'Dilatancy, brittle strength, and anisotropy of foliated rocks: Experimental deformation and micromechanical modeling', *Journal of Geophysical Research*, 107(B10), p. 2234. doi: 10.1029/2001JB000472.

Renard, F. *et al.* (2001) *Enchanced pressure solution creep rates induced by clay particles: Experimental evidence in salt aggregates*, *Geophysical Research Letters*. doi: 10.1029/2000GL012394.

Renard, F., Ortoleva, P. and Gratier, J. P. (1997) 'Pressure solution in sandstones: influence of clays and dependence on temperature and stress', *Tectonophysics*, 280(3–4), pp. 257–266. doi: 10.1016/S0040-1951(97)00039-5.

Rennie, S. F., Fagereng, A. and Diener, J. F. A. (2013) 'Strain distribution within a km-scale, mid-crustal shear zone: The Kuckaus Mylonite Zone, Namibia', *Journal of Structural Geology*. Elsevier Ltd, 56, pp. 57–69. doi: 10.1016/j.jsg.2013.09.001.

Richter, B., Stünitz, H. and Heilbronner, R. (2016) 'Stresses and pressures at the quartz-to-coesite phase transformation in shear deformation experiments', *Journal of Geophysical Research: Solid Earth*, 121, pp. 8105–8033. doi: 10.1002/2016JB013084.

Robie, R. A., Bethke, P. M. and Beardsley, K. M. (1967) 'Selected X-ray Crystallographic Data, Molar Volumes and Densities of Minerals and Related Substances', *US Geological Survey Bulletin*, 1248.

de Ronde, A. A. *et al.* (2005) 'Reaction-induced weakening of plagioclase-olivine composites', *Tectonophysics*, 409(1–4), pp. 85–106. doi: 10.1016/j.tecto.2005.08.008.

Ruiz-Agudo, E., Putnis, C. V. and Putnis, A. (2014) 'Coupled dissolution and precipitation at mineral–fluid interfaces', *Chemical Geology*, 383, pp. 132–146. doi: 10.1016/j.chemgeo.2014.06.007.

Rupke, L. H. *et al.* (2004) 'Serpentine and the subduction zone water cycle', *Earth and Planetary Science Letters*, 223(1–2), pp. 17–34. doi: 10.1016/j.epsl.2004.04.018.

Rutter, E. *et al.* (2007) 'Large-scale folding in the upper part of the Ivrea-Verbano zone, NW Italy', *Journal of Structural Geology*, 29(1), pp. 1–17. doi: http://dx.doi.org/10.1016/j.jsg.2006.08.013.

Rutter, E. H. (1976) 'The Kinetics of Rock Deformation by Pressure Solution', *Philosophical Transactions of the Royal Society A: Mathematical, Physical and Engineering Sciences*,

283(1312), pp. 203–219. doi: 10.1098/rsta.1976.0079.

Rutter, E. H. (1983) 'Pressure solution in nature, theory and experiment', *Journal of the Geological Society*, 140(5), pp. 725–740. doi: 10.1144/gsjgs.140.5.0725.

Rutter, E. H. *et al.* (2013) 'Reduction of friction on geological faults by weak-phase smearing'. doi: 10.1016/j.jsg.2013.03.008.

Rutter, E. H. and Brodie, K. H. (1988) 'The role of tectonic grain size reduction in the rheological stratification of the lithosphere', *Geologische Rundschau*, 77(1), pp. 295–307. doi: 10.1007/BF01848691.

Rutter, E. H. and Maddock, R. H. (1992) 'On the mechanical properties of synthetic kaolinite/ quartz fault gouge', *Terra Nova*, 4, pp. 489–500.

Rybacki, E. and Dresen, G. (2000) 'Dislocation and diffusion creep of synthetic anorthite aggregates', *JOURNAL OF GEOPHYSICAL RESEARCH*, 105, pp. 17–26. doi: 10.1029/2000JB900223.

Salomon, E., Koehn, D. and Passchier, C. (2015) 'Brittle reactivation of ductile shear zones in NW Namibia in relation to South Atlantic rifting', *Tectonics*, 34(1), pp. 70–85. doi: 10.1002/2014TC003728.

Schmid, D. W. *et al.* (2009) 'Matrix rheology effects on reaction rim growth II: coupled diffusion and creep model', *Journal of Metamorphic Geology*, 27, pp. 83–91. doi: 10.1111/j.1525-1314.2008.00805.x.

Schmid, S. M. and Casey, M. (1986) 'Analysis of Some Commonly Observed Quartz C-Axis ( a )', *Mineral and rock deformation: Laboratory studies*, 36, pp. 263–286.

Scholz, C. H. (1988) 'The brittle-plastic transition and the depth of seismic faulting', *Geologische Rundschau*, 77(1), pp. 319–328.

Scholz, C. H. (1998) 'Earthquakes and friction laws', *Nature*, 391, pp. 37–42. doi: 10.1038/34097.

Schrank, C. E., Handy, M. R. and Fusseis, F. (2008) 'Multiscaling of shear zones and the evolution of the brittle-to-viscous transition in continental crust', *Journal of Geophysical Research: Solid Earth*, 113(1), pp. 1–23. doi: 10.1029/2006JB004833.

Scruggs, V. . and Tullis, T. . (1998) 'Correlation between velocity dependence of friction and strain localization in large displacement experiments on feldspar, muscovite and biotite gouge', *Tectonophysics*, 295(1–2), pp. 15–40. doi: 10.1016/S0040-1951(98)00113-9.

Seward, G. G. E. *et al.* (2002) 'High-Temperature Electron Backscatter Diffraction and Scanning

Electron Microscopy Imaging Techniques: In-situ Investigations of Dynamic Processes', *Scanning*, 24, pp. 232–240.

Seward, G. G. E. *et al.* (2004) 'In situ SEM-EBSD observations of the hcp to bcc phase transformation in commercially pure titanium', *Acta Materialia*, 52, pp. 821–832.

Shau, Y. H., Peacor, D. R. and Essene, E. J. (1990) 'Corrensite and mixed-layer chlorite/corrensite in metabasalt from northern Taiwan: TEM/AEM, EMPA, XRD, and optical studies', *Contributions to Mineralogy and Petrology*, 105(2), pp. 123–142. doi: 10.1007/BF00678980.

Shea, W. T. and Kronenberg, A. K. (1992) 'Rheology and deformation mechanisms of an isotropic mica schist', *Journal of Geophysical Research*, 97(B11), p. 15201. doi: 10.1029/92JB00620.

Shea, W. T. and Kronenberg, A. K. (1993) 'Strength and anisotropy of foliated rocks with varied mica contents', *Journal of Structural Geology*, 15(9–10), pp. 1097–1121. doi: 10.1016/0191-8141(93)90158-7.

Shimizu, I. (1995) 'Kinetics of pressure solution creep in quartz: theoretical considerations', *Tectonophysics*, 245, pp. 121–134.

Sibson, R. H. (1977) 'Fault rocks and fault mechanisms', *Journal of the Geological Society of London*, 133, pp. 191–213.

Sibson, R. H. (1984) 'Roughness at the base of the seismogenic zone: contributing factors.', *Journal of Geophysical Research*, 89(B7), pp. 5791–5799. doi: 10.1029/JB089iB07p05791.

Siegesmund, S. *et al.* (2008) 'Exhumation and deformation history of the lower crustal section of the Valstrona di Omegna in the Ivrea Zone, southern Alps', *Tectonic Aspects of the Alpine-Dinaride-Carpathian System*, 298(1), pp. 45–68. doi: DOI: 10.1144/SP298.3.

Siivola, J. and Schmid, R. (2007) 'List of Mineral Abbreviations', *Recommendations of the International Union of Geological Sciences Subcommission on the Systematics of Metamorphic Rocks: Web version 01.02.07*.

Simpson, C. and Wintsch, R. P. (1989) 'Evidence for deformation-induced K-feldspar replacement by myrmekite', *Journal of Metamorphic Geology*, 7(2), pp. 261–275. doi: 10.1111/j.1525-1314.1989.tb00588.x.

Skemer, P. *et al.* (2005) 'The misorientation index: Development of a new method for calculating the strength of lattice-preferred orientation'. doi: 10.1016/j.tecto.2005.08.023.

Smith, C. S. (1948) 'Grains, phases, and interphases: an interpretation of microstructure.', *Transactions of the American Institute of Mining and Metallurgical Engineers*, 175, pp. 15–

51.

Song, W. J. and Ree, J. H. (2007) 'Effect of mica on the grain size of dynamically recrystallized quartz in a quartz-muscovite mylonite', *Journal of Structural Geology*, 29(12), pp. 1872–1881. doi: 10.1016/j.jsg.2007.09.011.

Spiers, C. J. *et al.* (2008) *Experimental determination of constitutive parameters governing creep of rocksalt by pressure solution*, *Geological Society, London, Special Publications*. doi: 10.1144/gsl.sp.1990.054.01.21.

Spruzeniece, L., Piazolo, S. and Maynard-Casely, H. E. (2017) 'Deformation-resembling microstructure created by fluid-mediated dissolution-precipitation reactions', *Nature CommunicationsNature Communications*, 8, pp. 1–9. doi: 10.1038/ncomms14032.

Stenvall, C. A., Fagereng, Å. and Diener, J. F. A. (2019) 'Weaker Than Weakest: On the Strength of Shear Zones', *Geophysical Research Letters*, 46(13), pp. 7404–7413. doi: 10.1029/2019GL083388.

Stipp, M. *et al.* (2002) 'The eastern Tonale fault zone: A "natural laboratory" for crystal plastic deformation of quartz over a temperature range from 250 to 700 °C', *Journal of Structural Geology*, 24(12), pp. 1861–1884. doi: 10.1016/S0191-8141(02)00035-4.

Stunitz, H. and Fitz Gerald, J. D. (1993) 'Deformation of granitoids at low metamorphic grade. II: Granular flow in albite-rich mylonites', p. 221.

Sullivan, W. A., Boyd, A. S. and Monz, M. E. (2013) 'Strain localization in homogeneous granite near the brittle-ductile transition: A case study of the Kellyland fault zone, Maine, USA', *Journal of Structural Geology*. Elsevier Ltd, 56, pp. 1–19.

Sutherland, R. *et al.* (2012) 'Drilling reveals fluid control on architecture and rupture of the Alpine fault, New Zealand', *Geology*, 40(12), pp. 1143–1146. doi: 10.1130/G33614.1.

Tajčmanová, L. *et al.* (2013) 'Grain-scale pressure variations and chemical equilibrium in high-grade metamorphic rocks', *Journal of Metamorphic Geology*, 32(2), pp. 195–207. doi: 10.1111/jmg.12066.

Tapponnier, P. and Brace, W. F. (1976) 'Development of stress-induced microcrakcs in Westerly granite.pdf', *International Journal of Rock Mechanics and Mining Sciences & Geomechanics Abstracts.*, 13(4), pp. 103–112.

Tesei, T. *et al.* (2012) 'Frictional strength and healing behavior of phyllosilicate-rich faults', *Journal of Geophysical Research: Solid Earth*, 117(9), pp. 1–13. doi: 10.1029/2012JB009204.

Tielke, J. *et al.* (2019) 'The Influence of Water on the Strength of Olivine Dislocation Slip Systems', *Journal of Geophysical Research: Solid Earth*, p. 2019JB017436. doi: 10.1029/2019JB017436.

Tielke, J. A., Zimmerman, M. E. and Kohlstedt, D. L. (2017) 'Hydrolytic weakening in olivine single crystals', *Journal of Geophysical Research: Solid Earth*, 122(5), pp. 3465–3479. doi: 10.1002/2017JB014004.

Trimby, P. W. (2012) 'Orientation mapping of nanostructured materials using transmission Kikuchi diffraction in the scanning electron microscope', *Ultramicroscopy*. Elsevier, 120, pp. 16–24. doi: 10.1016/j.ultramic.2012.06.004.

Trimby, P. W., Drury, M. R. and Spiers, C. J. (2000) 'Misorientations across etched boundaries in deformed rocksalt: a study using electron backscatter di raction', *Journal of Structural Geology*, 22, pp. 81–89.

Trimby, P. W. and Prior, D. J. (1999) 'Microstructural imaging techniques: a comparison between light and scanning electron microscopy', *Tectonophysics*, 303, pp. 71–81.

Tullis, J. and Yund, R. A. (1989) 'Hydrolytic weakening of quartz aggregates: the effects of water and pressure on recovery', *Geophysical research letters*, 16(11), pp. 1343–1346.

Tullis, T. E., Horowitz, F. G. and Tullis, J. (1991) 'Flow laws of polyphase aggregates from end-member flow laws', *Journal of Geophysical Research*, 96(B5), pp. 8081–8096. doi: 10.1029/90JB02491.

Urai, J. L., Means, W. D. and Lister, G. S. (1986) 'Dynamic recrystallisation of minerals', *Geophysical Monograph*, 36, pp. 161–199.

Vaughan, P. J., Greeen, H. W. and Coe, R. S. (1984) 'Anisotropic growth in the olivine-spinel transformation of Mg2GeO4 under nonhydrostatic stress', *Tectonophysics*, 108(3–4), pp. 299–322. doi: 10.1016/0040-1951(84)90241-5.

Viegas, G., Menegon, L. and Archanjo, C. (2015) 'Brittle grain size reduction of feldspar, phase mixing and strain localization in granitoids at mid-crustal conditions (Pernambuco shear zone, NE Brazil)', *Solid Earth*, 7, pp. 375–396. doi: 10.5194/sed-7-2953-2015.

Vitale, S. and Mazzoli, S. (2010) 'Strain analysis of heterogeneous ductile shear zones based on the attitudes of planar markers', *Journal of Structural Geology*. Elsevier Ltd, 32(3), pp. 321–329. doi: 10.1016/j.jsg.2010.01.002.

Vrijmoed, J. C. and Podladchikov, Y. Y. (2015) 'Thermodynamic equilibrium at heterogeneous

pressure', *Contributions to Mineralogy and Petrology*. Springer Berlin Heidelberg, 170(1), pp. 1–27. doi: 10.1007/s00410-015-1156-1.

Warren, J. M. and Hirth, G. (2006) 'Grain size sensitive deformation mechanisms in naturally deformed peridotites', *Earth and Planetary Science Letters*, 248(1–2), pp. 438–450. doi: 10.1016/j.epsl.2006.06.006.

Wassmann, S. and Stöckhert, B. (2013) 'Low stress deformation of garnet by incongruent dissolution precipitation creep', *Journal of Structural Geology*. Elsevier Ltd, 46, pp. 200–219. doi: 10.1016/j.jsg.2012.09.002.

Weiss, L. E. (1980) 'Nucleation and growth of kink bands', *Tectonophysics*, 65(1–2), pp. 1–38. doi: 10.1016/0040-1951(80)90221-8.

Wenk, H. R. *et al.* (2008) 'Preferred Orientations and Anisotropy in Shales: Callovo-Oxfordian Shale (France) and Opalinus Clay (Switzerland)', *Clays and Clay Minerals*, 56(3), pp. 285–306. doi: 10.1346/CCMN.2008.0560301.

Wenk, H. R., Kanitpanyacharoen, W. and Voltolini, M. (2010) 'Preferred orientation of phyllosilicates: Comparison of fault gouge, shale and schist', *Journal of Structural Geology*. Elsevier Ltd, 32(4), pp. 478–489. doi: 10.1016/j.jsg.2010.02.003.

Wex, S. *et al.* (2019) 'Interplay between seismic fracture and aseismic creep in the Woodroffe Thrust, central Australia – Inferences for the rheology of relatively dry continental mid-crustal levels', *Tectonophysics*. Elsevier B.V., 758, pp. 55–72. doi: 10.1016/j.tecto.2018.10.024.

Wheeler, J. (1992) 'Importance of pressure solution and coble creep in the deformation of polymineralic rocks', *Journal of Geophysical Research*, 97(B4), p. 4579. doi: 10.1029/91JB02476.

Wheeler, J. *et al.* (2001) 'The petrological significance of misorientations between grains', *Contributions to Mineralogy and Petrology*, 141(1), pp. 109–124. doi: 10.1007/s004100000225.

Wheeler, J. (2009) 'The preservation of seismic anisotropy in the Earth's mantle during diffusion creep', *Geophys. J. Int*, 178, pp. 1723–1732. doi: 10.1111/j.1365-246X.2009.04241.x.

Wheeler, J. (2014) 'Dramatic effects of stress on metamorphic reactions', *Geology*, 42(8), pp. 647–650. doi: 10.1130/G35718.1.

Wheeler, J. (2018) 'The effects of stress on reactions in the Earth: Sometimes rather mean, usually

normal, always important', *Journal of Metamorphic Geology*, 36(4), pp. 439–461. doi: 10.1111/jmg.12299.

White, S. H. *et al.* (1980) 'On mylonites in ductile shear zones', 2(1), pp. 175–187.

Wibberley, C. (1999) 'Are feldspar-to-mica reactions necessarily reaction-softening processes in fault zones?', *Journal of Structural Geology*, 21(8–9), pp. 1219–1227. doi: 10.1016/S0191-8141(99)00019-X.

Wibberley, C. A. . and Shimamoto, T. (2003) 'Internal structure and permeability of major strike-slip fault zones: the Median Tectonic Line in Mie Prefecture, Southwest Japan', *Journal of Structural Geology*, 25(1), pp. 59–78. doi: 10.1016/S0191-8141(02)00014-7.

Wilson, C. J. L. and Bell, I. A. (1979) 'Deformation of biotite and muscovite: Optical microstructure', *Tectonophysics*, 58(1–2), pp. 179–200. doi: 10.1016/0040-1951(79)90328-7.

Wilson, J. T. (1965) 'A new class of faults and their bearing on continental drift', *Nature*, 207, pp. 343–347.

Wintsch, R. P., Christoffersen, R. and Kronenberg, a. K. (1995) 'Fluid-rock reaction weakening of fault zones', *Journal of Geophysical Research*, 100(B7), p. 13021. doi: 10.1029/94JB02622.

Wintsch, R. P. and Yi, K. (2002) 'Dissolution and replacement creep: A significant deformation mechanism in mid-crustal rocks', *Journal of Structural Geology*, 24(6–7), pp. 1179–1193. doi: 10.1016/S0191-8141(01)00100-6.

Wolterbeek, T. K. T., Reinier Van Noort, • and Spiers, C. J. (2018) 'Reaction-driven casing expansion: potential for wellbore leakage mitigation', *Acta Geotechnica*, 13, pp. 341–366. doi: 10.1007/s11440-017-0533-5.

Zingg, A. (1983) 'The Ivrea and Strona-Ceneri Zones (Southern Alps, Ticino and N-Italy): a review', *Schweiz. Mineral. Petrogr. Mitt.* Leemann, 63(2–3), pp. 361–392. doi: 10.2217/fon-2016-0295.

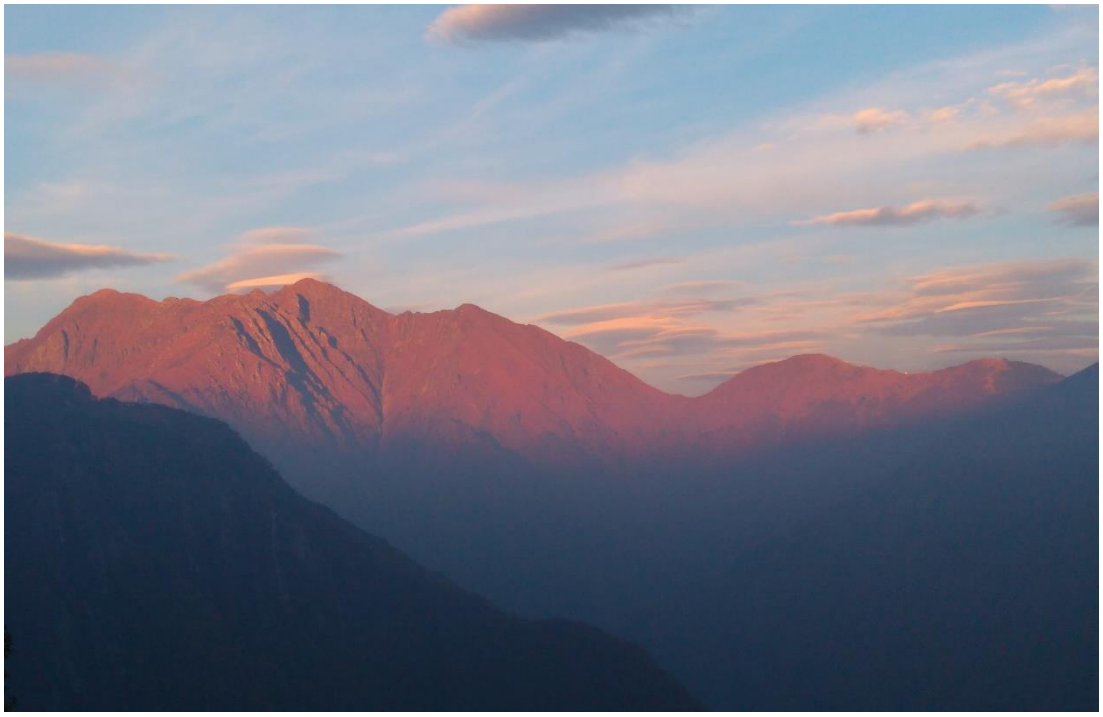

Monte Zeda at dusk